

# **Cytotoxic and Mechanistic studies of Novel Phenanthroline-Derived Oxovanadium(IV) Complexes**

**By**

**Kristy-Lyn Barry**

**DOCTOR OF PHILOSOPHY**

**December 2022**



**School of Chemistry and Physics  
Pietermaritzburg**

# **Cytotoxic and Mechanistic studies of Novel Phenanthroline-Derived Oxovanadium(IV) Complexes**

**By**

**Kristy-Lyn Barry**  
BScHons, MSc (UKZN)

Submitted in the fulfilment of the academic requirements for the degree of  
Doctor of Philosophy  
in the College of Agriculture, Engineering and Science  
School of Chemistry and Physics  
University of KwaZulu-Natal

Pietermaritzburg  
December 2022

*This work is dedicated to the following very special people:*

***To dad***

*Dad, I started this journey while you were still with us and now, I end it with you not here. I know you would have been proud of me. I know you did not have doubts that I would finish. I did it dad, I finally got to the end. Thank you for all the life lessons. May I work as hard to run our household as you did with us growing up. I love you and miss you dearly.*

***To my special mom***

*Thank you for all your support, encouragement, phone calls, bible study prayers and your own devoted prayers. Your prayers helped me to keep moving forward and were gratefully received! Thank you for being so proud of me and for cheering me on. Thank you also for always being interested and showing off my work. Thank you for all you have done to support me and my family. I hope that I can have the same capacity and energy for life that you have! I hope one day that I can be a mother to my children like you are to me. Thank you – love you my precious mommy!*

***To my two wonderful sisters, Michelle and Candice***

*Michelle - my fun, full of life sister. Thank you for checking in on me, being a source of encouragement, letting me rant and for helping me keep my priorities in check. I love you!*

*Candice – my globe-trotting sister. Thank-you for the advice and for having you to commiserate with. I love you!*

***To Gareth***

*To my darling husband - thank you. Thank you for all you have done for me. You have been here with me through another degree, now as my husband. Thank you for the hours of listening, your advice, encouragement, checking in on me and for your shoulder to cry on. Thank you for helping me keep things in perspective and see the bigger picture. Thank you for entertaining our boys so I could work. You are my best friend and my love. You can book our trip now!*

***To My dear children, Daniel and Nathan***

*My Daniel – thank you for all your wonderful support - asking how things are going with my PhD, for all the cups of tea, charging lights for me of your own initiative, checking in on me, giving me advice, being interested in my work and for being patient and flexible with your turn at the computer around mommy's work. You are growing up to be a fine young man. I love you and am so proud of you!*

*My Nathan – thank you for checking in on me, being interested in my work, for being patient and flexible with your gaming time, and for being quiet and independent so mommy could work. Keep your fun-loving spirit! I love you and am so proud of you!*

***Peace I leave with you; my peace I give you. I do not give to you as the world gives. Do not let your hearts be troubled and do not be afraid. John 14:27.***

# *Table of Contents*

<i>Declaration 1 – Plagiarism</i>	<i>i</i>
<i>Declaration 2 – Publications</i>	<i>ii</i>
<i>Acknowledgements</i>	<i>iii</i>
<i>Abstract</i>	<i>v</i>
<i>Conference and Publication Contributions</i>	<i>viii</i>
<i>List of Abbreviations and Symbols</i>	<i>ix</i>
<i>List of Figures</i>	<i>xiv</i>
<i>List of Schemes</i>	<i>xxxi</i>
<i>List of Tables</i>	<i>xxxii</i>
<b><i>Chapter 1: Introduction</i></b>	<b><i>1</i></b>
<b>1.1 Preface</b>	<b>1</b>
<b>1.2 Metals in Medicine</b>	<b>2</b>
<b>1.3 Vanadium in Nature</b>	<b>5</b>
<b>1.4 Applications of Vanadium</b>	<b>6</b>
1.4.1 Technical Applications of Vanadium	6
1.4.2 Medicinal Applications of Vanadium	7
<b>1.5 Speciation of Vanadium Compounds <i>In Vivo</i></b>	<b>9</b>
<b>1.6 Vanadium Compounds in Cancer Treatment</b>	<b>13</b>
1.6.1 Oxovanadium(IV) Anticancer Complexes	16
<b>1.7 Anticancer Mechanisms of Vanadium Complexes</b>	<b>17</b>
1.7.1 Reactive Oxygen Species (ROS)	19
<b>1.8 DNA Binding Modes of Metallopharmaceuticals</b>	<b>21</b>
1.8.1 Covalent Modes of Binding to DNA	21
1.8.2 Non-Covalent Modes of Binding to DNA	22
<b>1.9 Oxovanadium(IV) Complexes with Phenanthroline-Derived Co-ligands</b>	<b>24</b>
<b>1.10 Ternary Oxovanadium(IV) Schiff Base Complexes of Phenanthroline-Derived Co-ligands</b>	<b>26</b>

1.10.1	<i>O,N,O'</i> -Tridentate Schiff Base Oxovanadium(IV) Complexes with Phenanthroline-Derived Co-ligands	27
1.10.2	Cationic Oxovanadium(IV) Complexes with Phenanthroline-Derived Co-ligands	39
1.11	<b>Aims and Objectives</b>	42
1.12	<b>References</b>	45

## ***Chapter Two: Synthesis*** **63**

2.1	<b>Synthesis of 1,10-Phenanthroline-5,6-dione (PDO)</b>	63
2.2	<b>Schiff Base Condensation Reactions</b>	65
2.2.1	Synthesis of the Bidentate <i>N,N</i> -Donor Co-ligand DPQ	67
2.2.2	Synthesis of the Bidentate <i>N,N</i> -Donor Co-ligand DPPZ	68
2.2.3	Synthesis of the Tridentate <i>O,N,O'</i> -Donor Schiff Base Ligands	68
2.2.4	Synthesis of the Tridentate <i>O,N,N'</i> -Donor Schiff Base Ligands	70
2.3	<b>Synthesis of the Oxovanadium(IV) Complexes</b>	72
2.3.1	Synthesis of the Neutral Oxovanadium(IV) DPQ Complexes	73
2.3.2	Synthesis of the Neutral Oxovanadium(IV) DPPZ Complex	74
2.3.3	Synthesis of the Cationic Oxovanadium(IV) Complexes	75
2.4	<b>Summary of the Synthetic Procedures</b>	77
2.5	<b>References</b>	79

## ***Chapter Three: Experimental Methods*** **82**

3.1	<b>General Procedure</b>	82
3.2	<b>Instrumentation</b>	82
3.3	<b>Synthesis of the Bidentate <i>N,N</i>-Donor Co-ligands</b>	83
3.3.1	Synthesis of 1,10-Phenanthroline-5,6-dione Precursor (PDO)	83
3.3.2	Synthesis of Dipyrido[3,2- <i>d</i> :2',3'- <i>f</i> ]quinoxaline (DPQ)	84
3.3.3	Synthesis of Dipyrido[3,2- <i>a</i> :2',3'- <i>c</i> ]phenazine (DPPZ)	85
3.4	<b>Synthesis of the <i>O,N,O'</i>-Tridentate Schiff Base Ligands</b>	86
3.4.1	Synthesis of 2- $\{(E)-[(2\text{-hydroxyphenyl)imino}]methyl\}$ phenol (PHA)	87

3.4.2	Synthesis of 2-{[(1 <i>E</i> )-(2-hydroxyphenyl)methylene]amino}-4-methylphenol (MEA)	88
3.4.3	Synthesis of 4- <i>tert</i> -butyl-2-{[(1 <i>E</i> )-(2-hydroxyphenyl)methylene]amino}phenol (TERTA)	89
3.4.4	Synthesis of 4-chloro-2-{[(1 <i>E</i> )-(2-hydroxyphenyl)methylene]amino}phenol (CLA)	90
3.4.5	Synthesis of 4-(ethylsulfonyl)-2-{[(1 <i>E</i> )-(2-hydroxyphenyl)methylene]amino}phenol (SOA)	91
3.4.6	Synthesis of 3-{[(1 <i>E</i> )-(2-hydroxyphenyl)methylene]amino}-2-naphthol (NAA)	92
3.4.7	Synthesis of 3-{[(1 <i>E</i> )-(2-hydroxyphenyl)methylene]amino}biphenyl-4-ol (PHPHA)	93
<b>3.5</b>	<b>Synthesis of the <i>O,N,N'</i>-Tridentate Schiff Base Ligands</b>	<b>94</b>
3.5.1	Synthesis of 2-{[(1 <i>E</i> )-(1-methyl-1 <i>H</i> -imidazol-2-yl)methylene]amino}phenol (PHCA)	94
3.5.2	Synthesis of 4-methyl-2-{[(1 <i>E</i> )-(1-methyl-1 <i>H</i> -imidazol-2-yl)methylene]amino}phenol (MECA)	95
3.5.3	Synthesis of 4- <i>tert</i> -butyl-2-{[(1 <i>E</i> )-(1-methyl-1 <i>H</i> -imidazol-2-yl)methylene]amino}phenol (TERTCA)	96
3.5.4	Synthesis of 3-{[(1 <i>E</i> )-(1-methyl-1 <i>H</i> -imidazol-2-yl)methylene]amino}biphenyl-4-ol (PHPHCA)	97
<b>3.6</b>	<b>Synthesis of the Neutral Oxovanadium(IV) Complexes</b>	<b>98</b>
3.6.1	Synthesis of (2-{( <i>E</i> )-[(2-oxidophenyl)imino]methyl}phenolate)(dipyrido[3,2- <i>d</i> :2',3'- <i>f</i> ]quinoxaline) oxovanadium(IV) ([VO(PHA)(DPQ)])	98
3.6.2	Synthesis of (4-methyl-2-{[(1 <i>E</i> )-(2-oxidophenyl)methylene]amino}phenolate)(dipyrido[3,2- <i>d</i> :2',3'- <i>f</i> ]quinoxaline) oxovanadium(IV) ([VO(MEA)(DPQ)])	99
3.6.3	Synthesis of (4- <i>tert</i> -butyl-2-{[(1 <i>E</i> )-(2-oxidophenyl)methylene]amino}phenolate)(dipyrido[3,2- <i>d</i> :2',3'- <i>f</i> ]quinoxaline) oxovanadium(IV) ([VO(TERTA)(DPQ)])	100
3.6.4	Synthesis of (4-chloro-2-{[(1 <i>E</i> )-(2-oxidophenyl)methylene]amino}phenolate)(dipyrido[3,2- <i>d</i> :2',3'- <i>f</i> ]quinoxaline) oxovanadium(IV) ([VO(CLA)(DPQ)])	101

3.6.5	Synthesis of (4-(ethylsulfonyl)-2-{{(1 <i>E</i> )-(2-oxidophenyl)methylene}amino}phenolate)(dipyrido[3,2- <i>d</i> :2',3'- <i>f</i> ]quinoxaline) oxovanadium(IV) ([VO(SOA)(DPQ)])	102
3.6.6	Synthesis of (3-{{(1 <i>E</i> )-(2-oxidophenyl)methylene}amino}naphthalen-2-olate)(dipyrido[3,2- <i>d</i> :2',3'- <i>f</i> ]quinoxaline) oxovanadium(IV) ([VO(NAA)(DPQ)])	103
3.6.7	Synthesis of (3-{{(1 <i>E</i> )-(2-oxidophenyl)methylene}amino}biphenyl-4-olate)(dipyrido[3,2- <i>d</i> :2',3'- <i>f</i> ]quinoxaline) oxovanadium(IV) ([VO(PHPHA)(DPQ)])	104
3.6.8	Synthesis of (4-methyl-2-{{(1 <i>E</i> )-(2-oxidophenyl)methylene}amino}phenolate)(dipyrido[3,2- <i>a</i> :2',3'- <i>c</i> ]phenazine) oxovanadium(IV) ([VO(MEA)(DPPZ)])	105
<b>3.7</b>	<b>Synthesis of the Cationic Oxovanadium(IV) Complexes</b>	<b>106</b>
3.7.1	Synthesis of (2-{{(1 <i>E</i> )-(1-methyl-1 <i>H</i> -imidazol-2-yl)methylene}amino}phenolate)(1,10-phenanthroline) oxovanadium(IV) hexafluorophosphate ([VO(PHCA)(PHEN)](PF <sub>6</sub> ))	106
3.7.2	Synthesis of (4-methyl-2-{{(1 <i>E</i> )-(1-methyl-1 <i>H</i> -imidazol-2-yl)methylene}amino}phenolate)(1,10-phenanthroline) oxovanadium(IV) hexafluorophosphate ([VO(MECA)(PHEN)](PF <sub>6</sub> ))	108
3.7.3	Synthesis of (4- <i>tert</i> -butyl-2-{{(1 <i>E</i> )-(1-methyl-1 <i>H</i> -imidazol-2-yl)methylene}amino}phenolate)(1,10-phenanthroline) oxovanadium(IV) hexafluorophosphate ([VO(TERTCA)(PHEN)](PF <sub>6</sub> ))	110
3.7.4	Synthesis of (3-{{(1 <i>E</i> )-(1-methyl-1 <i>H</i> -imidazol-2-yl)methylene}amino}biphen-4-olate)(1,10-phenanthroline) oxovanadium(IV) hexafluorophosphate ([VO(PHPHCA)(PHEN)](PF <sub>6</sub> ))	112
3.7.5	Synthesis of (4-methyl-2-{{(1 <i>E</i> )-(1-methyl-1 <i>H</i> -imidazol-2-yl)methylene}amino}phenolate)(dipyrido[3,2- <i>d</i> :2',3'- <i>f</i> ]quinoxaline) oxovanadium(IV) hexafluorophosphate ([VO(MECA)(DPQ)](PF <sub>6</sub> ))	114

3.7.6	Synthesis of (4- <i>tert</i> -butyl-2-{[(1 <i>E</i> )-(1-methyl-1 <i>H</i> -imidazol-2-yl)methylene]amino}phenolate)(dipyrido[3,2- <i>d</i> :2',3'- <i>f</i> ]quinoxaline)oxovanadium(IV) hexafluorophosphate ([VO(TERTCA)(DPQ)](PF <sub>6</sub> ))	116
3.7.7	Synthesis of (4-methyl-2-{[(1 <i>E</i> )-(1-methyl-1 <i>H</i> -imidazol-2-yl)methylene]amino}phenolate)(dipyrido[3,2- <i>a</i> :2',3'- <i>c</i> ]phenazine)oxovanadium(IV) chloride ([VO(MECA)(DPPZ)](Cl))	118
<b>3.8</b>	<b>References</b>	<b>120</b>

## ***Chapter Four: Spectroscopic Characterisation*** **121**

<b>4.1</b>	<b>Introduction to Spectroscopy</b>	<b>121</b>
<b>4.2</b>	<b>Nuclear Magnetic Resonance Spectroscopy</b>	<b>121</b>
4.2.1	NMR Spectroscopy of the <i>N,N</i> -Bidentate Co-ligands	122
4.2.2	NMR Spectroscopy of the <i>O,N,O'</i> -Tridentate Ligands	123
4.2.3	NMR Spectroscopy of the <i>O,N,N'</i> -Tridentate Ligands	125
4.2.4	NMR Spectroscopic Hydrogen Bonding Study of the <i>O,N,N'</i> Ligands	128
<b>4.3</b>	<b>Infrared Spectroscopy of the Tridentate Ligands and Oxovanadium(IV) Complexes</b>	<b>130</b>
<b>4.4</b>	<b>UV/visible Spectroscopy</b>	<b>136</b>
4.4.1.	UV/visible Spectra of the <i>O,N,O'</i> -Tridentate Ligands and Neutral [VO(ONO)(NN)] Complexes	136
4.4.2.	UV/visible Spectra of the <i>O,N,N'</i> -Tridentate Ligands and Cationic [VO(ONN)(NN)](PF <sub>6</sub> /Cl) Complexes	140
<b>4.5</b>	<b>Electron Paramagnetic Resonance Spectroscopy of the Oxovanadium(IV) Complexes</b>	<b>143</b>
<b>4.6</b>	<b>Conclusions of Spectroscopic Characterisation</b>	<b>150</b>
4.6.1.	Spectroscopic Characterisation of the Bidentate and Tridentate Ligands	150
4.6.2.	Spectroscopic Characterisation of the Oxovanadium(IV) Complexes	151
<b>4.7</b>	<b>References</b>	<b>153</b>

## ***Chapter Five: X-ray Diffraction*** **157**

<b>5.1</b>	<b>General Experimental Procedure</b>	<b>157</b>
<b>5.2</b>	<b><i>O,N,O'</i>-Tridentate Ligands</b>	<b>157</b>
5.2.1	Introduction to <i>O,N,O'</i> -Tridentate Ligands	157
5.2.2	Experimental Procedures for the <i>O,N,O'</i> -Tridentate Ligands	160
5.2.3	Results and Discussion of the Solid-State Structures of the <i>O,N,O'</i> - Tridentate Ligands	160
<b>5.3</b>	<b><i>O,N,N'</i>-Tridentate Ligands</b>	<b>166</b>
5.3.1	Introduction to <i>O,N,N'</i> -Tridentate Ligands	166
5.3.2	Experimental Procedures for the <i>O,N,N'</i> -Tridentate Ligands	168
5.3.3	Results and Discussion of the Solid-State Structures of the <i>O,N,N'</i> - Tridentate Ligands	168
<b>5.4</b>	<b>[VO(ONO)(DPQ/DPPZ)] Complexes</b>	<b>177</b>
5.4.1	Introduction to [VO(ONO)(DPQ/DPPZ)] Complexes	177
5.4.2	Experimental Procedures for the [VO(ONO)(DPQ/DPPZ)] Complexes	177
5.4.3	Results and Discussion of the Solid-State Structures of the [VO(ONO)(DPQ/DPPZ)] Complexes	178
<b>5.5</b>	<b>[VO(ONN)(PHEN)](PF<sub>6</sub>) Complexes</b>	<b>184</b>
5.5.1	Introduction to [VO(ONN)(PHEN)](PF <sub>6</sub> ) Complexes	184
5.5.2	Experimental Procedures for the [VO(ONN)(PHEN)](PF <sub>6</sub> ) Complexes	185
5.5.3	Results and Discussion of the Solid-State Structures of the [VO(ONN)(PHEN)](PF <sub>6</sub> ) Complexes	186
<b>5.6</b>	<b>Conclusions</b>	<b>190</b>
<b>5.7</b>	<b>References</b>	<b>193</b>

## ***Chapter Six: Density Functional Theory*** **198**

<b>6.1</b>	<b>Introduction to Density Functional Theory</b>	<b>198</b>
<b>6.2</b>	<b>Experimental</b>	<b>199</b>
<b>6.3</b>	<b>DFT Studies of the Tridentate Schiff Base Ligands</b>	<b>200</b>

<b>6.4</b>	<b>DFT Studies of the [VO(ONO)(NN)] and [VO(ONN)(NN)]<sup>+</sup> Complexes</b>	<b>212</b>
<b>6.5</b>	<b>Conclusions</b>	<b>228</b>
<b>6.6</b>	<b>References</b>	<b>230</b>

## ***Chapter Seven: Stability of Oxovanadium(IV) Complexes*** **234**

<b>7.1</b>	<b>Introduction</b>	<b>234</b>
<b>7.2</b>	<b>Stabilities of Oxovanadium(IV) Complexes</b>	<b>235</b>
<b>7.3</b>	<b>Mass Spectrometry Stability Studies of the Oxovanadium(IV) Complexes</b>	<b>241</b>
<b>7.4</b>	<b>UV/visible Spectroscopy Stability Studies of the Oxovanadium(IV) Complexes</b>	<b>247</b>
<b>7.5</b>	<b>NMR Spectroscopy Stability Studies of the Oxovanadium(IV) Complexes</b>	<b>251</b>
<b>7.6</b>	<b>Conclusions on Stability of the Oxovanadium(IV) Complexes</b>	<b>254</b>
<b>7.7</b>	<b>References</b>	<b>255</b>

## ***Chapter Eight: Cytotoxicity and DNA Interaction Studies*** **258**

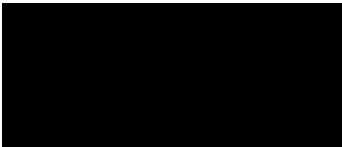
<b>8.1</b>	<b>Introduction</b>	<b>258</b>
<b>8.2</b>	<b>Cell Cytotoxicity Studies</b>	<b>259</b>
	8.2.1 Introduction and Experimental Cell Cytotoxicity Studies	<b>259</b>
	8.2.2 Results and Discussion Cell Cytotoxicity Studies	<b>260</b>
<b>8.3</b>	<b>UV/visible Spectroscopic DNA Binding Studies</b>	<b>265</b>
	8.3.1 Introduction and Experimental Absorption DNA Binding Studies	<b>265</b>
	8.3.2 Results and Discussion Absorption DNA Binding Studies	<b>266</b>
<b>8.4</b>	<b>Competitive DNA Binding by Ethidium Bromide Displacement</b>	<b>269</b>
	8.4.1 Introduction Fluorescence Emission Studies	<b>269</b>
	8.4.2 Determination of the DNA Binding Constant of Ethidium Bromide	<b>270</b>
	8.4.3 Experimental Fluorescence Emission Studies of the Oxovanadium(IV) Complexes	<b>272</b>

8.4.4	Results and Discussion Fluorescence Emission Studies of the Oxovanadium(IV) Complexes	273
<b>8.5</b>	<b>Viscosity DNA Binding Studies</b>	<b>275</b>
8.5.1	Introduction and Experimental DNA Viscosity	275
8.5.2	Results and Discussion DNA Viscosity	276
<b>8.6</b>	<b>Molecular Docking Studies</b>	<b>280</b>
<b>8.7</b>	<b>Gel Electrophoresis DNA Cleavage Studies</b>	<b>288</b>
8.7.1	Introduction and Experimental DNA Cleavage Studies	288
8.7.2	Results and Discussion DNA Cleavage Studies	289
<b>8.8</b>	<b>Mechanistic Studies of DNA Cleavage</b>	<b>294</b>
8.8.1	Introduction and Experimental Gel Electrophoresis Mechanistic Studies of DNA Cleavage	294
8.8.2	Results and Discussion Gel Electrophoresis Mechanistic Studies of DNA Cleavage	295
8.8.3	Introduction and Experimental Spin-Trapping Mechanistic Studies	298
8.8.4	Results and Discussion Spin-Trapping Mechanistic Studies	299
<b>8.9</b>	<b>Conclusions</b>	<b>300</b>
<b>8.10</b>	<b>References</b>	<b>302</b>
 <b><i>Chapter Nine: Conclusions and Future Work</i></b>		<b>307</b>
<b>9.1</b>	<b>Summary and Conclusions</b>	<b>307</b>
<b>9.2</b>	<b>Future Work</b>	<b>311</b>
<b>9.3</b>	<b>Research Outputs</b>	<b>314</b>
9.3.1	Conference Contributions	314
9.3.2	Publications	314
<b>9.4</b>	<b>References</b>	<b>315</b>
 <b>Appendix A: Characterisation Data</b>		<b>A1</b>
<b>Appendix B: EPR Spectra</b>		<b>B1</b>
<b>Appendix C: Crystal Data and Structure Refinement</b>		<b>C1</b>
<b>Appendix D: Density Functional Theory Results</b>		<b>D1</b>
<b>Appendix E: Stability and DNA Binding Studies</b>		<b>E1</b>

## *Declaration 1 – Plagiarism*

I, Kristy-Lyn Barry, declare that:

1. The research reported in this dissertation, except where otherwise indicated, is my original research, conducted within the School of Chemistry and Physics at the University of KwaZulu-Natal, Pietermaritzburg, from 2015 to 2022, under the supervision of Professor Orde Munro and Professor Matthew Akerman. The viscosity studies were conducted by myself at the School of Chemistry, Wits University under the guidance of Professor Orde Munro and Dr Cathy Slabber. Where use has been made of the work of others, it is duly acknowledged in the text.
2. This thesis has not been submitted in any form for any degree, diploma or examination at any other university.
3. This thesis does not contain other persons data, pictures, graphs or other information, unless specifically acknowledged as being sourced from other persons.
4. This thesis does not contain other persons writing, unless specifically acknowledged as being sourced from other researchers. Where other written sources have been quoted, then:
  - (a) Their words have been re-written, but the general information attributed to them has been referenced.
  - (b) Where their exact words have been used, then their writing has been placed in italics and inside quotation marks, and referenced.
5. This thesis does not contain text, graphics or tables copied and pasted from the Internet, unless specifically acknowledged, and the source being detailed in the thesis and in the References sections.

Signed: \_\_\_\_\_  


Kristy-Lyn Barry

## **Declaration 2 – Publications**

1. Barry, K.L., Grimmer, C.D., Munro, O.Q. and Akerman, M.P., “Self-assembled supramolecular structures of O,N,N' tridentate imidazole-phenol Schiff base compounds”, *RSC Adv.*, **2020**, *10*, 7867.

The free-ligands reported in the aforementioned manuscript have been synthesised, characterised and analysed by myself at the University of KwaZulu-Natal. The single crystal X-ray diffraction analyses were run and solved by Prof Matthew Akerman from the University of KwaZulu-Natal. The NMR spectra were run by Craig Grimmer, University of KwaZulu-Natal. I prepared the initial drafts of the manuscripts, which was proof-read by my supervisor, Professor Matthew Akerman.

## *Acknowledgements*

I wish to express my sincere gratitude to the following people:

- My supervisor Prof Matthew Akerman for your guidance, training, X-ray determinations, funding for chemicals, conferences and characterisations, and for very thorough corrections.
- My supervisor Prof Orde Munro for your training, X-ray determinations, funding, flying me up to Joburg for further training, advice and help.
- My extended family for always asking how things are going and for all your prayers and encouragement.
- Caryl Janse van Rensburg for your assistance with mass spectrometry and many elemental analysis samples!
- Craig Grimmer: for running all the NMR samples, help with software and helping me check all NMR assignments.
- Dr Alex Xulu for your help with the EPR measurements.
- Support staff, Shawn Ball, Hashim Desai, Saideshnee Naidoo: for all your help, with equipment and chemicals.
- Paul and Clarence: for setting up my vacuum line and for repairing glassware.
- Jayshree Naicker: for all your help with administration with the cost centre.
- Academic staff at the Chemistry department, School of Chemistry and Physics for encouragement and advice.
- Fellow friends and researchers Leigh Hunter and Sandipa Bhikraj for your input, help and guidance into this project. May we once again sit and drink wine next to a hotel pool in Cape Town.
- Dr Sanam Maikoo: for your help with PatchDock and thesis layout.
- Warren lab postgrads Lesly, Mince, Shivani, Tim for help with equipment and chemicals.
- Dr Cathy Slabber for your invaluable training and help in running agarose gels and viscosity studies. And for your knowledge and company at Indaba 9 Kruger conference.
- Dr Alex Delpont for your training and help with gel electrophoresis and for running the cytotoxicity studies.
- Dr Raymond Hewer for letting me invade your lab and run gels, and for provision of chemicals and the cytotoxicity studies.

- My friends and dear book-club ladies - thank you all for all your encouragement, checking-in and prayers.
- To my dear colleague, now Dr Muvhango Rasalanavho. Thank you for encouraging me, guiding me, protecting me, filling in for me and keeping my eyes on the prize on this journey. Your support has been invaluable, and I will always treasure it.
- To the School of Chemistry and physics for providing me with a laboratory space and equipment to conduct this study.
- The invaluable financial assistance and capacity development of the Thuthuka Funding instrument, National Research Foundation (NRF) and University of KwaZulu-Natal towards this research is hereby gratefully acknowledged. Opinions expressed and conclusions arrived at, are those of the author and are not necessarily to be attributed to the NRF.
- University Capacity development Grant (UCDP), University of KwaZulu-Natal for the invaluable financial assistance towards teaching relief to complete this PhD.
- School of Chemistry and Physics, University of KwaZulu-Natal for the invaluable financial contribution towards teaching relief to allow me to research towards this PhD. This degree would not have been possible without this assistance. Thank-You!

**And finally, to my Lord Jesus Christ who carried me through this project. Thank-you for keeping my head above water amongst the many set-backs – loss of my dad, Covid, riots, load-shedding and demotivation. You gave me strength to carry on and complete this project. Thank you, this work is Yours.**

## *Abstract*

In this work, a new series of ternary oxovanadium(IV) complexes of the type [VO(ONO)(DPQ/DPPZ)], [VO(ONN)(PHEN/DPQ)](PF<sub>6</sub>) and [VO(ONN)(DPPZ)](Cl) have been synthesised and characterised for the purpose of developing novel anticancer agents. ONO represents a tridentate Schiff base ligand derived from salicylaldehyde and various 4-substituted-2-aminophenols. ONN represents a tridentate Schiff base ligand derived from 1-methyl-2-imidazolecarboxaldehyde and various 4-substituted-2-aminophenols. PHEN represents 1,10-phenanthroline, DPQ represents dipyrido[3,2-*d*:2',3'-*f*]quinoxaline and DPPZ represents dipyrido[3,2-*a*:2',3'-*c*]phenazine. The bidentate *N,N*-donor polypyridyl co-ligands were incorporated to enhance DNA binding and to stabilise the vanadium(IV) metal centre.

The known *N,N*-bidentate ligands were synthesised and characterised by ESI-mass, <sup>1</sup>H and <sup>13</sup>C NMR spectroscopy. The tridentate *O,N,O'* and *O,N,N'* ligands were synthesised and characterised by ESI-mass, NMR, IR, and UV/visible spectroscopic techniques, elemental analysis and single crystal X-ray crystallography. Single crystal X-ray diffraction, <sup>1</sup>H NMR and DFT simulations confirmed the *O,N,N'* ligands in this work form dimeric hydrogen-bonded supramolecular structures that are stable in solution. The oxovanadium(IV) complexes were characterised by elemental analysis, UV/visible, FT-IR and EPR spectroscopy as well as mass spectrometry. Elemental analysis and mass spectrometry confirmed the identity and purity of the complexes. EPR spectroscopy confirmed the monomeric V<sup>IV</sup>O-bound species. IR and UV/visible spectroscopy confirmed coordination of the ligands to the metal centre. High-resolution solid-state structures were elucidated for the cationic complexes with PHEN co-ligands and the 4-chloro and 4-*tert*-butyl derivatives of the [VO(ONO)(DPQ)] complexes. The crystal structures of the complexes showed a monomeric vanadium(IV) species with the bidentate *N,N*-donor co-ligand and respective dianionic *O,N,O'*- or monoanionic *O,N,N'*-tridentate Schiff base ligand coordinated to the oxovanadium centre in a distorted octahedral geometry. The respective neutral V<sup>IV</sup>O<sub>3</sub>N<sub>3</sub> and monocationic V<sup>IV</sup>O<sub>2</sub>N<sub>4</sub><sup>+</sup> species were formed.

A least-squares fit of the solid-state and DFT-simulated (B3LYP-/6-311G(dp)) structures of the oxovanadium chelates indicate the experimental and simulated structures are in good agreement.

DFT-simulated structures were determined for those complexes where X-ray data are not available. The geometry-optimised structures for the neutral and cationic complexes all indicate that the respective bidentate polypyridyl ligands are free from steric hindrance by the tridentate ligand and should be available to bind DNA, which is their proposed cellular target. DFT simulations indicated the neutral complexes have larger HOMO-LUMO energy gaps than the corresponding cationic complexes, suggesting that the neutral complexes are more stable with respect to ligand substitution than the cationic complexes. Experimental mass spectrometry and UV/visible spectroscopy confirmed slower solvolysis processes for the neutral complexes versus the cationic analogues.  $^{51}\text{V}$  NMR studies indicate partial oxidation of the vanadium(IV) species in DMSO to  $\text{V}^{\text{V}}\text{O}_2(\text{ONO}/\text{ONN})(\text{DMSO})$  analogues. The cationic complexes with PHEN and DPQ co-ligands were deemed suitable to proceed with absorption DNA binding studies.

The cytotoxicity screening of the oxovanadium complexes in this work revealed that, in general, the neutral complexes with DPQ co-ligands are cytotoxic against the triple-negative breast cancer MDA-MB and neuroblastoma SH-SY5Y tumour cell lines and non-toxic towards the cervical cancer HeLa cell line. The charge of the complexes was found to influence the cytotoxic properties. The cationic complexes with PHEN and DPQ co-ligands are cytotoxic towards the HeLa cell line as well as the MDA-MB and SH-SY5Y cell lines. The neutral DPQ and cationic complexes with PHEN and DPQ co-ligands were found to be more cytotoxic towards MDA-MB cell lines than cisplatin and the cationic complexes were found to be more cytotoxic towards the HeLa cell line than cisplatin. Steric bulk of the Schiff base functional group influences cytotoxicity with larger functional groups, such as *tert*-butyl and sulfonyl, leading to lower cytotoxicity. The *N,N*-donor co-ligand and steric bulk of the Schiff base functional group also influenced the selectivity index of the cationic complexes. The cationic oxovanadium-DPQ complex with a methyl substituent on the tridentate ligand is significantly more toxic to the carcinoma cell lines than the healthy renal cell line HEK293. In comparison, the cationic oxovanadium-PHEN analogue with a methyl substituent and the cationic oxovanadium-DPQ analogue with a bulky *tert*-butyl substituent are less selective in their cytotoxicity.

The DNA binding studies show that the neutral and cationic DPQ compounds do have an affinity for DNA.

A positive correlation between antitumour activity and DNA binding affinity was found. The [VO(ONN)(DPQ)](PF<sub>6</sub>) analogue with a bulky *tert*-butyl substituent has a lower intrinsic *ct*-DNA binding constant than the [VO(ONN)(DPQ)](PF<sub>6</sub>) analogue with a methyl substituent ( $1.3 \times 10^4 \text{ M}^{-1}$  and  $2.8 \times 10^4 \text{ M}^{-1}$  respectively). The cationic DPQ derivatives also bind more strongly to DNA than the cationic complexes with PHEN co-ligands.

The steric effect is also evident in the neutral complexes. The [VO(ONO)(DPQ)] complex with a *tert*-butyl substituent has a lower apparent binding constant than the [VO(ONO)(DPQ)] complex with no substituents on the Schiff base ligand. The cationic charge also led to a higher apparent binding constant for the [VO(ONO)(DPQ)](PF<sub>6</sub>) complex with a *tert*-butyl functional group than for the corresponding neutral [VO(ONO)(DPQ)] analogue with a *tert*-butyl functional group.

Absorption and fluorescence spectroscopic and DNA viscosity studies indicate at least a partial DNA intercalative ability for the cationic oxovanadium-DPQ derivatives and the neutral oxovanadium-DPQ complexes with less bulky substituents. Molecular docking studies further highlighted the affinity of the metal chelates towards DNA, including interactions between DNA and the tridentate ligand. The lowest energy molecular docking poses range from *ca.* -48 to -67 kJ mol<sup>-1</sup>.

Gel electrophoresis studies showed the cationic vanadium complexes with DPQ co-ligands (unlike the neutral DPQ and cationic PHEN analogues) were able to cleave plasmid DNA without adding external oxidising or reducing reagents. Experimental data suggest a singlet oxygen pathway is the most likely. It was also shown that the combination of metal ion and ligand is needed to induce DNA cleavage. The neutral [VO(ONO)(DPQ)] derivative with a methyl functional group on the Schiff base was shown to oxidatively cleave supercoiled plasmid DNA in the presence of H<sub>2</sub>O<sub>2</sub> through the generation of hydroxyl radicals. EPR spin-trapping studies with DMPO further support the idea that hydroxyl radicals are formed from reaction of the oxovanadium complex and H<sub>2</sub>O<sub>2</sub>.

In summary the charge of the complex, type of substituent on the tridentate ligand and the identity of the *N,N*-donor heterocyclic ligand affected the stability, cytotoxic properties, selectivity, DNA binding, DNA cleavage abilities and DNA cleavage mechanism of the oxovanadium compounds in this study.

# **Conference and Publication Contributions**

## **Conference Contributions**

1. The Inorganic Chemistry Conference 2017 & Carman Physical Chemistry Symposium of the South African Chemical Institute (SACI), 25 – 29 June 2017, Arabella Hotel & Spa, Hermanus, Western Cape, South Africa. Barry, K.L., Akerman, M. and Munro, O., Poster entitled: “Synthesis and Structure of Novel Oxovanadium(IV) Complexes”.
2. Indaba 9 Conference, Modeling of Structures and Properties, 2 – 7 September 2018, Skukuza, Kruger National Park, South Africa. Barry, K.L., Akerman, M., Munro, O., Hwer, R. and Delpont, A., Poster entitled: “Synthesis and Structure of Novel Oxovanadium(IV) Complexes”.

## **Publications**

1. Barry, K.L., Grimmer, C.D., Munro, O.Q. and Akerman, M.P., “Self-assembled supramolecular structures of O,N,N' tridentate imidazole-phenol Schiff base compounds”, *RSC Adv.*, **2020**, *10*, 7867.

## *List of Abbreviations and Symbols*

$\alpha$	– alpha
A <sub>a</sub>	– absorbance of vanadium complex (in the presence of DNA)
A <sub>f</sub>	– absorbance of free vanadium complex (in the absence of DNA)
ABTS <sup>•+</sup>	– 2,2-azinobis(3-ethylbenzothiazoline-6-sulfonic acid)
AFM	– atomic force microscopy
ATP	– adenosinetriphosphatase
ATPase	– enzyme that hydrolyses adenosinetriphosphatase
$\beta$	– beta
B3LYP	– Becke, three parameter hybrid functional with the non-local correlation functional of Lee-Yang-Parr
BMOV	– bis(maltolato)oxovanadium(IV)
B-DNA	– anti-parallel, right-handed deoxyribonucleic acid helix
BEOV	– bis(ethylmaltolato)oxovanadium(IV)
BIOV	– bis(isopropylmaltolato)oxovanadium(IV)
BMOV	– bis(maltolato)oxovanadium(IV)
BnBOV	– bis(n-butylmaltolato)oxovanadium(IV)
bipy	– 2,2'-bipyridine
CDCl <sub>3</sub>	– deuterated chloroform
CH <sub>2</sub> Cl <sub>2</sub>	– dichloromethane
CH <sub>3</sub> CN	– acetonitrile
cisplatin	– <i>cis</i> -diamminedichloroplatinum(II)
CLA	– 4-chloro-2-{{(E)-(2-hydroxyphenyl)methylene}-amino}phenol
<i>ct</i> -DNA	– calf thymus deoxyribonucleic acid
DFT	– density functional theory
DMF	– dimethylformamide
DMPO	– 5,5-dimethyl-1-pyrroline N-oxide
DMSO	– dimethylsulfoxide
DNA	– deoxyribonucleic acid

dp	– single first polarisation and diffuse function
DPPH	– 1,1-diphenyl-2-picrylhydrazyl
DPPZ	– dipyrido[3,2- <i>a</i> :2',3'- <i>c</i> ]phenazine
DPQ	– dipyrido[3,2- <i>d</i> :2',3'- <i>f</i> ]quinoxaline
$\varepsilon$	– molar absorptivity
$\varepsilon_a$	– extinction coefficient of the absorption band at a given [DNA]
$\varepsilon_f$	– extinction coefficient of the free ethidium bromide (with no <i>ct</i> -DNA)
$\varepsilon_b$	– extinction coefficient of the fully intercalated ethidium bromide
EB	– ethidium bromide
ESP	– electrostatic potential
ESR	– electron spin resonance
EtOH	– ethanol
FT-IR	– fourier-transform infrared
GGA	– generalised gradient approximation
$h$	– Planck's constant ( $6.626 \times 10^{-34}$ J.s)
HF	– Hartree-Fock
HMG	– high-mobility group
HOMO	– highest occupied molecular orbital
HSA	– human serum albumin
IR	– infrared
$K_{app}$	– apparent binding constant
$K_b$	– intrinsic binding constant
L	– ligand
L'	– low molecular mass ligand present in blood serum
LMCT	– ligand-to-metal charge transfer
LUMO	– lowest unoccupied molecular orbital
MEA	– 2-{[(E)-(2-hydroxyphenyl)methylene]amino-4-methylphenol
MECA	– 4-methyl-2-{[(1E)-(1-methyl-1 <i>H</i> -imidazol-2-yl)methylene]amino}phenol

Metvan	– [VO(SO <sub>4</sub> )(Me <sub>2</sub> -Phen) <sub>2</sub> ]
NAMI-A	– [imidazoleH][ <i>trans</i> -RuCl <sub>4</sub> (dmsO-S)(imidazole)]
NKP-1339	– Na[ <i>trans</i> -RuCl <sub>4</sub> (indazole) <sub>2</sub> ]
NAA	– 3-{[( <i>E</i> )-(2-hydroxyphenyl)methylidene]amino}naphthalen-2-ol
NADH	– nicotinamide adenine dinucleotide hydride
NADPH	– nicotinamide adenine dinucleotide phosphate
NaOH	– sodium hydroxide
NMR	– nuclear magnetic resonance
PCM	– Polarizable Continuum Model
PDO	– 1,10-phenanthroline-5,6-dione
PDT	– photo dynamic therapy
PHA	– 2-{(E)-[(2-hydroxyphenyl)imino]methyl}phenol
PHCA	– 2-{[(1 <i>E</i> )-(1-methyl-1 <i>H</i> -imidazol-2-yl)methylene]amino}phenol
PHEN	– 1,10-phenanthroline
PHPHA	– 3-{[( <i>E</i> )-(2-hydroxyphenyl)methylidene]amino}biphenyl-4-ol
PHPHCA	– 3-{[(1 <i>E</i> )-(1-methyl-1 <i>H</i> -imidazol-2-yl)methylene]amino}-biphenyl-4-ol
PTK	– protein tyrosine kinase
PTP-1B	– protein tyrosine phosphatase 1B
PTPS	– protein tyrosine phosphatases
RMSD	– root-mean-square deviations
ROS	– reactive oxygen species
<i>s</i>	– binding site size (number of nucleotides per ethidium bromide)
SOA	– 4-(ethylsulfonyl)-2-{[( <i>E</i> )-(2-hydroxyphenyl)methylidene]amino}phenol
TERTA	– 4- <i>tert</i> -butyl-2-{[( <i>E</i> )-(2-hydroxyphenyl)methylene]amino}phenol
TERTCA	– 4- <i>tert</i> -butyl-2-{[(1 <i>E</i> )-(1-methyl-1 <i>H</i> -imidazol-2-yl)methylene] amino}phenol

Tf	– transferrin protein
UV	– ultraviolet
Vis	– visible
VO(acac) <sub>2</sub>	– vanadyl acetylacetonate
[VO(PHA)(DPQ)]	– (2- <i>{(E)-[(2-oxidophenyl)imino]methyl}</i> phenolate) (dipyrido[3,2- <i>d</i> :2',3'- <i>f</i> ]quinoxaline) oxovanadium(IV)
[VO(MEA)(DPQ)]	– (4-methyl-2- <i>{[(1E)-(2-oxidophenyl)methylene]</i> <i>amino}</i> phenolate)(dipyrido[3,2- <i>d</i> :2',3'- <i>f</i> ]quinoxaline) oxovanadium(IV)
[VO(TERTA)(DPQ)]	– (4- <i>tert</i> -butyl-2- <i>{[(1E)-(2-oxidophenyl)methylene]</i> <i>amino}</i> phenolate)(dipyrido[3,2- <i>d</i> :2',3'- <i>f</i> ]quinoxaline) oxovanadium(IV)
[VO(CLA)(DPQ)]	– (4-chloro-2- <i>{[(1E)-(2-oxidophenyl)methylene]</i> <i>amino}</i> phenolate)(dipyrido[3,2- <i>d</i> :2',3'- <i>f</i> ]quinoxaline) oxovanadium(IV)
[VO(SOA)(DPQ)]	– (4-(ethylsulfonyl)-2- <i>{[(1E)-(2-oxidophenyl)methylene]</i> <i>amino}</i> phenolate)(dipyrido[3,2- <i>d</i> :2',3'- <i>f</i> ]quinoxaline) oxovanadium(IV)
[VO(NAA)(DPQ)]	– (3- <i>{[(1E)-(2-oxidophenyl)methylene]</i> <i>amino}</i> naphtalen-2-olate)(dipyrido[3,2- <i>d</i> :2',3'- <i>f</i> ]quinoxaline) oxovanadium(IV)
[VO(PHPHA)(DPQ)]	– (3- <i>{[(1E)-(2-oxidophenyl)methylene]</i> <i>amino}</i> biphenyl-4-olate)(dipyrido[3,2- <i>d</i> :2',3'- <i>f</i> ]quinoxaline) oxovanadium(IV)
[VO(MEA)(DPPZ)]	– (4-methyl-2- <i>{[(1E)-(2-oxidophenyl)methylene]</i> <i>amino}</i> phenolate)(dipyrido[3,2- <i>a</i> :2',3'- <i>c</i> ]phenazine) oxovanadium(IV)
[VO(PHCA)(PHEN)]- (PF <sub>6</sub> )	– (2- <i>{[(1E)-(1-methyl-1H-imidazol-2-yl)methylene]</i> <i>amino}</i> phenolate)(1,10-phenanthroline) oxovanadium(IV) hexafluorophosphate
[VO(MECA)- (PHEN)](PF <sub>6</sub> )	– (4-methyl-2- <i>{[(1E)-(1-methyl-1H-imidazol-2-yl)]</i> <i>methylene]</i> <i>amino}</i> phenolate)(1,10-phenanthroline) oxovanadium(IV) hexafluorophosphate

- [VO(TERTCA)-  
(PHEN)](PF<sub>6</sub>) – (4-*tert*-butyl-2- {[*(1E)*-(1-methyl-1*H*-imidazol-2-yl)  
methylene]amino}phenolate)(1,10-phenanthroline)  
oxovanadium(IV) hexafluorophosphate
- [VO(PHPHCA)-  
(PHEN)](PF<sub>6</sub>) – (3- {[*(1E)*-(1-methyl-1*H*-imidazol-2-yl)methylene]  
amino}biphen-4-olate)(1,10-phenanthroline)  
oxovanadium(IV) hexafluorophosphate
- [VO(MECA)-  
(DPQ)](PF<sub>6</sub>) – (4-methyl-2- {[*(1E)*-(1-methyl-1*H*-imidazol-2-yl)  
methylene]amino}phenolate)(dipyrido[3,2-*d*:2',3'-  
*f*]quinoxaline) oxovanadium(IV) hexafluorophosphate
- [VO(TERTCA)-  
(DPQ)](PF<sub>6</sub>) – (4-*tert*-butyl-2- {[*(1E)*-(1-methyl-1*H*-imidazol-2-yl)  
methylene]amino}phenolate)(dipyrido[3,2-*d*:2',3'-  
*f*]quinoxaline) oxovanadium(IV) hexafluorophosphate
- [VO(MECA)-  
(DPPZ)](Cl) – (4-methyl-2- {[*(1E)*-(1-methyl-1*H*-imidazol-2-yl)  
methylene]amino}phenolate)(dipyrido[3,2-*a*:2',3'-  
*c*]phenazine) oxovanadium(IV) chloride

## *List of Figures*

<b>Figure #</b>	<b>Title</b>	<b>Page #</b>
<b>Figure 1.1</b>	The structure of <i>cis</i> -diamminedichloroplatinum(II) (cisplatin), the first metallodrug approved for clinical use in treating cancer.	<b>2</b>
<b>Figure 1.2</b>	Second- and third-generation platinum compounds approved for clinical use in treating cancer.	<b>4</b>
<b>Figure 1.3</b>	NAMI-A and NKP-1339, Ru(III) chemotherapeutic agents selected for clinical trials.	<b>5</b>
<b>Figure 1.4</b>	Structure of BEOV, an oxovanadium(IV) complex that entered phase IIa human clinical trials for diabetes treatment.	<b>8</b>
<b>Figure 1.5</b>	Summary of the uptake, distribution and excretion of vanadium compounds <i>in vivo</i> .	<b>10</b>
<b>Figure 1.6</b>	Vanadocene dichloride, a metallocene with cytotoxic properties.	<b>15</b>
<b>Figure 1.7</b>	Vanadocene compounds patented for the treatment of some cancers by Uckun and co-workers.	<b>15</b>
<b>Figure 1.8</b>	Possible mechanisms of action for the antitumour effects of vanadium compounds. Image reproduced from Evangelou.	<b>18</b>
<b>Figure 1.9</b>	Number of publications showing the surge in research into DNA interactions of oxovanadium compounds in the last decade.	<b>20</b>
<b>Figure 1.10</b>	Cisplatin intrastrand adduct with DNA at the N(7) atoms of guanine bases. Image reproduced from García-Ramos <i>et al.</i>	<b>21</b>
<b>Figure 1.11</b>	Schematic representation of non-covalent binding modes between small molecules and DNA. Image reproduced from de Almeida <i>et al.</i>	<b>23</b>
<b>Figure 1.12</b>	Schematic representation of a groove-binding metal complex and a metallointercalator. Image reproduced from Zeglis <i>et al.</i>	<b>23</b>

<b>Figure #</b>	<b>Title</b>	<b>Page #</b>
<b>Figure 1.13</b>	Bidentate <i>N,N</i> -donor ligands, which are known to enhance DNA binding.	<b>24</b>
<b>Figure 1.14</b>	Structure of Metvan, a promising oxovanadium(IV) anticancer agent.	<b>25</b>
<b>Figure 1.15</b>	[VO(ONO)(NN)] complexes for which DNA intrinsic binding constants have been determined by Sasmal and co-workers ( <i>a</i> ), ( <i>b</i> ), ( <i>c</i> ); Guo <i>et al.</i> ( <i>d</i> ); Liao <i>et al.</i> ( <i>f</i> ), ( <i>g</i> ) and Dong and co-workers ( <i>e</i> ), ( <i>h</i> ), ( <i>i</i> ), ( <i>j</i> ). Intrinsic DNA binding constants ( $K_b$ ) are indicated alongside each structure.	<b>29</b>
<b>Figure 1.16</b>	[VO(ONO)(NN)] complexes for which DNA binding modes have been determined by Li and co-workers ( <i>a</i> ), ( <i>b</i> ), ( <i>c</i> ), ( <i>d</i> ); Aboafia <i>et al.</i> ( <i>e</i> ); Liao <i>et al.</i> ( <i>f</i> ), ( <i>g</i> ) and Banerjee <i>et al.</i> ( <i>h</i> ) – ( <i>k</i> ). Intrinsic DNA binding constants ( $K_b$ ) are indicated alongside each structure.	<b>30</b>
<b>Figure 1.17</b>	[VO(ONO)(NN)] complexes reported to have antitumoural properties.	<b>34</b>
<b>Figure 1.18</b>	Oxovanadium(IV) complexes reported to have antiparasitic and antitumoural properties.	<b>36</b>
<b>Figure 1.19</b>	Oxovanadium(IV) complexes of <i>O,N,O'</i> -donor hydrazone ligands reported to have antimicrobial ( <i>a</i> ), anticancer ( <i>a</i> ), ( <i>b</i> ), ( <i>c</i> ) and antidiabetic properties ( <i>d</i> ) and ( <i>e</i> ).	<b>38</b>
<b>Figure 1.20</b>	Cationic oxovanadium(IV) complexes studied by Sasmal and co-workers of the type [VO(ONO)(NN)] <sup>+</sup> ( <i>a</i> ) and [VO(ONN)(NN)] <sup>+</sup> ( <i>b</i> ) and ( <i>c</i> ).	<b>40</b>
<b>Figure 1.21</b>	<i>O,N,O'</i> -tridentate Schiff base ligands to be synthesised.	<b>42</b>
<b>Figure 1.22</b>	<i>O,N,N'</i> -tridentate Schiff base ligands to be synthesised.	<b>43</b>
<b>Figure 1.23</b>	Neutral and novel cationic oxovanadium(IV) complexes to be synthesised in the present study.	<b>44</b>
<b>Figure 2.1</b>	Hydrated PHCA indicating the cage-like structure with a trapped, hydrogen-bonded water molecule bridging two ligands.	<b>72</b>

<b>Figure #</b>	<b>Title</b>	<b>Page #</b>
<b>Figure 2.2</b>	X-ray structure of 2-amino-4-methylphenol coordinated to the VO(MECA) centre.	<b>76</b>
<b>Figure 3.1</b>	Structure and atom numbering scheme of 1,10-phenanthroline-5,6-dione.	<b>83</b>
<b>Figure 3.2</b>	Structure and atom numbering scheme of DPQ.	<b>84</b>
<b>Figure 3.3</b>	Structure and atom numbering scheme of DPPZ.	<b>85</b>
<b>Figure 3.4</b>	Structure and atom numbering scheme of the ligand designated PHA.	<b>87</b>
<b>Figure 3.5</b>	Structure and atom numbering scheme of the ligand designated MEA.	<b>88</b>
<b>Figure 3.6</b>	Structure and atom numbering scheme of the ligand designated TERTA.	<b>89</b>
<b>Figure 3.7</b>	Structure and atom numbering scheme of the ligand designated CLA.	<b>90</b>
<b>Figure 3.8</b>	Structure and atom numbering scheme of the ligand designated SOA.	<b>91</b>
<b>Figure 3.9</b>	Structure and atom numbering scheme of the ligand designated NAA.	<b>92</b>
<b>Figure 3.10</b>	Structure and atom numbering scheme of the ligand designated PHPHA.	<b>93</b>
<b>Figure 3.11</b>	Structure and atom numbering scheme of the ligand designated PHCA.	<b>94</b>
<b>Figure 3.12</b>	Structure and atom numbering scheme of the ligand designated MECA.	<b>95</b>
<b>Figure 3.13</b>	Structure and atom numbering scheme of the ligand designated TERTCA.	<b>96</b>
<b>Figure 3.14</b>	Structure and atom numbering scheme of the ligand designated PHPHCA.	<b>97</b>
<b>Figure 3.15</b>	Structure of the complex designated [VO(PHA)(DPQ)].	<b>98</b>
<b>Figure 3.16</b>	Structure of the complex designated [VO(MEA)(DPQ)].	<b>99</b>
<b>Figure 3.17</b>	Structure of the complex designated [VO(TERTA)(DPQ)].	<b>100</b>

<b>Figure #</b>	<b>Title</b>	<b>Page #</b>
<b>Figure 3.18</b>	Structure of the complex designated [VO(CLA)(DPQ)].	<b>101</b>
<b>Figure 3.19</b>	Structure of the complex designated [VO(SOA)(DPQ)].	<b>102</b>
<b>Figure 3.20</b>	Structure of the complex designated [VO(NAA)(DPQ)].	<b>103</b>
<b>Figure 3.21</b>	Structure of the complex designated [VO(PHPHA)(DPQ)].	<b>104</b>
<b>Figure 3.22</b>	Structure of the complex designated [VO(MEA)(DPPZ)].	<b>105</b>
<b>Figure 3.23</b>	Structure of the complex designated [VO(PHCA)(PHEN)](PF <sub>6</sub> ).	<b>106</b>
<b>Figure 3.24</b>	Structure of the complex designated [VO(MECA)(PHEN)](PF <sub>6</sub> ).	<b>108</b>
<b>Figure 3.25</b>	Structure of the complex designated [VO(TERTCA)(PHEN)](PF <sub>6</sub> ).	<b>110</b>
<b>Figure 3.26</b>	Structure of the complex designated [VO(PHPHCA)(PHEN)](PF <sub>6</sub> ).	<b>112</b>
<b>Figure 3.27</b>	Structure of the complex designated [VO(MECA)(DPQ)](PF <sub>6</sub> ).	<b>114</b>
<b>Figure 3.28</b>	Structure of the complex designated [VO(TERTCA)(DPQ)](PF <sub>6</sub> ).	<b>116</b>
<b>Figure 3.29</b>	Structure of the complex designated [VO(MECA)(DPPZ)](Cl).	<b>118</b>
<b>Figure 4.1</b>	<sup>1</sup> H NMR spectra of DPPZ (top) and DPQ (bottom) in CDCl <sub>3</sub> . Inset structures show the atom numbering scheme.	<b>123</b>
<b>Figure 4.2</b>	Fully assigned <sup>1</sup> H NMR spectrum of TERTA in DMSO- <i>d</i> <sub>6</sub> .	<b>124</b>
<b>Figure 4.3</b>	Fully assigned <sup>13</sup> C NMR spectrum of TERTA in DMSO- <i>d</i> <sub>6</sub> .	<b>125</b>
<b>Figure 4.4</b>	Fully assigned <sup>1</sup> H NMR spectrum of TERTCA in DMSO- <i>d</i> <sub>6</sub> .	<b>126</b>
<b>Figure 4.5</b>	Fully assigned <sup>13</sup> C NMR spectrum of TERTCA in DMSO- <i>d</i> <sub>6</sub> .	<b>127</b>
<b>Figure 4.6</b>	Stacked <sup>1</sup> H NMR spectra of TERTCA depicting the concentration dependence of the chemical shift and line width of the OH signal.	<b>128</b>

<b>Figure #</b>	<b>Title</b>	<b>Page #</b>
<b>Figure 4.7</b>	Overlay of the IR spectra of the <i>O,N,O'</i> tridentate ligand TERTA and the neutral complex [VO(TERTA)(DPQ)] indicating the general shift to lower stretching frequencies following coordination of the electron deficient metal ion. The V=O, V–O and V–N stretching frequencies are also indicated and confirm successful metal ion coordination.	<b>132</b>
<b>Figure 4.8</b>	Overlay of the IR spectra of the <i>O,N,N'</i> -tridentate TERTCA ligand and the [VO(TERTCA)(PHEN)](PF <sub>6</sub> ) complex highlighting the lower C=N stretching frequency and appearance of the V=O, V–O and P–F stretching frequencies in the complex.	<b>133</b>
<b>Figure 4.9</b>	IR spectra of the neutral complex [VO(TERTA)(DPQ)] showing the lower V=O stretching frequency and absence of the P–F stretch when compared to the [VO(TERTCA)(DPQ)](PF <sub>6</sub> ) complex.	<b>135</b>
<b>Figure 4.10</b>	Overlay of the UV/visible spectra of the <i>O,N,O'</i> -tridentate ligand CLA and the neutral complex [VO(CLA)(DPQ)] indicating formation of the LMCT band in the complex.	<b>137</b>
<b>Figure 4.11</b>	Overlay of the UV/visible spectra of the neutral complexes [VO(MEA)(DPQ)] and [VO(MEA)(DPPZ)] highlighting the changes as a result of the increased conjugation of DPPZ compared to DPQ.	<b>139</b>
<b>Figure 4.12</b>	Overlay of the UV/visible spectra of the <i>O,N,N'</i> -tridentate ligand MECA and the cationic complexes: [VO(MECA)(PHEN)](PF <sub>6</sub> ), [VO(MECA)(DPQ)](PF <sub>6</sub> ) and [VO(MECA)(DPPZ)](Cl).	<b>140</b>
<b>Figure 4.13</b>	Overlay of the UV/visible spectra of the cationic complexes with a PHEN co-ligand: [VO(ONN)(PHEN)](PF <sub>6</sub> ), where ONN = PHCA, MECA, TERTCA and PHPHCA.	<b>142</b>

<b>Figure #</b>	<b>Title</b>	<b>Page #</b>
<b>Figure 4.14</b>	Overlay of the UV/visible spectra of the neutral complex [VO(MEA)(DPQ)] and [VO(MECA)(DPQ)](PF <sub>6</sub> ). This highlights the shift in the LMCT band as a consequence of coordinating a monoanionic versus dianionic ligand to the metal centre.	<b>143</b>
<b>Figure 4.15</b>	A <i>d</i> -orbital splitting diagram for VO <sup>2+</sup> .	<b>146</b>
<b>Figure 4.16</b>	X-band EPR spectra of [VO(MEA)(DPQ)] (a) and [VO(MECA)(DPQ)](PF <sub>6</sub> ) (b) in the solid-state at 298 K.	<b>148</b>
<b>Figure 4.17</b>	EPR spectra of [VO(MEA)(DPQ)] in dichloromethane (a) and [VO(MECA)(DPQ)](PF <sub>6</sub> ) in acetonitrile (b) at 298 K.	<b>149</b>
<b>Figure 5.1</b>	Thermal displacement plots (50% probability) showing the structure and atom numbering schemes of NAA and SOA. Hydrogen atoms are shown as spheres of arbitrary radius.	<b>161</b>
<b>Figure 5.2</b>	Dimeric structures of NAA indicating the intra- and intermolecular hydrogen bonds represented as dashed green lines. Atoms are shown as spheres of arbitrary radius.	<b>164</b>
<b>Figure 5.3</b>	Intermolecular hydrogen bonds (O2–H102···O1), intramolecular hydrogen bonds (N1–H101···O1) and C7–H···O3 intermolecular attractions in SOA, shown as dashed green lines. Atoms are shown as spheres of arbitrary radius.	<b>165</b>
<b>Figure 5.4</b>	Reported crystal structure of a Schiff base ligand containing the 1-methyl-imidazol-2-yl methylidene amino moiety (PILBEU).	<b>166</b>
<b>Figure 5.5</b>	Thermal displacement plots (50% probability) showing the structure and atom numbering schemes of PHCA, PHCA·0.5H <sub>2</sub> O, MECA, TERTCA and PHPHCA. Hydrogen atoms are shown as spheres of arbitrary radius. The symmetry completed (2-fold symmetry) water molecule in PHCA is shown.	<b>170</b>

<b>Figure #</b>	<b>Title</b>	<b>Page #</b>
<b>Figure 5.6</b>	Mean planes of the imidazole (red) and phenol (yellow) rings of PHCA(a) and PHCA(b).	<b>171</b>
<b>Figure 5.7</b>	Complimentary hydrogen bonds forming dimeric structures of PHCA, MECA, TERTCA and PHPHCA. The hydrogen bonds are shown as dashed green lines. Atoms are shown as spheres of arbitrary radius.	<b>174</b>
<b>Figure 5.8</b>	Dimeric hydrogen-bonded units of PHCA linked by C–H···O interactions to form one-dimensional columns (viewed down the <i>c</i> -axis). The intermolecular interactions are shown as dashed green lines. Atoms are rendered as spheres of arbitrary radius.	<b>176</b>
<b>Figure 5.9</b>	One-dimensional supramolecular structure comprising water-bridged PHCA dimers cross-linked by C–H...N interactions, viewed down the <i>a</i> -axis. Intermolecular interactions are shown as dashed green lines. All atoms are rendered as spheres of arbitrary radius.	<b>176</b>
<b>Figure 5.10</b>	Previously reported X-ray structures of neutral oxovanadium complexes of the form [VO(ONO)(NN)]. (a) RIVVUO with a DPQ co-ligand and (b) NAGZIG with a DPPZ co-ligand.	<b>177</b>
<b>Figure 5.11</b>	Low resolution structures of [VO(PHA)(DPQ)].	<b>178</b>
<b>Figure 5.12</b>	Thermal displacement plots (50% probability) showing the structure and atom numbering schemes of [VO(CLA)(DPQ)] and [VO(TERTA)(DPQ)]. Both structures show an octahedral coordination geometry.	<b>179</b>
<b>Figure 5.13</b>	Intermolecular interactions in [VO(TERTA)(DPQ)]. The attractions between the C–H of DPQ and O2 are shown as green lines and the $\pi$ – $\pi$ interactions are shown as orange lines. Atoms are shown as spheres of arbitrary radius.	<b>183</b>
<b>Figure 5.14</b>	Low resolution structures of [VO(MEA)(DPPZ)].	<b>184</b>

<b>Figure #</b>	<b>Title</b>	<b>Page #</b>
<b>Figure 5.15</b>	Previously reported X-ray crystal structures of oxovanadium complexes IRAGAK (a) HINXIN (b) of the general formula [VO(ONN)(PHEN)](ClO <sub>4</sub> ).	<b>185</b>
<b>Figure 5.16</b>	Thermal displacement plots (50% probability) showing the structure and atom numbering schemes of [VO(PHCA)(PHEN)](PF <sub>6</sub> ), [VO(MECA)(PHEN)](PF <sub>6</sub> ) and [VO(TERTCA)(PHEN)](PF <sub>6</sub> ). Hydrogen atoms are shown as spheres of arbitrary radius. The disordered CH <sub>2</sub> Cl <sub>2</sub> molecule in [VO(MECA)(PHEN)](PF <sub>6</sub> ) was omitted for clarity.	<b>187</b>
<b>Figure 6.1</b>	Least-squares-fits of the DFT-simulated (yellow) and X-ray crystal structures (blue) of the monomeric <i>O,N,N'</i> ligands. Root mean square deviations (RMSD) for all non-hydrogen atoms are indicated on the diagram.	<b>201</b>
<b>Figure 6.2</b>	Atom numbering used for PHPHCA.	<b>202</b>
<b>Figure 6.3</b>	Relative energy of PHPHCA as a function of the C9-C10-C12-C17 torsion angle. The energy maxima and minima are highlighted in magenta with their corresponding structures. All energy values are referenced against the lowest energy conformation.	<b>203</b>
<b>Figure 6.4</b>	Relative energy of PHCA as a function of the C5-N3-C6-C7 torsion angle. The energy maxima and minima are highlighted in magenta with their corresponding structures. All energy values are referenced against the lowest energy conformation.	<b>204</b>
<b>Figure 6.5</b>	Least-squares-fits of the DFT-simulated (yellow) and X-ray crystal structures (blue) of the dimeric <i>O,N,N'</i> ligand species. Root mean square deviations (RMSD) for all non-hydrogen atoms are indicated on the diagram.	<b>206</b>
<b>Figure 6.6</b>	Electrostatic potential map from the total SCF density for the PHPHCA dimer, highlighting the zones of positive (blue) and negative (red) potential.	<b>207</b>

<b>Figure #</b>	<b>Title</b>	<b>Page #</b>
<b>Figure 6.7</b>	Superposition plots of the experimental and the TD-DFT-simulated (CH <sub>3</sub> CN solvent continuum) simulated UV/visible spectra of MECA for both the monomeric and dimeric species.	<b>209</b>
<b>Figure 6.8</b>	DFT-simulated HOMO and LUMO plots for the geometry-optimised (gas phase) dimer of MECA. The energy gap between the two orbitals is indicated on the diagram.	<b>211</b>
<b>Figure 6.9</b>	Least-squares-fits of the DFT-optimised (yellow) and solid-state (blue) structures of [VO(CLA)(DPQ)], [VO(TERTA)(DPQ)], [VO(PHCA)(PHEN)] <sup>+</sup> , [VO(MECA)(PHEN)] <sup>+</sup> and [VO(TERTCA)(PHEN)] <sup>+</sup> complexes. Root mean square deviations (RMSD) for all non-hydrogen atoms are indicated on the diagram.	<b>213</b>
<b>Figure 6.10</b>	DFT-simulated geometry-optimised structures (B3LYP/6-311G(dp) level of theory) of [VO(MEA)(DPQ)], [VO(SOA)(DPQ)], [VO(NAA)(DPQ)], [VO(PHPHA)(DPQ)], [VO(MECA)(DPQ)] <sup>+</sup> , [VO(TERTCA)(DPQ)] <sup>+</sup> and [VO(MECA)(DPPZ)] <sup>+</sup> .	<b>217</b>
<b>Figure 6.11</b>	ESP maps from the total SCF density for the neutral complexes [VO(MEA)(DPQ)] and [VO(SOA)(DPQ)] and the cationic complex [VO(MECA)(DPQ)] <sup>+</sup> highlighting the zones of positive (blue) and negative (red) electrostatic potential.	<b>220</b>
<b>Figure 6.12</b>	Superposition plots of the experimental and the TD-DFT-simulated (CH <sub>3</sub> CN solvent continuum) UV/visible spectra of [VO(MEA)(DPQ)].	<b>221</b>
<b>Figure 6.13</b>	Superposition plots of the experimental and the TD-DFT-simulated (CH <sub>3</sub> CN solvent continuum) UV/visible spectra of [VO(MECA)(DPQ)] <sup>+</sup> .	<b>221</b>

Figure #	Title	Page #
<b>Figure 6.14</b>	DFT-simulated alpha HOMO and LUMO plots for the geometry-optimised (gas phase) of [VO(PHA)(DPQ)], [VO(MEA)(DPQ)] and [VO(SOA)(DPQ)].	<b>225</b>
<b>Figure 6.15</b>	DFT-simulated (B3LYP-/6-311G(dp)) alpha HOMO-3, HOMO-2, HOMO-1, HOMO, LUMO, LUMO+1 and LUMO+2 plots for [VO(MECA)(DPQ)] <sup>+</sup> . The energy gap of the frontier molecular orbitals is 2.77 eV.	<b>226</b>
<b>Figure 7.1</b>	[VO(ONO)(NN)] complexes reported, by Sasmal and co-workers to be stable in solution.	<b>235</b>
<b>Figure 7.2</b>	Cationic oxovanadium(IV) complexes of the type [VO(ONO)(NN)](Cl) ( <i>a</i> ) and [VO(ONN)(NN)](ClO <sub>4</sub> ) ( <i>b</i> ) for which stabilities were reported by Sasmal and co-workers.	<b>236</b>
<b>Figure 7.3</b>	[VO(ONO)(NN)] complexes for which stabilities have been studied with pH considerations.	<b>237</b>
<b>Figure 7.4</b>	Hydrazone oxovanadium(IV) complexes for which stabilities with pH considerations were reported by Szklarzewicz and co-workers.	<b>238</b>
<b>Figure 7.5</b>	[VO(ONO)(NN)] complexes where stability has been studied, as reported by Costa Pessoa and co-workers.	<b>239</b>
<b>Figure 7.6</b>	Structure of BEOV, an oxovanadium(IV) complex that entered phase IIa human clinical trials for diabetes. This compound acts as a pro-drug.	<b>240</b>
<b>Figure 7.7</b>	ESI mass spectrum of [VO(PHA)(DPQ)] in chloroform indicating the prominent molecular ion peaks of 510.0792 <i>m/z</i> and 511.0858 <i>m/z</i> corresponding to [M] <sup>+</sup> and [M+H] <sup>+</sup> respectively.	<b>242</b>
<b>Figure 7.8</b>	ESI mass spectra of [VO(TERTA)(DPQ)] in 10%DMSO/90%water (v/v) and in chloroform (inset) indicating the prominent singular molecular ion peak [M] <sup>+</sup> at 566.1644 <i>m/z</i> .	<b>243</b>

<b>Figure #</b>	<b>Title</b>	<b>Page #</b>
<b>Figure 7.9</b>	ESI mass spectra at 30 minutes and 24 hours after dissolution of [VO(TERTA)(DPQ)] in a 10%DMSO/90%water (v/v) solvent system indicating the disappearance of the [VO(TERTA)(DPQ)] 566.1667 <i>m/z</i> peak overtime and the appearance of the solvolysis species [VO(TERTA)(DMSO)] <sup>+</sup> at 412.1020 <i>m/z</i> .	<b>244</b>
<b>Figure 7.10</b>	ESI mass spectra of [VO(TERTCA)(DPQ)](PF <sub>6</sub> ) in (a): acetonitrile indicating the singular [M] <sup>+</sup> peak at 555.1563 <i>m/z</i> . (b):10%DMSO/90%water (v/v) – the [VO(TERTCA)(DPQ)] <sup>+</sup> peak at 555.1624 <i>m/z</i> is indicated, along with many solvolysis/decomposition species including the [DPQ+H] <sup>+</sup> peak at 233.0846 <i>m/z</i> . This illustrates the effect of solvent on the complex structure.	<b>245</b>
<b>Figure 7.11</b>	ESI mass spectra at 2 minutes and 24 hours after dissolution of [VO(MECA)(DPPZ)](Cl) in water, indicating the stability of the prominent molecular ion peak of 563.1601 <i>m/z</i> corresponding to [VO(MECA)(DPPZ)] <sup>+</sup> .	<b>247</b>
<b>Figure 7.12</b>	UV/visible spectra of [VO(TERTCA)(PHEN)](PF <sub>6</sub> ) (15 μM) in 10% v/v DMSO, 0.1 M Tris Buffer solution (pH = 7.1) at 37 °C at t = 1 min, 15 min, 1 hr and thereafter every hour until 18 hr after dissolution.	<b>248</b>
<b>Figure 7.13</b>	UV/visible spectra of [VO(TERTCA)(DPQ)](PF <sub>6</sub> ) (14 μM) in 10% v/v DMSO, 0.1 M Tris Buffer solution (pH = 7.1) at 37 °C, at t = 1, 15 min, 1 hr and thereafter every hour until 18 hr after dissolution.	<b>249</b>
<b>Figure 7.14</b>	UV/visible spectra of [VO(TERTA)(DPQ)] (30 μM) in 10% v/v DMSO,0.1 M Tris Buffer solution (pH = 7.1) at 37 °C at t = 1 min, 15 min, 1 hr and thereafter every hour until 18 hr after dissolution. <i>Inset</i> : Absorbance versus time plots at 396 nm.	<b>250</b>

Figure #	Title	Page #
<b>Figure 7.15</b>	$^{51}\text{V}$ NMR spectra indicating the progressive oxidation of [VO(PHA)(DPQ)] (2 mM) in DMSO- $d_6$ , over 21 hours. The minor peak appearing further upfield is attributed to the formation of vanadium oligomers.	<b>251</b>
<b>Figure 7.16</b>	$^{51}\text{V}$ NMR spectra indicating the progressive oxidation of [VO(TERTA)(DPQ)] (2 mM) in DMSO- $d_6$ , over 21 hours.	<b>252</b>
<b>Figure 7.17</b>	$^{51}\text{V}$ NMR spectra indicating the small amount of oxidised [VO(TERTCA)(PHEN)]( $\text{PF}_6$ ) (2 mM) in DMSO- $d_6$ , over 21 hours.	<b>253</b>
<b>Figure 7.18</b>	$^{51}\text{V}$ NMR spectra indicating the small amount of oxidised [VO(TERTCA)(DPQ)]( $\text{PF}_6$ ) (2 mM) in DMSO- $d_6$ , over 21 hours.	<b>253</b>
<b>Figure 8.1</b>	Plot of $-\text{Log}(\text{EC}_{50})$ data showing the cytotoxicity of the oxovanadium compounds synthesised in this work compared to commercially available drugs. The data is shown for cell line MDA-MB.	<b>263</b>
<b>Figure 8.2</b>	UV/visible absorbance spectra of [VO(MECA)(DPQ)]( $\text{PF}_6$ ) (15 $\mu\text{M}$ ) in the absence and presence of <i>ct</i> -DNA (0-65 $\mu\text{M}$ ) in 10% v/v DMSO/Tris buffer (pH 7.1) at 37 °C. <i>Inset</i> : Plots of $[\text{DNA}] / (\epsilon_a - \epsilon_f)$ versus $[\text{DNA}]$ for the titration of [VO(MECA)(DPQ)]( $\text{PF}_6$ ) with <i>ct</i> -DNA at 254 nm. This plot was used to calculate the intrinsic DNA binding constant of $2.8 \times 10^4 \text{ M}^{-1}$ .	<b>267</b>
<b>Figure 8.3</b>	UV/visible absorbance spectra of [VO(TERTA)(DPQ)] (30 $\mu\text{M}$ ) in the absence and presence of <i>ct</i> -DNA (0-165 $\mu\text{M}$ ) in 10% v/v DMSO, 100 mM Tris buffer (pH 7.1) at 37 °C. <i>Inset</i> : Plots of $[\text{DNA}] / (\epsilon_a - \epsilon_f)$ versus $[\text{DNA}]$ for the titration of [VO(TERTA)(DPQ)] with <i>ct</i> -DNA at 428 nm. Based on these spectral changes, a tentative DNA intrinsic constant of $6.5 \times 10^3 \text{ M}^{-1}$ was calculated.	<b>269</b>

<b>Figure #</b>	<b>Title</b>	<b>Page #</b>
<b>Figure 8.4</b>	UV/visible absorbance spectra of ethidium bromide (96 $\mu\text{M}$ ) as a function of <i>ct</i> -DNA concentration (0 – 929 $\mu\text{M}$ ) in 10% v/v DMSO and pH 7.0 Tris buffer at 25 °C. <i>Inset</i> : Plot of $(\epsilon_a - \epsilon_f) / (\epsilon_b - \epsilon_f)$ versus [DNA] and the non-linear fit for the titration of ethidium bromide with <i>ct</i> -DNA at 492 nm.	<b>271</b>
<b>Figure 8.5</b>	Fluorescence emission spectra of ethidium bromide bound to <i>ct</i> -DNA in Tris-HCl buffer (25 mM, pH 7.0) and maximum 5.1% DMSO in the presence of increasing concentrations of [VO(TERTCA)(DPQ)](PF <sub>6</sub> ) (0 – 18 $\mu\text{M}$ ) at 25 °C. <i>Inset</i> : Plot of emission intensity of the EB-DNA adduct versus concentration of [VO(TERTCA)(DPQ)](PF <sub>6</sub> ) with an exponential decay fit at 614 nm.	<b>273</b>
<b>Figure 8.6</b>	Effect of increasing concentrations of [VO(PHA)(DPQ)] and [VO(SOA)(DPQ)] (0 – 300 $\mu\text{M}$ ) on the relative viscosities of <i>ct</i> -DNA (237 $\mu\text{M}$ ) in 1X TAE buffer (pH 8.3) containing 10% v/v DMSO at 37 °C.	<b>276</b>
<b>Figure 8.7</b>	Effect of increasing concentrations of [VO(TERTA)(DPQ)], [VO(CLA)(DPQ)] and [VO(NAA)(DPQ)] (0 – 300 $\mu\text{M}$ ) on the relative viscosities of <i>ct</i> -DNA (237 $\mu\text{M}$ ) in 1X TAE buffer (pH 8.3) containing 10% v/v DMSO at 37 °C.	<b>277</b>
<b>Figure 8.8</b>	Effect of increasing concentrations of [VO(MEA)(DPQ)] ( <i>a</i> ) and [VO(MECA)(DPQ)](PF <sub>6</sub> ) ( <i>b</i> ) (0 – 200 $\mu\text{M}$ ) on the relative viscosities of <i>ct</i> -DNA (237 $\mu\text{M}$ ) in 1X TAE buffer (pH 8.3) containing 10% v/v DMSO at 37 °C.	<b>278</b>
<b>Figure 8.9</b>	Effect of increasing concentration of [VO(TERTCA)(DPQ)]-(PF <sub>6</sub> ) ( <i>b</i> ) (0 – 300 $\mu\text{M}$ ) on the relative viscosities of <i>ct</i> -DNA (237 $\mu\text{M}$ ) in 1X TAE buffer (pH 8.3) containing 10% v/v DMSO at 37 °C.	<b>279</b>

Figure #	Title	Page #
<b>Figure 8.10</b>	Effect of increasing concentrations of [VO(PHCA)(PHEN)]-(PF <sub>6</sub> ), [VO(MECA)(PHEN)](PF <sub>6</sub> ) and [VO(TERTCA)(PHEN)](PF <sub>6</sub> ) (0 – 300 μM) on the relative viscosities of <i>ct</i> -DNA (237 μM) in 1X TAE buffer (pH 8.3) containing 10% v/v DMSO at 37 °C.	<b>280</b>
<b>Figure 8.11</b>	[VO(PHA)(DPQ)] (shown as a green, capped-sticks model) docked into the minor groove of B-DNA: (a) molecular surface view of DNA. (b) DNA in Ball and stick view. Global energy = -53.94 kJ mol <sup>-1</sup> .	<b>283</b>
<b>Figure 8.12</b>	[VO(MEA)(DPQ)] (shown as a green, capped-sticks model) docked into the minor groove of B-DNA: (a) molecular surface view of DNA. (b) DNA in ball and stick view. Global energy = -51.01 kJ mol <sup>-1</sup> .	<b>283</b>
<b>Figure 8.13</b>	[VO(TERTA)(DPQ)] (shown as a green, capped-sticks model) docked into the minor groove of B-DNA: (a) molecular surface view of DNA. (b) DNA in ball and stick view. Global energy = -57.31 kJ mol <sup>-1</sup> .	<b>284</b>
<b>Figure 8.14</b>	[VO(MECA)(PHEN)] <sup>+</sup> (shown as a green, capped-sticks model) docked into the minor groove of B-DNA: (a) molecular surface view of DNA. (b) DNA in ball and stick view. Global energy = -51.50 kJ mol <sup>-1</sup> .	<b>284</b>
<b>Figure 8.15</b>	[VO(TERTCA)(PHEN)] <sup>+</sup> (shown as a green, capped-sticks model) docked into the minor groove of B-DNA: (a) molecular surface view of DNA. (b) DNA in ball and stick view. Global energy = -48.28 kJ mol <sup>-1</sup> .	<b>285</b>
<b>Figure 8.16</b>	[VO(MECA)(DPQ)] <sup>+</sup> (shown as a green, capped-sticks model) docked into the minor groove of B-DNA: (a) molecular surface view of DNA. (b) DNA in ball and stick view. Global energy = -49.80 kJ mol <sup>-1</sup> .	<b>285</b>

Figure #	Title	Page #
<b>Figure 8.17</b>	[VO(TERTCA)(DPQ)] <sup>+</sup> (shown as a green, capped-sticks model) docked into the minor groove of B-DNA: (a) molecular surface view of DNA. (b) DNA in ball and stick view. Global energy = -60.49 kJ mol <sup>-1</sup> .	<b>286</b>
<b>Figure 8.18</b>	[VO(MEA)(DPPZ)] (shown as a green, capped-sticks model) docked into the minor groove of B-DNA: (a) molecular surface view of DNA. (b) DNA in ball and stick view. Global energy = -66.73 kJ mol <sup>-1</sup> .	<b>286</b>
<b>Figure 8.19</b>	[VO(MECA)(DPPZ)] <sup>+</sup> (shown as a green, capped-sticks model) docked into the minor groove of B-DNA: (a) molecular surface view of DNA. (b) DNA in ball and stick view. Global energy = -63.00 kJ mol <sup>-1</sup> .	<b>287</b>
<b>Figure 8.20</b>	Hydrogen bonding of the oxygen atom from the <i>O,N,O'</i> -donor ligand in [VO(TERTA)(DPQ)] ( <i>a</i> ) and the nitrogen atom from the DPPZ ligand of [VO(MECA)(DPPZ)] <sup>+</sup> ( <i>b</i> ) to a H <sub>amine</sub> atom from a guanine residue of B-DNA. Hydrogen bonds are shown as pale-yellow dashed lines.	<b>288</b>
<b>Figure 8.21</b>	Agarose gel electrophoresis experiments showing cleavage of pcDNA_APP (0.15 μg) by [VO(MECA)(DPQ)](PF <sub>6</sub> ) and [VO(TERTCA)(DPQ)](PF <sub>6</sub> ) above concentrations of 50 μM in comparison to [VO(SOA)(DPQ)], [VO(TERTA)(DPQ)] and [VO(TERTCA)(PHEN)](PF <sub>6</sub> ), which show no cleavage. Incubation was in 1X TAE buffer (pH 8.0) containing 10% DMSO, at 37 °C, for 30 minutes.	<b>290</b>
<b>Figure 8.22</b>	The converging concentration-dependent effect of [VO(TERTCA)(DPQ)](PF <sub>6</sub> ) on pcDNA_APP plasmid DNA (0.15 μg) in 1X TAE buffer (pH 8.0) containing 10% v/v DMSO incubated at 37 °C for 30 min. The intensities were measured using the ImageJ software.	<b>291</b>

<b>Figure #</b>	<b>Title</b>	<b>Page #</b>
<b>Figure 8.23</b>	Agarose gel electrophoresis pattern showing cleavage of pcDNA_APP (0.15 µg) by [VO(MECA)(DPQ)](PF <sub>6</sub> ) and [VO(TERTCA)(DPQ)](PF <sub>6</sub> ) (300 µM) in comparison to VOSO <sub>4</sub> and the MECA, TERTCA and DPQ ligands (300 µM). Incubation was in 1X TAE buffer (pH 8.0) containing 10% v/v dmsO at 37 °C for 30 minutes.	<b>292</b>
<b>Figure 8.24</b>	Agarose gel electrophoresis pattern showing cleavage of pcDNA_APP (0.15 µg) by [VO(MECA)(DPQ)](PF <sub>6</sub> ) (300 µM) and [VO(TERTCA)(DPQ)](PF <sub>6</sub> ) (300 µM). Incubation was in 1X TAE buffer (pH 8.0) containing 10% v/v dmsO at 37 °C for 15, 30, 45, 60, 75, 90, 105 and 120 minutes.	<b>293</b>
<b>Figure 8.25</b>	The converging time-dependent effect of [VO(TERTCA)(DPQ)](PF <sub>6</sub> ) and [VO(MECA)(DPQ)](PF <sub>6</sub> ) (300 µM) on pcDNA_APP plasmid DNA (0.15 µg) in 1X TAE buffer (pH 8.0) containing 10% v/v DMSO incubated at 37 °C for 15, 30, 45, 60, 75, 90, 105 and 120 minutes. The intensities were measured using the ImageJ software by Alexandré Delport (Biochemistry, UKZN).	<b>294</b>
<b>Figure 8.26</b>	Agarose gel electrophoresis pattern showing cleavage of pcDNA_APP (0.15 µg) by [VO(MECA)(DPQ)](PF <sub>6</sub> ) (150 µM) in the presence of various additives. Incubation was in 1X TAE buffer (pH 8.0) containing 10% v/v dmF at 37 °C for 60 minutes. Lane 1: DNA control; Lane 2: DNA + 10% v/v DMF; Lane 3: DNA + [VO(MECA)(DPQ)](PF <sub>6</sub> ); Lane 4: DNA + [VO(MECA)-(DPQ)](PF <sub>6</sub> ) + DABCO (0.5 mM); Lane 5: DNA + [VO(MECA)(DPQ)](PF <sub>6</sub> ) + DMSO (10% v/v).	<b>296</b>

<b>Figure #</b>	<b>Title</b>	<b>Page #</b>
<b>Figure 8.27</b>	Agarose gel electrophoresis pattern of pcDNA_APP (0.15 $\mu$ g) with [VO(MEA)(DPQ)] (V) (150 $\mu$ M) in the absence (lane 6) and presence of various additives (H <sub>2</sub> O <sub>2</sub> (30 mM); DABCO (0.5 mM); 10% and 20% v/v DMSO. Incubation was in 1X TAE buffer (pH 8.0) containing 10% dmf at 37 °C for 60 minutes. V = [VO(MEA)(DPQ)].	<b>297</b>
<b>Figure 8.28</b>	EPR spectra of [VO(MEA)(DPQ)] at room temperature in acetonitrile ( <i>a</i> ) and of [VO(MEA)(DPQ)] (0.5 mM) following its reaction with H <sub>2</sub> O <sub>2</sub> (100 mM) in the presence of DMPO (50 mM) in acetonitrile ( <i>b</i> ).	<b>299</b>
<b>Figure 9.1</b>	[VO(ONN)(DPQ)](PF <sub>6</sub> /Cl) oxovanadium complexes with various substituents on the tridentate ligand where R = H, Cl, OH, CH <sub>3</sub> .	<b>311</b>

## *List of Schemes*

<b>Scheme #</b>	<b>Title</b>	<b>Page #</b>
<b>Scheme 2.1</b>	Synthesis of 1,10-phenanthroline-5,6-dione via oxidation of 5-amino-1,10-phenanthroline.	<b>63</b>
<b>Scheme 2.2</b>	One-pot synthesis of 1,10-phenanthroline-5,6-dione as reported by Yamada and co-workers.	<b>64</b>
<b>Scheme 2.3</b>	Formation of a Schiff base from an aldehyde or ketone and primary amine.	<b>66</b>
<b>Scheme 2.4</b>	Mechanism for imine bond formation from an aldehyde and primary amine.	<b>66</b>
<b>Scheme 2.5</b>	Schiff base condensation reaction of 1,10-phenanthroline-5,6-dione with ethylenediamine to form DPQ.	<b>67</b>
<b>Scheme 2.6</b>	Schiff base condensation reaction of 1,10-phenanthroline-5,6-dione with 1,2-phenylenediamine to form DPPZ.	<b>68</b>
<b>Scheme 2.7</b>	Schiff base condensation reaction between salicylaldehyde and 2-aminophenol substituted in the 4-position to form <i>O,N,O'</i> -tridentate Schiff base ligands. These ligands will later be coordinated to oxovanadium(IV).	<b>69</b>
<b>Scheme 2.8</b>	Enol-keto tautomerism of <i>O,N,O'</i> -tridentate Schiff base ligands.	<b>70</b>
<b>Scheme 2.9</b>	Schiff base condensation reaction of 1-methyl-2-imidazole carboxaldehyde and 4-substituted amino phenol to form <i>O,N,N'</i> -tridentate Schiff base ligands.	<b>70</b>
<b>Scheme 2.10</b>	Synthetic procedure to form the neutral oxovanadium(IV) DPQ complexes.	<b>73</b>
<b>Scheme 2.11</b>	Synthetic procedure to form the oxovanadium(IV) DPPZ neutral complex.	<b>74</b>
<b>Scheme 2.12</b>	Conversion of vanadyl sulfate to vanadyl chloride.	<b>75</b>
<b>Scheme 2.13</b>	Synthetic procedure to form the cationic oxovanadium(IV) PHEN, DPQ and DPPZ complexes.	<b>77</b>
<b>Scheme 8.1</b>	Spin-trapping of hydroxyl radicals to produce the DMPO-OH adduct.	<b>298</b>

## *List of Tables*

<b>Table #</b>	<b>Title</b>	<b>Page #</b>
<b>Table 1.1</b>	DNA intrinsic binding constants ( $K_b$ ) and related IC <sub>50</sub> values of oxovanadium(IV) hydrazide complexes against SH-SY5Y and MCF-7 human cancer cell lines after a 48-hour incubation, measured by MTT assay. Each IC <sub>50</sub> value expressed as the mean $\pm$ standard deviation of three independent experiments.	<b>33</b>
<b>Table 4.1</b>	Frequencies (cm <sup>-1</sup> ) of the imine C=N stretching vibrations in the tridentate ligands, and the neutral and cationic complexes.	<b>131</b>
<b>Table 4.2</b>	Selected frequencies (cm <sup>-1</sup> ) of V=O, V-O, V-N and P-F stretching vibrations in the neutral and cationic complexes.	<b>134</b>
<b>Table 4.3</b>	Summary of $\lambda_{\max}$ (nm) and $\epsilon$ (M <sup>-1</sup> cm <sup>-1</sup> ) values for the LMCT and $\pi \rightarrow \pi^*$ bands of the neutral oxovanadium(IV) complexes.	<b>138</b>
<b>Table 4.4</b>	Summary of $\lambda_{\max}$ (nm) and $\epsilon$ (M <sup>-1</sup> cm <sup>-1</sup> ) values for the LMCT and $\pi \rightarrow \pi^*$ bands of the cationic oxovanadium(IV) complexes.	<b>141</b>
<b>Table 4.5</b>	$g$ -Factors of the VO <sup>2+</sup> complexes in the solid-state at 298 K.	<b>148</b>
<b>Table 4.6</b>	$g_{iso}$ -Values of the VO <sup>2+</sup> complexes in either dichloromethane or acetonitrile (as indicated) at room temperature.	<b>150</b>
<b>Table 5.1</b>	Reported tautomers in the reported structures of PHA.	<b>158</b>
<b>Table 5.2</b>	Reported X-ray crystal structures of MEA, CLA and TERTA.	<b>159</b>
<b>Table 5.3</b>	Reported C-O bond lengths (Å) of PHA, MEA, CLA and TERTA.	<b>159</b>
<b>Table 5.4</b>	Selected torsion angles for SOA and NAA.	<b>161</b>
<b>Table 5.5</b>	Selected bond lengths (Å) for SOA and NAA.	<b>162</b>
<b>Table 5.6</b>	Selected bond angles (°) for SOA and NAA.	<b>163</b>
<b>Table 5.7</b>	Intramolecular hydrogen bond lengths (Å) and bond angles (°) for SOA and NAA.	<b>164</b>
<b>Table 5.8</b>	Bond parameters describing the intermolecular interactions of SOA and NAA.	<b>165</b>

<b>Table #</b>	<b>Title</b>	<b>Page #</b>
<b>Table 5.9</b>	Reported X-ray crystal structures of 2-aminophenol-derived Schiff Base Ligands.	<b>167</b>
<b>Table 5.10</b>	Selected crystal data for the <i>O,N,N'</i> Schiff Base Ligands.	<b>168</b>
<b>Table 5.11</b>	Selected bond lengths (Å) and angles (°) for PHCA and PHCA·0.5H <sub>2</sub> O.	<b>171</b>
<b>Table 5.12</b>	Selected bond lengths (Å) and angles (°) for MECA, TERTCA and PHPHCA.	<b>172</b>
<b>Table 5.13</b>	Hydrogen bond lengths (Å) and bond angles (°) for the intermolecular interactions of PHCA, PHCA·0.5H <sub>2</sub> O MECA, TERTCA and PHPHCA.	<b>175</b>
<b>Table 5.14</b>	Selected bond lengths (Å) and angles (°) for [VO(CLA)(DPQ)] and [VO(TERTA)(DPQ)].	<b>181</b>
<b>Table 5.15</b>	$\pi$ - $\pi$ Interactions in [VO(TERTA)(DPQ)] and [VO(CLA)(DPQ)].	<b>184</b>
<b>Table 5.16</b>	Selected crystal data for the [VO(ONN)(PHEN)](PF <sub>6</sub> ) Complexes.	<b>186</b>
<b>Table 5.17</b>	Selected bond lengths (Å) and bond angles (°) for the [VO(ONN)(PHEN)](PF <sub>6</sub> ) complexes.	<b>188</b>
<b>Table 6.1</b>	Summary of the major TD-DFT-simulated (CH <sub>3</sub> CN solvent continuum) electronic transitions and oscillator strengths for the monomeric and dimeric structures of MECA and the corresponding molecular orbitals.	<b>210</b>
<b>Table 6.2</b>	Comparison of selected bond parameters for the solid-state and DFT-simulated structures of [VO(CLA)(DPQ)]. Atom numbers are indicated in the appended structure.	<b>214</b>
<b>Table 6.3</b>	C=N, V=O and V-O stretching frequencies (cm <sup>-1</sup> ) for the DFT-simulated and solid-state oxovanadium complexes.	<b>216</b>
<b>Table 6.4</b>	A comparison of selected dft-simulated V=O, V-O and V-N bond lengths (Å) for the analogous neutral and cationic oxovanadium(IV) complexes.	<b>218</b>

<b>Table #</b>	<b>Title</b>	<b>Page #</b>
<b>Table 6.5</b>	Partial NBO charges (e) of selected atoms in the neutral oxovanadium(IV) complexes.	<b>219</b>
<b>Table 6.6</b>	Partial NBO charges (e) of selected atoms in the cationic oxovanadium(IV) complexes.	<b>219</b>
<b>Table 6.7</b>	Summary of the major TD-DFT-simulated (CH <sub>3</sub> CN solvent continuum) electronic transitions, oscillator strengths and the corresponding molecular orbitals for [VO(MEA)(DPQ)].	<b>223</b>
<b>Table 6.8</b>	Summary of the major TD-DFT-simulated (CH <sub>3</sub> CN solvent continuum) electronic transitions, oscillator strengths and the corresponding molecular orbitals for [VO(MECA)(DPQ)] <sup>+</sup> .	<b>224</b>
<b>Table 6.9</b>	Energy gap (in eV) between the frontier molecular orbitals for the oxovanadium(IV) compounds.	<b>227</b>
<b>Table 8.1</b>	EC <sub>50</sub> of cisplatin (control) and oxovanadium(IV) compounds against healthy and cancer cell lines. Selectivity index of the cationic oxovanadium compounds towards various tumour cell lines.	<b>261</b>
<b>Table 8.2</b>	Selectivity index of the cationic oxovanadium compounds towards various tumour cell lines.	<b>264</b>
<b>Table 8.3</b>	Apparent DNA Binding Constants ( $K_{app}$ ) for selected neutral and cationic oxovanadium(IV) complexes.	<b>274</b>
<b>Table 8.4</b>	Lowest global energy states for the docking of selected neutral and cationic oxovanadium(IV) species into B-DNA.	<b>281</b>

## Chapter One: Introduction

### 1.1 Preface

Cancer (abnormal cells that divide uncontrollably) is one of the main causes of death in humans.<sup>1</sup> The discovery of the antitumour activity of *cis*-diamminedichloroplatinum(II) (cisplatin) by Rosenberg *et al.* in the 1960s led to the realisation that transition metal complexes offer real possibilities for the discovery of novel anticancer drugs.<sup>2-5</sup> However, the toxic side effects, narrow range of antitumour activity and high rates of resistance of cisplatin led to an increase in the search for more effective and less toxic anticancer drugs.<sup>6-16</sup> To date, there has been limited success in developing broad-spectrum platinum-based anticancer agents capable of overcoming drug resistance with fewer side effects.<sup>17,18</sup> Current research in the field of metallopharmaceuticals has thus shifted to coordination compounds of other transition metals such as titanium, gold, germanium, copper, iron, ruthenium, cobalt and vanadium.<sup>19</sup>

In this work, oxovanadium(IV) has been selected as the metal centre for the design of novel anticancer agents. Vanadium is a biocompatible metal ion with antidiabetic, antiparasitic and cytotoxic properties.<sup>20,21</sup> The V<sup>IV</sup>O<sup>2+</sup> core was selected due to its stability in cells and lower toxicity in comparison to other oxidation states of vanadium.<sup>22-24</sup> Coordination of ligands to the oxovanadium(IV) centre has been shown to improve anticancer activities in comparison to the free ligands and VO<sup>2+</sup> starting material.<sup>2,25-41</sup> 1,10-Phenanthroline (PHEN), dipyrido[3,2-*d*:2',3'-*f*]quinoxaline (DPQ) and dipyrido[3,2-*a*:2',3'-*c*]phenazine (DPPZ) were chosen as the co-ligands in this work based on these ligand's ability to bind to DNA.<sup>20</sup> The mechanism of action of vanadium-based chemotherapeutics typically involves the VO<sup>2+</sup> complexes binding to DNA *via* non-covalent interactions, followed by oxidative DNA cleavage, which induces cell death.<sup>42</sup> DNA binding, cleavage and complex stability studies were, therefore, incorporated in this work to determine the strength and mode of DNA binding by the complexes. The mechanism of DNA cleavage of selected oxovanadium complexes was, additionally, assessed.

Tridentate Schiff base ligands were chosen to complete the distorted octahedron of the oxovanadium(IV) heteroleptic complexes. These ligands modulate the charge in the complexes and stabilise the  $VO^{2+}$  metal centre by blocking coordination sites. Two series of Schiff base ligands, tridentate  $O,N,O'$ - and  $O,N,N'$ -donor ligands, were used to create neutral and cationic complexes, respectively. Neutral and cationic complexes each have unique physicochemical properties which will influence their behaviour in a biological environment.<sup>43</sup> Neutral complexes tend to cross biological membranes more efficiently.<sup>44,45</sup> The cationic charge of the second series of complexes was designed to target the negatively charged sugar-phosphate backbone of DNA.<sup>46,47</sup>

The anticancer potential of the oxovanadium complexes were evaluated by *in vitro* cytotoxicity assays against breast, cervical, neuroblastoma carcinoma and healthy cell lines. The selectivity index of the chelates may then be established. Various electron-donating and electron-withdrawing substituents on the tridentate ligands were chosen to assess the electronic and steric effects of these substituents on cytotoxicity, aqueous stability, DNA binding and DNA-cleavage activities of the complexes.

## 1.2 Metals in Medicine

The application of metals in medicine can be traced back almost 5000 years.<sup>48</sup> The pharmaceutical industry has, however, traditionally been dominated by organic chemistry. The discovery of the antitumour activity of cisplatin (*Figure 1.1*) in the 1960s stimulated research in medicinal inorganic chemistry.<sup>5,12</sup>

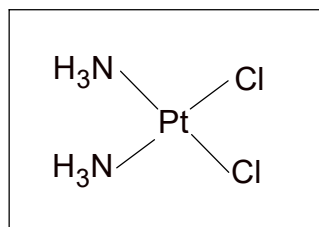


**Figure 1.1** The structure of *cis*-diamminedichloroplatinum(II) (cisplatin), the first metallodrug approved for clinical use in treating cancer.<sup>12</sup>

Cisplatin was the first drug used to cure testicular cancer with a cure rate of over 80% of testicular cancer patients. It was also the first compound to effectively treat small cell lung cancer. Patients with head, neck, ovarian and bladder cancers have also shown improved outcomes when treated with cisplatin. Cisplatin has additionally found application in the treatment of primary bone sarcomas and in upper gastrointestinal-tract, cervical and endometrial cancers.<sup>12,49</sup>

Unfortunately, cisplatin has dose-limiting toxicity, limited aqueous solubility, a limited spectrum of antitumour activity and high rates of intrinsic or acquired resistance.<sup>8,11,14,50</sup> The need for less toxic metallodrugs capable of treating a wider range of cancers while overcoming cisplatin-based resistance is therefore required. Initially, this search involved elucidating and understanding structure-activity relationships of cisplatin analogues, with the result that more than 3000 platinum complexes have been synthesised and tested for antitumour activity since the early 1970s.<sup>6,7,9,49,51</sup> The success of these analogues has been limited, with less than 1% entering into clinical trials. Only carboplatin and oxaliplatin (*Figure 1.2*) have been approved for clinical use worldwide. The compounds nedaplatin, lobaplatin and heptaplatin (*Figure 1.2*) have been approved for use in selected regions.<sup>4,18,52-54</sup>

The modest success of the cisplatin analogues has forced research to move away from designing metallodrugs which use a cisplatin architecture.<sup>55,56</sup> These include *trans*-platinum compounds, charged compounds, platinum(IV) complexes, multinuclear platinum complexes with bridging linkers and complexes with biologically active carrier ligands.<sup>4,18,49,57,58</sup>

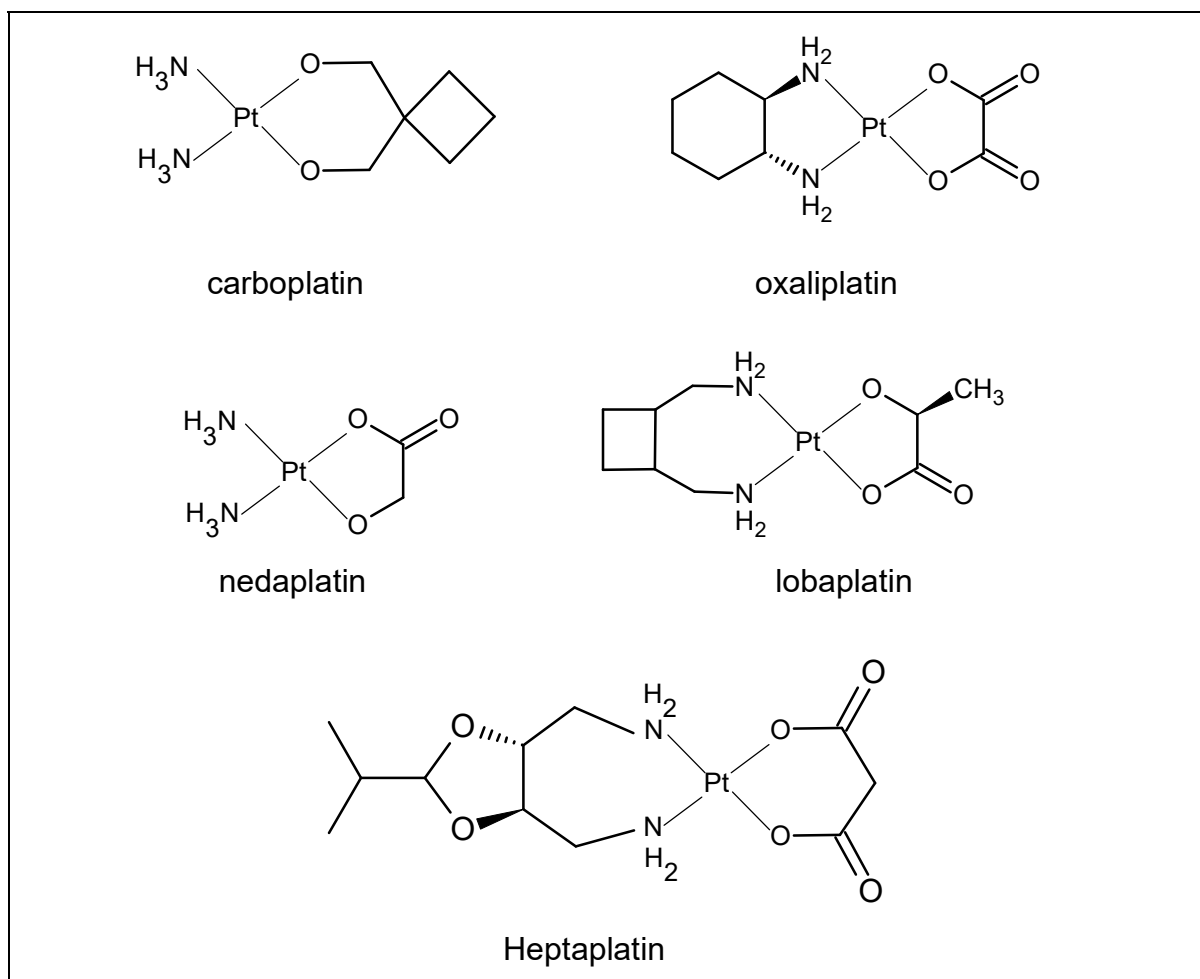


**Figure 1.2** Second- and third-generation platinum compounds approved for clinical use in treating cancer.<sup>52,54</sup>

Researchers have also turned to other metals such as ruthenium, gold, copper and vanadium.<sup>19</sup> The ruthenium(III) complexes NAMI-A and NKP-1339 (*Figure 1.3*) have entered into clinical trials.<sup>59-61</sup> However, despite the antimetastatic potential of NAMI-A, it was deemed too toxic to progress to market.<sup>59</sup> NKP-1339 was more successful with better efficacy and patient tolerability than NAMI-A.<sup>59,62</sup>

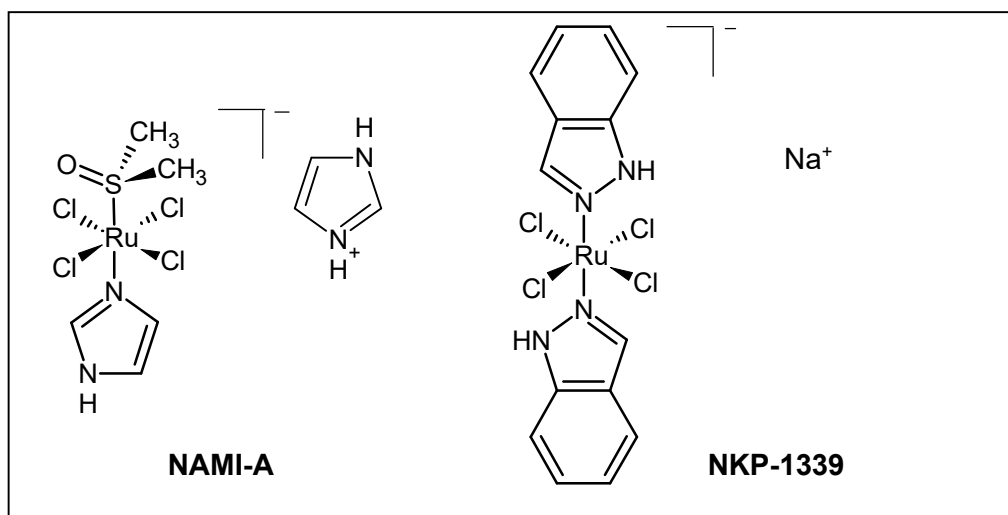


**Figure 1.3** NAMI-A and NKP-1339, Ru(III) chemotherapeutic agents selected for clinical trials.<sup>59</sup>

Vanadium-based anticancer drugs have become of considerable interest in recent years owed to the rich chemistry of vanadium with its varied coordination geometry and versatile redox and photophysical properties.<sup>21,63</sup> Research on vanadium has centered on the behaviour and function of vanadium in biological systems and the use of vanadium complexes in catalytic and pharmaceutical applications.<sup>64</sup>

### 1.3 Vanadium in Nature

Vanadium, a  $d^5$  transition metal, was first discovered in 1801 by del Rio in vanadinite, although misidentified at the time.<sup>65,66</sup> Sefström, who re-discovered the metal in 1830, named the metal after the Norse goddess of beauty and fertility.<sup>65,67-69</sup> Vanadium is the 22<sup>nd</sup> most abundant element in the earth's crust and the second most abundant transition element in marine environments.<sup>67</sup> It is found in soil, fossils, crude oil, fresh water, salt water, air and living organisms.<sup>28</sup>

Vanadium was first discovered in biological systems, in 1888, by Lippman in sugar beet plants.<sup>70</sup> In 1911, Henze reported a vanadium compound in the blood of sea squirts.<sup>71</sup> Vanadium also accumulates in fan worms and *Amanita* mushrooms, such as the fly agaric.<sup>72</sup> Interestingly, vanadium occurs in these organisms in the unusual forms of vanadium(III) and non-oxido vanadium(IV) compounds.<sup>72</sup>

Vanadium rich foods include shellfish, dill seeds, black pepper, fruits, mushrooms, grains, spinach and parsley.<sup>68</sup> This omnipresence of vanadium in food leads to ingestion being the main source of vanadium in the human body.<sup>66,68,73</sup> Vanadium can also be absorbed into the human body through inhalation and drinking water.<sup>72,74</sup> The average vanadium concentration in the human body of *ca.* 1 mg V per 70 kg human is non-toxic.<sup>66,72,74</sup> However, toxic effects can occur in industrial environments, where burning of fuels releases vanadium oxides that can be inhaled as dust particles loaded with VO<sub>x</sub>.<sup>66,68</sup> The limit value for no toxic effects on human health is 35 mg of V m<sup>-3</sup> breathing air.<sup>66,74</sup> The threshold for oral intake is 10 mg V per kg body mass per day and for intravenous application is 7 mg V kg<sup>-1</sup>.<sup>66,74</sup>

Despite vanadium compounds only been detected in a small number of organisms, vanadium has been established as a micronutrient required for normal metabolism, growth and development in mammals.<sup>72,73</sup> The discovery of vanadium nitrogenases in nitrogen fixation in 1933 and of vanadium-dependent haloperoxidase enzymes in marine macroalgae in 1983 further suggests that vanadium performs specific physiological functions in higher organisms.<sup>65-68,74-76</sup>

## ***1.4 Applications of Vanadium***

### **1.4.1 Technical Applications of Vanadium**

The first application of vanadium compounds was in 1835 in the making of black ink. Later, vanadium was utilised in oxidation catalysis from 1890.<sup>65,67</sup> The discovery of vanadate-dependent haloperoxidases stimulated new developments in vanadium catalyses, such as in sulfuric acid production and polymerisation catalysis.<sup>68,76</sup> Other technical applications of vanadium include high performance batteries, metal-organic frameworks for separation of gas mixtures, quantum information systems and as a component of superconducting alloys and as a steel additive. Environmental applications include detoxification of soils and water and using VO<sub>x</sub>-based catalysts in the conversion of exhaust gases.<sup>68,77</sup>

## 1.4.2 Medicinal Applications of Vanadium

The first biological experiments using vanadium began in 1876 by Priestley.<sup>78</sup> Priestley noted the inhibition of the germination of lettuce and mustard seeds by sodium vanadate and the toxic effects of large doses of sodium vanadate to animals such as cats.<sup>67</sup>

The medicinal applications of vanadium in humans began as early as 1897 with the use of sodium vanadate for the treatment of anaemia, tuberculosis, rheumatism, neurasthenia and diabetes mellitus.<sup>66,67,79,80</sup> The use of vanadium-based metallopharmaceuticals was then revived in the late 1970s when vanadate ( $\text{V}^{\text{V}}\text{O}_4^{3-}$ ) was found to inhibit sodium and potassium ATPase enzymes.<sup>23,81</sup> This prompted many enzyme studies. Vanadium has been revealed to exhibit a wide variety of biological functions, such as to activate protein tyrosine phosphorylation and protein kinases.<sup>22-24,73,82-86</sup>

One of the most important physiological roles discovered is the insulinomimetic and antidiabetic properties of vanadium complexes of oxidation states III, IV ( $\text{VO}^{2+}$ ) and V ( $\text{VO}_3^-$  or  $\text{VO}_4^{3-}$ ).<sup>22-24,82,84,87</sup> Most studies conclude that the inhibition of phosphatases by vanadate is the main mechanism by which these vanadium complexes have insulin enhancing effects.<sup>28,68</sup> Vanadate is similar in structure, charge and volume to phosphate and so can substitute phosphate in binding sites in enzymes and therefore inhibit enzyme activity.<sup>39,67</sup> Vanadate and the enzyme form a stable transition state (unlike phosphate) as vanadium can expand its coordination geometry to form stable 5-coordinate complexes when bound to the active site of the enzyme.<sup>28,66</sup>

Cohen *et al.* reported in 1995 on the treatment of non-insulin-dependent (type 2) diabetic human patients with vanadyl sulfate.<sup>88</sup> It was shown that well-tolerated doses of vanadyl sulfate improved glucose metabolism. Although some patients experienced mild gastrointestinal symptoms, this did not require the treatment to be terminated.<sup>66</sup> Goldfine and co-workers tested sodium metavanadate on insulin-dependent (type 1) and type 2 diabetic patients.<sup>89</sup> Improved insulin sensitivity was observed in type 2 and some of the type 1 patients but with mild gastrointestinal intolerance.<sup>67,80,82</sup> In 2013, Soveid *et al.* determined vanadyl sulfate was effective and safe for long-term therapy in type 1 diabetic patients.<sup>90</sup>

Variable responses in bioavailability and pharmacological response of vanadyl sulfate in humans have also been reported.<sup>82,91</sup>

The potential toxicity of inorganic vanadate species, the degradation of peroxido vanadates in the gastrointestinal tract, and the low absorption of inorganic vanadium ions in the gut led to studies on the insulin-enhancing properties of vanadium to focus on coordination compounds with organic ligands.<sup>80,91</sup> Chelated vanadium compounds have been shown to be more potent than free vanadium salts in facilitating insulin-like effects.<sup>92,93</sup> One such complex, bis(ethylmaltolato)oxovanadium(IV) (BEOV) (Figure 1.4), has successfully passed phase IIa clinical trials for diabetes treatment.<sup>65,66,68,94</sup>

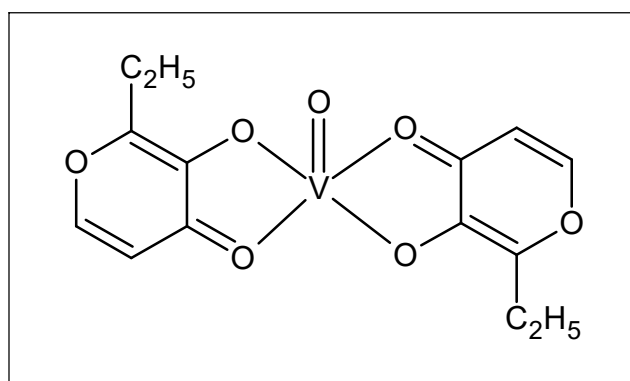


**Figure 1.4** Structure of BEOV, an oxovanadium(IV) complex that entered phase IIa human clinical trials for diabetes treatment.<sup>66</sup>

The results were promising with reduced blood glucose levels, enough stability for pro-drug use (which improves absorption) and BEOV was consistently well-tolerated by patients.<sup>74,94-96</sup> The tests have, however, been abandoned due to mild renal problems in some of the test patients and lack of financial incentives.<sup>66,80,82,94,95,97</sup> Recently, BEOV has been shown to alleviate neuronal apoptosis in a mouse Alzheimer's disease model.<sup>98</sup>

Other vanadium compounds that have been tested on diabetic and healthy humans include sodium orthovanadate, ammonium vanadyl tartrate and vanadium-albumin.<sup>73,97</sup>

The fact that vanadate-species interfere with phosphate-regulated enzymatic activity coupled with the positive results of vanadium compounds in the treatment of diabetic animals and humans, stimulated research into further medicinal applications of vanadium complexes.<sup>66,72</sup>

*In vitro* studies (with cell cultures) and *in vivo* studies (with various animals) have shown that vanadium complexes have potential in a wide variety of medicinal applications. These include treatment of cancer; parasitic tropical diseases such as leishmaniasis, Chagas' disease and amoebiasis; bacterial diseases such as tuberculosis; viral infections such as Dengue fever, SARS, HIV and influenza; antifungal infections; antiobesity; cardio-vascular and neuronal disorders. Vanadium complexes have also been found to reduce hyperlipidaemia, modulate blood pressure - restoring blood flow to tissues, and stimulating bone cell proliferation and bone collagen synthesis.<sup>2,24,28,39,66,72-74,83,99-105</sup> Vanadyl sulfate is also currently used as a food additive by body builders, although this practice is controversial with less than 1% of the vanadium absorbed.<sup>39,80,106</sup> The applications in cancer treatment are most relevant to the present study and are discussed in further detail in *Section 1.6*.

For a vanadium compound to be considered as a metallopharmaceutical - it must have low toxicity, balanced hydrophilicity versus lipophilicity and sufficient stability to survive passage from the blood serum into target cells and tissue structures.<sup>39</sup> The therapeutic or toxic effects will depend on how much vanadium reaches the cells, the type of tissue and if the original ligands are present or not.<sup>28</sup> Although numerous pharmacokinetic and toxicity studies of vanadium compounds in animal models have been performed, only a small number of clinical trials on human subjects have been conducted. Thus, little is known on the speciation and effects of vanadium compounds in the human body.<sup>28,73</sup> The uptake and distribution of vanadium in the body's organs is, therefore, poorly understood.<sup>28</sup>

## ***1.5 Speciation of Vanadium Compounds In Vivo***

The speciation of vanadium in biological systems is complex since vanadium can easily undergo reduction/oxidation reactions between oxidation states III, IV and V, expand its coordination sphere beyond tetrahedral geometries and readily form polymeric species.<sup>72,107</sup> There are numerous possible interactions between vanadium compounds and serum components; the main pathways of which are summarised in *Figure 1.5*.

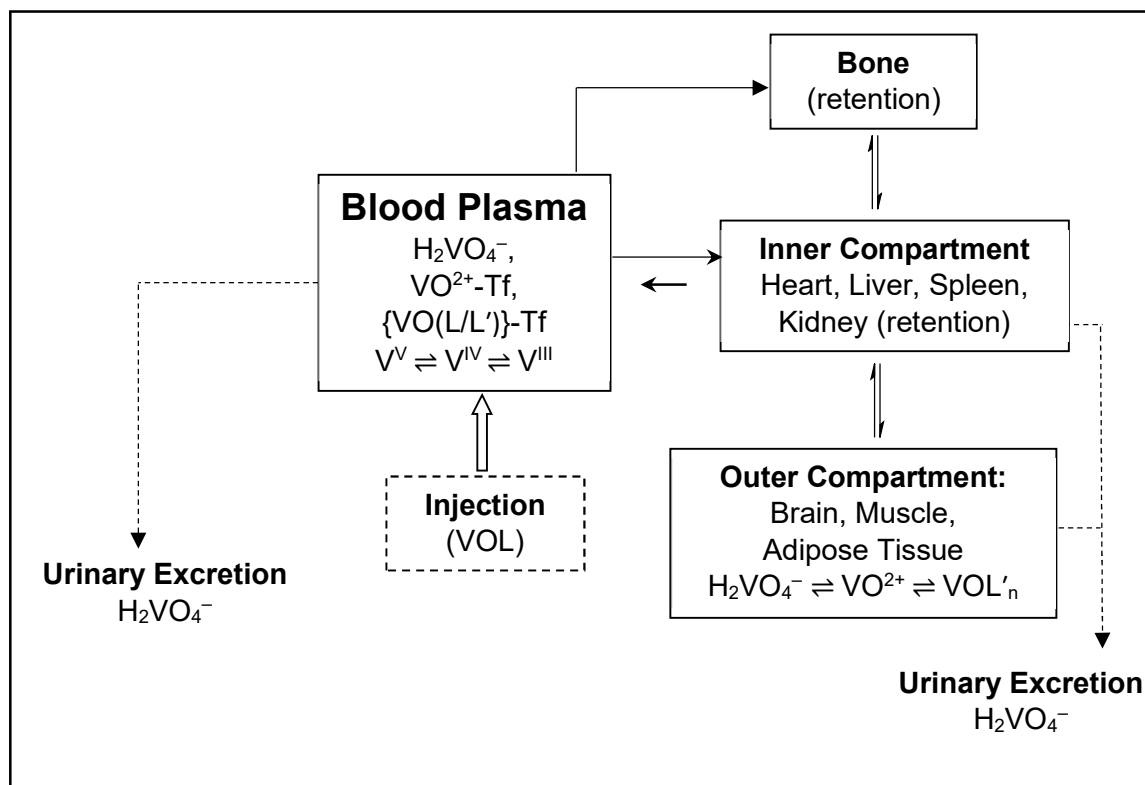


**Figure 1.5** Summary of the uptake, distribution and excretion of vanadium compounds *in vivo*. Tf = transferrin; L = ligand in vanadium pharmaceutical; L' = low molecular mass ligand present in blood serum;  $\{VO(L/L')\}$  =  $VO^{2+}$  complex with L and/or L'.<sup>39,66,80</sup>

Most commonly, vanadium pharmaceuticals are pro-drugs, where the active species is not the same as the administered compound. For example, vanadate ( $H_2V^VO_4^-$ ) is the bioactive form of the antidiabetic drug BEOV.<sup>68</sup>

When vanadium(IV) compounds are ingested, redox processes and ligand exchange take place in the slightly alkaline gastrointestinal tract, saliva and acidic stomach environment. Most of the compound is then converted to sparingly soluble  $V^{IV}O(OH)_2$ , which is unabsorbed and excreted.<sup>39,68,108,109</sup> The remaining vanadium enters the blood stream as vanadate ( $H_2V^VO_4^-$ ) and stable oxovanadium(IV) complexes either with endogenous ligands and/or the original ligand of the medication.<sup>39,74,80</sup>

Most of the vanadium compound that enters the blood, through injection or ingestion, undergoes speciation and redox interconversion between the +4 and +5 oxidation states.<sup>28,39,66,72,80</sup> One of the main products formed in the blood serum is vanadate ( $\text{H}_2\text{V}^{\text{V}}\text{O}_4^-$ ) through hydrolysis, ligand removal and oxidation of oxovanadium(IV) complexes.<sup>28,65</sup>

Vanadate ( $\text{V}^{\text{V}}$ ) and oxovanadium ( $\text{V}^{\text{IV}}$ ) can be interconverted by oxygen and reducing agents such as ascorbate, glutathione and NADH in the blood.<sup>28,67,74</sup> The other main species formed in the blood is vanadyl ( $\text{VO}^{2+}$ ) bound to transferrin (Tf, an iron transport protein).<sup>110-112</sup> Despite serum albumin being the most abundant protein in blood plasma, transferrin is the predominant ligand for exchange as it binds strongly to vanadyl and is one of the main constituents in blood.<sup>113</sup>

Most of the initial vanadyl complex will therefore release its original ligands and the  $\text{VO}^{2+}$  core will then coordinate to free ferric sites of transferrin.<sup>28,65,67,114,115</sup>  $\text{V}^{\text{IV}}\text{O-Tf}$  species are also susceptible to oxidation, despite glutathione being present.<sup>116</sup> At higher vanadium concentrations in the whole blood,  $\text{VO}^{2+}$  can also be coordinated to other high molecular mass proteins such as albumin and immunoglobulin G, low molecular mass constituents lactate and citrate as well as red blood cells.<sup>39,68,74,117</sup> At therapeutic concentrations, transferrin is the main transporter of vanadium drugs in the blood.<sup>28,80,94,117,118</sup>

The vanadium species are then transported from the blood plasma into blood and tissue cells.<sup>66</sup> It is distributed to tissues of the inner compartment (heart, liver, spleen and kidney) and outer compartment (brain, muscle, adipose tissues) and bones. Typically, within 24 hours vanadium concentrations are reduced to about 30% of the initial dose.<sup>66</sup> The resorbed vanadium is excreted *via* the urinary tract. Bone can serve as a long-term delivery system for vanadium as bone accumulates vanadate and vanadyl species. Bone can store vanadium for about a month.<sup>39,67,80,114</sup> Vanadium is also stored to some extent in the kidneys. A free ligand may then be used to chelate the speciated vanadate or  $\text{VO}^{2+}$  to mobilise the vanadium for excretion from the kidneys.<sup>74</sup>

The interaction of vanadium compounds with serum proteins impacts the drug distribution, biotransformation and mechanism of action of vanadium pharmaceuticals.<sup>67</sup> The administered complex may not reach the target tissue intact in appreciable amounts.<sup>67</sup>

The loss of the original ligands from vanadium complexes *in vivo* can be delayed – either kinetically or with outer-sphere interactions, such as hydrogen bonding or  $\pi$ -stacking between the original complex ligands and protein moieties. Using this approach, an appreciable amount of the complex may be taken up by a cell with the original ligands still intact.<sup>67,80</sup> The hydrophobic environment of cellular membranes may also delay disintegration. A compound that is less thermodynamically stable in the hydrophilic aqueous environments of the cytoplasm can be stabilised by entrapment in the hydrophobic environments near membranes or proteins.<sup>119</sup>

After speciation of vanadium complexes in the blood serum VO-Tf and  $\text{H}_2\text{VO}_4^-$  are the main vanadium species that target cells.<sup>66,74</sup> From the blood serum, a vanadium complex can enter a cell in one of four ways:<sup>28,74,80,120</sup>

- 1) Vanadate ( $\text{H}_2\text{VO}_4^-$ ) formed enters the cell through phosphate and/or sulfate anion channels.<sup>65,66,83,107</sup>
- 2) Transferrin-bound vanadium species enter cells *via* transferrin-receptor mediated endocytosis. These species include  $\text{VO}^{2+}$  or neutral or charged  $\text{V}^{\text{IV}}\text{O}(\text{L})$  species bound to transferrin after the oxovanadium complex has lost its ligands completely or in part in the blood. L is the original ligand of the vanadium complex or a low molecular mass blood serum constituent, such as lactate.<sup>68,80,117</sup>
- 3) A stable complex containing a lipophilic coordination sphere remains intact (at least in part) and crosses the cell membrane through diffusion.<sup>66</sup> Neutral vanadium complexes bound to proteins may also enter cells through passive diffusion.<sup>95</sup>
- 4) A stable complex which includes a biologically compatible moiety that is recognised by cell receptors may enter the cell through endo- or exocytosis.<sup>66</sup>

Once in the cell, the mode of action of the active species is dependent on the cellular distribution of the vanadium complex.<sup>119</sup> There are various intracellular speciation pathways including oxidation, reduction, hydrolysis, ligand exchange and re-coordination of the vanadium species.<sup>28,67</sup> A vanadium(IV) species may undergo hydrolytic degradation or be oxidised by reactive oxygen species (ROS) to vanadate in a cell.<sup>80,107</sup> Vanadate is reduced to vanadyl ( $\text{V}^{\text{IV}}\text{O}^{2+}$ ) in the cytoplasm, typically by the endogenous reducing agent glutathione. A small amount of  $\text{V}^{\text{IV}}(\text{OH})_3^-$  may also be present and  $\text{H}_2\text{VO}_4^-$  may also be re-formed. ATP present in cells also efficiently bonds to  $\text{VO}^{2+}$ .<sup>28,65,67,80,83,95,107</sup>

Vanadium(IV) may also be stabilised by NAD(P)H and ascorbate or other proteins.<sup>71, 104 72,107</sup> Vanadium exists mainly as the vanadyl VO<sup>2+</sup> cation in cells.<sup>104</sup>

Given the complex *in vivo* chemistry of vanadium species described above, and the fact that pharmaceuticals may be given chronically, more mechanistic studies and larger, longer-term clinical trials are required before any meaningful conclusions can be made on the effects of administering vanadium pharmaceuticals to humans.<sup>28,39,73,96,106,121</sup>

## ***1.6 Vanadium Compounds in Cancer Treatment***

Vanadium salts were found to have antineoplastic properties in 1965.<sup>122</sup> Later, in 1980, Thompson and co-workers found that vanadyl sulfate inhibited breast cancer growth.<sup>123</sup> Since then, research has shown that vanadium compounds have the potential to be a new class of non-platinum metal-based anticancer agents.<sup>2,73,83</sup> The lower costs and specific subcellular interactions of vanadium compounds show they have potential as selective and specific chemotherapeutics.<sup>28,97</sup>

Several vanadium-based compounds have shown promise during *in vitro* studies with low IC<sub>50</sub> values reported against several carcinoma cell lines.<sup>73,104</sup> Preclinical *in vivo* studies in animal models have shown vanadium compounds have great potential to prevent and treat a wide variety of cancers.<sup>31,73,104,124</sup> Experimental findings suggest that low doses of vanadium reduce the risk of developing breast, colon and liver cancer in humans.<sup>73,74</sup> Vanadium compounds are also able to reduce or have absent potency to induce cellular resistance.<sup>83</sup>

Contrarily, vanadium compounds have potential mutagenic, teratogenic, anti-apoptotic and suspected carcinogenic properties dependent on cell type, stage of cancer, type of vanadium compound and its dose.<sup>28,66,105,121,125</sup> This is because vanadium compounds activate numerous signalling pathways and transcription factors and so induce non-specific antagonistic effects on different cell structures.<sup>28,77</sup>

Vanadium compounds may exhibit some potential carcinogenic properties, but they are known to generally damage DNA in tumour cells to a greater extent than in normal cells, and vanadium accumulates in cancerous tissue more so than in normal tissue.<sup>28,31,66,121,126</sup>

Vanadium compounds also decrease harmful ROS.<sup>28,31,66,121,127</sup> Vanadium is not classified as a human carcinogen and toxic side effects of vanadium are quickly reversed upon stopping treatment.<sup>73</sup> Toxic effects may include mild gastrointestinal and renal problems, but these are mediated by low absorption rates of dietary vanadium and efficient desorption of vanadium from blood and body tissues.<sup>66</sup> There is no evidence yet to classify vanadium compounds as harmful if the administered doses are carefully considered.<sup>66</sup> Therefore, the application of vanadium compounds as anticancer agents is still viable.<sup>77</sup>

Novel vanadium-based anticancer agents include vanadium nanoparticles and vanadium compounds with oncolytic viruses.<sup>97,128</sup> Vanadyl compounds have also shown application as contrast agents to enhance *in vivo* magnetic resonance images for early detection of tumours.<sup>73</sup> Compounds of <sup>48</sup>V have shown potential as tumour-imaging agents in the imaging of small tumours due to the positron-emitting property of this radio isotope of vanadium.<sup>73,129,130</sup>

Studies have shown that vanadium complexes with organic ligands have lower toxicity, increased stability and bioavailability to comparable doses of inorganic vanadyl or vanadate salts alone.<sup>28,80,96,121,131</sup> Chelated metal compounds may have hydrophilic and lipophilic properties.<sup>132,133</sup> This allows for transport of the metal species to target cells and tissues. Lipophilic properties allow for cellular uptake of drugs across biological membranes, whereby the ligands act as a carrier system.<sup>44,45,65,80,132-135</sup> Lipophilicity is also an important parameter for intramolecular attractions, drug metabolism and biological activity.<sup>44,45</sup> The ligands designed to coordinate vanadium allow for fine-tuning of these properties as well as solubility; compatibility with physiological functions; recognition of peripheral groups by cell membrane receptors, and stability against hydrolysis, redox processes and ligand exchange.<sup>65,80,133-135</sup>

The first report of a vanadium compound with organic ligands that showed cytotoxic effects came in the early 1980s. This was developed by Köpf-Maier and co-workers and was a vanadium(IV) compound stabilised with two cyclopentadienide ligands – vanadocene dichloride (Cp<sub>2</sub>VCl<sub>2</sub> shown in *Figure 1.6*).<sup>136,137</sup>

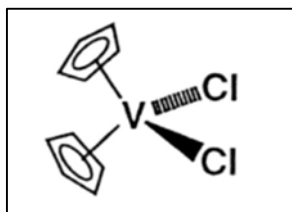


**Figure 1.6** Vanadocene dichloride, a metallocene with cytotoxic properties.<sup>138</sup>

Vanadocene dichloride has since been found to exhibit strong tumour-inhibiting properties against Ehrlich ascites tumours (breast carcinoma) in mice and in testicular cancer cell lines compared to other metallocenes, such as titanocene dichloride.<sup>28,73,139</sup> Vanadocene dichloride has also been found to significantly extend the life span of mice xenografted with leukaemia and exhibit antitumour effects against transplanted colon and lung cancers in mice.<sup>73,137</sup> A vanadium(IV) complex of 2-methylaminopyridine has also been reported to significantly decrease Ehrlich ascites tumour cell volume and viability in complex-treated mice.<sup>73,140</sup> These data highlight the potential of vanadium compounds as metallodrugs.

Köpf-Maier and Köpf were the first to systematically investigate the application of vanadium compounds as anticancer agents.<sup>136,141</sup> Two decades since these early reports, Uckun and co-workers patented a method for the treatment or prevention of metastatic cancer using vanadium complexes.<sup>142-144</sup> The patent involved vanadocene compounds of the type in *Figure 1.7*. Vanadocene ( $V^{IV}$ ) dihalides and pseudohalide type complexes exhibit significant cytotoxicity (comparable to cisplatin) and have spermicidal potential.<sup>133,145-147</sup>

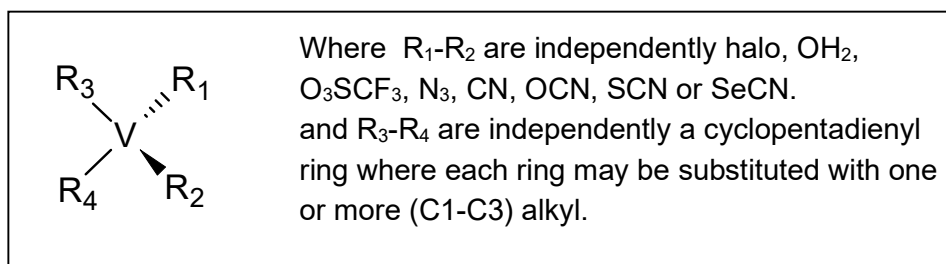


**Figure 1.7** Vanadocene compounds patented for the treatment of some cancers by Uckun and co-workers.<sup>142,143</sup>

## 1.6.1 Oxovanadium(IV) Anticancer Complexes

Of the six possible oxidation states of vanadium ranging from  $-3$  to  $+5$ , the oxidation states of  $+4$  and  $+5$  are the most biologically relevant.<sup>66,73</sup>  $V^{III}$  plays very limited role as  $V^{IV}$  is not easily reduced to  $V^{III}$  under biological conditions.<sup>66</sup> The vanadyl form ( $V^{IV}O^{2+}$ ) is used most extensively in the development of pharmaceuticals due to its stability in cells, efficacy in animal models and lower toxicity than  $V^V$ .<sup>66</sup> Therefore, for the purposes of this work, oxovanadium(IV) was chosen as the metal centre for the design of novel anticancer agents.

The coordination of ligands to an oxovanadium(IV) centre has been shown to improve anticancer activities in comparison to the free ligands against various carcinoma cell lines.<sup>2,25-31,33-41,125</sup> It is thought the anticancer activity of the respective ligand is enhanced upon coordination to the metal as the conjugation in the ligand skeleton is increased upon coordination.<sup>29</sup> Also, stronger hydrogen bonding improves biological activity through the partial positive charge of the metal influencing the ligand's ability to carry protons.<sup>30</sup> Coordination of ligands to  $VO^{2+}$  also enhanced the cytotoxic activities in comparison to the  $VO^{2+}$  starting material.<sup>26-28,31-34,38-41</sup>

There are numerous reports of oxovanadium(IV) complexes with organic ligands which have antitumour properties. Oxovanadium(IV) complexes have been found to be cytotoxic towards human breast, liver, leukemia, melanoma, myeloma, lung, ovarian, cervical, neuroblastoma, bladder, gastric, pancreatic, prostate, bone and colon carcinoma cell lines.<sup>25-27,29,32-34,36-38,40,41,43,63,77,100,120,135,139,148-175</sup>

Studies suggest that oxovanadium(IV) complexes are selectively cytotoxic towards cancerous cells in comparison to normal cells.<sup>26,32,33,38,40,100,120,156,157,161,170,172,176-179</sup> This high selectivity index is critical in the development of new drugs. Oxovanadium(IV) complexes have also been found to be more cytotoxic than cisplatin against various neoplastic cell lines including breast, liver, colorectal, neuroblastoma, and cisplatin-resistant ovarian carcinoma cell lines.<sup>33,34,37,63,152,156,177,178</sup> Oxovanadium(IV) complexes can also overcome multidrug resistance.<sup>156</sup> In addition, oxovanadium(IV) complexes have application in photodynamic therapy (PDT).<sup>167,180-184</sup>

*In vivo* anticancer studies of oxovanadium(IV) complexes include a ternary oxovanadium(IV) complex of a thiosemicarbazone ligand and a 2-(4-nitrophenyl)-imidazo[4,5-f]1,10-phenanthroline ligand that significantly inhibited tumour growth in cervical cancer xenograft mice models.<sup>26,27</sup>

Recent patents covering oxovanadium complexes highlight the renewed interest in vanadium anticancer agents. Bis(maltolato)oxovanadium(IV) (BMOV) and related vanadium-containing compounds such as BEOV, bis(isopropylmaltolato)oxovanadium(IV), (BIOV), and bis(n-butylmaltolato)oxovanadium(IV) (BnBOV) have been identified in recent research as therapeutic agents able to treat or prevent certain cancers such as ovarian, endometrial, brain, bone, lung and melanoma cancers in animals and humans.<sup>153</sup> Oxovanadium (IV) complexes of tetradentate hydrazone ligands have been shown to have applications in the treatment of Alzheimer's disease, diabetes and in preventing metastasis in various types of cancer and have been patented.<sup>185</sup>

## ***1.7 Anticancer Mechanisms of Vanadium Complexes***

While there is some understanding of the mechanism of action of the insulin-mimetic properties of vanadium, far less is known about vanadium's mechanism in cancer treatment.<sup>74</sup> The anticancer mechanisms of vanadium compounds have been investigated to some extent on a variety of cell lines and multiple modes of action have been proposed.<sup>28,31,39,43,66,67,73,74,77,83,104,172,186,187</sup> These different mechanisms are represented in *Figure 1.8*.

The growth of cancerous cells are inhibited *via* different pathways depending on the concentration of the vanadyl complex, the oxidation state of vanadium, the type of organic ligands coordinated to vanadium, the spatial structure of the complex and the type of cancer.<sup>32,172,187</sup> Oxovanadium(IV) complexes can induce apoptosis ("programmed cell death") and necrosis of cancer cells, cause cell cycle arrest, depolarisation of mitochondrial membranes of cancer cells, shift cancer cell metabolism and inhibit topoisomerase IB activity.<sup>26,31-33,38,120,149,155,164-166,173,174,176</sup> They also decrease the ratio of glutathione to oxidised glutathione and activate caspase 3, triggering apoptosis.<sup>26,31,33,169,170</sup>

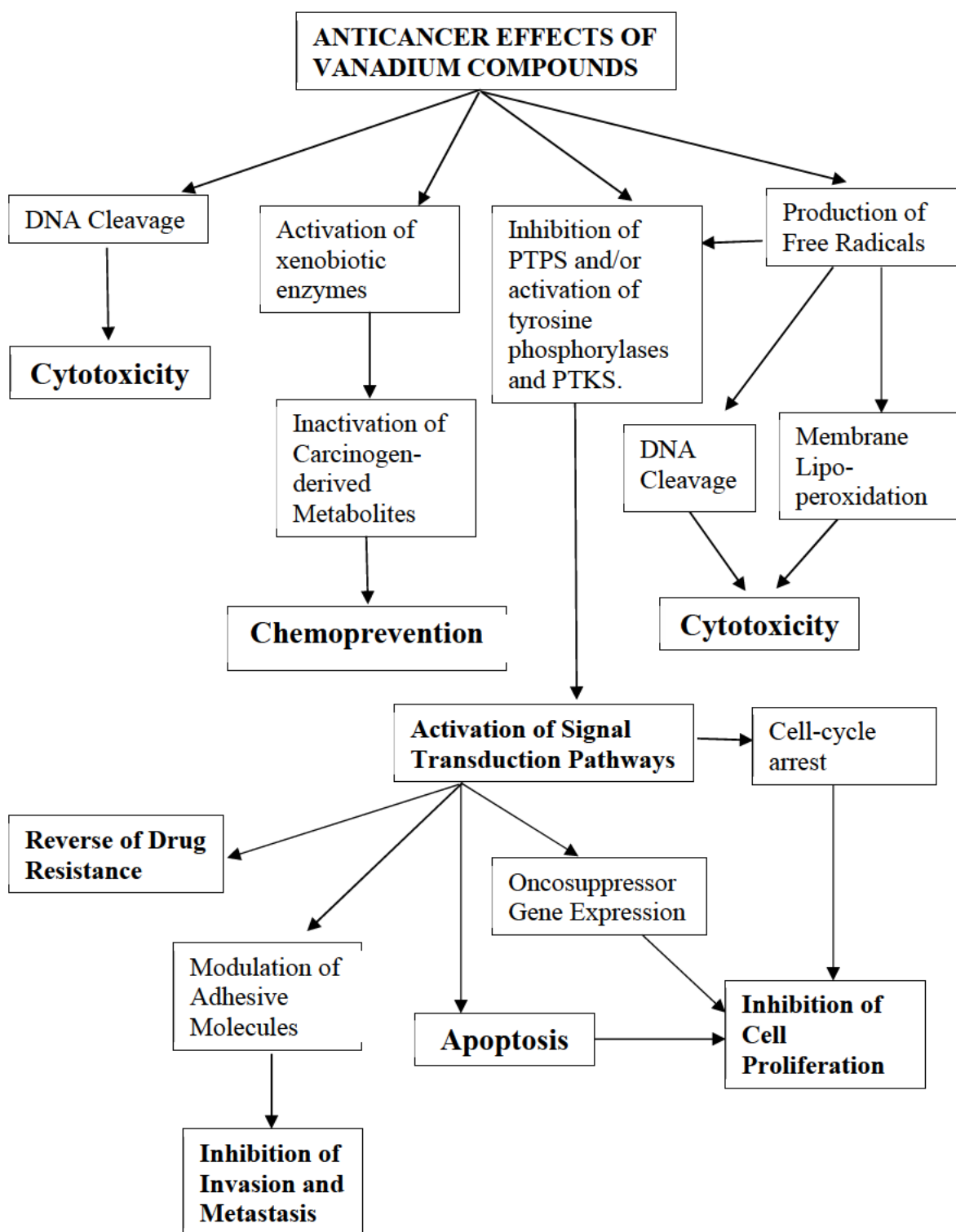


**Figure 1.8** Possible mechanisms of action for the antitumour effects of vanadium compounds. PTPS = protein tyrosine phosphatases and PTKS = protein kinases. Image reproduced from Evangelou.<sup>83</sup>

Oxovanadium compounds that are less stable are still able to exhibit cytotoxic effects through indirect modes of action. This includes interference of the speciated vanadium complex/vanadate inhibiting phosphatases and activating kinases.<sup>39,74</sup>

### 1.7.1 Reactive Oxygen Species (ROS)

The antiproliferative and cytotoxic effects of oxovanadium anticancer agents may also be caused by indirect interaction with DNA components. The fact that vanadium compounds, especially those with aromatic ligands, are active against certain forms of cancer and parasites which cause tropical diseases implies that DNA is the compounds' biological target.<sup>39</sup> The antitumor properties of oxovanadium complexes have further been found to be associated with their DNA cleavage activity, DNA binding abilities and DNA binding mode.<sup>26,34,35,40,162,188</sup>

DNA may be cleaved through either oxidative or hydrolytic cleavage. In hydrolytic cleavage, DNA is cut by hydrolysis of the phosphodiester bond. In oxidative cleavage, oxidation of deoxyribose sugars occurs through removal of a sugar hydrogen atom, or DNA nucleobases are oxidised by reactive oxygen species (ROS).<sup>42,99,181,189</sup>

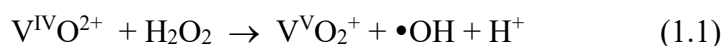
ROS such as singlet oxygen, superoxide, and hydroxyl radicals are generated through external co-reactants such as reducing or oxidising agents, for example, peroxide.<sup>181</sup> Peroxide can form in living systems through reduction of oxygen in the respiration chain, reduction of superoxide or dimerisation of hydroxyl radicals.<sup>67,121</sup>

Oxidative cleavage can also be photoactivated. In the type I pathway, direct electron transfer occurs from a DNA base to the photoexcited state of the complex, and in this process free radicals are produced.<sup>181</sup> This type of pathway is useful for hypoxic cancer cell environments.<sup>181</sup>

In the type II process, energy transfer occurs from the excited state of the photosensitiser to molecular oxygen in its triplet state to convert it to the reactive singlet oxygen state. Singlet oxygen then oxidises a DNA base, such as guanine.<sup>42,99,181</sup> To be effective the photosensitisers must show low dark cellular toxicity and cancerous cells must selectively uptake the photosensitiser over normal cells.<sup>181</sup>

In the photo-redox pathway, the redox-active photo-excited complex is oxidised causing reduction of cytosine, thymine or molecular oxygen to cytotoxic superoxide and hydroxyl radicals.<sup>42,99,181</sup> An oxovanadium(IV) complex may even undergo reduction, where the photo-activated oxovanadium(IV) complex forms a reactive V<sup>III</sup> species that can generate hydroxyl radicals.<sup>99,180</sup>

The cleavage of DNA caused by ROS leads to cell death.<sup>181</sup> Other effects of ROS include membrane lipoperoxidation, protein denaturation, cell membrane disintegration and membrane protein damage.<sup>34,83</sup> Free radical production can also cause systemic effects in organisms, some diametrically opposite, such as both antitumour and carcinogenic properties.<sup>28,121</sup> Interestingly, oxovanadium(IV) complexes can act as both scavengers and generators of reactive oxygen species depending on the pH and the structure of the ligands bound to vanadium.<sup>67,169,170,190</sup> The delivery of vanadium compounds into the DNA helix allows for oxidative cleavage of DNA to take place by ROS.<sup>19,181</sup> Superoxide and singlet oxygen ROS are formed when some vanadium species react with O<sub>2</sub>.<sup>66,67,80</sup> Hydroxyl radicals are generated in cells by the oxidation of vanadium components reacting with hydrogen peroxide in Fenton-type reactions. The Fenton mechanism is illustrated in *Equations 1.1* and *1.2*.<sup>28,65,67,83,107,191-198</sup>



Research into the interactions of oxovanadium complexes with DNA has increased dramatically in the last decade, as indicated by a literature search on Scifinder<sup>n</sup> (*Figure 1.9*).<sup>199</sup>

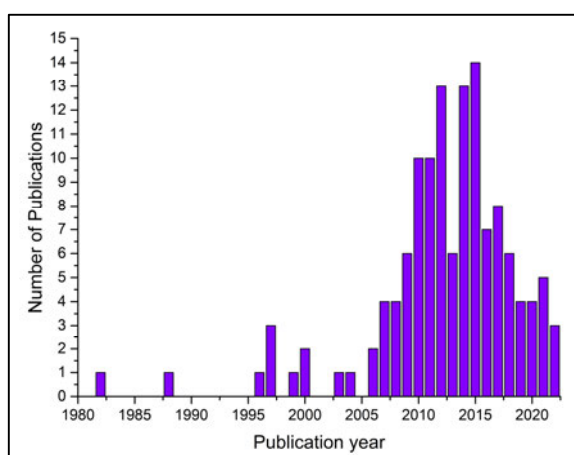


**Figure 1.9** Number of publications showing the surge in research into DNA interactions of oxovanadium compounds in the last decade.<sup>199</sup>

The study of the interaction of metal complexes with DNA forms the core of recent research in bioinorganic chemistry and was therefore included in the scope of this project.<sup>135,200,201</sup> Metal-based anticancer agents bind to DNA in covalent and various non-covalent modes of interaction.<sup>63</sup> These are discussed in *Section 1.8*.

## 1.8 DNA Binding Modes of Metallopharmaceuticals

### 1.8.1 Covalent Modes of Binding to DNA

A metal complex may bind to DNA by forming strong covalent bonds.<sup>181</sup> The key mechanism of the anticancer action of cisplatin is direct covalent binding of cisplatin fragments to DNA. Upon entry into the cell, the neutral form of cisplatin hydrolyses. The *cis*-[Pt(NH<sub>3</sub>)<sub>2</sub>]<sup>2+</sup> unit formed binds to DNA, preferentially at two neighbouring guanine bases at their N(7) atoms to form intrastrand cross-links (*Figure 1.10*).<sup>12,15,49,202</sup>

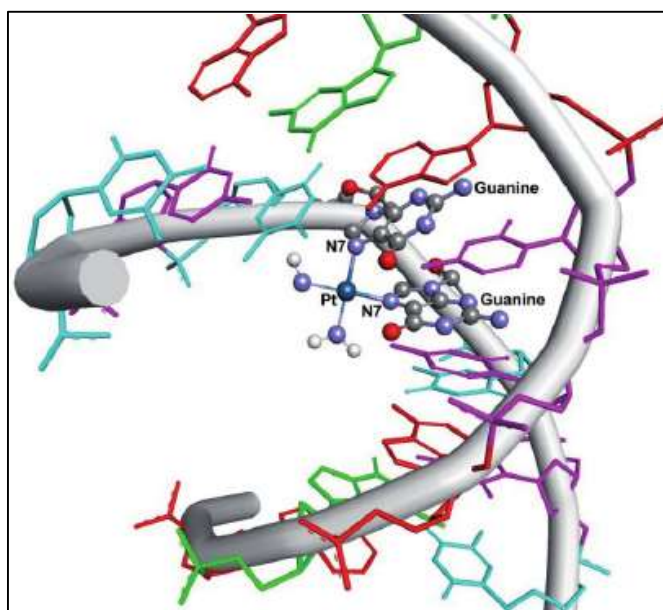


**Figure 1.10** Cisplatin intrastrand adduct with DNA at the N(7) atoms of guanine bases. Image reproduced from García-Ramos *et al.*<sup>203</sup>

The consequence of the bifunctional adduct formation is a distortion of the double helix structure of DNA.<sup>204</sup> The kinked DNA is recognised by proteins, causing the bending of the helix to increase significantly. This binding of proteins prevents DNA repair by nuclear excision repair enzymes, and eventually leads to cell death by apoptosis.<sup>8,205</sup>

The mechanism of action of vanadocenes was thought to be similar to that of cisplatin. The chloride ligands undergo hydrolysis while the cyclopentadienyl rings stay coordinated to the vanadium ion in biofluids.<sup>80</sup> It was proposed that the vanadocene moiety then directly binds to DNA by binding to the phosphate ester backbone of DNA to form outer-sphere complexes *via* a water group or *via* hydrogen bonds. This binding causes a kink in DNA which defunctionalises it and activates the tumour antigen p53 (a protein that suppresses tumours).<sup>31,39,47,65</sup> However, further research has indicated that vanadocene induces apoptosis through a yet unknown mechanism as the apoptotic signal is not triggered by primary DNA damage and does not require p53 induction.<sup>28,206</sup> Oxidative damage and inhibition of tyrosine phosphatase are possible mechanisms.<sup>31</sup>

## 1.8.2 Non-Covalent Modes of Binding to DNA

Covalent binding is not the only mechanism of action of cytotoxic metallopharmaceuticals. Despite few natural examples of non-covalent interactions between free-standing transition metal complexes and DNA, there are distinct advantages to this approach. The metal centre can act as an anchor for the ligands that may bear recognition elements for DNA and the transition metal centre allows for photophysical and electrochemical reactions rather than being only passive agents.<sup>207</sup> There are several non-covalent DNA binding modes of metal complexes, of which the most important are electrostatic, groove and intercalative binding (*Figure 1.11*).<sup>208</sup>

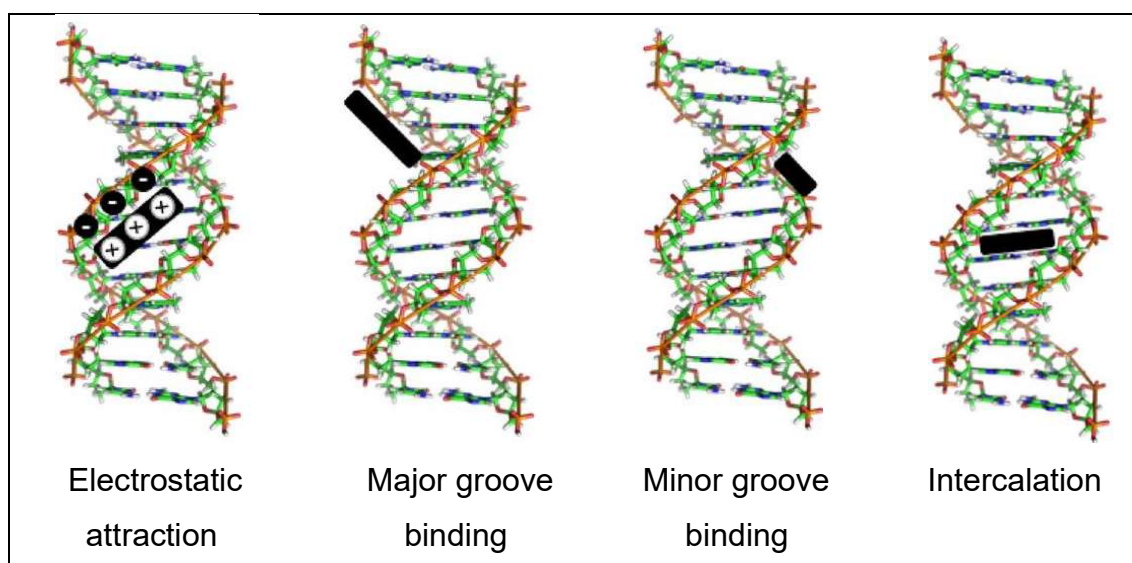


**Figure 1.11** Schematic representation of non-covalent binding modes between small molecules and DNA. Image reproduced from de Almeida *et al.*<sup>1</sup>

In electrostatic binding, the attraction is between a cationic metal complex and the negatively charged phosphate backbone of DNA. This binding is non-directional and so is generally weak.<sup>209</sup> Groove binding occurs when small metal complexes sit in either the major or minor groove of DNA, with intermolecular attractions to both the sugar-phosphate backbone and the functional groups of the nucleobases that are exposed at the bottom of the groove (*Figure 1.11* and *1.12*).<sup>209,210</sup> The functional groups of the exposed nucleobases are able to hydrogen bond to groove binders as either donor or acceptor groups. This can lead to highly stabilised DNA/drug conjugates.<sup>209</sup>

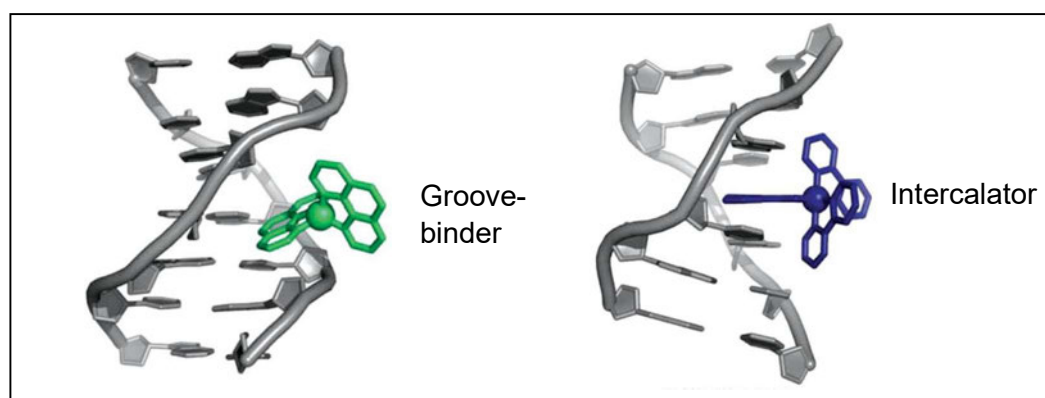


**Figure 1.12** Schematic representation of a groove-binding metal complex and a metallointercalator.<sup>207,209</sup> Image reproduced from Zeglis *et al.*<sup>207</sup>

Metal complexes with extended planar aromatic ligands can also intercalate into DNA, inducing a kink in the DNA.<sup>34,39,66,162</sup> In this mode of binding, the planar section of the complex inserts between two base pairs of DNA with the rest of the complex situated in the major or minor groove (*Figure 1.10* and *1.11*). The DNA backbone extends to accommodate the extra “base pair”. Intercalation leads to strong binding due to the interaction between the pi-systems of the intercalator and nucleobases. The binding strength can also be increased if the outer portion of the small molecule is oriented perpendicularly to the intercalated region and is able to simultaneously groove bind.<sup>209</sup>

### 1.9 Oxovanadium(IV) Complexes with Phenanthroline-Derived Co-ligands

Planar nitrogen-donor heterocyclic aromatic ligands such as 1,10-phenanthroline (PHEN), dipyrido[3,2-*d*:2',3'-*f*]quinoxaline (DPQ) and dipyrido[3,2-*a*:2',3'-*c*]phenazine (DPPZ) (*Figure 1.13*) enable vanadium (and indeed other metal) complexes to bind to DNA through intercalative or groove binding modes.<sup>2,20,21,34,42,99,100,113,134,135,167,171,182-184,211-226</sup> It has been consistently shown that the inclusion of phenanthroline-derived ligands improves the DNA binding affinity of oxovanadium(IV) complexes.<sup>227</sup> Phenanthroline-type ligands also enhance the lipophilic character of the complexes, enabling the drug to enter lipophilic cellular membranes.<sup>39</sup>

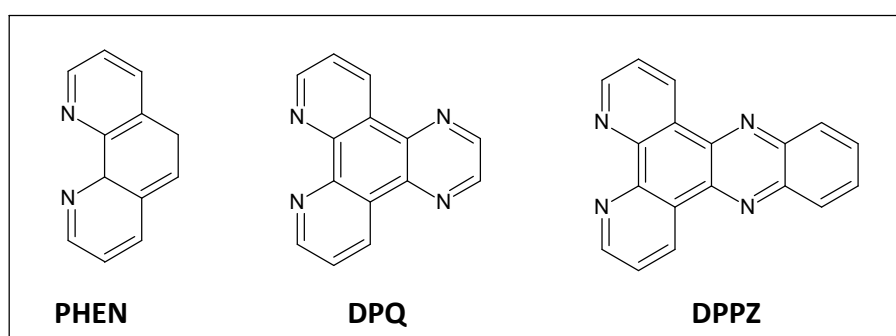


**Figure 1.13** Bidentate *N,N*-donor ligands, which are known to enhance DNA binding.<sup>21,167</sup>

Numerous oxovanadium(IV) complexes of phenanthroline and derivatives thereof have been shown to be cytotoxic towards neoplastic tissue both *in vitro* and *in vivo*.<sup>32,43,135,182,183,228</sup>

Exchanging the chloride ligands of vanadocene dichloride with phenanthroline has been found to stabilise the complex and improve cytotoxicity.<sup>31,229</sup> Oxovanadium(IV) complexes of *N,N*-bidentate ligands also have DNA photolase and chemical nuclease activity with high DNA binding affinities.<sup>19,21,158,162,171,180-183,215,230</sup> Antitumour activity of these metal complexes generally increases with increasing aromaticity of the *N,N*-donor ligand with the *N,N*-donor intercalator being mechanistically important to the biological activity.<sup>28,31,32,38,39,158,231</sup>

The patent by Uckun *et al.* included vanadium compounds with *N*-donor oligodentate aromatic ligands, such as PHEN.<sup>142-144</sup> The design of the vanadium compounds was based on the direct interaction of the stable vanadium-ligand fragments with the DNA of cancer cells.<sup>66,67,142,232,233</sup> Metvan,  $[\text{VO}(\text{SO}_4)(\text{Me}_2\text{-PHEN})_2]$  (Figure 1.14) has been identified as one of the most promising anticancer vanadium compounds with the potential to be the first vanadium-based compound used in chemotherapy.<sup>232,233</sup>

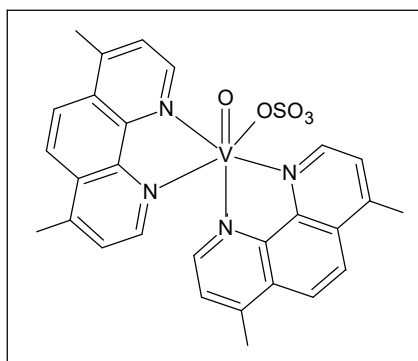


**Figure 1.14** Structure of Metvan, a promising oxovanadium(IV) anticancer agent.<sup>232</sup>

Metvan has antiproliferative properties, broad-spectrum anticancer activity, low toxicity to healthy cells and favourable pharmacodynamic features.<sup>28,73,232</sup> Metvan is cytotoxic, even at low doses, against numerous tumour cell lines including leukaemia, myeloma and solid tumour cells such as glioblastoma, breast, ovarian, prostate and testicular cancer, this includes testicular and ovarian cancers resistant to cisplatin.<sup>28,66,80,121,214,232-234</sup> Metvan also showed significant antitumour activity, delayed tumour progression and increased survival time in mouse xenograft studies of human glioblastoma and breast cancer.<sup>28,73,235</sup> The mechanism of action of Metvan is attributed to the intercalation of the PHEN ligands into DNA, generation of ROS, depletion of glutathione and loss of mitochondrial transmembrane potential, which collectively lead to apoptosis.<sup>28,121,214,232,233,236</sup>

PHEN, DPQ and DPPZ have been chosen to coordinate to the  $\text{VO}^{2+}$  core in the proposed structures for this work, based on the ability of oxovanadium complexes with planar *N,N*-bidentate ligands to bind DNA.

Metal complexes that have been found to bind DNA include those with a stable, rigid octahedral structure.<sup>207</sup> Schiff base ligands are used to increase stability of oxovanadium(IV) complexes with bidentate *N,N*-donor co-ligands.<sup>45,167,237</sup> Tridentate Schiff base ligands are preferred over bidentate Schiff bases to further increase stability of the complexes in culture media.<sup>45</sup> Schiff bases, themselves are models of biological systems and exhibit a wide range of physicochemical properties and so, could aid targeted delivery of the drug to DNA.<sup>17,132,223,238</sup> Metal complexes with rigid Schiff bases of aromatic systems enable tuning of the electronic effects of the complexes. This allows the complexes to be potential probes for nucleic acids with better DNA binding characteristics.<sup>2,100,186</sup> Metal complexes of Schiff bases have found application in a wide variety of fields including medicinal biological chemistry and catalysis.<sup>239</sup> Studies have shown that chelation of a Schiff base ligand and bidentate *N,N*-donor co-ligand to the oxovanadium(IV) core improves antibacterial, antifungal, antidiabetic, antitrypanosomal and antitumoural activity.<sup>28,36</sup>

### ***1.10 Ternary Oxovanadium(IV) Schiff Base Complexes of Phenanthroline-Derived Co-ligands***

Lipophilic, polar, electronic and steric factors of both the tridentate Schiff base and planar bidentate *N,N*-donor co-ligand influence interactions of ternary oxovanadium(IV) complexes with DNA.<sup>240</sup> The intercalative ability of the polypyridyl ligand influences the strength and type of binding of the ternary complexes to DNA.<sup>20,21,34,99,162,167,171,183,222,223</sup> Oxovanadium(IV) complexes of DPPZ bind to DNA primarily in an intercalative mode with intrinsic binding constants in the order of  $10^5 \text{ M}^{-1}$ .<sup>21,167</sup> The DPQ and PHEN complexes generally bind in a groove and/or surface binding fashion with intrinsic binding constants in the order of  $10^4 - 10^5 \text{ M}^{-1}$  for the DPQ complexes and  $10^4 \text{ M}^{-1}$  for the PHEN complexes.<sup>2,20,21,34,42,99,167,183,211,215,216,222,223,241,242</sup> These data highlight the link between the extent of ligand aromaticity and the affinity of the metal chelate towards DNA.

Numerous oxovanadium(IV) complexes of *N,N*-bidentate polypyridyl-derived and *O,N,S*-donor<sup>20,27,40,41,63,149,162,171,173,174,188,215,243-246</sup> or *O,N,O'*-donor<sup>2,21,26,34-36,38,43,45,100,113,127,150,165,167,176,178,189,211-213,216-219,221,225-227,237,238,240-242,247-286</sup> Schiff base ligands have been reported. Ternary Schiff base complexes of the type [VO(ONN)(NN)],<sup>36,287,288</sup> [VO(OOO)(NN)]<sup>32,158,231,289-294</sup> and [VO(OSO)(NN)]<sup>32,289</sup> have also been reported.

Hard acid metal ions preferentially bind to hard base ligands according to Pearson's principle.<sup>295</sup> The VO<sup>2+</sup> core is considered a hard acid and so the vanadium core preferentially binds to hard atoms such as oxygen.<sup>66,296</sup> Thiodiacetate [VO(OSO)(NN)] complexes have been found to be less stable than corresponding oxydiacetate [VO(OOO)(NN)] analogues due to the softer nature of sulfur in the thioether donor atom as compared to the oxygen donor atom.<sup>231</sup> *O,N,O'*-donor Schiff base ligands were chosen over *O,N,S*-donor Schiff base ligands to coordinate to the VO<sup>2+</sup> centre to form the neutral complexes in this work, in order to stabilise the VO<sup>2+</sup> metal centre and block coordination sites. The design of the complexes is similar to the framework of Prasad *et al.* in *Figure 1.15(a)*.<sup>167</sup>

Changing the architecture of ligands coordinated to vanadium can increase the antitumor activity of oxovanadium complexes.<sup>40</sup> The type of substituents, steric bulk and presence of aromatic moieties on the tridentate Schiff base ligand of ternary oxovanadium complexes have been found to influence the DNA binding affinity of the complexes.<sup>2,21,34,113,167,171,211,215,217,218,241</sup> These factors are discussed in further detail below for neutral [VO(ONO)(NN)], and cationic oxovanadium(IV) complexes in *Sections 1.10.1* and *1.10.2*, respectively.

### 1.10.1 *O,N,O'*-Tridentate Schiff Base Oxovanadium(IV) Complexes with Phenanthroline-Derived Co-ligands

Ternary oxovanadium(IV) complexes of *O,N,O'*-tridentate and planar *N,N*-bidentate co-ligands have been reported to have antidiabetic,<sup>45,221,225,226,269</sup> antiparasitic,<sup>36,100,240,247,248</sup> antitumour<sup>2,21,34,36,38,100,150,167,242,250</sup> and catalytic properties.<sup>189,252,261,268,273,279,282,286</sup>

[VO(ONO)(NN)] complexes for which DNA binding studies have been reported include those depicted in *Figures 1.15* and *1.16*.<sup>2,21,34,35,113,167,211-213,216-219,227,241,242,272</sup> The complexes in *Figures 1.15 (e), (j)* and *Figures 1.16 (h) – (k)* have also been determined to bind to bovine serum albumin.<sup>113,216,241</sup> Studies on the interactions of transition metal complexes with bovine serum albumin are important as serum albumins are the most abundant proteins in blood and have the ability to transport and deposit drugs.<sup>113,242</sup> Such studies can provide information on the features that determine the therapeutic effect of vanadium drugs.<sup>113,241</sup>

The complexes in *Figures 1.15 (d), (f), (g)* and in *Figures 1.16 (b), (c), (d), (f) – (k)* bound to DNA intercalatively.<sup>2,34,35,212,213,217,218,241,272</sup> Not all ternary oxovanadium complexes of DPPZ bind to DNA as classical intercalators. The DPPZ complex in *Figure 1.15 (a)* as well as the PHEN complexes in *Figures 1.15 (e), (h), (i), (j)* and *Figure 1.16 (a)* were found to bind to DNA in a partial/weak intercalative binding mode.<sup>113,167,211,216,219</sup> The DPPZ complexes in *Figures 1.15 (b)* and *(c)* and the PHEN and DPQ complexes in *Figures 1.15 (a) – (c)* were found to be groove binders.<sup>21,167</sup> Electrostatic attraction to DNA was also noted in some cases.<sup>21,113,227</sup> The OH substituent in the complex in *Figure 1.15 (e)* has the potential to form hydrogen bonds to the phosphate backbone of DNA.<sup>113</sup>

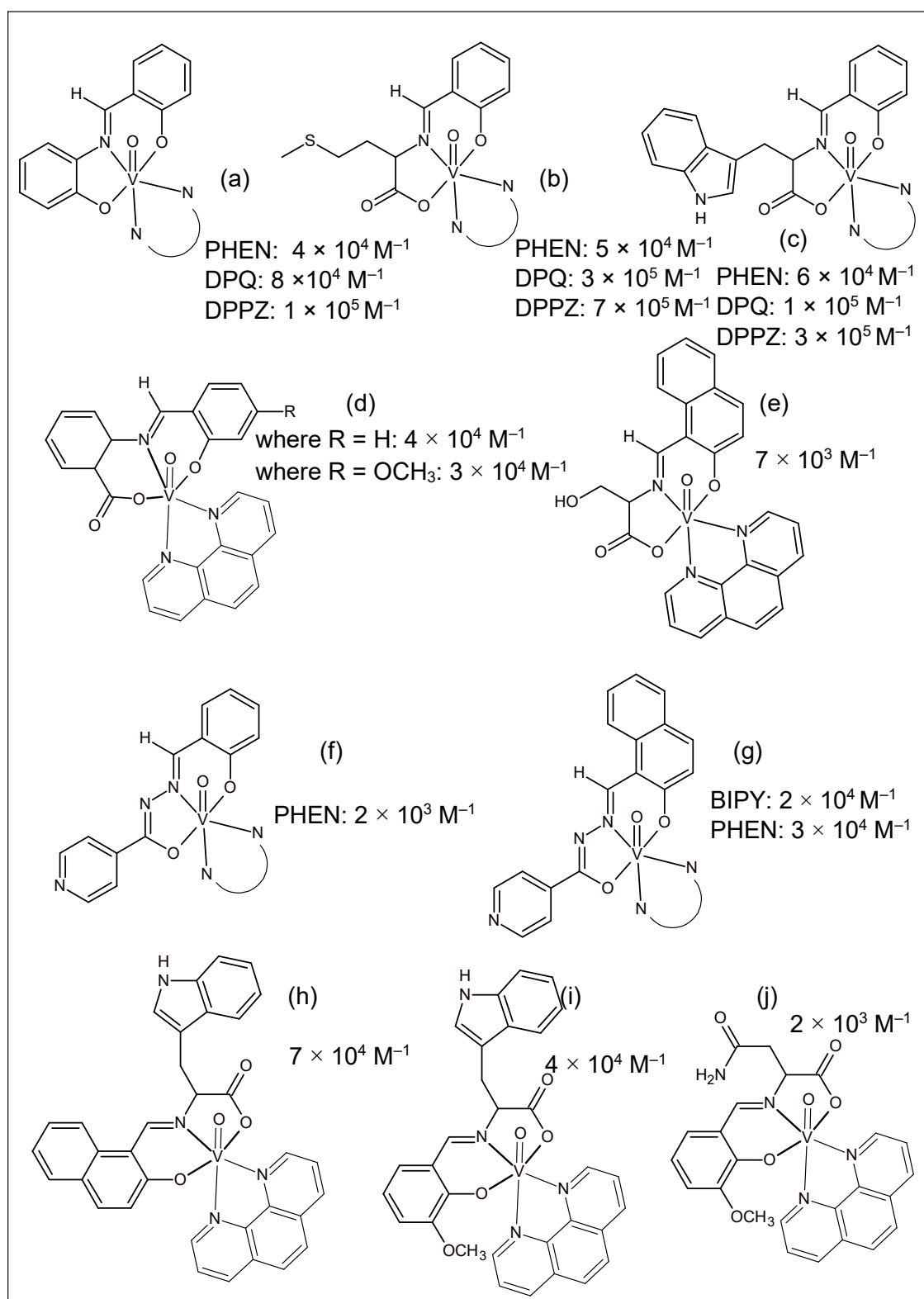


**Figure 1.15** [VO(ONO)(NN)] complexes for which DNA intrinsic binding constants have been determined by Sasmal and co-workers (a),<sup>167</sup> (b), (c);<sup>21</sup> Guo *et al.* (d);<sup>2</sup> Liao *et al.* (f), (g)<sup>34</sup> and Dong and co-workers (e),<sup>113</sup> (h), (i),<sup>211</sup> (j).<sup>216</sup> Intrinsic DNA binding constants ( $K_b$ ) are indicated alongside each structure.

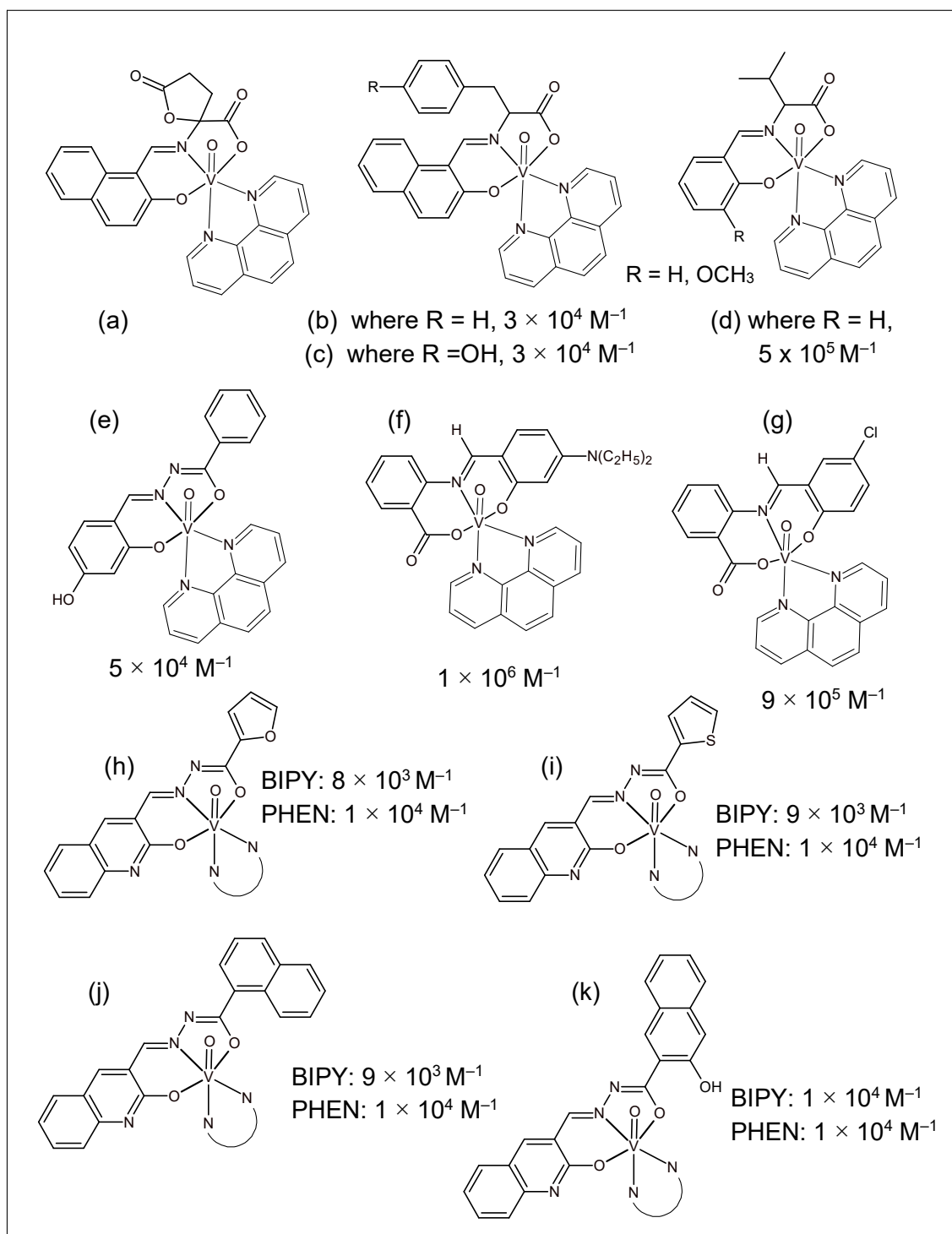


**Figure 1.16** [VO(ONO)(NN)] complexes for which DNA binding modes have been determined by Li and co-workers (a),<sup>219</sup> (b),<sup>212</sup> (c),<sup>213</sup> (d),<sup>217,218,272</sup> Aboafia *et al.* (e);<sup>227</sup> Liao *et al.* (f), (g)<sup>35</sup> and Banerjee *et al.* (h) – (k).<sup>241</sup> Intrinsic DNA binding constants ( $K_b$ ) are indicated alongside each structure.

The extent of aromaticity of the *N,N*-bidentate polypyridyl co-ligand was a factor in determining DNA binding ability of the [VO(ONO)(NN)] derivatives.<sup>21,34,167</sup> The DNA binding ability of the complexes generally increased in the order BIPY < PHEN < DPQ < DPPZ for the complexes in *Figures 1.15 (a), (b), (c), (f) and (g)*.<sup>21,34,167</sup>

Interactions of the complexes with DNA could also be through the *O,N,O'*-tridentate ligand.<sup>34</sup> The salicylidene-PHEN complex in *Figure 1.16 (d)* interacted with DNA weaker than the PHEN complexes reported in *Figures 1.15 (d), (h) and (i)* and *Figure 1.16 (c)*.<sup>2,211,213,217</sup> Appending aromatic moieties on the tridentate ligand can improve the affinity of the compounds towards DNA.<sup>34,35,211</sup> For example, the BIPY complex with the naphthalene moiety on the tridentate azine ligand in *Figure 1.15 (g)* had a higher intrinsic DNA binding constant than the salicylidene-PHEN complex in *Figure 1.15 (f)*.<sup>34</sup>

However, complexes with aromatic moieties on the tridentate ligand do not always ensure stronger binders. The complexes with the less sterically hindered thiomethyl moiety on the *N*-salicylidene tridentate ligand in *Figure 1.15 (b)* had higher DNA binding constants than those with the aromatic indole analogues in *Figure 1.15 (c)*.<sup>21</sup> Steric factors were also seen to impact the DNA binding constant in the work of Zhai and co-workers.<sup>113</sup> The naphthalene derivative in *Figure 1.15 (e)* bound to DNA with a modest intrinsic binding constant of  $7 \times 10^3 \text{ M}^{-1}$ , despite the planar naphthalene moiety.<sup>113</sup> Lu and co-workers also found lower DNA binding constants for the [VO(ONO)(PHEN)] type complexes in *Figure 1.15 (d)* with aromatic tridentate ligands than those reported for [VO(ONO)(PHEN)] complexes with fewer aromatic groups.<sup>2,100</sup>

The DNA binding affinities of the [VO(ONO)(NN)] complexes are also associated with the electronic effect of substituents on the tridentate ligand, although the effect is not definitive. Electron-withdrawing groups, such as chlorine in the complex in *Figure 1.16 (g)* resulted in a lower binding constant than the complex in *Figure 1.16 (f)*.<sup>35</sup> However, the electron-donating methoxy substituent on the tridentate ligand of the complexes in *Figure 1.15 (d)* and *Figure 1.16 (d)* decreased the binding ability to DNA in comparison to the salicylidene analogues, where R = H.<sup>2,217,218</sup>

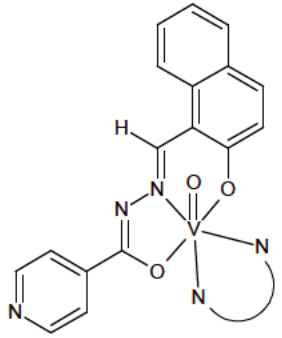
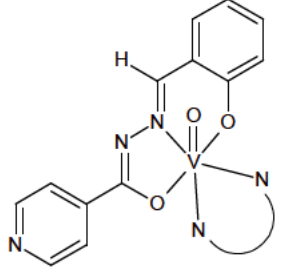
The electron-donating OH substituent on the tridentate ligand in the complexes in *Figure 1.16 (k)* led to higher DNA binding affinities in comparison to the corresponding complexes in *Figure 1.16 (j)*.<sup>241</sup> The latter may be a consequence of hydrogen bonding to the DNA helix leading to a more stable chelate.

The above data show that there are multiple factors affecting the DNA binding affinity of the metallodrugs, suggesting that the design of complexes with high DNA affinities is not a trivial matter.

Electron-withdrawing or donating groups changes the electron density of the aromatic chromophore of the tridentate ligand and so alters the pi-stacking interaction of the ligand with the base-pairs of DNA.<sup>215</sup> To study the electronic effects of substituents on the drug/DNA interactions of the complexes in this work, a range of electron-donating and withdrawing substituents have been included on the Schiff base ligand.

A positive correlation between DNA binding ability and antitumour activity of the [VO(ONO)(NN)] complexes has been reported.<sup>2,34,35,257</sup> IC<sub>50</sub> data is presented in *Table 1.1* for the complexes depicted in *Figures 1.15 (f)* and *(g)*. The data indicates that the complexes with the higher intrinsic DNA binding constants were more cytotoxic towards neuroblastoma and breast carcinoma cell lines.<sup>34</sup>

**Table 1.1** DNA intrinsic binding constants ( $K_b$ ) and related  $IC_{50}$  values of oxovanadium(IV) hydrazone complexes against SH-SY5Y and MCF-7 human cancer cell lines after a 48-hour incubation, measured by MTT assay.<sup>34</sup> Each  $IC_{50}$  value expressed as the mean  $\pm$  standard deviation of three independent experiments.

Complex	Co-ligand	$K_b$ ( $M^{-1}$ )	$IC_{50}$ ( $\mu M$ ) SH-SY5Y neuroblastoma	$IC_{50}$ ( $\mu M$ ) MCF-7 breast
	PHEN	$(2.70 \pm 0.10) \times 10^4$	$3.95 \pm 0.14$	$1.97 \pm 0.21$
	BIPY	$(2.10 \pm 0.10) \times 10^4$	$6.90 \pm 0.38$	$11.5 \pm 0.94$
	PHEN	$(1.60 \pm 0.10) \times 10^3$	$8.86 \pm 0.31$	$26.5 \pm 0.62$

The PHEN complexes in *Figures 1.17 (a), (b) and (c)* were also more cytotoxic than the corresponding BIPY derivatives against liver, breast, and ovarian cancer cells.<sup>38,178,257</sup> However, this is not always the case. The BIPY analogue of the complex in *Figure 1.15 (f)* and the BIPY complex in *Figure 1.17 (b)*, where  $R = H$ , are more cytotoxic against a human breast carcinoma cell line and interacted with DNA differently compared to the PHEN analogues.<sup>34,257</sup> The BIPY complex in *Figure 1.17 (b)* where  $R = Br$  is selective towards ovarian, breast and prostate cancer cell lines over normal kidney cells in comparison to the corresponding PHEN complex.<sup>178</sup> This variability shows that the mechanism of action extends beyond that of passive DNA binding. The ability of the complex to reach the intended cellular target and then produce ROS is also a vital factor in cytotoxicity.

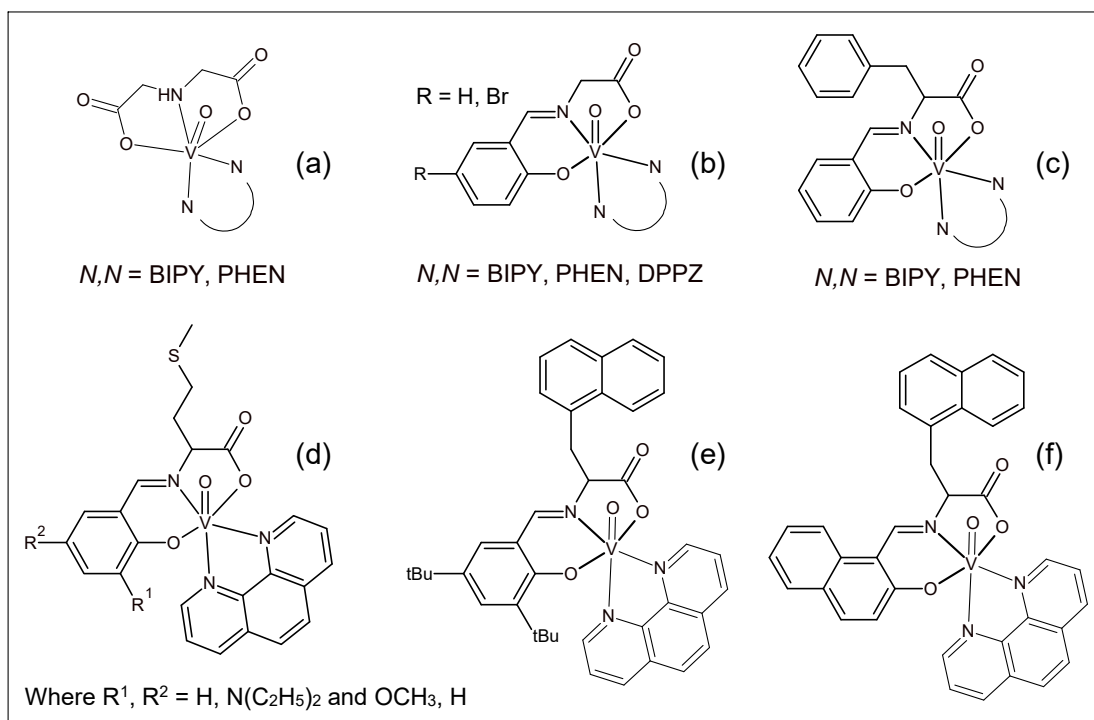


**Figure 1.17**  $[VO(ONO)(NN)]$  complexes reported to have antitumoural properties, (a),<sup>38</sup> (b),<sup>178,257</sup> (c)<sup>257</sup> and (d, e, f).<sup>150</sup>

Substituents on the tridentate ligand also influence the cytotoxicity of  $[VO(ONO)(NN)]$ -type complexes. The carboxyl group on the salicylidene ring of the complexes shown in Figures 1.16 (f) and (g) is thought to improve their hydrophilicity and so improve cytotoxicity against myeloma and gliomas cancer cell lines.<sup>35</sup> The complex in Figure 1.16 (f) with the diethyl amine substituent showed better inhibitory effect against myeloma and gliomas cell lines than the complex in Figure 1.16 (g) with the chloro substituent. This is possibly due to complex (f) being a stronger DNA binder than complex (g).<sup>35</sup> The complex with the methoxy substituent in Figure 1.15 (d) was a less potent inhibitor of myeloma and gliomas cell lines than the corresponding unsubstituted derivative, correlating with it being a weaker DNA binder.<sup>2</sup> The addition of an electron-withdrawing bromo substituent on the tridentate ligand in the BIPY and PHEN complexes in Figures 1.17 (b) resulted in higher cytotoxicity than the corresponding unsubstituted derivatives against ovarian and breast carcinoma cell lines.<sup>178,257</sup> Also, the complex in Figure 1.17 (d) with the methoxy substituent was significantly more cytotoxic against human liver cancer cells than the corresponding complex with a diethyl amine substituent.<sup>150</sup>

The complex in *Figure 1.17 (f)* with the extra naphthalene moiety was less cytotoxic against liver cancer cells than the complex with *tert*-butyl substituents in *Figure 1.17 (e)*.<sup>150</sup> Yet, the complexes in *Figure 1.15 (g)* with the extra naphthalene moiety were more cytotoxic against neuroblastoma cancer cell lines than the corresponding salicylidene analogues in *Figure 1.15 (f)* (*Table 1.1*).<sup>34</sup> These data show that through relatively minor variations of the Schiff base ligand, the physicochemical and the subsequent cytotoxic properties of complexes may easily be tuned.

Oxovanadium complexes that are reported to be strong DNA binders also have higher DNA cleavage activities.<sup>184,227</sup> It is thought the bioavailability of ROS is improved as the strength of the DNA binding ability of the vanadium complex is increased.<sup>184</sup> The phenanthroline-derived complex in *Figure 1.16 (e)* exhibited higher DNA binding affinity and induced more DNA oxidative cleavage than the parallel  $[V^V O_2(ONO)]$  complex.<sup>227</sup> In addition, the phenanthroline derivatives depicted in *Figures 1.17 (b)* and *(c)* were able to cleave plasmid DNA more effectively than the BIPY derivatives in the presence of the oxidising agent oxone and reducing agent 3-mercaptopropionic acid.<sup>257</sup>

The DNA cleavage efficacy was also dependent on the the nature of the tridentate ligand. The salicylidene-glycine-DPPZ compound shown in *Figure 1.17 (b)*, was able to induce moderate DNA cleavage without external agents, whilst the bromo DPPZ derivative did not.<sup>178</sup> The phenylalanine-BIPY derivative in *Figure 1.17 (c)* was also more active than the BIPY derivative in *Figure 1.17 (b)* where R = H in the presence of oxone.<sup>257</sup>

The complexes depicted in *Figure 1.15 (h)* and *(i)* and in *Figure 1.16 (b)* and *(c)* were also shown to cleave plasmid DNA.<sup>211-213</sup> The complex in *Figure 1.16 (d)*, where R = H, cleaves plasmid DNA and the nuclease activity of the complex was further enhanced by the addition of hydrogen peroxide.<sup>272</sup> Other complexes that could oxidatively cleave plasmid DNA in the presence of hydrogen peroxide include those shown in *Figure 1.15 (d)* and *Figure 1.16 (e)*, both through the catalytic production of hydroxyl radicals.<sup>2,227</sup> The complexes *(f)* and *(g)* in *Figure 1.16* could oxidatively cleave plasmid DNA in the presence of hydrogen peroxide after irradiation with UV radiation and subsequent production of hydroxyl radicals.<sup>35</sup>



The presence of the  $\text{VO}^{2+}$  core with the *N,N*-bidentate and tridentate ligands was needed for activity.<sup>36,186</sup> This indicates the intact oxovanadium(IV) complex is associated with the biological activity at least until the compounds are taken up by the cells.<sup>247</sup> A parabolic relationship between the biological response of these compounds and lipophilicity was also noted.<sup>100,240,247,248</sup> This parabolic relationship is interesting and highlights the conflicting role of lipophilicity. To be effective, compounds need to travel in aqueous blood serum and then be able to cross phospholipid bilayers and penetrate the hydrophobic core of the DNA helix to reach the final biological target.

DNA was found to be the potential parasite and tumour cell target with the bidentate polypyridyl ligand allowing interaction of the complexes with DNA.<sup>36,100,134,186,240,248</sup> DNA interaction atomic force microscopy studies of the PHEN complexes depicted in *Figure 1.18 (a)* indicate that an absence of substituents on the semicarbazone tridentate ligand improved intercalative ability of the complexes.<sup>100</sup> In contrast, the DNA interactions of the DPPZ analogues in *Figure 1.18 (a)* were modestly affected by a change in substituents on the tridentate semicarbazone ligand.<sup>240</sup> The order of biological activity was dependant on the type of *N,N*-bidentate ligand and almost independent of the substituents on the phenol moiety of the *O,N,O'*-tridentate ligand.<sup>36,100,240,247,248</sup> Interestingly, the order of antitrypanosomal activity of the complexes was  $\text{PHEN} > \text{DPPZ} \gg \text{BIPY}$ . The antitrypanosomal activity of the compounds is thus more closely aligned to the aqueous stability of the  $[\text{VO}(\text{ONO})(\text{NN})]$  complexes. This indicates the importance of aqueous stability on the biological efficacy of vanadium-based metallodrugs. The PHEN compounds were determined to be the most stable to oxidation and solvolysis and were correspondingly the most biologically active.<sup>36,100,240,247,248</sup>

What is not known about the complexes described above, is whether the higher biological activity of the PHEN complexes is due to intrinsic bioactivity of the complexes or to a higher bioavailability and/or interaction with DNA. The correlation with stability is established, but the causation is not yet understood. The vanadium(IV) complexes could act as pro-drugs in biological media and the active species in the cells may not contain the original ligands (*Section 1.5*).<sup>39,247</sup> The stability of oxovanadium complexes is an important aspect of their chemistry and will be further discussed in *Chapter 7*.



The complex in *Figure 1.19 (b)* was similarly shown to be more cytotoxic towards a lung cancer cell line compared to either the free tridentate ligand or metal precursor, indicating that the combination of the two is required for cytotoxicity.<sup>242</sup> The hydrazone-BIPY complex in *Figure 1.19 (c)* was able to induce apoptosis in human papillomavirus infected cervical cancer cells.<sup>165</sup> The hydrazone-PHEN complexes in *Figures 1.19 (d)* and *(e)* displayed antidiabetic properties.<sup>45,269</sup> The complex in *Figure 1.19 (d)* is able to inhibit human recombinant protein tyrosine phosphatase 1B (PTP-1B) and is likely a key step in the mechanism of action.<sup>45</sup> The *tert*-butyl group of this compound is thought to aid glucose utilisation. The *tert*-butyl substituent increases the lipophilicity of the complex, and so may aid transport across cell membranes.<sup>45</sup>

Whilst neutral complexes may enable metallodrugs to cross biological membranes, cationic metallodrugs, inclusive of vanadium complexes, can target the negatively charged phosphate backbone of DNA.<sup>44-47,223,298</sup>

### 1.10.2 Cationic Oxovanadium(IV) Complexes with Phenanthroline-Derived Co-ligands

Marks and co-workers reported that the aqueous form of vanadocene,  $[(C_5H_5)_2V(OH_2)_2]^{2+}$  ions, interacted with the phosphate groups of DNA nucleotides, and is likely part of their mechanism of action.<sup>46,47</sup>

Several cationic oxovanadium(IV) complexes with bidentate *N,N*-donor polypyridyl ligands forming part of their coordination sphere have been reported.<sup>42,99,180,183,184,222,223,299-304</sup> Oxovanadium complexes of the type  $[VO(ONO)(NN)]^+$  and  $[VO(ONN)(NN)]^+$  with phenanthroline-derived ligands, for which DNA binding studies have been reported, are indicated in *Figure 1.20*.<sup>181,222,223,302</sup>

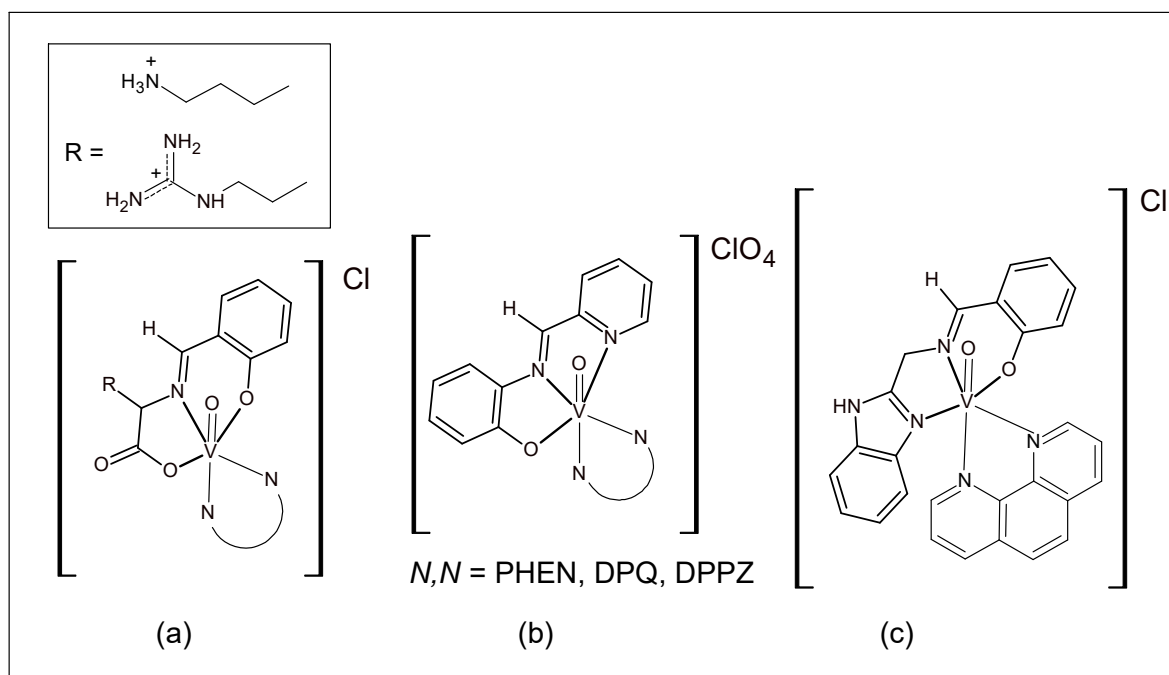


**Figure 1.20** Cationic oxovanadium(IV) complexes studied by Sasmal and co-workers of the type  $[\text{VO}(\text{ONO})(\text{NN})]^+$  (a) and  $[\text{VO}(\text{ONN})(\text{NN})]^+$  (b) and (c).<sup>222,223,302</sup>

The complexes in *Figure 1.20* bind to calf thymus DNA in a primarily groove binding mode with intrinsic binding constants of  $10^4$  to  $10^5 \text{ M}^{-1}$  in the order  $\text{PHEN} < \text{DPQ} < \text{DPPZ}$ .<sup>222,223</sup> The DPPZ complex in *Figure 1.20* (b) was found to be a partial intercalator.<sup>222</sup> The cationic guanidinium or amine moiety of the complexes depicted in *Figure 1.20* (a), is thought to enable those complexes to target specific DNA base pairs.<sup>223</sup> The complexes show higher binding affinity towards adenine-thymine base pairs than guanine-cytosine base pairs.<sup>223</sup>

The DPQ and DPPZ analogues in *Figure 1.20* (a) were found to be efficient plasmid DNA photocleavers in both UV-A and near-IR light, *via* a singlet oxygen mechanistic pathway.<sup>109</sup> These cationic DPPZ complexes are significantly better photocleavers of DNA in red light than the neutral DPPZ analogue depicted in *Figure 1.15* (b).<sup>21,223</sup>

The  $[\text{VO}(\text{ONN})(\text{NN})]\text{ClO}_4$  DPQ and DPQ complexes in *Figure 1.20* (b) were also able to photocleave DNA with UV-A radiation, forming both  $^1\text{O}_2$  and hydroxyl radicals and under near-IR radiation by a hydroxyl radical mechanism.<sup>222</sup> No hydrolytic cleavage of DNA was suggested for the complexes in *Figure 1.20* (a) and (b) based on their poor chemical nuclease activity in the dark in the presence of oxidising or reducing agents.<sup>222,223</sup>

The PHEN ligand is known to be photo-inactive when bound to a metal ion.<sup>223</sup> The PHEN complexes in *Figure 1.15 (a), (b) and (c)* and in *Figure 1.20 (b) and (c)* were thus inactive with respect to DNA photocleavage.<sup>21,167,222,302</sup> Yet, the PHEN complexes in *Figure 1.20 (a)* showed slight DNA cleavage in UV-A light. This was possibly a result of the photosensitising nature of the tridentate amino acid ligands.<sup>223</sup>

The DPPZ complexes in *Figure 1.20 (a) and (b)* exhibited photocytotoxicity (in visible light) towards cervical cancer cells.<sup>222,223</sup> The VO<sup>2+</sup> moiety was noted to enhance the photodynamic therapy effect of DPPZ.<sup>222</sup> The PHEN and DPQ complexes did not show any significant photocytotoxic activity.<sup>222,223</sup> The photocytotoxicity of the DPPZ complexes is attributed to greater lipophilicity and DNA binding strength of the DPPZ moiety in comparison to the PHEN and DPQ complexes.<sup>222</sup> The DPPZ ligand may enable increased internalisation of the complexes into the cell.<sup>222</sup> Studies have shown that the DPPZ complexes can cross the cellular membrane and concentrate in the cell in greater quantities when compared to the ligands alone.<sup>180</sup> The above data are the basis for the selection of the range of *N,N*-bidentate co-ligands used in the present study.

For the purposes of this project, monoanionic *O,N,N'*-tridentate Schiff base ligands were chosen to coordinate to the VO<sup>2+</sup> core to form the cationic set of complexes. The *O,N,N'*-tridentate Schiff bases are *N*-methyl imidazole aminophenols. The purpose of the *N*-methyl group on the imidazole moiety is to prevent ionisation of the nitrogen upon coordination to the metal centre.<sup>305</sup> In recent years, derivatives of the 1-methyl-1*H*-imidazol-2-yl)methanimine Schiff base ligand have been coordinated to various metals for a wide variety of applications. These include molecular magnets,<sup>306-309</sup> catalysis,<sup>310-314</sup> anticancer agents,<sup>315</sup> bioimaging probes<sup>316</sup> and enzyme modelling.<sup>317</sup>

The cationic metal chelates will have significantly different physicochemical properties when compared to their neutral analogues. They should exhibit improved aqueous solubility and the potential electrostatic attraction of the cationic complexes to the negatively charged phosphate backbone of the DNA helix would serve to stabilise the DNA/drug conjugate.

These previous studies show that predicting DNA binding modes and the likely mechanism of action of anticancer agents is more complex than the structure of the primary and ancillary ligands of the oxovanadium(IV) complexes alone. The type of polypyridyl ligand, tridentate Schiff base ligand, and type of substituents on the tridentate ligand influence many factors such as the electron density, stability, lipophilicity, and steric bulk of the complexes. These in turn influence the DNA binding modes, DNA cleavage and cytotoxicity of the complexes.

### 1.11 Aims and Objectives

The main aim of this work is to synthesise novel neutral and cationic oxovanadium(IV) complexes which are designed to bind DNA for the purposes of developing anticancer agents. The aims and objectives of the study are listed:

1. To optimise the synthesis of the *N,N*-bidentate ligands DPQ and DPPZ.
2. To synthesise *O,N,O'*-donor salicylidene tridentate ligands (*Figure 1.21*).

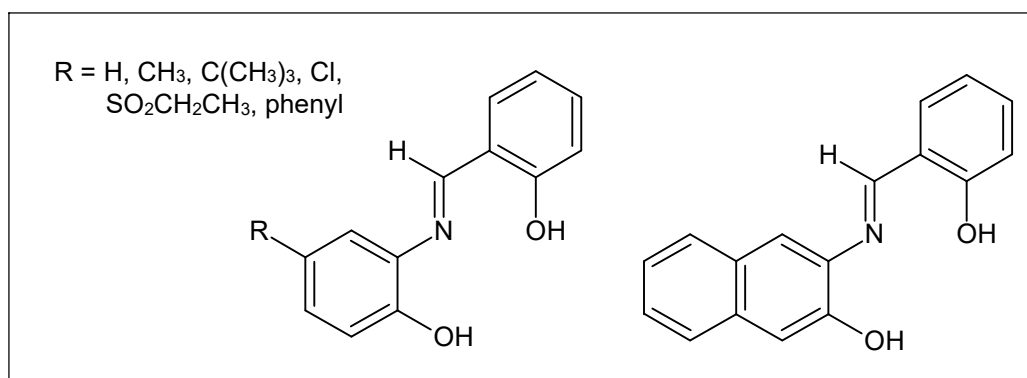


**Figure 1.21** *O,N,O'*-tridentate Schiff base ligands to be synthesised.

3. To synthesise known (R = H) and novel (R = CH<sub>3</sub>, C(CH<sub>3</sub>)<sub>3</sub>, phenyl) *O,N,N'*-donor imidazole tridentate ligands (*Figure 1.22*).

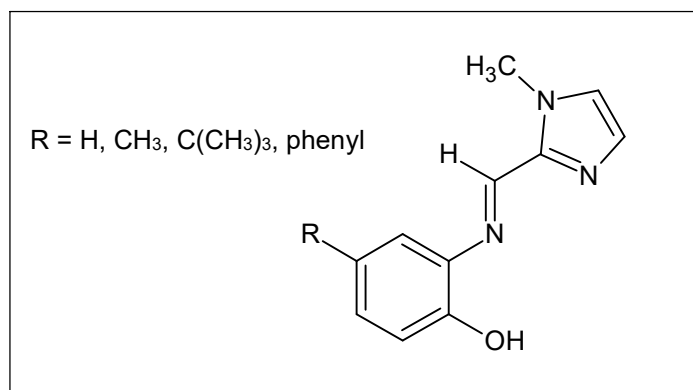


**Figure 1.22** *O,N,N'*-tridentate Schiff base ligands to be synthesised.

4. To characterise the ligands by means of <sup>1</sup>H and <sup>13</sup>C NMR spectroscopy, elemental analysis, UV/Visible and FT-IR spectroscopy, and mass spectrometry. Where possible, single crystal X-ray crystallography will also be used to characterise the ligands.
5. To synthesise novel (except when R = H), neutral oxovanadium(IV) complexes with the *O,N,O'*-tridentate ligands and DPQ or DPPZ co-ligands and novel cationic oxovanadium(IV) complexes with *O,N,N'*-tridentate ligands and PHEN, DPQ or DPPZ co-ligands (*Figure 1.23*).

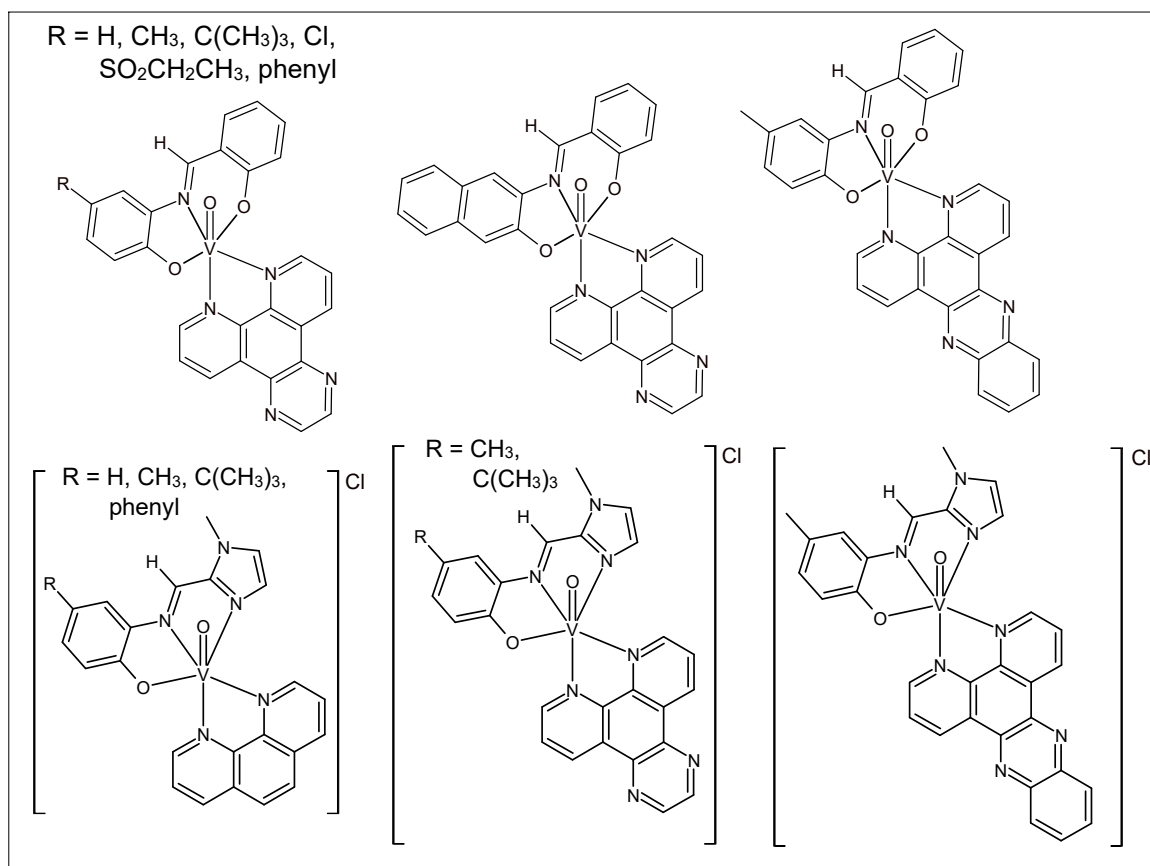


**Figure 1.23** Neutral and novel cationic oxovanadium(IV) complexes to be synthesised in the present study.

6. To fully characterise the oxovanadium(IV) complexes by means of elemental analysis, UV/Visible, FT-IR and EPR spectroscopy as well as mass spectrometry, and where possible X-ray crystallography.
7. To determine the DNA binding affinity and mode of DNA binding of the complexes using absorption spectroscopy, competitive fluorescence emission spectroscopy, DNA viscosity studies and molecular simulations.
8. To measure the ability of selected complexes to cleave DNA by gel electrophoresis.
9. To investigate the stability of selected complexes in solution.
10. To perform molecular simulations of the complexes and selected ligands using the DFT method. The experimental structures will be used in conjunction with the DFT-calculated structures to provide a clear analysis of the structural and electronic attributes of the compounds that might impact on their interaction with DNA.
11. The vanadium complexes will also be screened against several healthy and tumour cell lines to determine their cytotoxicity and selectivity index.

## 1.12 References

1. de Almeida, S.M.V., Ribeiro, A.G., de Lima Silva, G.C., Ferreira Alves, J.E., Beltrão, E.I.C., de Oliveira, J.F., de Carvalho Junior, L.B., de Lima, Md.C.A., , *Biomed. Pharmacother.* , **2017**, *96*, 1538.
2. Guo, H., Lu, J., Ruan, Z., Zhang, Y., Liu, Y., Zang, L., Jiang, J. and Huang, J., *J. Coord. Chem.*, **2012**, *65*, 191.
3. Guo, Z. and Sadler, P.J., *Angew. Chem., Int. Ed.*, **1999**, *38*, 1512.
4. Kostova, I., *Recent Pat. Anti-Cancer Drug Discovery*, **2006**, *1*, 1.
5. Rosenberg, B., Vancamp, L., Trosko, J.E. and Mansour, V.H., *Nature*, **1969**, *222*, 385.
6. Connors, T.A., Jones, M., Ross, W.C.J., Braddock, P.D., Khokhar, A.R. and Tobe, M.L., *Chem.-Biol. Interact.*, **1972**, *5*, 415.
7. Costa, L.A., Rocha, W.R., De Almeida, W.B. and Dos Santos, H.F., *J. Inorg. Biochem.*, **2005**, *99*, 575.
8. Fuertes, M.A., Alonso, C. and Perez, J.M., *Chem. Rev.*, **2003**, *103*, 645.
9. Gray, H.B. and Ballhausen, C.J., *J. Am. Chem. Soc.*, **2002**, *85*, 260.
10. Jones, T.W., Chopra, S., Kaufman, J.S., Flamenbaum, W. and Trump, B.F., *Lab. Invest.*, **1985**, *52*, 363.
11. Kockerbauer, R. and Bednarski, P.J., *J. Pharm. Sci.*, **1995**, *84*, 819.
12. Lippert, B., *Cisplatin. The Chemistry and Biochemistry of a Leading Anticancer Drug*, Wiley-VCH, **1999**, V, 3, 6-8, 12-58, 73-75, 111-115, 183, 184, 339-359.
13. Loehrer, P.J. and Einhorn, L.H., *Ann. Intern. Med.*, **1984**, *100*, 704.
14. Petrovic, D., Stojimirovic, B., Petrovic, B., Bugarcic, Z.M. and Bugarcic, Z.D., *Bioorg. Med. Chem.*, **2007**, *15*, 4203.
15. Reedijk, J., *Chem. Commun.*, **1996**, 801.
16. Reedijk, J., *Chem. Rev.*, **1999**, *99*, 2499.
17. Cao, Y., Liu, H., Yuan, Z. and Wei, G., *Aust. J. Chem.*, **2017**, *70*,
18. Pasetto, L.M., D'Andrea, M.R., Brandes, A.A., Rossi, E. and Monfardini, S., *Crit. Rev. Oncol. Hematol.*, **2006**, *60*, 59.
19. Sakurai, H., Tamura, H. and Okatani, K., *Biochem. Biophys. Res. Commun.*, **1995**, *206*, 133.
20. Sasmal, P.K., Patra, A.K. and Chakravarty, A.R., *J. Inorg. Biochem.*, **2008**, *102*, 1463.

21. Sasmal, P.K., Patra, A.K., Nethaji, M. and Chakravarty, A.R., *Inorg. Chem.*, **2007**, *46*, 11112.
22. Sakurai, H., *Expert Opin. Drug Discov.*, **2007**, *2*, 873.
23. Sakurai, H., *J. Health Sci.*, **2010**, *56*, 129.
24. Sakurai, H., Yoshikawa, Y. and Yasui, H., *Chem. Soc. Rev.*, **2008**, *37*, 2383.
25. Adly, O.M.I., El-Shafiy, H.F. and Shebl, M., *J. Mol. Struct.*, **2019**, *1196*, 805.
26. Bai, Y., Zhang, H., Wang, Y., Zhu, L., Shi, T., Wei, H., Xiao, J., Zhang, Y. and Wang, Z., *Front. Pharmacol.*, **2020**, *11*, 608218.
27. Bai, Y.-L., Zhang, Y.-W., Xiao, J.-Y., Guo, H.-W., Liao, X.-W., Li, W.-J. and Zhang, Y.-C., *Trans. Met. Chem.*, **2018**, *43*, 171.
28. Costa Pessoa, J., Etcheverry, S. and Gambino, D., *Coord. Chem. Rev.*, **2015**, *301*, 24.
29. El-Shafiy, H.F. and Shebl, M., *J. Mol. Struct.*, **2018**, *1156*, 403.
30. Ibrahim, M.A., Emara, A.A.A., Taha, A., Adly, O.M.I., Nabeel, A.I. and Salah, N., *Appl. Organomet. Chem.*, **2022**, *36*,
31. Kioseoglou, E., Petanidis, S., Gabriel, C. and Salifoglou, A., *Coord. Chem. Rev.*, **2015**, *301-302*, 87.
32. Kowalski, S., Hac, S., Wyrzykowski, D., Zauszkiewicz-Pawlak, A. and Inkielewicz-Stepniak, I., *Oncotarget*, **2017**, *8*, 60324.
33. León, I.E., Cadavid-Vargas, J.F., Tiscornia, I., Porro, V., Castelli, S., Katkar, P., Desideri, A., Bollati-Fogolín, M. and Etcheverry, S.B., *J. Biol. Inorg. Chem.*, **2015**, *20*, 1175.
34. Liao, X., Lu, J., Ying, P., Zhao, P., Bai, Y., Li, W. and Liu, M., *J. Biol. Inorg. Chem.*, **2013**, *18*, 975.
35. Liao, X., Pan, W., He, R., Guo, H., Ying, P. and Lu, J., *Chem. Biol. Drug Res.*, **2014**, *83*, 367.
36. Machado, I., Fernández, M., Becco, L., Garat, B., Brissos, R.F., Zabarska, N., Gamez, P., Marques, F., Correia, I., Costa Pessoa, J. and Gambino, D., *Inorg. Chim. Acta*, **2014**, *420*, 39.
37. Mohamadi, M., Yousef Ebrahimipour, S., Torkzadeh-Mahani, M., Foro, S. and Akbari, A., *RSC Adv.*, **2015**, *5*, 101063.
38. Ni, L., Zhao, H., Tao, L., Li, X., Zhou, Z., Sun, Y., Chen, C., Wei, D., Liu, Y. and Diao, G., *Dalton Trans.*, **2018**, *47*, 10035.
39. Rehder, D., *Future Med. Chem.*, **2016**, *8*, 325.

40. Wang, J., Huang, B., Wang, L., Jiang, G., Cheng, J., Xiong, Y., Wang, J. and Liao, X., *J. Chem. Res.*, **2021**, *45*, 1016.
41. Ying, P., Zeng, P., Lu, J., Chen, H., Liao, X. and Yang, N., *Chem. Biol. Drug Res.*, **2015**, *86*, 926.
42. Banik, B., Somyajit, K., Koley, D., Nagaraju, G. and Chakravarty, A.R., *Inorg. Chim. Acta*, **2012**, *393*, 284.
43. Kostrzewa, T., Jonczyk, J., Drzezdzon, J., Jacewicz, D., Gorska-Ponikowska, M., Kolaczkowski, M. and Kuban-Jankowska, A., *Int. J. Mol. Sci.*, **2022**, *23*,
44. Bisel, P., Al-Momani, L. and Muller, M., *Org. Biomol. Chem.*, **2008**, *6*, 2655.
45. Szklarzewicz, J., Jurowska, A., Hodorowicz, M., Gryboś, R., Kruczała, K., Głuch-Lutwin, M. and Kazek, G., *J. Coord. Chem.*, **2020**, *73*, 986.
46. Murugavel, R., Choudhury, A., Walawalkar, M.G., Pothiraja, R. and Rao, C.N., *Chem. Rev.*, **2008**, *108*, 3549.
47. Toney, J.H., Brock, C.P. and Marks, T.J., *J. Am. Chem. Soc.*, **1986**, *108*, 7263.
48. Colotti, G., Illari, A., Boffi, A. and Morea, V., *Mini-Rev. Med. Chem.*, **2013**, *13*, 211.
49. de Boer, K.-L., *An Investigation into the Influence of Ligand Substituents on the Substitution Reactions of Pt(II) Diamine and Terpyridine Chloro Complexes*, MSc Thesis, University of KwaZulu-Natal, **2007**, 1-2.
50. Perez, R.P., *Eur. J. Cancer*, **1998**, *34*, 1535.
51. Farrell, N., *Transition Metal Complexes as Drugs and Chemotherapeutic Agents*, Kluwer, **1989**, 54, 67, 70, 71.
52. Ahmad, S., *Polyhedron*, **2017**, *138*, 109.
53. Novokmet, S., Stojic, I., Radonjic, K., Savic, M. and Jeremic, J., *Serb. J. Exp. Clin. Res*, **2017**, *18*, 191.
54. Wheate, N.J., Walker, S., Craig, G.E. and Oun, R., *Dalton Trans.*, **2010**, *39*, 8113.
55. Costa, L.A.S., Rocha, W.R., De Almeida, W.B. and Dos Santos, H.F., *Chem. Phys. Lett.*, **2004**, *387*, 182.
56. Galanski, M., Jakupec, M.A. and Keppler, B.K., *Curr. Med. Chem.*, **2005**, *12*, 2075.
57. Hambley, T.W., *Coord. Chem. Rev.*, **1997**, *166*, 181.
58. Reedijk, J., *Proc. Natl. Acad. Sci. USA*, **2003**, *100*, 3611.
59. Coverdale, J., Laroiya-McCarron, T. and Romero-Canelón, I., *Inorganics*, **2019**, *7*,
60. Sava, G., Capozzi, I., Clerici, K., Gagliardi, G., Alessio, E. and Mestroni, G., *Clin. Exp. Metastasis*, **1998**, *16*, 371.

61. Trondl, R., Heffeter, P., Kowol, C.R., Jakupec, M.A., Berger, W. and Keppler, B.K., *Chem. Sci.*, **2014**, 5, 2925.
62. Levina, A., Mitra, A. and Lay, P.A., *Metallomics*, **2009**, 1, 458.
63. Sarhan, A.M., Elsayed, S.A., Mashaly, M.M. and El-Hendawy, A.M., *Appl. Organomet. Chem.*, **2019**, 33,
64. El-Deen, I.M., Shoair, A.F. and El-Bindary, M.A., *J. Mol. Struct.*, **2019**, 1180, 420.
65. Rehder, D., *Dalton Trans.*, **2013**, 42, 11749.
66. Rehder, D., *Met. Ions Life Sci.*, **2013**, 13, 139.
67. Rehder, D., *Bioinorganic Vanadium Chemistry*, John Wiley & Sons, **2008**, 2, 5, 8, 9, 10, 13, 20, 21, 26, 30, 31, 160, 161, 165, 166, 169, 172, 173, 176, 177, 182, 190, 191, 193, 194.
68. Rehder, D., *Inorg. Chim. Acta*, **2017**, 455, 378.
69. Sefström, N.G., *Kgl. Vetensk. Acad. Handl.*, , **1830**, 255.
70. von Lippmann, E.O., *Ber. Dtsch. Chem. Ges.*, , **1888**, 21, 3492.
71. Henze, M., *Z. Physiol. Chem.*, **1911**, 72, 494.
72. Rehder, D., *Metallomics*, **2015**, 7, 730.
73. Bishayee, A., Waghay, A., Patel, M.A. and Chatterjee, M., *Cancer Lett.*, **2010**, 294, 1.
74. Rehder, D., *Future Med. Chem.*, **2012**, 4, 1823.
75. Bortels, H., *Zentralbl. Bakteriол. Parasitenk. Infektionskr.* , **1933**, 87, 476.
76. Vilter, H., Glombitza, K.-W. and Grawe, A., *Bot. Mar.*, **1983**, 26, 331.
77. Costa Pessoa, J., *J. Inorg. Biochem.*, **2015**, 147, 4.
78. Priestly, J., *Philos Trans. R. Soc. London.*, **1876**, 166, 495.
79. Lyonnet, B., Martz, X. and Martin, E., *La Presse Méd.*, **1899**, 32, 191.
80. Rehder, D., 3.27 - Biological Activities of V and Cr. In: Reedijk, J. and Poeppelmeier, K., eds., *Comprehensive Inorganic Chemistry II* (Second Edition), Elsevier, **2013**, 821-824, 826-831, 833.
81. Cantley, L.C., Josephson, L., Warner, R., Yanagisawa, M., Lechene, C. and Guidotti, G., *J. Biol. Chem.*, **1977**, 252, 7421.
82. Domingo, J.L. and Gomez, M., *Food Chem. Toxicol.*, **2016**, 95, 137.
83. Evangelou, A.M., *Crit. Rev. Oncol. Hematol.*, **2002**, 42, 249.
84. Islam, M.N., Kumbhar, A.A., Kumbhar, A.S., Zeller, M., Butcher, R.J., Dusane, M.B. and Joshi, B.N., *Inorg. Chem.*, **2010**, 49, 8237.
85. Mehdi, M.Z. and Srivastava, A.K., *Arch. Biochem. Biophys.*, **2005**, 440, 158.

86. Treviño, S., Díaz, A., Sánchez-Lara, E., Sanchez-Gaytan, B.L., Perez-Aguilar, J.M. and González-Vergara, E., *Biol. Trace Elem. Res.*, **2019**, *188*, 68.
87. Heyliger, C.E., Tahiliani, A.G. and McNeill, J.H., *Science*, **1985**, *227*, 1474.
88. Cohen, N., Halberstam, M., Shlimovich, P., Chang, C.J., Shamoon, H. and Rossetti, L., *J. Clin. Invest.*, **1995**, *95*, 2501.
89. Goldfine, A.B., Simonson, D.C., Folli, F., Patti, M.E. and Kahn, C.R., *J. Clin. Endocrinol. Metab.*, **1995**, *80*, 3311.
90. Soveid, M., Dehghani, G.A. and Omrani, G.R., *Arch. Iran. Med.*, **2013**, *16*, 408.
91. Scior, T., Guevara-Garcia, J.A., Do, Q.T., Bernard, P. and Laufer, S., *Curr. Med. Chem.*, **2016**, *23*, 2874.
92. El-Shafey, E.S. and Elsherbiny, E.S., *Biomaterials*, **2020**, *33*, 123.
93. Shechter, Y., *Coord. Chem. Rev.*, **2003**, *237*, 3.
94. Thompson, K.H., Lichter, J., LeBel, C., Scaife, M.C., McNeill, J.H. and Orvig, C., *J. Inorg. Biochem.*, **2009**, *103*, 554.
95. Jakusch, T. and Kiss, T., *Coord. Chem. Rev.*, **2017**, *351*, 118.
96. Vincent, J.B., *Nutritional and Therapeutic Interventions for Diabetes and Metabolic Syndrome* (Second Edition), Academic Press, Elsevier, **2018**, 365, 370-373.
97. Crans, D.C., Yang, L., Haase, A. and Yang, X. Health Benefits of Vanadium and Its Potential as an Anticancer Agent. In: Sigel, A., Sigel, H., Freisinger, E. and Sigel, R.K.O., eds. *Metal Ions in Life Sciences*. Walter de Gruyter GmbH; **2018**, 251.
98. He, Z., Song, J., Li, X., Li, X., Zhu, H., Wu, C., Xiao, W., Du, X., Ni, J., Li, N. and Liu, Q., *J. Biol. Inorg. Chem.*, **2021**, *26*, 551.
99. Banerjee, S., Hussain, A., Prasad, P., Khan, I., Banik, B., Kondaiah, P. and Chakravarty, A.R., *Eur. J. Inorg. Chem.*, **2012**, *2012*, 3899.
100. Benítez, J., Becco, L., Correia, I., Leal, S.M., Guiset, H., Pessoa, J.C., Lorenzo, J., Tanco, S., Escobar, P., Moreno, V., Garat, B. and Gambino, D., *J. Inorg. Biochem.*, **2011**, *105*, 303.
101. Brichard, S.M. and Henquin, J.-C., *Trends Pharmacol. Sci.*, **1995**, *16*, 265.
102. da S. Maia, P.I., Pavan, F.R., Leite, C.Q.F., Lemos, S.S., de Sousa, G.F., Batista, A.A., Nascimento, O.R., Ellena, J., Castellano, E.E., Niquet, E. and Deflon, V.M., *Polyhedron*, **2009**, *28*, 398.

103. Ross, A., Soares, D.C., Covelli, D., Pannecouque, C., Budd, L., Collins, A., Robertson, N., Parsons, S., De Clercq, E., Kennepohl, P. and Sadler, P.J., *Inorg. Chem.*, **2010**, *49*, 1122.
104. Ścibior, A., Pietrzyk, Ł., Plewa, Z. and Skiba, A., *J. Trace Elem. Med. Biol.*, **2020**, *61*, 126508.
105. Gruzewska, K., Michno, A., Pawelczyk, T., & Bielarczyk, H. , *J. Physiol. Pharmacol.*, **2014**, *65*, 603.
106. Willsky, G.R., Goldfine, A.B. and Kostyniak, P.J. Pharmacology and Toxicology of Oxovanadium Species: Oxovanadium Pharmacology. *Vanadium Compounds*. American Chemical Society; **1998**, 278:chap 22. *Acs Symposium Series*; vol. 711.
107. Nechay, B.R., *Ann. Rev. Pharmac. Toxicol.*, **1984**, *24*, 501.
108. Levina, A., McLeod, A.I., Kremer, L.E., Aitken, J.B., Glover, C.J., Johannessen, B. and Lay, P.A., *Metallomics*, **2014**, *6*, 1880.
109. Levina, A., McLeod, A.I., Pulte, A., Aitken, J.B. and Lay, P.A., *Inorg. Chem.*, **2015**, *54*, 6707.
110. Chéry, C.C., De Cremer, K., Dumont, E., Cornelis, R. and Moens, L., *Electrophoresis*, **2002**, *23*, 3284.
111. De Cremer, K., Van Hulle, M., Chery, C., Cornelis, R., Strijckmans, K., Dams, R., Lameire, N. and Vanholder, R., *J. Biol. Inorg. Chem.*, **2002**, *7*, 884.
112. Kiss, T., Jakusch, T., Bouhsina, S., Sakurai, H. and Enyedy, É.A., *Eur. J. Inorg. Chem.*, **2006**, *2006*, 3607.
113. Zhai, S., Guo, Q., Dong, J., Xu, T. and Li, L., *Trans. Met. Chem.*, **2014**, *39*, 271.
114. Chasteen, N.D., DeKoch, R.J., Rogers, B.L. and Hanna, M.W., *J. Am. Chem. Soc.*, **1973**, *95*, 1301.
115. Liboiron, B.D., Thompson, K.H., Hanson, G.R., Lam, E., Aebischer, N. and Orvig, C., *J. Am. Chem. Soc.*, **2005**, *127*, 5104.
116. Costa Pessoa, J., Gonçalves, G., Roy, S., Correia, I., Mehtab, S., Santos, M.F.A. and Santos-Silva, T., *Inorg. Chim. Acta*, **2014**, *420*, 60.
117. Azevedo, C.G., Correia, I., Dos Santos, M.M.C., Santos, M.F.A., Santos-Silva, T., Douth, J., Fernandes, L., Santos, H.M., Capelo, J.L. and Pessoa, J.C., *J. Inorg. Biochem.*, **2018**, *180*, 211.
118. Sanna, D., Micera, G. and Garribba, E., *Inorg. Chem.*, **2010**, *49*, 174.

119. Crans, D.C., Trujillo, A.M., Pharazyn, P.S. and Cohen, M.D., *Coord. Chem. Rev.*, **2011**, 255, 2178.
120. Rozzo, C., Sanna, D., Garribba, E., Serra, M., Cantara, A., Palmieri, G. and Pisano, M., *J. Inorg. Biochem.*, **2017**, 174, 14.
121. Korbecki, J., Baranowska-Bosiacka, I., Gutowska, I. and Chlubek, D., *Acta Biochim. Pol.*, **2012**, 59, 195.
122. Kieler, J., Gromek, A. and Nissen, N.I., *Acta Chir. Scand. Suppl.*, **1965**, 343, 154.
123. Thompson, H.J., Chasteen, N.D. and Meeker, L.D., *Carcinogenesis*, **1984**, 5, 849.
124. Chakraborty, T., Ghosh, S., Datta, S., Chakraborty, P. and Chatterjee, M., *J. Exp. Ther. Oncol.*, **2003**, 3, 346.
125. Etcheverry, S.B., Ferrer, E.G., Naso, L., Rivadeneira, J., Salinas, V. and Williams, P.A., *J. Biol. Inorg. Chem.*, **2008**, 13, 435.
126. Rizk, S.L. and Sky-Peck, H.H., *Cancer Res.*, **1984**, 44, 5390.
127. Drzeżdżon, J., Pawlak, M., Matyka, N., Sikorski, A., Gawdzik, B. and Jacewicz, D., *Int. J. Mol. Sci.*, **2021**, 22, 9886.
128. Chen, Y., Cheng, L., Dong, Z., Chao, Y., Lei, H., Zhao, H., Wang, J. and Liu, Z., *Angew. Chem., Int. Ed.*, **2017**, 56, 12991.
129. Iwai, K., Ido, T., Iwata, R., Kawamura, M. and Kimura, S., *Nucl. Med. Biol.*, **1989**, 16, 783.
130. Iwai, K., Kimura, S., Ido, T. and Iwata, R., *Nucl. Med. Biol.*, **1990**, 17, 775.
131. Abakumova, O.Y., Podobed, O.V., Belayeva, N.F. and Tochilkin, A.I., *Biochem. (Mosc.) Suppl. B: Biomed. Chem.*, **2012**, 6, 166.
132. Mishra, A.P. and Soni, M., *Met Based Drugs*, **2008**, 2008, 875410.
133. Rehder, D., *Inorg. Chem. Commun.*, **2003**, 6, 604.
134. Benítez, J., Correia, I., Becco, L., Fernández, M., Garat, B., Gallardo, H., Conte, G., Kuznetsov, M.L., Neves, A., Moreno, V., Costa Pessoa, J. and Gambino, D., *Z. Anorg. Allg. Chem.*, **2013**, 639, 1417.
135. Benítez, J., Guggeri, L., Tomaz, I., Costa Pessoa, J., Moreno, V., Lorenzo, J., Avilés, F.X., Garat, B. and Gambino, D., *J. Inorg. Biochem.*, **2009**, 103, 1386.
136. Köpf-Maier, P. and Köpf, H., *Drugs Future*, **1986**, 11, 297.
137. Köpf-Maier, P., Wagner, W., Hesse, B. and Köpf, H., *Eur. J. Cancer*, **1981**, 17, 665.
138. Djordjevic, C., Vanadium and Its Role in Life. In: Sigel, H. and Sigel, A., eds., *Metal Ions in Biological Systems*, vol. 31, Marcel Dekker, **1995**, 602.

139. Ghosh, P., D'Cruz, O.J., Narla, R.K. and Uckun, F.M., *Clin. Cancer Res.*, **2000**, *6*, 1536.
140. El-Naggar, M.M., El-Waseef, A.M., El-Halafawy, K.M. and El-Sayed, I.H., *Cancer Lett.*, **1998**, *133*, 71.
141. Köpf-Maier, P., Wagner, W. and Köpf, H., *Cancer Chemoth. Pharm.*, **1981**, *5*, 237.
142. Dong, Y., Gosh, P. and Uckun, F.M., inventors; Vanadium Compounds for Treating Cancer., *U.S. Pat. Appl. Publ.*, United States patent US 7091351 B2. patent application 10/857440, **2006/08/15**.
143. Navara, C.S., Narla, R.K., D'Cruz, O.J., Venkatachalam, T.K. and Uckun, F.M., inventors; Vanadium Compounds for Treating Cancer, WO patent WO 2000/035930 A1. patent application US 9919016 W, **2000/06/22**.
144. Uckun, F.M., Dong, Y. and Gosh, P., inventors; Vanadium compounds for treating cancer. *U.S. Pat. Appl. Publ.*, United States patent application US 2004/0235815 A1. patent application 10/857440, **2004/11/25**.
145. D'Cruz, O.J., Ghosh, P. and Uckun, F.M., *Biol. Reprod.*, **1998**, *58*, 1515.
146. Köpf-Maier, P. and Köpf, H., *Chem. Rev.*, **1987**, *87*, 1137.
147. Kopf-Maier, P., Wagner, W. and Liss, E., *J. Cancer Res. Clin. Oncol.*, **1983**, *106*, 44.
148. Al-abbasi, A.A., Tahir, M.I.M., Kayed, S.F. and Kassim, M.B., *Appl. Organomet. Chem.*, **2022**, *36*, e6607.
149. Banerjee, A., Mohanty, M., Lima, S., Samanta, R., Garribba, E., Sasamori, T. and Dinda, R., *New J. Chem.*, **2020**, *44*, 10946.
150. Cao, Y., Yi, C., Liu, H., Li, H., Li, Q., Yuan, Z. and Wei, G., *Trans. Met. Chem.*, **2016**, *41*, 531.
151. Clark, O., Park, I., Di Florio, A., Cichon, A.C., Rustin, S., Jugov, R., Maeshima, R. and Stoker, A.W., *Cancer Lett.*, **2015**, *357*, 316.
152. Correia, I., Adão, P., Roy, S., Wahba, M., Matos, C., Maurya, M.R., Marques, F., Pavan, F.R., Leite, C.Q.F., Avecilla, F. and Costa Pessoa, J., *J. Inorg. Biochem.*, **2014**, *141*, 83.
153. Corsello, S., Spangler, R., Nagari, R. and Golub, T., inventors; Vanadium Compositions and Methods for Treatment of Cancer, World Intellectual Property Organization WO 2020/102295 A1. patent application PCT/US2019/061108, **2020/05/22**.
154. Ertik, O., Danişman Kalındemirtaş, F., Kaya, B., Yanardag, R., Erdem Kuruca, S., Şahin, O. and Ülküseven, B., *Polyhedron*, **2021**, *202*, 115192.
155. Fu, Y., Wang, Q., Yang, X.G., Yang, X.D. and Wang, K., *J. Biol. Inorg. Chem.*, **2008**, *13*, 1001.

156. Kalindemirtaş, F.D., Kaya, B., Sert, E., Şahin, O., Kuruca, S.E. and Ülküseven, B., *Chem. Biol. Interact.*, **2022**, *363*, 109997.
157. Kowalski, S., Wyrzykowski, D., Hac, S., Rychlowski, M., Radomski, M.W. and Inkielewicz-Stepniak, I., *Int. J. Mol. Sci.*, **2019**, *20*, 261.
158. León, I.E., Butenko, N., Di Virgilio, A.L., Muglia, C.I., Baran, E.J., Cavaco, I. and Etcheverry, S.B., *J. Inorg. Biochem.*, **2014**, *134*, 106.
159. León, I.E., Di Virgilio, A.L., Porro, V., Muglia, C.I., Naso, L.G., Williams, P.A., Bollati-Fogolín, M. and Etcheverry, S.B., *Dalton Trans.*, **2013**, *42*, 11868.
160. León, I.E., Porro, V., Di Virgilio, A.L., Naso, L.G., Williams, P.A., Bollati-Fogolín, M. and Etcheverry, S.B., *J. Biol. Inorg. Chem.*, **2014**, *19*, 59.
161. Lewis, N.A., Liu, F., Seymour, L., Magnusen, A., Erves, T.R., Arca, J.F., Beckford, F.A., Venkatraman, R., González-Sarriás, A., Fronczek, F.R., VanDerveer, D.G., Seeram, N.P., Liu, A., Jarrett, W.L. and Holder, A.A., *Eur. J. Inorg. Chem.*, **2012**, *2012*, 664.
162. Lu, J., Guo, H., Zeng, X., Zhang, Y., Zhao, P., Jiang, J. and Zang, L., *J. Inorg. Biochem.*, **2012**, *112*, 39.
163. Meshkini, A. and Yazdanparast, R., *Exp. Mol. Pathol.*, **2010**, *89*, 334.
164. Mirjalili, S., Dejamfekar, M., Moshtaghian, A., Salehi, M., Behzad, M. and Khaleghian, A., *Drug Res. (Stuttg)*, **2020**, *70*, 545.
165. Nair, R.S., Kuriakose, M., Somasundaram, V., Shenoi, V., Kurup, M.R. and Srinivas, P., *Life Sci.*, **2014**, *116*, 90.
166. Pattanayak, P., Pratihari, J.L., Patra, D., Mitra, S., Bhattacharyya, A., Lee, H.M. and Chattopadhyay, S., *Dalton Trans.*, **2009**, 6220.
167. Prasad, P., Sasmal, P.K., Majumdar, R., Dighe, R.R. and Chakravarty, A.R., *Inorg. Chim. Acta*, **2010**, *363*, 2743.
168. Rivas-García, L., Quiles, J.L., Varela-López, A., Arredondo, M., Lopez, P., Diéguez, A.R., Montes-Bayon, M., Aranda, P., Llopis, J. and Sánchez-González, C., *Food Chem. Toxicol.*, **2020**, *135*, 110900.
169. Sergi, B., Bulut, I., Xia, Y., Waller, Z.A.E., Yildizhan, Y., Acilan, C. and Lord, R.M., *ChemMedChem.*, **2021**, *16*, 2402.
170. Strianese, M., Basile, A., Mazzone, A., Morello, S., Turco, M.C. and Pellicchia, C., *J. Cell. Physiol.*, **2013**, *228*, 2202.

171. Zeng, P., He, L., Ye, Z., Yang, N., Song, Y. and Lu, J., *Trans. Met. Chem.*, **2015**, *40*, 779.
172. Zhang, Y., Wang, L., Zeng, K., Wang, K. and Yang, X., *J. Inorg. Biochem.*, **2018**, *188*, 76.
173. Zhang, Y., Wang, X., Fang, W., Cai, X., Chu, F., Liao, X. and Lu, J., *Bioinorg. Chem. Appl.*, **2013**, *2013*, 437134.
174. Zhang, Y.-L., Wang, X.-S., Fang, W., Cai, X.-Y., Li, H.-Z., Mao, J.-W., Jin, X.-B., Bai, Y.-L. and Lu, J.Z., *Pharmazie*, **2013**, *68*, 827.
175. Yamaguchi, T., Watanabe, S., Matsumura, Y., Tokuoka, Y. and Yokoyama, A., *Bioorg. Med. Chem.*, **2012**, *20*, 3058.
176. Bakhshi Aliabad, H., Khanamani Falahati-pour, S., Ahmadirad, H., Mohamadi, M., Hajizadeh, M.R. and Mahmoodi, M., *Biometals*, **2018**, *31*, 981.
177. Palion-Gazda, J., Luz, A., Raposo, L.R., Choroba, K., Nycz, J.E., Bienko, A., Lewinska, A., Erfurt, K., P, V.B., Machura, B., Fernandes, A.R., Shul'pina, L.S., Ikonnikov, N.S. and Shul'pin, G.B., *Molecules*, **2021**, *26*, 6364.
178. Scalese, G., Correia, I., Benítez, J., Rostán, S., Marques, F., Mendes, F., Matos, A.P., Costa Pessoa, J. and Gambino, D., *J. Inorg. Biochem.*, **2017**, *166*, 162.
179. Wang, Q., Liu, T.T., Fu, Y., Wang, K. and Yang, X.G., *J. Biol. Inorg. Chem.*, **2010**, *15*, 1087.
180. Banik, B., Sasmal, P.K., Roy, S., Majumdar, R., Dighe, R.R. and Chakravarty, A.R., *Eur. J. Inorg. Chem.*, **2011**, *2011*, 1425.
181. Chakravarty, A.R. and Roy, M., Photoactivated DNA Cleavage and Anticancer Activity of 3d Metal Complexes. In: Karlin, K.D., ed., *Progress in Inorganic Chemistry*, John Wiley and Sons Inc, **2011**, 119-202.
182. Sasmal, P.K., Saha, S., Majumdar, R., De, S., Dighe, R.R. and Chakravarty, A.R., *Dalton Trans.*, **2010**, *39*, 2147.
183. Sasmal, P.K., Saha, S., Majumdar, R., Dighe, R.R. and Chakravarty, A.R., *Inorg. Chem.*, **2010**, *49*, 849.
184. Sun, Y., Zheng, Y., Lei, W.H., Zhou, Q.X., Hou, Y.J., Zhang, B.W. and Wang, X.S., *Dalton Trans.*, **2012**, *41*, 651.
185. Yanardag, R., Ulkuseven, B., Sahin, O., Kaya, B. and Tunali, S., inventors; Vanadium Complexes for Treating Alzheimer's Disease with Anti-Diabetic Specification and Its Synthesis Method. Turkey patent application TR2020-8804. **2020**.

186. Gambino, D., *Coord. Chem. Rev.*, **2011**, 255, 2193.
187. Kowalski, S., Wyrzykowski, D. and Inkielewicz-Stepniak, I., *Molecules*, **2020**, 25, 1757.
188. Lu, J.-Z., Du, Y.-F., Guo, H.-W., Jiang, J., Zeng, X.-D. and Zang, L.-Q., *J. Coord. Chem.*, **2011**, 64, 1229.
189. Bennie, R.B., Livingston, D.J., Joel, C., Jeyanthi, D. and Solomon, R.V., *Appl. Organomet. Chem.*, **2021**, 35, e6106.
190. Wu, J.-X., Hong, Y.-H. and Yang, X.-G., *J. Biol. Inorg. Chem.*, **2016**, 21, 919.
191. Brooks, H.B. and Sicilio, F., *Inorg. Chem.*, **1971**, 10, 2530.
192. Inamdar, P.R. and Sheela, A., *Int. J. Biol. Macromol.*, **2015**, 76, 269.
193. Keller, R.J., Coulombe, R.A., Sharma, R.P., Grover, T.A. and Piette, L.H., *Arch. Biochem. Biophys.*, **1989**, 271, 40.
194. Ozawa, T. and Hanaki, A., *Chem. Pharm. Bull.*, **1989**, 37, 1407.
195. Sakurai, H., *Envir. Health Perspect.*, **1994**, 102 Suppl 3, 35.
196. Sakurai, H. and Tsuchiya, K., *FEBS Lett.*, **1990**, 260, 109.
197. Sutton, H.C. and Winterbourne, C.C., *Free Rad. Biol. & Med.*, **1989**, 6, 53.
198. Walling, C., *Acc. Chem. Res.*, **1975**, 8, 125.
199. <https://scifinder-n.cas.org/search/reference/637785e264596205a1733f28/1>. Accessed 11 November 2022, 2022.
200. Ribeiro, N., Bulut, I., Pósa, V., Sergi, B., Sciortino, G., Pessoa, J.C., Maia, L.B., Ugone, V., Garribba, E., Enyedy, E.A., Acilan, C. and Correia, I., *J. Inorg. Biochem.*, **2022**, 235, 111932.
201. Shahabadi, N., Hakimi, M., Morovati, T. and Fatahi, N., *Nucleosides Nucleotides Nucleic Acids*, **2017**, 36, 497.
202. McGowan, G., Parsons, S. and Sadler, P.J., *Inorg. Chem.*, **2005**, 44, 7459.
203. García-Ramos, J.C., Galindo-Murillo, R., Cortés-Guzmán, F. and Ruiz-Azuara, L., *J. Mex. Chem. Soc.*, **2013**, 57, 245.
204. Mello, J.A., Lippard, S.J. and Essigmann, J.M., *Biochemistry*, **1995**, 34, 14783.
205. Jamieson, E.R. and Lippard, S.J., *Chem. Rev.*, **1999**, 99, 2467.
206. Aubrecht, J., Narla, R.K., Ghosh, P., Stanek, J. and Uckun, F.M., *Toxicol. Appl. Pharmacol.*, **1999**, 154, 228.
207. Zeglis, B.M., Pierre, V.C. and Barton, J.K., *Chem. Commun.*, **2007**, 4565.

208. Rehman, S.U., Yaseen, Z., Husain, M.A., Sarwar, T., Ishqi, H.M. and Tabish, M., *PloS One*, **2014**, 9, e93913.
209. Metzler-Nolte, N. and Schatzschneider, U., *Bioinorganic Chemistry: A Practical Course*, Walter de-Gruyter, **2009**, 32-34.
210. Pages, B.J., Ang, D.L., Wright, E.P. and Aldrich-Wright, J.R., *Dalton Trans.*, **2015**, 44, 3505.
211. Bian, L., Li, L., Zhang, Q., Dong, J., Xu, T., Li, J. and Kong, J., *Trans. Met. Chem.*, **2012**, 37, 783.
212. Bian, L., Li, L.-Z., Wang, X., Huang, L., Pu, X.-W. and Dong, J.-F., *Chinese J. Inorg. Chem.*, **2011**, 27, 649.
213. Bian, L., Li, L.-Z., Zhang, Q.-F., Liu, H.-L. and Wang, D.-Q., *Acta Chim. Sinica*, **2011**, 69, 1661.
214. Dong, Y., Narla, R.K., Sudbeck, E. and Uckun, F.M., *J. Inorg. Biochem.*, **2000**, 78, 321.
215. Du, Y.-f., Lu, J.-Z., Guo, H.-w., Jiang, J., Chao, P., Chen, F. and Pan, J.-M., *Trans. Met. Chem.*, **2010**, 35, 859.
216. Guo, Q., Li, L., Dong, J., Liu, H., Xue, Z. and Xu, T., *Acta Chim. Sinica*, **2012**, 70, 1617.
217. Jing, B., Dong, J., Li, J., Xu, T. and Li, L., *J. Coord. Chem.*, **2013**, 66, 520.
218. Jing, B., Dong, J., Wei, Q., Xu, T. and Li, L., *Trans. Met. Chem.*, **2014**, 39, 605.
219. Li, L., Guo, Z., Zhang, Q., Xu, T. and Wang, D., *Inorg. Chem. Commun.*, **2010**, 13, 1166.
220. Li, L., Niu, S.-Y., Shi, Z.-F., Gong, L.-C., Jin, J., Chi, Y.-X. and Xing, Y.-H., *Polyhedron*, **2011**, 30, 976.
221. Lu, L., Yue, J., Yuan, C., Zhu, M., Han, H., Liu, Z. and Guo, M., *J. Inorg. Biochem.*, **2011**, 105, 1323.
222. Prasad, P., Sasmal, P.K., Khan, I., Kondaiah, P. and Chakravarty, A.R., *Inorg. Chim. Acta*, **2011**, 372, 79.
223. Sasmal, P.K., Majumdar, R., Dighe, R.R. and Chakravarty, A.R., *Dalton Trans.*, **2010**, 39, 7104.
224. Sasmal, P.K., Saha, S., Majumdar, R., Dighe, R.R. and Chakravarty, A.R., *Chem. Commun.*, **2009**, 1703.
225. Yuan, C., Lu, L., Gao, X., Wu, Y., Guo, M., Li, Y., Fu, X. and Zhu, M., *J. Biol. Inorg. Chem.*, **2009**, 14, 841.

226. Yuan, C., Lu, L., Wu, Y., Liu, Z., Guo, M., Xing, S., Fu, X. and Zhu, M., *J. Inorg. Biochem.*, **2010**, *104*, 978.
227. Aboafia, S.A., Elsayed, S.A., El-Sayed, A.K.A. and El-Hendawy, A.M., *J. Mol. Struct.*, **2018**, *1158*, 39.
228. Scrivens, P.J., Alaoui-Jamali, M.A., Giannini, G., Wang, T., Loignon, M., Batist, G. and Sandor, V.A., *Mol. Cancer Ther.*, **2003**, *2*, 1053.
229. Ghosh, P., Kotchevar, A.T., DuMez, D.D., Ghosh, S., Peiterson, J. and Uckun, F.M., *Inorg. Chem.*, **1999**, *38*, 3730.
230. Kuwahara, J., Suzuki, T. and Sugiura, Y., *Biochem. Biophys. Res. Commun.*, **1985**, *129*, 368.
231. Pranczk, J., Tesmar, A., Wyrzykowski, D., Inkielewicz-Stępnia, I., Jacewicz, D. and Chmurzyński, L., *Biol. Trace Elem. Res.*, **2016**, *174*, 251.
232. D'Cruz, O.J. and Uckun, F.M., *Expert Opin. Invest. Drugs*, **2002**, *11*, 1829.
233. Narla, R.K., Dong, Y., D'Cruz, O.J., Navara, C. and Uckun, F.M., *Clin. Cancer Res.*, **2000**, *6*, 1546.
234. Narla, R.K., Dong, Y., Klis, D. and Uckun, F.M., *Clin. Cancer Res.*, **2001**, *7*, 1094.
235. Narla, R.K., Chen, C.-L., Dong, Y. and Uckun, F.M., *Clin. Cancer Res.*, **2001**, *7*, 2124.
236. Butenko, N., Tomaz, A.I., Nouri, O., Escribano, E., Moreno, V., Gama, S., Ribeiro, V., Telo, J.P., Costa Pesssoa, J. and Cavaco, I., *J. Inorg. Biochem.*, **2009**, *103*, 622.
237. Szklarzewicz, J., Jurowska, A., Hodorowicz, M., Gryboś, R. and Matoga, D., *J. Mol. Struct.*, **2019**, *1180*, 839.
238. Gryboś, R., Szklarzewicz, J., Jurowska, A. and Hodorowicz, M., *J. Mol. Struct.*, **2018**, *1171*, 880.
239. Demir, S., Yazicilar, T.K. and Tas, M., *Inorg. Chim. Acta*, **2014**, *409*, 399.
240. Fernández, M., Becco, L., Correia, I., Benítez, J., Piro, O.E., Echeverria, G.A., Medeiros, A., Comini, M., Lavaggi, M.L., González, M., Cerecetto, H., Moreno, V., Pessoa, J.C., Garat, B. and Gambino, D., *J. Inorg. Biochem.*, **2013**, *127*, 150.
241. Banerjee, A., Dash, S.P., Mohanty, M., Sanna, D., Sciortino, G., Ugone, V., Garribba, E., Reuter, H., Kaminsky, W. and Dinda, R., *J. Inorg. Biochem.*, **2019**, *199*, 110786.
242. Lima, S., Banerjee, A., Mohanty, M., Sahu, G., Kausar, C., Patra, S.K., Garribba, E., Kaminsky, W. and Dinda, R., *New J. Chem.*, **2019**, *43*, 17711.
243. Jang, Y.-J., Lee, U. and Koo, B.-K., *Bull. Korean Chem. Soc.*, **2005**, *26*, 72.

244. Parma, L., Peters, H.A.B., Johansson, M.E., Gutiérrez, S., Meijerink, H., de Kimpe, S., de Vries, M.R. and Quax, P.H.A., *Int. J. Mol. Sci.*, **2020**, *21*, 4643.
245. Tasiopoulos, A.J., Troganis, A.N., Evangelou, A., Raptopoulou, C.P., Terzis, A., Deligiannakis, Y. and Kabanos, T.A., *Chem. Eur. J.*, **1999**, *5*, 910.
246. Tasiopoulos, A.J., Vlahos, A.T., Keramidas, A.D., Kabanos, T.A., Deligiannakis, Y.G., Raptopoulou, C.P. and Terzis, A., *Angew. Chem., Int. Ed. Engl.*, **1996**, *35*, 2531.
247. Benítez, J., Cavalcanti de Queiroz, A., Correia, I., Alves, M.A., Alexandre-Moreira, M.S., Barreiro, E.J., Lima, L.M., Varela, J., Gonzalez, M., Cerecetto, H., Moreno, V., Pessoa, J.C. and Gambino, D., *Eur. J. Med. Chem.*, **2013**, *62*, 20.
248. Benítez, J., Guggeri, L., Tomaz, I., Arrambide, G., Navarro, M., Costa Pessoa, J., Garat, B. and Gambino, D., *J. Inorg. Biochem.*, **2009**, *103*, 609.
249. Bian, L., Li, L., Zhang, Q. and Wang, D., *Acta Cryst.*, **2010**, *E66*, m1051.
250. Biswas, N., Bera, S., Sepay, N., Mukhopadhyay, T.K., Acharya, K., Ghosh, S., Acharyya, S., Biswas, A.K., Drew, M.G.B. and Ghosh, T., *New J. Chem.*, **2019**, *43*, 16714.
251. Bitu, M.N.A., Hossain, M.S., Asraf, M.A., Hossen, M.F. and Zahan, M.K.-E., *Croat. Chem. Acta*, **2020**, *93*, 231.
252. Cao, Y.-Z., Zhao, H.-Y., Bai, F.-Y., Xing, Y.-H., Wei, D.-M., Niu, S.-Y. and Shi, Z., *Inorg. Chim. Acta*, **2011**, *368*, 223.
253. Cavaco, I., Costa Pessoa, J., Costa, D., Duarte, M.T., Gillard, R.D. and Matias, P., *J. Chem. Soc., Dalton Trans.*, **1994**,
254. Cavaco, I., Costa Pessoa, J., Duarte, M.T., Henriques, R.T., Matias, P.M. and Gillard, R.D., *J. Chem. Soc., Dalton Trans.*, **1996**, 1989.
255. Chakravarty, J., Dutta, S., Chandra, S.K., Basu, P. and Chakravorty, A., *Inorg. Chem.*, **1993**, *32*, 4249.
256. Chatterjee, M., Ghosh, S., Wu, B.-M. and Mak, T.C.W., *Polyhedron*, **1998**, *17*, 1369.
257. Correia, I., Roy, S., Matos, C.P., Borovic, S., Butenko, N., Cavaco, I., Marques, F., Lorenzo, J., Rodriguez, A., Moreno, V. and Pessoa, J.C., *J. Inorg. Biochem.*, **2015**, *147*, 134.
258. Costa Pessoa, J., Calhorda, M.J., Cavaco, I., Correia, I., Duarte, M.T., Felix, V., Henriques, R.T., Piedade, M.F.M. and Tomaz, I., *J. Chem. Soc., Dalton Trans.*, **2002**, 4407.

259. Costa Pessoa, J., Calhorda, M.J., Cavaco, I., Costa, P.J., Correia, I., Costa, D., Vilas-Boas, L.F., Felix, V., Gillard, R.D., Henriques, R.T. and Wiggins, R., *Dalton Trans.*, **2004**, 2855.
260. Costa Pessoa, J., Cavaco, I., Correia, I., Duarte, M.T., Gillard, R.D., Henriques, R.T., Higes, F.J., Madeira, C. and Tomaz, I., *Inorg. Chim. Acta*, **1999**, 293, 1.
261. Drzeżdżon, J., Gawdzik, B., Rybiński, P., Malinowski, J. and Jacewicz, D., *J. Therm. Anal. Calorim.*, **2021**, 146, 1623.
262. Drzeżdżon, J., Pawlak, M., Gawdzik, B., Wypych, A., Kramkowski, K., Kowalczyk, P. and Jacewicz, D., *Materials (Basel)*, **2022**, 15, 1379.
263. Dutta, S., Mondal, S. and Chakravorty, A., *Polyhedron*, **1995**, 14, 1163.
264. Gryboś, R., Matoga, D., Szklarzewicz, J. and Hodorowicz, M., *CSD Communication*, **2018**, CCDC 1851403 and 1851408,
265. Gryboś, R., Szklarzewicz, J. and Hodorowicz, M., *CSD Communication*, **2017**, CCDC 1588193,
266. Hoof, D.L. and Walton, R.A., *Inorg. Chim. Acta*, **1975**, 12, 71.
267. Li, L.Z., Jing, B.Q., Li, L.W. and Xu, T., *Z. Kristallogr.- New Cryst. Struct.*, **2006**, 221, 520.
268. Ma, X.T., Xing, N., Yan, Z.D., Zhang, X.X., Wu, Q. and Xing, Y.H., *New J. Chem.*, **2015**, 39, 1067.
269. Meng, X.-F., Liu, Q.-F., Liu, J.-L., Sun, M.-H. and Ma, J.-J., *Inorg. Nano-Met. Chem.*, **2017**, 47, 1585.
270. Pranczk, J., Jacewicz, D., Wyrzykowski, D., Wojtczak, A., Tesmar, A. and Chmurzyński, L., *Eur. J. Inorg. Chem.*, **2015**, 2015, 3343.
271. Pranczk, J., Wyrzykowski, D., Jacewicz, D., Sikorski, A., Tesmar, A. and Chmurzyński, L., *Polyhedron*, **2015**, 100, 74.
272. Saha, U. and Mukherjea, K.K., *Int. J. Biol. Macromol.*, **2014**, 66, 166.
273. Saha, U., Si, T.K., Nandi, P.K. and Mukherjea, K.K., *Inorg. Chem. Commun.*, **2013**, 38, 43.
274. Scalese, G., Benitez, J., Rostan, S., Correia, I., Bradford, L., Vieites, M., Minini, L., Merlino, A., Coitino, E.L., Birriel, E., Varela, J., Cerecetto, H., Gonzalez, M., Pessoa, J.C. and Gambino, D., *J. Inorg. Biochem.*, **2015**, 147, 116.
275. Seená, E.B., Mathew, N., Kuriakose, M. and Kurup, M.R.P., *Polyhedron*, **2008**, 27, 1455.

276. Shit, M., Bera, S., Maity, S., Maji, S., Weyhermüller, T. and Ghosh, P., *Eur. J. Inorg. Chem.*, **2016**, 2016, 330.
277. Shit, M., Maity, S., Bera, S., Weyhermüller, T. and Ghosh, P., *New J. Chem.*, **2016**, 40, 10305.
278. Sreeja, P.B. and Kurup, M.R., *Spectrochim. Acta A Mol. Biomol. Spectrosc.*, **2005**, 61, 331.
279. Sutradhar, M., Martins, L.M.D.R.S., Guedes da Silva, M.F.C. and Pombeiro, A.J.L., *Appl. Catal. A-Gen.*, **2015**, 493, 50.
280. Takjoo, R., Mague, J.T., Akbari, A. and Ebrahimipour, S.Y., *J. Coord. Chem.*, **2013**, 66, 2852.
281. Wang, C.Y., Jing, B.Q., Dong, J.F. and Li, L.Z., *Acta Cryst.*, **2012**, E68, m907.
282. Wang, Y., Lin, X.-M., Bai, F.-Y. and Sun, L.-X., *J. Mol. Struct.*, **2017**, 1149, 379.
283. Xu, T., Li, L.-Z., Zhou, S.-F., Guo, G.-Q. and Niu, M.-J., *J. Chem. Crystallogr.*, **2005**, 35, 263.
284. Yuan, Z., *CSD Communication*, **2015**, CCDC 1438252, 1052037, 1429158, 1429159,
285. Yuan, Z. and Cao, Y., *CSD Communication*, **2015**, CCDC 1437051, 1437052 and 1437053,
286. Zhao, H.-Y., Xing, Y.-H., Cao, Y.-Z., Li, Z.-P., Wei, D.-M., Zeng, X.-Q. and Ge, M.-F., *J. Mol. Struct.*, **2009**, 938, 54.
287. Tasiopoulos, A.J., Tolis, E.J., Tsangaris, J.M., Evangelou, A., Woollins, D., Slawin, A.M., Pessoa, C., Correia, I. and Kabanos, T.A., *J. Biol. Inorg. Chem.*, **2002**, 7, 363.
288. Tasiopoulos, A.J., Troganis, A.N., Deligiannakis, Y., Evangelou, A., Kabanos, T.A., Woollins, J.D. and Slawin, A., *J. Inorg. Biochem.*, **2000**, 79, 159.
289. Álvarez, L., Grirrane, A., Moyano, R., Álvarez, E., Pastor, A. and Galindo, A., *Polyhedron*, **2010**, 29, 3028.
290. del Río, D., Galindo, A., Vicente, R., Mealli, C., Ienco, A. and Masi, D., *Dalton Trans.*, **2003**, 1813.
291. León, I.E., Etcheverry, S.B., Parajón-Costa, B.S. and Baran, E.J., *Biol. Trace Elem. Res.*, **2012**, 147, 403.
292. León, I.E., Etcheverry, S.B., Parajón-Costa, B.S. and Baran, E.J., *J. Mex. Chem. Soc.*, **2013**, 57, 175.
293. Siddiqi, Z.A., Sharma, P.K., Shahid, M., Khalid, M. and Kumar, S., *J. Mol. Struct.*, **2011**, 994, 295.

294. Wyrzykowski, D., Inkielewicz-Stepniak, I., Pranczk, J., Żamojć, K., Zieba, P., Tesmar, A., Jacewicz, D., Ossowski, T. and Chmurzyński, L., *Biometals*, **2015**, *28*, 307.
295. Pearson, R.G., *J. Am. Chem. Soc.*, **1963**, *85*, 3533.
296. Huheey, J.E., Keiter, E.A. and Keiter, R.L. *Inorganic Chemistry: Principles of Structure and Reactivity* (Fourth edition), HarperCollins College; **1993**, 345-347.
297. Akerman, K.J., Fagenson, A.M., Cyril, V., Taylor, M., Muller, M.T., Akerman, M.P. and Munro, O.Q., *J. Am. Chem. Soc.*, **2014**, *136*, 5670.
298. Roess, D.A., Smith, S.M.L., Winter, P., Zhou, J., Dou, P., Baruah, B., Trujillo, A.M., Levinger, N.E., Yang, X., Barisas, B.G. and Crans, D.C., *Chem. Biodivers.*, **2008**, *5*, 1558.
299. Avgoulas, D., Katsipis, G., Halevas, E., Geromichalou, E.G., Geromichalos, G.D. and Pantazaki, A.A., *J. Inorg. Biochem.*, **2021**, *221*, 111402.
300. Jan, R., Khan, M.S., Hassan, N., Mushtaq, U., Khanday, F.A. and Bhat, M.A., *J. Mol. Liq.*, **2021**, *331*, 115696.
301. Katsipis, G., Tsalouxiidou, V., Halevas, E., Geromichalou, E., Geromichalos, G. and Pantazaki, A.A., *Appl. Microbiol. Biotechnol.*, **2021**, *105*, 147.
302. Prasad, P., Khan, I., Kondaiah, P. and Chakravarty, A.R., *Chemistry*, **2013**, *19*, 17445.
303. Sanasam, B., Raza, M.K., Musib, D. and Roy, M., *J. Chem. Sci.*, **2021**, *133*, 42.
304. Yang, L., Jin, W.-T. and Zhou, Z.-H., *J. Mol. Struct.*, **2020**, *1207*, 127805.
305. Koderá, M., Terasako, N., Kita, T., Tachi, Y., Kano, K., Yamazaki, M., Koikawa, M. and Tokii, T., *Inorg. Chem.*, **1997**, *36*, 3861.
306. Gu, Z.-G., Pang, C.-Y., Qiu, D., Zhang, J., Huang, J.-L., Qin, L.-F., Sun, A.-Q. and Li, Z., *Inorg. Chem. Commun.*, **2013**, *35*, 164.
307. Howson, S.E., Allan, L.E., Chmel, N.P., Clarkson, G.J., Deeth, R.J., Faulkner, A.D., Simpson, D.H. and Scott, P., *Dalton Trans.*, **2011**, *40*, 10416.
308. Qin, L.-F., Pang, C.-Y., Han, W.-K., Zhang, F.-L., Tian, L., Gu, Z.-G., Ren, X. and Li, Z., *Cryst. Eng. Comm.*, **2015**, *17*, 7956.
309. Tian, L., Pang, C.-Y., Zhang, F.-L., Qin, L.-F., Gu, Z.-G. and Li, Z., *Inorg. Chem. Commun.*, **2015**, *53*, 55.
310. Becerra, A., Contreras, R., Carmona, D., Lahoz, F.J. and García-Orduna, P., *Dalton Trans.*, **2013**, *42*, 11640.
311. Boudier, A., Breuil, P.-A.R., Magna, L., Olivier-Bourbigou, H. and Braunstein, P., *J. Organometal. Chem.*, **2012**, *718*, 31.

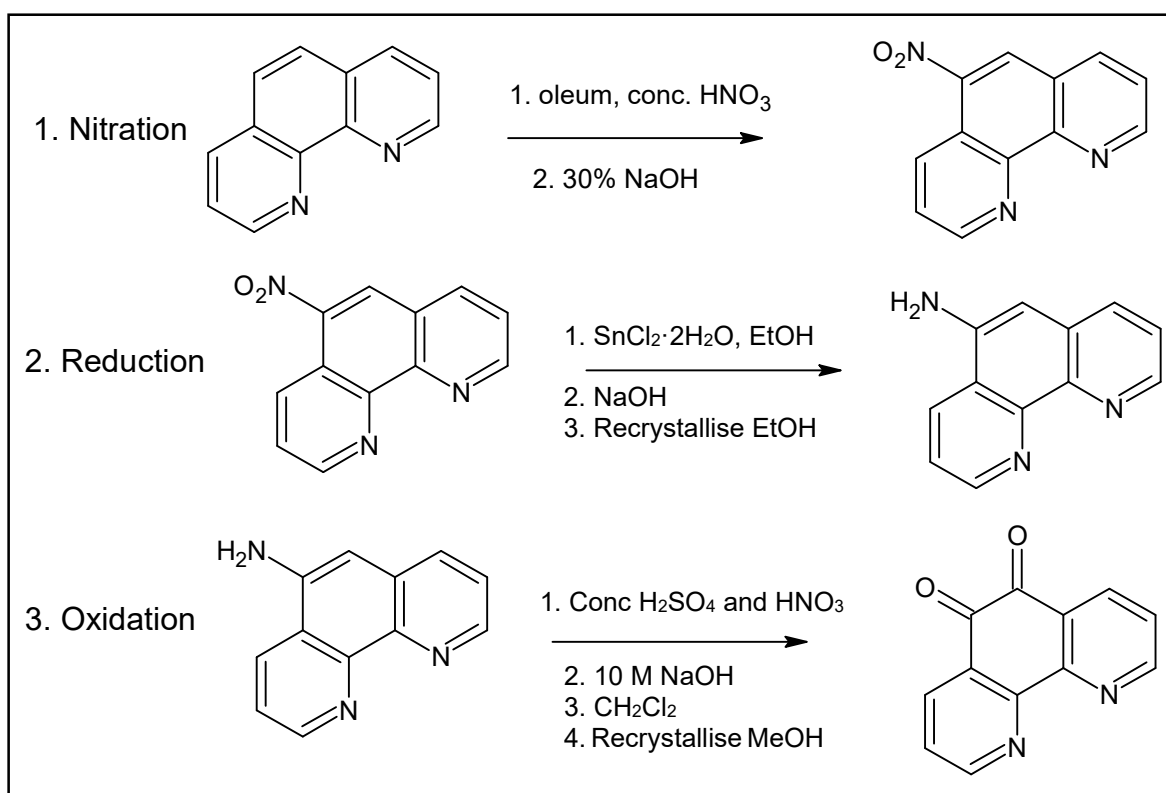
312. Choy, S.W.S., Page, M.J., Bhadbhade, M. and Messerle, B.A., *Organometallics*, **2013**, 32, 4726.
313. Kennedy, D.F., Messerle, B.A. and Rumble, S.L., *New J. Chem.*, **2009**, 33,
314. Kennedy, D.F., Messerle, B.A. and Smith, M.K., *Eur. J. Inorg. Chem.*, **2007**, 2007, 80.
315. Kozlyuk, N., Lopez, T., Roth, P. and Acquaye, J.H., *Inorg. Chim. Acta*, **2015**, 428, 176.
316. Mandal, S., Poria, D.K., Seth, D.K., Ray, P.S. and Gupta, P., *Polyhedron*, **2014**, 73, 12.
317. Kloskowski, M., Pursche, D., Hoffmann, R.-D., Pöttgen, R., Läge, M., Hammerschmidt, A., Glaser, T. and Krebs, B., *Z. Anorg. Allg. Chem.*, **2007**, 633, 106.

## Chapter Two: Synthesis

### 2.1 Synthesis of 1,10-Phenanthroline-5,6-dione (PDO)

Of the *N,N*-bidentate ligands required for this study, 1,10-phenanthroline (PHEN) was purchased from Sigma Aldrich and used as received. The co-ligands dipyrido[3,2-*d*:2',3'-*f*]quinoxaline (DPQ) and dipyrido[3,2-*a*:2',3'-*c*]phenazine (DPPZ) were synthesised. The synthesis of DPQ and DPPZ first involved synthesising the 1,10-phenanthroline-5,6-dione (PDO) precursor.

The synthesis of PDO was first reported by Smith and Cagle in 1947, as a by-product from the nitration of 1,10-phenanthroline.<sup>1</sup> Less than 1% yield of the dione was obtained in this early work.<sup>1</sup> PDO was also reportedly synthesised, again as a by-product, from the oxidation of 5-methoxy-1,10-phenanthroline.<sup>2,3</sup> Two decades later, Dickenson and Summers reported a method with improved yields to synthesise the dione (*Scheme 2.1*).<sup>4</sup>



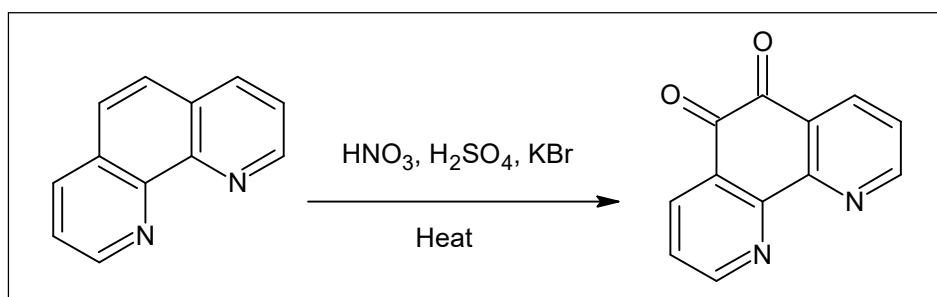
**Scheme 2.1** Synthesis of 1,10-phenanthroline-5,6-dione *via* oxidation of 5-amino-1,10-phenanthroline.<sup>1, 4, 5</sup>

The multi-step method involved converting 1,10-phenanthroline into 5-nitro-1,10-phenanthroline.<sup>1</sup> The nitro group was thereafter reduced using stannous chloride dihydrate to form 5-amino-1,10-phenanthroline.<sup>5</sup> Alternatively, the nitro group may be reduced by sodium borohydride.<sup>6,7</sup> The isolated 5-amino adduct was then oxidised with fuming nitric acid in concentrated sulfuric acid to form the dione. This method improved the yield of the dione from 1,10-phenanthroline to 15%.<sup>4,8</sup>

Gillard and co-workers also described a method to synthesise the dione by oxidising phenanthroline coordinated to a cobalt(III) metal centre with nitric and sulfuric acids in the presence of the bromide anion.<sup>6</sup> The free 1,10-phenanthroline-5,6-quinone hydrate ligand was then isolated by complexing the cobalt(III) with ethylenediaminetetraacetate (EDTA).<sup>6</sup>

Amouyal and co-workers developed a one-step procedure where 1,10-phenanthroline monohydrate was oxidised by nitric acid in 20% oleum.<sup>9</sup> The solution was neutralised with 30% NaOH, following which, crude 5-amino-1,10-phenanthroline was isolated as a precipitate. The filtrate, which contained the dione, was extracted with CH<sub>2</sub>Cl<sub>2</sub>. Upon re-crystallisation from methanol, the dione was isolated at 20% yield. The improved yield was accredited to the lower temperature reaction conditions and higher oleum concentration at the start of the reaction.<sup>9</sup>

A breakthrough in the yield of the dione came when Yamada and co-workers adapted Gillard and co-workers' procedure.<sup>6,10</sup> In the adapted procedure the free 1,10-phenanthroline ligand was oxidised instead of (+)-[Co(PHEN)<sub>3</sub>](ClO<sub>4</sub>)<sub>3</sub> (Scheme 2.2). The 1,10-phenanthroline and potassium bromide were cooled to *ca.* 4 °C prior to the addition of sulfuric and nitric acids. The acids were added dropwise to the reaction mixture before heating. The yield improved to 86%.<sup>10</sup>



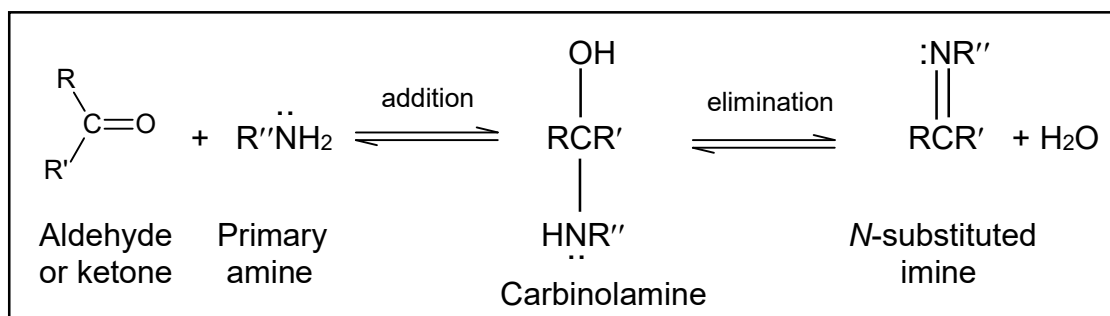
**Scheme 2.2** One-pot synthesis of 1,10-phenanthroline-5,6-dione as reported by Yamada and co-workers.<sup>10</sup>

Hiort and co-workers also used a one-pot synthesis method comprising the nitrating agent and bromide ion but did not cool the acids prior to their addition.<sup>11</sup> They achieved a yield of 45%. Calderazzo *et al.*, however, cooled the sulfuric acid with liquid nitrogen before the phenanthroline/KBr mixture was added.<sup>12</sup> With this method, they achieved a 56% yield. These two contrasting results show the significance of cooling the reaction mixture.

In this work, 1,10-phenanthroline-5,6-dione was synthesised using modified procedures of previously reported methods.<sup>11-15</sup> Nitric and sulfuric acid in a 1:2 ratio were combined and cooled using liquid nitrogen.<sup>12-15</sup> Potassium bromide and 1,10-phenanthroline (PHEN) were added to the frozen acids in a 1.5:1 ratio.<sup>13,14</sup> After slowly warming the mixture to room temperature, the solution was refluxed for six hours, following which the pH of the solution was increased to six with the dropwise addition of 10 M NaOH.<sup>11,14,15</sup> Care was taken not to go above pH 7 as this resulted in the formation of undesired by-products.<sup>13</sup> After filtering, the precipitate was washed with boiling water.<sup>11,15</sup> The combined aqueous extracts were extracted with dichloromethane and dried over anhydrous magnesium sulfate.<sup>12,13,15</sup> After evaporation of the solvent, the crude product was recrystallised from methanol to give a 64% yield of the dione.<sup>13,14</sup>

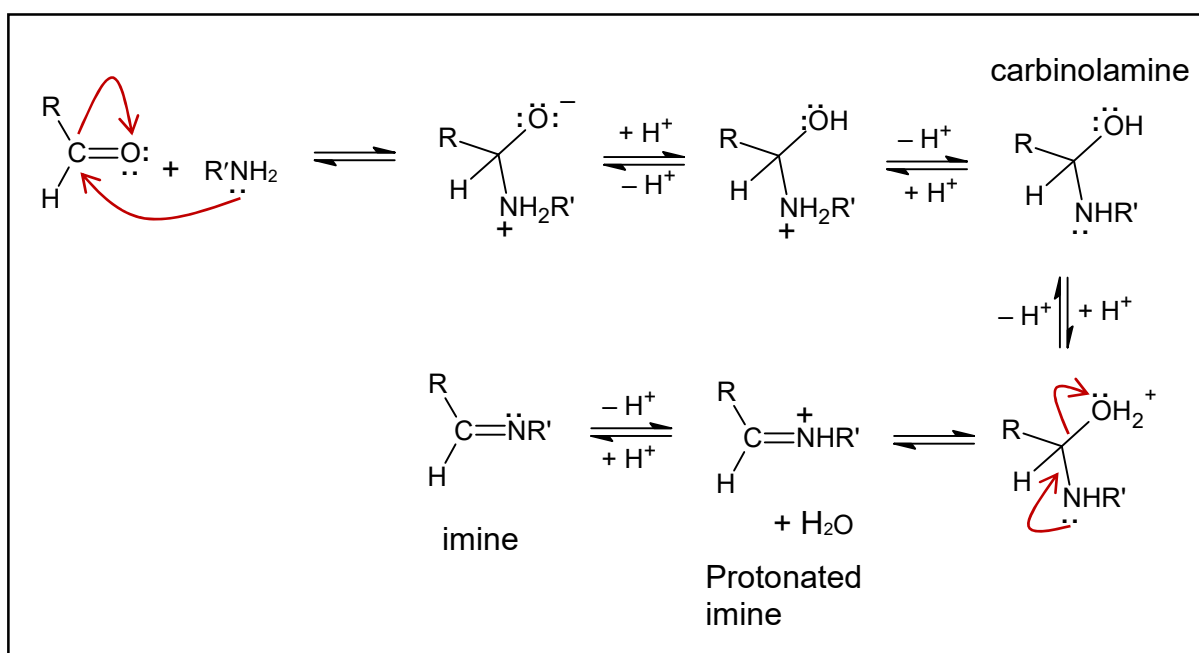
## 2.2 Schiff Base Condensation Reactions

The synthesis of the DPQ and DPPZ co-ligands as well as the *O,N,O'*- and *O,N,N'*-tridentate ligands in this work involved Schiff base condensation reactions. As mentioned in *Chapter One*, a Schiff base (named after its discoverer Hugo Schiff)<sup>16,17</sup> is an *N*-substituted imine obtained from the reaction of an aldehyde or ketone with a primary amine.<sup>18,19</sup> The formation of the *N*-substituted imine is a two-stage reaction.<sup>19</sup> In the first stage, a carbinolamine forms from the nucleophilic addition of the amine to the carbonyl group. The carbinolamine then undergoes dehydration to form the *N*-alkyl- or *N*-aryl-substituted imine (*Scheme 2.3*).<sup>18,19</sup>



**Scheme 2.3** Formation of a Schiff base from an aldehyde or ketone and primary amine.<sup>18</sup>

The mechanism for imine formation is outlined in *Scheme 2.4*. In the first step, the carbinolamine is formed by the nucleophilic attack of the carbonyl carbon by a primary amine. The oxyanion gains a proton, and the ammonium ion loses a proton to form the neutral tetrahedral carbinolamine. The carbinolamine is an unstable intermediate. Protonation on the oxygen atom followed by dehydration of this intermediate forms a protonated imine, which loses a proton to yield the imine.<sup>19</sup>

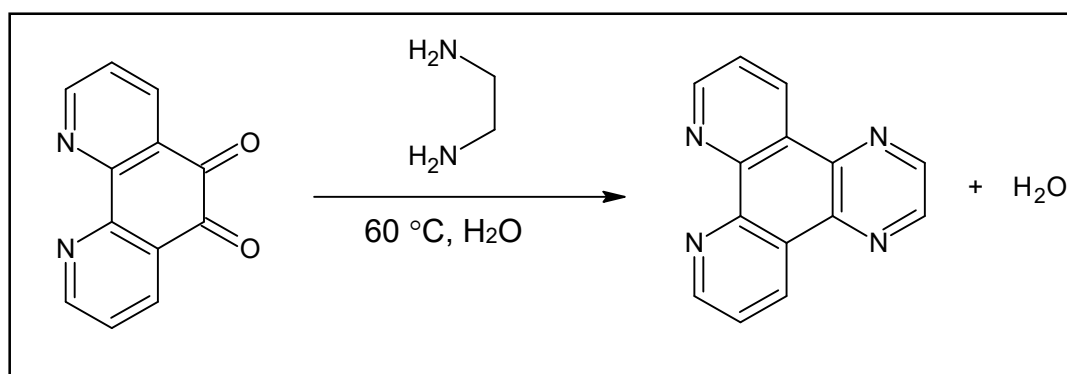


**Scheme 2.4** Mechanism for imine bond formation from an aldehyde and primary amine.<sup>19</sup>

The carbinolamine favours protonation on the nitrogen atom as nitrogen is more basic than oxygen. The oxygen can be protonated to form the imine, by removing water or by precipitation of the imine. The addition and elimination phases of the reaction are also accelerated by acid catalysis. This gives a reasonable equilibrium concentration of the protonated aldehyde or ketone and protonates the carbinolamine to form  $\text{H}_2\text{O}$  and not  $\text{OH}^-$ , which acts as the leaving group. The amine, however, will be converted to its non-nucleophilic protonated form in the presence of excess acid.<sup>18,19</sup>

### 2.2.1 Synthesis of the Bidentate *N,N*-Donor Co-ligand DPQ

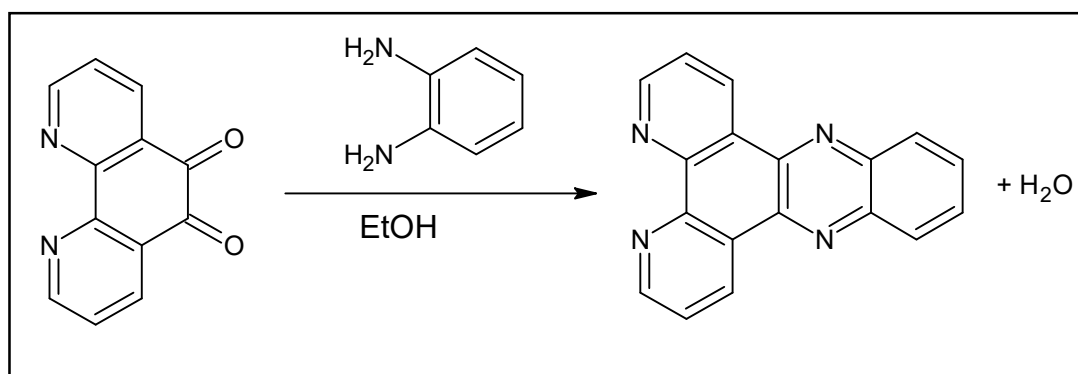
The formation of dipyrido[3,2-*d*:2',3'-*f*]quinoxaline (DPQ) follows a Schiff base condensation reaction of 1,10-phenanthroline-5,6-dione and ethylenediamine (*Scheme 2.5*). Collins and co-workers synthesised DPQ using the above condensation reaction in ethanol followed by the addition of methanol/water (10/90) and recrystallisation of the crude DPQ from methanol.<sup>20</sup> Using this method, much lower yields were obtained in this work than those reported (33% vs 91%).<sup>20</sup> The method adopted by Molphy *et al.* was, therefore, utilised in this work.<sup>21</sup> This method entailed stirring the dione and a 4:1 excess of ethylene diamine in water for twelve hours at 60 °C.<sup>21</sup> The DPQ was isolated as a precipitate and washed with water and diethyl ether to isolate DPQ at a high yield of 89%.



**Scheme 2.5** Schiff base condensation reaction of 1,10-phenanthroline-5,6-dione with ethylenediamine to form DPQ.<sup>21</sup>

### 2.2.2 Synthesis of the Bidentate *N,N*-Donor Co-ligand DPPZ

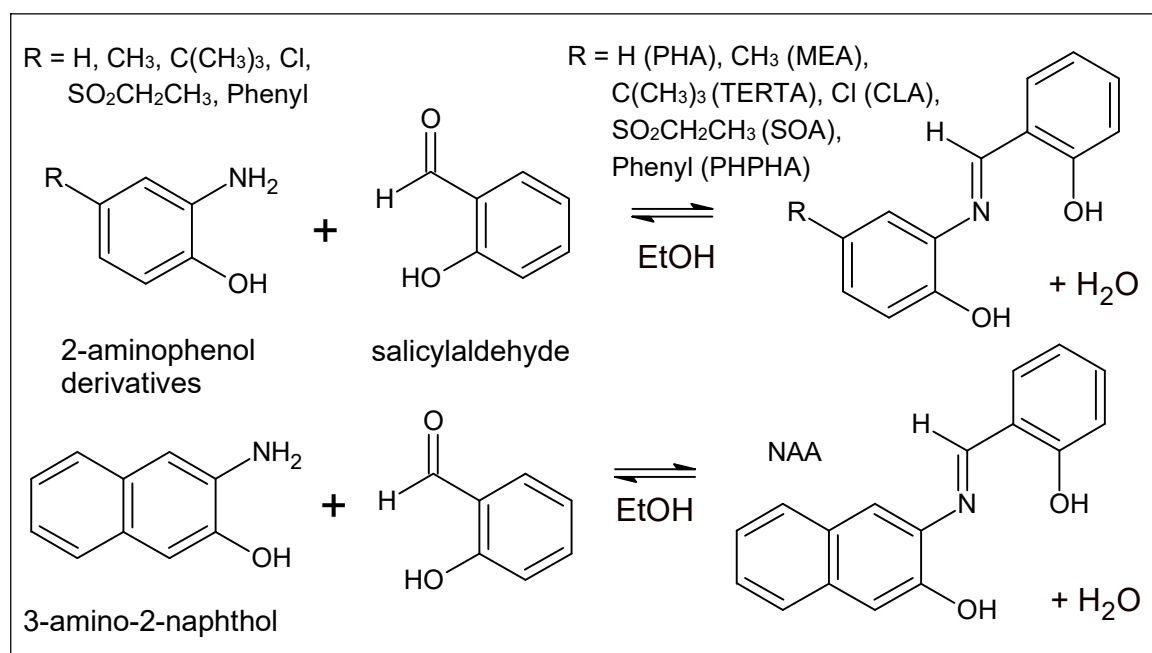
The dipyrido[3,2-*a*:2',3'-*c*]phenazine (DPPZ) ligand is synthesised by a Schiff base condensation reaction between 1,10-phenanthroline-5,6-dione and 1,2-phenylenediamine (*Scheme 2.6*). DPPZ was synthesised according to the method reported by Summers and co-workers.<sup>4</sup> Therein, a 2:1 dione:diamine ratio in refluxing ethanol was used, followed by recrystallisation from methanol to give a yield of 75%.



**Scheme 2.6** Schiff base condensation reaction of 1,10-phenanthroline-5,6-dione with 1,2-phenylenediamine to form DPPZ.<sup>4</sup>

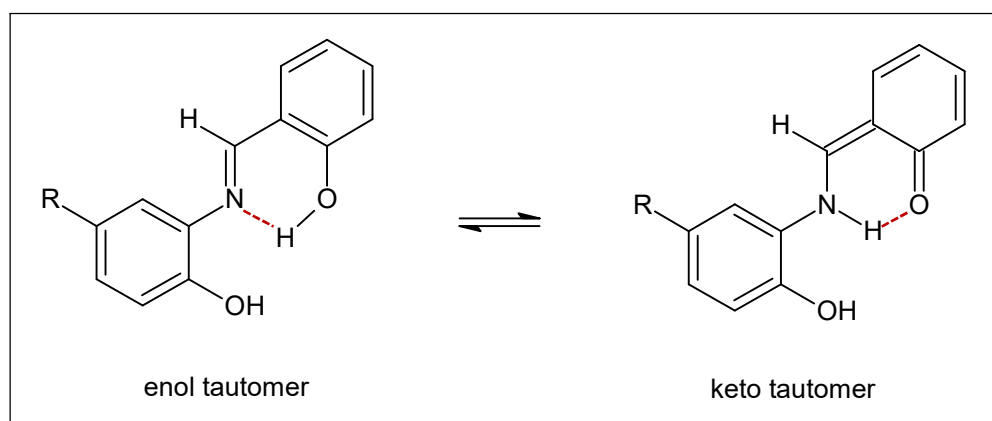
### 2.2.3 Synthesis of the Tridentate *O,N,O'*-Donor Schiff Base Ligands

Salicylidene Schiff base ligands such as 2- $\{(E)-[(2\text{-hydroxyphenyl})\text{imino}]\text{methyl}\}$  phenol are well known having been used extensively in the preparation of transition metal complexes.<sup>22-27</sup> The *O,N,O'*-tridentate Schiff base ligands in this work were synthesised *via* the general procedure of reacting equimolar quantities of salicylaldehyde with the corresponding 2-aminophenol derivative (*Scheme 2.7*) in refluxing ethanol or methanol.<sup>22,28</sup> No further dehydration methods (such as Dean and stark apparatus) were necessary to form the imine. The imine bond is stabilised through electron delocalisation from the electron-dense aryl groups. Owing to the possible delocalisation of electrons, Schiff bases synthesised from aromatic amines and aldehydes generally result in higher yields compared to those synthesised from aliphatic precursors.<sup>29</sup>



**Scheme 2.7** Schiff base condensation reaction between salicylaldehyde and 2-aminophenols substituted in the 4-position to form *O,N,O'*-tridentate Schiff base ligands. These ligands will later be coordinated to oxovanadium(IV).

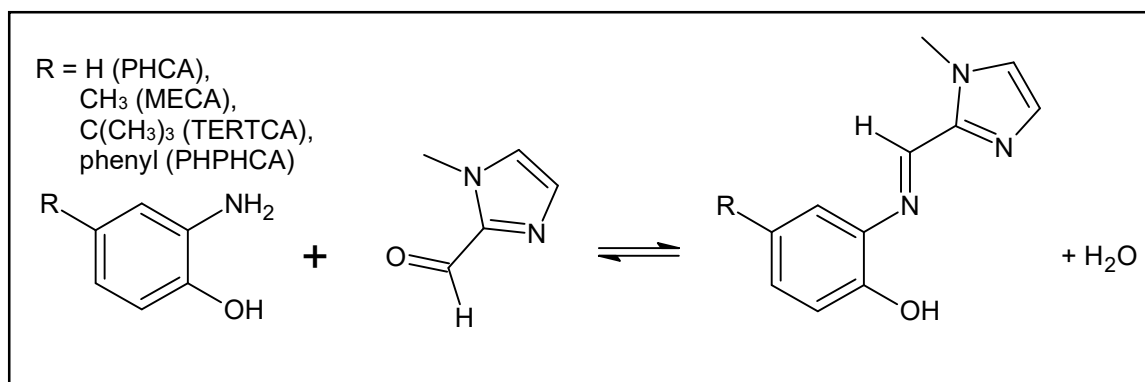
The *O,N,O'*-tridentate ligands derived from salicylaldehyde typically form  $\text{O-H}\cdots\text{N}$  intramolecular hydrogen bonds.<sup>22</sup> Salicylidene Schiff bases are also known to form keto-enol tautomers with  $\text{N-H}\cdots\text{O}$  intramolecular hydrogen bonds in the keto-amine tautomer (Scheme 2.8). Kabak and co-workers, reported that the keto tautomer is predominant over the enol form in the solid-state for 2- $\{[(1E)-(2\text{-hydroxyphenyl)methylene]amino}\}$ -4-methylphenol (MEA) and 4-chloro-2- $\{[(1E)-(2\text{-hydroxyphenyl)methylene]amino}\}$ phenol (CLA).<sup>30,31</sup> Böhme and Fels also reported the isolation of the keto-amine tautomer for 4-*tert*-butyl-2- $\{[(1E)-(2\text{-hydroxyphenyl)methylene]amino}\}$ phenol (TERTA).<sup>32</sup> In agreement with the literature, the *O,N,O'*-donor ligands synthesised in this work crystallised as the keto-amine tautomer (reported in Section 5.1). The phenol-imine solid-state structures of CLA and 2- $\{(E)-[(2\text{-hydroxyphenyl)imino]methyl}\}$ phenol (PHA) have also been reported with small AM1 calculated energy barrier between the keto and enol arrangements.<sup>22,23,30,31</sup> While the *O,N,O'*-donor ligands synthesised in this work crystallised as the keto-amine tautomer (Section 5.1), the NMR spectra of the *O,N,O'*-donor ligands indicate the enol-imine form in solution (Appendix A, Figures A10, A16, A22, A28, A34, A40 and A46), as reported in the literature.<sup>33</sup> The abundance of examples in literature of both the keto and enol tautomers suggests that the energy barrier for this rearrangement is relatively low.



**Scheme 2.8** Enol-keto tautomerism of  $O,N,O'$ -tridentate Schiff base ligands.<sup>30,31</sup> Hydrogen bonds are shown as dashed red lines.

### 2.2.4 Synthesis of the Tridentate $O,N,N'$ -Donor Schiff Base Ligands

The  $O,N,N'$ -tridentate ligands were synthesised by a condensation reaction between 1-methyl-2-imidazolecarboxaldehyde and the corresponding 2-aminophenol (*Scheme 2.9*).



**Scheme 2.9** Schiff base condensation reaction of 1-methyl-2-imidazole carboxaldehyde and 4-substituted 2-aminophenol to form  $O,N,N'$ -tridentate Schiff base ligands.

The novel 4-methyl-2-{[(1*E*)-(1-methyl-1*H*-imidazol-2-yl)methylene]amino}phenol (MECA) and 4-*tert*-butyl-2-{[(1*E*)-(1-methyl-1*H*-imidazol-2-yl)methylene]amino}phenol (TERTCA) ligand derivatives were synthesised *via* the common synthetic route of refluxing the carboxaldehyde and respective 2-aminophenol in ethanol.<sup>30</sup> The ligand, however, did not precipitate out of solution upon cooling. Instead, a viscous oil was formed upon removal of the solvent under reduced pressure. The isolation of the product as an oil is not unusual for this class of compounds.<sup>34-38</sup> Upon cooling to -20 °C the ligands crystallised.

These crystals remained stable when warmed to room temperature. This crystallisation process simplified their handling during further chemical manipulations. The synthetic procedure of MECA and TERTCA in this study has been published.<sup>39</sup>

As previously mentioned, imine bonds are stabilised through electron delocalisation from electron-dense aryl groups.<sup>29</sup> The stabilising effect of the electron-donating methyl and *tert*-butyl substituents in MECA and TERTCA, respectively, is observed with the relative ease with which MECA and TERTCA formed upon refluxing the carboxaldehyde and the corresponding 2-aminophenol derivative in ethanol. Attempts to synthesise 2-{{[(1*E*)-(1-methyl-1*H*-imidazol-2-yl)methylene]amino}phenol (PHCA) and 3-{{[(1*E*)-(1-methyl-1*H*-imidazol-2-yl)methylene]amino}biphenyl-4-ol (PHPHCA) in ethanol, methanol or dichloromethane did not yield the target compounds. Whilst MECA, TERTCA and PHPHCA are novel, PHCA has been previously described. The reported method to synthesise PHCA involved reacting a 1:1 molar ratio of the carboxaldehyde and 2-aminophenol in water, followed by extraction of PHCA with CHCl<sub>3</sub> and recrystallisation from CH<sub>2</sub>Cl<sub>2</sub>/hexane.<sup>40,41</sup> This is an unusual method as imine bonds are susceptible to hydrolysis and the presence of water would shift the reaction equilibrium to the reactants. An improved method was thus developed.

An efficient solid-state method adapted from Akerman and Chiazzari was rather employed to synthesise PHCA and PHPHCA in this work.<sup>42</sup> This method was chosen due to the reduced number of synthetic steps and minimal work-up required to isolate the target compound. A slight excess of 1-methyl-2-imidazole-carboxaldehyde was reacted with 2-aminophenol or 2-amino-4-phenylphenol to form PHCA and PHPHCA, respectively. The imidazole, which is soluble in toluene, was added in excess. This further simplified the purification process as the target ligands are sparingly soluble in toluene. The excess 1-methyl-2-imidazolecarboxaldehyde could thus be easily removed by washing with toluene.

The ligands were then obtained by recrystallisation from toluene. If this recrystallisation process was done at room temperature, X-ray crystallography showed that the PHCA crystals contained water, even with the use of molecular sieves in the toluene. The crystal structure showed the unit cell had a cage-like structure with a trapped hydrogen-bonded water molecule bridging two ligands (*Figure 2.1*).<sup>39</sup> The structure of the hemihydrate form of PHCA is further discussed in *Section 5.2*.

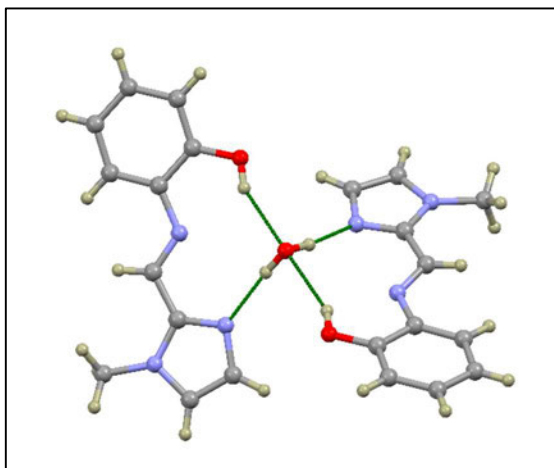


**Figure 2.1** Hydrated PHCA indicating the cage-like structure with a trapped, hydrogen-bonded water molecule bridging two ligands.<sup>39</sup>

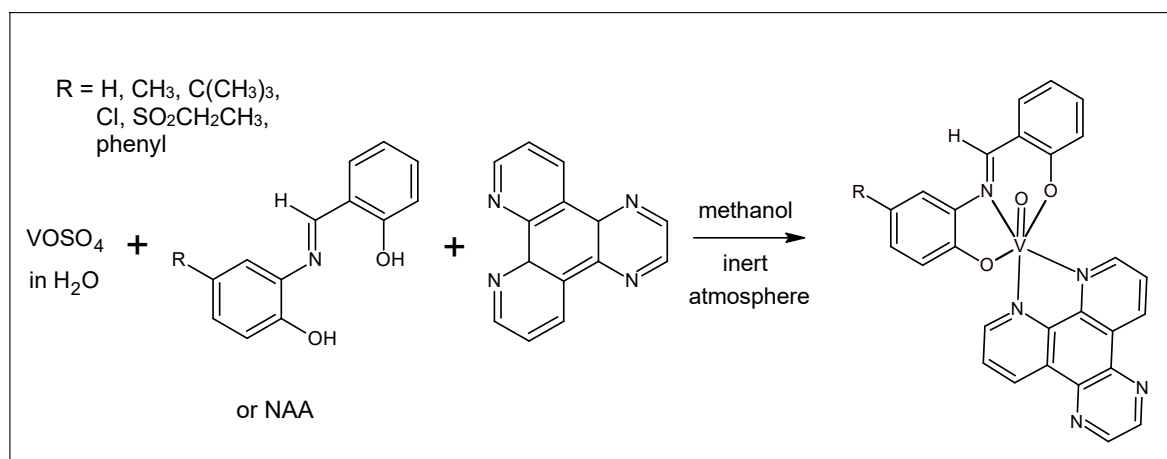
The anhydrous samples of PHCA and PHPHCA ligands were obtained by dissolving the respective crude products in toluene with 3Å molecular sieves and refluxing the resultant solution for 30 minutes. Crystals of anhydrous PHCA and PHPHCA formed upon slow cooling of the hot solution respectively. This adapted synthetic method has been published for PHCA.<sup>39</sup> The cage-like crystal structure with extensive hydrogen-bonding between the ligand and water molecules explains the stability of the hemihydrate. The additional energy afforded by heating the sample was required to break this motif apart and remove the water trapped in the lattice.

### 2.3 Synthesis of the Oxovanadium(IV) Complexes

The formation of octahedral oxovanadium(IV) complexes generally starts from an aqueous solution of vanadyl sulfate or VO(acac)<sub>2</sub>.<sup>43-53</sup> Vanadyl sulfate hydrate (vanadium(IV) oxide sulfate hydrate) was chosen as the metal salt precursor for the synthesis of both the neutral and cationic metal complexes in this work. VO<sup>2+</sup> is considered a hard acid.<sup>54</sup> According to Pearson's principle, hard acid metal ions prefer to bind to hard base ligands.<sup>55</sup> The vanadium core preferentially binds to hard atoms such as oxygen donor ligands and to a lesser extent, heterocyclic nitrogen donor ligands (pyridine is considered a borderline base).<sup>54</sup>

### 2.3.1 Synthesis of the Neutral Oxovanadium(IV) DPQ Complexes

The neutral heteroleptic oxovanadium(IV) complexes with a DPQ co-ligand were prepared by an adapted method of Sasmal and co-workers.<sup>52,53</sup> The synthetic procedure was a one-pot method starting with dissolving vanadyl sulfate hydrate in ultrapure water (*Scheme 2.10*).<sup>52</sup> The relevant *O,N,O'*-tridentate ligand, dissolved in methanol, was then added dropwise, over thirty minutes, to the vanadyl sulfate solution.<sup>52,53</sup> No base was necessary to deprotonate the phenol OH groups. The <sup>1</sup>H NMR spectra of the tridentate ligands indicate that the tridentate ligands are predominantly the enol tautomer in solution, rather than the keto tautomer (*Section 4.2.2*). The metal was found to be sufficiently acidic to deprotonate the phenolic OH groups of the tridentate ligand. Chelation was immediate at room temperature, indicated by the change in colour of the blue vanadyl solution to orange. Similar methods were used for related compounds.<sup>52, 53</sup> Once all the tridentate ligand had been added, solid DPQ was added.<sup>52,53</sup> The solution was then refluxed for two hours under an inert atmosphere to stop vanadium(IV) from oxidising to vanadium(V).<sup>45,46</sup> The metal octahedron comprised the dianionic, tridentate Schiff base ligand; the monodentate, dianionic oxo ligand and the neutral, bidentate DPQ ligand to yield a neutral vanadium(IV) metal chelate.



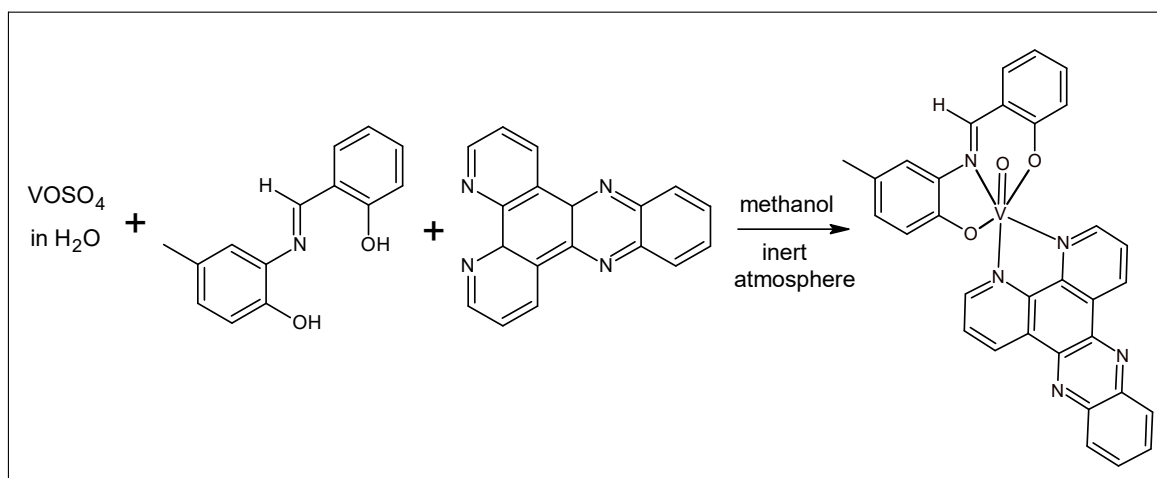
**Scheme 2.10** Synthetic procedure to form the neutral oxovanadium(IV) DPQ complexes.

Both the tridentate Schiff base and DPQ ligands are soluble in methanol and could be separated from the sparingly soluble oxovanadium(IV) DPQ target compound, which precipitates from solution as a red microcrystalline powder. The purity of the product, as indicated by ESI-mass spectroscopy, was further improved when the synthesis was executed under inert conditions.

The isolated vanadyl complexes were shown by X-ray crystallography to form a  $\text{VN}_3\text{O}_3$ , six-coordinate distorted octahedron with the  $O,N,O'$ -tridentate Schiff base ligand occupying three of the equatorial coordination sites of the  $\text{VO}^{2+}$  core and the  $N,N$ -donor DPQ ligand *trans* to the oxo ligand.

### 2.3.2 Synthesis of the Neutral Oxovanadium(IV) DPPZ Complex

The neutral oxovanadium(IV) DPPZ complex was prepared *via* the same procedure as the neutral oxovanadium(IV) DPQ complexes in this work, adapted from Sasmal and co-workers.<sup>52,53</sup> Vanadyl sulfate hydrate was first dissolved in ultrapure water.<sup>45</sup> MEA, dissolved in methanol, was then added dropwise, over 30 minutes, to the vanadyl sulfate solution. After chelation of MEA, solid-state DPPZ was added to the reaction mixture and the solution was heated to reflux under an inert atmosphere for two hours (*Scheme 2.11*). The sparingly soluble oxovanadium(IV)-DPPZ adduct precipitated from solution as a red, microcrystalline precipitate.

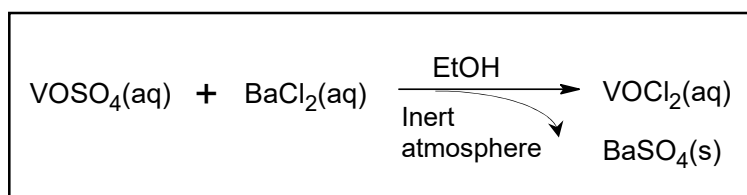


**Scheme 2.11** Synthetic procedure to form the oxovanadium(IV) DPPZ neutral complex.

### 2.3.3 Synthesis of the Cationic Oxovanadium(IV) Complexes

The chelation of a monoanionic *O,N,N'*-tridentate ligand (in place of a dianionic *O,N,O'*-tridentate ligand) and an *N,N*-bidentate co-ligand (PHEN, DPQ or DPPZ) to the  $\text{VO}^{2+}$  core yields a six-coordinate, monocationic complex. The metal chelate was isolated as the hexafluorophosphate(V) metal salt for the PHEN and DPQ complexes due to the ease of isolation of the hexafluorophosphate adduct as compared to the chloride derivative. The DPPZ complex was easily isolated as the chloride salt.

The first step in the synthesis of the monocationic complexes is conversion of the sulfate anion to chloride using barium chloride in a metathesis reaction, under an inert atmosphere (*Scheme 2.12*).<sup>45,46</sup>  $\text{BaSO}_4$  precipitates from the aqueous reaction medium as a fine solid and must be removed by filtration through either a Millipore filter or Celite.<sup>46</sup> The vanadyl chloride remains in the ethanol/water-based solution.



**Scheme 2.12** Conversion of vanadyl sulfate to vanadyl chloride.

The corresponding *O,N,N'*-tridentate ligand, dissolved in ethanol, was then added dropwise to the vanadyl chloride solution under an inert atmosphere, over thirty minutes. The tridentate ligand coordinates immediately to the oxovanadium core as evidenced by the solution changing colour from blue to red.

Past literature reports suggest that refluxing vanadyl chloride and an *O,N,N'*-donor Schiff base ligand, for one hour before adding the *N,N*-donor phenanthroline base is an effective synthetic method.<sup>56</sup> However, in this work, the bidentate *N,N*-donor co-ligand (PHEN, DPQ or DPPZ) was added to the reaction mixture earlier than one hour (no more than thirty minutes after the first addition of the tridentate ligand), to stabilise the vanadium(IV) centre.

If the *N,N*-donor co-ligand was added to the reaction mixture later, the imine bond in the tridentate ligand was found to hydrolyse without the *N,N*-donor co-ligand available for coordination. A sample of a species formed from vanadyl chloride and the *O,N,N'*-tridentate MECA ligand in 11% water/ 89% ethanol (v/v), is shown in *Figure 2.2*. In this case the structure comprises 2-amino-4-methylphenol coordinated to the oxovanadium centre, along with the *O,N,N'*-tridentate ligand MECA. It must be noted that MECA was carefully purified prior to addition to the vanadium reaction mixture. The  $^1\text{H}$  and  $^{13}\text{C}$  NMR spectra of MECA (in *Figures A58* and *A59*, *Appendix A*, respectively) clearly indicate the MECA ligand purity.

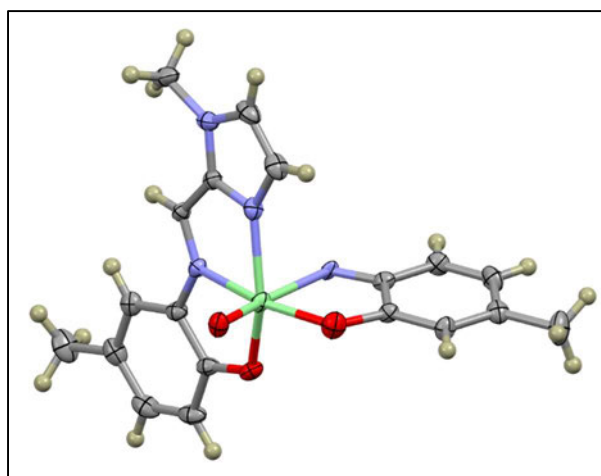
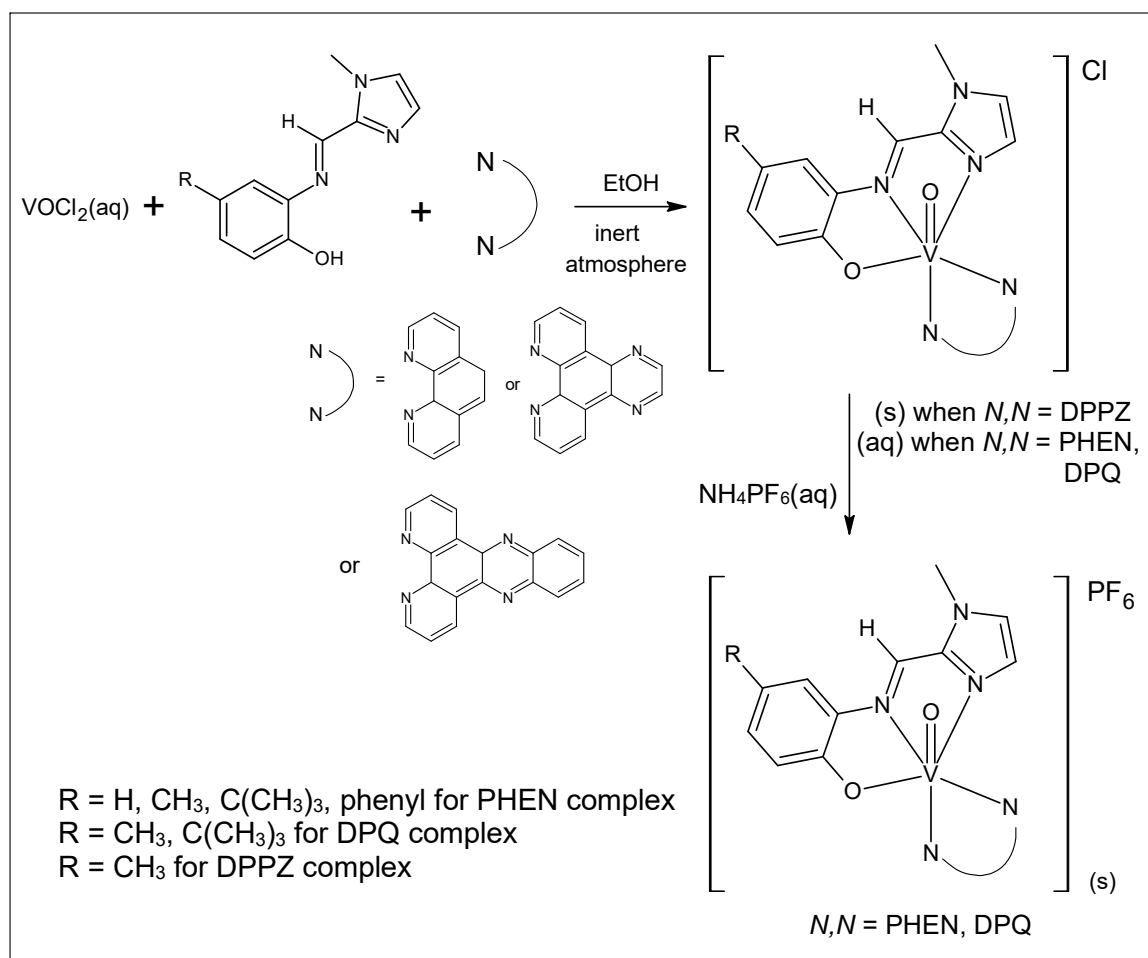


**Figure 2.2** X-ray structure of 2-amino-4-methylphenol coordinated to the VO(MECA) centre. (green = V, red = O, purple = N, grey = C, beige = H).

After the addition of the bidentate *N,N*-donor co-ligand as a solid to the reaction mixture, the reaction mixture was heated to reflux for two hours under an inert atmosphere (*Scheme 2.13*).<sup>45,46,52</sup> The reaction was performed under an inert atmosphere to ensure the formation of the oxovanadium(IV) chelate and not a vanadium(V) derivative.

The chloride salt of the complex with the DPPZ co-ligand precipitated from the ethanol/water solution as a maroon, microcrystalline powder upon reduction of the solvent volume. For the PHEN and DPQ complexes, aqueous ammonium hexafluorophosphate was added to the reaction mixture. The target compounds precipitated from the reaction mixture as the maroon hexafluorophosphate(V) salts (*Scheme 2.13*).



**Scheme 2.13** Synthetic procedure to form the cationic oxovanadium(IV) PHEN, DPQ and DPPZ complexes.

## 2.4 Summary of the Synthetic Procedures

The bidentate and tridentate ligands were synthesised *via* condensation reactions of the respective carbonyl compounds and amines using adaptations of reported methods for DPQ,<sup>21</sup> DPPZ,<sup>4</sup> *O,N,O'*<sup>22,28</sup> and *O,N,N'* ligands.<sup>30,39,42</sup> The neutral DPQ and DPPZ oxovanadium complexes were synthesised using procedures reported for related compounds.<sup>52,53</sup> The complexes were synthesised in methanol, under an inert atmosphere. First, the vanadyl sulfate was dissolved in water. The respective *O,N,O'*-tridentate ligand, dissolved in methanol, was then added. Finally, the addition of solid-state DPQ or DPPZ, formed the respective target compound after heating to reflux.

The PHEN, DPQ and DPPZ complexes with an *O,N,N'*-tridentate ligand were synthesised using adaptations of procedures reported for related compounds.<sup>45,46,52,56</sup> First, the sulfate anion was exchanged to chloride using barium chloride.<sup>45,46</sup> BaSO<sub>4</sub> was removed by filtration. The vanadyl chloride was then reacted with the corresponding *O,N,N'*-tridentate ligand in ethanol, under an inert atmosphere. PHEN, DPQ or DPPZ were added as a solid to the reaction mixture under an inert atmosphere.<sup>45,46,52</sup> After refluxing for two hours under an inert atmosphere, the maroon-coloured complex with a DPPZ co-ligand was precipitated as the chloride salt upon reduction of the solvent volume. The PHEN and DPQ complexes were isolated as the respective hexafluorophosphate salts by the addition of ammonium hexafluorophosphate to the reaction mixture.

## 2.5 References

1. Smith, G.F and Cagle, F.W., *J. Org. Chem.*, **1947**, *12*, 781.
2. Druey, J. and Schmidt, P., *Helv. Chim. Acta*, **1950**, *33*, 1080.
3. Ciba Ltd., British Patent 688,802 (1953) (*Chem. Abstr.*, **1954**, *48*, 4009).
4. Dickenson, J.E. and Summers, L.A., *Aust. J. Chem.*, **1970**, *23*, 1023.
5. Koft, E. and Case, F.H., *J. Org. Chem.*, **1962**, *27*, 865.
6. Gillard, R.D., Hill, R.E.E. and Maskill, R., *J. Chem. Soc. (A)*, **1970**, 1447.
7. Gillard, R.D. and Hill, R.E.E., *J. Chem. Soc., Dalton Trans.*, **1974**, 1217.
8. Katritzky, A.R and Boulton, A.J., *Advances in Heterocyclic Chemistry*, Academic Press, New York, **1978**, *22*, p 35.
9. Amouyal, E., Homsy, A., Chambron, J.-C. and Sauvage, J.-P., *J. Chem. Soc., Dalton Trans.*, **1990**, 1841.
10. Yamada, M., Tanaka, Y., Yashimoto, Y, Kuroda, S and Shimao, I., *Bull. Chem. Soc. Jpn.*, **1992**, *65*, 1006.
11. Hiort, C., Lincoln, P. and Nordén, B., *J. Am. Chem. Soc.*, **1993**, *115*, 3448.
12. Calderazzo, F., Marchetti, F., Pampaloni, G. and Passarelli, V., *J. Chem. Soc., Dalton Trans.*, **1999**, 4389.
13. Metzler-Nolte, N. and Schatzschneider, U., *Bioinorganic Chemistry. A Practical Course.*, Walter de Gruyter, **2009**, *40*, 41.
14. Calucci, L., Pampaloni, G., Pinzino, C. and Prescimone, A., *Inorg. Chim. Acta*, **2006**, *359*, 3911.
15. Yang, C. Luo, J., Ma, J., Zhu, D., Miao, L., Zhang, Y., Liang, L. and Lu, M., *Synth. Met.*, **2012**, *162*, 1097.
16. Tidwell, T., *Angew. Chem. Int. Ed.*, **2008**, *47*, 1016.
17. Schiff, H., *Justus Liebigs Ann. Chem.*, **1864**, *131*, 118.
18. Carey, F.A., *Organic Chemistry* (Fourth edition), McGraw-Hill, **2000**, 672, 673, 689.
19. Bruice, P.Y., *Organic Chemistry* (Second edition), Prentice-Hall, **1998**, 740 – 742.
20. Collins, J.G., Sleeman, A.D., Aldrich-Wright, J.R., Greguric, I. and Hambley, T.W., *Inorg. Chem.*, **1998**, *37*, 3133.
21. Molphy, Z., Prisecaru, A., Slator, C., Barron, N., McCann, M., Colleran, J., Chandran, D., Gathergood, N. and Kellet, A., *Inorg. Chem.*, **2014**, *53*, 5392.
22. Tunç, T., Sari, M., Sadikoğlu and Büyükgüngör, O., *J. Chem. Cryst.*, **2009**, *39*, 672.

23. Elerman, Y. and Elmali, A., *Acta Cryst.*, **1995**, C51, 2344.
24. Kovacic, J.E., *Spectrochim. Acta*, **1967**, 23A, 183.
25. Westland, A.D. and Tarafder, M.T.H., *Inorg. Chem.*, **1981**, 20, 3992.
26. Gündüz, T., Gündüz, N., Kiliç, E. and Atakol, O., *Anal. Chim. Acta*, **1991**, 249, 427.
27. González-Hernández, A., León-Negrete, A., Roman-Bravo, P., Galván-Hidalgo, J.M., Gómez, E. and Barba, V., *Inorg. Chim. Acta.*, **2020**, 501, 119266.
28. Barba, V., Cuahutle, D., Santillan, R. and Farfán, N., *Can. J. Chem.*, **2001**, 79, 1229.
29. Demir, S., Yazicilar, T.K. and Taş, M., *Inorg. Chim. Acta*, **2014**, 409, 399.
30. Kabak, M., Elmali, A. and Elerman, Y., *J. Molec. Struc.*, **1999**, 477, 151.
31. Elmali, A., Kabak, M., Kavlakoglu, E., Elerman, Y. and Durlu, T.N., *J. Molec. Struc.*, **1999**, 510, 207.
32. Böhme, U. and Fels, S., *Acta Cryst.*, **2008**, E64, o14.
33. Öztürk, B. Ö., Bucak, E. and Karabulut, S., *J. Mol. Catal. A-Chem.*, **2013**, 376, 53.
34. Howson, S.E., Allan, L.E., Chmel, N.P., Clarkson, G.J., Deeth, R.J., Faulkner, A.D., Simpson, D.H. and Scott, P., *Dalton Trans.*, **2011**, 40, 10416.
35. Becerra, A., Contreras, R., Carmona, D., Lahoz, F.J. and García-Orduna, P., *Dalton Trans.*, **2013**, 42, 11640.
36. Kennedy, D.F., Messerle, B.A. and Smith, M.K., *Eur. J. Inorg. Chem.*, **2007**, 80.
37. Boudier, A., Breuil, P.-A.R., Magna, L., Olivier-Bourbigou, H. and Braunstein, P., *J. Organometal. Chem.*, **2012**, 718, 31.
38. Kozlyuk, N., Lopez, T., Roth, P. and Acquaye, J.H., *Inorg. Chim. Acta.*, **2015**, 428, 176.
39. Barry, K.-L., Grimmer, C.D., Munro, O.Q. and Akerman, M.P., *RSC Adv.*, **2020**, 10, 7867.
40. Kloskowski, M., Pursche, D., Hoffmann, R.-D., Pöttgen, R., Läge, M., Hammerschmidt, A., Glaser, T. and Krebs, B., *Z. Anorg. Allg. Chem.*, **2007**, 106.
41. Pitt, C.G., Bao, Y., Thompson J., Wani, M.C., Rosenkrantz, H. and Metterville, J., *J. Med. Chem.*, **1986**, 29, 1231.
42. Akerman, M.P. and Chiazzari, V.A., *J. Mol. Struct.*, **2014**, 1058, 22.
43. Benítez, J., Guggeri, L., Tomaz, I., Pessoa, J.C., Moreno, V., Lorenzo, J., Avilés, F.X., Garat, B. and Gambino, D., *J. Inorg. Biochem.*, **2009**, 103, 1386.
44. Benítez, J., Correia, I., Becco, L., Fernández, M., Garat, B., Gallardo, H., Conte, G., Kuznetsov, M.L., Neves, A., Moreno, V., Pessoa, J.C. and Gambino, D., *Z. Anorg. Allg. Chem.*, **2013**, 639, 1417.

45. Banerjee, S., Hussain, A., Prasad, P., Khan, I., Banik, B., Kondaiah, P. and Chakravarty, A.R., *Eur. J. Inorg. Chem.*, **2012**, 24, 3899.
46. Banik, B., Somyajit, K., Koley, D., Nagaraju, G. and Chakravarty, A.R., *Inorg. Chim. Acta*, **2012**, 393, 284.
47. Sasmal, P., Patra, A.K., Nethaji, M. and Chakravarty, A.R., *Inorg. Chem.*, **2007**, 46, 11112.
48. Yuan, C., Lu, L., Gao, X., Wu, Y., Guo, M., Li, Y., Fu, X. and Zhu, M., *J. Biol. Inorg. Chem.*, **2009**, 14, 841.
49. Lu, L., Yue, J., Yuan, C., Zhu, M., Han, H., Liu, Z. and Guo, M., *J. Inorg. Biochem.*, **2011**, 105, 1323.
50. Yuan, C., Lu, L., Wu, Y., Liu, Z., Guo, M., Xing S., Fu, X. and Zhu, M., *J. Inorg. Biochem.*, **2010**, 104, 978.
51. Sasmal, P.K., Saha, A., Majumdar, R., De, S., Dighe, R.R. and Chakravarty, A.R., *Dalton Trans.*, **2010**, 39, 2147.
52. Prasad, P., Sasmal, P.K., Majumdar, R., Dighe, R.R. and Chakravarty, A.R., *Inorganica Chim. Acta*, **2010**, 363, 2743.
53. Sasmal, P., Patra, A.K. and Chakravarty, A.R., *J. Inorg. Biochem.*, **2008**, 102, 1463.
54. Huheey, J.E., Keiter, E.A. and Keiter, R.L., *Inorganic Chemistry: principles of structure and reactivity* (Fourth Edition), HarperCollins College, **1993**, 345 – 347.
55. Pearson, R.G., *J. Am. Chem. Soc.*, **1963**, 85, 3533.
56. Prasad, P., Sasmal, P.K., Khan, I., Kondaiah, P. and Chakravarty, A.R., *Inorg. Chim. Acta*, **2011**, 372, 79.

## Chapter Three: Experimental Methods

### 3.1 General Procedure

1,10-Phenanthroline-5,6-dione<sup>1-4</sup>, dipyrido[3,2-*d*:2',3'-*f*]quinoxaline (DPQ)<sup>5</sup>, dipyrido[3,2-*a*:2',3'-*c*]phenazine (DPPZ)<sup>6</sup>, the *O,N,O'* and *O,N,N'* ligands<sup>7-10</sup> as well as the oxovanadium(IV) complexes<sup>11-13</sup> were synthesised using adaptations of reported procedures. All other reagents and methanol (chromasolv grade) were purchased from Sigma Aldrich. Magnesium sulfate (anhydrous) and all other solvents (AR grade) were purchased from Merck. All reagents and solvents were used as received. Ultrapure water was collected from Elga PURELAB<sup>®</sup> Ultra (DV35) water purification system at 18 MΩ. Reactions were carried out under standard atmospheric conditions unless otherwise specified.

### 3.2 Instrumentation

NMR spectra of the ligands were recorded either with a Bruker Avance III 400 spectrometer, equipped with a Bruker magnet (9.4 T), at frequencies of 400 MHz for <sup>1</sup>H and 100 MHz for <sup>13</sup>C NMR spectra or with a Bruker Avance III 500 spectrometer, equipped with an Oxford magnet (11.7 T), at frequencies of 500 MHz for <sup>1</sup>H and 125 MHz for <sup>13</sup>C. The 9.4 T spectrometer used a 5 mm BBOZ probe <sup>19</sup>F/<sup>31</sup>P-<sup>109</sup>Ag/{<sup>1</sup>H}. The 11.7 T spectrometer used a 5 mm BBOZ probe <sup>31</sup>P-<sup>109</sup>Ag/{<sup>1</sup>H}. The spectra were recorded at 30 °C. All NMR spectra were processed through Topspin 2.1, patch level 6.<sup>14</sup> The proton and carbon shifts were calibrated to the residual DMSO solvent signal of 2.50 ppm for <sup>1</sup>H and 39.51 ppm for <sup>13</sup>C and to the CHCl<sub>3</sub> solvent signal of 7.26 ppm for <sup>1</sup>H and 77.16 ppm for <sup>13</sup>C. FTIR spectra were recorded using a Bruker Alpha FTIR spectrometer equipped with an ATR platinum Diamond 1 reflectance accessory. Data was collected using 128 scans at a resolution of 2 cm<sup>-1</sup>. Electronic spectra for the PHEN and DPQ complexes were recorded from 700 – 200 nm using a Perkin Elmer UV/Vis Lambda 25 double beam spectrometer (1.0 cm path length cuvette) equipped with a Perkin Elmer PTP-1 Peltier Temperature Programmer set to 25.0 °C. The UV WinLab-Run-Scan-Lambda 25 programme was used to record the spectra. Electronic spectra for the DPPZ complexes were recorded from 700 – 200 nm using a Shimadzu UV-1800 double beam Spectrometer (1.0 cm path length cuvette) equipped with a Shimadzu CPS Temperature Controller set to 25.0 °C.

The UV-Probe Ver 2.33 programme was used to record the spectra. Elemental analysis data was acquired using a Thermo Scientific Flash 2000 Organic Elemental CHNS-O Analyser. High Resolution mass spectra were recorded using a Waters Micromass LCT Premier time-of-flight mass spectrometer with electrospray ionisation in positive or negative mode (as specified) with direct injection.

### 3.3 Synthesis of the Bidentate *N,N*-Donor Co-ligands

#### 3.3.1 Synthesis of 1,10-Phenanthroline-5,6-dione Precursor (PDO)

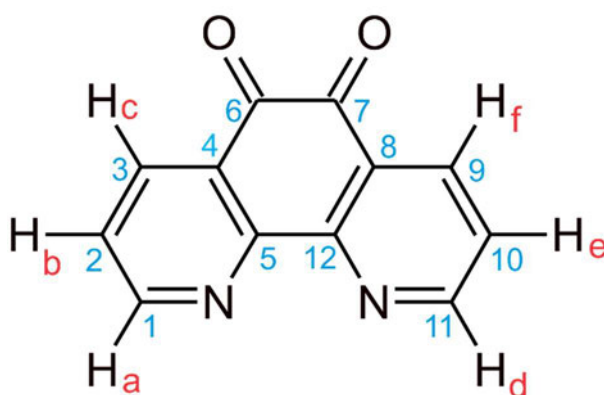


**Figure 3.1** Structure and atom numbering scheme of 1,10-phenanthroline-5,6-dione.

1,10-Phenanthroline-5,6-dione was synthesised using modified procedures reported by Calderazzo *et al.*<sup>1</sup>, Metzler-Nolte and Schatzschneider,<sup>2</sup> Calucci *et al.*<sup>3</sup> and Hiort *et al.*<sup>4</sup>. Concentrated sulfuric acid (40 mL, 96-98%) and nitric acid (20 mL, 70%) were mixed, in a 250 mL, two-neck round bottom flask. The acids were cooled by placing the flask in liquid nitrogen. Solid-state 1,10-phenanthroline (PHEN), (3.994 g, 0.0222 mol) and potassium bromide (3.995 g, 0.0336 mol) were added to the frozen acid mixture. The reaction mixture was then removed from the cooling liquid nitrogen and allowed to warm to room temperature. The solution was then stirred at room temperature for thirty minutes and then heated to reflux for seven hours. The reflux condenser was temporarily removed after six hours of refluxing to allow bromine vapours to escape. The reaction mixture was slowly cooled to room temperature and left standing for fifteen hours. The acidic yellow mixture was then poured over ice (400 g) in a large beaker. Sodium hydroxide solution (10 M, approximately 150 mL) was used to neutralise the solution to pH 6. The resulting murky yellow solution was left to stand for thirty minutes. A yellow solid was then separated from the aqueous solution by vacuum filtration.

The yellow solid was further washed with  $3 \times 100$  mL aliquots of boiling water. The insoluble yellow material was separated from the aqueous extract by vacuum filtration after each extraction. The aqueous filtrate fractions, containing the desired product, were combined and extracted with  $6 \times 100$  mL aliquots of dichloromethane. The combined organic fractions were dried over anhydrous magnesium sulfate, filtered and the solvent removed under reduced pressure. The resultant yellow residue was recrystallised from methanol (270 mL) to yield yellow needles. The crystals were dried for at least one hour under vacuum at  $50$  °C. Yield: 2.994 g, 64.3 %.

$^1\text{H NMR}$  (400 MHz,  $\text{CDCl}_3$ , 303 K) [ $\delta$ , ppm]: 9.12 (dd, 2H,  $H_a$  and  $H_d$ ,  $J_A = 1.8$  Hz,  $J_B = 4.7$  Hz), 8.50 (dd, 2H,  $H_c$  and  $H_f$ ,  $J_A = 1.8$  Hz,  $J_B = 7.9$  Hz), 7.59 (dd, 2H,  $H_b$  and  $H_e$ ,  $J_A = 4.7$  Hz,  $J_B = 7.9$  Hz).  $^{13}\text{C NMR}$  (100 MHz,  $\text{DMSO-}d_6$ , 303 K) [ $\delta$ , ppm]: 178.86 ( $C_6$  and  $C_7$ ), 156.58 ( $C_1$  and  $C_{11}$ ), 153.11 ( $C_5$  and  $C_{12}$ ), 137.46 ( $C_3$  and  $C_9$ ), 128.27 ( $C_2$  and  $C_{10}$ ), 125.75 ( $C_4$  and  $C_8$ ).<sup>15</sup>  $\text{ESI-MS}$  in MeOH:  $[\text{M}+\text{H}]^+$  211.0514  $m/z$  (calc. 211.0508  $m/z$ ).

### 3.3.2 Synthesis of Dipyrido[3,2-*d*:2',3'-*f*]quinoxaline (DPQ)

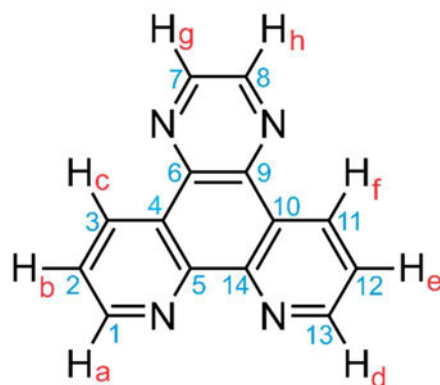


**Figure 3.2** Structure and atom numbering scheme of DPQ.

DPQ was synthesised according to the literature method reported by Molphy *et al.*<sup>5</sup> 1,10-Phenanthroline-5,6-dione (PDO), (1.020 g, 4.853 mmol) was added to distilled water (70 mL) at  $60$  °C, forming a yellow suspension. Ethylenediamine (1.40 mL, 20.9 mmol) was then added to the suspension. The dione immediately dissolved and the solution turned clear brown. A beige solid started to precipitate from solution after fifteen minutes. The reaction mixture was stirred overnight at  $60$  °C.

The suspension was cooled to room temperature, and the resultant beige precipitate was collected by vacuum filtration and washed with distilled water (10 mL) and diethyl ether (2 mL). Yield: 1.007 g, 89.4 %.

$^1\text{H NMR}$  (400 MHz,  $\text{CDCl}_3$ , 303 K) [ $\delta$ , ppm]: 9.47 (dd, 2H,  $H_c$  and  $H_f$ ,  $J_A = 1.7$  Hz,  $J_B = 8.2$  Hz), 9.28 (d, 2H,  $H_a$  and  $H_d$ ,  $J = 2.9$  Hz), 8.96 (s, 2H,  $H_g$  and  $H_h$ ), 7.78 (dd, 2H,  $H_b$  and  $H_e$ ,  $J_A = 4.4$  Hz,  $J_B = 8.2$  Hz).  $^{13}\text{C NMR}$  (100 MHz,  $\text{DMSO}-d_6$ , 303 K) [ $\delta$ , ppm]: 152.46 ( $C_1$  and  $C_{13}$ ), 147.57 ( $C_5$  and  $C_{14}$ ), 144.65 ( $C_7$  and  $C_8$ ), 140.67 ( $C_6$  and  $C_9$ ), 133.30 ( $C_3$  and  $C_{11}$ ), 127.15 ( $C_4$  and  $C_{10}$ ), 124.11 ( $C_2$  and  $C_{12}$ ). **ESI-MS** in DMSO:  $[\text{M}+\text{Na}]^+$  255.0638  $m/z$  (calc. 255.0647  $m/z$ ).

### 3.3.3 Synthesis of Dipyrido[3,2-*a*:2',3'-*c*]phenazine (DPPZ)

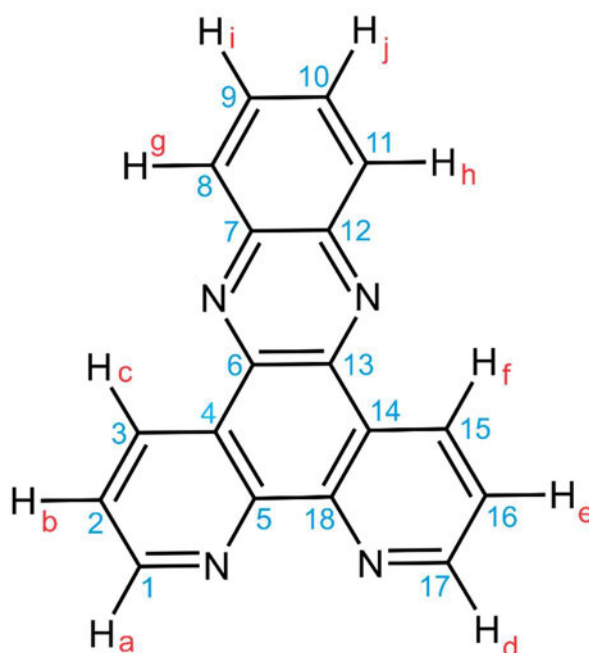


**Figure 3.3** Structure and atom numbering scheme of DPPZ.

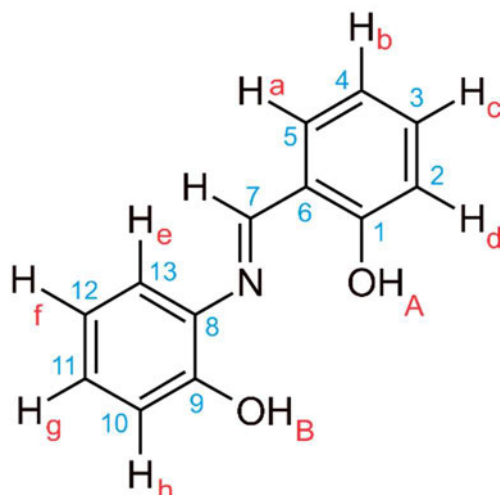
DPPZ was synthesised according to a modified procedure reported by Dickeson and Summers.<sup>6</sup> 1,10-Phenanthroline-5,6-dione (PDO), (2.046 g, 9.734 mmol) was added to 100 mL of dry acetonitrile to give a yellow suspension. 1,2-phenylenediamine (2.046 g, 18.92 mmol) was dissolved in 90 mL dry acetonitrile and added slowly to the dione suspension. The dione dissolved upon addition of the diamine to give a dark brown solution. The solution was heated to reflux for fifteen minutes during which the solution turned amber in colour.

Upon cooling the solution overnight, the product appeared as a beige precipitate. The target compound was collected by vacuum filtration and washed with water, methanol, and diethyl ether. The collected precipitate was then dried under vacuum for four hours at 50 °C. Yield: 2.299 g, 83.7 %.

**<sup>1</sup>H NMR** (400 MHz, CDCl<sub>3</sub>, 303 K) [δ, ppm]: 9.65 (dd, 2H, *Hc* and *Hf*,  $J_A = 1.8$  Hz,  $J_B = 8.1$  Hz), 9.27 (dd, 2H, *Ha* and *Hd*,  $J_A = 1.8$  Hz,  $J_B = 4.4$  Hz), 8.38 – 8.34 (m, 2H, *Hg* and *Hh*), 7.95 – 7.90 (m, 2H, *Hi* and *Hj*), 7.80 (dd, 2H, *Hb* and *He*,  $J_A = 4.4$  Hz,  $J_B = 8.1$  Hz).<sup>16</sup> **<sup>13</sup>C NMR** (100 MHz, DMSO-*d*<sub>6</sub>, 303 K) [δ, ppm]: 152.74 (*C*<sub>1</sub> and *C*<sub>17</sub>), 148.63 (*C*<sub>5</sub> and *C*<sub>18</sub>), 142.69 (*C*<sub>7</sub> and *C*<sub>12</sub>), 141.35 (*C*<sub>6</sub> and *C*<sub>13</sub>), 133.93 (*C*<sub>3</sub> and *C*<sub>15</sub>), 130.81 (*C*<sub>9</sub> and *C*<sub>10</sub>), 129.73 (*C*<sub>8</sub> and *C*<sub>11</sub>), 127.78 (*C*<sub>4</sub> and *C*<sub>14</sub>), 124.30 (*C*<sub>2</sub> and *C*<sub>16</sub>). **ESI-MS** in MeOH: [M+Na]<sup>+</sup> 305.0797 *m/z* (calc. 305.0803 *m/z*).

### 3.4 Synthesis of the *O,N,O'*-Tridentate Schiff Base Ligands

The *O,N,O'* Schiff Base ligands were synthesized *via* a general procedure of reacting equimolar quantities of the corresponding 2-aminophenol with salicylaldehyde as per previously described methods.<sup>7,8</sup>

3.4.1 Synthesis of 2-*{(E)-[(2-hydroxyphenyl)imino]methyl}*phenol (PHA)

**Figure 3.4** Structure and atom numbering scheme of the ligand designated PHA.

2-Aminophenol (0.327 g, 3.00 mmol) was dissolved in ethanol (20 mL) and the resulting clear yellow solution was continuously stirred. Salicylaldehyde (0.33 mL, 3.1 mmol) was then added to this solution and the resulting mixture was heated to reflux for thirty minutes. The solution was then allowed to cool to room temperature. After several days, orange crystals of the target compound were collected by vacuum filtration. Yield: 0.521 g, 81.4 %.

**<sup>1</sup>H NMR** (500 MHz, DMSO-*d*<sub>6</sub>, 303 K) [δ, ppm]: 13.74 (s, br, 1H, *OH*<sub>A</sub>), 9.69 (s, br, 1H, *OH*<sub>B</sub>), 8.96 (s, 1H, N=C-H), 7.61 (dd, 1H, *J*<sub>A</sub> = 1.7 Hz, *J*<sub>B</sub> = 7.6 Hz), 7.40 – 7.34 (m, 2H), 7.14 – 7.11 (m, 1H), 6.97 – 6.93 (m, 3H), 6.89 – 6.86 (m, 1H), phenyl protons *Ha–Hh*. **<sup>13</sup>C NMR** (125 MHz, DMSO-*d*<sub>6</sub>, 303 K) [δ, ppm]: 161.66 (*C*<sub>7</sub>), 160.66 (*C*<sub>1</sub>), 151.04 (*C*<sub>9</sub>), 134.96 (*C*<sub>8</sub>), 119.47 (*C*<sub>6</sub>), 132.76, 132.23, 127.96, 119.57, 119.54, 118.66, 116.62, 116.48 (*C*<sub>2</sub>, *C*<sub>3</sub>, *C*<sub>4</sub>, *C*<sub>5</sub>, *C*<sub>10</sub>, *C*<sub>11</sub>, *C*<sub>12</sub> or *C*<sub>13</sub>). **IR** (cm<sup>-1</sup>): 3044 (O–H); 2836 (C–H); 1626, 1610, 1589 (N=C–H, C=O, N–H bend); 1270 (C–OH); 1134 (C–N); 737 (aromatic C–H bend). **UV-Vis** (CH<sub>3</sub>CN) [λ<sub>max</sub>, ε]: 210 nm, 1.95 × 10<sup>4</sup> M<sup>-1</sup> cm<sup>-1</sup>; 232 nm, 1.36 × 10<sup>4</sup> M<sup>-1</sup> cm<sup>-1</sup>; 268 nm, 1.02 × 10<sup>4</sup> M<sup>-1</sup> cm<sup>-1</sup>; 348 nm, 1.07 × 10<sup>4</sup> M<sup>-1</sup> cm<sup>-1</sup>. **Melting point**: 185.7 – 186.2 °C (lit<sup>8</sup> = >186 °C). **ESI-MS** in 90% CHCl<sub>3</sub> and 10% MeOH: [M–H]<sup>-</sup> 212.0715 *m/z* (calc. 212.0712 *m/z*). **Elemental Analysis**: Calculated for C<sub>13</sub>H<sub>11</sub>NO<sub>2</sub>: C, 73.222; H, 5.200; N, 6.570 %. Found: C, 72.808; H, 5.199; N, 6.513 %.

### 3.4.2 Synthesis of 2-[[*(1E)*-(2-hydroxyphenyl)methylene]amino]-4-methylphenol (MEA)

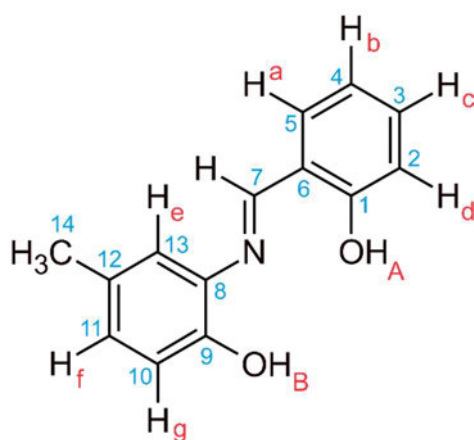


**Figure 3.5** Structure and atom numbering scheme of the ligand designated MEA.

2-Amino-4-methylphenol (0.367 g, 2.98 mmol) was dissolved in ethanol (25 mL) and the resulting solution was continuously stirred. Salicylaldehyde (0.32 mL, 3.0 mmol) was then added to this solution. There was an immediate colour change, from pale yellow to bright yellow. The solution was then heated to reflux for thirty minutes. The solvent was removed *via* rotary evaporation under reduced pressure. The remaining orange powder was recrystallised from methanol (15 mL). After several days, red brick-like crystals were collected by vacuum filtration. Subsequent recrystallisation from the filtrate yielded more needle-like red crystals. Yield: 0.603 g, 89.1%.

**<sup>1</sup>H NMR** (500 MHz, DMSO-*d*<sub>6</sub>, 303 K) [δ, ppm]: 13.80 (s, br, 1H, OH<sub>A</sub>), 9.45 (s, br, 1H, OH<sub>B</sub>), 8.95 (s, 1H, N=C-H), 7.60 (dd, 1H, H<sub>a</sub>, *J*<sub>A</sub> = 1.7 Hz, *J*<sub>B</sub> = 7.6 Hz), 7.39 – 7.36 (m, 1H, H<sub>c</sub>), 7.18 (d, 1H, H<sub>e</sub>, *J* = 1.7 Hz), 6.96 – 6.92 (m, 3H, H<sub>b</sub>, H<sub>d</sub> and H<sub>f</sub>), 6.85 (d, 1H, H<sub>g</sub>, *J* = 8.1 Hz), 2.25 (s, 3H, CH<sub>3</sub>). **<sup>13</sup>C NMR** (125 MHz, DMSO-*d*<sub>6</sub>, 303 K) [δ, ppm]: 161.32 (C<sub>7</sub>), 160.72 (C<sub>1</sub>), 148.77 (C<sub>9</sub>), 134.46 (C<sub>12</sub>), 132.68 (C<sub>3</sub>), 132.18 (C<sub>5</sub>), 128.42 (C<sub>11</sub>), 128.26 (C<sub>8</sub>), 119.81 (C<sub>13</sub>), 119.50 (C<sub>6</sub>), 118.63 (C<sub>2</sub>), 116.63 (C<sub>4</sub>), 116.34 (C<sub>10</sub>), 20.11 (C<sub>14</sub>). **IR** (cm<sup>-1</sup>): 3051 (O-H); 2909 (C-H); 1611, 1597 (N=C-H, C=O, N-H bend); 1278 (C-OH); 1142 (C-N); 760 (aromatic C-H bend). **UV-Vis** (CH<sub>3</sub>CN) [λ<sub>max</sub>, ε]: 212 nm, 2.35 × 10<sup>4</sup> M<sup>-1</sup> cm<sup>-1</sup>; 268 nm, 1.18 × 10<sup>4</sup> M<sup>-1</sup> cm<sup>-1</sup>; 353 nm, 1.14 × 10<sup>4</sup> M<sup>-1</sup> cm<sup>-1</sup>. **Melting point**: 158.8 – 159.3 °C (lit<sup>7</sup> = 162 – 165 °C). **ESI-MS** in 50% MeOH and 50% DMSO: [M+H]<sup>+</sup> 228.1027 *m/z* (calc. 228.1025 *m/z*). **Elemental Analysis**: Calculated for C<sub>14</sub>H<sub>13</sub>NO<sub>2</sub>: C, 73.988; H, 5.766; N, 6.165 %. Found: C, 73.689; H, 5.463; N, 6.163 %.

### 3.4.3 Synthesis of 4-*tert*-butyl-2-[[*(1E)*-(2-hydroxyphenyl)methylene]-amino]phenol (TERTA)

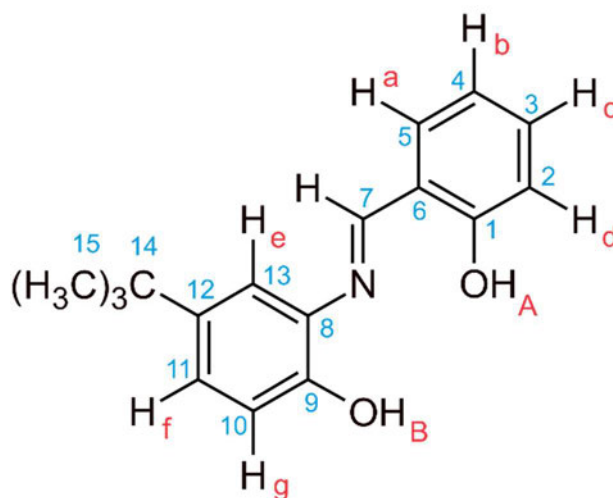


**Figure 3.6** Structure and atom numbering scheme of the ligand designated TERTA.

2-Amino-4-*tert*-butylphenol (0.496 g, 3.00 mmol) was dissolved in ethanol (25 mL) and the resulting yellow solution continuously stirred. Salicylaldehyde (0.32 mL, 3.0 mmol) was then added to this solution and the resulting mixture was heated to reflux for thirty minutes. The solvent was removed *via* rotary evaporation under reduced pressure. The remaining bright orange powder was recrystallised from methanol (20 mL). After several days, orange crystals were collected by vacuum filtration. Yield: 0.670 g, 82.9 %.

**<sup>1</sup>H NMR** (500 MHz, DMSO-*d*<sub>6</sub>, 303 K) [δ, ppm]: 13.86 (s, br, 1H, OH<sub>A</sub>), 9.48 (s, br, 1H, OH<sub>B</sub>), 8.99 (s, 1H, N=C-H), 7.63 (dd, 1H, H<sub>a</sub>, J<sub>A</sub> = 1.6 Hz, J<sub>B</sub> = 7.6 Hz), 7.39 – 7.36 (m, 1H, H<sub>c</sub>), 7.33 (d, 1H, H<sub>e</sub>, J = 2.3 Hz), 7.14 (dd, 1H, H<sub>f</sub>, J<sub>A</sub> = 2.3 Hz, J<sub>B</sub> = 8.5 Hz), 6.96 – 6.92 (m, 2H, H<sub>b</sub> and H<sub>d</sub>), 6.88 (d, 1H, H<sub>g</sub>, J = 8.4 Hz), 1.29 (s, 9H, (CH<sub>3</sub>)<sub>3</sub>). **<sup>13</sup>C NMR** (125 MHz, DMSO-*d*<sub>6</sub>, 303 K) [δ, ppm]: 161.51 (C<sub>7</sub>), 160.77 (C<sub>1</sub>), 148.60 (C<sub>9</sub>), 142.01 (C<sub>12</sub>), 134.11 (C<sub>8</sub>), 132.63 (C<sub>3</sub>), 132.25 (C<sub>5</sub>), 124.65 (C<sub>11</sub>), 119.51 (C<sub>6</sub>), 118.58 (C<sub>2</sub>), 116.62 (C<sub>4</sub>), 116.45 (C<sub>13</sub>), 115.97 (C<sub>10</sub>), 33.90 (C<sub>14</sub>), 31.31 (C<sub>15</sub>). **IR** (cm<sup>-1</sup>): 3044 (O-H); 2954 (C-H); 1614, 1594 (N=C-H, C=O, N-H bend); 1282 (C-OH); 1144 (C-N); 756 (aromatic C-H bend). **UV-Vis** (CH<sub>3</sub>CN) [λ<sub>max</sub>, ε]: 212 nm, 2.30 × 10<sup>4</sup> M<sup>-1</sup> cm<sup>-1</sup>; 268 nm, 1.16 × 10<sup>4</sup> M<sup>-1</sup> cm<sup>-1</sup>; 353 nm, 1.11 × 10<sup>4</sup> M<sup>-1</sup> cm<sup>-1</sup>. **Melting point**: 141.2 – 141.9 °C (lit<sup>17</sup> = 139 °C). **ESI-MS** in MeOH: [M+H]<sup>+</sup> 270.1496 *m/z* (calc. 270.1494 *m/z*). **Elemental Analysis**: Calculated for C<sub>17</sub>H<sub>19</sub>NO<sub>2</sub>: C, 75.806; H, 7.111; N, 5.202 %. Found: C, 75.516; H, 7.183; N, 5.225 %.

### 3.4.4 Synthesis of 4-chloro-2-[(1*E*)-(2-hydroxyphenyl)methylene]amino-phenol (CLA)

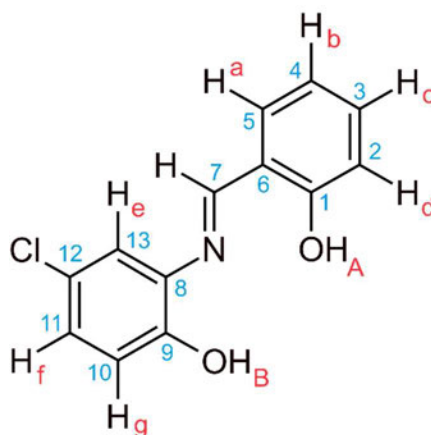


**Figure 3.7** Structure and atom numbering scheme of the ligand designated CLA.

2-Amino-4-chlorophenol (0.431 g, 3.00 mmol) was added to ethanol (60 mL) and the resulting murky brown solution was continuously stirred. Salicylaldehyde (0.32 mL, 3.0 mmol) was then added to this solution and the resulting mixture was heated to reflux for thirty minutes. The solvent volume was reduced by half, and the solution was allowed to cool, during which the product precipitated from solution. After several days, amber crystals were collected by vacuum filtration, and washed with ethanol (5 mL) and diethyl ether (5 mL). The crystals were then crushed and dried under vacuum for three hours at 50 °C. Yield: 0.477 g, 64.2 %.

**<sup>1</sup>H NMR** (400 MHz, DMSO-*d*<sub>6</sub>, 303 K) [δ, ppm]: 13.41 (s, br, 1H, *OH*<sub>A</sub>), 9.97 (s, br, 1H, *OH*<sub>B</sub>), 8.99 (s, 1H, N=C–H), 7.62 (dd, 1H, *H*<sub>a</sub>, *J*<sub>A</sub> = 1.6 Hz, *J*<sub>B</sub> = 7.6 Hz), 7.46 (d, 1H, *H*<sub>e</sub>, *J* = 2.5 Hz), 7.43 – 7.38 (m, 1H, *H*<sub>c</sub>), 7.16 (dd, 1H, *H*<sub>f</sub>, *J*<sub>A</sub> = 2.6 Hz, *J*<sub>B</sub> = 8.6 Hz), 6.98 – 6.93 (m, 3H, *H*<sub>b</sub>, *H*<sub>d</sub> and *H*<sub>g</sub>). **<sup>13</sup>C NMR** (100 MHz, DMSO-*d*<sub>6</sub>, 303 K) [δ, ppm]: 162.99 (*C*<sub>7</sub>), 160.55 (*C*<sub>1</sub>), 150.11 (*C*<sub>9</sub>), 136.28 (*C*<sub>8</sub>), 133.16 (*C*<sub>3</sub>), 132.48 (*C*<sub>5</sub>), 127.25 (*C*<sub>11</sub>), 123.04 (*C*<sub>12</sub>), 119.38 (*C*<sub>6</sub>), 119.21 (*C*<sub>13</sub>), 118.85 (*C*<sub>2</sub>), 117.74 (*C*<sub>4</sub>), 116.64 (*C*<sub>10</sub>). **IR** (cm<sup>-1</sup>): 3040 (O–H); 1614, 1589 (N=C–H, C=O, N–H bend); 1276 (C–OH); 1134 (C–N); 741 (aromatic C–H bend). **UV-Vis** (CH<sub>3</sub>CN) [λ<sub>max</sub>, ε]: 211 nm, 2.27 × 10<sup>4</sup> M<sup>-1</sup> cm<sup>-1</sup>; 230 nm, 1.78 × 10<sup>4</sup> M<sup>-1</sup> cm<sup>-1</sup>; 269 nm, 1.23 × 10<sup>4</sup> M<sup>-1</sup> cm<sup>-1</sup>; 352 nm, 1.10 × 10<sup>4</sup> M<sup>-1</sup> cm<sup>-1</sup>. **Melting point**: 161.1 – 161.9 °C (lit<sup>7</sup> = 221 – 223 °C). **ESI-MS** in 90% CHCl<sub>3</sub> and 10% MeOH: [M+H]<sup>+</sup> 248.0480 *m/z* (calc. 248.0478 *m/z*). **Elemental Analysis**: Calculated for C<sub>13</sub>H<sub>10</sub>NO<sub>2</sub>Cl: C, 63.040; H, 4.070; N, 5.657 %. Found: C, 63.021; H, 3.961; N, 5.411 %.

### 3.4.5 Synthesis of 4-(ethylsulfonyl)-2-[(1*E*)-(2-hydroxyphenyl)-methylene]amino}phenol (SOA)

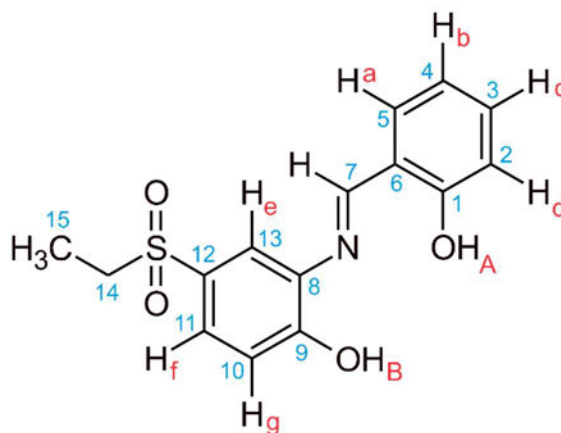


**Figure 3.8** Structure and atom numbering scheme of the ligand designated SOA.

2-Amino-4-ethylsulfonylphenol (0.604 g, 3.00 mmol) was added to ethanol (20 mL) with stirring. Salicylaldehyde (0.37 mL, 3.5 mmol) was added to the clear brown solution and the resulting mixture was heated to reflux for forty-five minutes. The solvent was removed *via* rotary evaporation under reduced pressure. The remaining powder was recrystallised from methanol (32 mL). After several days, amber crystals were collected by vacuum filtration, and washed with diethyl ether (5 mL). The crystals were then crushed and dried under vacuum for three hours at 50 °C. Yield: 0.682 g, 74.5 %.

**<sup>1</sup>H NMR** (400 MHz, DMSO-*d*<sub>6</sub>, 303 K) [δ, ppm]: 13.27 (s, 1H, *OH*<sub>A</sub>), 10.88 (s, 1H, *OH*<sub>B</sub>), 9.06 (s, 1H, N=C–H), 7.82 (d, 1H, *He*, *J* = 2.3 Hz), 7.70 (dd, 1H, *Ha*, *J*<sub>A</sub> = 1.5 Hz, *J*<sub>B</sub> = 7.6 Hz), 7.63 (dd, 1H, *Hf*, *J*<sub>A</sub> = 2.2 Hz, *J*<sub>B</sub> = 8.5 Hz), 7.44 – 7.40 (m, 1H, *Hc*), 7.16 (d, 1H, *Hg*, *J* = 8.5 Hz), 7.00 – 6.95 (m, 2H, *Hb* and *Hd*), 3.26 (q, 2H, *CH*<sub>2</sub>), 1.12 (t, 3H, *CH*<sub>3</sub>).  
**<sup>13</sup>C NMR** (100 MHz, DMSO-*d*<sub>6</sub>, 303 K) [δ, ppm]: 163.74 (*C*<sub>7</sub>), 160.52 (*C*<sub>1</sub>), 155.61 (*C*<sub>9</sub>), 135.79 (*C*<sub>8</sub>), 133.38 (*C*<sub>3</sub>), 132.54 (*C*<sub>5</sub>), 129.08 (*C*<sub>12</sub>), 127.77 (*C*<sub>11</sub>), 119.49 (*C*<sub>13</sub>), 119.40 (*C*<sub>6</sub>), 118.96 (*C*<sub>4</sub>), 116.67 (*C*<sub>2</sub>), 116.57 (*C*<sub>10</sub>), 49.50 (*C*<sub>14</sub>), 7.23 (*C*<sub>15</sub>). **IR** (cm<sup>-1</sup>): 3058 (O–H); 2925 (C–H); 1612, 1584 (N=C–H, C=O, N–H bend); 1296 (C–OH); 1138 (C–N); 733 (aromatic C–H bend).  
**UV-Vis** (CH<sub>3</sub>CN) [λ<sub>max</sub>, ε]: 219 nm, 3.19 × 10<sup>4</sup> M<sup>-1</sup> cm<sup>-1</sup>; 232 nm, 2.60 × 10<sup>4</sup> M<sup>-1</sup> cm<sup>-1</sup>; 251 nm, 2.03 × 10<sup>4</sup> M<sup>-1</sup> cm<sup>-1</sup>; 269 nm, 1.69 × 10<sup>4</sup> M<sup>-1</sup> cm<sup>-1</sup>; 346 nm, 1.41 × 10<sup>4</sup> M<sup>-1</sup> cm<sup>-1</sup>.  
**Melting point**: 177.1 – 177.6 °C. **ESI-MS** in CH<sub>3</sub>CN: [M–H]<sup>-</sup> 304.0642 *m/z* (calc. 304.0644 *m/z*). **Elemental Analysis**: Calculated for C<sub>15</sub>H<sub>15</sub>NO<sub>4</sub>S: C, 58.998; H, 4.952; N, 4.588; S, 10.503 %. Found: C, 58.931; H, 4.962; N, 4.839; S, 10.409 %.

### 3.4.6 Synthesis of 3-[[*(1E)*-(2-hydroxyphenyl)methylene]amino]-2-naphthol (NAA)

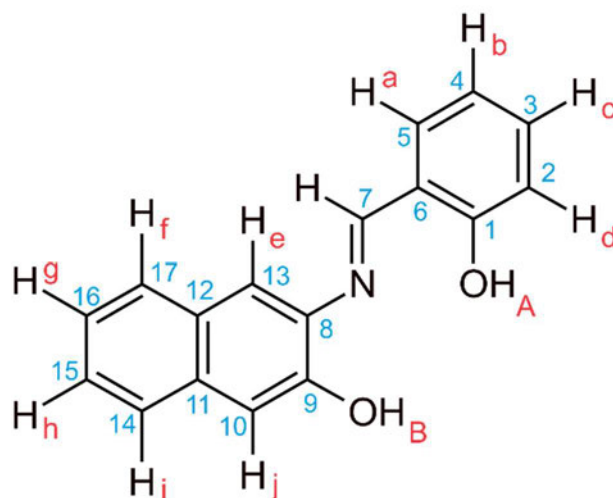


**Figure 3.9** Structure and atom numbering scheme of the ligand designated NAA.

3-Amino-2-naphthol (0.478 g, 3.00 mmol) was added to ethanol (25 mL) and the resulting murky brown suspension was continuously stirred. Salicylaldehyde (0.32 mL, 3.0 mmol) was then added to this solution and the resulting mixture was heated to reflux for forty minutes. Upon heating, the solution turned clear amber. After refluxing, the solution was set aside to cool to allow the product to crystallise. After several days, red crystals were collected by vacuum filtration and washed with diethyl ether (8 mL). The crystals were then crushed and dried under vacuum for four hours at 50 °C. Yield: 0.640 g, 81.0 %.

**<sup>1</sup>H NMR** (500 MHz, DMSO-*d*<sub>6</sub>, 303 K) [δ, ppm]: 13.58 (s, br, 1H, *OH*<sub>A</sub>), 10.05 (s, 1H, *OH*<sub>B</sub>), 9.07 (s, 1H, N=C-H), 7.82 – 7.80 (m, 2H, *H*<sub>j</sub> and *H*<sub>f</sub> or *H*<sub>i</sub>), 7.71 – 7.68 (m, 2H, *H*<sub>a</sub> and *H*<sub>f</sub> or *H*<sub>i</sub>), 7.44 – 7.41 (m, 1H, *H*<sub>c</sub>), 7.40 – 7.37 (m, 1H, *H*<sub>g</sub> or *H*<sub>h</sub>), 7.32 – 7.28 (m, 2H, *H*<sub>e</sub> and *H*<sub>g</sub> or *H*<sub>h</sub>), 7.00 – 6.97 (m, 2H, *H*<sub>b</sub> and *H*<sub>d</sub>). **<sup>13</sup>C NMR** (100 MHz, DMSO-*d*<sub>6</sub>, 303 K) [δ, ppm]: 163.17 (*C*<sub>7</sub>), 160.74 (*C*<sub>1</sub>), 149.98 (*C*<sub>9</sub>), 137.97 (*C*<sub>8</sub>), 133.22 (*C*<sub>11</sub> or *C*<sub>12</sub>), 133.18 (*C*<sub>3</sub>), 132.42 (*C*<sub>5</sub>), 127.94 (*C*<sub>11</sub> or *C*<sub>12</sub>), 127.58 (*C*<sub>14</sub> or *C*<sub>17</sub>), 125.87 (*C*<sub>15</sub> or *C*<sub>16</sub>), 125.67 (*C*<sub>14</sub> or *C*<sub>17</sub>), 123.34 (*C*<sub>15</sub> or *C*<sub>16</sub>), 119.49 (*C*<sub>6</sub>), 118.86 (*C*<sub>4</sub>), 117.12 (*C*<sub>10</sub>), 116.71 (*C*<sub>2</sub>), 109.92 (*C*<sub>13</sub>). **IR** (cm<sup>-1</sup>): 3047 (O-H); 1630, 1608, 1595 (N=C-H, C=O, N-H bend); 1340 (C-OH); 1133 (C-N); 743 (aromatic C-H bend). **UV-Vis** (CH<sub>3</sub>CN) [λ<sub>max</sub>, ε]: 228 nm, 5.71 × 10<sup>4</sup> M<sup>-1</sup> cm<sup>-1</sup>; 269 nm, 3.18 × 10<sup>4</sup> M<sup>-1</sup> cm<sup>-1</sup>; 351 nm, 2.12 × 10<sup>4</sup> M<sup>-1</sup> cm<sup>-1</sup>. **Melting point**: 203.9 – 204.5 °C. **ESI-MS** in methanol: [M+H]<sup>+</sup> 264.1021 *m/z* (calc. 264.1025 *m/z*). **Elemental Analysis**: Calculated for C<sub>17</sub>H<sub>13</sub>NO<sub>2</sub>: C, 77.547; H, 4.977; N, 5.321 %. Found: C, 77.390; H, 5.021; N, 5.297 %.

### 3.4.7 Synthesis of 3-[[*(1E)*-(2-hydroxyphenyl)methylene]amino] biphenyl-4-ol (PHPHA)

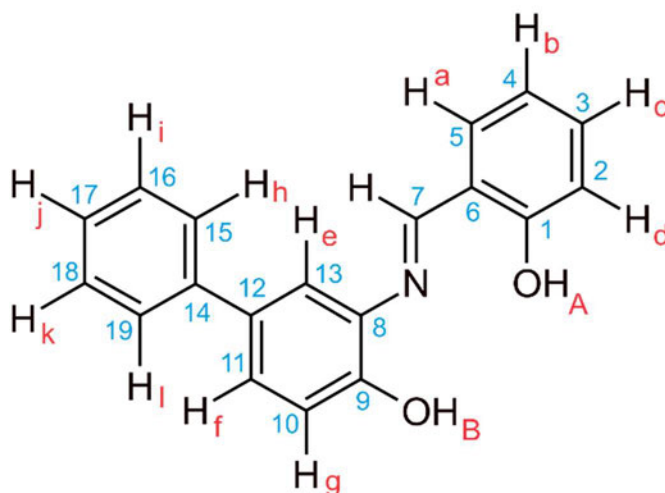


**Figure 3.10** Structure and atom numbering scheme of the ligand designated PHPHA.

2-Amino-4-phenylphenol (0.556 g, 3.00 mmol) was dissolved in ethanol (25 mL) and the resulting clear brown solution was continuously stirred. Salicylaldehyde (0.32 mL, 3.0 mmol) was then added to this solution and the resulting mixture was heated to reflux for thirty minutes. The solution was then slowly cooled, and after several days brown crystals were collected by vacuum filtration and washed with diethyl ether (5 mL). The crystals were then crushed and dried under vacuum for four hours at 50 °C. Yield: 0.644 g, 74.2 %.

**<sup>1</sup>H NMR** (500 MHz, DMSO-*d*<sub>6</sub>, 303 K) [δ, ppm]: 13.79 (s, 1H, OH<sub>A</sub>), 9.88 (s, 1H, OH<sub>B</sub>), 9.11 (s, 1H, N=C-H), 7.70 – 7.68 (m, 3H), 7.64 (d, 1H, *J* = 7.4 Hz), 7.47 – 7.38 (m, 4H), 7.31 (t, 1H, *J* = 7.3 Hz), 7.06 (d, 1H, *J* = 8.4 Hz), 6.98 – 6.95 (m, 2H), phenyl protons *H*<sub>a</sub>–*H*<sub>l</sub>. **<sup>13</sup>C NMR** (125 MHz, DMSO-*d*<sub>6</sub>, 303 K) [δ, ppm]: 162.23 (*C*<sub>7</sub>), 160.76 (*C*<sub>1</sub>), 150.77 (*C*<sub>9</sub>), 135.32 (*C*<sub>8</sub>), 139.74, 131.76, 119.53 (*C*<sub>6</sub>, *C*<sub>12</sub> or *C*<sub>14</sub>), 132.85, 132.34, 128.73, 126.66, 126.17, 126.11, 118.69, 117.68, 116.90, 116.67 (*C*<sub>2</sub>–*C*<sub>5</sub>, *C*<sub>10</sub>, *C*<sub>11</sub>, *C*<sub>13</sub>, *C*<sub>15</sub>–*C*<sub>19</sub>). **IR** (cm<sup>-1</sup>): 3045 (O–H); 1612, 1594 (N=C–H, C=O, N–H bend); 1287 (C–OH); 1137 (C–N); 755 (aromatic C–H bend). **UV-Vis** (CH<sub>3</sub>CN) [λ<sub>max</sub>, ε]: 223 nm, 2.18 × 10<sup>4</sup> M<sup>-1</sup> cm<sup>-1</sup>; 269 nm, 2.63 × 10<sup>4</sup> M<sup>-1</sup> cm<sup>-1</sup>; 356 nm, 1.02 × 10<sup>4</sup> M<sup>-1</sup> cm<sup>-1</sup>. **Melting point**: 166.7 – 167.7 °C. **ESI-MS** in CHCl<sub>3</sub>: [M+H]<sup>+</sup> 290.1176 *m/z* (calc. 290.1181 *m/z*). **Elemental Analysis**: Calculated for C<sub>19</sub>H<sub>15</sub>NO<sub>2</sub>: C, 78.871; H, 5.226; N, 4.842 %. Found: C, 78.495; H, 5.240; N, 4.943 %.

### 3.5 Synthesis of the *O,N,N'*-Tridentate Schiff Base Ligands

The *O,N,N'* Schiff Base ligands were synthesized *via* a solid-state reaction between the corresponding 2-aminophenol and 1-methyl-2-imidazole-carboxaldehyde.<sup>9,10,11</sup>

#### 3.5.1 Synthesis of 2-[[*(1E)*-(1-methyl-1*H*-imidazol-2-yl)methylene]amino}phenol (PHCA)

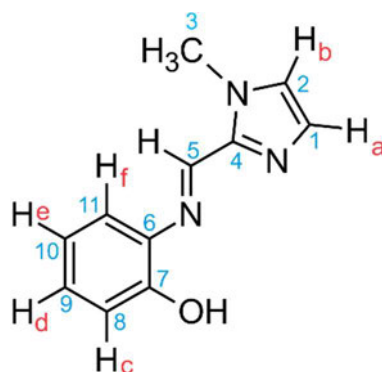


**Figure 3.11** Structure and atom numbering scheme of the ligand designated PHCA.

1-Methyl-2-imidazolecarboxaldehyde (0.487 g, 4.42 mmol) and 2-aminophenol (0.326 g, 2.99 mmol) were ground together in an agate pestle and mortar for approximately ten minutes, during which a paste was formed. As the paste dried under ambient conditions, a yellow powder formed. The crude product was dissolved in toluene (16 mL), and the resulting mixture was heated to reflux for thirty minutes over activated 3Å molecular sieves. Once the volume of the solution was reduced to approximately 10 mL, the molecular sieves were removed from the hot solution by vacuum filtration. The refined product crystallised from the yellow filtrate upon standing at room temperature overnight. The volume of the filtrate was further reduced by boiling off approximately half of the solvent, allowing additional product to crystallise. Yellow crystals were collected by vacuum filtration. The crystals were crushed and dried under vacuum at 50 °C for three hours. Yield: 0.425 g, 70.6 %.

**<sup>1</sup>H NMR** (500 MHz, DMSO-*d*<sub>6</sub>, 303 K) [δ, ppm]: 8.97 (s, br, 1H, *OH*), 8.54 (s, 1H, N=C-H), 7.41 (s, br, 1H, *Hb*), 7.14 (m, 1H, *Ha*), 7.12 (d, 1H, *Hf*, *J* = 1.6 Hz), 7.09 – 7.06 (m, 1H, *Hd*), 6.91 (dd, 1H, *Hc*, , *J*<sub>A</sub> = 1.3Hz, *J*<sub>B</sub> = 8.0 Hz), 6.85 – 6.82 (m, 1H, *He*), 4.08 (s, 3H, N-CH<sub>3</sub>). **<sup>13</sup>C NMR** (125 MHz, DMSO-*d*<sub>6</sub>, 303 K) [δ, ppm]: 150.93 (*C*<sub>5</sub>), 150.53 (*C*<sub>7</sub>), 143.02 (*C*<sub>4</sub>), 138.14 (*C*<sub>6</sub>), 129.45 (*C*<sub>1</sub>), 127.26 (*C*<sub>9</sub>), 126.33 (*C*<sub>2</sub>), 119.79 (*C*<sub>11</sub>), 119.61 (*C*<sub>10</sub>), 116.14 (*C*<sub>8</sub>), 35.24 (*C*<sub>3</sub>). **IR** (cm<sup>-1</sup>): 3140 (O-H); 1634 (C=N); 1450, 1431 (C=C phenol); 755 (imidazole C-H bend).

**UV-Vis** (CH<sub>3</sub>CN) [ $\lambda_{\max}$ ,  $\epsilon$ ]: 297 nm,  $1.08 \times 10^4 \text{ M}^{-1} \text{ cm}^{-1}$ ; 348 nm,  $1.35 \times 10^4 \text{ M}^{-1} \text{ cm}^{-1}$ .

**Melting point:** 120.1 – 120.7 °C. **ESI-MS** in DMSO:  $[\text{M}+\text{Na}]^+$  224.0801  $m/z$  (calc. 224.0800  $m/z$ ). **Elemental Analysis:** Calculated for C<sub>11</sub>H<sub>11</sub>N<sub>3</sub>O: C, 65.651; H, 5.510; N, 20.887 %. Found: C, 65.625; H, 5.240; N, 20.851 %.

### 3.5.2 Synthesis of 4-methyl-2-[(1*E*)-(1-methyl-1*H*-imidazol-2-yl)methylene]amino}phenol (MECA)

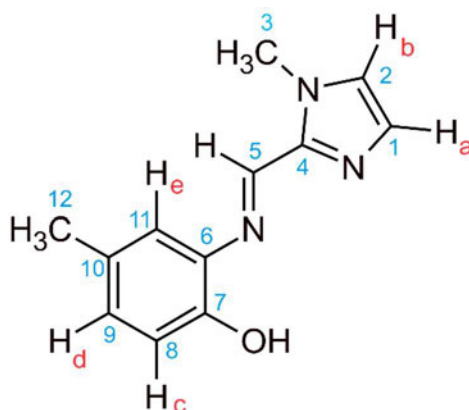


**Figure 3.12** Structure and atom numbering scheme of the ligand designated MECA.

2-Amino-4-methylphenol (0.369 g, 3.00 mmol) was dissolved in ethanol (15 mL) with constant stirring. 1-Methyl-2-imidazolecarboxaldehyde (0.330 g, 3.00 mmol), dissolved in ethanol (10 mL), was added to the yellow phenol solution and the resulting mixture was heated to reflux for ninety minutes. The solvent was then removed *via* rotary evaporation under reduced pressure. The resulting orange, viscous oil was cooled to  $-20 \text{ }^\circ\text{C}$  for fifteen hours, upon which yellow crystals formed. These crystals remained stable upon warmth to room temperature. The crystals were dried under vacuum at  $50 \text{ }^\circ\text{C}$  for four hours. Yield: 0.622 g, 96.3%.

**<sup>1</sup>H NMR** (400 MHz, DMSO-*d*<sub>6</sub>, 303 K) [ $\delta$ , ppm]: 8.76 (s, br, 1H, OH), 8.54 (s, 1H, N=C-H), 7.40 (s, br, 1H, H<sub>b</sub>), 7.14 (s, br, 1H, H<sub>a</sub>), 6.95 (d, 1H, H<sub>e</sub>,  $J = 1.6 \text{ Hz}$ ), 6.88 (dd, 1H, H<sub>d</sub>,  $J_A = 1.5 \text{ Hz}$ ,  $J_B = 8.2 \text{ Hz}$ ), 6.79 (d, 1H, H<sub>c</sub>,  $J = 8.1 \text{ Hz}$ ), 4.07 (s, 3H, N-CH<sub>3</sub>), 2.23 (s, 3H, C-CH<sub>3</sub>). **<sup>13</sup>C NMR** (100 MHz, DMSO-*d*<sub>6</sub>, 303 K) [ $\delta$ , ppm]: 150.70 (C<sub>5</sub>), 148.21 (C<sub>7</sub>), 143.04 (C<sub>4</sub>), 137.67 (C<sub>6</sub>), 129.42 (C<sub>1</sub>), 128.25 (C<sub>10</sub>), 127.66 (C<sub>9</sub>), 126.28 (C<sub>2</sub>), 120.25 (C<sub>11</sub>), 115.96 (C<sub>8</sub>), 35.23 (C<sub>3</sub>), 20.07 (C<sub>12</sub>). **IR** (cm<sup>-1</sup>): 3137 (O-H); 1620 (C=N); 1424, 1406 (C=C phenol); 754 (imidazole C-H bend). **UV-Vis** (CH<sub>3</sub>CN) [ $\lambda_{\max}$ ,  $\epsilon$ ]: 298 nm,  $1.57 \times 10^4 \text{ M}^{-1} \text{ cm}^{-1}$ ; 357 nm,  $1.62 \times 10^4 \text{ M}^{-1} \text{ cm}^{-1}$ . **Melting point:** 129.3 – 129.9 °C. **ESI-MS** in methanol:  $[\text{M}+\text{Na}]^+$  238.0959  $m/z$  (calc. 238.0956  $m/z$ ). **Elemental Analysis:** Calculated for C<sub>12</sub>H<sub>13</sub>N<sub>3</sub>O: C, 66.953; H, 6.088; N, 19.526 %. Found: C, 66.694; H, 5.773; N, 19.157 %.

### 3.5.3 Synthesis of 4-*tert*-butyl-2-[[*(1E)*-(1-methyl-1*H*-imidazol-2-yl)methylene]amino}phenol (TERTCA)

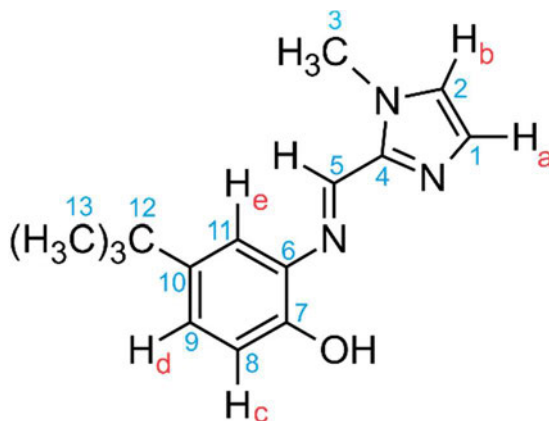


**Figure 3.13** Structure and atom numbering scheme of the ligand designated TERTCA.

2-Amino-4-*tert*-butylphenol (0.496 g, 3.00 mmol) was dissolved in ethanol (15 mL) with stirring. 1-Methyl-2-imidazolecarboxaldehyde (0.330 g, 3.00 mmol), dissolved in ethanol (10 mL), was added to the yellow phenol solution at room temperature, with stirring. The resulting mixture was heated to reflux for ninety minutes. The solvent was then removed by rotary evaporation under reduced pressure. The resulting orange, viscous oil was cooled to  $-20\text{ }^{\circ}\text{C}$  for fifteen hours, upon which yellow crystals formed. The crystals remained stable upon warmth to room temperature. The crystals were dried under vacuum for three hours. Yield: 0.721 g, 93.4%.

**$^1\text{H}$  NMR** (400 MHz,  $\text{DMSO-}d_6$ , 303 K) [ $\delta$ , ppm]: 8.78 (s, br, 1H, OH), 8.56 (s, 1H, N=C-H), 7.41 (s, br, 1H, H<sub>b</sub>), 7.14 (s, br, 1H, H<sub>a</sub>), 7.10 – 7.09 (m, 2H, H<sub>d</sub> and H<sub>e</sub>), 6.83 – 6.81 (m, 1H, H<sub>c</sub>), 4.08 (s, 3H, N-CH<sub>3</sub>), 1.27 (s, 9H, C(CH<sub>3</sub>)<sub>3</sub>).  **$^{13}\text{C}$  NMR** (100 MHz,  $\text{DMSO-}d_6$ , 303 K) [ $\delta$ , ppm]: 150.94 (C<sub>5</sub>), 147.99 (C<sub>7</sub>), 143.07 (C<sub>4</sub>), 141.96 (C<sub>10</sub>), 137.38 (C<sub>6</sub>), 129.38 (C<sub>1</sub>), 126.24 (C<sub>2</sub>), 123.86 (C<sub>11</sub>), 116.87 (C<sub>9</sub>), 115.61 (C<sub>8</sub>), 35.26 (C<sub>3</sub>), 33.81 (C<sub>12</sub>), 31.31 (C<sub>13</sub>). **IR** ( $\text{cm}^{-1}$ ): 3140 (O-H); 2952 (C-H); 1618 (C=N); 1436 (C=C phenol); 759 (imidazole C-H bend). **UV-Vis** ( $\text{CH}_3\text{CN}$ ) [ $\lambda_{\text{max}}$ ,  $\epsilon$ ]: 296 nm,  $1.28 \times 10^4\text{ M}^{-1}\text{ cm}^{-1}$ ; 355 nm,  $1.24 \times 10^4\text{ M}^{-1}\text{ cm}^{-1}$ . **Melting point**: 136.2 – 136.4  $^{\circ}\text{C}$ . **ESI-MS** in methanol:  $[\text{M-H}]^-$  256.1446  $m/z$  (calc. 256.1450  $m/z$ ). **Elemental Analysis**: Calculated for  $\text{C}_{15}\text{H}_{19}\text{N}_3\text{O}$ : C, 70.007; H, 7.443; N, 16.333 %. Found: C, 70.096; H, 7.169; N, 16.126 %.

### 3.5.4 Synthesis of 3-[[*(1E)*-(1-methyl-1*H*-imidazol-2-yl)methylene]amino]biphenyl-4-ol (PHPHCA)

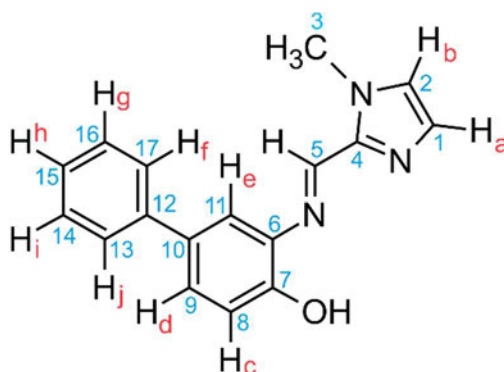


**Figure 3.14** Structure and atom numbering scheme of the ligand designated PHPHCA.

1-Methyl-2-imidazolecarboxaldehyde (0.440 g, 4.00 mmol) and 2-amino-4-phenylphenol (0.556 g, 3.00 mmol) were ground together in an agate pestle and mortar for approximately ten minutes, during which a paste was formed. As the paste dried under ambient conditions, a brown powder formed. The crude product was dissolved in toluene (150 mL), and the resulting mixture was heated to reflux for thirty minutes over activated 3Å molecular sieves. Once the volume of the solution was reduced to approximately 35 mL, the molecular sieves were removed from the hot solution by vacuum filtration. The refined product crystallised from the filtrate upon standing at room temperature for fifteen hours. The volume of the filtrate was further reduced to approximately 10 mL, by boiling off solvent, allowing additional product to crystallise. Brown crystals were collected by vacuum filtration. The crystals were dried under vacuum at 50 °C for four hours. Yield: 0.552 g, 66.3 %.

**<sup>1</sup>H NMR** (400 MHz, DMSO-*d*<sub>6</sub>, 303 K) [δ, ppm]: 9.17 (s, br, 1H, *OH*), 8.66 (s, 1H, N=C-H), 7.68 – 7.66 (m, 2H), 7.43 – 7.39 (m, 5H), 7.31 – 7.29 (m, 1H), 7.16 (d, 1H, *J* = 0.8 Hz), 6.99 (d, 1H, *J* = 8.2 Hz), phenyl protons *Ha–Hj*, 4.10 (s, 3H, N-CH<sub>3</sub>). **<sup>13</sup>C NMR** (100 MHz, DMSO-*d*<sub>6</sub>, 303 K) [δ, ppm]: 151.56 (*C*<sub>5</sub>), 150.18 (*C*<sub>7</sub>), 143.05, 139.85, 138.54, 131.75 (*C*<sub>4</sub>, *C*<sub>6</sub>, *C*<sub>10</sub>, or *C*<sub>12</sub>), 129.51, 126.54, 126.36, 125.33, 118.13, 116.58 (*C*<sub>1</sub>, *C*<sub>2</sub>, *C*<sub>8</sub>, *C*<sub>9</sub>, *C*<sub>11</sub>, *C*<sub>15</sub>), 128.71, 126.14 (*C*<sub>13,17</sub> or *C*<sub>14,16</sub>), 35.28 (*C*<sub>3</sub>). **IR** (cm<sup>-1</sup>): 3140 (O-H); 1614 (C=N); 1450, 1406 (C=C phenol); 752 (imidazole C-H bend). **UV-Vis** (CH<sub>3</sub>CN) [λ<sub>max</sub>, ε]: 276 nm, 1.85 × 10<sup>4</sup> M<sup>-1</sup> cm<sup>-1</sup>; 364 nm, 1.09 × 10<sup>4</sup> M<sup>-1</sup> cm<sup>-1</sup>. **Melting point**: 165.1 – 165.8 °C. **ESI-MS** in DMSO: [M-H]<sup>-</sup> 276.1141 *m/z* (calc. 276.1137 *m/z*). **Elemental Analysis**: Calculated for C<sub>17</sub>H<sub>15</sub>N<sub>3</sub>O: C, 73.623; H, 5.452; N, 15.156 %. Found: C, 73.737; H, 5.375; N, 15.100 %.

### 3.6 Synthesis of the Neutral Oxovanadium(IV) Complexes

The neutral DPQ and DPPZ oxovanadium complexes were synthesised using adaptations of reported methods.<sup>11, 13</sup>

#### 3.6.1 Synthesis of (2-*{(E)-[(2-oxidophenyl)imino]methyl}phenolate*) (dipyrido[3,2-*d*:2',3'-*f*]quinoxaline) oxovanadium(IV) ([VO(PHA)(DPQ)])

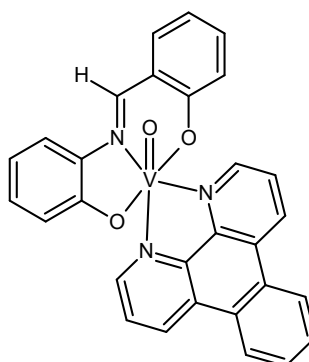


**Figure 3.15** Structure of the complex designated [VO(PHA)(DPQ)].

Vanadium(IV) oxide sulfate hydrate (0.082 g, 0.50 mmol) was dissolved in ultrapure water (5 mL) and the solution was degassed and saturated with nitrogen. PHA ligand (0.107 g, 0.502 mmol) was dissolved in HPLC grade methanol (22 mL). The resulting yellow solution was filtered and purged with nitrogen for ten minutes. The ligand solution was then added dropwise to the blue vanadyl sulfate solution over thirty minutes, under a nitrogen atmosphere, *via* a cannula. The solution changed from clear blue to murky green during this procedure. Solid-state DPQ (0.116 g, 0.499 mmol) was then added to the solution. The resulting mixture was heated to reflux under a nitrogen atmosphere. A red precipitate began to form after ten minutes of heating. The mixture was heated to reflux for two hours, under a nitrogen atmosphere. The red, microcrystalline powder was collected by vacuum filtration and washed with ultrapure water (5 mL) and diethyl ether (7 mL). The precipitate was crushed and dried for three hours, under vacuum, at 50 °C. Yield: 0.171 g, 67.1%.

**IR** (cm<sup>-1</sup>): 1600 (C=N); 958 (V=O); 532 (V-O); 424 (V-N). **UV-Vis** (CH<sub>3</sub>CN) [ $\lambda_{\text{max}}$ ,  $\epsilon$ ]: 202 nm,  $4.98 \times 10^4 \text{ M}^{-1} \text{ cm}^{-1}$ ; 225 nm,  $4.36 \times 10^4 \text{ M}^{-1} \text{ cm}^{-1}$ ; 256 nm,  $6.01 \times 10^4 \text{ M}^{-1} \text{ cm}^{-1}$ ; 291 nm,  $2.46 \times 10^4 \text{ M}^{-1} \text{ cm}^{-1}$ ; 450 nm,  $9.14 \times 10^3 \text{ M}^{-1} \text{ cm}^{-1}$ . **ESI-MS** in chloroform: [M]<sup>+</sup> 510.0792 *m/z* (calc. 510.0771 *m/z*). **Elemental Analysis:** Calculated for VC<sub>27</sub>H<sub>17</sub>N<sub>5</sub>O<sub>3</sub>: C, 63.533; H, 3.357; N, 13.725 %. Found: C, 63.753; H, 3.699; N, 15.456 %.

### 3.6.2 Synthesis of (4-methyl-2-[(1E)-(2-oxidophenyl)methylene]amino} phenolate)(dipyrido[3,2-d:2',3'-f]quinoxaline) oxovanadium(IV) ([VO(MEA)(DPQ)])

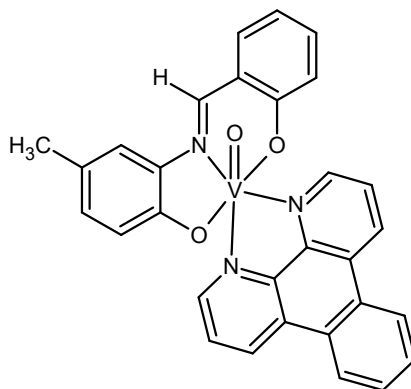


**Figure 3.16** Structure of the complex designated [VO(MEA)(DPQ)].

Vanadium(IV) oxide sulfate hydrate (0.082 g, 0.50 mmol) was dissolved in ultrapure water (5 mL) and the solution was degassed and saturated with nitrogen. MEA ligand (0.114 g, 0.502 mmol) was dissolved in methanol (20 mL). The resulting yellow solution was purged with nitrogen for ten minutes. The ligand solution was then added dropwise to the blue vanadyl sulfate solution *via* a cannula over thirty minutes, under a nitrogen atmosphere. The solution changed from clear blue to murky orange during this procedure. Solid-state DPQ (0.116 g, 0.499 mmol) was then added to the solution. The resulting mixture was heated to reflux, under a nitrogen atmosphere for two hours. The red product precipitated from solution during this procedure. The red, microcrystalline powder was collected by vacuum filtration and washed with distilled water (5 mL), methanol (degassed, 3 mL) and diethyl ether (5 mL). The precipitate was dried for three hours, under vacuum. Yield: 0.131 g, 50.0 %.

**IR** ( $\text{cm}^{-1}$ ): 1599 (C=N); 955 (V=O); 533 (V-O); 425 (V-N). **UV-Vis** ( $\text{CH}_3\text{CN}$ ) [ $\lambda_{\text{max}}$ ,  $\epsilon$ ]: 204 nm,  $5.02 \times 10^4 \text{ M}^{-1} \text{ cm}^{-1}$ ; 224 nm,  $4.21 \times 10^4 \text{ M}^{-1} \text{ cm}^{-1}$ ; 256 nm,  $6.01 \times 10^4 \text{ M}^{-1} \text{ cm}^{-1}$ ; 292 nm,  $2.45 \times 10^4 \text{ M}^{-1} \text{ cm}^{-1}$ ; 400 nm (s),  $6.26 \times 10^3 \text{ M}^{-1} \text{ cm}^{-1}$ ; 464 nm,  $9.64 \times 10^3 \text{ M}^{-1} \text{ cm}^{-1}$ . **ESI-MS** in chloroform:  $[\text{M}]^+$  524.0948  $m/z$  (calc. 524.0928  $m/z$ ). **Elemental Analysis:** Calculated for  $\text{VC}_{28}\text{H}_{19}\text{N}_5\text{O}_3$ : C, 64.124; H, 3.652; N, 13.358 %. Found: C, 63.651; H, 3.251; N, 13.011 %.

### 3.6.3 Synthesis of (4-*tert*-butyl-2-[(1*E*)-(2-oxidophenyl)methylene]amino}phenolate)(dipyrido[3,2-*d*:2',3'-*f*]quinoxaline)oxovanadium(IV) ([VO(TERTA)(DPQ)])

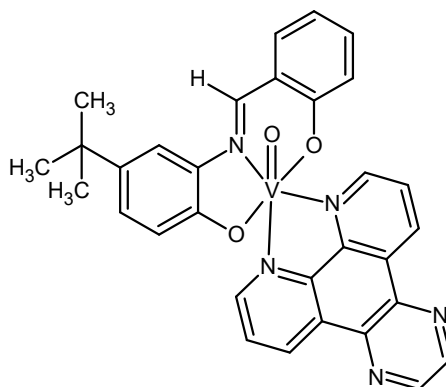


**Figure 3.17** Structure of the complex designated [VO(TERTA)(DPQ)].

Vanadium(IV) oxide sulfate hydrate (0.082 g, 0.50 mmol) was dissolved in ultrapure water (5 mL) and the solution was degassed and saturated with nitrogen. TERTA ligand (0.135 g, 0.501 mmol) was dissolved in HPLC grade methanol (25 mL). The resulting yellow solution was filtered and purged with nitrogen for ten minutes. The ligand solution was then added dropwise to the blue vanadyl sulfate solution *via* a cannula over thirty minutes, under a nitrogen atmosphere. The solution changed from clear blue to murky orange during this procedure. Solid-state DPQ (0.116 g, 0.499 mmol) was then added to the solution. The resulting mixture was heated to reflux for two hours, under a nitrogen atmosphere. The red product precipitated from solution during this procedure. The red, microcrystalline powder was collected by vacuum filtration and washed with distilled water (5 mL) and diethyl ether (7 mL). The precipitate was crushed and dried for four hours, under vacuum, at 50 °C. Yield: 0.157 g, 55.5 %.

**IR** (cm<sup>-1</sup>): 1603 (C=N); 949 (V=O); 535 (V-O); 425 (V-N). **UV-Vis** (CH<sub>3</sub>CN) [ $\lambda_{\text{max}}$ ,  $\epsilon$ ]: 204 nm,  $4.53 \times 10^4 \text{ M}^{-1} \text{ cm}^{-1}$ ; 226 nm,  $3.99 \times 10^4 \text{ M}^{-1} \text{ cm}^{-1}$ ; 256 nm,  $5.68 \times 10^4 \text{ M}^{-1} \text{ cm}^{-1}$ ; 292 nm,  $2.75 \times 10^4 \text{ M}^{-1} \text{ cm}^{-1}$ ; 406 nm (s),  $6.76 \times 10^3 \text{ M}^{-1} \text{ cm}^{-1}$ ; 464 nm,  $1.07 \times 10^4 \text{ M}^{-1} \text{ cm}^{-1}$ . **ESI-MS** in chloroform: [M]<sup>+</sup> 566.1382 *m/z* (calc. 566.1397 *m/z*). **Elemental Analysis:** Calculated for VC<sub>31</sub>H<sub>25</sub>N<sub>5</sub>O<sub>3</sub>: C, 65.721; H, 4.448; N, 12.365 %. Found: C, 65.428; H, 4.451; N, 12.294 %.

### 3.6.4 Synthesis of (4-chloro-2-[[*(1E)*-(2-oxidophenyl)methylene]amino]phenolate)(dipyrido[3,2-*d*:2',3'-*f*]quinoxaline) oxovanadium(IV) ([VO(CLA)(DPQ)])

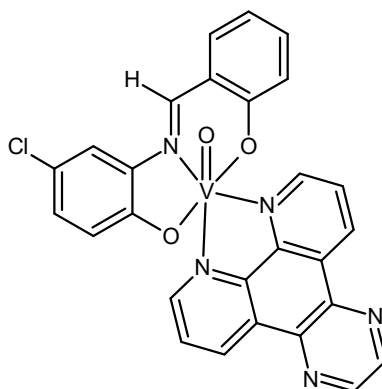


**Figure 3.18** Structure of the complex designated [VO(CLA)(DPQ)].

Vanadium(IV) oxide sulfate hydrate (0.082 g, 0.50 mmol) was dissolved in ultrapure water (5 mL) and the solution was degassed and saturated with nitrogen. CLA ligand (0.124 g, 0.501 mmol) was dissolved in methanol (20 mL). The resulting yellow solution was purged with nitrogen for ten minutes. The ligand solution was then added dropwise to the vanadyl sulfate solution over thirty minutes, under a nitrogen atmosphere, *via* a cannula. The solution changed from clear blue to murky orange during this procedure. Solid-state DPQ (0.116 g, 0.499 mmol) was then added to the solution. The resulting mixture was heated to reflux for two hours under a nitrogen atmosphere. The red product precipitated from solution during this procedure. The red, microcrystalline powder was collected by vacuum filtration and washed with distilled water (5 mL), methanol (degassed, 3 mL) and diethyl ether (5 mL). The precipitate was dried for four hours, under vacuum, at 50 °C. Yield: 0.150 g, 55.1 %.

**IR** (cm<sup>-1</sup>): 1599 (C=N); 945 (V=O); 532 (V-O); 424 (V-N). **UV-Vis** (CH<sub>3</sub>CN) [ $\lambda_{\text{max}}$ ,  $\epsilon$ ]: 203 nm,  $4.81 \times 10^4 \text{ M}^{-1} \text{ cm}^{-1}$ ; 224 nm,  $4.07 \times 10^4 \text{ M}^{-1} \text{ cm}^{-1}$ ; 256 nm,  $5.78 \times 10^4 \text{ M}^{-1} \text{ cm}^{-1}$ ; 294 nm,  $2.51 \times 10^4 \text{ M}^{-1} \text{ cm}^{-1}$ ; 400 nm (s),  $6.16 \times 10^3 \text{ M}^{-1} \text{ cm}^{-1}$ ; 464 nm,  $9.76 \times 10^3 \text{ M}^{-1} \text{ cm}^{-1}$ . **ESI-MS** in chloroform: [M]<sup>+</sup> 544.0385 *m/z* (calc. 544.0381 *m/z*). **Elemental Analysis:** Calculated for VC<sub>27</sub>H<sub>16</sub>N<sub>5</sub>O<sub>3</sub>Cl: C, 59.517; H, 2.960; N, 12.857 %. Found: C, 59.820; H, 2.894; N, 12.558 %.

### 3.6.5 Synthesis of (4-(ethylsulfonyl)-2-([(1E)-(2-oxidophenyl)methylene]amino}phenolate)(dipyrido[3,2-d':3'-f]quinoxaline)oxovanadium(IV) ([VO(SOA)(DPQ)])

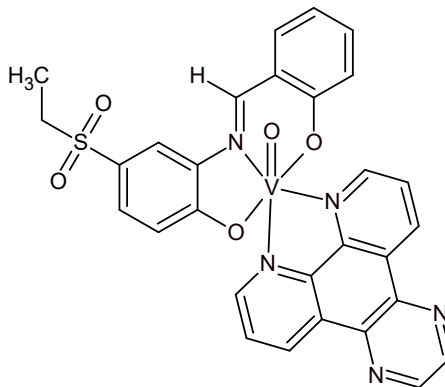


**Figure 3.19** Structure of the complex designated [VO(SOA)(DPQ)].

Vanadium(IV) oxide sulfate hydrate (0.082 g, 0.50 mmol) was dissolved in ultrapure water (5 mL) and the solution was degassed and saturated with nitrogen. SOA ligand (0.153 g, 0.501 mmol) was dissolved in methanol (25 mL). The resulting yellow solution was purged with nitrogen for ten minutes. The ligand solution was then added dropwise to the vanadyl sulfate solution over fifty minutes, under a nitrogen atmosphere, *via* a cannula. The solution changed from clear blue to clear brown during this procedure. Solid-state DPQ (0.116 g, 0.499 mmol) was then added to the solution. The resulting mixture was heated to reflux, under a nitrogen atmosphere. A red precipitate began to form after five minutes of heating. The mixture was refluxed for two hours, under a nitrogen atmosphere. The red powder was collected by vacuum filtration and washed with distilled water (5 mL), methanol (degassed, 3mL) and diethyl ether (5 mL). The precipitate was dried for four hours, under vacuum, at 50 °C. Yield: 0.194 g, 64.5 %.

**IR** (cm<sup>-1</sup>): 1600 (C=N); 953 (V=O); 533 (V-O); 435 (V-N). **UV-Vis** (CH<sub>3</sub>CN) [ $\lambda_{\text{max}}$ ,  $\epsilon$ ]: 201 nm,  $5.78 \times 10^4 \text{ M}^{-1} \text{ cm}^{-1}$ ; 225 nm,  $5.03 \times 10^4 \text{ M}^{-1} \text{ cm}^{-1}$ ; 256 nm,  $8.40 \times 10^4 \text{ M}^{-1} \text{ cm}^{-1}$ ; 288 nm (s),  $3.91 \times 10^4 \text{ M}^{-1} \text{ cm}^{-1}$ ; 384 nm,  $7.43 \times 10^3 \text{ M}^{-1} \text{ cm}^{-1}$ ; 450 nm,  $1.30 \times 10^4 \text{ M}^{-1} \text{ cm}^{-1}$ . **ESI-MS** in methanol: [M+Na]<sup>+</sup> 625.0589 *m/z* (calc. 625.0601). **Elemental Analysis:** Calculated for VC<sub>29</sub>H<sub>21</sub>N<sub>5</sub>O<sub>5</sub>S: C, 57.806; H, 3.513; N, 11.626; S, 5.323 %. Found: C, 57.808; H, 3.486; N, 11.827; S, 5.522 %.

### 3.6.6 Synthesis of (3-{{(1E)-(2-oxidophenyl)methylene}amino}naphthalen-2-olate)(dipyrido[3,2-d:2',3'-f]quinoxaline) oxovanadium(IV) ([VO(NAA)(DPQ)])

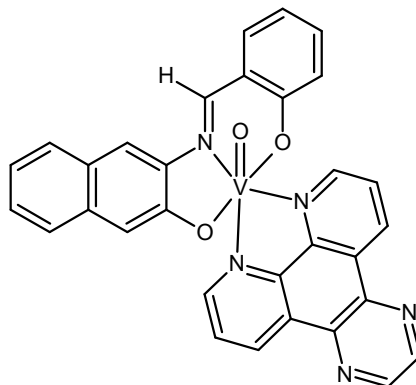


**Figure 3.20** Structure of the complex designated [VO(NAA)(DPQ)].

Vanadium(IV) oxide sulfate hydrate (0.082 g, 0.50 mmol) was dissolved in ultrapure water (5 mL) and the solution was degassed and saturated with nitrogen. NAA ligand (0.132 g, 0.501 mmol) was dissolved in ethanol (30 mL). The resulting yellow solution was filtered and purged with nitrogen for twenty minutes. The ligand solution was then added dropwise to the blue vanadyl sulfate solution over thirty minutes, under a nitrogen atmosphere, *via* a cannular. The solution changed from blue to murky yellow during this procedure. Solid-state DPQ (0.115 g, 0.495 mmol) was then added to the solution. The resulting mixture was heated to reflux under a nitrogen atmosphere. A red precipitate began to form after ten minutes of heating. The mixture was heated to reflux for three hours under a nitrogen atmosphere. The red, microcrystalline powder was collected by vacuum filtration and washed with distilled water (5 mL), absolute ethanol (degassed, 3 mL) and diethyl ether (5 mL). The precipitate was crushed and dried for four hours, under vacuum, at 50 °C. Yield: 0.108 g, 39.0 %.

**IR** (cm<sup>-1</sup>): 1600 (C=N); 954 (V=O); 565 (V-O); 425 (V-N). **UV-Vis** (CH<sub>3</sub>CN) [ $\lambda_{\max}$ ,  $\epsilon$ ]: 226 nm,  $4.50 \times 10^4 \text{ M}^{-1} \text{ cm}^{-1}$ ; 256 nm,  $6.79 \times 10^4 \text{ M}^{-1} \text{ cm}^{-1}$ ; 289 nm (s),  $3.01 \times 10^4 \text{ M}^{-1} \text{ cm}^{-1}$ ; 330 nm,  $1.17 \times 10^4 \text{ M}^{-1} \text{ cm}^{-1}$ ; 442 nm,  $1.14 \times 10^4 \text{ M}^{-1} \text{ cm}^{-1}$ . **ESI-MS** in chloroform: [M]<sup>+</sup> 560.0939 *m/z* (calc. 560.0928 *m/z*). **Elemental Analysis**: Calculated for VC<sub>31</sub>H<sub>19</sub>N<sub>5</sub>O<sub>3</sub>: C, 66.430; H, 3.417; N, 12.499 %. Found: C, 66.037; H, 3.351; N, 12.371 %.

### 3.6.7 Synthesis of (3-{{(1E)-(2-oxidophenyl)methylene}amino}biphenyl-4-olate)(dipyrido[3,2-d:2',3'-f]quinoxaline) oxovanadium(IV) ([VO(PHPHA)(DPQ)])

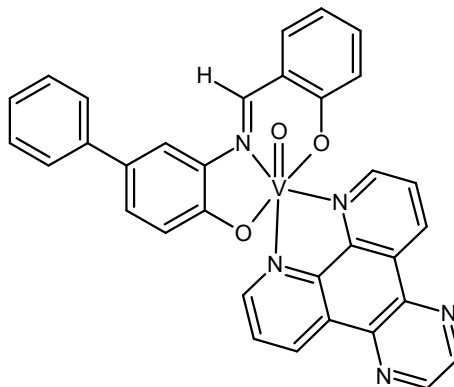


**Figure 3.21** Structure of the complex designated [VO(PHPHA)(DPQ)].

Vanadium(IV) oxide sulfate hydrate (0.082 g, 0.50 mmol) was dissolved in ultrapure water (5 mL) and the solution was degassed and saturated with nitrogen. PHPHA ligand (0.145 g, 0.501 mmol) was dissolved in HPLC grade methanol (35 mL). The resulting orange solution was filtered and purged with nitrogen for ten minutes. The ligand solution was then added dropwise to the blue vanadyl sulfate solution over thirty minutes, under a nitrogen atmosphere, *via* a canular. The solution changed from clear blue to clear brown during this procedure. Solid-state DPQ (0.116 g, 0.499 mmol) was then added to the solution. The resulting mixture was heated to reflux under a nitrogen atmosphere. A red precipitate began to form after five minutes of heating. The mixture was heated to reflux for two hours under a nitrogen atmosphere. The red, microcrystalline powder was collected by vacuum filtration and washed with ultrapure water (5 mL) and diethyl ether (6 mL). The precipitate was dried for four hours, under vacuum, at 50 °C. Yield: 0.172 g, 58.7 %.

**IR** ( $\text{cm}^{-1}$ ): 1597 (C=N); 959 (V=O); 534 (V-O); 435 (V-N). **UV-Vis** ( $\text{CH}_3\text{CN}$ ) [ $\lambda_{\text{max}}$ ,  $\epsilon$ ]: 225 nm (s),  $4.30 \times 10^4 \text{ M}^{-1} \text{ cm}^{-1}$ ; 256 nm,  $6.17 \times 10^4 \text{ M}^{-1} \text{ cm}^{-1}$ ; 294 nm,  $3.84 \times 10^4 \text{ M}^{-1} \text{ cm}^{-1}$ ; 464 nm,  $9.57 \times 10^3 \text{ M}^{-1} \text{ cm}^{-1}$ . **ESI-MS** in acetonitrile:  $[\text{M}]^+$  586.1088  $m/z$  (calc. 586.1084  $m/z$ ). **Elemental Analysis:** Calculated for  $\text{VC}_{33}\text{H}_{21}\text{N}_5\text{O}_3 \cdot \text{CH}_3\text{OH}$ : C, 66.018; H, 4.074; N, 11.325 %. Found: C, 66.073; H, 3.734; N, 11.373 %.

### 3.6.8 Synthesis of (4-methyl-2-[(1E)-(2-oxidophenyl)methylene]amino} phenolate)(dipyrido[3,2-a:2',3'-c]phenazine) oxovanadium(IV) ([VO(MEA)(DPPZ)])

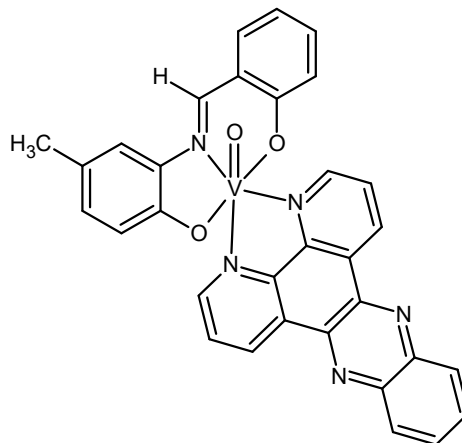


**Figure 3.22** Structure of the complex designated [VO(MEA)(DPPZ)].

Vanadium(IV) oxide sulfate hydrate (0.0408 g, 0.250 mmol) was dissolved in ultrapure water (2.5 mL) and the solution was degassed and saturated with nitrogen. MEA ligand (0.0568 g, 0.250 mmol) was dissolved in methanol (10 mL). The resulting yellow solution was purged with nitrogen for thirty minutes. The ligand solution was then added dropwise to the vanadyl sulfate solution, over thirty minutes, under a nitrogen atmosphere, *via* a cannula. The solution changed from clear blue to murky orange during this procedure. A methanol suspension (26 mL) of the DPPZ ligand (0.0706 g, 0.250 mmol), previously degassed and saturated with nitrogen, was added dropwise to the vanadyl reaction mixture. The resulting mixture was heated to reflux, under a nitrogen atmosphere. A red precipitate began to form after ten minutes of heating. The mixture was heated to reflux for two hours, under a nitrogen atmosphere. The red, microcrystalline powder was collected by vacuum filtration and washed with ultrapure water (2 mL), methanol (2 mL) and diethyl ether (2 mL). The precipitate was dried for four hours, under vacuum, at 50 °C. Yield: 0.0665 g, 46.3 %.

**IR** (cm<sup>-1</sup>): 1601 (C=N); 948 (V=O); 533 (V-O); 424 (V-N). **UV-Vis** (CH<sub>3</sub>CN) [ $\lambda_{\max}$ ,  $\epsilon$ ]: 203 nm,  $4.89 \times 10^4 \text{ M}^{-1} \text{ cm}^{-1}$ ; 234 nm,  $3.80 \times 10^4 \text{ M}^{-1} \text{ cm}^{-1}$ ; 271 nm,  $6.38 \times 10^4 \text{ M}^{-1} \text{ cm}^{-1}$ ; 357 nm,  $1.28 \times 10^4 \text{ M}^{-1} \text{ cm}^{-1}$ ; 374 nm,  $1.36 \times 10^4 \text{ M}^{-1} \text{ cm}^{-1}$ ; 459 nm,  $8.62 \times 10^3 \text{ M}^{-1} \text{ cm}^{-1}$ . **ESI-MS** in dichloromethane: 574.1088 [M]<sup>+</sup> *m/z* (calc. 574.1084 *m/z*). **Elemental Analysis:** Calculated for VC<sub>32</sub>H<sub>21</sub>N<sub>5</sub>O<sub>3</sub>: C, 66.899; H, 3.685; N, 12.194%. Found: C, 65.992; H, 3.720; N, 12.687 %.

### 3.7 Synthesis of the Cationic Oxovanadium(IV) Complexes

The cationic complexes with a PHEN, DPQ or DPPZ co-ligand and a *O,N,N'*-tridentate ligand were synthesised using adaptations of reported methods.<sup>12, 13</sup>

#### 3.7.1 Synthesis of (2-{{(1*E*)-(1-methyl-1*H*-imidazol-2-yl)methylene}amino}phenolate)(1,10-phenanthroline) oxovanadium(IV) hexafluorophosphate ([VO(PHCA)(PHEN)](PF<sub>6</sub>))

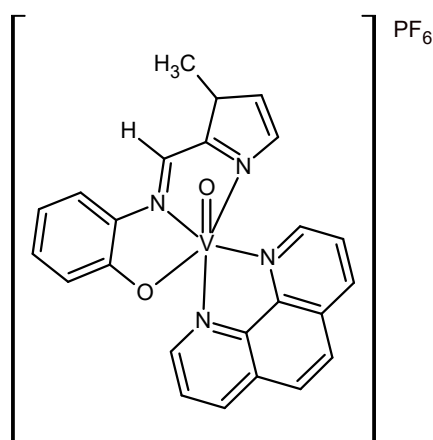


**Figure 3.23** Structure of the complex designated [VO(PHCA)(PHEN)](PF<sub>6</sub>).

Vanadium(IV) oxide sulfate hydrate (0.082 g, 0.50 mmol) was dissolved in a mixture of ultrapure water (5 mL) and ethanol (3 mL). The resulting blue solution was degassed and saturated with nitrogen for ten minutes. Barium chloride dihydrate (0.122 g, 0.500 mmol), ethanol (5 mL) and ultrapure water (1 mL) was then added to the vanadyl sulfate solution. A white precipitate of barium sulfate immediately formed. The suspension was stirred under a nitrogen atmosphere at room temperature for ninety minutes. The fine white precipitate was removed by vacuum filtration using a fritted glass filter support with nylon filter paper (0.45 μm). The reaction flask was washed with ethanol (2 mL) and the barium sulfate residue removed by vacuum filtration using nylon filter paper (0.45 μm). The filtrate from this solution was added to the bulk of the vanadyl chloride filtrate. The clear blue vanadyl chloride filtrate was transferred to a two-neck, round-bottomed flask. The filtration side-arm flask that contained the vanadyl chloride filtrate was washed with ethanol (2 mL) and this solution was added to the bulk vanadyl chloride filtrate.

The vanadyl chloride filtrate was then degassed and saturated with nitrogen for ten minutes. PHCA ligand (0.101 g, 0.502 mmol) was dissolved in ethanol (6 mL, previously degassed and saturated with nitrogen for ten minutes) to form a clear yellow solution. This ligand solution was further purged with nitrogen for ten minutes. The PHCA ligand solution was then added dropwise to the blue vanadyl chloride solution over twenty minutes, under a nitrogen atmosphere, at room temperature. The vanadyl chloride solution immediately changed from clear blue to red upon addition of the PHCA ligand solution. Solid-state 1,10-phenanthroline (PHEN), (0.090 g, 0.50 mmol) was added to the red solution and the resulting mixture was heated to reflux under a nitrogen atmosphere for two hours. PHEN dissolved upon heating the solution. The solution was then allowed to cool under a nitrogen atmosphere for five minutes. Ultrapure water (25 mL) was added to the solution and the solution was degassed and saturated with nitrogen for ten minutes. This solution was then filtered through nylon filter paper (0.45  $\mu\text{m}$ ). An excess of ammonium hexafluorophosphate (0.252 g, 1.55 mmol), dissolved in a minimum of ultrapure water (*ca.* 4 mL), was then added to the clear, dark red filtrate. A red precipitate of the target compound immediately formed. The precipitate was collected by vacuum filtration and washed with ultrapure water (5 ml), HPLC grade methanol (1 mL) and diethyl ether (5 ml). The precipitate was dried for four hours, under vacuum, at 50 °C. Yield: 0.100 g, 33.8 %.

**IR** ( $\text{cm}^{-1}$ ): 1582 (C=N); 959 (V=O); 831 (P-F stretch); 555 (V-O); 427 (V-N). **UV-Vis** ( $\text{CH}_3\text{CN}$ ) [ $\lambda_{\text{max}}$ ,  $\epsilon$ ]: 202 nm,  $5.88 \times 10^4 \text{ M}^{-1} \text{ cm}^{-1}$ ; 227 nm,  $5.10 \times 10^4 \text{ M}^{-1} \text{ cm}^{-1}$ ; 271 nm,  $3.61 \times 10^4 \text{ M}^{-1} \text{ cm}^{-1}$ ; 294 nm (s),  $1.44 \times 10^4 \text{ M}^{-1} \text{ cm}^{-1}$ ; 354 nm,  $1.28 \times 10^4 \text{ M}^{-1} \text{ cm}^{-1}$ ; 484 nm,  $9.49 \times 10^3 \text{ M}^{-1} \text{ cm}^{-1}$ . **ESI-MS** in acetonitrile:  $[\text{M}]^+$  447.0905  $m/z$  (calc. 447.0900  $m/z$ ). **Elemental Analysis:** Calculated for  $\text{VC}_{23}\text{H}_{18}\text{N}_5\text{O}_2\text{PF}_6$ : C, 46.634; H, 3.063; N, 11.826%. Found: C, 46.309; H, 3.042; N, 11.916 %.

### 3.7.2 Synthesis of (4-methyl-2-[(1*E*)-(1-methyl-1*H*-imidazol-2-yl)methylene]amino}phenolate)(1,10-phenanthroline) oxovanadium(IV) hexafluorophosphate ([VO(MECA)(PHEN)](PF<sub>6</sub>))

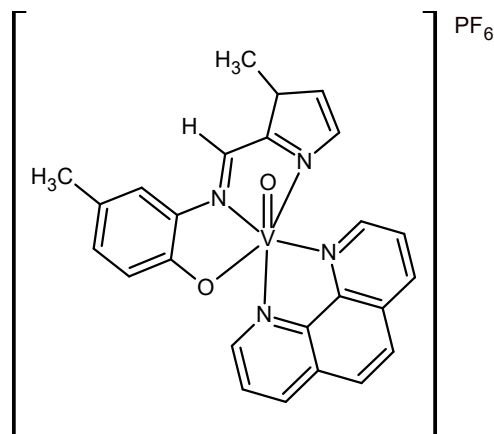


**Figure 3.24** Structure of the complex designated [VO(MECA)(PHEN)](PF<sub>6</sub>).

Vanadium(IV) oxide sulfate hydrate (0.082 g, 0.50 mmol) was dissolved in a mixture of ultrapure water (5 mL) and ethanol (3 mL), previously degassed and saturated with nitrogen for ten minutes. The resulting blue solution was further degassed and saturated with nitrogen for ten minutes. Barium chloride dihydrate (0.122 g, 0.500 mmol) and ethanol (5 mL) was then added to the vanadyl sulfate solution. A white precipitate of barium sulfate immediately formed. The suspension was stirred under a nitrogen atmosphere at room temperature for ninety minutes. The fine white precipitate was removed using two regenerated cellulose syringe filters (0.45  $\mu\text{m}$ ). The filters were rinsed with ethanol (2 mL each) and the filtered solutions were added to the bulk vanadyl chloride filtrate. The clear blue vanadyl chloride filtrate was then degassed and saturated with nitrogen for ten minutes in a two-neck, round-bottomed flask. MECA ligand (0.108 g, 0.502 mmol) was dissolved in ethanol (4 mL) to form a clear yellow solution. This ligand solution was degassed and saturated with nitrogen for ten minutes. The MECA ligand solution was then added dropwise to the blue vanadyl chloride solution over thirty minutes, under a nitrogen atmosphere at room temperature. The vanadyl chloride solution immediately changed from clear blue to red upon addition of the MECA ligand solution. Solid-state PHEN (0.090 g, 0.50 mmol) was then added to the red solution.

Upon dissolution of PHEN the reaction mixture was heated to reflux under a nitrogen atmosphere for two hours. The solution was then cooled under a nitrogen atmosphere for thirty minutes. Ultrapure water (30 mL) was added to the solution and the resulting solution was filtered using vacuum filtration. An excess of ammonium hexafluorophosphate (0.247 g, 1.52 mmol), dissolved in a minimum of ultrapure water (*ca.* 1 mL), was then added to the clear, dark red filtrate. A red precipitate of the target compound immediately formed. The precipitate was collected by vacuum filtration and washed with ultrapure water (5 ml), HPLC grade methanol (2 mL) and diethyl ether (5 ml). The precipitate was dried for three hours, under vacuum, at 50 °C. Yield: 0.121 g, 39.9 %.

**IR** ( $\text{cm}^{-1}$ ): 1604 (C=N); 961 (V=O); 833 (P-F stretch); 557 (V-O); 430 (V-N). **UV-Vis** ( $\text{CH}_3\text{CN}$ ) [ $\lambda_{\text{max}}$ ,  $\epsilon$ ]: 202 nm,  $4.37 \times 10^4 \text{ M}^{-1} \text{ cm}^{-1}$ ; 230 nm,  $4.37 \times 10^4 \text{ M}^{-1} \text{ cm}^{-1}$ ; 266 nm,  $2.75 \times 10^4 \text{ M}^{-1} \text{ cm}^{-1}$ ; 294 nm (s),  $1.16 \times 10^4 \text{ M}^{-1} \text{ cm}^{-1}$ ; 357 nm,  $1.07 \times 10^4 \text{ M}^{-1} \text{ cm}^{-1}$ ; 500 nm,  $6.57 \times 10^3 \text{ M}^{-1} \text{ cm}^{-1}$ . **ESI-MS** in acetonitrile:  $[\text{M}]^+$  461.1053  $m/z$  (calc. 461.1053  $m/z$ ). **Elemental Analysis:** Calculated for  $\text{VC}_{24}\text{H}_{20}\text{N}_5\text{O}_2\text{PF}_6$ : C, 47.536; H, 3.325; N, 11.553%. Found: C, 47.141; H, 3.630; N, 11.096 %.

### 3.7.3 Synthesis of (4-*tert*-butyl-2-[(1*E*)-(1-methyl-1*H*-imidazol-2-yl)methylene]amino}phenolate)(1,10-phenanthroline) oxovanadium(IV) hexafluorophosphate ([VO(TERTCA)(PHEN)](PF<sub>6</sub>))

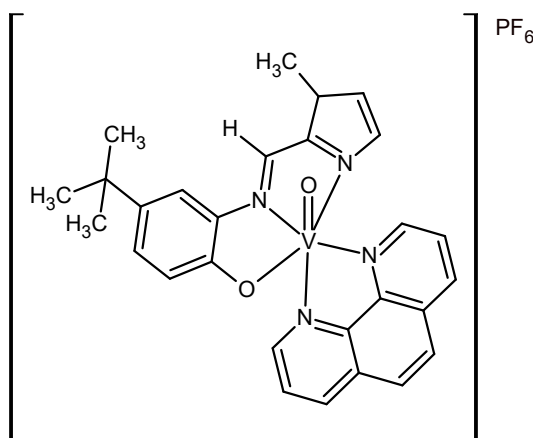


**Figure 3.25** Structure of the complex designated [VO(TERTCA)(PHEN)](PF<sub>6</sub>).

Vanadium(IV) oxide sulfate hydrate (0.082 g, 0.50 mmol) was dissolved in ultrapure water (5 mL), previously degassed and saturated with nitrogen for ten minutes. Ethanol (3 mL) was added to the resulting blue vanadyl sulfate solution and the solution was further degassed and saturated with nitrogen for ten minutes. Barium chloride dihydrate (0.122 g, 0.500 mmol) and ethanol (5 mL) was then added to the vanadyl sulfate solution. A white precipitate of barium sulfate immediately formed. The suspension was stirred under a nitrogen atmosphere at room temperature for ninety minutes. The fine white precipitate was removed using two regenerated cellulose syringe filters (0.45  $\mu\text{m}$ ). The filters were rinsed with ethanol (2 mL each) and the filtered solutions were added to the bulk vanadyl chloride filtrate. The clear blue vanadyl chloride filtrate was then degassed and saturated with nitrogen for ten minutes in a two-neck, round-bottomed flask. TERTCA ligand (0.127 g, 0.494 mmol) was dissolved in ethanol (4 mL) to form a clear orange solution. This ligand solution was degassed and saturated with nitrogen for ten minutes. The TERTCA ligand solution was then added dropwise to the blue vanadyl chloride solution over twenty minutes, under a nitrogen atmosphere at room temperature. The vanadyl chloride solution immediately changed from clear blue to red upon addition of the TERTCA ligand solution.

Solid-state PHEN (0.089 g, 0.49 mmol) was then added to the red solution. Upon dissolution of PHEN, the reaction mixture was heated to reflux under a nitrogen atmosphere for two hours. The solution was then cooled under a nitrogen atmosphere for thirty minutes. Ultrapure water (30 mL) was added to the solution and the solution was degassed and saturated with nitrogen for ten minutes. This solution was then filtered using vacuum filtration. An excess of ammonium hexafluorophosphate (0.247 g, 1.52 mmol), dissolved in a minimum of ultrapure water (*ca.* 4 mL), was then added to the clear, dark red filtrate. A red precipitate of the target compound immediately formed. The precipitate was collected by vacuum filtration and washed with ultrapure water (5 ml), HPLC grade methanol (2 mL) and diethyl ether (5 ml). The precipitate was dried for three hours, under vacuum, at 50 °C. Yield: 0.174 g, 54.4 %.

**IR** ( $\text{cm}^{-1}$ ): 1600 (C=N); 968 (V=O); 831 (P-F stretch); 557 (V-O); 427 (V-N). **UV-Vis** ( $\text{CH}_3\text{CN}$ ) [ $\lambda_{\text{max}}$ ,  $\epsilon$ ]: 203 nm,  $5.67 \times 10^4 \text{ M}^{-1} \text{ cm}^{-1}$ ; 229 nm,  $5.06 \times 10^4 \text{ M}^{-1} \text{ cm}^{-1}$ ; 271 nm,  $3.53 \times 10^4 \text{ M}^{-1} \text{ cm}^{-1}$ ; 293 nm (s),  $1.42 \times 10^4 \text{ M}^{-1} \text{ cm}^{-1}$ ; 357 nm,  $1.21 \times 10^4 \text{ M}^{-1} \text{ cm}^{-1}$ ; 499 nm,  $7.78 \times 10^3 \text{ M}^{-1} \text{ cm}^{-1}$ . **ESI-MS** in acetonitrile:  $[\text{M}]^+$  503.1536  $m/z$  (calc. 503.1526  $m/z$ ). **Elemental Analysis:** Calculated for  $\text{VC}_{27}\text{H}_{26}\text{N}_5\text{O}_2\text{PF}_6$ : C, 50.008; H, 4.042; N, 10.803%. Found: C, 49.716; H, 3.852; N, 10.668 %.

### 3.7.4 Synthesis of (3-[[*(1E)*-(1-methyl-1*H*-imidazol-2-yl)methylene]amino}biphen-4-olate)(1,10-phenanthroline) oxovanadium(IV) hexafluorophosphate ([VO(PHPHCA)(PHEN)](PF<sub>6</sub>))

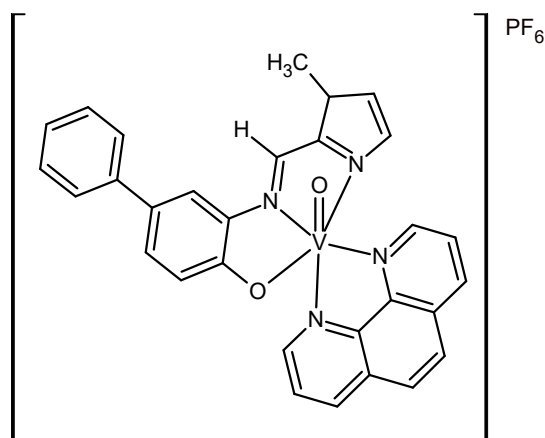


**Figure 3.26** Structure of the complex designated [VO(PHPHCA)(PHEN)](PF<sub>6</sub>).

Vanadium(IV) oxide sulfate hydrate (0.082 g, 0.50 mmol) was dissolved in a mixture of ultrapure water (5 mL) and ethanol (3 mL). The resulting blue solution was degassed and saturated with nitrogen for ten minutes. Barium chloride dihydrate (0.122 g, 0.500 mmol), ethanol (5 mL) and ultrapure water (1 mL) was then added to the vanadyl sulfate solution. A white precipitate of barium sulfate immediately formed. The suspension was stirred under a nitrogen atmosphere at room temperature for ninety minutes. The fine white precipitate was removed by vacuum filtration using a fritted glass filter support with nylon filter paper (0.45  $\mu\text{m}$ ). The clear blue vanadyl chloride filtrate was transferred to a two-neck, round-bottomed flask. The filtration side-arm flask that contained the vanadyl chloride filtrate was washed with ethanol (2 mL) and this solution was added to the bulk vanadyl chloride filtrate. The vanadyl chloride solution was then degassed and saturated with nitrogen for ten minutes. PHPHCA ligand (0.139 g, 0.501 mmol) was dissolved in ethanol (20 mL, previously degassed and saturated with nitrogen for ten minutes) to form a clear yellow solution. This ligand solution was further purged with nitrogen for ten minutes. The PHPHCA ligand solution was then added dropwise to the blue vanadyl chloride solution over thirty minutes, under a nitrogen atmosphere, *via* a cannular at room temperature. The vanadyl chloride solution immediately changed from clear blue to red upon addition of the PHPHCA ligand solution.

Solid-state PHEN (0.090 g, 0.50 mmol) was then added to the red solution and the reaction mixture was heated to reflux under a nitrogen atmosphere for two hours. PHEN dissolved upon heating. The solution was then allowed to cool under a nitrogen atmosphere for ten minutes. Ultrapure water (30 mL, previously degassed and saturated with nitrogen for fifteen minutes) was added to the dark red solution, *via* a cannular. The solution was further degassed and saturated with nitrogen for ten minutes. The solution was then filtered through nylon filter paper (0.45  $\mu\text{m}$ ). An excess of ammonium hexafluorophosphate (0.252 g, 1.55 mmol), dissolved in a minimum of ultrapure water (*ca.* 4 mL), was then added to the clear, dark red filtrate. A maroon precipitate of the target compound immediately formed. The precipitate was collected by vacuum filtration and washed with distilled water (5 ml), HPLC grade methanol (1 mL) and diethyl ether (5 ml). The precipitate was dried for three hours, under vacuum, at 50 °C. Yield: 0.142 g, 42.5 %.

**IR** ( $\text{cm}^{-1}$ ): 1601 (C=N); 965 (V=O); 833 (P-F stretch); 556 (V-O); 432 (V-N). **UV-Vis** ( $\text{CH}_3\text{CN}$ ) [ $\lambda_{\text{max}}$ ,  $\epsilon$ ]: 226 nm,  $4.96 \times 10^4 \text{ M}^{-1} \text{ cm}^{-1}$ ; 272 nm,  $4.27 \times 10^4 \text{ M}^{-1} \text{ cm}^{-1}$ ; 295 nm (s),  $2.49 \times 10^4 \text{ M}^{-1} \text{ cm}^{-1}$ ; 356 nm,  $1.33 \times 10^4 \text{ M}^{-1} \text{ cm}^{-1}$ ; 507 nm,  $7.24 \times 10^3 \text{ M}^{-1} \text{ cm}^{-1}$ . **ESI-MS** in acetonitrile:  $[\text{M}]^+$  523.1207  $m/z$  (calc. 523.1213  $m/z$ ). **Elemental Analysis:** Calculated for  $\text{VC}_{29}\text{H}_{22}\text{N}_5\text{O}_2\text{PF}_6$ : C, 52.106; H, 3.318; N, 10.480%. Found: C, 49.145; H, 3.303; N, 10.127 %.

**3.7.5 Synthesis of (4-methyl-2-[(1*E*)-(1-methyl-1*H*-imidazol-2-yl)methylene]amino}phenolate)(dipyrido[3,2-*d*:2',3'-*f*]quinoxaline)oxovanadium(IV) hexafluorophosphate ([VO(MECA)(DPQ)](PF<sub>6</sub>))**

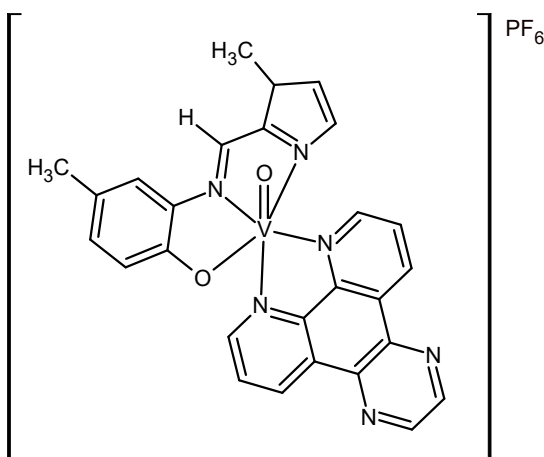


**Figure 3.27** Structure of the complex designated [VO(MECA)(DPQ)](PF<sub>6</sub>).

Vanadium(IV) oxide sulfate hydrate (0.082 g, 0.50 mmol) was dissolved in a mixture of ultrapure water (5 mL) and ethanol (3 mL). The resulting blue solution was degassed and saturated with nitrogen for ten minutes. Barium chloride dihydrate (0.122 g, 0.500 mmol), ethanol (5 mL) and ultrapure water (1 mL) was then added to the vanadyl sulfate solution. A white precipitate of barium sulfate immediately formed. The suspension was stirred under a nitrogen atmosphere at room temperature for ninety minutes. The fine white precipitate was removed using vacuum filtration using a fritted glass filter support with nylon filter paper (0.45 μm). The flask that contained the barium sulfate suspension was rinsed with ethanol (2 mL) and this solution was also filtered using nylon filter paper (0.45 μm) and the filtrate combined with the bulk vanadyl chloride filtrate. The clear blue vanadyl chloride filtrate was transferred to a two-neck, round-bottomed flask. The filtration side-arm flask that contained the vanadyl chloride filtrate was washed with ethanol (2 mL) and this solution was added to the bulk vanadyl chloride filtrate. The vanadyl chloride solution was then degassed and saturated with nitrogen for ten minutes. MECA ligand (0.107 g, 0.497 mmol) was dissolved in ethanol (7 mL) to form a clear yellow solution. This ligand solution was degassed and saturated with nitrogen for ten minutes.

The MECA ligand solution was then added dropwise to the blue vanadyl chloride solution over twenty minutes under a nitrogen atmosphere at room temperature. The vanadyl chloride solution immediately changed from clear blue to red upon addition of the MECA ligand solution. Solid-state DPQ (0.115 g, 0.495 mmol) was then added to the red solution and the resulting mixture was heated to reflux under a nitrogen atmosphere for three hours. DPQ dissolved upon heating. The solution was then allowed to cool under a nitrogen atmosphere for five minutes. Ultrapure water (30 mL) was added to the solution and the solution was degassed and saturated with nitrogen for ten minutes. This solution was then filtered through nylon filter paper (0.45  $\mu\text{m}$ ). An excess of ammonium hexafluorophosphate (0.255 g, 1.56 mmol), dissolved in a minimum of ultrapure water (*ca.* 3 mL), was then added to the dark red filtrate. A maroon precipitate of the target compound immediately formed. The precipitate was collected by vacuum filtration and washed with ultrapure water (5 ml) and diethyl ether (6 ml). The precipitate was dried for five hours, under vacuum, at 50 °C. Yield: 0.161 g, 49.9 %.

**IR** ( $\text{cm}^{-1}$ ): 1581 (C=N); 967 (V=O); 835 (P-F stretch); 556 (V-O); 438 (V-N). **UV-Vis** ( $\text{CH}_3\text{CN}$ ) [ $\lambda_{\text{max}}$ ,  $\epsilon$ ]: 205 nm,  $5.14 \times 10^4 \text{ M}^{-1} \text{ cm}^{-1}$ ; 223 nm (s),  $4.26 \times 10^4 \text{ M}^{-1} \text{ cm}^{-1}$ ; 256 nm,  $6.43 \times 10^4 \text{ M}^{-1} \text{ cm}^{-1}$ ; 296 nm (s),  $2.42 \times 10^4 \text{ M}^{-1} \text{ cm}^{-1}$ ; 340 nm,  $1.13 \times 10^4 \text{ M}^{-1} \text{ cm}^{-1}$ ; 371 nm (s),  $8.35 \times 10^3 \text{ M}^{-1} \text{ cm}^{-1}$ ; 503 nm,  $6.14 \times 10^3 \text{ M}^{-1} \text{ cm}^{-1}$ . **ESI-MS** in acetonitrile:  $[\text{M}]^+$  513.1129  $m/z$  (calc. 513.1118  $m/z$ ). **Elemental Analysis:** Calculated for  $\text{VC}_{26}\text{H}_{20}\text{N}_7\text{O}_2\text{PF}_6$ : C, 47.427; H, 3.062; N, 14.895%. Found: C, 47.047; H, 3.307; N, 15.264 %.

**3.7.6 Synthesis of (4-*tert*-butyl-2-[(1*E*)-(1-methyl-1*H*-imidazol-2-yl)methylene]amino}phenolate)(dipyrido[3,2-*d*:2',3'-*f*]quinoxaline)oxovanadium(IV) hexafluorophosphate ([VO(TERTCA)(DPQ)](PF<sub>6</sub>))**

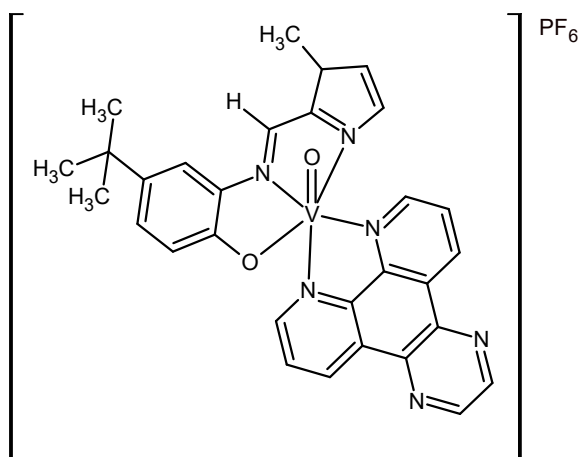


**Figure 3.28** Structure of the complex designated [VO(TERTCA)(DPQ)](PF<sub>6</sub>).

Vanadium(IV) oxide sulfate hydrate (0.082 g, 0.50 mmol) was dissolved in a mixture of ultrapure water (5 mL) and ethanol (3 mL). The resulting blue solution was degassed and saturated with nitrogen for ten minutes. Barium chloride dihydrate (0.122 g, 0.500 mmol), ethanol (5 mL) and distilled water (1 mL) was then added to the vanadyl sulfate solution. A white precipitate of barium sulfate immediately formed. The suspension was stirred under a nitrogen atmosphere at room temperature for ninety minutes. The fine white precipitate was removed by vacuum filtration using a fritted glass filter support with nylon filter paper (0.45 μm). The flask that contained the barium sulfate suspension was rinsed with ethanol (2 mL) and this solution was also filtered using nylon filter paper (0.45 μm) and the filtrate combined with the bulk vanadyl chloride filtrate. The clear blue vanadyl chloride filtrate was transferred to a two-neck, round-bottomed flask. The filtration side-arm flask that contained the vanadyl chloride filtrate was washed with ethanol (2 mL) and this solution was added to the bulk vanadyl chloride filtrate. The vanadyl chloride solution was then degassed and saturated with nitrogen for ten minutes. TERTCA ligand (0.127 g, 0.494 mmol) was dissolved in ethanol (7 mL) to form a clear orange solution. This ligand solution was degassed and saturated with nitrogen for ten minutes.

The TERTCA ligand solution was then added dropwise to the blue vanadyl chloride solution over twenty minutes under a nitrogen atmosphere at room temperature. The vanadyl chloride solution immediately changed from clear blue to red upon addition of the TERTCA ligand solution. Solid-state DPQ (0.115 g, 0.495 mmol) was then added to the red solution and the reaction mixture was heated to reflux under a nitrogen atmosphere for three hours. DPQ dissolved upon heating. The solution was then allowed to cool under a nitrogen atmosphere for five minutes. Ultrapure water (30 mL) was added to the solution and the solution was degassed and saturated with nitrogen for ten minutes. This solution was then filtered through nylon filter paper (0.45  $\mu\text{m}$ ). An excess of ammonium hexafluorophosphate (0.247 g, 1.52 mmol), dissolved in a minimum of ultrapure water (*ca.* 3 mL), was then added to the dark red filtrate. A maroon precipitate of the target compound immediately formed. The precipitate was collected by vacuum filtration and washed with ultrapure water (5 ml) and diethyl ether (5 ml). The precipitate was dried for four and a half hours, under vacuum, at 50 °C. Yield: 0.209 g, 60.4 %.

**IR** ( $\text{cm}^{-1}$ ): 1581 (C=N); 967 (V=O); 834 (P-F stretch); 556 (V-O); 437 (V-N). **UV-Vis** ( $\text{CH}_3\text{CN}$ ) [ $\lambda_{\text{max}}$ ,  $\epsilon$ ]: 205 nm,  $5.22 \times 10^4 \text{ M}^{-1} \text{ cm}^{-1}$ ; 223 nm (s),  $4.41 \times 10^4 \text{ M}^{-1} \text{ cm}^{-1}$ ; 256 nm,  $6.53 \times 10^4 \text{ M}^{-1} \text{ cm}^{-1}$ ; 295 nm (s),  $2.49 \times 10^4 \text{ M}^{-1} \text{ cm}^{-1}$ ; 340 nm,  $1.14 \times 10^4 \text{ M}^{-1} \text{ cm}^{-1}$ ; 369 nm (s),  $8.61 \times 10^3 \text{ M}^{-1} \text{ cm}^{-1}$ ; 501 nm,  $5.98 \times 10^3 \text{ M}^{-1} \text{ cm}^{-1}$ . **ESI-MS** in acetonitrile:  $[\text{M}]^+$  555.1592  $m/z$  (calc. 555.1588  $m/z$ ). **Elemental Analysis:** Calculated for  $\text{VC}_{29}\text{H}_{26}\text{N}_7\text{O}_2\text{PF}_6$ : C, 49.722; H, 3.741; N, 14.000%. Found: C, 49.638; H, 3.820; N, 14.004 %.

### 3.7.7 Synthesis of (4-methyl-2-[(1*E*)-(1-methyl-1*H*-imidazol-2-yl)methylene]amino}phenolate)(dipyrido[3,2-*a*:2',3'-*c*]phenazine)oxovanadium(IV) chloride ([VO(MECA)(DPPZ)](Cl))

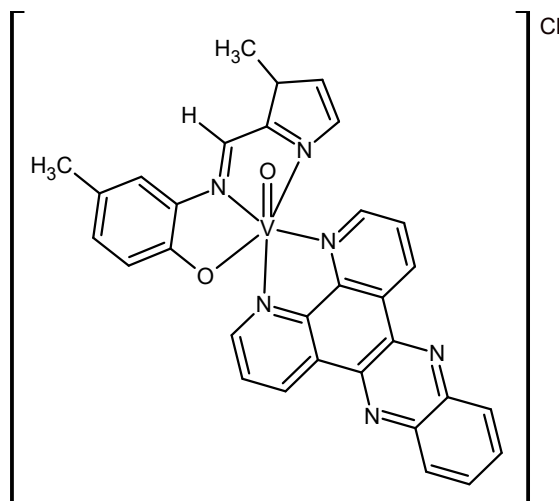


**Figure 3.29** Structure of the complex designated [VO(MECA)(DPPZ)](Cl).

Vanadium(IV) oxide sulfate hydrate (0.082 g, 0.50 mmol) was dissolved in ultrapure water (5 mL). The resulting blue solution was degassed and saturated with nitrogen for ten minutes. Barium chloride dihydrate (0.122 g, 0.500 mmol) and ethanol (10 mL) was then added to the vanadyl sulfate solution. A white precipitate of barium sulfate immediately formed. The suspension was stirred under a nitrogen atmosphere at room temperature for ninety minutes. The fine white precipitate was removed using a regenerated cellulose syringe filter (0.45  $\mu\text{m}$ ). The filter was rinsed with ethanol (4 mL) and the filtered solution was added to the bulk vanadyl chloride filtrate. The clear blue vanadyl chloride filtrate was then degassed and saturated with nitrogen for ten minutes in a two-neck, round-bottomed flask. MECA ligand (0.108 g, 0.502 mmol) and ethanol (5 mL) were added to the blue vanadyl chloride solution at room temperature. The vanadyl chloride solution immediately changed from clear blue to red upon addition of the MECA ligand. DPPZ (0.141 g, 0.499 mmol) and ethanol (4 mL) were then added to the red solution. The resulting mixture was heated to reflux under a nitrogen atmosphere for three hours. DPPZ dissolved upon heating. After three hours the reflux condenser was removed, and the solvent volume was reduced to about 5 mL. The solution was then allowed to cool to *ca.* 4  $^{\circ}\text{C}$  on ice.

A maroon precipitate of the target compound formed upon cooling. The product was collected by vacuum filtration and dried for four hours, under vacuum. Yield: 0.195 g, 65.2 %.

**IR** ( $\text{cm}^{-1}$ ): 3085 (C–H); 1577 (C=N); 966 (V=O); 605 (V–O); 423 (V–N). **UV-Vis** ( $\text{CH}_3\text{CN}$ ) [ $\lambda_{\text{max}}$ ,  $\epsilon$ ]: 239 nm,  $2.64 \times 10^4 \text{ M}^{-1} \text{ cm}^{-1}$ ; 270 nm,  $4.79 \times 10^4 \text{ M}^{-1} \text{ cm}^{-1}$ ; 359 nm,  $1.66 \times 10^4 \text{ M}^{-1} \text{ cm}^{-1}$ ; 376 nm (s),  $1.44 \times 10^4 \text{ M}^{-1} \text{ cm}^{-1}$ ; 500 nm,  $5.17 \times 10^3 \text{ M}^{-1} \text{ cm}^{-1}$ . **ESI-MS** in acetonitrile:  $[\text{M}]^+$  563.1281  $m/z$  (calc. 563.1275  $m/z$ ). **Elemental Analysis:** Calculated for  $\text{VC}_{30}\text{H}_{22}\text{N}_7\text{O}_2\text{Cl}$ : C, 60.157; H, 3.703; N, 16.374%. Found: C, 57.366; H, 4.263; N, 16.419 %.

### 3.8 References

1. Calderazzo, F., Marchetti, F., Pampaloni, G. and Passarelli, V., *J. Chem. Soc., Dalton Trans.*, **1999**, 4389.
2. Metzler-Nolte, N. and Schatzschneider, U., *Bioinorganic Chemistry. A Practical Course.*, Walter de Gruyter, Berlin, New York, **2009**, p 40, 41.
3. Calucci, L., Pampaloni, G., Pinzino, C. and Prescimone, A., *Inorg. Chim. Acta*, **2006**, 359, 3911.
4. Hiort, C., Lincoln, P. and Nordén, B., *J. Am. Chem. Soc.*, **1993**, 115, 3448.
5. Molphy, Z., Prisecaru, A. Slator, C., Barron, N., McCann, M., Colleran, J., Chandran, D., Gathergood, N and Kellett, A. *Inorg. Chem.*, **2014**, 53, 5392.
6. Dickeson, J.E. and Summers, L.A., *Aust. J. Chem.*, **1970**, 23, 1023.
7. Barba, V., Cuahutle, D., Santillan, R. and Farfán, N., *Can. J. Chem.*, **2001**, 79, 1229.
8. Tunç, T., Sari, M., Sadikoğlu and Büyükgüngör, O., *J. Chem. Cryst.*, **2009**, 39, 672.
9. Akerman, M.P. and Chiazzari, V.A., *J. Mol. Struct.*, **2014**, 1058, 22.
10. Kabak, M., Elmali, A. and Elerman, Y., *J. Mol. Struct.*, **1999**, 477, 151.
11. Prasad, P., Sasmal, P.K., Majumdar, R., Dighe, R.R. and Chakravarty, A.R., *Inorganica Chim. Acta*, **2010**, 363, 2743.
12. Banerjee, S., Hussain, A., Prasad, P., Khan, I., Banik, B., Kondaiah, P. and Chakravarty, A.R., *Eur. J. Inorg. Chem.*, **2012**, 24, 3899.
13. Banik, B., Somyajit, K., Koley, D., Nagaraju, G. and Chakravarty, A.R., *Inorg. Chim. Acta*, **2012**, 393, 284.
14. Bruker Topspin 2.1 (pl6), Java version 1.6.0\_03, Sun Microsystems Inc., from Bruker BioSpin, 2010.
15. Ocakoglu, K., Zafer, C., Cetinkaya, B. and Icli, S., *Dyes Pigm.*, **2007**, 75, 385.
16. Arancibia, A., Concepción, J., Daire, N., Leiva, G., Leiva, A.M., Loeb, B., Del Río, R., Díaz, R., Francois, A. and Saldivia, M., *J. Coord. Chem.*, **2011**, 54, 323.
17. Rodríguez, M., Ochoa; M.E., Santillan R.; Farfán, N. and Barba, V., *J. Organomet. Chem.*, **2005**, 690, 2975.

## ***Chapter Four: Spectroscopic Characterisation***

### ***4.1 Introduction to Spectroscopy***

The spectroscopic techniques employed in this work to characterise the ligands include nuclear magnetic resonance (NMR), UV/visible and infrared spectroscopy, and electrospray ionisation mass spectrometry (ESI-MS). ESI-MS, UV/visible, infrared and electron paramagnetic resonance (EPR) spectroscopic techniques were used to characterise the oxovanadium complexes. Ultraviolet (190 – 400 nm) and visible (400-800 nm) radiation causes electron transitions between electronic energy levels within a molecule. In infrared spectroscopy, compounds will absorb radiation between 2.5 – 15  $\mu\text{m}$  wavelengths, corresponding to stretching and bending vibration frequencies of the covalent bonds in the molecule. EPR utilises an applied magnetic field, and radio-frequency radiation (in GHz range), to study transitions between electronic spin states split by the magnetic field of unpaired electrons. NMR also utilises an applied magnetic field, but utilises lower radio frequencies (MHz range) of longer wavelengths (1 – 5 m) to cause nuclear spin transitions in a compound.<sup>1-3</sup>

### ***4.2 Nuclear Magnetic Resonance Spectroscopy***

$^1\text{H}$  and  $^{13}\text{C}$  NMR spectroscopy was used to characterise the diamagnetic dione precursor, bidentate and tridentate ligands. NMR can be used for atomic nuclei with odd atomic numbers or mass based on these nuclei having a quantised spin angular momentum. This technique can provide information on each type of atom that is magnetically distinct and the immediate environment surrounding the nucleus.<sup>1</sup> When a magnetic field is applied the spin states of a nucleus split into states of unequal energy. Taking hydrogen as an example, the spin state of  $-\frac{1}{2}$  has higher energy than the spin state  $+\frac{1}{2}$  as it is opposed to the magnetic field. When the magnetic field is applied, the nucleus begins to precess (wobble) about its own axis. An oscillating electrical field is generated by this precession, as the nucleus has a charge. When radio frequencies are applied, the nuclei that are aligned with the applied magnetic field absorb energy and change their spin orientation.<sup>1</sup>

This absorption of energy is quantised, and so, the energy can only be absorbed if the frequency of the radio waves matches the frequency of the electric field of the precessing nucleus (resonance). Not all protons have the same electronic environment and, therefore, resonate at different frequencies. In addition, the applied magnetic field causes valence electrons of protons to circulate, creating a magnetic field that is opposed to the applied magnetic field. This generated magnetic field (diamagnetic anisotropy) causes a shielding of the protons from the applied magnetic field. The greater the electron density around a nucleus, the greater the shielding from the applied magnetic field. Protons that are shielded by a higher electron density resonate at lower frequencies due to the lower net applied field.<sup>1</sup>

In pulsed Fourier transform instruments, all of the magnetic nuclei in a molecule are excited simultaneously by a pulse and undergo resonance at the same time. The excited nuclei then relax and return to their original spin state by emitting radiation, when the pulse is discontinued. The emitted radiation occurs at various frequencies depending on the environment of the nuclei. The free-induction decay (FID) signal generated is the difference between the frequencies emitted by the excited nuclei and the frequency of the pulse.<sup>1</sup>

The FID signal is then computed through Fourier transform analysis into the chemical shifts of the different nuclei in ppm. The signal is represented as a chemical shift, as they are independent of the strength of the applied magnetic field. The sensitivity of the NMR spectrometer instrument is increased with stronger resonance signals, with increasing applied frequencies to observe nuclei such as <sup>13</sup>C that is low in abundance.<sup>1</sup> The NMR spectrometers used in this work use high field strength and operating frequencies of 9.4 T magnet at frequencies of 400 MHz for <sup>1</sup>H and 100 MHz for <sup>13</sup>C NMR spectra and 11.7 T magnet at frequencies of 500 MHz for <sup>1</sup>H and 125 MHz for <sup>13</sup>C.

#### 4.2.1 NMR Spectroscopy of the *N,N*-Bidentate Co-ligands

DPQ and DPPZ are symmetrical ligands (two-fold symmetry). Four <sup>1</sup>H peaks and seven <sup>13</sup>C peaks are expected for DPQ (C<sub>14</sub>H<sub>8</sub>N<sub>4</sub>). Five <sup>1</sup>H peaks and nine <sup>13</sup>C peaks are expected for DPPZ (C<sub>18</sub>H<sub>10</sub>N<sub>4</sub>). The signals recorded correspond with those reported in the literature for DPQ<sup>4</sup> and DPPZ<sup>5</sup> (Figure 4.1). The full <sup>1</sup>H and <sup>13</sup>C NMR spectra are available in Figures A4, A5, A7 and A8 for DPQ and DPPZ, respectively, in Appendix A.

The reference literature assigns H<sub>c</sub>/H<sub>f</sub> of DPQ as the lowest-field signal (refer to *Figure 4.1*) due to the quinoxaline nitrogen atoms increasing the *para* effect of the bipyridine nitrogen atoms. In the <sup>13</sup>C NMR spectrum of DPQ, the C–H<sub>c</sub>/C–H<sub>f</sub> signal appears upfield of the C–H<sub>a</sub>/C–H<sub>d</sub> signal.<sup>4</sup> In the DPPZ <sup>1</sup>H NMR spectrum the H<sub>c</sub>/H<sub>f</sub> protons in the bipyridine moiety of DPPZ are the most affected by the addition of a benzene ring on DPQ, shifting downfield in comparison to the H<sub>c</sub>/H<sub>f</sub> protons in the bipyridine moiety of DPQ.

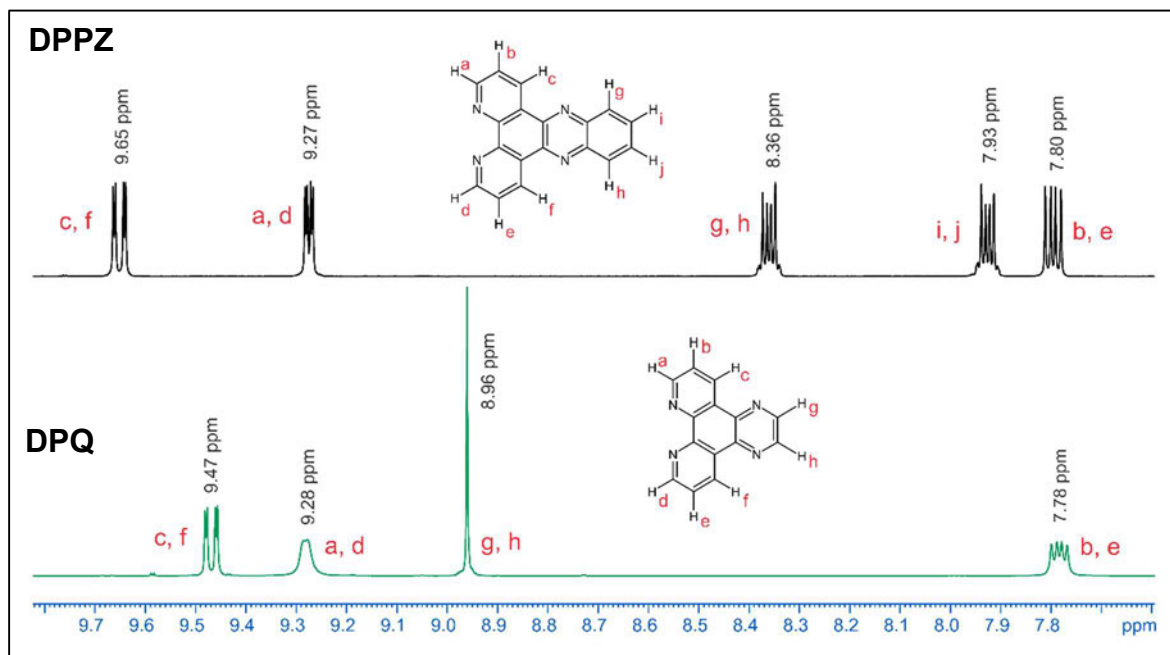


**Figure 4.1** <sup>1</sup>H NMR spectra of DPPZ (top) and DPQ (bottom) in CDCl<sub>3</sub>. Inset structures show the atom numbering scheme.

#### 4.2.2 NMR Spectroscopy of the *O,N,O'*-Tridentate Ligands

The <sup>1</sup>H and <sup>13</sup>C spectra of PHA, MEA, TERTA, and CLA have been reported in literature.<sup>6-13</sup> The reported spectra, however, have not been fully assigned. The <sup>1</sup>H and <sup>13</sup>C NMR spectra of the *O,N,O'*-tridentate ligands in this work are fully assigned, where possible. In addition, the <sup>1</sup>H and <sup>13</sup>C assignments in this work have improved on those reported. The most notable examples are the assignments in the <sup>1</sup>H and <sup>13</sup>C NMR spectra of ligands MEA and TERTA (*Figures A16, A17, A22 and A23, Appendix A*). <sup>1</sup>H, <sup>13</sup>C, and additional NMR cosy, dept, hsqc and hmbc experiments were conducted on all *O,N,O'* ligands in this work to remove any ambiguity. Assigned <sup>1</sup>H and <sup>13</sup>C spectra for all *O,N,O'* ligands are reported in *Appendix A*.

All of the  $^1\text{H}$  NMR spectra of the  $O,N,O'$  ligands in this work exhibited a singlet signal between 8.95 – 9.11 ppm, assigned to the imine proton.<sup>10</sup> In addition, all of the  $O,N,O'$  ligands have two broad singlets downfield. These are assigned to the two OH groups present with the furthest downfield signal assigned to the OH of the salicylidene group.<sup>13</sup> A representative  $^1\text{H}$  NMR spectrum is shown in *Figure 4.2* for TERTA.

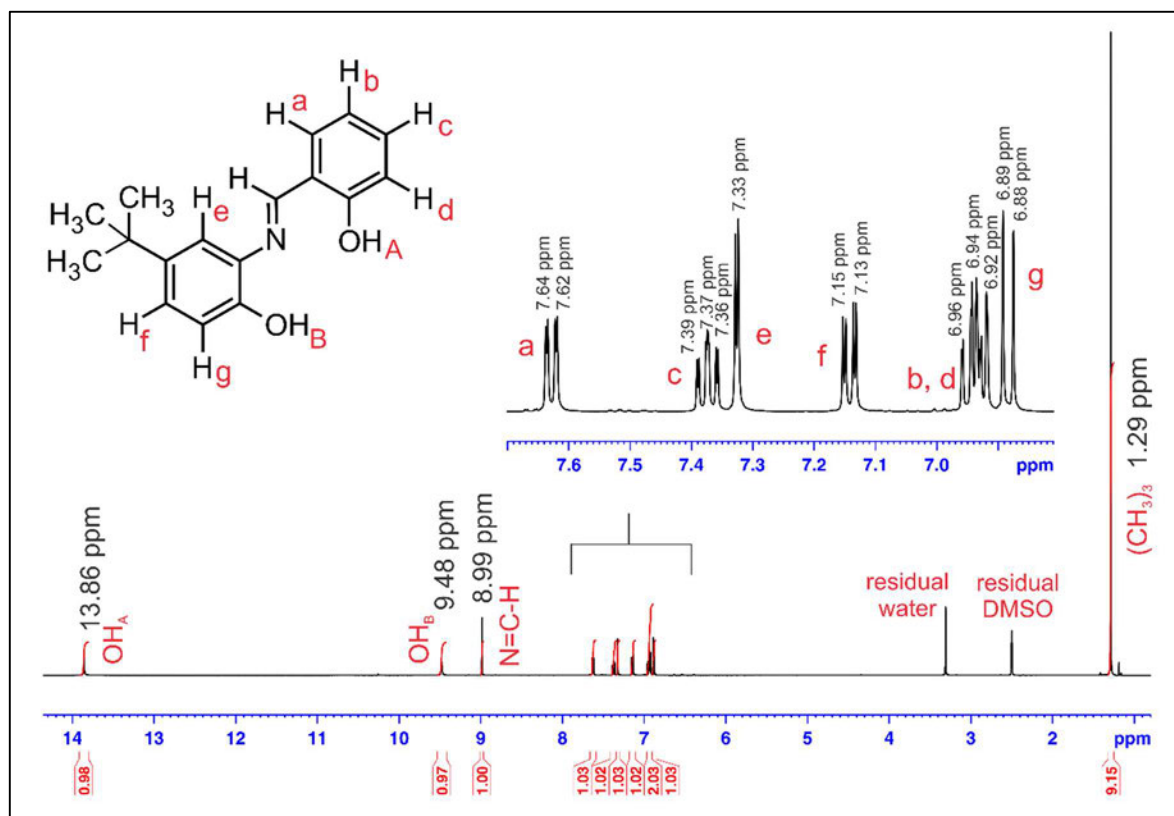


**Figure 4.2** Fully assigned  $^1\text{H}$  NMR spectrum of TERTA in  $\text{DMSO-}d_6$ .

Although the  $O,N,O'$  ligands crystallised as the keto tautomer (refer to *Chapter 5, Section 5.2*), the  $O,N,O'$  ligands were found as the enol tautomer in solution. This was confirmed by the presence of the two broad singlets downfield (in the ranges 13.27 – 13.86 ppm and 9.45 – 10.88 ppm), characteristic of phenol hydrogens.<sup>6,8,9</sup> The OH shifts for the  $O,N,O'$  ligands in this work differed to those in the literature. The literature reports either zero<sup>10</sup> or one reported phenol signal,<sup>7,12,13</sup> or different chemical shifts of the two phenol signals.<sup>6,11</sup> This deviation may be due to solvents<sup>1</sup> or the presence of the zwitterion derivative.<sup>12</sup> The chemical shift of the OH hydrogen atoms in general are also dependant on concentration and temperature.<sup>1</sup> A representative  $^{13}\text{C}$  NMR spectrum is shown in *Figure 4.3* for TERTA.

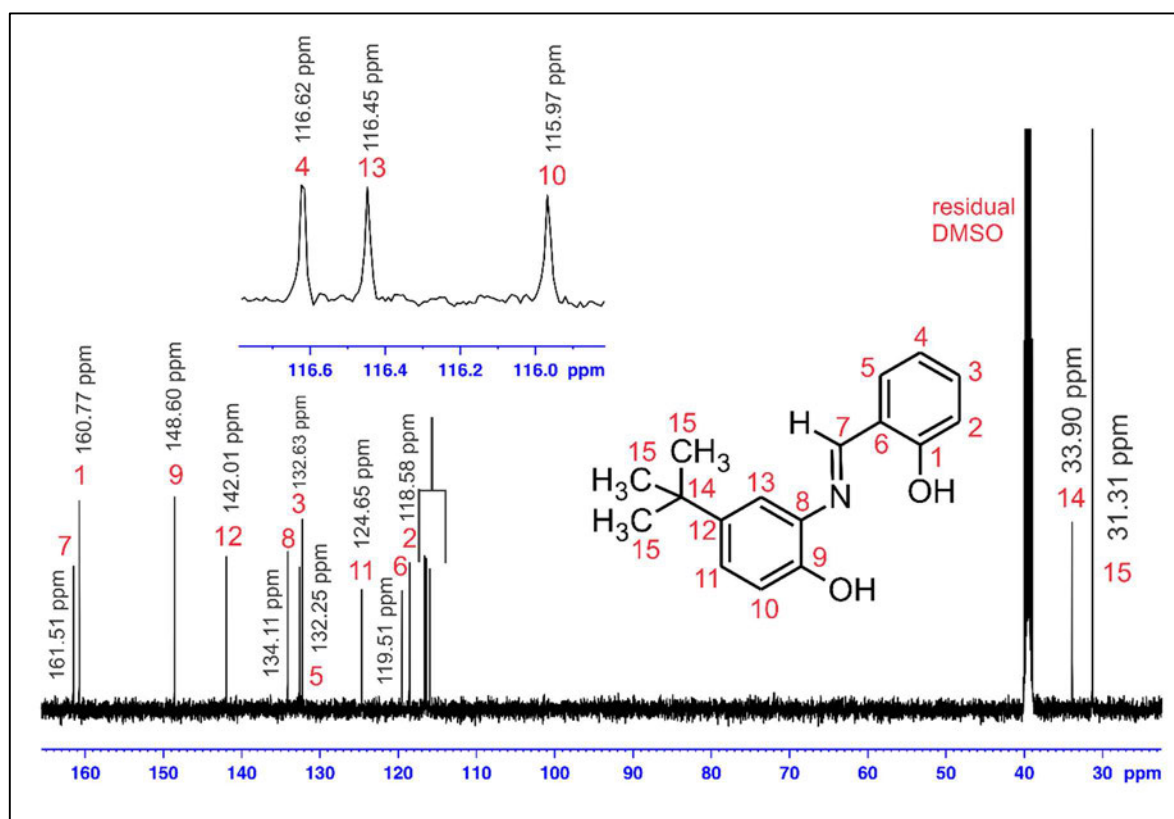


**Figure 4.3** Fully assigned  $^{13}\text{C}$  NMR spectrum of TERTA in  $\text{DMSO-}d_6$ .

The imine carbon atom signal is furthest downfield in the  $^{13}\text{C}$  NMR spectra of the  $O,N,O'$  ligands as it is the most deshielded. In contrast alkyl groups, such as  $-\text{CH}_3$  groups are furthest upfield. The electron withdrawing effects of the OH groups mean that carbon atoms C1 and C9 are further downfield than the other aromatic carbon atoms. The other aromatic carbon atoms are in more similar chemical environments and are closely spaced - between 142 and 116 ppm, in the case of TERTA.

### 4.2.3 NMR Spectroscopy of the $O,N,N'$ -Tridentate Ligands

The NMR data for the novel  $O,N,N'$ -tridentate ligands in this study has been published for PHCA, MECA and TERTCA as part of this PhD project.<sup>14</sup> Full  $^1\text{H}$  and  $^{13}\text{C}$  NMR spectra of the  $O,N,N'$  ligands, with assignments are given in *Appendix A*. The  $^1\text{H}$  chemical shifts for the imine and hydroxyl group show that, as in the solid-state, the hydroxyl proton remained on the oxygen in solution and the OH hydrogen atom chemical shift appeared furthest downfield.

The imine nitrogen was not protonated as had been reported for the *O,N,O'*-donor PHA derivative of the ligand in solution.<sup>12</sup> Previously reported similar *O,N,N'* ligands with an NH,N imidazole moiety also indicate that the OH group is protonated in solution.<sup>15,16</sup>

Comparing the <sup>1</sup>H chemical shift of the imine CH atoms of the *O,N,O'* and *O,N,N'* ligands, those of the *O,N,N'* ligands are further upfield than in the corresponding *O,N,O'* ligands. For example, 8.56 ppm for the imine C–H of the *O,N,N'*-donor TERTCA ligand compared to 8.99 ppm for the equivalent atom in the *O,N,O'*-donor TERTA ligand. This is likely a consequence of the electron withdrawing effect of the OH group which would deshield the imine CH in the latter. The <sup>1</sup>H NMR spectrum of TERTCA is shown in Figure 4.4 for TERTCA.

The addition of the electron-donating methyl and *tert*-butyl groups in MECA and TERTCA, respectively, at the 4' position on the aminophenol ring, did not affect the imine CH hydrogen atom chemical shift significantly (8.54 and 8.56 ppm for MECA and TERTCA, respectively, compared to 8.54 ppm for unsubstituted PHCA). The addition of an electron-withdrawing phenyl ring in PPHCA, however, caused a downfield shift of the imine hydrogen atom (8.66 ppm for PPHCA).

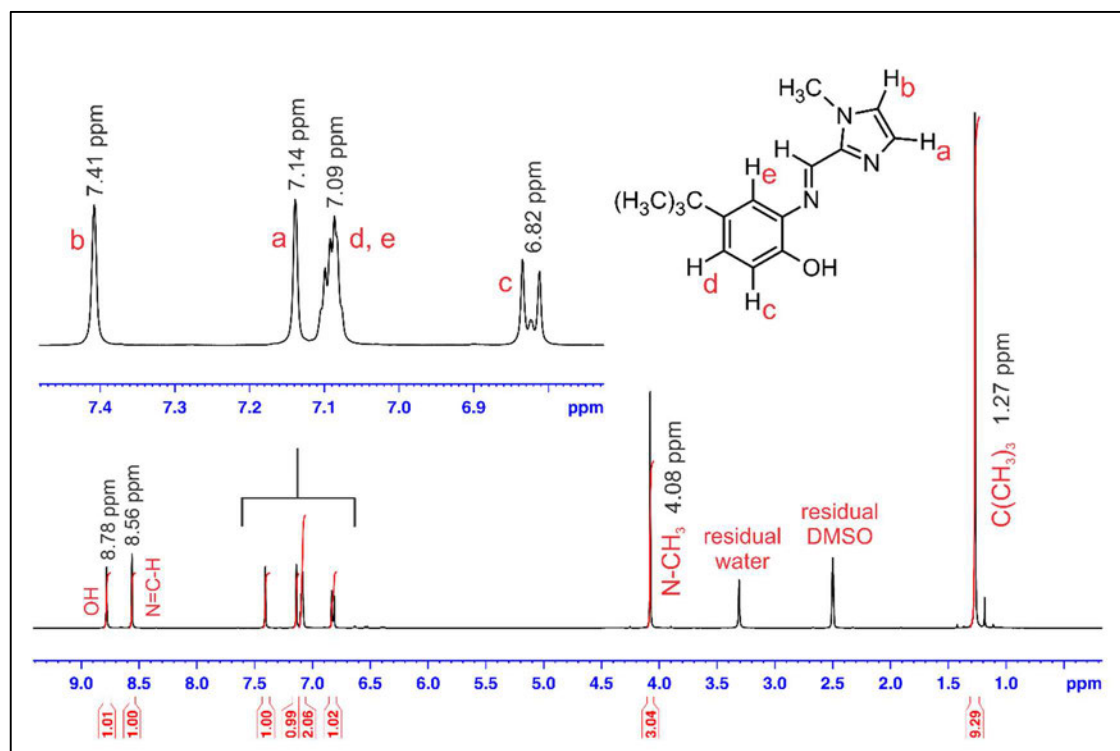
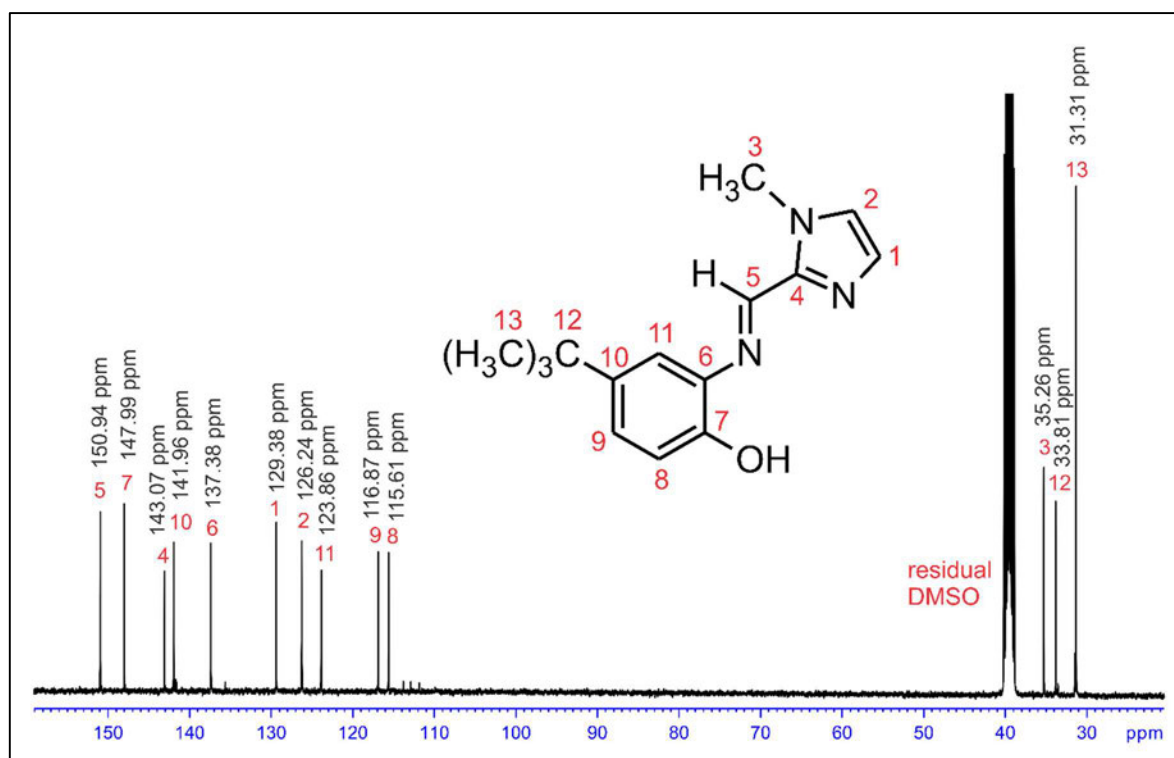


Figure 4.4 Fully assigned <sup>1</sup>H NMR spectrum of TERTCA in DMSO-*d*<sub>6</sub>.

The effect of adding a phenyl ring in PHPHCA similarly affected the hydroxyl chemical shift. The chemical shift of the hydroxyl hydrogen atom was similar for MECA and TERTCA (8.76 ppm and 8.78 ppm, respectively), but further downfield for PHCA at 8.97 ppm and even further downfield for PHPHCA at 9.17 ppm. The electron-donating methyl and *tert*-butyl groups of MECA and TERTCA, respectively, *para* to the hydroxyl group lead to shielding compared to the unsubstituted phenol ring in PHCA. The phenyl substituent has a deshielding effect on the OH group. A similar trend is noted in the C–OH  $^{13}\text{C}$  chemical shifts (150.53 ppm, 148.21 ppm, 147.99 ppm and 150.18 ppm for PHCA, MECA, TERTCA and PHPHCA, respectively). A representative  $^{13}\text{C}$  NMR spectrum is shown in *Figure 4.5* for TERTCA. The  $^1\text{H}$  and  $^{13}\text{C}$  chemical shifts of the imidazole moiety did not seem to be affected by the addition of electron-donating substituents at the 4' position on the aminophenol ring.



**Figure 4.5** Fully assigned  $^{13}\text{C}$  NMR spectrum of TERTCA in  $\text{DMSO-}d_6$ .

As with the  $O,N,O'$  ligands the imine carbon atom is furthest downfield in the  $^{13}\text{C}$  NMR spectra of the  $O,N,N'$  ligands as it is the most deshielded. Alkyl groups such as  $-\text{CH}_3$  groups are furthest upfield.

The addition of the electron-withdrawing phenyl ring in PHPHCA, also caused a downfield shift of the imine carbon atom as it did for the imine hydrogen atom as compared to the other *O,N,N'* ligands in the series: 150.93, 150.70, 150.94 and 151.56 ppm for the imine  $^{13}\text{C}$  shift of PHCA, MECA, TERTCA and PHPHCA, respectively.

#### 4.2.4 NMR Spectroscopic Hydrogen Bonding Study of the *O,N,N'* Ligands

The crystal structures of the *O,N,N'* ligands revealed the compounds spontaneously dimerise in the solid-state (further discussed in *Chapter 5*). A  $^1\text{H}$  NMR titration study was, therefore, conducted on TERTCA to determine if dimerisation also occurs in the solution phase. TERTCA was selected as the *tert*-butyl functionality allowed for more solubility in the chosen solvent, chloroform, allowing for a wider range of concentrations. As mentioned previously, the chemical shifts of atoms involved in hydrogen bonding vary based on several factors. The line shapes and chemical shifts of the OH group were followed over a concentration range of *ca.*  $3 \times 10^{-3} - 4 \times 10^{-1}$  M based on the mass of the monomeric unit of TERTCA (*Figure 4.6*). NMR spectra for this study were recorded with a Bruker Avance III 500 spectrometer at 30 °C in dry  $\text{CDCl}_3$ . The solvent was dried over calcium hydride. This is an important step as water in the samples may interfere with the hydrogen bonding pattern. The  $^1\text{H}$  NMR spectra were processed through TopSpin 3.2, patch level 7.<sup>17</sup> The results of this study have been published.<sup>14</sup>

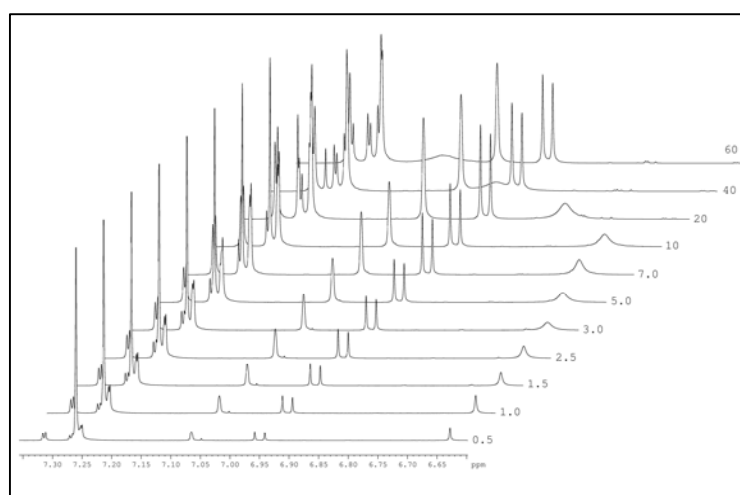


**Figure 4.6** Stacked  $^1\text{H}$  NMR spectra of TERTCA depicting the concentration dependence of the chemical shift and line width of the OH signal.<sup>14</sup>

The data indicated that the chemical shift of the OH group moves downfield, and line broadening occurs as the concentration of TERTCA increases (*Figure 4.6*). The original OH chemical shift, of 6.62 ppm at  $3.24 \times 10^{-3}$  M, shifted downfield to a final chemical shift of 7.11 ppm at  $3.88 \times 10^{-1}$  M. The chemical shifts and line widths of the hydrogen atoms not involved in hydrogen bonding remained unchanged. The significant downfield shift of the OH group was attributed to the deshielding effect of intermolecular hydrogen bonding within the dimers. The line broadening of the OH hydrogen atom is attributed to a greater rate of exchange between the monomer and dimer units in relation to the timescale of the 500 MHz  $^1\text{H}$  NMR spectra acquisition. The signal observed is the weighted time average of the monomer and dimer.<sup>14</sup>

The equilibrium constant for the dimerisation process was estimated using the above data. The chemical shift of the OH group was plotted against the concentration of TERTCA. The data were fitted using Origin 9.1 to a non-linear least-squares fit of the following equation to determine the equilibrium constant,  $K$ .<sup>14,18</sup>

$$\delta = \delta_D + \frac{\delta_D - \delta_M}{4KC} (1 - \sqrt{1 + 8KC})$$

Where  $\delta$  = the weighted average chemical shift of the hydroxyl proton

$\delta_D$  = chemical shift of the hydroxyl proton of the dimer

$\delta_M$  = chemical shift of the hydroxyl proton of the monomer

$C$  = concentration of the monomer in solution

The equilibrium constant was calculated as  $0.16(5) \text{ M}^{-1}$  for the 1:1 dimerisation process at 30 °C. The  $\delta_D$  and  $\delta_M$  chemical shifts were estimated to be 11.4(9) ppm and 6.62(1) ppm respectively at 30 °C. The dimerisation process at 30 °C was also determined to be endergonic with a  $\Delta G$  value of *ca.* 4.6 kJ mol<sup>-1</sup>. The slightly endergonic process may explain why relatively high concentrations of TERTCA were required to observe a significant change in the chemical shift of the hydroxyl proton.

The  $^1\text{H}$  NMR study strongly suggests that dimerisation of TERTCA takes place in solution. It is also suspected that dimerisation in solution would occur for PHCA and MECA as the hydrogen bonding parameters and molecular geometry in the solid-state are similar for PHCA, MECA and TERTCA (refer to *Chapter 5*).<sup>14</sup>

### 4.3 Infrared Spectroscopy of the Tridentate Ligands and Oxovanadium(IV) Complexes

The relevant range for vibrational infrared spectroscopy extends from about 4000 to 400  $\text{cm}^{-1}$ .<sup>1</sup> A molecule will absorb selected frequencies of infrared radiation that match the natural vibration frequencies of the bonds in the molecule.<sup>1</sup> The absorbed energy enhances the amplitude of the natural vibrations with energy changes between 8 to 40  $\text{kJ mol}^{-1}$ .<sup>1</sup> Only bonds that have a dipole moment that changes as a function of time at the same frequency as the incoming radiation can absorb infrared radiation.<sup>1</sup> Each different type of molecule will produce a unique infrared spectrum as every type of bond has a different natural frequency of vibration and the same type of bond in a different molecule would be in a different chemical environment. The absorption frequency of each type of bond are thus found over a range dependent on the chemical environment, such as C=N in the range 1650 – 1550  $\text{cm}^{-1}$ .<sup>1</sup>

The infrared spectra of the synthesised ligands and complexes are shown in *Appendix A*. The infrared spectra of the tridentate ligands were compared with the spectra of the corresponding complexes to assess successful coordination of the ligand to the oxovanadium(IV) centre. Due to the paramagnetic nature of the metal chelates, IR spectroscopy is an important characterisation tool.

The first notable difference in the infrared spectra of the uncoordinated tridentate ligands and the respective complexes is the stretching vibrations of the imine bond in the Schiff base ligand. This shifts to a lower frequency in the complexes, by at least 8  $\text{cm}^{-1}$  (*Table 4.1*). For example, the stretching frequency of the imine bond in the *O,N,O'* tridentate ligand TERTA is 1614  $\text{cm}^{-1}$ . This shifts to a lower frequency of 1603  $\text{cm}^{-1}$  in the neutral [VO(TERTA)(DPQ)] complex. Note - there may be some single bond character for the imine bond in the *O,N,O'* ligands due to the keto-enol tautomerism of the *O,N,O'* ligands (see *Section 5.2*). Therefore, the band at 1614  $\text{cm}^{-1}$  may contain C=O stretching frequency character due to the presence of the carbonyl bond in the keto tautomer. The *O,N,O'* ligands were determined as the keto form in the solid-state structures (*Section 5.2.3*).

**Table 4.1** Frequencies ( $\text{cm}^{-1}$ ) of the imine C=N stretching vibrations in the tridentate ligands, and the neutral and cationic complexes.

<b>Tridentate O,N,O'</b> <b>Ligand</b>	<b><math>\nu</math> (C=N)</b> <b>(<math>\text{cm}^{-1}</math>)</b>	<b>Neutral Complex</b>	<b><math>\nu</math> (C=N)</b> <b>(<math>\text{cm}^{-1}</math>)</b>
PHA	1610	[VO(PHA)(DPQ)]	1600
MEA	1611	[VO(MEA)(DPQ)]	1599
TERTA	1614	[VO(TERTA)(DPQ)]	1603
CLA	1614	[VO(CLA)(DPQ)]	1599
SOA	1612	[VO(SOA)(DPQ)]	1600
NAA	1608	[VO(NAA)(DPQ)]	1600
PHPHA	1612	[VO(PHPHA)(DPQ)]	1597
MEA	1611	[VO(MEA)(DPPZ)]	1601
<b>Tridentate O,N,N'</b> <b>Ligand</b>	<b><math>\nu</math> C=N</b> <b>(<math>\text{cm}^{-1}</math>)</b>	<b>Cationic Complex</b>	<b><math>\nu</math> C=N</b> <b>(<math>\text{cm}^{-1}</math>)</b>
PHCA	1634	[VO(PHCA)(PHEN)](PF <sub>6</sub> )	1582
MECA	1620	[VO(MECA)(PHEN)](PF <sub>6</sub> )	1604
TERTCA	1618	[VO(TERTCA)(PHEN)](PF <sub>6</sub> )	1600
PHPHCA	1614	[VO(PHPHCA)(PHEN)](PF <sub>6</sub> )	1601
MECA	1620	[VO(MECA)(DPQ)](PF <sub>6</sub> )	1581
TERTCA	1618	[VO(TERTCA)(DPQ)](PF <sub>6</sub> )	1581
MECA	1620	[VO(MECA)(DPPZ)](Cl)	1577

The shifting of the imine bond stretching frequency to lower wavenumbers in the metal complexes indicates coordination of the imine nitrogen to the vanadium centre as the carbon to nitrogen bond order decreases upon coordination.<sup>6,19</sup> The decrease in bond order is a consequence of the electron deficient metal centre removing electron density from the ligand. The imine C=N group is directly coordinated to the metal and thus experiences a relatively large change compared to other bonds. The sharp imine C=N stretching vibrations for the complexes in this work are consistent with the imine frequencies in similar oxovanadium(IV) compounds with Schiff base ligands found in the literature.<sup>19-21</sup>

The second difference to note between the free ligand and metal complex IR spectra is the appearance of the strong V=O stretching vibration<sup>19,20,22-25</sup>, in the range 945 – 968  $\text{cm}^{-1}$ . For example, the V=O stretching vibration appears at 949  $\text{cm}^{-1}$  in the [VO(TERTA)(DPQ)] spectrum, this is not present in the spectra of the free TERTA ligand (*Figure 4.7*).

The presence of the V–N stretch in the range 423 – 438  $\text{cm}^{-1}$  and the V–O stretch in the range 532 – 557  $\text{cm}^{-1}$  also indicate coordination of the tridentate Schiff base ligands to the vanadium centre.<sup>24,26–28</sup>

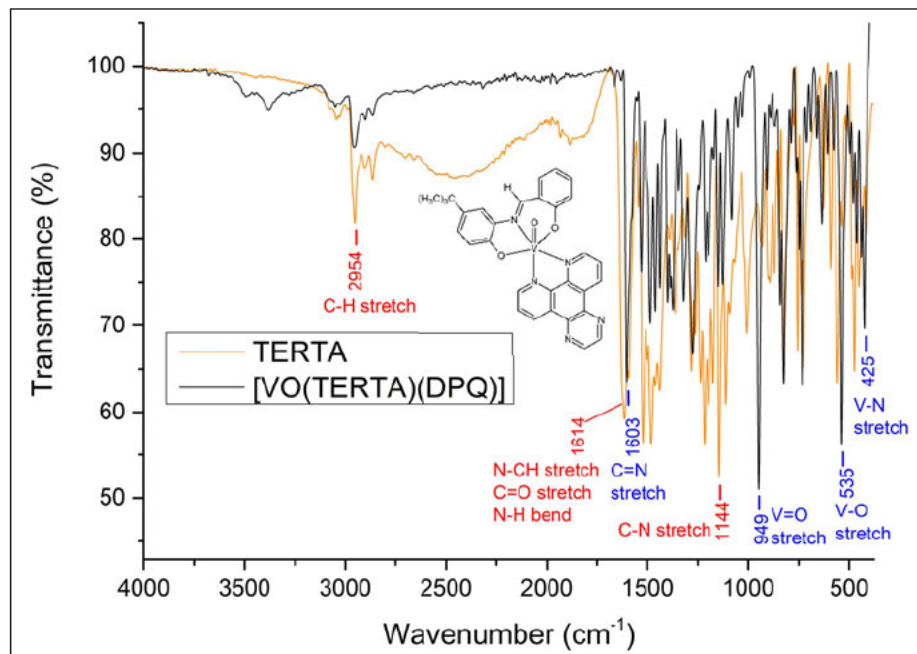


**Figure 4.7** Overlay of the IR spectra of the  $O,N,O'$  tridentate ligand TERTA and the neutral complex  $[\text{VO}(\text{TERTA})(\text{DPQ})]$  indicating the general shift to lower stretching frequencies following coordination of the electron deficient metal ion. The V=O, V–O and V–N stretching frequencies are also indicated and confirm successful metal ion coordination.

The cationic PHEN and DPQ complexes also have an additional intense peak in the region 831 – 835  $\text{cm}^{-1}$  that is not present in the free ligand spectra. This is assigned to the P–F stretch of the hexafluorophosphate counter ion.<sup>29–31</sup> Representative IR spectra giving a comparison of the  $O,N,N'$ -tridentate ligand TERTCA and the  $[\text{VO}(\text{TERTCA})(\text{PHEN})](\text{PF}_6)$  complex are shown in *Figure 4.8*. The general shift to lower frequencies and appearance of the V=O, V–O and P–F stretching frequencies are indicative of successful metal complex formation.

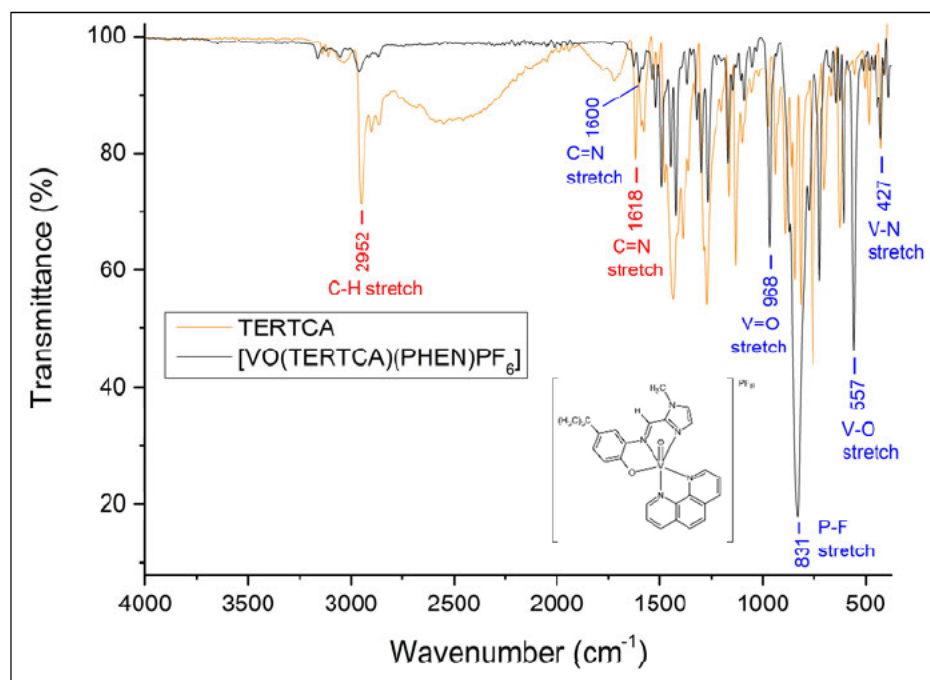


**Figure 4.8** Overlay of the IR spectra of the *O,N,N'*-tridentate TERTCA ligand and the [VO(TERTCA)(PHEN)](PF<sub>6</sub>) complex highlighting the lower C=N stretching frequency and appearance of the V=O, V–O and P–F stretching frequencies in the complex.

The V=O, V–O, V–N and P–F stretching frequencies of the complexes are listed in *Table 4.2*. The intense P–F stretch that is present in the spectra of the hexafluorophosphate PHEN and DPQ complexes is not present in the neutral DPQ complexes, nor in the cationic DPPZ chloride complex spectra.

The frequency of the V=O stretch gives an indication of the sigma donor capacity of the donor *trans* to the vanadyl oxygen.<sup>32</sup> The greater the sigma donor capacity of the ligand, the lesser the frequency of V=O stretching vibration.<sup>32</sup> Crystal structures obtained of the complexes in this work (*Chapter 5*) indicate the nitrogen donor of the bidentate ligand is *trans* to the vanadyl oxygen. A decrease in  $\nu(\text{V}=\text{O})$  was seen for [VO(MEA)(DPPZ)] in comparison to [VO(MEA)(DPQ)], but most differences in the V=O stretching frequency for analogous complexes with PHEN, DPQ and DPPZ co-ligands were marginal (*Table 4.2*).

**Table 4.2** Selected frequencies ( $\text{cm}^{-1}$ ) of V=O, V–O, V–N and P–F stretching vibrations in the neutral and cationic complexes.

Neutral Complexes	$\nu$ V=O ( $\text{cm}^{-1}$ )	$\nu$ V–O ( $\text{cm}^{-1}$ )	$\nu$ V–N ( $\text{cm}^{-1}$ )	$\nu$ P–F ( $\text{cm}^{-1}$ )
[VO(PHA)(DPQ)]	958	532	424	N/A
[VO(MEA)(DPQ)]	955	533	425	N/A
[VO(TERTA)(DPQ)]	949	535	425	N/A
[VO(CLA)(DPQ)]	945	532	424	N/A
[VO(SOA)(DPQ)]	953	533	435	N/A
[VO(NAA)(DPQ)]	954	565	425	N/A
[VO(PHPHA)(DPQ)]	959	534	435	N/A
[VO(MEA)(DPPZ)]	948	533	424	N/A
Cationic Complexes	$\nu$ V=O ( $\text{cm}^{-1}$ )	$\nu$ V–O ( $\text{cm}^{-1}$ )	$\nu$ V–N ( $\text{cm}^{-1}$ )	$\nu$ P–F ( $\text{cm}^{-1}$ )
[VO(PHCA)(PHEN)]( $\text{PF}_6$ )	959	555	427	831
[VO(MECA)(PHEN)]( $\text{PF}_6$ )	961	557	430	833
[VO(TERTCA)(PHEN)]( $\text{PF}_6$ )	968	557	427	831
[VO(PHPCA)(PHEN)]( $\text{PF}_6$ )	965	556	432	833
[VO(MECA)(DPQ)]( $\text{PF}_6$ )	967	556	438	835
[VO(TERTCA)(DPQ)]( $\text{PF}_6$ )	967	556	437	834
[VO(MECA)(DPPZ)](Cl)	966	557	423	N/A

The position of the V=O band is often correlated with the V=O bond length.<sup>32,33</sup> In this work the V=O bond length increased in the order [VO(TERTCA)(PHEN)]( $\text{PF}_6$ ) < [VO(MECA)(PHEN)]( $\text{PF}_6$ ) < [VO(PHCA)(PHEN)]( $\text{PF}_6$ ) while the  $\nu(\text{V}=\text{O})$  decreased in energy in the same order. Bond length typically increases as bond order (or bond strength) decreases. This lowering in bond order lowers the energy of the stretching frequency. There is seemingly a relationship between the electronic properties of the substituents on the Schiff base ligand and the stretching frequency: electron donating groups lead to shorter V=O bonds in the cationic PHEN complexes.

Comparing the infrared spectra of the neutral and cationic complexes, the V=O and V–O stretching frequencies occur at lower wavenumbers in the neutral complexes than in the cationic set of complexes (Table 4.2). For example,  $\nu(\text{V}=\text{O})$  was  $949 \text{ cm}^{-1}$  versus  $967 \text{ cm}^{-1}$  and  $\nu(\text{V}-\text{O})$  was  $535 \text{ cm}^{-1}$  versus  $556 \text{ cm}^{-1}$  for the neutral [VO(TERTA)(DPQ)] and cationic [VO(TERTCA)(DPQ)]( $\text{PF}_6$ ) complexes, respectively (Figure 4.9).

This is consistent with the literature where a decrease in the V=O stretching frequency occurred from the neutral complex [VO(PHA)(DPQ)] to the cationic *N*-2-pyridylmethylidene-2-hydroxyphenylamine oxovanadium(IV) DPQ derivative.<sup>19,20</sup> It is probable this difference is caused by the tridentate ligand  $\sigma$ -donor ability.

The appearance of the P–F intense peak in the [VO(TERTCA)(DPQ)](PF<sub>6</sub>) spectra at 834 cm<sup>-1</sup> that is not visible in the neutral analogue [VO(TERTCA)(DPQ)] spectra is also noted (Figure 4.9).

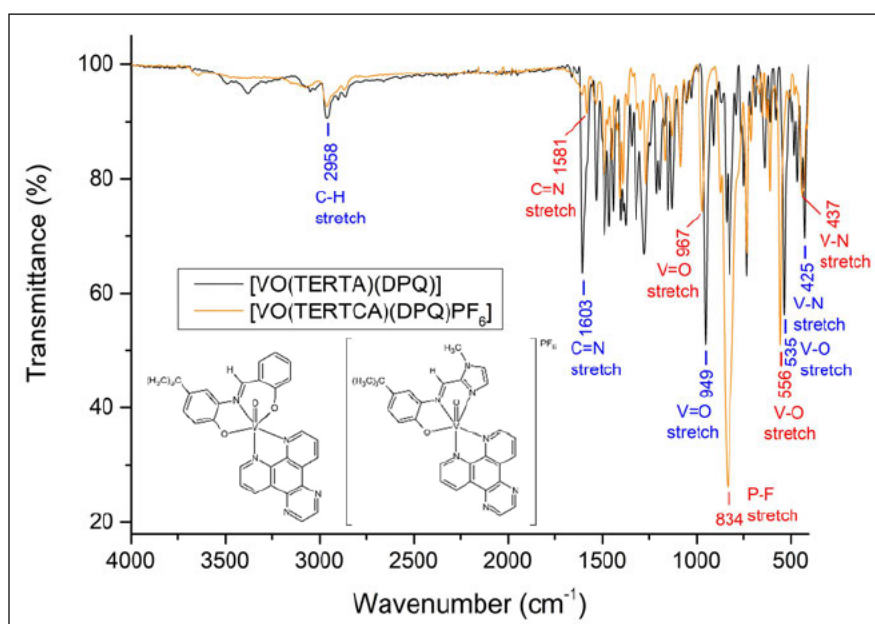


**Figure 4.9** IR spectra of the neutral complex [VO(TERTCA)(DPQ)] showing the lower V=O stretching frequency and absence of the P–F stretch when compared to the [VO(TERTCA)(DPQ)](PF<sub>6</sub>) complex.

Bands assigned to the co-ligand (PHEN, DPQ and DPPZ) are also present in the infrared spectra. For example, the bands at 1490, 1423 and 724 cm<sup>-1</sup> in the IR spectra of [VO(TERTCA)(PHEN)](PF<sub>6</sub>) (Figure 4.8) agree with characteristic bands of the phenanthroline ligand.<sup>21,33</sup>

The bands slightly higher than 3000 cm<sup>-1</sup> are assigned to aromatic C–H stretching vibrations of the phenyl rings and the bands slightly lower than 3000 cm<sup>-1</sup> are assigned to C–H stretching vibrations of the alkyl groups.<sup>28,34,35</sup>

## 4.4 UV/visible Spectroscopy

In UV/visible spectroscopy, continuous radiation (200 – 700 nm region of interest) is passed through a sample. This radiation induces transitions between electronic energy levels within the molecule being studied. An electron in a molecule moves to greater potential energy from occupied molecular orbitals to the lowest unoccupied molecular orbitals (LUMO) as the molecule absorbs energy, resulting in an absorption spectrum.<sup>1</sup> Molecules have many excited modes of vibration and rotation at room temperature and so a molecule undergoes electronic and vibrational-rotation excitation at the same time. Absorption phenomena in UV/visible spectroscopy, therefore, occurs over a wide range of wavelengths. Nuclei, held together by bonding electrons, determine the spacing between ground and excited energy states and so determine which wavelengths of radiation may be absorbed.<sup>1</sup>

The UV/visible absorption spectra of all ligands and complexes in this work were recorded in acetonitrile and are available in *Appendix A*. Acetonitrile was chosen as the solvent as it does not absorb radiation in the region of interest for this study (cut off 190 nm).<sup>1</sup> The applicability of Beer-Lambert's law was also conducted by plotting absorbance versus concentration for  $\lambda_{\text{max}}$  of all ligands and complexes. All ligands and complexes obeyed Beer-Lambert's law indicating a single species in solution.<sup>1</sup> Beer-Lambert straight-line graphs are also available in *Appendix A* for the ligands and complexes in this work.

### 4.4.1 UV/visible Spectra of the *O,N,O'*-Tridentate Ligands and Neutral [VO(ONO)(NN)] Complexes

The absorption spectra of the *O,N,O'* ligands consist of at least four bands. A representative absorption spectrum for an *O,N,O'* ligand is shown in *Figure 4.10* for CLA. The higher energy absorption bands at *ca.* 230 and 269 nm are assigned to  $\sigma \rightarrow \sigma^*$  and  $\pi \rightarrow \pi^*$  benzenoid transitions, respectively.<sup>6</sup> Bands at 269 nm could also include imine  $\pi \rightarrow \pi^*$  transitions.<sup>36</sup> Bands around 211 nm may be due to  $\pi \rightarrow \pi^*$  transitions of the ring containing phenolate oxygen.<sup>36</sup> The band at around 352 nm in the *O,N,O'* ligands is attributed to  $n \rightarrow \pi^*$  transitions between the lone pair of electrons of the N-atom in the imine group and a conjugated  $\pi$  bond of the phenyl rings.<sup>37</sup>

The UV/visible spectra of the  $O,N,O'$  ligands and the corresponding neutral complex were compared to determine if successful coordination of the ligand to the oxovanadium(IV) centre occurred. The first noticeable difference between absorption spectra of the free  $O,N,O'$  ligands and the corresponding  $[VO(ONO)(NN)]$  complexes is the appearance of the ligand-to-metal charge transfer (LMCT) band at 442 – 464 nm in the neutral metal complexes. For example, the LMCT band appears at *ca.* 464 nm in the  $[VO(CLA)(DPQ)]$  complex spectrum that is not present in the CLA ligand absorption spectrum. The LMCT band is attributed to a ligand-to-metal charge transfer from the phenolate oxygen to an empty  $d$ -orbital of vanadium ( $ONO \rightarrow V^{IV}$ ). The LMCT band is also possibly mixed with  $d_{xy}$  to  $d_z^2$  and  $d_x^2 - d_y^2$  transitions. It is generally thought that transitions occur from  $d_{xy}$  to  $d_{xz}$ ,  $d_{yz}$ ;  $d_{xy}$  to  $d_x^2 - d_y^2$  and  $d_{xy}$  to  $d_z^2$  orbitals in increasing energies for vanadyl(IV) complexes.<sup>19,20,26,36,38-40</sup>

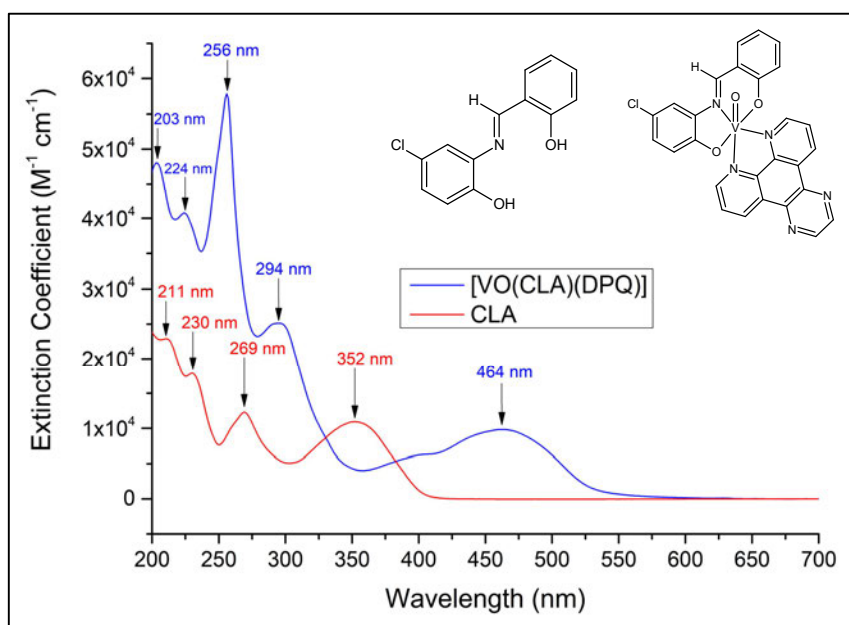


**Figure 4.10** Overlay of the UV/visible spectra of the  $O,N,O'$ -tridentate ligand CLA and the neutral complex  $[VO(CLA)(DPQ)]$  indicating formation of the LMCT band in the complex.

The increase in the number of bands for the complexes in comparison to the respective free ligand also indicates successful metallation. The  $\sigma \rightarrow \sigma^*$  and  $\pi \rightarrow \pi^*$  bands may have merged in the complex to form the intense band at 256 nm as the formation of the band around 256 nm in the complexes is midway between the  $\sigma \rightarrow \sigma^*$  band at 230 nm and the  $\pi \rightarrow \pi^*$  band at 269 nm of the corresponding free ligand. The hypsochromic shift of the  $\pi \rightarrow \pi^*$  benzenoid band in the complex could be due to the unsymmetrical nature of the metal-ligand bonding or increased metal-ligand  $\pi$ -interactions and conjugation.<sup>6</sup>

The remaining bands in the UV region of the complexes are attributed to intra-ligand  $\pi \rightarrow \pi^*$  transitions of the aromatic chromophores of the respective  $N,N'$  ligands and tridentate ligands. The formation of the bands around 291 nm are assigned to bidentate ligand  $\pi \rightarrow \pi^*$  transitions.<sup>19,20,26,36,38-40</sup> The  $n \rightarrow \pi^*$  band around 352 nm in the free ligands undergoes a bathochromic shift upon coordination to vanadium.<sup>37</sup> The shoulder at 400 nm in the complexes could be attributed to the imine band as the imine band normally appears at  $390 \pm 10$  nm with  $\epsilon = 1400 - 1800 \text{ M}^{-1} \text{ cm}^{-1}$  in  $[\text{VO}(\text{ONO})(\text{BIPY})]$  complexes.<sup>41</sup>

The  $\lambda_{\text{max}}$  (nm) and  $\epsilon$  ( $\text{M}^{-1} \text{ cm}^{-1}$ ) values for the LMCT and  $\pi \rightarrow \pi^*$  bands for the neutral complexes are summarised in *Table 4.3*.

**Table 4.3** Summary of  $\lambda_{\text{max}}$  (nm) and  $\epsilon$  ( $\text{M}^{-1} \text{ cm}^{-1}$ ) values for the LMCT and  $\pi \rightarrow \pi^*$  bands of the neutral oxovanadium(IV) complexes.

Neutral Complex	$\lambda_{\text{max}}, \epsilon$ ( $\text{M}^{-1} \text{ cm}^{-1}$ )	$\lambda_{\text{max}}, \epsilon$ ( $\text{M}^{-1} \text{ cm}^{-1}$ )
	LMCT band	$\pi \rightarrow \pi^*$
$[\text{VO}(\text{PHA})(\text{DPQ})]$	450 nm, $9.14 \times 10^3$	256 nm, $6.01 \times 10^4$
$[\text{VO}(\text{MEA})(\text{DPQ})]$	464 nm, $9.64 \times 10^3$	256 nm, $6.01 \times 10^4$
$[\text{VO}(\text{TERTA})(\text{DPQ})]$	464 nm, $1.07 \times 10^4$	256 nm, $5.68 \times 10^4$
$[\text{VO}(\text{CLA})(\text{DPQ})]$	464 nm, $9.76 \times 10^3$	256 nm, $5.78 \times 10^4$
$[\text{VO}(\text{SOA})(\text{DPQ})]$	450 nm, $1.30 \times 10^4$	256 nm, $8.40 \times 10^4$
$[\text{VO}(\text{NAA})(\text{DPQ})]$	442 nm, $1.14 \times 10^4$	256 nm, $6.79 \times 10^4$
$[\text{VO}(\text{PHPHA})(\text{DPQ})]$	464 nm, $9.57 \times 10^3$	256 nm, $6.17 \times 10^4$
$[\text{VO}(\text{MEA})(\text{DPPZ})]$	459 nm, $8.62 \times 10^3$	271 nm, $6.38 \times 10^4$

Comparing the spectra of the neutral complexes, the addition of electron-donating substituents such as methyl and *tert*-butyl and electron-withdrawing chloro on the 4' position of the phenyl ring caused the LMCT band to shift from 450 nm to 464 nm in comparison to  $[\text{VO}(\text{PHA})(\text{DPQ})]$ . The addition of the aromatic naphthalene rings caused the LMCT band to shift from 450 nm in  $[\text{VO}(\text{PHA})(\text{DPQ})]$  to 442 nm in  $[\text{VO}(\text{NAA})(\text{DPQ})]$ .

The additional  $\pi$  bonds in [VO(SOA)(DPQ)], [VO(NAA)(DPQ)] and [VO(PHPHA)(DPQ)] are also apparent in the amplified intensity of the  $\pi \rightarrow \pi^*$  transitions in comparison to [VO(PHA)(DPQ)], [VO(MEA)(DPQ)], [VO(TERTA)(DPQ)] and [VO(CLA)(DPQ)] (Table 4.3).

The extended conjugation of DPPZ in comparison to DPQ is also evident in the bathochromic shift of the  $\pi \rightarrow \pi^*$  band from 256 nm for [VO(MEA)(DPQ)] to 271 nm for [VO(MEA)(DPPZ)] (Figure 4.11). This is due to the gap in energy levels of a chromophore moving closer together with an increase in  $\pi$ -conjugation.<sup>1</sup> The energy of the transitions will therefore decrease, leading to a longer wavelength of absorption. The intensity of the absorption for the  $\pi \rightarrow \pi^*$  bands also increases as shown in Figure 4.11 ( $\epsilon$  is  $6.01 \times 10^4 \text{ M}^{-1} \text{ cm}^{-1}$  at 256 nm for [VO(MEA)(DPQ)] and is  $6.38 \times 10^4 \text{ M}^{-1} \text{ cm}^{-1}$  at 271 nm for [VO(MEA)(DPPZ)]). [VO(MEA)(DPPZ)] displays additional bands at 357 nm and 374 nm (Figure 4.11). DPQ and DPPZ complexes are known to exhibit additional bands near 350 nm due to  $n \rightarrow \pi^*$  transitions of the quinoxaline and phenazine moieties.<sup>19,20</sup>

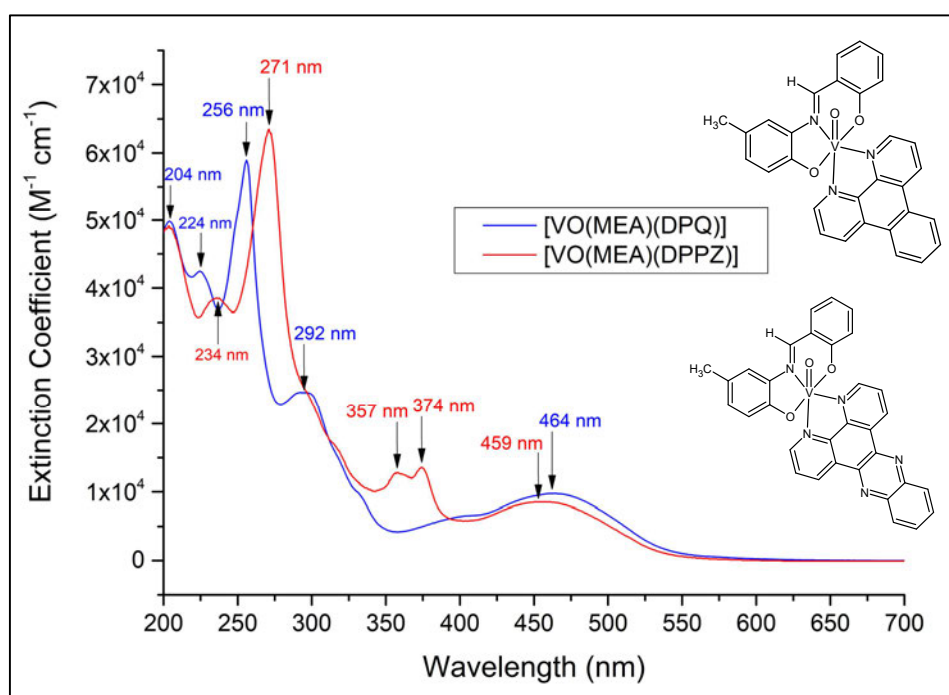


**Figure 4.11** Overlay of the UV/visible spectra of the neutral complexes [VO(MEA)(DPQ)] and [VO(MEA)(DPPZ)] highlighting the changes as a result of the increased conjugation of DPPZ compared to DPQ.

#### 4.4.2 UV/visible Spectra of the *O,N,N'*-Tridentate Ligands and Cationic [VO(ONN)(NN)](PF<sub>6</sub>/Cl) Complexes

In comparing the UV/visible spectra of the free *O,N,N'* ligands and corresponding cationic complexes the appearance of the LMCT (ONN → V<sup>IV</sup>) bands at 484 – 507 nm in the metal complex spectra are indicative of successful metallation. For example, a band formed at *ca.* 500 nm in the [VO(MECA)(PHEN)](PF<sub>6</sub>), [VO(MECA)(DPQ)](PF<sub>6</sub>) and [VO(MECA)(DPPZ)](Cl) complex spectra, which was absent from the MECA ligand spectrum (*Figure 4.12*). Considering that the wavelength of maximum absorption for the LMCT band was independent of the bidentate co-ligand supports the notion that the charge transfer is from the tridentate ligand to the metal ion. The increase in the number of bands for the complexes in comparison to the respective free ligand is also present for the cationic complexes, further indicating successful metallation.

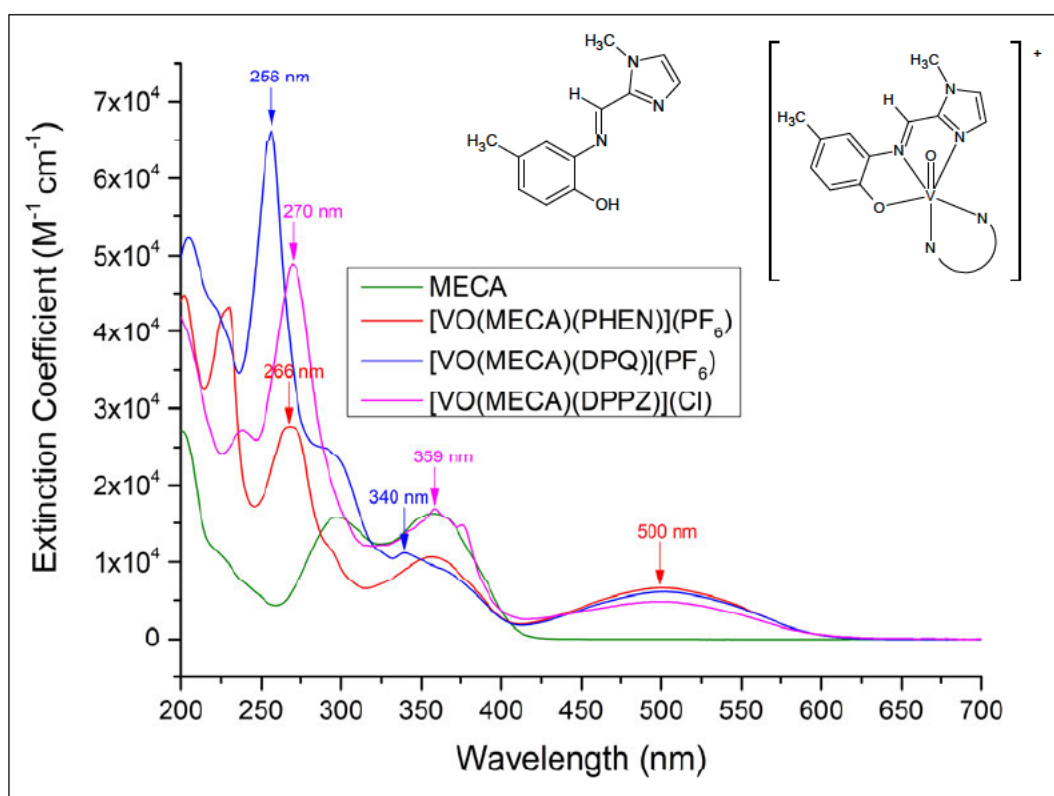


**Figure 4.12** Overlay of the UV/visible spectra of the *O,N,N'*-tridentate ligand MECA and the cationic complexes: [VO(MECA)(PHEN)](PF<sub>6</sub>), [VO(MECA)(DPQ)](PF<sub>6</sub>) and [VO(MECA)(DPPZ)](Cl).

The extended conjugation of DPPZ in comparison to DPQ is also evident in the metal chelate spectra by the bathochromic shift of the  $\pi \rightarrow \pi^*$  band from 256 nm for [VO(MECA)(DPQ)](PF<sub>6</sub>) to 270 nm for [VO(MECA)(DPPZ)](Cl) (Figure 4.12).<sup>1</sup> The  $\lambda_{\text{max}}$  (nm) and  $\epsilon$  (M<sup>-1</sup> cm<sup>-1</sup>) values for the LMCT and  $\pi \rightarrow \pi^*$  bands for the cationic complexes are listed in Table 4.4.

**Table 4.4** Summary of  $\lambda_{\text{max}}$  (nm) and  $\epsilon$  (M<sup>-1</sup> cm<sup>-1</sup>) values for the LMCT and  $\pi \rightarrow \pi^*$  bands of the cationic oxovanadium(IV) complexes.

Cationic Complex	$\lambda_{\text{max}}, \epsilon$ (M <sup>-1</sup> cm <sup>-1</sup> )	$\lambda_{\text{max}}, \epsilon$ (M <sup>-1</sup> cm <sup>-1</sup> )
	LMCT band	$\pi \rightarrow \pi^*$
[VO(PHCA)(PHEN)](PF <sub>6</sub> )	484 nm, $9.49 \times 10^3$	271 nm, $3.61 \times 10^4$
[VO(MECA)(PHEN)](PF <sub>6</sub> )	500 nm, $6.57 \times 10^3$	266 nm, $2.75 \times 10^4$
[VO(TERTCA)(PHEN)](PF <sub>6</sub> )	499 nm, $7.78 \times 10^3$	271 nm, $3.53 \times 10^4$
[VO(PHPHCA)(PHEN)](PF <sub>6</sub> )	507 nm, $7.24 \times 10^3$	272 nm, $4.27 \times 10^4$
[VO(MECA)(DPQ)](PF <sub>6</sub> )	503 nm, $6.14 \times 10^3$	256 nm, $6.43 \times 10^4$
[VO(TERTCA)(DPQ)](PF <sub>6</sub> )	501 nm, $5.98 \times 10^3$	256 nm, $6.53 \times 10^4$
[VO(MECA)(DPPZ)](Cl)	500 nm, $5.17 \times 10^3$	270 nm, $4.79 \times 10^4$

Comparing the electronic spectra of the cationic species with PHEN co-ligands, the addition of electron-donating substituents on the 4' position of the phenyl ring of the *O,N,N'* Schiff base ligand caused the LMCT band to drop in intensity and shift to a longer wavelength (Figure 4.13). The addition of a phenyl ring in [VO(PHPHCA)(PHEN)](PF<sub>6</sub>) leads to an increase in the intensity of the  $\pi \rightarrow \pi^*$  band at 272 nm (Table 4.4, Figure 4.13).

As mentioned for the neutral complexes, DPQ and DPPZ complexes are known to exhibit additional bands near 350 nm due to  $n \rightarrow \pi^*$  transitions within the quinoxaline and phenazine moieties. The cationic complexes with a PHEN co-ligand also have a band at 354–358 nm (Figure 4.13), which may be due to a charge transfer from the imidazole moiety of the Schiff base ligand to the vanadium centre. This band is seemingly obscured by the  $n \rightarrow \pi^*$  transitions in the absorption spectra of the analogous cationic DPQ and DPPZ complexes.<sup>19,20</sup> For example, [VO(MECA)(DPPZ)](Cl) displays a band at 359 nm (Figure 4.12). The *O,N,N'* ligands also exhibit a band in the region 348–364 nm, which could be attributed to  $n \rightarrow \pi^*$  transitions between the lone pair of electrons of the N-atom in the imine group and the conjugated  $\pi$  system of the phenyl rings.<sup>37</sup>

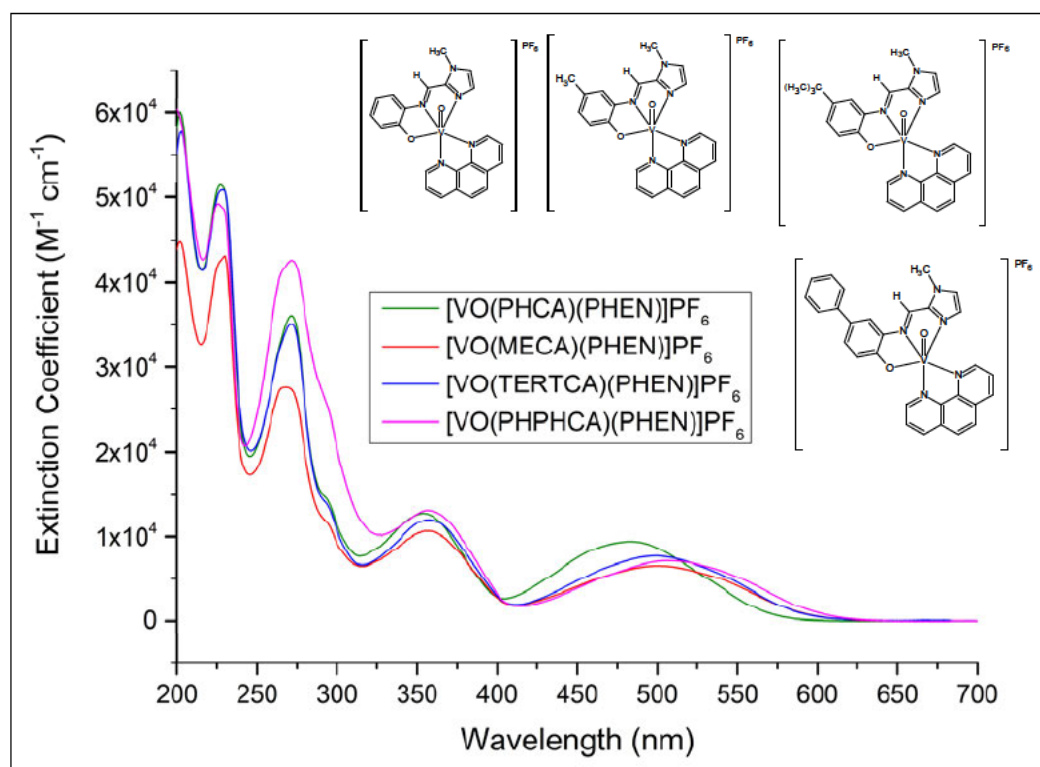


**Figure 4.13** Overlay of the UV/visible spectra of the cationic complexes with a PHEN co-ligand:  $[\text{VO}(\text{ONN})(\text{PHEN})](\text{PF}_6)$ , where ONN = PHCA, MECA, TERTCA and PHPHCA.

Comparison of the analogous cationic and neutral species shows that the absorption bands in the UV range are similar. The LMCT band, however, becomes a weaker chromophore (lower extinction coefficient) and shifts to a longer wavelength in the cationic species. For example, the LMCT band at 464 nm for the neutral complex  $[\text{VO}(\text{MEA})(\text{DPQ})]$  appears at 503 nm for the cationic complex  $[\text{VO}(\text{MECA})(\text{DPQ})](\text{PF}_6)$  (Figure 4.14). This could be due to increased metal-ligand  $\pi$ -interactions in the neutral  $[\text{VO}(\text{ONO})(\text{DPQ})]$  complexes.<sup>6</sup> The band at 340 nm in the absorption spectrum of  $[\text{VO}(\text{MECA})(\text{DPQ})](\text{PF}_6)$  may be a charge transfer band from the imidazole moiety of the ligand to the vanadium centre.<sup>20</sup>

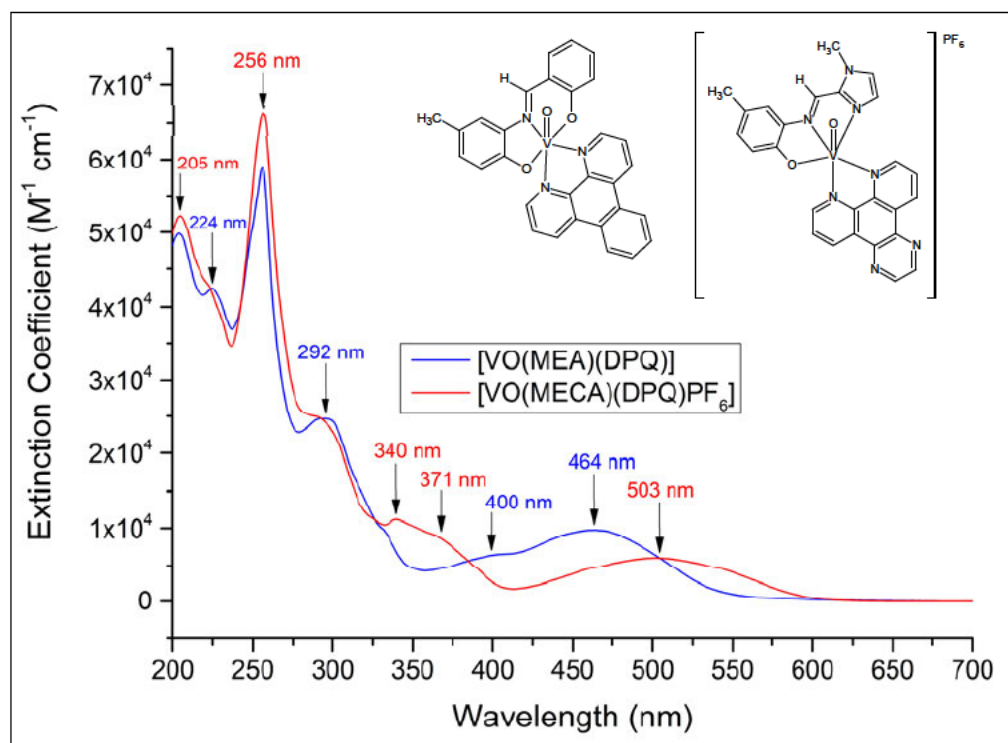


**Figure 4.14** Overlay of the UV/visible spectra of the neutral complex [VO(MEA)(DPQ)] and [VO(MECA)(DPQ)](PF<sub>6</sub>). This highlights the shift in the LMCT band as a consequence of coordinating a monoanionic versus dianionic ligand to the metal centre.

In an effort to better understand the nature of the electronic transitions in the ligands and metal complexes, DFT methods have been applied. These data are presented and discussed in Chapter 6.

#### 4.5 Electron Paramagnetic Resonance Spectroscopy of the Oxovanadium(IV) Complexes

Electron paramagnetic resonance (EPR) spectra of the oxovanadium compounds in this work were recorded to confirm the oxidation state and coordination geometry of the vanadium(IV) metal centre. The oxovanadium(IV) complexes have a  $d^1$  electron configuration and are therefore paramagnetic.

EPR spectroscopy utilises a magnetic field and radio-frequency radiation to analyse paramagnetic species. In EPR, the frequency is fixed (usually 9 GHz – X band) and the applied magnetic field strength is varied to probe electron spin properties of substances with unpaired electron spins rather than nuclear spin, as in NMR. When a magnetic field is applied in EPR, the ground electronic state splits into a set of more closely spaced energy levels than the excited electronic states. The resultant smaller transition energies lead to high sensitivity in EPR. The focus is then on the interactions between the external magnetic field and the unpaired electron. These interactions depend on the chemical environment of the electron.<sup>2,42</sup> Essentially, EPR spectroscopy probes the transitions that occur between electron spin states that have been separated by an applied magnetic field.<sup>3</sup>

An electron has an orbital magnetic moment originating from it spinning around the nucleus and it has a spin magnetic moment from spinning around its own axis. The magnetic moment of the spinning electron interacts with the applied magnetic field. For a spin of  $\frac{1}{2}$  for a single unpaired electron, there are two possible energy states.<sup>2,42</sup> The energy difference between the two energy states increases as the intensity of the magnetic field increases. When the energy difference matches the wavelength of the microwave radiation, absorption of photons occurs and an EPR signal is generated.<sup>42</sup> To improve the signal to noise ratio, a modulation technique is used whereby the spectra are shown in the first-derivative form. The maximum of the simple absorption peak would then be the point at which the central trace crosses the baseline in the first-derivative spectra.<sup>2,42</sup>

The energy difference between the states is dependent on the strength of the applied magnetic field and the *g*-value for the particular species.<sup>3</sup> *g*-Values for the unpaired electron are determined from the EPR spectra and are dependent on the chemical environment of the paramagnetic atom.<sup>2</sup> The *g*-value (also called *g*-factor) also has the advantage of being independent of the microwave frequency. The *g*-factor, therefore, is a better unit than magnetic field to use for identification of a compound through unique “fingerprints”.<sup>43</sup> A *g*-value reflects the nature of the orbital in which the unpaired electron resides and accounts for the coupling between the orbital and spin angular momenta of the electrons.<sup>2,42</sup> Not only does the *g*-value take into account the total magnetic dipole moment of a paramagnetic species, but it also takes into account the local environment of the spin system, such as ligand fields, which can change the effective magnetic field experienced by the unpaired electron.<sup>42</sup>

For *d*-series elements, such as vanadium, the ligands considerably influence the behaviour of the unpaired electrons, and so the orbital contribution may be reduced or even quenched. For a free electron in a vacuum  $g = 2.0023$ .<sup>2</sup> Measured *g*-values for a chemical species deviate from that of a free electron due to the spin-orbit coupling between the ground and excited states. The extent of mixing is dependent on the relative orientation of the spin and magnetic field axes.<sup>2,43</sup>

For every paramagnetic molecule, there exists a unique axis system called the principal axis system. *g*-Factors are measured along the principal axis system which are labelled as  $g_x$ ,  $g_y$  and  $g_z$ . If the molecules are in a fixed position, such as in a frozen solution or solid-state, each molecule will have its own random orientation with its own *g*-value. The observed spectrum would then be an average of all molecules. The magnitude of mixing of the spin-orbit coupling between the ground and excited states would then be direction-dependant and is said to be anisotropic. The *g*-value then depends on the relative orientation of the magnetic field and principal axis of the system.<sup>2,43</sup>

Samples may be isotropic, axial or rhombic. In isotropic symmetry, all of the principal *g*-factors are the same ( $g_x = g_y = g_z$ ). If there are three unique axes, the symmetry is classified as rhombic and three different *g*-factors would be recorded ( $g_x \neq g_y \neq g_z$ ). If the *x*- and *y*-directions are equivalent but different from the *z*-axis, the symmetry is axial ( $g_x = g_y \neq g_z$ ). In this case, there would be two principal *g*-values for the two electronically distinct axes in the molecular frame of reference ( $g_z$  and  $g_{x,y}$ ).<sup>2,43</sup>

In the case of axial symmetry, the magnetic field may be parallel to the *z*-axis or parallel to either the *x*- or *y*-axes. If the field and spin angular momentum (generalised to molecular) axes are parallel, then the signal on the EPR spectrum occurs at  $g_{\parallel}$ . The *g*-factor along the unique (*z*) axis is said to be parallel with the *z*-axis, so  $g_z$  is also labelled as  $g_{\parallel}$ .<sup>2,43</sup> When the field and symmetry molecular axes are perpendicular to each other the signal is labelled as  $g_{\perp}$ . The *x*- or *y*-direction would then be parallel to the field ( $g_{\perp} = g_{x,y}$ ). Most molecules will have their principal axes perpendicular to the applied field. Fewer molecules would have their principal axes parallel to the field (*z*-axis parallel to the field). Therefore  $g_{x,y}$  will typically have a more intense absorption peak than  $g_z$ .<sup>2,3,43</sup>

In the first-derivative spectrum of an axial system, for either powder or frozen solution samples, two principal  $g$ -values ( $g_{\parallel}$  and  $g_{\perp}$ ) can be obtained from the centre of each signal.<sup>2,3,43,44</sup>

Axial symmetry is usually observed for vanadyl ( $\text{VO}^{2+}$ ) complexes due to the strong  $\text{V}=\text{O}$  interaction, although three principal  $g$ -values are also possible.<sup>2,3</sup> For the parallel transitions in an axial system, the  $\text{V}=\text{O}$  bond is parallel to the applied magnetic field.<sup>2,3</sup> The  $d$ -orbital splitting diagram for the  $d^1$  system for  $\text{VO}^{2+}$  is shown in *Figure 4.15*.

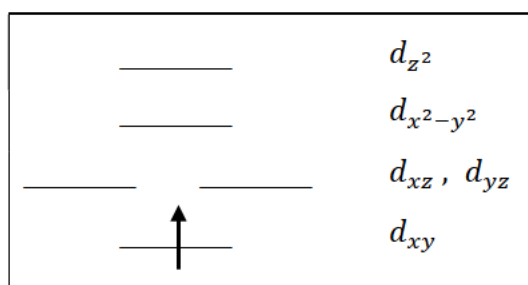


**Figure 4.15** A  $d$ -orbital splitting diagram for  $\text{VO}^{2+}$ .<sup>2,3</sup>

In the ground state, the unpaired electron of vanadium(IV) occupies the  $d_{xy}$  orbital and the excited states correspond to the occupation of the other orbitals.  $g_{\parallel}$  Depends on the energy of  $d_{x^2-y^2}$  because the  $d_{x^2-y^2}$  orbital has angular momentum about the  $z$ -axis (the parallel direction). This dependence is an inverse relationship. In the same way,  $g_{\perp}$  depends on the energy of  $d_{xz}$  and  $d_{yz}$  as  $d_{xz}$  and  $d_{yz}$  have angular momenta about the  $y$ - and  $x$ -axes equal to the angular momentum of  $d_{xy}$  about the  $y$ - and  $x$ -axes.<sup>2</sup> Both  $g_{\parallel}$  and  $g_{\perp}$  are expected to be smaller than the free-electron value of  $g = 2.0023$  and  $g_{\parallel}$  is expected to be smaller than  $g_{\perp}$  for an axially compressed  $d_{xy}^1$  vanadium configuration.<sup>2,45</sup>

As mentioned previously, there are two possible energy states for a spin of  $\frac{1}{2}$  for a single unpaired electron.<sup>2,42</sup> If the atom on which the unpaired spin is centred has a nucleus that also has a spin, then the electron states could be split by their interaction with the spin of the nucleus. This hyperfine coupling between the electron spin and the nuclear spin results in  $2I + 1$  lines ( $I =$  spin of the nucleus) in the hyperfine EPR spectrum. For vanadium, the most abundant isotope is  $^{51}\text{V}$ . Therefore, vanadium(IV) with the nuclear spin of  $I = 7/2$  for  $^{51}\text{V}$  will result in 8 different energy states.<sup>2,3,46,47</sup>

Further splitting of the states, such as by neighbouring ligands containing  $^{14}\text{N}$ , is not resolved in a 9 GHz spectrum due to the unpaired electron sitting in a  $\sigma$ -non-bonding orbital that points away from the ligands in the equatorial ( $xy$ ) plane. A hyperfine 8-line spectrum is, therefore, expected for a vanadium(IV) complex.<sup>3</sup> In a frozen solution the eight components of the parallel hyperfine spectra superimpose the eight components of the perpendicular signal for axial spectra. The two superimposed spectra will have different hyperfine splittings with the perpendicular peaks being more closely spaced than the parallel peaks.<sup>2,3,43,45</sup>

If the solution is not frozen the molecules can continuously tumble at rates greater than the frequency of the spectrometer. Anisotropy is then averaged to 0 during the time required to excite the system. Even though molecules have all possible orientations relative to the magnetic field, the molecules appear isotropic and so only one average  $g$ -value is obtained and is reported as  $g_{iso}$ .<sup>2,43,48,49</sup>

The EPR spectra of all compounds in this work were recorded in the solid-state and solution at room temperature. Dichloromethane was used to prepare samples of the neutral complexes and acetonitrile was used for the cationic complexes. The X-band EPR spectra were collected on a Bruker EMX Premium X spectrometer at 298 K at 9 GHz. Instrument settings: microwave bridge frequency, 9.9 GHz; modulation frequency, 100 kHz and centre field, 3500 G. Modulation amplitude was 3 G for the solution spectra of the neutral DPQ complexes and 5 G for the remaining spectra.

The  $g$ -values were calculated by converting the magnetic field using the formula:<sup>2,3</sup>

$$g = \frac{\Delta E}{\mu_B B}$$

$$g = \frac{h\nu}{\mu_B B}$$

Where  $\Delta E$  = the difference in J between two energy states

$h$  = planck's constant =  $6.626 \times 10^{-34}$  J s

$\nu$  = microwave frequency (in Hz)

$\mu_B$  = Bohr magnetron constant =  $9.274 \times 10^{-24}$  J T<sup>-1</sup>

$B$  = Magnetic field (in T)

The EPR spectra of the oxovanadium complexes in this work, in the solid-state, exhibited signals with  $S = \frac{1}{2}$  centred on an average of  $g = 1.98$  (Table 4.5).

**Table 4.5**  $g$ -Factors of the  $\text{VO}^{2+}$  complexes in the solid-state at 298 K.

[VO(ONO)(NN)] Complexes	$g$ -factor	[VO(ONN)(NN)](PF <sub>6</sub> /Cl) Complexes	$g$ -factor
[VO(PHA)(DPQ)]	1.980	[VO(PHCA)(PHEN)](PF <sub>6</sub> )	1.974
[VO(MEA)(DPQ)]	1.980	[VO(MECA)(PHEN)](PF <sub>6</sub> )	1.994
[VO(TERTA)(DPQ)]	1.987	[VO(TERTCA)(PHEN)](PF <sub>6</sub> )	1.986
[VO(CLA)(DPQ)]	1.982	[VO(PHPHCA)(PHEN)](PF <sub>6</sub> )	1.986
[VO(SOA)(DPQ)]	1.986	[VO(MECA)(DPQ)](PF <sub>6</sub> )	1.980
[VO(NAA)(DPQ)]	1.977	[VO(TERTCA)(DPQ)](PF <sub>6</sub> )	1.981
[VO(PHPHA)(DPQ)]	1.977	[VO(MECA)(DPPZ)](Cl)	1.977
[VO(MEA)(DPPZ)]	1.978		

The  $g$ -factors obtained for each compound in the solid-state (Table 4.5) are consistent with the literature  $g$ -factor values of 1.98, 1.99, and 2.00 for related  $[\text{V}^{\text{IV}}\text{O}(\text{ONO})(\text{NN})]$  compounds under similar experimental conditions.<sup>25,40,50,51</sup> Representative EPR spectra are shown in Figure 4.16 of solid samples of [VO(MEA)(DPQ)] (a) and [VO(MECA)(DPQ)](PF<sub>6</sub>) (b) at room temperature. The absence of hyperfine structures in the EPR spectra in the solid-state are thought to be a consequence of strong spin-spin interactions.<sup>40</sup>

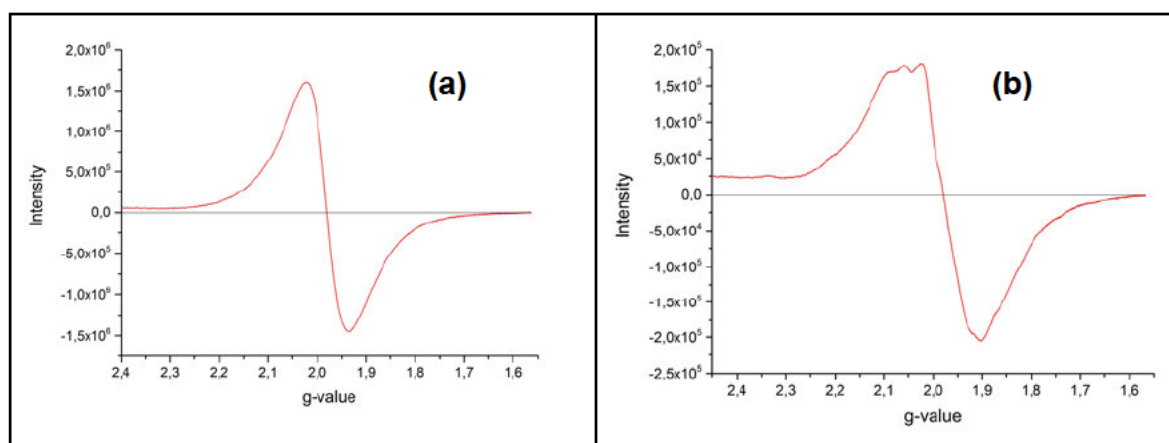


**Figure 4.16** X-band EPR spectra of [VO(MEA)(DPQ)] (a) and [VO(MECA)(DPQ)](PF<sub>6</sub>) (b) in the solid-state at 298 K.

All of the EPR spectra of the oxovanadium compounds in solution in this work exhibited hyperfine 8-line patterns, which indicate monomeric  $V^{IV}O$ -bound species with a  $d_{xy}^1$  ground-state electron configuration.<sup>40,47</sup> Representative isotropic EPR spectra are shown of  $[VO(MEA)(DPQ)]$  in dichloromethane in *Figure 4.17* (a) and of  $[VO(MECA)(DPQ)](PF_6)$  in acetonitrile in *Figure 4.17* (b) at room temperature. The individual splittings in the spectra are not equal, possibly due to small degrees of anisotropy, insufficient rapid tumbling of molecules in solution or coupling with the nuclear quadrupole moment. The splittings may be averaged out to an appropriate value.<sup>2,3</sup> The coupling constants ( $A_{iso}$ ) obtained in this work are  $89 \times 10^{-4} \text{ cm}^{-1}$  for the neutral complexes and  $88 \times 10^{-4} \text{ cm}^{-1}$  for the cationic complexes, which is consistent with the literature.<sup>49,50,52</sup>

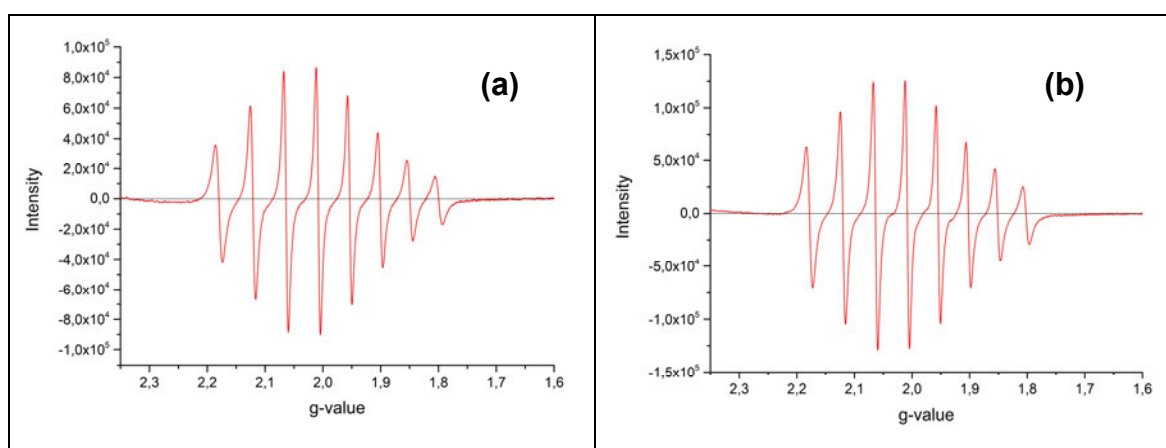


**Figure 4.17** EPR spectra of  $[VO(MEA)(DPQ)]$  in dichloromethane (a) and  $[VO(MECA)(DPQ)](PF_6)$  in acetonitrile (b) at 298 K.

For solutions measured at room temperature the average  $g$ -value is obtained and is reported as  $g_{iso}$ .<sup>2,48,49</sup> The experimental  $g_{iso}$ -values measured for the complexes in solution at room temperature are listed in *Table 4.6*. The  $g_{iso}$ -values are very similar for all complexes ( $g_{iso}$  (avg) = 1.99) and are consistent with  $g$ -values of 1.97, 1.98 and 1.99 for related  $[V^{IV}O(ONO)(NN)]$  compounds also measured in dichloromethane at room temperature.<sup>49,50,52,53</sup>

**Table 4.6**  $g_{iso}$ -Values of the  $VO^{2+}$  complexes in either dichloromethane or acetonitrile (as indicated) at room temperature.

<b>[VO(ONO)(NN)] Complexes in <math>CH_2Cl_2</math></b>	$g_{iso}$	<b>[VO(ONN)(NN)](<math>PF_6/Cl</math>) Complexes in <math>CH_3CN</math></b>	$g_{iso}$
[VO(PHA)(DPQ)]	1.990	[VO(PHCA)(PHEN)]( $PF_6$ )	1.990
[VO(MEA)(DPQ)]	1.990	[VO(MECA)(PHEN)]( $PF_6$ )	1.991
[VO(TERTA)(DPQ)]	1.990	[VO(TERTCA)(PHEN)]( $PF_6$ )	1.990
[VO(CLA)(DPQ)]	1.991	[VO(PHPHCA)(PHEN)]( $PF_6$ )	1.991
[VO(SOA)(DPQ)]	1.991	[VO(MECA)(DPQ)]( $PF_6$ )	1.990
[VO(NAA)(DPQ)]	1.990	[VO(TERTCA)(DPQ)]( $PF_6$ )	1.991
[VO(PHPHA)(DPQ)]	1.991	[VO(MECA)(DPPZ)]( $Cl$ )	1.992
[VO(MEA)(DPPZ)]	1.990		

The remaining EPR spectra for all compounds (solid-state and in solution-state) are available in *Appendix B*. The EPR spectra of the oxovanadium complexes in this work confirm the presence of the  $VO^{2+}$  core both in the solid-state and in solution. The stability of the oxovanadium(IV) complexes in solution is further discussed in *Chapter 7*.

## 4.6 Conclusions of Spectroscopic Characterisation

### 4.6.1 Spectroscopic Characterisation of the Bidentate and Tridentate Ligands

The known *N,N*-bidentate ligands were characterised by ESI-mass,  $^1H$  and  $^{13}C$  NMR spectroscopy. The tridentate *O,N,O'* and *O,N,N'* ligands were characterised by ESI-mass, NMR, IR, and UV/visible spectroscopic techniques as well as elemental analysis.

The key findings from the spectroscopic studies which indicate successful condensation reactions to form the Schiff base imine ligands include:

- Detection of prominent molecular ion peaks in the mass spectra corresponding with the monoisotopic mass of each ligand (refer to *Section 3.3, 3.4 and 3.5 of Chapter Three and Appendix A*).
- The  $^1\text{H}$  and  $^{13}\text{C}$  NMR spectra were consistent with the proposed structures of the ligands, including the presence of the imine  $^1\text{H}$  singlet and  $^{13}\text{C}$  chemical shifts.
- The  $^1\text{H}$  NMR hydrogen bonding study of TERTCA strongly suggests that dimerisation of the *O,N,N'* ligands takes place in solution as in the solid-state.
- The imine stretching frequency was present in the IR spectra in the range of 1608 – 1614  $\text{cm}^{-1}$  for the *O,N,O'*-tridentate ligands and 1614 – 1634  $\text{cm}^{-1}$  for the *O,N,N'* tridentate ligands.
- The UV/visible spectra of the *O,N,O'* and *O,N,N'* ligands exhibited at least four absorption bands with the band at *ca.* 269 nm characteristic of  $\pi \rightarrow \pi^*$  benzenoid and imine transitions. The band at around 352 nm in the *O,N,O'* ligands and around 353 nm in the *O,N,N'* ligands is attributed to  $n \rightarrow \pi^*$  transitions between the lone pair of electrons of the imine-N and the  $\pi$ -system of the phenyl rings.

#### 4.6.2 Spectroscopic Characterisation of the Oxovanadium(IV) Complexes

The coordination of the tridentate and bidentate co-ligands to the oxovanadium(IV) metal centre was confirmed by ESI-MS, IR, UV/visible and EPR spectroscopic characterisation as well as elemental analysis. The key findings of the spectroscopic studies are:

- Detection of prominent molecular ion peaks in the mass spectra corresponding with the monoisotopic mass of each complex (Full data available in *Section 3.6 and Section 3.7 of Chapter Three and Appendix A*).
- The imine stretching frequency in the IR spectra in the free tridentate ligands shifted to a lower frequency by at least 8  $\text{cm}^{-1}$  in the metal complexes, which suggest coordination of the imine nitrogen atom to the vanadium centre.

- The presence of the V=O, V–O and V–N stretching vibrations at 945 – 968  $\text{cm}^{-1}$ , 532 – 557  $\text{cm}^{-1}$  and 423 – 438  $\text{cm}^{-1}$ , respectively in the metal complex IR spectra indicate ligand chelation to the  $\text{VO}^{2+}$  core. In the case of some cationic chelates, P–F stretches associated with the hexafluorophosphate anions also appear.
- The appearance of the LMCT band in the UV/visible absorption spectra at 442 – 464 nm for the neutral complexes and at 484 – 507 nm for the cationic complexes, which are attributed to charge transfer from the phenolate oxygen to the vanadium centre.
- The extended conjugation of the DPPZ ligand in comparison to DPQ and PHEN is evident in the bathochromic shift of the  $\pi \rightarrow \pi^*$  band, in the UV/visible spectra for the DPPZ complexes  $[\text{VO}(\text{MEA})(\text{DPPZ})]$  and  $[\text{VO}(\text{MECA})(\text{DPPZ})](\text{Cl})$  in comparison to the DPQ and PHEN complexes.
- The EPR spectra of the oxovanadium compounds in the solid-state exhibited  $S = \frac{1}{2}$  signals indicative of the paramagnetic  $\text{V}^{\text{IV}}\text{O}^{2+}$  species with a  $d^1$  system.
- The EPR spectra of the oxovanadium compounds in solution exhibited hyperfine 8-line spectra indicative of monomeric  $\text{V}^{\text{IV}}\text{O}$ -bound species with a  $d_{xy}^1$  ground-state electron configuration coupled with the vanadium nuclear spin of  $7/2$ .

The above data all indicate successful syntheses and also highlight the rich photophysical properties of vanadium(IV) and the associated Schiff base ligands. Elemental analysis (refer to *Chapter Three*) confirmed the identity and purity of the complexes, which is critical prior to biological testing.

## 4.7 References

1. Pavia, D.L., Lampman, G.M. and Kriz, G.S., *Introduction to Spectroscopy*, 3<sup>rd</sup> Ed., Harcourt College Publishers, Orlando, **2001**, p. 13 – 15, 102-104, 106 – 110, 113, 114, 144, 353, 355, 356, 358, 359, 362.
2. Parish, R.V., *NMR, NQR, EPR, and Mössbauer Spectroscopy in Inorganic Chemistry*, Ellis Horwood Limited, **1990**, 12, 168 - 171, 173, 175 - 180, 185, 186.
3. Smith II, T.S.S., LoBrutto, R. and Pecoraro, V.L., *Coord. Chem. Rev.*, **2002**, 228, 1.
4. Delgadillo, A., Romo, P., Leiva, A.M. and Loeb, B., *Hel. Chim. Acta*, **2003**, 86, 2110.
5. Arancibia, A., Concepción, J., Daire, N., Leiva, G., Leiva, A.M., Loeb, B., Del Río, R., Díaz, R., Francois, A. and Saldivia, M., *J. Coord. Chem.*, **2011**, 54, 323.
6. Biradar, N.S., Mahale, V.B. and Kulkarni, V.H., *Inorg. Chim. Acta*, **1973**, 7, 267.
7. Aslam, M., Anis, I., Afza, N., Hussain, M.T., Mehmood, R., Hussain, A., Yousuf, S., Iqbal, L., Iqbal, S. and Khan, I., *J. Chil. Chem. Soc.*, **2013**, 58, 1867.
8. Öztürk, B.Ö, Bucak, E. and Karabulut, S., *J. Mol. Catal. A: Chem.*, **2013**, 376, 53.
9. Alyea, E.C. and Malek, A., *Can. J. Chem.*, **1975**, 53, 939.
10. Barba, V., Cuahutle, D., Santillan, R. and Farfán, N., *Can. J. Chem.*, **2001**, 79, 1229.
11. Rodríguez, M., Ochoa, M.E., Santillan, R., Farfán, N and Barba, V., *J. Organometal. Chem.*, **2005**, 690, 2975.
12. Mayer, P., Potgieter, K.C. and Gerber, T.I.A., *Polyhedron*, **2010**, 29, 1423.
13. Böhme, U. and Fels, S., *Acta Cryst.*, **2008**, E64, o14.
14. Barry, K.-L., Grimmer, C.D., Munro, O.Q. and Akerman, M.P., *RSC Adv.*, **2020**, 10, 7867.
15. Demir, S., Yazicilar, T.K. and Taş, M., *Inorg. Chim. Acta*, **2014**, 409, 399.
16. García-Deibe, A.M., Portela-García, C., Fondo, M., Mota, A.J. and Sanmartín-Matalobos, J., *Chem. Commun.*, **2012**, 48, 9915.
17. *Bruker Topspin 3.2 (pl7)*, from Bruker BioSpin, Sun Microsystems Inc., 2010.
18. Bednar, V., Elliott, K.W., Byrd, E. and Woodford, J.N., *Chem. Phys. Lett.*, **2012**, 547, 24.
19. Prasad, P., Sasmal, P.K., Majumdar, R., Dighe, R. and Chakravarty, A.R., *Inorg. Chim. Acta*, **2010**, 363, 2743.

20. Prasad, P., Sasmal, P.K., Khan, I., Kondaiah, P. and Chakravarty, A.R., *Inorg. Chim. Acta*, **2011**, 372, 79.
21. Jing, B., Dong, J., Wei, Q., Xu, T. and Li, L., *Transit. Met. Chem.*, **2014**, 39, 605.
22. Triantafillou, G.D., Tolis, E.I., Terzis, A., Deligiannakis, Y., Raptopoulou, C.P., Sigalas, M.P. and Kabanos, T.A., *Inorg. Chem.*, **2004**, 43, 79.
23. Doadrio, A.L., Sotelo, J. and Fernández-Ruano, A., *Quim. Nova*, **2002**, 25, 525.
24. Lozano, R., Martínez, J., Román, J., Martínez, A., and Doadrio, A. and Peña, J. L., *Polyhedron*, **1986**, 5, 1341.
25. Gryboś, R., Szklarzewicz, J., Jurowska, A. and Hodorowicz, M., *J. Mol. Struct.*, **2018**, 1171, 880.
26. Cao, Y.-Z., Zhao, H.-Y, Bai, F.-Y., Xing, Y.-H., Wei, D.-M., Niu, S.-Y. and Shi, Z., *Inorg. Chim. Acta*, **2011**, 368, 223.
27. Zhao, H.-Y., Xing, Y.-H., Cao, Y.-Z., Li, Z.-P., Wei, D.-M., Zeng, X.-Q. and Ge, M.-F., *J. Mol. Struct.*, **2009**, 938, 54.
28. Wang, Y., Lin, X.-M., Bai, F.-Y. and Sun, L.-X., *J. Mol. Struct.*, **2017**, 1149, 379.
29. Grant, G.J., Galas, D.F., Jones, M.W., Loveday, K.D., Pennington, W.T., Schimek, G.L., Eagle, C.T. and VanDerveer, D.G., *Inorg. Chem.*, **1998**, 37, 5299.
30. Uršič, M., Lipeč, T., Meden, A. and Turel, I., *Molecules*, **2017**, 22, 326.
31. Nakamoto, K. *Applications in inorganic chemistry. In Infrared and Raman Spectra of Inorganic and Coordination Compounds*; John Wiley & Sons, Inc., Hoboken, New Jersey, **2008**, p. 222, 223.
32. Chatterjee, M., Ghosh, S., Wu, B.-M., and Mak., T.C.W, *Polyhedron*, **1998**, 17, 1369.
33. Szklarzewicz, J., Jurowska, A., Hodorowicz, M., Gryboś, R. And Matoga, D., *J. Mol. Struct.*, **2019**, 1180, 839.
34. Pranczk, J., Jacewicz, D., Wyrzykowski, D., Wojtczak, A., Tesmar, A. and Chmurzyński, L., *Eur. J. Inorg. Chem.*, **2015**, 3343.
35. <https://orgchemboulder.com/Spectroscopy/irtutor/aromaticsir.shtml>, 21 April 2020.
36. Xu, T., Li, L.-Z., Zhou, S.-F., Guo, G.-Q. and Niu, M.-J., *J. Chem. Crystallogr.*, **2005**, 35, 263.
37. Sarwar, A., Shamsuddin, M.B. amd Lingtang, H., *Mod. Chem. Appl.*, **2018**, 6, 262.

38. Prasad, P., Khan, I., Kondaiah, P. and Chakravarty, A.R., *Chem. Eur. J.*, **2013**, *19*, 17445.
39. Tasiopoulus, A.J., Tolis, E.J., Tsangaris, J.M., Evangelou, A., Woollins, J.D., Slawin, A.M.Z., Costa Pessoa, J., Correia, I. and Kabanos, T.A., *J. Biol. Inorg. Chem.*, **2002**, *7*, 363.
40. Ni, L., Zhao, H., Tao, L., Li, X., Zhou, Z., Sun, Y., Chen, C., Wei, D., Liu, Y., and Diao, G., *Dalton Trans.*, **2018**, *47*, 10035.
41. Costa Pessoa, J., Cavaco, I., Correia, I., Duarte, M.T., Gillard, R.D., Henriques, R.T., Higes, F.J., Madeira, C. and Tomaz, I., *Inorg. Chim. Acta*, **1999**, *293*, 1.
42. [https://chem.libretexts.org/Bookshelves/Physical\\_and\\_Theoretical\\_Chemistry\\_Textbook\\_Maps/Supplemental\\_Modules\\_\(Physical\\_and\\_Theoretical\\_Chemistry\)/Spectroscopy/Magnetic\\_Resonance\\_Spectroscopies/Electron\\_Paramagnetic\\_Resonance/EPR%3A\\_Theory](https://chem.libretexts.org/Bookshelves/Physical_and_Theoretical_Chemistry_Textbook_Maps/Supplemental_Modules_(Physical_and_Theoretical_Chemistry)/Spectroscopy/Magnetic_Resonance_Spectroscopies/Electron_Paramagnetic_Resonance/EPR%3A_Theory), 14 October 2020.
43. Duin, E., Electron Paramagnetic Resonance Theory, [http://webhome.auburn.edu/~duinedu/epr/1\\_theory.pdf](http://webhome.auburn.edu/~duinedu/epr/1_theory.pdf), 14 October 2020.
44. McPhail, D.B., Linehan, D.J. and Goodman, B.A., *New Phytol.*, **1982**, *91*, 615.
45. Yuan, C., Lu, L., Wu, Y., Liu, Z., Guo, M and Xing, S., *J. Inorg. Biochem.*, **2010**, *104*, 978.
46. Holder, A.A., Taylor, P., Magnusen, A.R., Moffett, E.T., Meyer, K., Hong, Y., Ramsdale, S.E., Gordon, M., Stubbs, J., Seymour, L.A., Acharya, D., Weber, R.T., Smith, P.F., Dismukes, G.C., Ji, P., Menocal, L., Bai, F., Williams, J.L., Cropek, D.M., and Jarrett, W.L., *Dalton Trans.*, **2013**, *42*, 11881.
47. Saha, U., Si. T.K., Nandi, P.K. and Mukherjea, K.K., *Inorg. Chem. Commun.*, **2013**, *38*, 43.
48. Lu, L., Yue, J., Yuan, C., Zhu, M., Han, H., Liu, Z. and Guo, M., *J. Inorg. Biochem.*, **2011**, *105*, 1323.
49. Shit., M., Maity, S., Bera, S., Weyhermüller, T. And Ghosh, P., *New J. Chem.*, **2016**, *40*, 10305.
50. Aboafia, S.A., Elsayed, S.A., El-Sayed, A.K.A. and El-Hendawy, A.M., *J. Mol. Struct.*, **2018**, *1158*, 39.
51. Szklarzewicz, J., Jurowska, A., Hodorowicz, M., Gryboś, R, Kruczala, K., Gluch-Lutwin, M. and Kazek, G., *J. Coord. Chem.*, **2020**, *73*, 986.

52. Biswas, N., Bera, S., Sepay, N., Mukhopadhyay, T.K., Acharya, K., Ghosh, S., Acharyya, S., Biswas, A.K., Drew, M.G.B. and Ghosh, T., *New. J. Chem.*, **2019**, *43*, 16714.
53. Shit., M., Bera, S., Maity, S., Maji, S., Weyhermüller, T. and Ghosh, P., *Eur. J. Inorg. Chem.*, **2016**, 330.

## Chapter Five: X-ray Diffraction

### 5.1. General Experimental Procedure

In this work, selected *O,N,O'* and *O,N,N'* ligands and [VO(ONO)(DPQ)], [VO(MEA)(DPPZ)] and [VO(ONN)(PHEN)](PF<sub>6</sub>) complexes were studied by single-crystal X-ray diffraction. X-ray data were recorded on a Bruker Apex Duo diffractometer. The diffractometer was equipped with an Oxford Instruments Cryojet operating at 100(2) K and an Incoatec microsource operating at 30 W power. The data were collected with Mo K $\alpha$  ( $\lambda = 0.71073$  Å) radiation using omega and phi scans with exposures taken at 30 W X-ray power and 0.50° frame widths using APEX2.<sup>1</sup>

The data were reduced with the programme SAINT<sup>1</sup> using outlier rejection, scan speed scaling as well as standard Lorentz and polarisation correction factors. A SADABS semi-empirical multi-scan absorption correction was applied to the data. Direct methods, SHELX-2016<sup>2</sup> and WinGX<sup>3</sup>, were used to solve all structures. All non-hydrogen atoms were located in the difference density map and refined anisotropically. All hydrogen atoms were treated with the standard riding model in SHELX-2016, with C-H<sub>aromatic</sub> distances of 0.93 Å and U<sub>iso</sub> = 1.2 Ueq and C-H<sub>methyl</sub> distances of 0.98 Å and U<sub>iso</sub> = 1.5 Ueq. The O-H atoms were located in the density map and allowed to refine isotropically. All diagrams were rendered using Mercury CSD 2020.2.0.<sup>4</sup> V, O, N, C, Cl, S and H atoms are represented as green, red, purple, grey, dark green, yellow and beige atoms, respectively. The final structures were validated using an IUCr checkCIF<sup>5</sup>. Full crystal data, and crystal refinement tables are available in *Appendix C*.

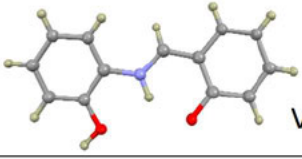
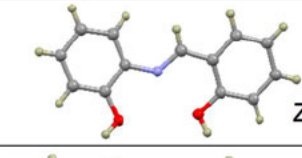
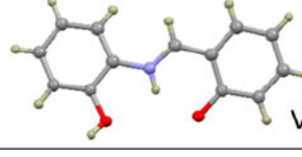
### 5.2. *O,N,O'*-Tridentate Ligands

#### 5.2.1 Introduction to *O,N,O'*-Tridentate Ligands

The crystal structures of *O,N,O'* salicylidene tridentate ligands are well known. A search of the Cambridge Structural Database (CSD),<sup>5</sup> using ConQuest 2020.2.0,<sup>6</sup> revealed published crystal structures for the PHA, MEA, TERTA and CLA ligands.<sup>7-22</sup>

Various tautomeric forms have been noted for (*E*)-[(2-hydroxyphenyl)iminomethyl]phenol (PHA) (*Table 5.1*) including the hydrochloride,<sup>7</sup> keto<sup>8-11</sup> and enol<sup>12-14</sup> tautomers. Resonance and intramolecular proton transfer allows for conversion between the keto and enol configurations.<sup>15</sup>

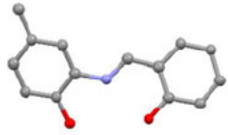
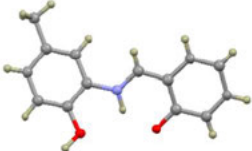
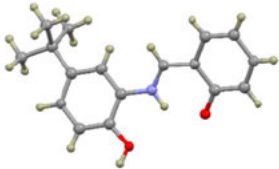
**Table 5.1** Reported tautomers in the reported structures of PHA.<sup>8-17</sup>

Structure	Type of Tautomer	CSD Ref. Code	Lit. Reference
 VAYJAG03	Ketone	VAYJAG	8
		VAYJAG01	9
		VAYJAG02	10
		VAYJAG03	11
 ZEXPEX02	Enol	ZEXPEX	12
		ZEXPEX01	13
		ZEXPEX02	14
 VAYJAG05	Zwitter Ion	VAYJAG04	15
		VAYJAG05	16
		VAYJAG06	17

Intramolecular proton transfer can also lead to zwitterionic molecules with the protonated imine nitrogen carrying a positive charge and the phenolate oxygen carrying a negative charge.<sup>15-17</sup> The X-ray crystal structures of the keto and zwitterion forms of MEA, the keto/enol tautomers of CLA and the ketone tautomer of TERTA have also been reported (*Table 5.2*).<sup>18-22</sup>

Reported C–O bond lengths for PHA, MEA, CLA and TERTA are summarised in *Table 5.3* for the respective keto, enol and zwitterion tautomers of these *O,N,O'* ligands.

**Table 5.2** Reported X-ray crystal structures of MEA, CLA and TERTA.

Structure	Type of Tautomer	CSD Ref. Code	Lit. Reference
 WOLYAX	Ketone MEA	WOLYAX	18
		WOLYAX01	19
	Zwitterion MEA	WOLYAX02	20
	Keto/Enol Tautomers CLA	XEWKEP	21
	Ketone TERTA	XISJIT	22

**Table 5.3** Reported C–O bond lengths (Å) of PHA, MEA, CLA and TERTA.<sup>8-22</sup>

Ketone (C=O)		Enol (C–OH)		Zwitterion (C–O <sup>-</sup> )	
PHA <sup>8</sup>	1.299(1) (A)*	PHA <sup>12</sup>	1.399(8)	PHA <sup>15</sup>	1.303(4) (A)
	1.301(2) (B)		1.411(6)		1.316(4) (B)
PHA <sup>9</sup>	1.294(2) (A)	PHA <sup>13</sup>	1.307(3)	PHA <sup>16</sup>	1.298(2) (A)
	1.297(2) (B)		1.370(2)		1.301(2) (B)
PHA <sup>10</sup>	1.278(2) (A)	PHA <sup>14</sup>	1.294(2) (A1)	PHA <sup>17</sup>	1.298(2) (A)
	1.286(2) (B)		1.356(3) (A2)		1.300(2) (B)
PHA <sup>11</sup>	1.299(3) (A)		1.298(2) (B1)	MEA <sup>20</sup>	1.291(2)
	1.301(3) (B)		1.346 (B2)		
MEA <sup>18</sup>	1.291(1)				
TERTA <sup>22</sup>	1.296(1)				
CLA <sup>21</sup>	1.299(2)				

\* Where there are multiple molecules in the asymmetric unit, the bond lengths of each are reported and designated (A) and (B).

## 5.2.2 Experimental Procedures for the *O,N,O'*-Tridentate Ligands

In this study, the structures of the free ligands MEA, TERTA, CLA, SOA and NAA were determined by single-crystal X-ray diffraction. Red crystals of MEA, orange crystals of TERTA and amber crystals of SOA were obtained upon slow evaporation of methanol following recrystallisation of the respective ligand in methanol. Amber crystals of CLA and red crystals of NAA were obtained upon slow evaporation of an ethanolic solution of the respective ligands. Data were recorded as per the general method in *Section 5.1*.

## 5.2.3 Results and Discussion of the Solid-State Structures of the *O,N,O'*-Tridentate Ligands

The free ligands MEA, TERTA, CLA, SOA and NAA were found exclusively as the ketone tautomers in this work. A search of the Cambridge Structural Database (CSD)<sup>5</sup> indicated that no free ligand crystal structures of SOA and NAA have been reported. The X-ray structures of SOA and NAA are discussed herein. The thermal displacement plots of SOA and NAA are shown in *Figure 5.1*. The full crystal data and structure refinement details of SOA and NAA are reported in *Appendix C*.

SOA crystallised in the monoclinic  $P2_1/n$  space group, with one independent molecule in the asymmetric unit ( $Z = 4$ ). NAA crystallised in the orthorhombic space group  $Pca2_1$ , with two hydrogen-bonded molecules in the asymmetric unit ( $Z = 8$ ). The main difference between the two molecules of the asymmetric unit of NAA is the relative orientation of the hydroxyl group. The hydroxyl group is rotated below the mean plane of the naphthalene moiety in one molecule and is rotated above in the other molecule.

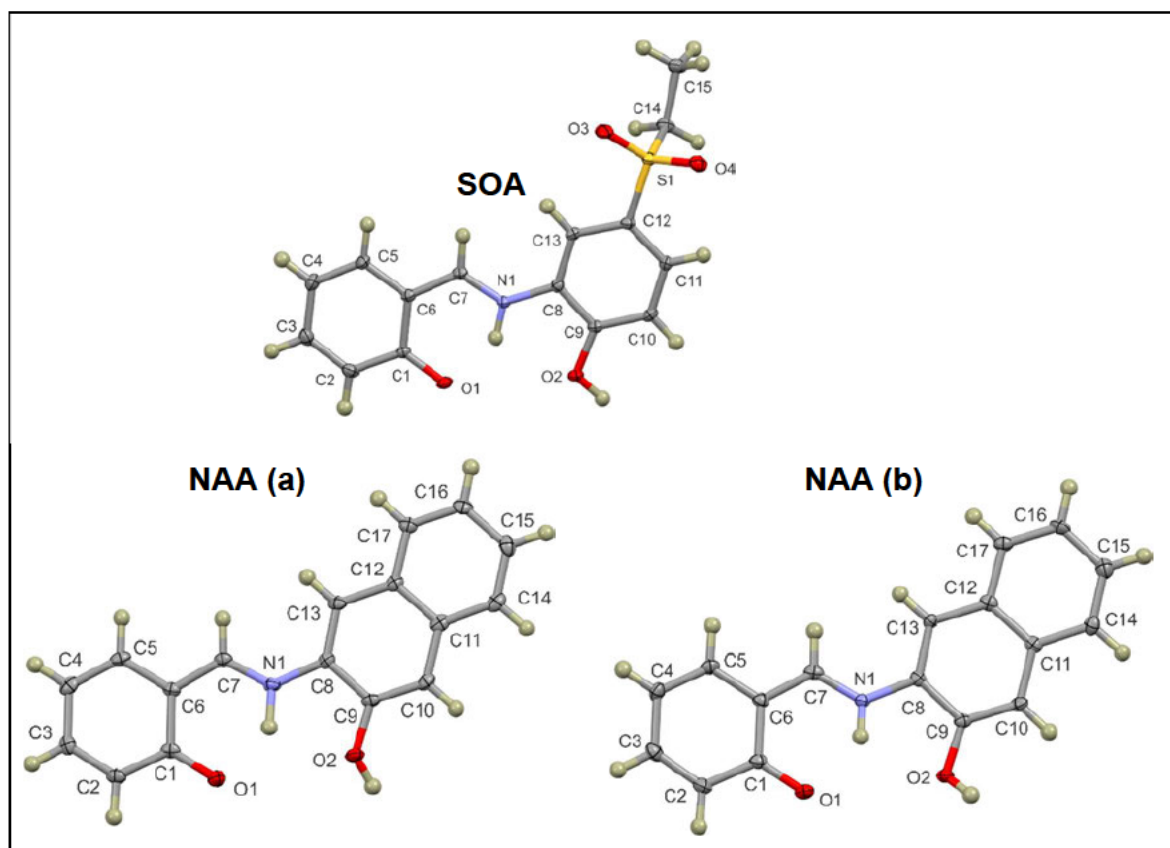


**Figure 5.1** Thermal displacement plots (50% probability) showing the structure and atom numbering schemes of NAA and SOA. Hydrogen atoms are shown as spheres of arbitrary radius.

The SOA and NAA molecules are approximately planar. The planarity of the molecules is illustrated by the angle between the two rings (O1, C1–C7) and (N1, O2, S1, C8–C13), which is 4.1°, 2.6° and 3.2° in SOA, NAA molecule (a) and NAA molecule (b), respectively. The torsion angles of C5–C6–C7–N1, C6–C7–N1–C8, C7–N1–C8–C13 and C7–N1–C8–C9 (Table 5.4) also indicate the planarity of the SOA and NAA molecules. In general, the structure of SOA deviates from planarity to a greater extent than NAA (refer to Table 5.4). This difference may be related to the bulky sulfonyl group which necessitates this to relieve steric strain.

**Table 5.4** Selected torsion angles for SOA and NAA.

	SOA	NAA (a)	NAA (b)
C5–C6–C7–N1	–177.8(1)	178.5(3)	179.4(3)
C6–C7–N1–C8	177.6(1)	179.0(3)	–178.6(3)
C7–N1–C8–C13	3.3(2)	0.3(5)	–2.2(5)
C7–N1–C8–C9	177.2(1)	–178.3(3)	177.6(3)

Molecular simulations have shown that for MEA, CLA, benzylideneaniline and related molecules, the most stable conformation is non-planar.<sup>18,21,23</sup> The X-ray structure of MEA has also been reported and shows a non-planar structure.<sup>18</sup> The non-planar conformation is likely due to non-bonded repulsion of the *ortho* hydrogen on the amino ring (H–C13) and the imine H-atom (H–C7). Conversely, the X-ray structure of CLA has been reported as nearly planar; the torsion angles thereof closely match those of SOA and NAA reported here.<sup>21</sup> A planar configuration allows for effective overlap of  $\pi$ -orbitals leading to delocalisation of electrons over a molecule.<sup>18</sup> Deviations from planarity are therefore typically related to steric factors as opposed to electronic effects. Selected bond lengths for SOA and NAA are summarised in *Table 5.5*.

**Table 5.5** Selected bond lengths (Å) for SOA and NAA.

Ligand	SOA	NAA(a)	NAA(b)
O1–C1	1.296(2)	1.282(4)	1.288(4)
C1–C2	1.419(2)	1.418(4)	1.425(5)
C2–C3	1.374(2)	1.378(4)	1.365(4)
C3–C4	1.408(2)	1.415(5)	1.413(5)
C4–C5	1.371(2)	1.367(5)	1.372(5)
C5–C6	1.415(2)	1.425(4)	1.418(4)
C1–C6	1.440(2)	1.449(4)	1.442(4)
C6–C7	1.418(2)	1.413(4)	1.414(4)
C7–N1	1.309(2)	1.310(4)	1.310(4)
N1–C8	1.406(2)	1.414(4)	1.413(4)
C <sub>ar</sub> –C <sub>ar</sub> (phenol) <sup>a</sup>	1.394(2)	1.408(4)	1.407(4)
C <sub>ar</sub> –C <sub>ar</sub> (ring 3) <sup>a</sup>	N/A	1.404(5)	1.406(4)
C9–O2	1.339(2)	1.357(4)	1.347(4)

<sup>a</sup> Mean C–C bond lengths of the phenyl rings.

The C1–O1 bond lengths of 1.296(2), 1.282(4) and 1.288(4) Å for SOA, NAA(a) and NAA(b), respectively are shorter than typical C–O bond lengths for enols of 1.362 Å, but greater than the mean C=O double bonds in benzoquinones of 1.222 Å.<sup>18,21,24,25</sup> In comparison, the C9–O2 bond length of the phenol ring of 1.339(2) Å, 1.357(4) and 1.347(4) Å for SOA, NAA(a) and NAA(b), respectively, are longer than the C1–O1 bond lengths. These suggest that the molecules are in the keto form, but there is some extent of electron delocalisation leading to a reduced bond order of C1–O1.<sup>18,21,24,25</sup> Previously reported structures of MEA, CLA and TERTA were similarly reported as keto tautomers with comparable C1–O1 bond lengths as SOA and NAA (*Table 5.3*).<sup>18,21,22</sup>

Protonation of the imine N atom in the keto form has reduced the bond order of the imine group. In SOA, the C6–C7 bond length measures 1.418(2) Å, which is shorter than the average  $C_{aromatic}-Csp^2$  value of 1.485 Å. The N1–C8 and C7–N1 bond lengths measure 1.406(2) Å and 1.309(2) Å, respectively. These are longer than the average  $C_{aromatic}-Nsp^2$  and  $Csp^2=N$  bond lengths, which are reported as 1.353 and 1.279 Å, respectively.<sup>24,25</sup> This indicates delocalisation along the imine moiety (C6–C7–N1–C8).<sup>25</sup> The above bond parameters closely match those reported for MEA, CLA and TERTA.<sup>18,21,22</sup>

Selected bond angles for SOA and NAA are summarised in *Table 5.6*. It is noted that the bond angles subtended by the atom C8 deviate from ideality for a  $sp^2$  hybridised carbon. This is seemingly a consequence of non-bonded repulsion between the hydrogen atoms on C7 of the imine and on C13 of the phenol ring.

**Table 5.6** Selected bond angles (°) for SOA and NAA.

Ligand	SOA	NAA(a)	NAA(b)
C6–C7–N1	121.1(1)	122.5(3)	121.5(3)
C7–N1–C8	128.5(1)	128.5(3)	127.6(3)
C2–C1–C6	116.9(1)	116.6(3)	117.1(3)
C5–C6–C7	118.8(1)	119.0(3)	119.0(3)
C7–C6–C1	120.7(1)	120.8(3)	121.1(3)
C4–C5–C6	120.6(1)	120.9(3)	121.2(3)
C6–C1–O1	120.5(1)	120.6(3)	120.5(3)
C2–C1–O1	122.6(1)	122.9(3)	122.4(3)
N1–C8–C9	114.7(1)	114.3(3)	114.4(3)
N1–C8–C13	124.2(1)	124.5(3)	124.4(3)
C8–C9–O2	116.1(1)	115.6(3)	115.7(3)
C10–C9–O2	124.3(1)	124.8(3)	125.0(3)

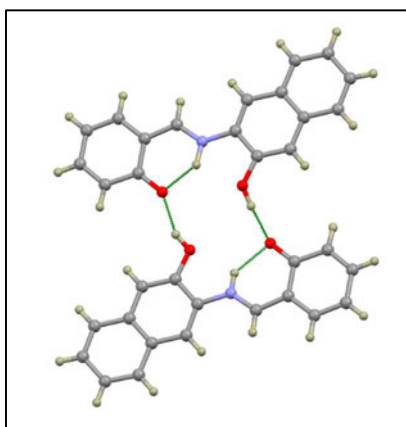
The structures of SOA and NAA show intramolecular hydrogen bonds between the imine N–H and ketone oxygen atom (N1–H101 $\cdots$ O1). Hydrogen bonds of this nature are common in this class of compounds.<sup>18,21,25</sup> The intramolecular hydrogen bonding parameters for SOA and NAA are listed in *Table 5.7*.

**Table 5.7** Intramolecular hydrogen bond lengths (Å) and bond angles (°) for SOA and NAA.

Ligand	D–H (Å)	H···A (Å)	D···A (Å)	D–H···A (°)
<b>SOA</b>				
N1–H101···O1	0.93(2)	1.72(2)	2.537(1)	145(2)
<b>NAA</b>				
N1A–H101A···O1A	1.02(6)	1.76(6)	2.578(4)	135(5)
N1B–H101B···Q1B	0.84(4)	1.87(5)	2.559(4)	138(4)

The N1···O1 intramolecular hydrogen bond distances for SOA and NAA are significantly shorter than the sum of the van der Waals radii of nitrogen and oxygen: 3.07 Å.<sup>18,26</sup> This interaction distance is, however, restricted by the geometry of the ligand and leads to a significant deviation from the ideal H-bond angle (180°).

Intermolecular hydrogen bonds in NAA result in an 18-membered hydrogen-bonded ring. The intra- and intermolecular hydrogen bonds of NAA are shown in *Figure 5.2*. These complementary O–H···O intermolecular hydrogen bonds between the ketone oxygen (H-bond acceptor) and the phenol OH of an adjacent molecule (H-bond donor) stabilise dimeric structures in the solid-state.

**Figure 5.2** Dimeric structures of NAA indicating the intra- and intermolecular hydrogen bonds represented as dashed green lines. Atoms are shown as spheres of arbitrary radius.

For SOA, complementary interactions between O3 of the sulfonyl moiety and the imine hydrogen atom (H–C7) of a neighbouring molecule result in a 16-membered ring. Each molecule in this dimer unit is then linked to two adjacent molecules through intermolecular O2–H102···O1 hydrogen bonds to form one-dimensional columns which traverse the *ac* plane (Figure 5.3). The intramolecular hydrogen bonds of SOA are also represented in Figure 5.3.

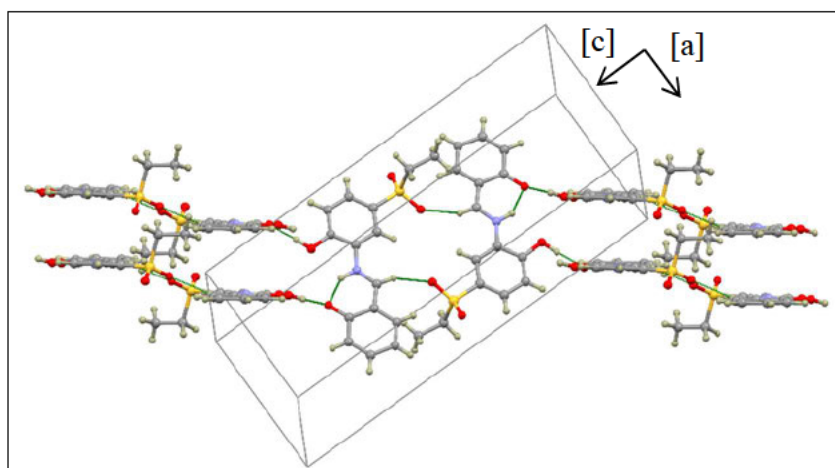


**Figure 5.3** Intermolecular hydrogen bonds (O2–H102···O1), intramolecular hydrogen bonds (N1–H101···O1) and C7–H···O3 intermolecular attractions in SOA, shown as dashed green lines. Atoms are shown as spheres of arbitrary radius.

The bonding parameters for the intermolecular O2–H102···O1 hydrogen bonds of SOA and NAA and the intermolecular C7–H···O3 interactions of SOA are listed in Table 5.8.

**Table 5.8** Bond parameters describing the intermolecular interactions of SOA and NAA.

Ligand	D–H (Å)	H···A (Å)	D···A (Å)	D–H···A (°)
<b>SOA</b>				
O2–H102···O1 <sup>i</sup>	0.93(3)	1.60(3)	2.526(1)	177(3)
C7–H···O3 <sup>ii</sup>	0.949	2.329	3.202(2)	152.66
<b>NAA</b>				
O2A–H102···O1B <sup>iii</sup>	0.89(7)	1.67(7)	2.559(3)	174(7)
O2B–H102···Q1A <sup>iv</sup>	0.840	1.768	2.557(3)	155.7
Symmetry operators: (i) $-x, \frac{1}{2} + y, \frac{1}{2} - z$ ; (ii) $1 - x, 1 - y, 1 - z$ (iii) $x, y, z$ ; (iv) $x, y, z$				

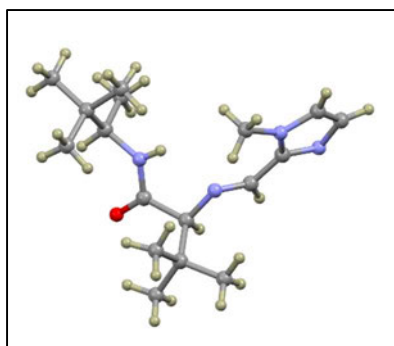
The O2–H102···O1 intermolecular hydrogen bonds are considerably shorter than the sum of the van der Waals radii of the interacting atoms.<sup>26</sup>

Although bond length is not always a reliable indicator of bond strength, due to packing constraints in the lattice, this short bond length coupled with the near-ideal bond angles suggest these interactions are moderately strong. The O–H···O bond angle for NAA is less than ideal at 155.7° due to the different orientation of the OH group in molecule (b).

### 5.3 *O,N,N'*-Tridentate Ligands

#### 5.3.1 Introduction to *O,N,N'*-Tridentate Ligands

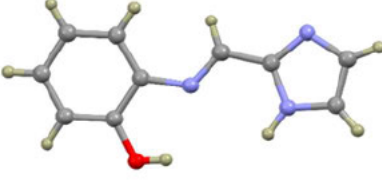
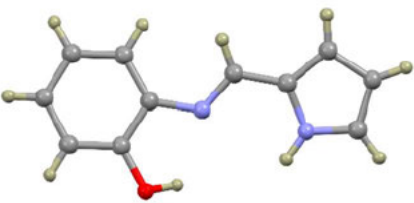
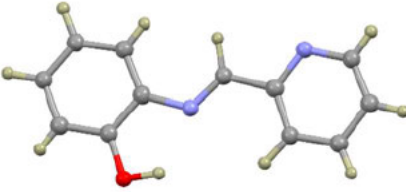
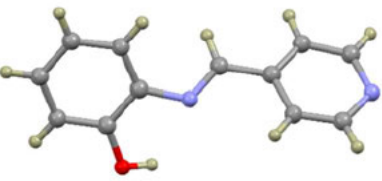
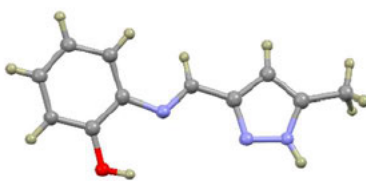
A search of the Cambridge Structural Database (CSD)<sup>5</sup> indicated there are no reported free ligand structures of tridentate *O,N,N'*-1-methyl-2-imidazole-aminophenol Schiff base molecules. PHCA has been previously synthesised by Kloskowski and co-workers.<sup>27</sup> However, no characterisation data were reported for this ligand. In the same work, an X-ray structure of a trinuclear Mn complex of PHCA is reported as an enzyme model (PETFUQ).<sup>27</sup> In general, very few free ligand structures containing the 1-methyl-imidazol-2-yl methylidene amino moiety have been reported. One of the few examples is PILBEU (*Figure 5.4*).<sup>28,29</sup>



**Figure 5.4** Reported crystal structure of a Schiff base ligand containing the 1-methyl-imidazol-2-yl methylidene amino moiety (PILBEU).<sup>28</sup>

A small number of compounds based on the 1-methyl-imidazol-2-yl methylidene amino moiety have been reported chelated to metal ions. The metals that have been coordinated include Ni(II), Fe(II), Rh(III), Ir(III), Rh(I) and Cu(II).<sup>30-38</sup> These metal complexes have been used for a wide range of applications such as hosts for racemic separation, catalysis, anticancer chemotherapeutic agents and bioimaging probes.<sup>30,33,35-40</sup> A few free ligand structures of *O,N,N'* and related Schiff base ligands derived from 2-aminophenol have been reported (*Table 5.9*).<sup>41-47</sup>

**Table 5.9** Reported X-ray crystal structures of 2-aminophenol-derived Schiff Base Ligands.

Structure	CSD Ref. Code	Lit. Reference
	DAYYAF	41,42
	JETLIE	43
	JUBKOG	44
	JOFZIP	45
	AFUROL	46
	MIKNOM	47

Literature on solid-state structures of *O,N,N'* ligands of this class is scarce. In this work, X-ray structures of PHCA, MECA, TERTCA and PHPHCA were elucidated by single-crystal X-ray diffraction and are discussed below.

### 5.3.2 Experimental Procedures for the *O,N,N'*-Tridentate Ligands

Yellow crystals of MECA and TERTCA were formed upon by cooling the oil samples to -20 °C overnight. The crystals remained stable upon warmth to room temperature. For PHCA dark yellow hexagonal-shaped crystals were formed by slow evaporation of toluene solution. The crystals formed were hydrated if the re-crystallisation process was performed at room temperature, even with the use of molecular sieves. Crystals of anhydrous PHCA could be obtained by dissolving the crude product in toluene with 3 Å molecular sieves and heating the solution to reflux for thirty minutes. Crystals of anhydrous PHCA formed upon slow cooling of the solution.<sup>48</sup> Dark yellow crystals of anhydrous PHPHCA also formed using the above method.

### 5.3.3 Results and Discussion of the Solid-State Structures of the *O,N,N'*-Tridentate Ligands

Crystal data details for hydrous and anhydrous PHCA, MECA, TERTCA and PHPHCA are summarised in *Table 5.10*. Full crystal data and structure refinement details are given in *Appendix C*. The crystal structures of PHCA (UHUGEM), PHCA·0.5H<sub>2</sub>O (UHUGOW), MECA (UHUGIQ) and TERTCA (UHUGAI) have been published as part of this PhD study.<sup>48</sup>

**Table 5.10** Selected crystal data for the *O,N,N'* Schiff Base Ligands.

Crystal data	PHCA	PHCA·0.5H <sub>2</sub> O	MECA	TERTCA	PHPHCA
Crystal system	Monoclinic	Monoclinic	Monoclinic	Monoclinic	Monoclinic
Space group	<i>P2<sub>1</sub>/c</i>	<i>C2/c</i>	<i>P2<sub>1</sub>/n</i>	<i>C2/c</i>	<i>P2<sub>1</sub>/n</i>
No of molecules in asymmetric unit	2	1 and ½ H <sub>2</sub> O solvate	2	1	2
<i>Z</i>	8	8	8	8	8

MECA and PHPHCA crystallised in the *P2<sub>1</sub>/n* space group with two independent molecules in the asymmetric unit. TERTCA crystallised in the monoclinic *C2/c* space group with one molecule in the asymmetric unit.

Anhydrous PHCA crystallised in the  $P2_1/c$  space group with two independent molecules in the asymmetric unit, while the hydrated PHCA crystallised in the  $C2/c$  space group with one molecule of PHCA and a half water molecule in the asymmetric unit. The thermal displacement plots of PHCA, PHCA·0.5H<sub>2</sub>O, MECA, TERTCA and PHPHCA are shown in *Figure 5.5*.

Previously reported  $O,N,N'$  free ligands, closely related to those in this work, such as DAYYAF<sup>41,42</sup> and JUBKOG<sup>44</sup> (*Table 5.9*) are approximately planar in geometry. However, in this study, most of the  $O,N,N'$  molecules deviated from planarity. The angle subtended by the imidazole and phenyl rings is approximately 15° for both MECA(a) and (b) and a similar angle of 22° for TERTCA. Although the subtended angle is the same for both MECA(a) and (b), the imidazole ring is rotated below the mean plane of the phenyl ring for MECA(a) and above for MECA(b). The most noticeable deviation from planarity is for PHCA(a) with the angle subtended by the imidazole and phenyl rings measuring *ca.* 66°. PHCA(b) has a significantly different geometry to PHCA(a). PHCA(b) is approximately planar with the angle subtended by the same rings measuring *ca.* 7° (*Figure 5.6*). The difference between the two independent molecules in the asymmetric unit in PHCA is also evident in the C5–N3–C6–C7 torsion angles. For the relatively planar molecule PHCA(b), this torsion angle is  $-7.6(2)^\circ$  and for the molecule (a) this torsion angle measures  $-59.1(2)^\circ$ .

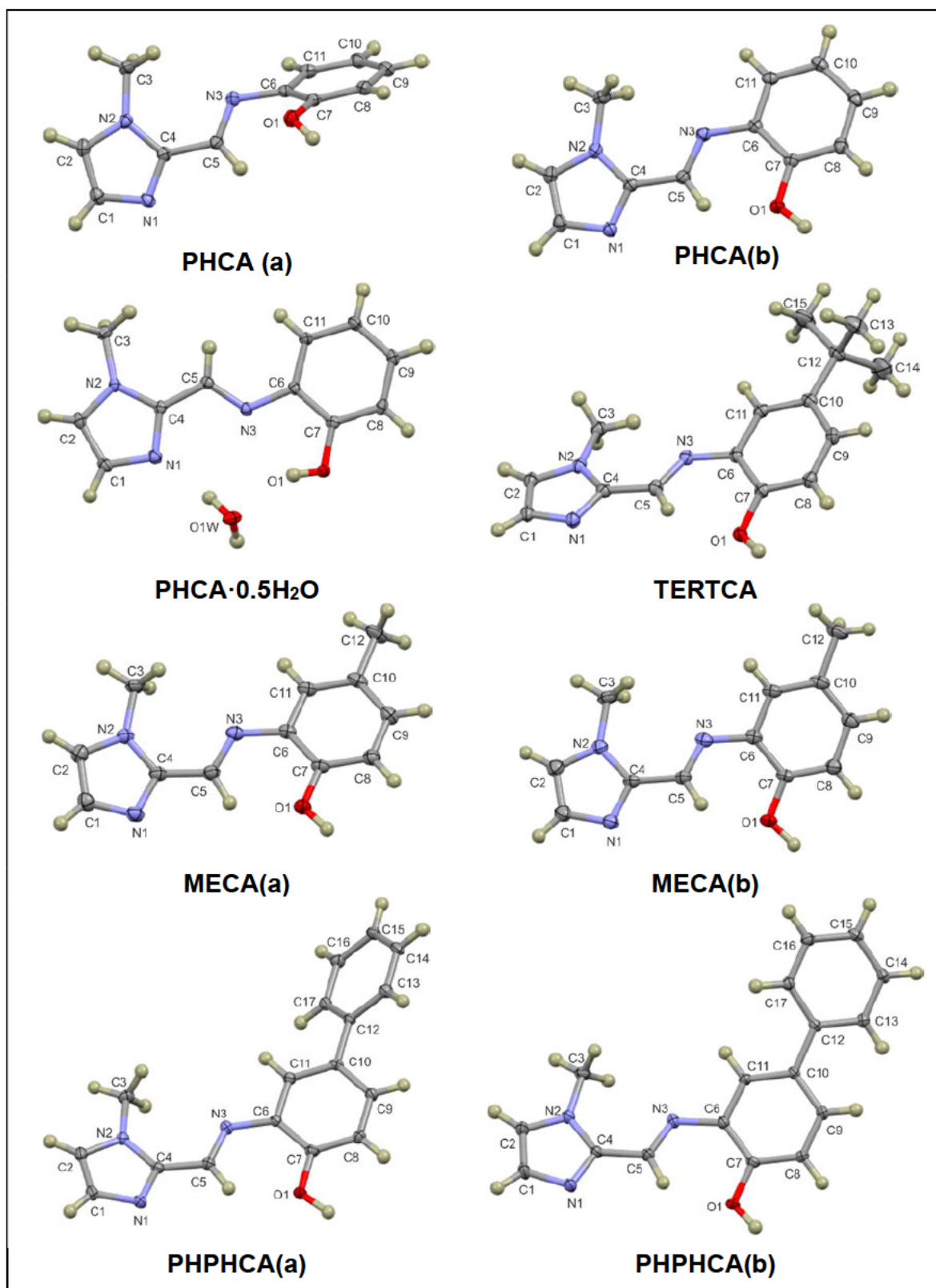


**Figure 5.5** Thermal displacement plots (50% probability) showing the structure and atom numbering schemes of PHCA, PHCA·0.5H<sub>2</sub>O, MECA, TERTCA and PHPHCA. Hydrogen atoms are shown as spheres of arbitrary radius. The symmetry completed (2-fold symmetry) water molecule in PHCA is shown.

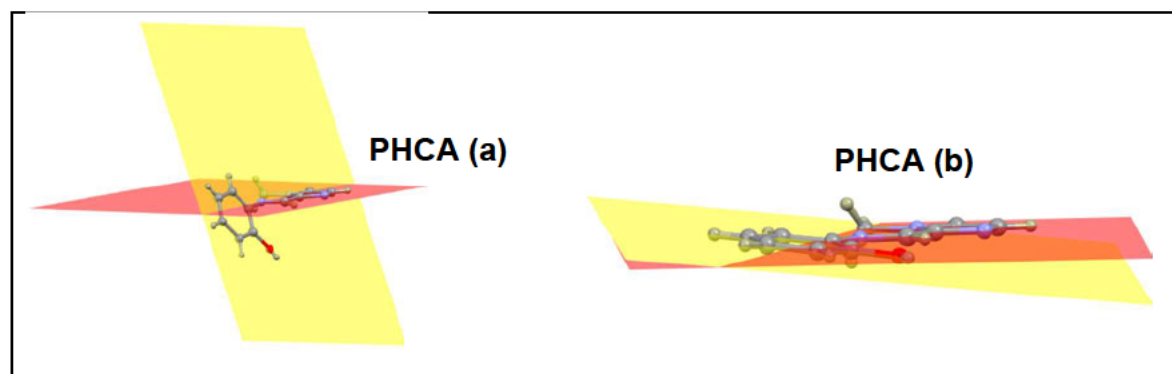


**Figure 5.6** Mean planes of the imidazole (red) and phenol (yellow) rings of PHCA(a) and PHCA(b).

When crystallised as the hydrate, PHCA is again approximately planar, with the angle subtended by the phenyl and imidazole rings measuring *ca.* 6°. The two independent molecules in the asymmetric unit of PHPHCA also have significantly different geometries. The angle subtended by the imidazole and phenyl mean planes are similar - *ca.* 14° and 16° for PHPHCA molecules (a) and (b), respectively. However, the angle subtended by the phenol and phenyl rings is significantly different; 40° for PHPHCA (a) and 17° for PHPHCA (b). Selected bond lengths and angles are reported in *Table 5.11* for PHCA and PHCA·0.5H<sub>2</sub>O and in *Table 5.12* for MECA, TERTCA and PHPHCA.

**Table 5.11** Selected bond lengths (Å) and angles (°) for PHCA and PHCA·0.5H<sub>2</sub>O.

Ligand	PHCA(a)	PHCA(b)	PHCA·0.5H <sub>2</sub> O
<b>Bond Lengths</b>			
N1–C1	1.375(2)	1.375(2)	1.369(2)
N1–C4	1.341(2)	1.340(2)	1.336(2)
C1–C2	1.367(2)	1.368(2)	1.370(2)
C2–N2	1.372(2)	1.373(2)	1.371(2)
N2–C3	1.463(2)	1.467(2)	1.463(2)
N2–C4	1.366(1)	1.367(2)	1.370(1)
C4–C5	1.460(2)	1.459(2)	1.457(2)
C5–N3	1.278(2)	1.281(2)	1.278(1)
N3–C6	1.426(1)	1.418(1)	1.412(2)
C <sub>ar</sub> –C <sub>ar</sub> <sup>a</sup>	1.399(2)	1.402(2)	1.398(2)
C7–O1	1.369(1)	1.357(1)	1.359(2)
<b>Bond Angles</b>			
C4–C5–N3	123.2(1)	122.3(1)	118.4(1)
C5–N3–C6	118.2(1)	123.4(1)	122.7(1)
C1–N1–C4	105.6(1)	106.2(1)	105.5(1)
C2–N2–C4	107.1(1)	107.0(1)	107.1(1)
N3–C6–C7	121.9(1)	127.3(1)	114.0(1)
N3–C6–C11	118.8(1)	114.4(1)	127.0(1)

<sup>a</sup> Mean C–C bond lengths of the phenyl rings.

**Table 5.12** Selected bond lengths (Å) and angles (°) for MECA, TERTCA and PHPHCA.

Ligand	MECA(a)	MECA(b)	TERTCA	PHPHCA(a)	PHPHCA(b)
<b>Bond Lengths</b>					
N1–C1	1.364(2)	1.364(2)	1.372(2)	1.372(2)	1.364(2)
N1–C4	1.334(2)	1.334(2)	1.341(2)	1.336(2)	1.332(2)
C1–C2	1.364(2)	1.361(2)	1.364(2)	1.360(2)	1.362(2)
C2–N2	1.367(2)	1.368(2)	1.373(2)	1.369(2)	1.367(2)
N2–C3	1.461(2)	1.459(2)	1.461(2)	1.462(2)	1.457(2)
N2–C4	1.361(2)	1.361(2)	1.362(2)	1.366(2)	1.357(2)
C4–C5	1.448(2)	1.451(2)	1.456(2)	1.457(2)	1.456(2)
C5–N3	1.281(2)	1.281(2)	1.284(2)	1.284(2)	1.274(2)
N3–C6	1.410(2)	1.411(2)	1.421(2)	1.416(2)	1.416(2)
C <sub>ar</sub> –C <sub>ar</sub> <sup>a</sup> (phenol)	1.395(2)	1.395(2)	1.400(2)	1.399(2)	1.398(2)
C <sub>ar</sub> –C <sub>ar</sub> <sup>a</sup> (phenyl)	N/A	N/A	N/A	1.392(2)	1.394(2)
C7–O1	1.352(1)	1.352(1)	1.354(2)	1.341(2)	1.350(2)
<b>Bond Angles</b>					
C4–C5–N3	122.5(1)	122.3(1)	123.4(1)	122.2(1)	121.5(1)
C5–N3–C6	122.4(1)	122.3(1)	120.8(1)	122.9(1)	122.4(1)
C1–N1–C4	106.0(1)	106.0(1)	106.2(1)	105.7(1)	106.1(1)
C2–N2–C4	106.9(1)	106.8(1)	107.0(1)	107.1(1)	107.1(1)
N3–C6–C7	126.8(1)	126.6(1)	126.8(1)	126.8(1)	127.7(1)
N3–C6–C11	115.1(1)	115.1(1)	114.6(1)	114.9(1)	114.0(1)
<sup>a</sup> Mean C–C bond lengths of the phenyl rings.					

The bond lengths of the *O,N,N'* ligands, in this work, compare favourably with each other and with those previously reported of related molecules.<sup>41-47</sup> The C5–N3 imine bond lengths in the *O,N,N'* ligands range from 1.274 – 1.284 Å, close to the average  $Csp^2=N$  bond length of 1.279 Å.<sup>24,25</sup> This coupled with the C4–C5–N3 bond angles, ranging from 121.5 – 123.4° clearly indicate the double bond character of the imine bond and  $sp^2$  hybridisation of the imine carbon atom. The isomerisation about the imine bond is an *E*-configuration for all the *O,N,N'* ligands. The *trans* configuration is favoured, as there would be non-bonded repulsion between the hydroxyl and imidazole N–CH<sub>3</sub> group in the *cis* configuration. The *trans* configuration also allows for stabilising intramolecular interactions between the imine C–H and phenol oxygen atoms except in the case of PHCA(a) and PHCA·H<sub>2</sub>O. The twist of the phenol moiety in PHCA(a) prevents this interaction. In the hydrated PHCA, the imine C–H is orientated on the opposite side of the molecule.

The bond angles of the *O,N,N'* ligands in this work compare favourably with each other and mostly with reported bond angles for similar compounds.<sup>41-47</sup> Noticeable differences are the N3–C6–C7 and N3–C6–C11 bond angles. In the structures of the previously reported 2-aminophenol-derived *O,N,N'* free ligands (*Table 5.9*), the N3–C6–C11 bond angle is more obtuse than the N3–C6–C7 bond angle due to steric crowding of the hydrogen atom at the *ortho* position of the phenyl ring and the imino group.<sup>41-47</sup> In this study, the N3–C6–C11 bond angle is significantly more acute than the N3–C6–C7 bond angle for PHCA (b), MECA, TERTCA and PHPHCA. This difference is likely caused by steric strain between the hydroxyl group and imine C–H as a consequence of these groups being on the same side of the molecule. The opening of the bond angle is less pronounced for molecule (a) of PHCA as the steric strain is released by the rotation of the phenol moiety out-of-plane (*Figure 5.6*).

As indicated in *Section 4.2.4*, the crystal structures of all the *O,N,N'* ligands exhibit intermolecular hydrogen bonds. Sixteen-membered supramolecular dimeric ring structures are formed with hydrogen bonds between the unsubstituted imidazole nitrogen and the phenol OH, on a neighbouring molecule. The dimeric structures are shown in *Figure 5.7*.

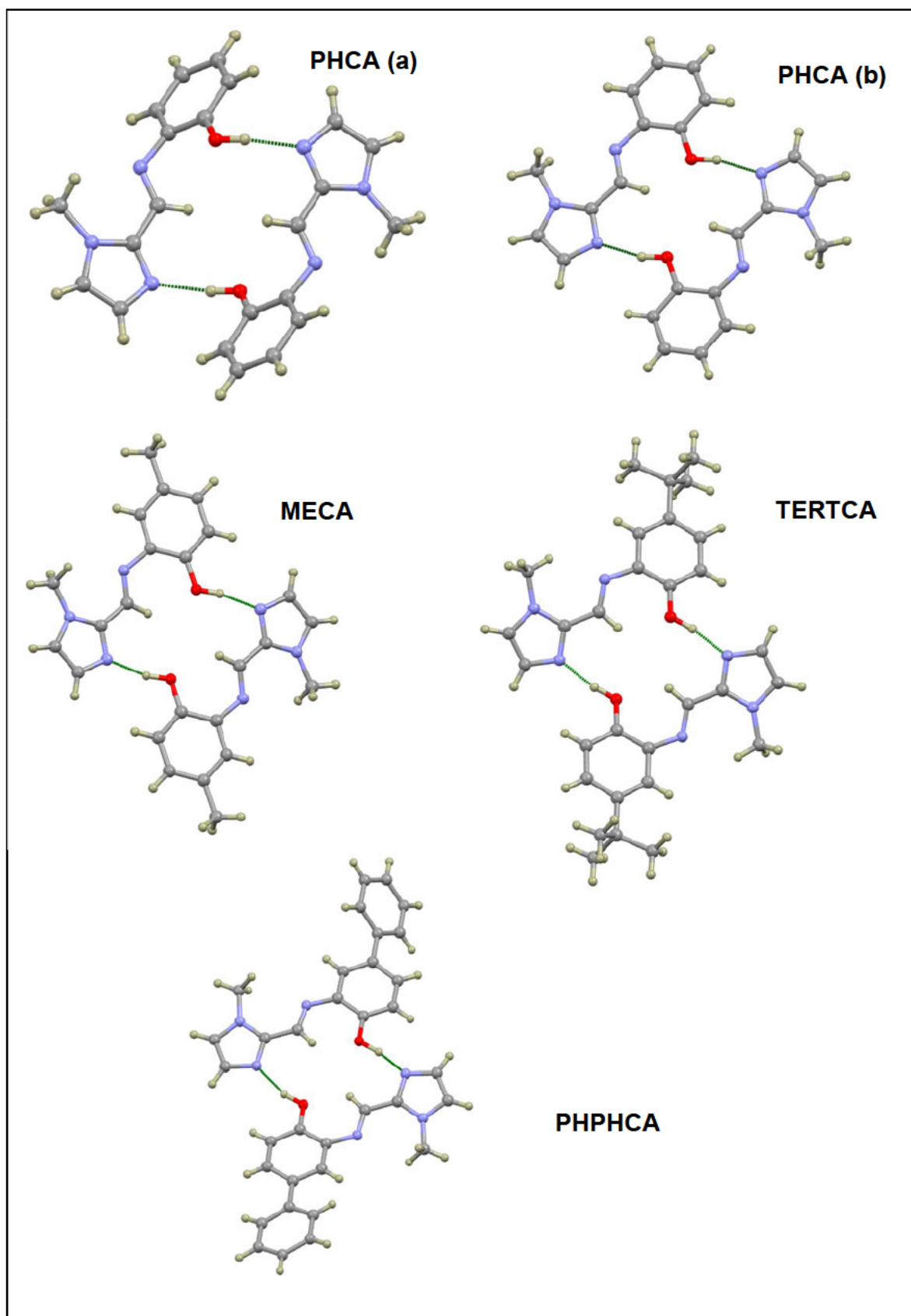


**Figure 5.7** Complementary hydrogen bonds forming dimeric structures of PHCA, MECA, TERTCA and PHPHCA. The hydrogen bonds are shown as dashed green lines. Atoms are shown as spheres of arbitrary radius.

MECA forms hydrogen bonds between two symmetry-independent molecules within the asymmetric unit. The two symmetry-independent molecules in the asymmetric unit of PHCA and PHPHCA form hydrogen bonds, not with each other, but with neighbouring molecules. TERTCA and anhydrous PHCA form hydrogen bonds with neighbouring symmetry-dependant molecules and, thus, form inversion dimers. PHPHCA forms hydrogen bonds between neighbouring symmetry-independent molecules. The hydrogen bonding parameters for these interactions are summarised in *Table 5.13*.

**Table 5.13** Hydrogen bond lengths (Å) and bond angles (°) for the intermolecular interactions of PHCA, PHCA·0.5H<sub>2</sub>O MECA, TERTCA and PHPHCA.

Ligand	D–H (Å)	H···A (Å)	D···A (Å)	D–H···A (°)
<b>PHCA</b>				
O1A–H101···N1A <sup>i</sup>	0.89(2)	1.81(2)	2.688(1)	170(2)
O1B–H102···N1B <sup>ii</sup>	0.95(2)	1.75(2)	2.672(1)	164(1)
<b>PHCA·0.5H<sub>2</sub>O</b>				
O1–H101···O1S	0.83(2)	2.18(2)	2.936(1)	151(2)
O1S–H1S···N1	0.89(2)	1.95(2)	2.832(1)	173(2)
<b>MECA</b>				
O1A–H101···N1B <sup>iii</sup>	0.93(2)	1.76(2)	2.672(2)	169(2)
O1B–H102···N1A <sup>iv</sup>	0.99(2)	1.69(2)	2.662(2)	166(2)
<b>TERTCA</b>				
O1–H101···N1 <sup>v</sup>	0.98(3)	1.70(3)	2.667(2)	168(3)
<b>PHPHCA</b>				
O1A–H101···N1B <sup>vi</sup>	1.01(3)	1.61(3)	2.608(2)	168(2)
O1B–H102···N1A <sup>vii</sup>	0.96(3)	1.77(2)	2.705(2)	163(2)
Symmetry operators:	(i) $1 - x, 2 - y, -z$ ; (ii) $-x, 1 - y, -z$ (iii) $1 + x, 1 + y, z$ ; (iv) $1 + x, 1 + y, z$ (v) $\frac{1}{2} - x, \frac{1}{2} - y, 1 - z$ ; (vi) $1 - x, -y, 1 - z$ (vii) $1 - x, -y, 1 - z$			

The intermolecular O1···N1 hydrogen bonds of the *O,N,N'* ligands are significantly shorter than the sum of the van der Waals radii for nitrogen and oxygen of 3.07 Å.<sup>18,26</sup> In addition the O–H···N<sub>imidazole</sub> hydrogen bond lengths, in this work, are significantly shorter than N–H···N; N–H···O; O–H···O and O–H···N hydrogen bonds, previously reported.<sup>41,43-47,49</sup> This as well as the near ideal (180°) hydrogen bond angles suggest the hydrogen bonds in PHCA, MECA, TERTCA and PHPHCA are strong interactions.

The dimer units of PHCA are further linked by C–H···O interactions between the phenol O-atom and an imidazole C–H to form one-dimensional columns, which traverse the *ab* plane (Figure 5.8).

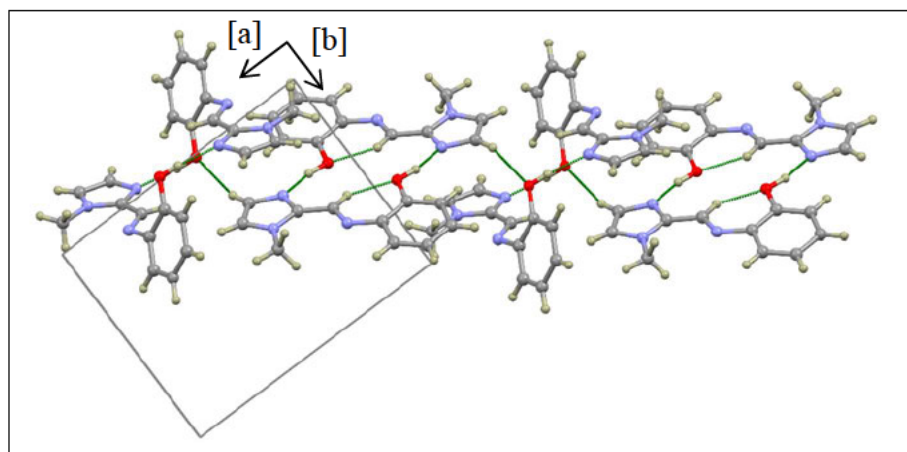


**Figure 5.8** Dimeric hydrogen-bonded units of PHCA linked by C–H···O interactions to form one-dimensional columns (viewed down the *c*-axis). The intermolecular interactions are shown as dashed green lines. Atoms are rendered as spheres of arbitrary radius.

The hemihydrate of PHCA forms water-bridged dimers in the solid-state. The central water molecule acts as an H-bond donor to the imidazole N-atoms (H-bond acceptor). The water molecule also acts as an H-bond acceptor, forming hydrogen bonds with the phenol OH. Each water molecule thus bridges two ligand molecules, supported by four hydrogen bonds. Weak C–H···N interactions link these dimers to form one-dimensional columns co-linear with the *c*-axis (Figure 5.9).

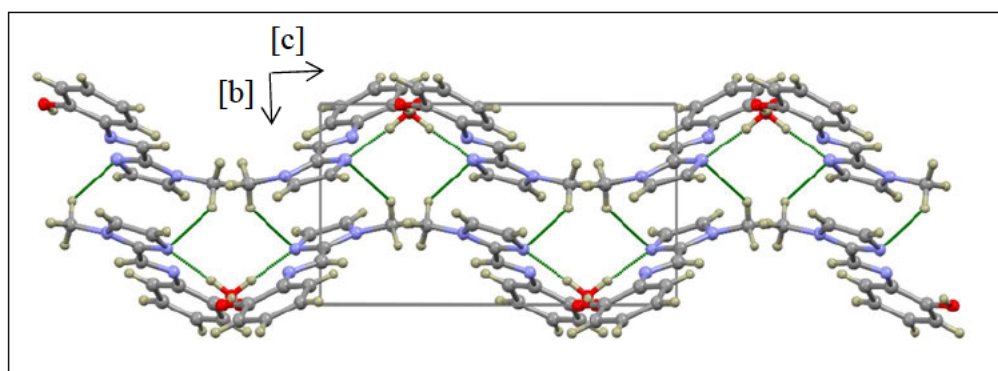


**Figure 5.9** One-dimensional supramolecular structure comprising water-bridged PHCA dimers cross-linked by C–H···N interactions, viewed down the *a*-axis. Intermolecular interactions are shown as dashed green lines. All atoms are rendered as spheres of arbitrary radius.

## 5.4 [VO(ONO)(DPQ/DPPZ)] Complexes

### 5.4.1 Introduction to [VO(ONO)(DPQ/DPPZ)] Complexes

A search of the Cambridge Structural Database (CSD)<sup>5</sup> indicates that numerous [VO(ONO)(PHEN)] complexes have been reported, mainly with a carboxylate tridentate Schiff base ligand. <sup>50-81</sup> Conversely, very few [VO(ONO)(DPQ)] and [VO(ONO)(DPPZ)] structures have been reported. Previously reported structures of an oxovanadium DPQ complex with a tridentate *O,N,O'*-donor *N*-salicylidene-*L*-methionate ligand (RIVVUO<sup>53</sup>) and a DPPZ complex with a *O,N,O'*-tridentate 2-(2-hydroxybenzylideneamino) phenol ligand (NAGZIG<sup>82</sup>) are shown in *Figure 5.10*. In both cases, the vanadium has a nominally octahedral geometry with three coordination sites occupied by the Schiff base ligand, two by the respective *N,N*-bidentate ligand. The final coordination site is occupied by the oxo ligand.

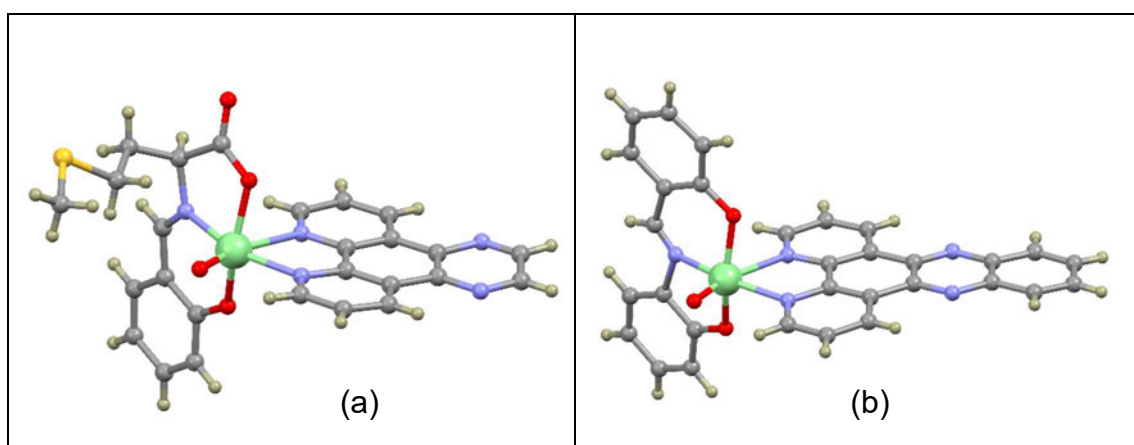


**Figure 5.10** Previously reported X-ray structures of neutral oxovanadium complexes of the form [VO(ONO)(NN)]. (a) RIVVUO with a DPQ co-ligand<sup>53</sup> and (b) NAGZIG with a DPPZ co-ligand.<sup>82</sup>

### 5.4.2 Experimental Procedures for the [VO(ONO)(DPQ/DPPZ)] Complexes

[VO(PHA)(DPQ)] (this was a low-resolution structure), [VO(CLA)(DPQ)], [VO(TERTA)(DPQ)] and [VO(MEA)(DPPZ)] (low resolution structure) were characterised by single-crystal X-ray diffraction.

Red crystals of [VO(PHA)(DPQ)], [VO(CLA)(DPQ)] and [VO(TERTA)(DPQ)] were grown by slow solvent diffusion of hexane into a dichloromethane solution of the target compound. Red crystals of [VO(MEA)(DPPZ)] were grown by slow liquid diffusion of diethyl ether into a 2-methoxy ethanol solution of [VO(MEA)(DPPZ)]. Crystal data and structure refinement details are reported in *Appendix C*.

### 5.4.3 Results and Discussion of the Solid-State Structures of the [VO(ONO)(DPQ/DPPZ)] Complexes

A combination of weak diffraction and structural disorder in the complex meant only a low-resolution structure of [VO(PHA)(DPQ)] was elucidated. The low-resolution structure shows two independent molecules in the asymmetric unit (*Figure 5.11*). The structures show a six-coordinate  $V^{IV}N_3O_3$  coordination geometry with the Schiff Base ligand coordinated in a tridentate manner with two deprotonated phenolate groups yielding a dianionic ligand. The bidentate DPQ ligand is shown to be coordinated to the metal centre with the oxo ligand occupying the sixth coordination site.

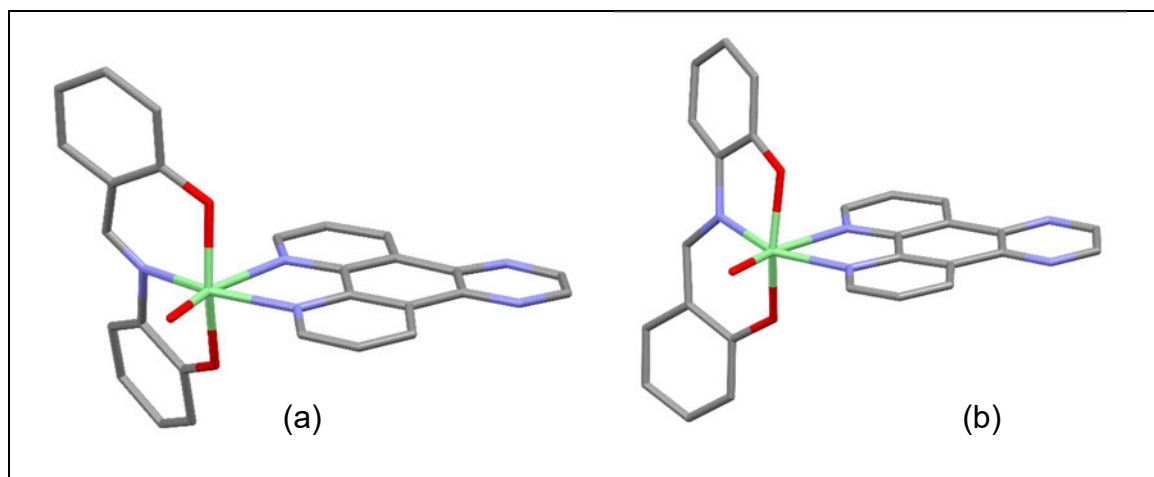


**Figure 5.11** Low resolution structures of [VO(PHA)(DPQ)].

The thermal displacement plots of [VO(CLA)(DPQ)] and [VO(TERTA)(DPQ)] are shown in *Figure 5.12*.

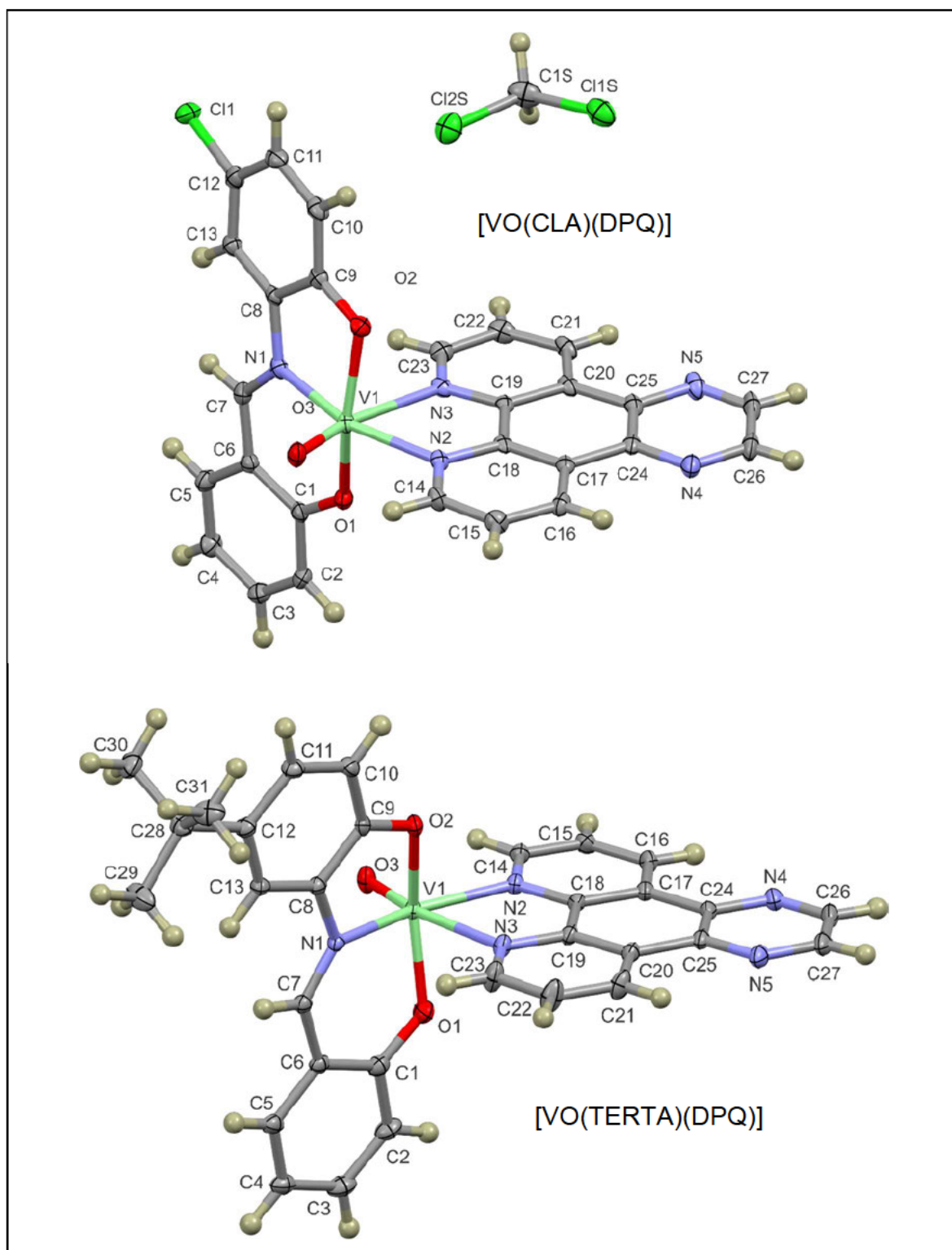


**Figure 5.12** Thermal displacement plots (50% probability) showing the structure and atom numbering schemes of  $[VO(CLA)(DPQ)]$  and  $[VO(TERTA)(DPQ)]$ . Both structures show an octahedral coordination geometry.

[VO(CLA)(DPQ)] crystallised in the monoclinic  $P2_1/c$  space group as the dichloromethane monosolvate, with one [VO(CLA)(DPQ)] molecule and one dichloromethane molecule in the asymmetric unit ( $Z = 4$ ). The dichloromethane solvent is involved in intermolecular interactions between a chlorine atom from  $\text{CH}_2\text{Cl}_2$  and a hydrogen atom from the DPQ moiety (H–C14). [VO(TERTA)(DPQ)] crystallised in the triclinic  $P-1$  space group with one independent molecule in the asymmetric unit ( $Z = 2$ ). There was a disordered dichloromethane solvent molecule in the lattice of [VO(TERTA)(DPQ)]. The PLATON/SQUEEZE procedure was used to suppress the reflections related to the solvent molecule. This process yielded a void of  $120 \text{ \AA}^3$ .

The crystal structures show a monomeric vanadium(IV) species with the *N,N*-bidentate DPQ ligand and respective dianionic tridentate *O,N,O'* ligand coordinated to the vanadyl ( $\text{VO}^{2+}$ ) core to form a  $\text{V}^{\text{IV}}\text{O}_3\text{N}_3$  six-coordinate distorted octahedron. The tridentate Schiff base is bound to the vanadium centre through the two phenolate oxygens and the imine nitrogen in a meridional binding mode. The DPQ ligand occupies two of the remaining sites with the oxo ligand in the sixth coordination site.

Selected bond distances and bond angles for [VO(CLA)(DPQ)] and [VO(TERTA)(DPQ)] are given in *Table 5.14*. The bond lengths and angles of [VO(CLA)(DPQ)] and [VO(TERTA)(DPQ)] compare favourably with each other and with those of closely related structures which have been previously reported. The double-bond character of the vanadyl group is highlighted by the short bond length. The  $\text{V}=\text{O}_3$  bond distance of  $1.608(2) \text{ \AA}$  for [VO(CLA)(DPQ)] and  $1.606(2) \text{ \AA}$  for [VO(TERTA)(DPQ)] are typical for oxovanadium complexes, where  $\text{V}=\text{O}$  bond lengths are commonly in the range  $1.57 \text{ \AA} - 1.62 \text{ \AA}$ .<sup>50,58,81</sup> The  $\text{V1}-\text{O1}$  and  $\text{V1}-\text{O2}$  bond lengths of the coordinated Schiff bases range from  $1.964(2) - 1.988(2) \text{ \AA}$  in the present complexes, which is typical for  $\text{V}-\text{O}$  single bonds.<sup>50,52,60,67,79,81</sup>

The *trans*  $\text{O3}=\text{V1}-\text{N3}$  bond angle of  $164.73(8)^\circ$  for [VO(CLA)(DPQ)] and  $167.30(6)^\circ$  for [VO(TERTA)(DPQ)] indicates the distorted octahedron. The deviation from  $90^\circ$  of the  $\text{O3}-\text{V1}-\text{N1}$ ,  $\text{O3}-\text{V1}-\text{N2}$ ,  $\text{O3}-\text{V1}-\text{O1}$  and  $\text{O3}-\text{V1}-\text{O2}$  bond angles also highlight the distorted octahedron.

**Table 5.14** Selected bond lengths (Å) and angles (°) for [VO(CLA)(DPQ)] and [VO(TERTA)(DPQ)].

Complex	[VO(CLA)(DPQ)]	[VO(TERTA)(DPQ)]
<b>Bond Lengths</b>		
V1–O1	1.964(2)	1.977(1)
V1–O2	1.988(2)	1.981(1)
V1–O3	1.608(2)	1.606(2)
V1–N1	2.079(2)	2.070(1)
V1–N2	2.143(2)	2.151(1)
V1–N3	2.365(2)	2.337(2)
C6–C7	1.433(4)	1.434(2)
C7–N1	1.303(4)	1.295(2)
N1–C8	1.432(3)	1.421(2)
C1–C2	1.418(4)	1.418(2)
C2–C3	1.375(4)	1.380(3)
C3–C4	1.407(3)	1.399(2)
C4–C5	1.366(4)	1.374(2)
C5–C6	1.416(4)	1.414(3)
C1–C6	1.430(3)	1.422(2)
C8–C9	1.415(4)	1.412(2)
C9–C10	1.405(4)	1.408(2)
C10–C11	1.393(3)	1.385(2)
C11–C12	1.394(4)	1.405(3)
C12–C13	1.379(4)	1.394(2)
C8–C13	1.396(3)	1.392(2)
<b>Bond Angles</b>		
O3–V1–N1	105.42(9)	103.68(6)
O3–V1–N2	92.84(9)	94.55(6)
O3–V1–N3	164.73(8)	167.30(6)
O3–V1–O1	100.51(8)	100.35(6)
O3–V1–O2	100.61(8)	102.14(6)
N2–V1–N3	71.90(7)	72.77(5)
N2–V1–N1	161.32(8)	161.69(6)
N2–V1–O1	93.00(8)	90.70(5)
N2–V1–O2	92.71(7)	94.21(5)
N3–V1–O1	81.33(7)	79.63(5)
N3–V1–O2	80.10(7)	79.93(5)
N3–V1–N1	89.77(8)	89.02(5)
O2–V1–N1	80.32(8)	80.44(5)
O2–V1–O1	157.80(7)	156.50(5)
O1–V1–N1	87.55(8)	87.75(5)
C6–C7–N1	125.4(2)	125.8(2)

The vanadium atom is displaced toward the O3 atom with V1 lying 0.341 Å above the equatorial plane (defined as O2–N1–O1–N2) in [VO(CLA)(DPQ)] and 0.355 Å in [VO(TERTA)(DPQ)]. This displacement is within the normal range for vanadyl complexes.<sup>81</sup>

The Schiff base ligand forms two chelate rings with the vanadium atom, one five-membered (V1/N1/C8/C9/O2) and one six-membered (V1/N1/C7/C6/C1/O1) ring. The O2–V1–N1 bond angles are acute, measuring 80.32(8)° and 80.44(5)° for [VO(CLA)(DPQ)] and [VO(TERTA)(DPQ)], respectively. This is a consequence of the small bite of the aminophenol moiety of the Schiff base ligand and resulting five-membered chelate ring. In comparison the O1–V1–N1, O1–V1–N1 and O1–V1–N2 bond angles are closer to 90°. This is a result of the larger six-membered iminomethyl phenol chelate ring. The five-membered chelate ring formed by coordination of DPQ again results in acute N2–V1–N3 bond angles, which measure 71.90(7)° and 72.77(5)° for [VO(CLA)(DPQ)] and [VO(TERTA)(DPQ)], respectively.

The dihedral angle between the two chelate ring planes (V1/N1/C8/C9/O2 and V1/N1/C7/C6/C1/O1) is 10.54° for [VO(CLA)(DPQ)] and 10.20° for [VO(TERTA)(DPQ)] indicating a slight twist of the Schiff base ligand. O2, N1, O1 of the Schiff base and N2 of DPQ are almost in the same equatorial plane with the sum of the equatorial angles almost equal to 360° (353.58(8)° for [VO(CLA)(DPQ)] and 353.10(5)° for [VO(TERTA)(DPQ)]). The delocalisation along the imino moiety (C6–C7–N1–C8) of the Schiff base is still evident in the C–C and C–N bond lengths. In [VO(TERTA)(DPQ)] the C6–C7 bond of 1.434(2) Å is shorter than the expected  $C_{aromatic}-Csp^2$  value of 1.485 Å and the N1–C8 bond, which measures 1.421(2) Å, is longer than the typical  $Nsp^2-C_{aromatic}$  value of 1.353 Å. The C=N imine bond, measures 1.295(2) Å, which is slightly longer than formal C=N bond length of 1.279 Å.<sup>24,25</sup>

The DPQ ligand is almost perpendicular to the equatorial plane with a dihedral angle to this plane of 86.21° for [VO(CLA)(DPQ)] and 89.70° for [VO(TERTA)(DPQ)].<sup>54,61,82</sup> The V–N bond *trans* to the vanadyl group (V1–N3) is significantly longer than the other V–N bonds in the respective structures. The V1–N3 bond length measures 2.365(2) Å versus 2.079(2) Å for V1–N1 and 2.143(2) Å for V1–N2 for [VO(CLA)(DPQ)]. This is due to the *trans* effect of the terminal oxo ligand. Similar trends have been reported for [VO(ONO)(NN)] complexes.<sup>50-54,59-61,65,66,68,70,73-77,80-82</sup>

In terms of intermolecular interactions, [VO(TERTA)(DPQ)] forms bifurcated interactions between the phenolate oxygen atom (O2) and an *ortho* hydrogen atom from the DPQ moiety of a neighbouring molecule (O2⋯H–C14) as well as with a hydrogen atom from the quinoxaline moiety of another neighbouring molecule (O2⋯H–C27).

These intermolecular interactions link the molecules into one-dimensional supramolecular structures co-linear with the  $c$ -axis. The  $\text{H}\cdots\text{O}$  bond distances are 2.482 Å for C14–H $\cdots$ O2 and 2.455 Å for C27–H $\cdots$ O2, shorter than the sum of the van der Waals radii for hydrogen and oxygen of 2.72 Å.<sup>26</sup> This suggests that the interactions are a genuine attraction.

In addition, the DPQ ligand moieties stack in [VO(TERTA)(DPQ)], creating  $\pi$ – $\pi$  inversion dimers. The centroid-centroid separation of 3.499 Å for C17–C18–C19–C20–C25–C24 and N4–C24–C25–N5–C27–C26 rings indicate a moderately strong  $\pi$ – $\pi$  interaction.<sup>80</sup> The intermolecular C–H $\cdots$ O and  $\pi$ – $\pi$  interactions are represented in *Figure 5.13* and the  $\pi$ – $\pi$  interaction parameters are listed in *Table 5.15*.

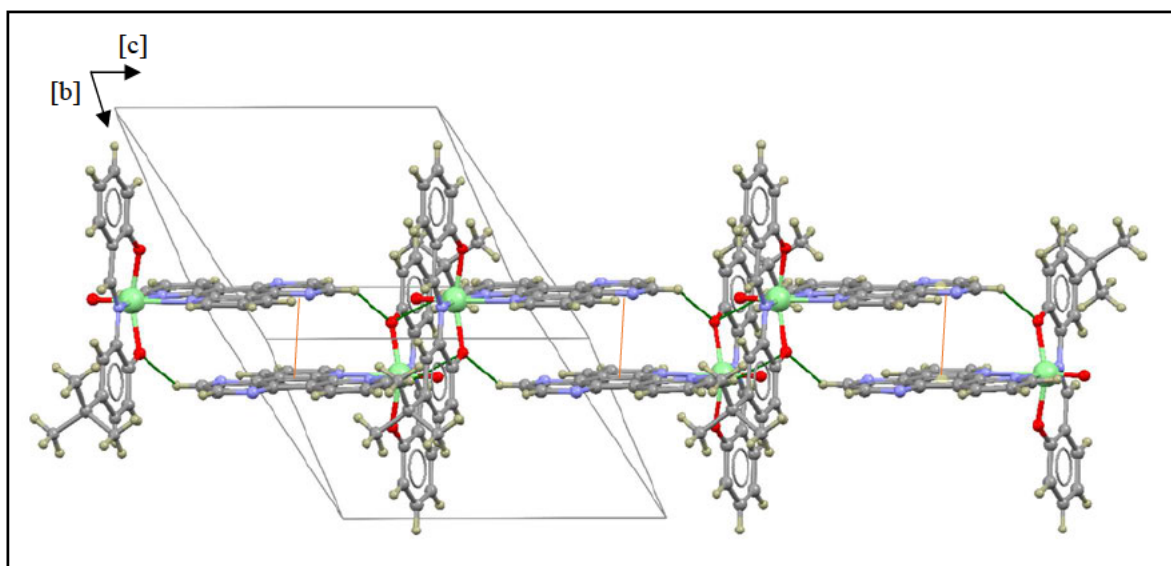


**Figure 5.13** Intermolecular interactions in [VO(TERTA)(DPQ)]. The attractions between the C–H of DPQ and O2 are shown as green lines and the  $\pi$ – $\pi$  interactions are shown as orange lines. Atoms are shown as spheres of arbitrary radius.

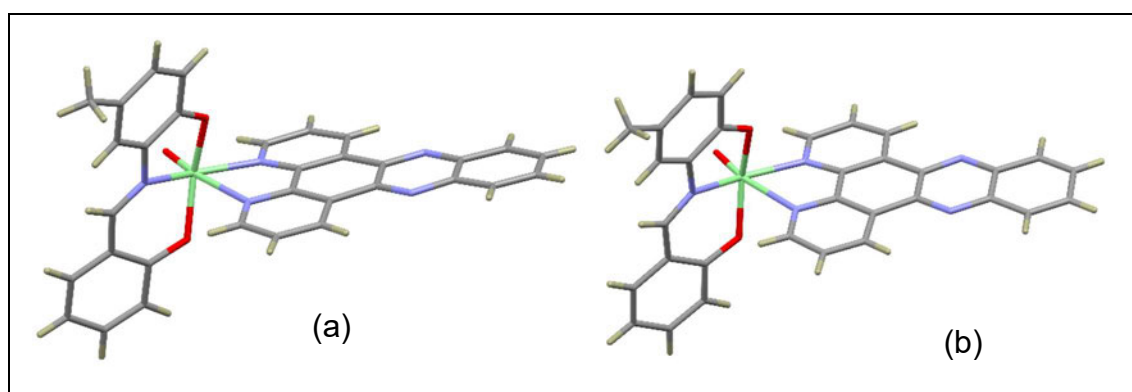
[VO(CLA)(DPQ)] also forms moderate  $\pi$ – $\pi$  interactions between the C17–C18–C19–C20–C25–C24 and N4–C24–C25–N5–C27–C26 rings of DPQ. The centroid-centroid separation is 3.518 Å. The  $\pi$ – $\pi$  interaction parameters are also listed in *Table 5.15* for [VO(CLA)(DPQ)].

**Table 5.15**  $\pi$ - $\pi$  Interactions in [VO(TERTA)(DPQ)] and [VO(CLA)(DPQ)].

Metal Complex	Centroid	$\pi$ - $\pi$ centroid- centroid (Å)	Mean Plane Separation (Å)	Ring Offset (Å)
[VO(TERTA)(DPQ)]	Cg(1)⋯Cg(2)	3.499	3.409	0.788
	Cg(2)⋯Cg(1)	3.499	3.404	0.810
[VO(CLA)(DPQ)]	Cg(1)⋯Cg(2)	3.518	3.429	0.786
	Cg(2)⋯Cg(1)	3.518	3.424	0.808

**Cg(1):** C17–C18–C19–C20–C25–C24  
**Cg(2):** N4–C24–C25–N5–C27–C26

Low resolution structures of [VO(MEA)(DPPZ)] were elucidated. The low-resolution structures of the two independent molecules in the asymmetric unit are shown in *Figure 5.14*. The structures show a six-coordinate  $V^{IV}N_3O_3$  coordination geometry with the Schiff Base ligand coordinated in a tridentate-*O,N,O* fashion to the oxovanadium(IV) centre. This configuration is closely related to the DPQ analogues described above.

**Figure 5.14** Low resolution structures of [VO(MEA)(DPPZ)].

## 5.5 [VO(ONN)(PHEN)](PF<sub>6</sub>) Complexes

### 5.5.1 Introduction to [VO(ONN)(PHEN)](PF<sub>6</sub>) Complexes

Although numerous crystal structures have been reported for neutral [VO(ONO)-(PHEN)]<sup>50-81</sup> complexes, very few have been reported for cationic complexes of the general form [VO(ONN)(PHEN)]<sup>+</sup>.

Previously reported examples of this class of compound include  $[\text{VO}(\text{ONN})(\text{PHEN})](\text{ClO}_4)$  complexes with a tridentate *N*-2-pyridylmethylidene-2-hydroxyphenylamine ligand (Figure 5.15 (a)) and a tridentate 2-{[(benzimidazol-2-yl)methylimino]-methyl}phenol ligand (Figure 5.15 (b)).<sup>83,84</sup> Other cationic oxovanadium complexes that have been reported include complexes of the type  $[\text{VO}(\text{ONO})(\text{PHEN})](\text{Cl})$  and  $[\text{VO}(\text{NNN})(\text{PHEN})]\text{X}$ , where  $\text{X} = (\text{Cl})_2$ ,  $(\text{ClO}_4)_2$  and  $(\text{ClO}_4)_{1.5}(\text{PF}_6)_{0.5}$ .<sup>85-88</sup> Crystal structures of neutral  $[\text{VO}(\text{ONN})(\text{PHEN})]$  complexes have also been reported.<sup>89-91</sup>

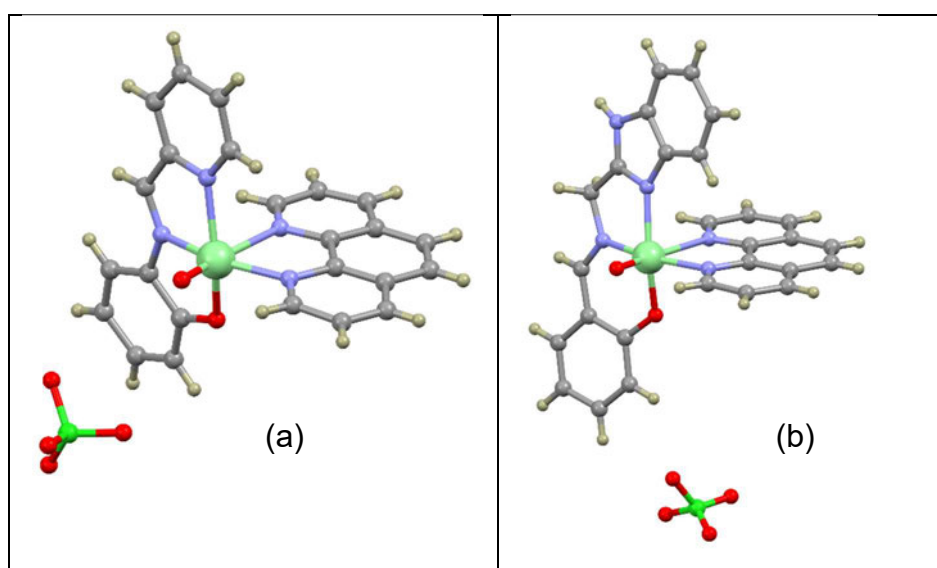


**Figure 5.15** Previously reported X-ray crystal structures of oxovanadium complexes IRAGAK<sup>83</sup> (a) HINXIN<sup>84</sup> (b) of the general formula  $[\text{VO}(\text{ONN})(\text{PHEN})](\text{ClO}_4)$ .

### 5.5.2 Experimental Procedures for the $[\text{VO}(\text{ONN})(\text{PHEN})](\text{PF}_6)$ Complexes

In this work, the complexes of  $[\text{VO}(\text{PHCA})(\text{PHEN})](\text{PF}_6)$ ,  $[\text{VO}(\text{MECA})(\text{PHEN})](\text{PF}_6)$  and  $[\text{VO}(\text{TERTCA})(\text{PHEN})](\text{PF}_6)$  were characterized by single-crystal X-ray diffraction. Red crystals of  $[\text{VO}(\text{PHCA})(\text{PHEN})](\text{PF}_6)$  and  $[\text{VO}(\text{MECA})(\text{PHEN})](\text{PF}_6)$  were formed upon slow solvent diffusion of hexane into a dichloromethane solution of the respective complexes. Red crystals of  $[\text{VO}(\text{TERTCA})(\text{PHEN})](\text{PF}_6)$  were grown by slow solvent diffusion of hexane into a chlorobenzene solution of  $[\text{VO}(\text{TERTCA})(\text{PHEN})](\text{PF}_6)$ .

### 5.5.3 Results and Discussion of the Solid-State Structures of the [VO(ONN)(PHEN)](PF<sub>6</sub>) Complexes

Selected crystal data for [VO(PHCA)(PHEN)](PF<sub>6</sub>), [VO(MECA)(PHEN)](PF<sub>6</sub>) and [VO(TERTCA)(PHEN)](PF<sub>6</sub>) are summarized in *Table 5.16*. Full crystal data and structure refinement details are reported in *Appendix C*.

**Table 5.16** Selected crystal data for the [VO(ONN)(PHEN)](PF<sub>6</sub>) Complexes.

Crystal data	[VO(PHCA)- (PHEN)](PF <sub>6</sub> )	[VO(MECA)- (PHEN)](PF <sub>6</sub> )	[VO(TERTCA)- (PHEN)](PF <sub>6</sub> )
Crystal system	Triclinic	Triclinic	Monoclinic
Space group	<i>P</i> -1	<i>P</i> -1	<i>P</i> 2 <sub>1</sub> / <i>n</i>
No of molecules in asymmetric unit	1 and 1 CH <sub>2</sub> Cl <sub>2</sub> solvate	1 and 1 CH <sub>2</sub> Cl <sub>2</sub> solvate	1 and 1 C <sub>6</sub> H <sub>5</sub> Cl solvate
<i>Z</i>	2	2	4

[VO(PHCA)(PHEN)](PF<sub>6</sub>) and [VO(MECA)(PHEN)](PF<sub>6</sub>) crystallised in the triclinic *P*-1 space group as [VO(ONN)(PHEN)](PF<sub>6</sub>)·CH<sub>2</sub>Cl<sub>2</sub> with one independent oxovanadium formula unit and one dichloromethane molecule in the asymmetric unit. The dichloromethane solvent molecule is disordered over two positions in the [VO(MECA)(PHEN)](PF<sub>6</sub>) asymmetric unit. [VO(TERTCA)(PHEN)](PF<sub>6</sub>) crystallised in the monoclinic *P*2<sub>1</sub>/*n* space group, with one independent oxovanadium formula unit and one chlorobenzene molecule in the asymmetric unit.

The thermal displacement plots of the [VO(ONN)(PHEN)](PF<sub>6</sub>) complexes are shown in *Figure 5.16*. The crystal structures for each of the [VO(ONN)(PHEN)](PF<sub>6</sub>) complexes show a monomeric, monocationic vanadium(IV) species, with the vanadium atom coordinated to one terminal oxo ligand, one *N,N*-bidentate phenanthroline ligand, and the respective monoanionic tridentate *O,N,N'*-donor Schiff base ligand.

The respective tridentate *O,N,N'* ligand is bound to the vanadium through the phenolate oxygen, the imine nitrogen, and the imidazole nitrogen in a meridional binding mode to form a V<sup>IV</sup>O<sub>2</sub>N<sub>4</sub><sup>+</sup> six-coordinate distorted octahedral geometry.

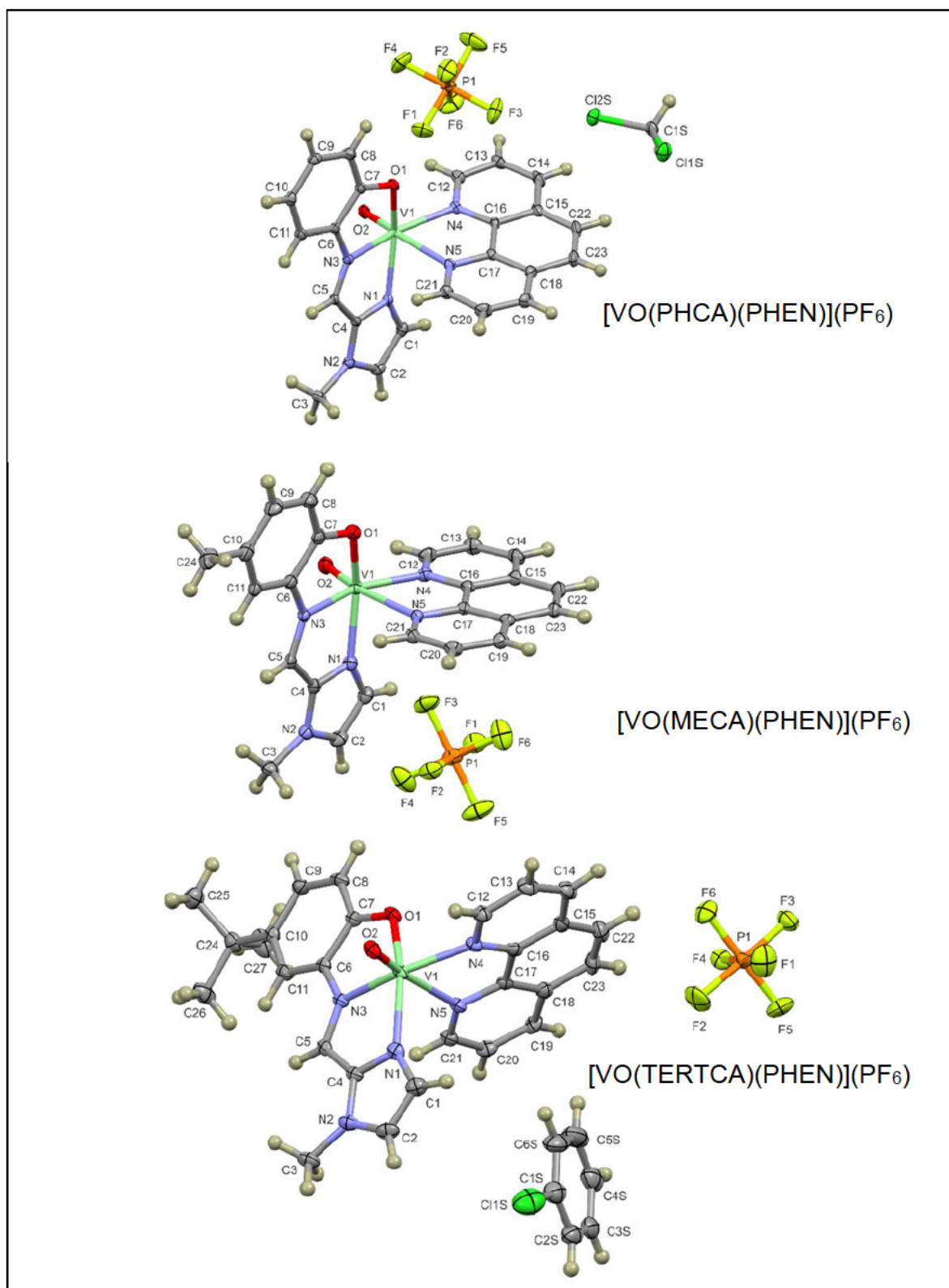


**Figure 5.16** Thermal displacement plots (50% probability) showing the structure and atom numbering schemes of [VO(PHCA)(PHEN)](PF<sub>6</sub>), [VO(MECA)(PHEN)](PF<sub>6</sub>) and [VO(TERTCA)(PHEN)](PF<sub>6</sub>). Hydrogen atoms are shown as spheres of arbitrary radius. The disordered CH<sub>2</sub>Cl<sub>2</sub> molecule in [VO(MECA)(PHEN)](PF<sub>6</sub>) was omitted for clarity.

Selected bond distances and bond angles for the complexes are summarised in *Table 5.17*. The double-bond character of the vanadyl moiety is again indicated by the short bond distance of V1=O2 in comparison to V1–O1. The V=O2 bond distances of 1.607(1) Å, 1.604(3) Å and 1.603(2) Å for [VO(PHCA)(PHEN)](PF<sub>6</sub>), [VO(MECA)(PHEN)](PF<sub>6</sub>) and [VO(TERTCA)(PHEN)](PF<sub>6</sub>), respectively are comparable to the V=O bond lengths of 1.588(5) Å and 1.586(4) Å for the previously reported complexes with the general formula [VO(ONN)(PHEN)](ClO<sub>4</sub>).<sup>83,84</sup> The V1–O1<sub>Schiffbase</sub> bond lengths of 1.951(1) Å, 1.967(2) Å and 1.952(2) Å for [VO(PHCA)(PHEN)](PF<sub>6</sub>), [VO(MECA)(PHEN)](PF<sub>6</sub>) and [VO(TERTCA)(PHEN)](PF<sub>6</sub>) respectively are also similar to the V–O single bond lengths of 1.951(4) Å and 1.930(4) Å in closely related compounds.<sup>83,84</sup>

**Table 5.17** Selected bond lengths (Å) and bond angles (°) for the [VO(ONN)(PHEN)](PF<sub>6</sub>) complexes.

Complex	[VO(PHCA)- (PHEN)](PF <sub>6</sub> )	[VO(MECA)- (PHEN)](PF <sub>6</sub> )	[VO(TERTCA)- (PHEN)](PF <sub>6</sub> )
<b>Bond Lengths</b>			
V1–O1	1.951(1)	1.967(2)	1.952(2)
V1–O2	1.607(1)	1.604(3)	1.603(2)
V1–N1	2.151(1)	2.122(3)	2.139(2)
V1–N3	2.085(1)	2.080(3)	2.087(2)
V1–N4	2.126(1)	2.116(3)	2.108(2)
V1–N5	2.301(1)	2.311(3)	2.312(3)
C4–C5	1.441(2)	1.445(5)	1.434(4)
C5–N3	1.290(2)	1.295(4)	1.293(3)
N3–C6	1.401(2)	1.404(4)	1.397(3)
<b>Bond Angles</b>			
O2–V1–N1	94.34(5)	96.1(1)	95.4(1)
O2–V1–N4	94.82(5)	91.8(1)	94.4(1)
O2–V1–N5	165.15(5)	165.5(1)	165.9(1)
O2–V1–O1	103.66(5)	101.9(1)	102.93(9)
O2–V1–N3	103.86(5)	106.9(1)	105.4(1)
N4–V1–N5	74.06(5)	73.9(1)	73.57(9)
N4–V1–N3	160.81(5)	160.5(1)	159.34(9)
N4–V1–N1	106.87(5)	95.7(1)	107.67(9)
N4–V1–O1	91.73(5)	102.5(1)	90.49(9)
N5–V1–N1	79.94(5)	84.0(1)	81.66(9)
N5–V1–O1	86.78(5)	83.2(1)	84.89(8)
N5–V1–N3	88.22(5)	87.2(1)	87.39(9)
O1–V1–N3	79.74(5)	79.5(1)	79.67(9)
O1–V1–N1	152.96(5)	153.8(1)	153.14(9)
N1–V1–N3	76.43(5)	77.1(1)	76.61(9)
C4–C5–N3	112.9(1)	113.1(3)	112.8(3)

The vanadium(IV) ion is displaced from the equatorial plane towards the terminal oxo group in the cationic complexes, but to a lesser extent than the neutral [VO(ONO)(DPQ)] complexes. The vanadium ion sits 0.312, 0.310 and 0.321 Å above the equatorial plane (defined as N1–N3–O1–N4) for [VO(PHCA)(PHEN)](PF<sub>6</sub>), [VO(MECA)(PHEN)](PF<sub>6</sub>) and [VO(TERTCA)(PHEN)](PF<sub>6</sub>), respectively. The deviation from 90° of the O2–V1–N3, O2–V1–N4, O2–V1–N5, O2–V1–N1 and O2–V1–O1 bond angles illustrates the distorted octahedral structure. The O1–V1–N1 and O2–V1–N5 *trans* bond angles exhibit an average *ca.* 27° and 14° deviation respectively from the expected *trans* angle of 180°. A distorted octahedral geometry is common in related structures.<sup>83-88</sup>

O1, N3, N1 and N4 of the tridentate ligand are almost in the same equatorial plane with the sum of the equatorial angles N1–V1–N3, N1–V1–N4, O1–V1–N4 and O1–V1–N3 almost equal to 360° (354.77(5)°, 354.8(1)° and 354.44(9)° for [VO(PHCA)(PHEN)](PF<sub>6</sub>), [VO(MECA)(PHEN)](PF<sub>6</sub>) and [VO(TERTCA)(PHEN)](PF<sub>6</sub>), respectively).

The Schiff base ligand forms two five-membered chelate rings with the vanadium atom (V1/N3/C6/C7/O1 and V1/N3/C5/C4/N1 rings). The dihedral angle between the two chelate ring planes in the [VO(ONN)(PHEN)](PF<sub>6</sub>) complexes tends more towards planarity than the neutral [VO(ONO)(DPQ)] complexes. The dihedral angle between the two chelate ring planes is 7.75°, 8.57° and 8.49° for [VO(PHCA)(PHEN)](PF<sub>6</sub>), [VO(MECA)(PHEN)](PF<sub>6</sub>) and [VO(TERTCA)(PHEN)](PF<sub>6</sub>), respectively. The bulky methyl and *tert*-butyl substituents on the phenol moiety of the tridentate ligand in [VO(MECA)(PHEN)](PF<sub>6</sub>) and [VO(TERTCA)(PHEN)](PF<sub>6</sub>), respectively, may be responsible for the larger deviation from planarity than in the unsubstituted phenol ring of [VO(PHCA)(PHEN)](PF<sub>6</sub>).

The small bite of the tridentate *O,N,N'* ligand yields 5-membered chelate rings and consequently acute bond angles. The O1–V1–N3 bond angles measure *ca.* 80° and the N1–V1–N3 bond angles measure *ca.* 77°. This necessitates the N1–V1–N4 bond angle becoming more obtuse; these measure *ca.* 103° in the cationic PHEN complexes.

The delocalisation of electrons in the imino moiety (C4–C5–N3–C6) is again evident in the cationic complexes. The respective C4–C5 bond lengths are shorter (average 1.440(7) Å) than the standard C<sub>aromatic</sub>–C<sub>sp<sup>2</sup></sub> value of 1.485 Å.<sup>24,25</sup>

The N3–C6 bond lengths are longer (average of 1.401(5) Å) than the typical  $Nsp^2-C_{aromatic}$  bond length of 1.353 Å and the C5=N3 imine bond lengths are slightly longer (average of 1.293(5) Å) than the expected C=N bond length of 1.279 Å.<sup>24,25</sup> The C4–C5–N3 imine bond angles also deviate from ideality (average of 113°).

As in the neutral complexes, the *trans* effect of the oxo ligand leads to a significantly longer V1–N5 bond *trans* to the vanadyl group in comparison to the other V–N bonds. The PHEN ligand is approximately perpendicular to the equatorial plane with the dihedral angles subtended by the two mean planes measuring 82.61°, 86.35° and 84.72° for [VO(PHCA)(PHEN)](PF<sub>6</sub>), [VO(MECA)(PHEN)](PF<sub>6</sub>) and [VO(TERTCA)(PHEN)](PF<sub>6</sub>), respectively.

The terminal oxo group (O2) in [VO(PHCA)(PHEN)](PF<sub>6</sub>) and [VO(TERTCA)(PHEN)](PF<sub>6</sub>) form C–H···O interactions with the imine hydrogen atom on C5 of a neighbouring molecule. The H···A (H···O2) bond lengths are 2.496 Å for [VO(PHCA)(PHEN)](PF<sub>6</sub>) and 2.509 Å for [VO(TERTCA)(PHEN)](PF<sub>6</sub>), shorter than the sum of the van der Waals radii for hydrogen and oxygen of 2.72 Å, suggesting that these are genuine intermolecular interactions.<sup>26</sup> In addition, there are also intermolecular interactions between the phenolate oxygen (O1) and the methylene C–H of the dichloromethane solvent in [VO(PHCA)(PHEN)](PF<sub>6</sub>). No significant  $\pi$ - $\pi$  interactions are noted in these compounds.

## 5.6 Conclusions

The *O,N,O'*-tridentate ligands SOA and NAA were successfully characterised by single crystal X-ray diffraction and were shown to be in the ketone form. The SOA and NAA molecules are approximately planar with delocalisation of electrons in the imino moiety (C6–C7–N1–C8). The crystal structures of SOA and NAA are further stabilised by intramolecular hydrogen bonds between the protonated imine and ketone oxygen (N1–H101···O1).

The lattice of NAA is further stabilised by complementary intermolecular O2–H102···O1 hydrogen bonds between neighbouring symmetry-independent molecules, resulting in an 18-membered hydrogen-bonded ring. SOA also exhibited intermolecular O2–H102···O1 hydrogen bonds.

In addition, intermolecular attractions between an oxygen atom of the sulfonyl moiety and the protonated imine of a neighbouring molecule results in 16-membered rings. These dimer units in SOA are then linked by the intermolecular interactions to form one-dimensional columns.

The *O,N,N'*-tridentate ligands PHCA, MECA, TERTCA, PHPHCA were successfully characterised by single crystal X-ray diffraction and were shown to generally deviate from planarity. The most noticeable deviation is for PHCA(a) with a large angle subtended by the imidazole and phenyl rings (*ca.* 66°). PHCA(b) is approximately planar. Stabilising intramolecular interactions are present in the *O,N,N'* ligands between the imine hydrogen atom (H–C) and oxygen except in the case of the non-planar molecule of PHCA. The crystal structures of all *O,N,N'* ligands in this work exhibited intermolecular hydrogen bonds between the un-substituted imidazole nitrogen and the phenol OH on a neighbouring molecule. Sixteen-membered supramolecular dimeric ring structures are stabilised through these hydrogen bonds. The dimer units of PHCA are further linked by intermolecular C–H···O interactions to form one-dimensional columns.

The hemihydrate form of PHCA was also studied. PHCA·0.5H<sub>2</sub>O is also approximately planar. The water molecule bridges two ligands, acting as both an H-bond donor and H-bond acceptor, forming a water-bridged dimer. Intermolecular C–H···N interactions link the water-bridged dimers to form one-dimensional columns.

Of the neutral oxovanadium complexes, high resolution structures of [VO(CLA)(DPQ)] and [VO(TERTA)(DPQ)] were elucidated. Low-resolution structures were obtained for [VO(PHA)(DPQ)] and [VO(MEA)(DPPZ)]. The crystal structures all showed a monomeric vanadium(IV) species with the bidentate *N,N*-donor co-ligand and respective dianionic *O,N,O'*-tridentate ligand coordinated to the vanadyl (VO<sup>2+</sup>) moiety to form a V<sup>IV</sup>O<sub>3</sub>N<sub>3</sub> six-coordinate distorted octahedral geometry. The V–N bond *trans* to the vanadyl group is significantly longer than the other V–N bonds due to the *trans* effect of the oxo ligand. [VO(CLA)(DPQ)] and [VO(TERTA)(DPQ)] form moderate  $\pi$ – $\pi$  interactions between the rings of DPQ.

The X-ray structures of [VO(PHCA)(PHEN)](PF<sub>6</sub>), [VO(MECA)(PHEN)](PF<sub>6</sub>) and [VO(TERTCA)(PHEN)](PF<sub>6</sub>) were elucidated. The structures of the [VO(ONN)(PHEN)](PF<sub>6</sub>) complexes show a monomeric, monocationic vanadium(IV) species with the vanadium atom coordinated to one oxo ligand, one bidentate *N,N*-donor phenanthroline ligand and the respective monoanionic tridentate *O,N,N'*-donor Schiff base ligand to form a V<sup>IV</sup>O<sub>2</sub>N<sub>4</sub><sup>+</sup> six-coordinate distorted octahedron.

As in the neutral complexes, the *trans* effect of the oxo ligand is evident with a significantly longer V1–N<sub>phen</sub> bond *trans* to the vanadyl group in comparison to the other V–N bonds in the respective structures. [VO(PHCA)(PHEN)](PF<sub>6</sub>) and [VO(TERTCA)(PHEN)](PF<sub>6</sub>) exhibit intermolecular interactions between the oxo group and the imine C–H to form 10-membered rings. There are also intermolecular attractions between the phenolate oxygen and a hydrogen atom of the dichloromethane solvent in [VO(PHCA)(PHEN)](PF<sub>6</sub>).

The X-ray structures of the [VO(ONO)(DPQ)], [VO(MEA)(DPPZ)] and [VO(ONN)(PHEN)](PF<sub>6</sub>) complexes are in agreement with the structures proposed based on UV/visible, IR, ESI-MS and EPR spectroscopic techniques and elemental analysis. The molecular structures also indicate that the aromatic rings of the respective PHEN, DPQ or DPPZ ligand are in a position where they will be able to form interactions with the DNA helix.

## 5.7 References

1. Bruker APEX2, SAINT and SADABS, Bruker AXS Inc., Madison, Wisconsin, USA, 2012.
2. G.M. Sheldrick, *Acta Cryst.*, **2015**, C71, 3.
3. L.J. Farrugia, *J. Appl. Cryst.*, **2012**, 45, 849.
4. *Mercury CSD 2.0 - new features for the visualisation and investigation of crystal structures*, Macrae, C.F., Bruno, I.J., Chisholm, J. A., Edgington, P. R., McCabe, P., Pidcock, E., Rodriguez-Monge, L., Taylor, R., van de Streek, J. and Wood, P.A., *J. Appl. Cryst.*, **2008**, 41, 466.
5. Groom, C.R., Bruno, I.J., Lightfoot, M.P. and Ward, S.C., *Acta Cryst.*, **2016**, B72, 171.
6. Bruno, I. J., Cole, J. C., Edgington, P. R., Kessler, M., Macrae, C. F., McCabe, P., Pearson, J. and Taylor, R., *Acta Cryst.*, **2002**, B58, 389.
7. Ondráček, J., Kovářová, Z., Maixner, J. and Jursik, F., *Acta Cryst.*, **1993**, C49, 1948.
8. Lindeman, S.V., Antipin, M.Y. and Struchkov, Y.T., *Kristallografiya, (Russ.) (Crystallogr. Rep.)*, **1988**, 33, 365.
9. Mukherjee, A.K., De, R.L., Banerjee, I., Samanta, C. and Nayak, N.P., *Acta Cryst.*, **1999**, C55, 407.
10. Maciejewska, D., Pawlak, D. and Koleva, V., *J. Phys. Org. Chem.*, **1999**, 12, 875.
11. Mayer, P., Potgieter, K.C. and Gerber, T.I.A., *Polyhedron*, **2010**, 29, 1423.
12. Elerman, Y. and Elmali, A., *Acta Cryst.*, **1995**, C51, 2344.
13. Gao, J. and Xu, T.-T., *Synth. React. Inorg., Met.-Org., Nano-Met. Chem.*, **2008**, 38, 550.
14. Tunç, T., Sari, M., Sadikoğlu, M., and Büyükgüngör, O., *J. Chem. Crystallogr.*, **2009**, 39, 672.
15. Sun, Y., Wang, Y., Liu, Z., Huang, C. and Yu, C., *Spectrochim. Acta A*, **2012**, 96, 42.
16. Aslam, M., Anis, I., Afza, N., Hussain, M.T., Mehmood, R., Hussain, A., Yousuf, S., Iqbal, L., Iqbal, S. and Khan, I., *J. Chil. Chem. Soc.*, **2013**, 58, 1867.
17. Girisha, M., Sagar, B.K., Yathirajan, H.S., Rathore, R.S., Kaur, M., Jasinski, J.P. and Glidewell, C., *Acta Cryst.*, **2018**, C74, 1094.
18. Kabak, M., Elmali, A., and Elerman, Y., *J. Mol. Struct.*, **1999**, 477, 151.
19. Böhme, U. and Fels, S., CSD Communication (Private Communication), **2006**.
20. Wujiu, J., Daizhi, K., Yonglan, F., Jianxi, Y., Fuxing, Z. and Xiaoming, Z., *Chin. J. Org. Chem.*, **2014**, 34, 2288.

21. Elmali, A., Kabak, M., Kavlakoglu, E., Elerman, Y. and Durlu, T.N., *J. Mol. Struct.*, **1999**, 510, 207.
22. Böhme, U. and Fels, S., *Acta Cryst.*, **2008**, E64, o14.
23. Bürgi, H.B. and Dunitz, J.D., *Helv. Chim. Acta*, **1971**, 54, 1255.
24. Allen, F.H., Kennard, O., Watson, D.G., Brammer, L., Orpen, A.G. and Taylor, R., *J. Chem. Soc. Perkin Trans. II*, **1987**, S1.
25. Gavranić, M., Kaitner, B. and Meštrović, E., *J. Chem. Crystallogr.*, **1996**, 26, 23.
26. Bondi, A., *J. Phys. Chem.*, **1964**, 68, 441.
27. Kloskowski, M., Pursche, D., Hoffmann, R.-D., Pöttgen, R., Läge, M., Hammerschmidt, A., Glaser, T. and Krebs, B., *Z. Anorg. Allg. Chem.*, **2007**, 106.
28. Juaristi, E., Fingerhut, A., Vargas-Capporali, J., Leyva-Ramirez, M.A. and Tsogoeva, S.B., *CSD Communication (Private Communication)*, **2018**.
29. Fingerhut, A., Vargas-Caporali, J., Leyva-Ramírez, M.A. Juaristi, E., and Tsogoeva, S.B., *Molecules*, **2019**, 24, 3182.
30. Boudier, A., Breuil, P.-A.R., Magna, L., Olivier-Bourbigou, H. and Braunstein, P., *J. Organometal. Chem.*, **2012**, 718, 31.
31. Howson, S.E., Allan, L.E.N., Chmel, N.P., Clarkson, G.J., Deeth, R.J., Faulkner, A.D., Simpson, D.H. and Scott, P. *Dalton Trans.*, **2011**, 40, 10416.
32. Gu, Z.-G., Pang, C.-Y., Qiu, D., Zhang, J., Huang, J.-L., Qin, L.-F., Sun, A.-Q., and Li, Z., *Inorg. Chem. Commun.*, **2013**, 35, 164.
33. Qin, L.-F., Pang, C.-Y., Han, W.-K., Zhang, F.-L., Tian, L., Gu, Z.-G., Ren, X. and Li, Z., *Cryst. Eng. Comm.*, **2015**, 17, 7956.
34. Tian, L., Pang, C.-Y., Zhang, F.-Li, Qin, L.-F, Gu, Z.-G and Li, Z., *Inorg. Chem. Commun.*, **2015**, 53, 55.
35. Becerra, A., Contreras, R., Carmona, D., Lahoz, F.J. and García-Orduna, P., *Dalton Trans.*, **2013**, 42, 11640.
36. Mandal, S., Poria, D.K., Seth, D.K., Ray, P.S. and Gupta, P., *Polyhedron*, **2014**, 73, 12.
37. Choy, S.W.S., Page, M.J., Bhadbhade, M. and Messerle, B.A., *Organometallics*, **2013**, 32, 4726.
38. Kozlyuk, N., Lopez, T., Roth, P., and Acquaye, J.H., *Inorg. Chim. Acta.*, **2015**, 428, 176.
39. Kennedy, D.F., Messerle, B.A. and Smith, M.K., *Eur. J. Inorg. Chem.*, **2007**, 80.
40. Kennedy, D.F., Messerle, B.A. and Rumble, S.L., *New J. Chem.*, **2009**, 33, 818.

41. García-Deibe, A.M., Portela-García, C., Fondo, M., Mota, A.J., and Sanmartín-Matalobos, J., *Chem. Commun.*, **2012**, *48*, 9915.
42. Sanmartín-Matalobos, J., Portela-García, C., Fondo, M., and García-Deibe, A.M., *Cryst. Growth Des.*, **2015**, *15*, 4318.
43. Gerlach, D., Brendler, E., Heine, T. and Wagler, J., *Organometallics*, **2007**, *26*, 234.
44. Orr Jr, L.B., Parsons, E.J. and Pennington, W.T., *Acta Crystallogr., Sect. C: Cryst. Struct. Commun.*, **1992**, *48*, 2042.
45. Yanga, G.-S., Liua, C.-B., Lia, H.N., Chena, Y., Huanga, D.-H. and Wen, H.-L., *Chin. J. Struct. Chem.*, **2014**, *33*, 528.
46. Mandal, S., Das, M., Das, P., Samanta, A., Butcher, R.J., Saha, M., Alswaidan, I.A., Rhyman, L., Ramasami, P. and Saha, N.C., *J. Mol. Struct.*, **2019**, *1178*, 100.
47. Wazalwar, S.S., Banpurkar, A.R. and Perdih, F., *J. Chem. Cryst.*, **2018**, *48*, 185.
48. Barry, K.L., Grimmer, C.D., Munro, O.Q. and Akerman, M.P., *RSC Adv.*, **2020**, *10*, 7867.
49. Akerman, M.P. and Chiazzari, V.A., *J. Mol. Struct.*, **2014**, *1058*, 22.
50. Yuan, C., Lu, L., Gao, X., Wu, Y., Guo, M., Li, Y., Fu, X and Zhu, M., *J. Biol. Inorg. Chem.*, **2009**, *14*, 841.
51. Yuan, C., Lu, L., Wu, Y., Liu, Z., Guoa, M., Xing, S., Fu, X. and Zhu, M., *J. Inorg. Biochem.*, **2010**, *104*, 978.
52. Lu, L., Yue, J., Yuan, C., Zhu, M., Han, H., Liu, Z. and Guo, M., *J. Inorg. Biochem.*, **2011**, *105*, 1323.
53. Sasmal, P., Patra, A.K., Nethaji, M. and Chakravarty, A.R., *Inorg. Chem.*, **2007**, *46*, 11112.
54. Zhai, S., Guo, Q., Dong, J., Xu, T. and Li, L., *Transit. Met. Chem.*, **2014**, *39*, 271.
55. Bian, L., Li, L., Zhang, Q., and Wang, D., *Acta Cryst.*, **2010**, *E66*, m1051.
56. Bian, L., Li, L., Zhang, Q., Liu, H. and Wang, D., *Acta Chim. Sinica*, **2011**, *69*, 1661.
57. Bian, L., Li, L.-Z., Wang, X., Huang, L., Pu, X.-W., Dong, J.-F., *Chinese J. Inorg. Chem.*, **2011**, *27*, 649.
58. Bian, L., Li, L., Zhang, Q., Dong, J., Xu, T., Li, J. and Kong, J., *Transit. Met. Chem.*, **2012**, *37*, 783.
59. Cao, Y.-Z., Zhao, H.-Y., Bai, F.-Y., Xing, Y.-H., Wei, D.-M., Niu, S.-Y. and Shi, Z., *Inorg. Chim. Acta*, **2011**, *368*, 223.

60. Cao, Y., Yi, C., Liu, H., Li, H., Li, Q., Yuan, Z. and Wei, G., *Transit. Met. Chem.*, **2016**, *41*, 531.
61. Chatterjee, M., Ghosh, S., Wu, B.-M., and Mak., T.C.W, *Polyhedron*, **1998**, *17*, 1369.
62. Feng, Y.X., Xue, L.W. and Zhang, C.X., *Russ. J. Coord. Chem.*, **2014**, *40*, 337.
63. Gryboś, R., Szklarzewicz, J., Jurowska, A. and Hodorowicz, M., *J. Mol. Struct.*, **2018**, *1171*, 880.
64. Guo, Q., Li, L., Dong, J., Liu, H., Xue, Z. and Xu, T., *Acta Chim. Sinica*, **2012**, *70*, 1617.
65. Jing, B.Q., Dong, J.F., Li, J.H., Xu T. and Li, L.Z., *J. Coord. Chem.*, **2013**, *66*, 520.
66. Jing, B., Dong, J., Wei, Q., Xu, T. and Li, L., *Transit. Met. Chem.*, **2014**, *39*, 605.
67. Li, L.-Z., Jing, B.-Q., Li, L.-W., and Xu, T., *Z. Kristallogr.- New Cryst. Struct.*, **2006**, *221*, 520.
68. Li, L., Guo, Z., Zhang, Q., Xu, T. and Wang, D., *Inorg. Chem. Commun.*, **2010**, *13*, 1166.
69. Ma, X.T., Xing, N., Yan, Z.D., Zhang, X.X., Wu, Q. And Xing, Y.H., *New J. Chem.*, **2015**, *39*, 1067.
70. Meng, X.-F., Liu, Q.-F., Liu, J.-L., Sun, M.-H. and Ma, J.-J., *Inorg. Nano-Met. Chem.*, **2017**, *47*, 1585.
71. Ni, L., Zhao, H., Tao, L., Li, X., Zhou, Z., Sun, Y., Chen, C., Wei, D., Liu, Y., and Diao, G., *Dalton Trans.*, **2018**, *47*, 10035.
72. Pranczk, J., Jacewicz, D., Wyrzykowski, D., Wojtczak, A., Tesmar, A. and Chmurzyński, L., *Eur. J. Inorg. Chem.*, **2015**, 3343.
73. Saha, U., Si. T.K., Nandi, P.K. and Mukherjea, K.K., *Inorg. Chem. Commun.*, **2013**, *38*, 43.
74. Shit., M., Bera, S., Maity, S., Maji, S., Weyhermüller, T. and Ghosh, P., *Eur. J. Inorg. Chem.*, **2016**, 330.
75. Shit., M., Maity, S., Bera, S., Weyhermüller, T. And Ghosh, P., *New J. Chem.*, **2016**, *40*, 10305.
76. Sutradhar, M., Martins, L.M.D.R.S., Guedes da Silva, M.F.C. and Pombeiro, A.J.L., *Appl. Catal. A-Gen.*, **2015**, *493*, 50.
77. Szklarzewicz, J., Jurowska, A., Hodorowicz, M., Gryboś, R. And Matoga, D., *J. Mol. Struc.*, **2019**, *1180*, 839.
78. Wang, C.-Y., Jing, B.-Q., Dong, J.-F. and Li, L.-Z., *Acta Cryst.*, **2012**, *E68*, m907.

79. Wang, Y., Lin, X.-M., Bai, F.-Y. and Sun, L.-X., *J. Mol. Struct.*, **2017**, 1149, 379.
80. Xu, T., Li, L.-Z., Zhou, S.-F., Guo, G.-Q. and Niu, M.-J., *J. Chem. Crystallogr.*, **2005**, 35, 263.
81. Zhao, H.-Y., Xing, Y.-H., Cao, Y.-Z., Li, Z.-P., Wei, D.-M., Zeng, X.-Q. and Ge, M.-F., *J. Mol. Struct.*, **2009**, 938, 54.
82. Prasad, P., Sasmal, P.K., Majumdar, R., Dighe, R.R. and Chakravarty, A.R., *Inorg. Chim. Acta*, **2010**, 363, 2743.
83. Prasad, P., Sasmal, P.K., Khan, I., Kondaiah, P. and Chakravarty, A.R., *Inorg. Chim. Acta*, **2011**, 372, 79.
84. Prasad, P., Khan, I., Kondaiah, P. and Chakravarty, A.R., *Chem. Eur. J.*, **2013**, 19, 17445.
85. Sasmal, P.K., Majumdar, R., Dighe, R.R. and Chakravarty, A.R., *Dalton Trans.*, **2010**, 39, 7104.
86. Sasmal, P.K., Saha, S., Majumdar, R., Dighe, R.R., and Chakravarty, A.R., *Inorg. Chem.*, **2010**, 49, 849.
87. Banerjee, S., Hussain, A., Prasad, P., Khan, I., Banik, B., Kondaiah, P. and Chakravarty, A.R., *Eur. J. Inorg. Chem.*, **2012**, 3899.
88. Banik, B., Sasmal, P.K., Roy, S., Majumdar, R., Dighe, R.R. and Chakravarty, A.R., *Eur. J. Inorg. Chem.*, **2011**, 1425.
89. Tasiopoulus, A.J., Tolis, E.J., Tsangaris, J.M., Evangelou, A., Woollins, J.D., Slawin, A.M.Z., Costa Pessoa, J., Correia, I. and Kabanos, T.A., *J. Biol. Inorg. Chem.*, **2002**, 7, 363.
90. Tasiopoulos, A.J., Troganis, A.N., Deligiannakis, Y., Evangelou, A., Kabanos, T.A., Woollins, J.D., and Slawin, A., *J. Inorg. Biochem.*, **2000**, 79, 159.
91. Tasiopoulos, A.J., Deligiannakis, Y.G., Woollins, J.D., Slawin, A.M.Z. and Kabanos, T.A., *Chem. Commun.*, **1998**, 569.

## Chapter Six: Density Functional Theory

### 6.1 Introduction to Density Functional Theory

As mentioned in *Chapter 1*, DNA binding constants for [VO(ONO)(NN)] complexes are dependent on steric and electronic properties of the coordinated ligands.<sup>1-8</sup> Molecular simulations using Density Functional Theory (DFT) were therefore employed to gain a further understanding of the molecular geometries, energies and spectroscopic properties of the [VO(ONO)(NN)] and [VO(ONN)(NN)]<sup>+</sup> complexes. The DFT simulations will also be used to predict the optimised structures of complexes for which X-ray data is unavailable. In addition, geometry optimisations, frequency and energy simulations were run for the dimeric and monomeric structures of the *O,N,N'* ligands to further probe the stability of these structures.

DFT has become the most common approach to quantum chemical simulations of electronic structure and properties.<sup>9</sup> DFT uses electron density as the primary quantity to determine the ground-state electronic energy of a molecule<sup>10-12</sup> instead of the many-body electronic wave function approach of traditional Hartree-Fock (HF)<sup>13,14</sup> and post-HF methods.<sup>12,15-17</sup> DFT is more accurate than HF calculations (which treat electron-electron interactions in an approximation). It does not, however, have the high computational demands as the more accurate post-HF methods such as Möller-Plesset perturbation theory and Configuration Interaction.<sup>15,16,18</sup>

In DFT, a density functional is used to calculate the energy for the electron density.<sup>17</sup> Electron density itself is a function of the position coordinate (functionals are functions of functions).<sup>15</sup> Several density functional methods exist with increasing degrees of accuracy to correlate the electron density and energy.<sup>12,18</sup> The B3LYP functional is a common choice for transition metal compounds and free ligands.<sup>16</sup> Previous studies of oxovanadium complexes with tridentate Schiff base ligands have used the B3LYP functional.<sup>19-23</sup> B3LYP is the Becke, three parameter hybrid functional with the non-local correlation functional of Lee-Yang-Parr.<sup>24-26</sup> It is a hybrid generalised gradient approximation (GGA) functional which mixes GGA with exact HF exchange. GGA functionals depend on the electron density and its reduced gradient.<sup>16-18</sup>

The electron density itself can be represented by a choice of several mathematical functions (basis sets).<sup>15</sup> A basis set is a set of functions used to describe the shape of the orbital in an atom.<sup>17</sup> The type of basis set used also influences the accuracy of the calculations.<sup>12</sup> Atom-centered, rather than planewave function, basis sets are more appropriate for calculations on molecules.<sup>15</sup> 6-311G was the basis set chosen for this study. It is applicable for atoms H to Kr<sup>17</sup> and is more sophisticated than the minimal Slater-type basis sets.<sup>27</sup> 6-311G is a triple split valence, Pople Style basis set where the core orbitals are a contraction of six primitive Gaussian-type orbitals with the valence split into three functions.<sup>12,17,27</sup>

## 6.2 Experimental

Geometry optimisations, frequency and energy DFT simulations were performed on the oxovanadium complexes and the monomeric and dimeric species of the *O,N,N'* ligands in this work using Gaussian 09 W.<sup>28</sup> Geometry optimisations were performed using the X-ray coordinates as the input structures for the *O,N,N'* ligands and [VO(CLA)(DPQ)], [VO(TERTA)(DPQ)], [VO(PHA)(DPQ)], [VO(MEA)(DPPZ)] and [VO(ONN)(PHEN)]<sup>+</sup> complexes. The counter ion of the cationic complexes and any solvent molecules of crystallisation were removed from the input files. The starting structures for the remaining complexes were generated using GaussView 5.0.<sup>29</sup> All simulations were run at the B3LYP/6-311G level of theory and single first polarisation and diffuse functions (dp) were added to the basis set.<sup>30</sup> Diffuse functions help describe orbitals with a large spatial extent. Polarisation functions have a higher angular momentum than the occupied orbitals, such as adding *d* orbitals to carbon, to better span the function space.<sup>17</sup> The geometries were optimised with a singlet spin state for the *O,N,N'* ligands and doublet spin state for the paramagnetic oxovanadium complexes. All input files were prepared, and output files analysed through GaussView 5.0.<sup>29</sup> The vibrational frequencies indicate that the geometry optimisations are true minima on the global potential energy surface based on the lack of negative Eigen values.

Electronic spectra were simulated for the *in-vacuo* geometry-optimised structures with 24 and 64 excited states for the *O,N,N* ligands and oxovanadium complexes, respectively, using the TD-SCF method at the same level of theory used for the geometry optimisations.<sup>31-39</sup> A Polarizable Continuum Model (PCM) was included in the simulations of transition energies and oscillator strengths to account for any solvent effects.<sup>38,39</sup>

An acetonitrile solvent continuum was used to mimic the experimental conditions. The molecular orbitals were assigned by studying the spatial distribution of their isosurfaces. Singlet excited states were considered for the  $O,N,N'$  ligands and alpha and beta spin states for the oxovanadium complexes.

### 6.3 DFT Studies of the Tridentate Schiff Base Ligands

Numerous reports of geometry optimisations and frequency simulations by AM1 molecular orbital semi-empirical quantum-mechanical and DFT methods have been reported for numerous  $O,N,O$  Schiff-base ligands.<sup>40-43</sup> The DFT simulations in this work therefore focus on the novel  $O,N,N'$  ligands. The DFT study for PHCA, MECA and TERTCA has been reported as part of this PhD study.<sup>44</sup>

Of the  $O,N,N'$  ligands in this work two distinct molecular configurations exist in the solid-state for PHPHCA and anhydrous PHCA (*Section 5.3.3*). Geometry optimisations and frequency simulations on the dimeric and monomeric structures of the  $O,N,N'$  ligands were, therefore, conducted to further probe the lowest energy conformations of this class of ligands. A comparison of the DFT-simulated and solid-state structures for the monomeric ligands are indicated in *Figure 6.1*. The least-square-fits were calculated using Mercury 2020.2.0.<sup>45</sup> The root-mean-square deviations (RMSD) indicate the experimental and lowest-energy simulated structures are generally in good agreement for the monomers, except for the PHCA(a) and PHPHCA (b) molecules. A comparison of the bond lengths and bond angles confirms the agreement (within 4%) between the experimental and simulated monomer structures. A summary of selected bond lengths and bond angles is reported in *Tables D1 – D4* in *Appendix D* for PHCA, MECA, TERTCA and PHPHCA. In addition, the vibrational frequency results of the experimental and simulated monomer and dimer structures are in good agreement with a 2-4% difference for the imine stretching frequency. A summary of the imine stretching frequencies for the experimental and DFT-simulated monomer and dimer  $O,N,N'$  molecules is reported in *Table D5, Appendix D*.

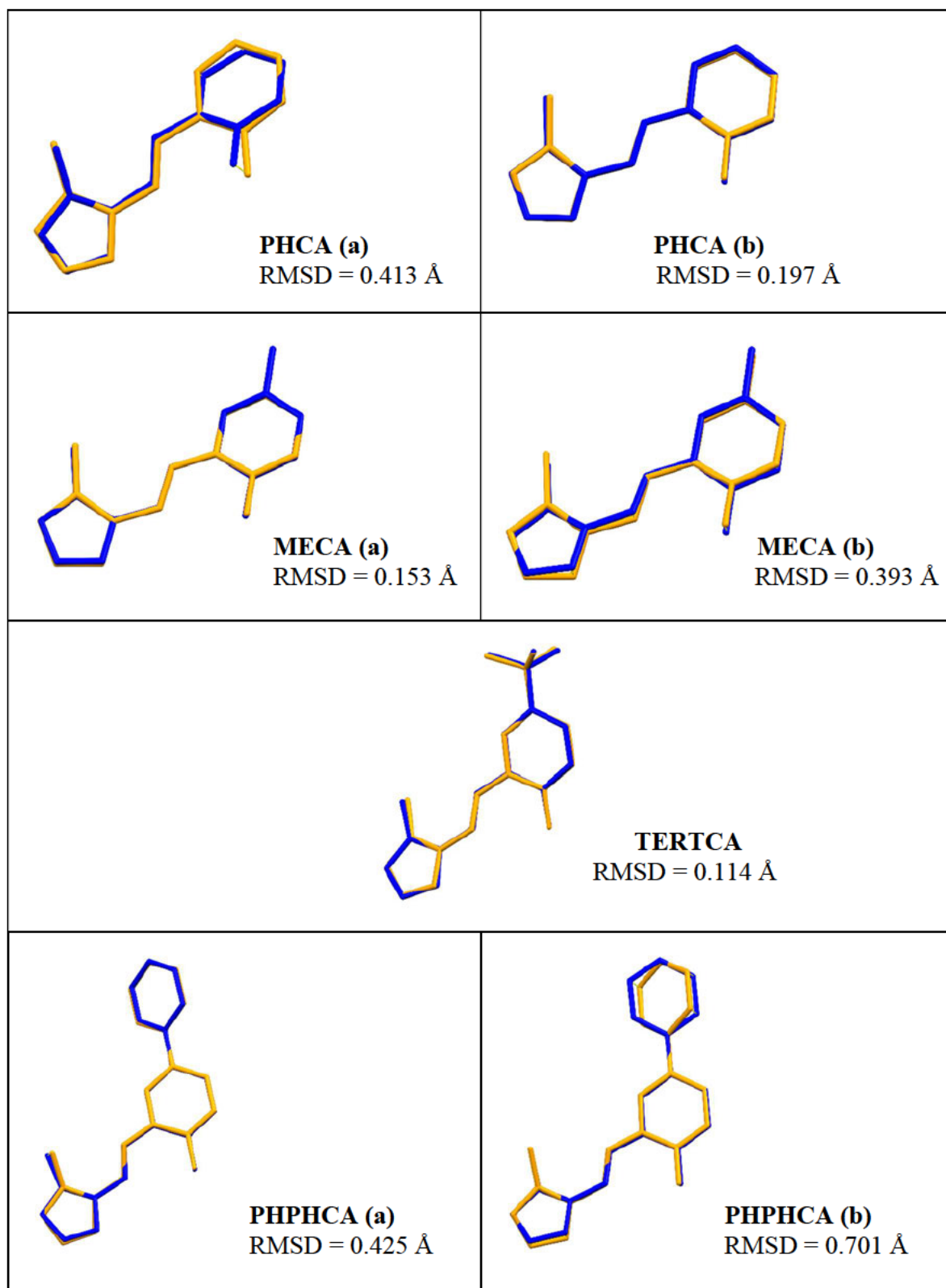


**Figure 6.1** Least-squares-fits of the DFT-simulated (yellow) and X-ray crystal structures (blue) of the monomeric *O,N,N'* ligands. Root mean square deviations (RMSD) for all non-hydrogen atoms are indicated on the diagram.

The two distinct molecular configurations that exist in the solid-state for PHCA and PHPHCA were probed, using scan simulations, to calculate the total energy of the molecule as a function of the phenol ring rotation for PHCA and of the phenyl ring rotation for PHPHCA to determine the lowest energy conformations.

The main difference between the two solid-state conformations of PHPHCA is the relative angle of the phenol and phenyl ring mean planes. The angle subtended by the mean planes of the non-hydrogen atoms of the phenol and phenyl rings in the solid-state structures is  $40^\circ$  for PHCA (a) and  $17^\circ$  for PHPHCA (b). The total energy of the molecules as a function of the relative angles of the phenyl and phenol rings was simulated for PHPHCA using  $10^\circ$  increments in the C9-C10-C12-C17 torsion angle. The atom numbering is indicated in *Figure 6.2* and the scan coordinate result is shown in *Figure 6.3*.

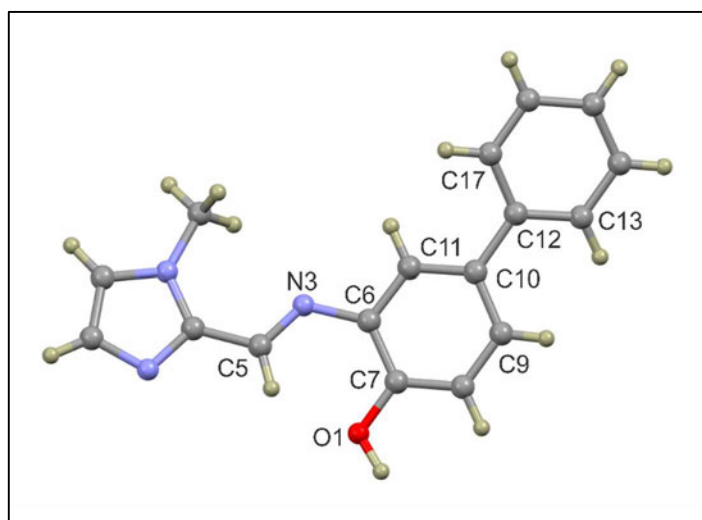


**Figure 6.2** Atom numbering used for PHPHCA.

The energy scan coordinate indicates that the highest energy conformations of PHPHCA are when the phenyl and phenol mean planes are in either a perpendicular or co-planar orientation. The perpendicular arrangement prevents overlap of the *p*-orbitals and breaks the  $\pi$ -conjugation of the molecule. In the co-planar arrangement, non-bonded repulsion occurs between H-C11 and H-C17 and between H-C9 and H-C13. The DFT-simulated lowest energy conformation has a C9-C10-C12-C17 torsion angle of  $141.05^\circ$ . This rotation of the phenyl ring decreases the steric repulsion whilst still maintaining some stabilising *p*-orbital overlap.

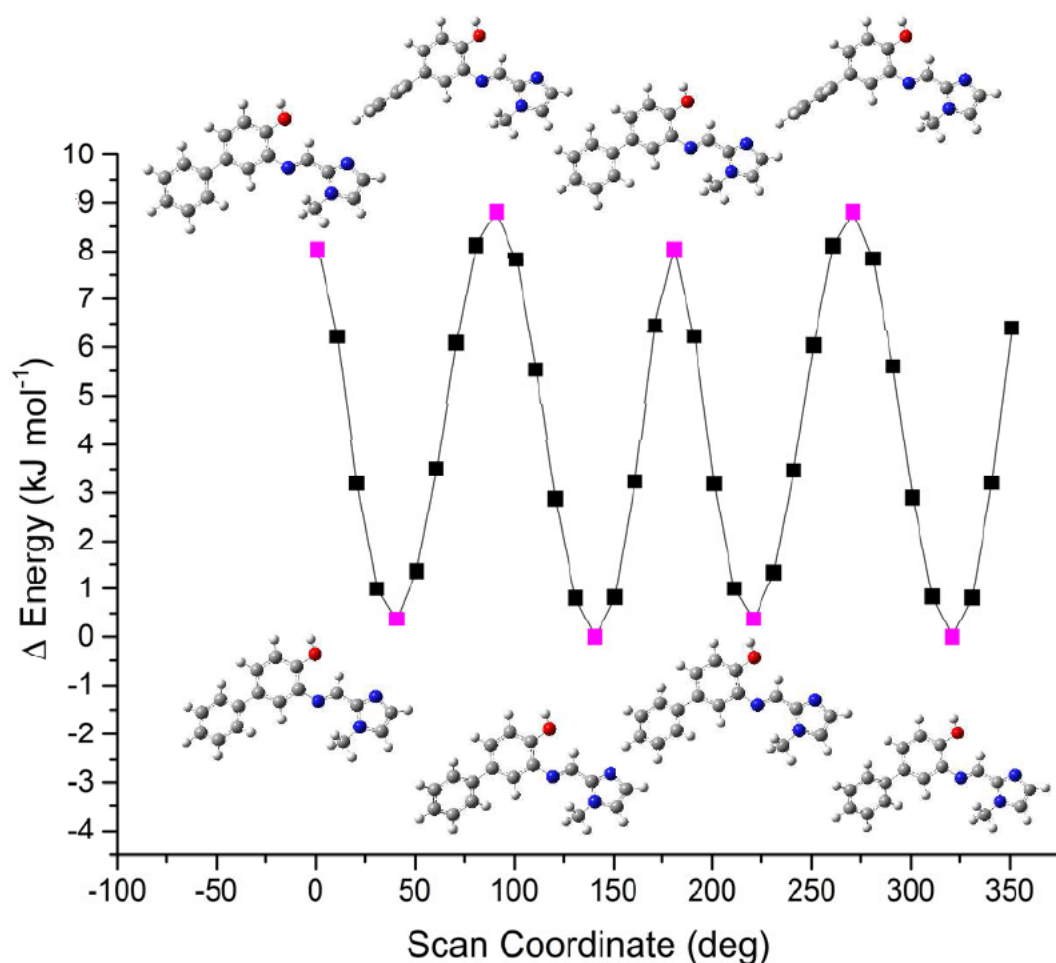


**Figure 6.3** Relative energy of PHPHCA as a function of the C9-C10-C12-C17 torsion angle. The energy maxima and minima are highlighted in magenta with their corresponding structures. All energy values are referenced against the lowest energy conformation.

The 141.05° C9-C10-C12-C17 torsion angle of the simulated lowest energy conformation matches very closely with the 141.7(1)° C9-C10-C12-C17 torsion angle of the solid-state PHPHCA (a) molecule. The other solid-state conformation of PHPHCA has a C9-C10-C12-C17 torsion angle of -161.5(1)°. The calculated energy difference between the solid-state conformations is relatively small: 3.9 kJ mol<sup>-1</sup>. This small energy difference may explain why PHPHCA was able to adopt different geometries in the solid-state. Deviations from the true lowest energy conformations in the solid-state can allow for more favourable packing of the molecules or stronger intermolecular interactions, which offset the energy difference.

The difference between the two independent solid-state structures of PHCA is the C5–N3–C6–C7 torsion angle (see atom numbering in *Figure 6.2*). This torsion angle measures  $-59.1(2)^\circ$  for molecule (a) and  $-7.6(2)^\circ$  for the relatively planar molecule (b). The total energy of the molecules as a function of this torsion angle was simulated by rotating the phenyl and imidazole rings in  $10^\circ$  increments. The relationship between energy and molecular geometry for PHCA as a function of the C5–N3–C6–C7 torsion angle is shown in *Figure 6.4*.

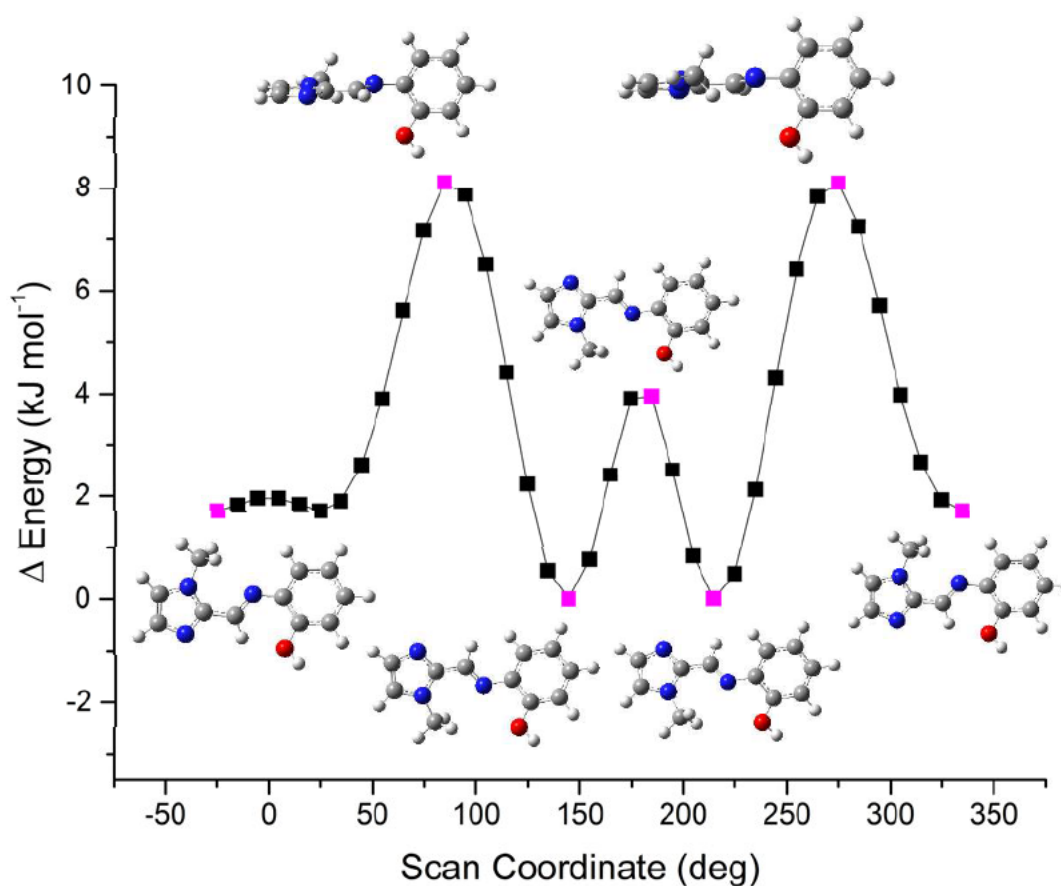


**Figure 6.4** Relative energy of PHCA as a function of the C5–N3–C6–C7 torsion angle. The energy maxima and minima are highlighted in magenta with their corresponding structures. All energy values are referenced against the lowest energy conformation.

In the solid-state structures of PHCA the imine C–H and hydroxy groups are in a *cis*-configuration to maximise complementary hydrogen bonding between the imidazole nitrogen and phenolic OH to form dimeric structures. This configuration also minimises repulsion between the OH and imidazole N–CH<sub>3</sub> groups.

The imine C–H and phenolic OH are also in a *cis*-configuration in the DFT-optimised structure with a C5-N3-C6-C7 torsion angle measuring  $-25.26^\circ$  (Step 1 in *Figure 6.4*). The energy scan revealed the true energy minimum is when the imine C–H and OH group are *trans*, with the C5-N3-C6-C7 torsion angle measuring  $144.74^\circ$  (Step 18 in *Figure 6.4*) in the absence of packing constraints. The energy difference between these conformations is a modest  $1.7 \text{ kJ mol}^{-1}$ .

MECA, TERTCA and PHPHCA have a similar out-of-plane rotation in the lowest energy conformations. The C5–N3–C6–C7 torsion angles measure:  $-22.33^\circ$ ,  $23.75^\circ$  and  $-28.53^\circ$  for MECA, TERTCA and PHPHCA, respectively. A co-planar arrangement of the phenol and imidazole rings would maximise *p*-orbital overlap of the imine and phenol ring. An out-of-plane rotation, however, decreases the steric repulsion between the imine C–H and phenol moiety leading to a more stable molecule. The difference in energy for PHCA with a co-planar arrangement of the phenyl and imidazole moieties and the non-planar arrangement (where the C5-N3-C6-C7 torsion angle is  $145^\circ$ ) is only  $2.0 \text{ kJ mol}^{-1}$ . This small energy difference may explain why both geometries are viable options in the solid-state. Previous studies of the geometry-optimised structures of MEA, CLA and closely related benzyldeneaniline molecules show that the most stable free-molecule conformation is similarly non-planar.<sup>40,41,46,47</sup>

The DFT-simulated dimeric structures have larger RMS deviations than the corresponding monomer species when compared to the solid-state structures (*Figure 6.5*). The major difference between the simulated and experimental dimeric structures is in the relative angle of rotation between the two molecules that comprise the dimer. The molecules that comprise the dimer in the solid-state can be considered approximately co-planar. The angle subtended by the two 15-atom mean planes of the non-hydrogen atoms of the imidazole, phenol and imine groups is  $0^\circ$  for PHCA and TERTCA,  $2^\circ$  for MECA and  $4^\circ$  for PHPHCA in the solid-state. This is in comparison to an average of  $35^\circ$  for the DFT-simulated lowest-energy conformations of the dimers. There is only a  $0.9 \text{ kJ mol}^{-1}$  difference in energy between the co-planar and lowest energy dimeric PHCA structures, where the angle subtended by the two 15-atom mean planes is  $34.10^\circ$ .

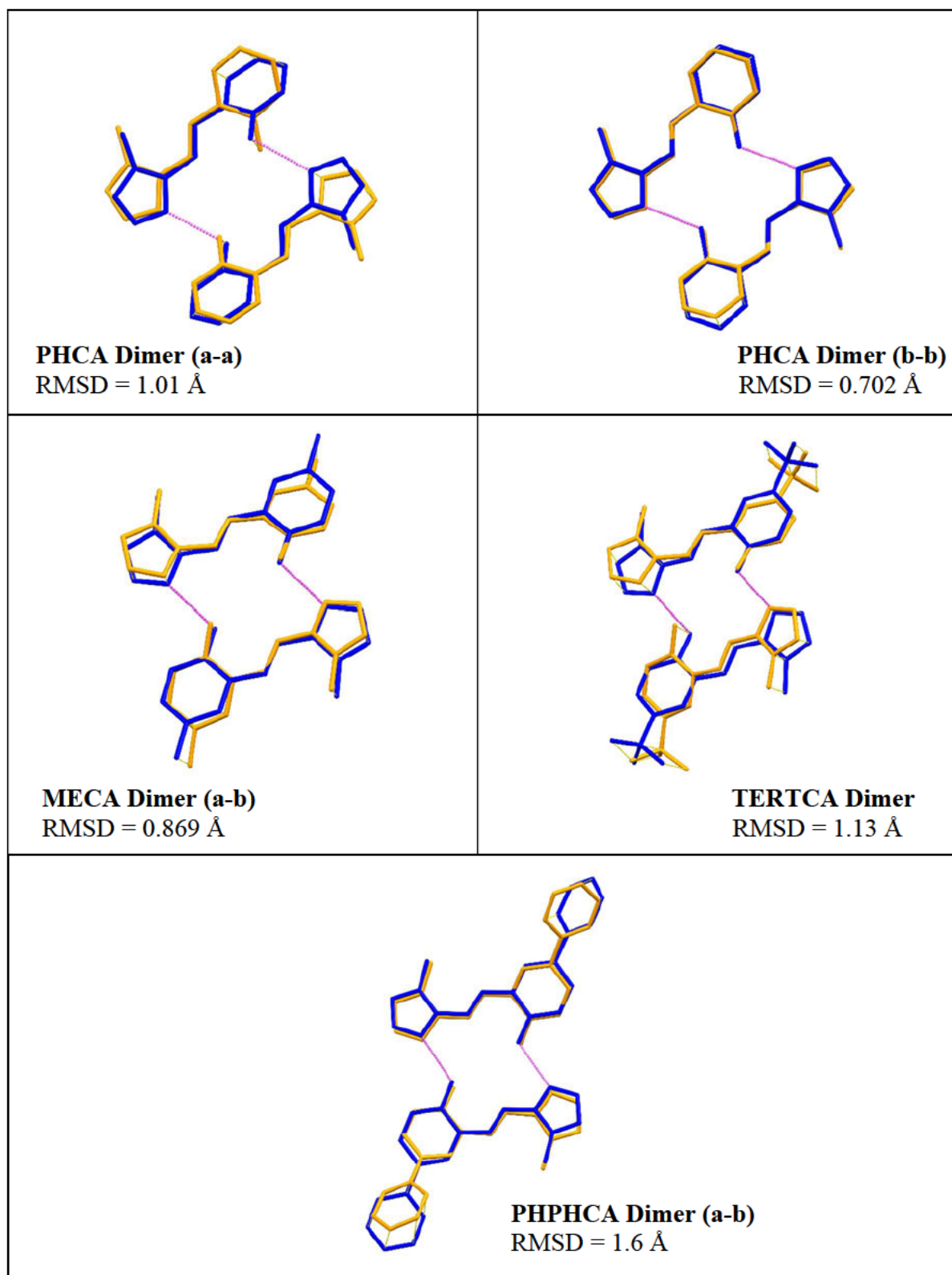


**Figure 6.5** Least-squares-fits of the DFT-simulated (yellow) and X-ray crystal structures (blue) of the dimeric *O,N,N'* ligand species. Root mean square deviations (RMSD) for all non-hydrogen atoms are indicated on the diagram.

There is also a difference in symmetry between the solid-state and DFT-simulated dimer structures. The solid-state dimers in TERTCA and PHCA are related by inversion symmetry while the molecules of the MECA and PHPHCA dimers are symmetry independent. The PHCA (a-a), MECA, TERTCA and PHPHCA DFT-simulated dimers are related through  $C_2$  symmetry. The PHCA (b-b) dimers are of  $C_i$  symmetry.

Despite the difference in symmetry of the solid-state and gas-phase dimer structures the hydrogen bonding motif is the same with two complementary O–H···N hydrogen bonds. The bond parameters are also comparable. The electrostatic potential (ESP) plots indicate that intermolecular hydrogen bonding between the imidazole nitrogen and the phenolic OH group is favourable (based on simple electrostatic arguments). The ESP plots are shown in *Figure 6.6* for PHPHCA and in *Figure D1, Appendix D* for PHCA, MECA and TERTCA.

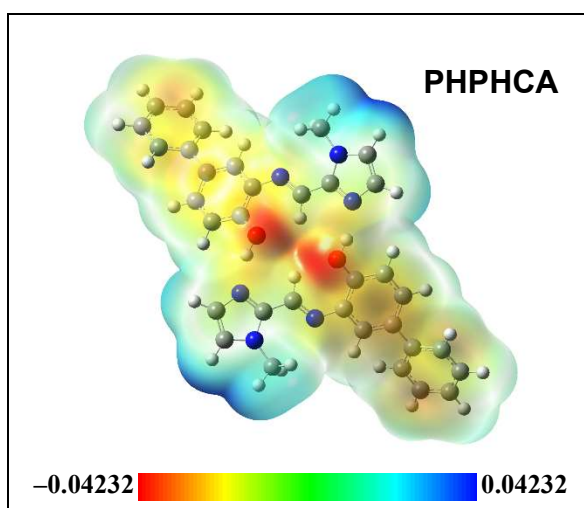


**Figure 6.6** Electrostatic potential map from the total SCF density for the PHPHCA dimer, highlighting the zones of positive (blue) and negative (red) potential.

The partial charge distribution (NBO charges, measured in electrons) indicates that in fact the oxygen atom carries the most negative partial charge. The imidazole N atom has the second highest partial negative charge in both the dimeric and monomeric species. The hydroxyl hydrogen atom has the highest positive partial charge. NBO charges are indicated in *Figure D2, Appendix D*. In the literature, (JUBKOG) hydrogen bonds are preferentially formed between the two phenols.<sup>48</sup>

Hydrogen bonds are, however, preferentially formed with the less negative nitrogen acting as the H-bond acceptor in this work. This is likely a result of being able to form complementary O-H $\cdots$ N interactions between the phenol and imidazole, as opposed to a single H-bond between the two phenols.

The stability gained by forming hydrogen bonds compensates for the individual molecules not being in their lowest energy conformation.<sup>49</sup> The DFT-simulated hydrogen-bonded dimers are significantly lower in energy than two independent monomers by an average of  $103\pm 1$  kJ mol<sup>-1</sup>. The small standard deviation indicates that in the gas phase the substituent on the phenol ring has effectively no influence on the strength of the hydrogen bonds.

DFT simulations were also used to better understand the electronic spectra of the free ligands. Superposition plots of the experimental and simulated UV/visible spectra are shown in *Figure 6.7* for MECA (as a representative example) and in *Figure D3, Appendix D* for PHCA, TERTCA and PHPHCA. The simulated spectra show good correlation with the experimental data in terms of the  $\lambda_{\text{max}}$  values, especially for the dimer conformations (the simulated data were not normalised). Considering that the DFT studies indicated the hydrogen-bonded dimeric structures are more stable than the monomers in the gas phase, and the experimental <sup>1</sup>H NMR study (*Section 4.2.4*) also shows dimerisation of the ligands takes place in solution it is expected that the UV/visible data should similarly indicate the dimer in solution. This is supported by the similarity of the experimental and simulated data for the dimeric species.

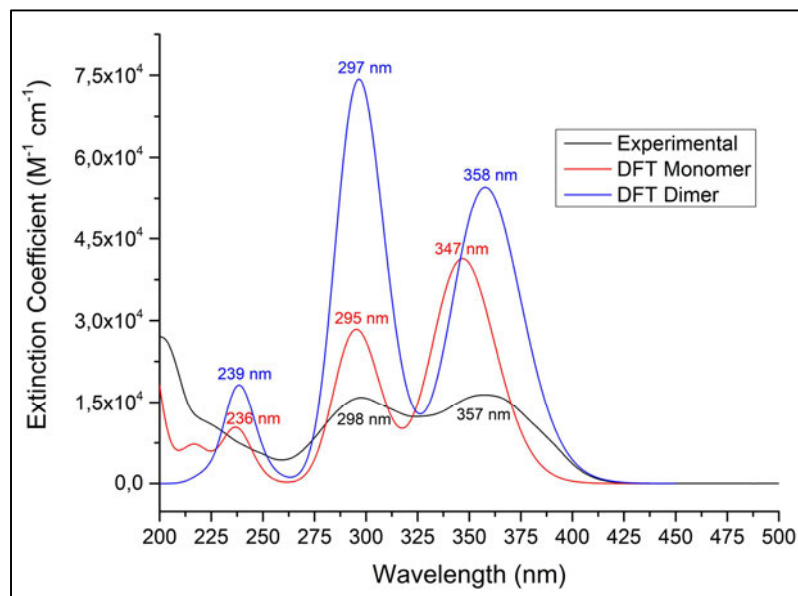


**Figure 6.7** Superposition plots of the experimental and the TD-DFT-simulated ( $CH_3CN$  solvent continuum) simulated UV/visible spectra of MECA for both the monomeric and dimeric species.

*Table 6.1* indicates the main TD-DFT-simulated transitions and oscillator strengths for the monomeric and dimeric species of MECA. The main transitions and oscillator strengths for the simulated monomeric and dimeric species of PHCA, TERTCA and PHPHCA are reported in *Tables D6 – D8, Appendix D*. These data show the absorption spectra are dominated by high energy  $\pi \rightarrow \pi^*$  transitions for both the monomeric and dimeric species.

**Table 6.1** Summary of the major TD-DFT-simulated (CH<sub>3</sub>CN solvent continuum) electronic transitions and oscillator strengths for the monomeric and dimeric structures of MECA and the corresponding molecular orbitals.

$\lambda$ (nm) <sup>a</sup>	Oscillator Strength, f	Molecular Orbitals	Contri- bution <sup>b</sup>	Assignment <sup>c</sup>
<b>MECA Monomer</b>				
346.80	0.5701	57 (HOMO) → 58 (LUMO)	91%	$\pi$ (Imd, Im, Phenol, Me) → $\pi^*$ (Imd, Im, Phenol)
294.22	0.3213	54 (HOMO-3) → 58 (LUMO)	11%	$\pi$ (N-Me, Imd, Im, Phen) → $\pi^*$ (Imd, Im, Phenol)
		55 (HOMO-2) → 58 (LUMO)	45%	$\pi$ (N-Me, Imd, Im, Phen) → $\pi^*$ (Imd, Im, Phenol)
		56 (HOMO-1) → 58 (LUMO)	32%	$\pi$ (Imd, Im, Phenol, Me) → $\pi^*$ (Imd, Im, Phenol)
237.08	0.1371	54 (HOMO-3) → 58 (LUMO)	36%	$\pi$ (N-Me, Imd, Im, Phen) → $\pi^*$ (Imd, Im, Phenol)
		55 (HOMO-2) → 58 (LUMO)	12%	$\pi$ (N-Me, Imd, Im, Phen) → $\pi^*$ (Imd, Im, Phenol)
		57 (HOMO) → 59 (LUMO+1)	34%	$\pi$ (Imd, Im, Phenol, Me) → $\pi^*$ (Phenol, Me)
<b>MECA Dimer</b>				
356.29	0.6102	113 (HOMO-1) → 115 (LUMO)	83%	$\pi$ (Imd, Im, Phenol, Me) → $\pi^*$ (Imd, Im, Phenol)
		114 (HOMO) → 116 (LUMO+1)	10%	$\pi$ (Imd, Im, Phenol, Me) → $\pi^*$ (Imd, Im, Phenol)
295.18	0.7453	109 (HOMO-5) → 116 (LUMO+1)	16%	$\pi$ (Imd, Im, Phenol) → $\pi^*$ (Imd, Im, Phenol)
		110 (HOMO-4) → 115 (LUMO)	20%	$\pi$ (N-Me, Imd, Im, Phenol) → $\pi^*$ (Imd, Im, Phenol)
		112 (HOMO-2) → 115 (LUMO)	44%	$\pi$ (Imd, Im, Phenol, Me) → $\pi^*$ (Imd, Im, Phenol)
238.57	0.2213	107 (HOMO-7) → 116 (LUMO+1)	13%	$\pi$ (Imd, Im, Phenol) → $\pi^*$ (Imd, Im, Phenol)
		108 (HOMO-6) → 115 (LUMO)	19%	$\pi$ (Imd, Im, Phenol) → $\pi^*$ (Imd, Im, Phenol)
		113 (HOMO-1) → 117 (LUMO+2)	11%	$\pi$ (Imd, Im, Phenol, Me) → $\pi^*$ (Phenol)
		114 (HOMO) → 118 (LUMO+3)	33%	$\pi$ (Imd, Im, Phenol, Me) → $\pi^*$ (Phenol)

<sup>a</sup> Three of the 24 simulated excited states with the highest oscillator strengths are listed.

HOMO: Highest occupied molecular orbital.

LUMO: Lowest unoccupied molecular orbital.

<sup>b</sup> Only orbitals with >10% contribution are listed.

<sup>c</sup> Imd = imidazole; Im = imine; Phenol = benzene ring + OH; Phen = benzene ring; N-Me = imidazole N-CH<sub>3</sub>; Me = phenolic methyl substituent.

The highest occupied molecular orbital (HOMO) and lowest unoccupied molecular orbital (LUMO) plots are shown in *Figure 6.8* for MECA and in *Figure D4, Appendix D* for PHCA, TERTCA and PHPHCA.

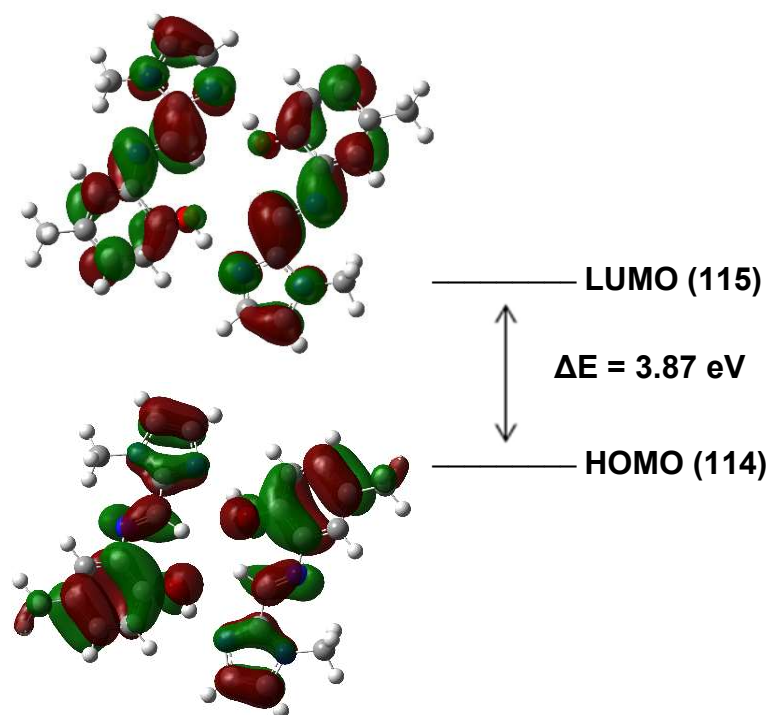


**Figure 6.8** DFT-simulated HOMO and LUMO plots for the geometry-optimised (gas phase) dimer of MECA. The energy gap between the two orbitals is indicated on the diagram.

The HOMO and LUMO plots of the dimers indicate they are of  $\pi$ -symmetry and that they span both molecules. The dimers can, therefore, be considered as supramolecular structures with  $\pi$ -electrons spread over both molecules as previously reported for pyrrole-imine Schiff base hydrogen-bonded dimers.<sup>49</sup> The dimeric structures also have smaller LUMO-HOMO energy gaps than the corresponding monomers by 0.13, 0.16, 0.15 and 0.18 eV for PHCA, MECA, TERTCA and PHPHCA, respectively. Considering a high level of theory was used and diffuse functions incorporated into the calculations, the results can be considered as reliable. This is further supported by the good correlation between the experimental and simulated data, as discussed above.

## 6.4 DFT Studies of the [VO(ONO)(NN)] and [VO(ONN)(NN)]<sup>+</sup> Complexes

One of the objectives of the DFT simulations was to elucidate the geometry-optimised structures of the oxovanadium complexes for which X-ray data were not available. A comparison of the DFT-simulated and solid-state structures was, therefore, performed for those complexes where experimental data were available. The simulations were run using the same level of formula as the ligands. The 6-311G(dp) basis set covers vanadium and imposes fewer restrictions on the electrons compared to methods like LanL2DZ where effective core potentials are applied.<sup>50</sup> Structural overlays (least-squares-fit) of the geometry-optimised and solid-state structures were calculated using Mercury 2020.2.0 and are reported in *Figure 6.9*.<sup>45</sup> The small root-mean-square deviations (non-H atoms) indicate the experimental and simulated structures are in good agreement. This suggests that the level of theory used is appropriate, and the simulated structures are likely to be accurate representations of the respective molecules.

Structural overlays were also performed for those complexes for which low-resolution experimental structures were obtained, namely [VO(PHA)(DPQ)], [VO(MEA)(DPPZ)] and [VO(PHPHCA)(PHEN)]<sup>+</sup>. The overlays are reported in *Figure D5, Appendix D*. The RMSDs range from 0.2450 Å to 0.4867 Å.

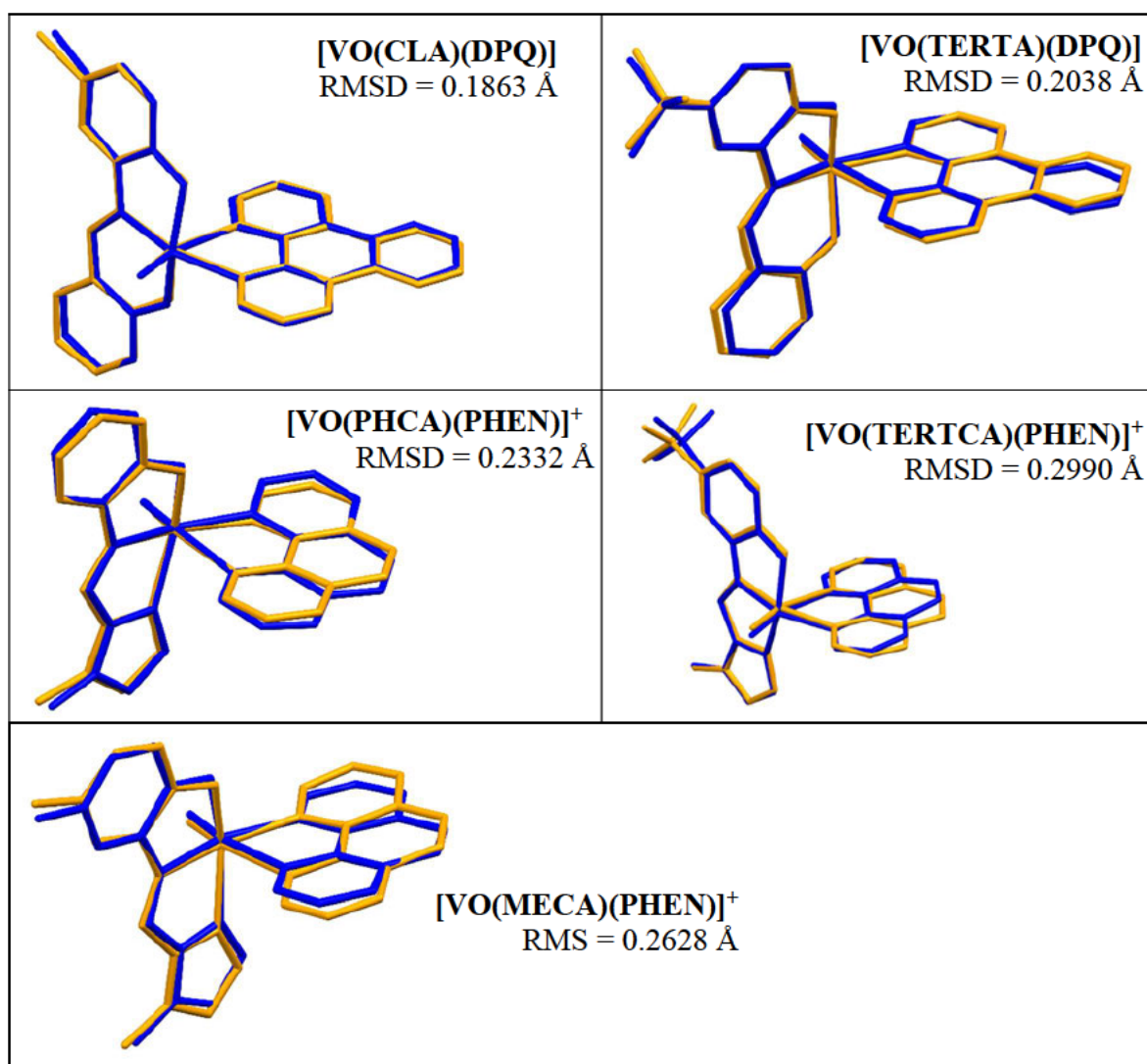


**Figure 6.9** Least-squares-fits of the DFT-optimised (yellow) and solid-state (blue) structures of [VO(CLA)(DPQ)], [VO(TERTA)(DPQ)], [VO(PHCA)(PHEN)]<sup>+</sup>, [VO(MECA)(PHEN)]<sup>+</sup> and [VO(TERTCA)(PHEN)]<sup>+</sup> complexes. Root mean square deviations (RMSD) for all non-hydrogen atoms are indicated on the diagram.

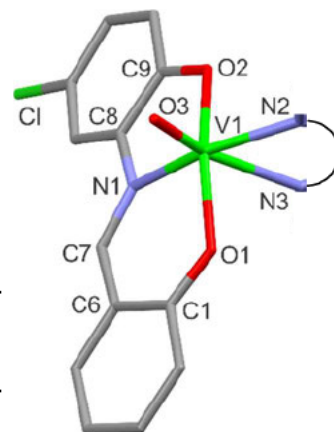
A comparison of selected bond lengths and bond angles for the DFT-simulated and solid-state structures is shown in *Table 6.2* below for [VO(CLA)(DPQ)] and in *Tables D9 – D12, Appendix D* for [VO(TERTA)(DPQ)], [VO(PHCA)(PHEN)]<sup>+</sup>, [VO(MECA)(PHEN)]<sup>+</sup> and [VO(TERTCA)(PHEN)]<sup>+</sup>. The bond lengths and bond angles are in good agreement, within 5% difference. This again highlights the suitability of the chosen DFT method.

**Table 6.2** Comparison of selected bond parameters for the solid-state and DFT-simulated structures of [VO(CLA)(DPQ)]. Atom numbers are indicated in the appended structure.

<b>Bond Lengths</b> (Å)	<b>Experimental</b>	<b>Simulated</b>	<b>% Difference</b>
V1–O1	1.964(2)	1.964	0
V1–O2	1.988(2)	1.960	1.4
V1–O3	1.608(2)	1.582	1.6
V1–N1	2.079(2)	2.096	-0.82
V1–N2	2.143(2)	2.199	-2.6
V1–N3	2.365(2)	2.449	-3.6
C6–C7	1.433(4)	1.430	0.21
C7–N1	1.303(4)	1.303	0
N1–C8	1.432(3)	1.415	1.2

<b>Bond Angles</b> (°)	<b>Experimental</b>	<b>Simulated</b>	<b>% Difference</b>
O3–V1–N1	105.42(9)	104.09	1.3
O3–V1–N2	92.84(9)	91.25	1.7
O3–V1–N3	164.73(8)	161.46	2.0
O3–V1–O1	100.51(8)	102.17	-1.7
O3–V1–O2	100.61(8)	104.66	-4.0
C6–C7–N1	125.4(2)	126.05	-0.5



\* % difference = (experimental – simulated / experimental x 100)

The double-bond character of the vanadyl moiety is evident in the DFT-simulated structures with shorter vanadyl (V=O3) bond distances in comparison to the other V–O bond lengths in the optimised structures. The elongation of the V–N3 bond *trans* to the oxo ligand in comparison to the other V–N bonds in the structure is also evident.

A distorted octahedral geometry is also noted in the simulated structures with deviations from 90° of the O–V–N and O–V–O bond angles (these are explained by the same arguments used in the X-ray section, *Chapter 5*). The simulated structures indicate a displacement of the vanadium ion out of the equatorial plane towards the oxo ligand. The vanadium atom is 0.362 Å and 0.364 Å above the O2–N1–O1–N2 equatorial plane in comparison to the experimental values of 0.341 Å and 0.355 Å for [VO(CLA)(DPQ)] and [VO(TERTA)(DPQ)], respectively. The displacement of the V atom out of the equatorial plane (N<sub>imidazole</sub>–N<sub>imine</sub>–O<sub>phenol</sub>–N<sub>DPQ</sub>) is 0.319 Å, 0.320 Å and 0.322 Å for the DFT-simulated structures in comparison to 0.312 Å, 0.310 Å and 0.321 Å for the solid-state structures of [VO(PHCA)(PHEN)]<sup>+</sup>, [VO(MECA)(PHEN)]<sup>+</sup> and [VO(TERTCA)(PHEN)]<sup>+</sup>, respectively.

The slight twist of the *O,N,O'*-tridentate ligand was also observed in the DFT-simulated neutral oxovanadium complexes. The dihedral angle between the two chelate rings of the tridentate Schiff base ligand with vanadium (V1/N1/C8/C9/O2 and V1/N1/C7/C6/C1/O1) is 12.07° and 12.33° for the simulated structures of [VO(CLA)(DPQ)] and [VO(TERTA)(DPQ)], respectively. This is similar to the 10.54° and 10.20° dihedral angles for the solid-state structures of [VO(CLA)(DPQ)] and [VO(TERTA)(DPQ)], respectively. The DFT-simulated structures for the cationic oxovanadium complexes have a smaller dihedral angle between the two chelate rings of the *O,N,N'* Schiff base ligand, as reported for the solid-state structures. The dihedral angle between the two 5-membered chelate ring planes of the *O,N,N'* ligand is 9.46°, 9.62° and 9.42° for the simulated structures versus 7.75°, 8.57° and 8.49° for the experimental structures for [VO(PHCA)(PHEN)]<sup>+</sup>, [VO(MECA)(PHEN)]<sup>+</sup> and [VO(TERTCA)(PHEN)]<sup>+</sup>, respectively.

The delocalisation along the imino moiety of the respective Schiff base ligands is evident in the DFT-simulated metal structures. The respective C-C<sub>imine</sub> bond lengths are shorter, and the C-N<sub>imine</sub> bond lengths are longer than expected values.<sup>51,52</sup>

The *N,N* ligands in the optimised structures are perpendicular to the equatorial plane as in the solid-state structures. The dihedral angles of the mean plan of DPQ to the equatorial plane (defined as O<sub>2phenol</sub>-N<sub>imine</sub>-O<sub>1phenol</sub>-N<sub>DPQ</sub>) range from 87 - 89° in the geometry-optimised structures and 83 - 90° in the experimental, solid-state structures.

The slight deviations between the DFT-simulated lowest energy conformations and the solid-state structures could be due to the absence of intra- and intermolecular attractions in the DFT (gas phase) structures. In the experimental structures there is, for example,  $\pi$ - $\pi$  stacking of the DPQ rings in [VO(TERTA)(DPQ)] and [VO(CLA)(DPQ)] and various C-H $\cdots$ X intermolecular interactions between complex and solvent molecules.

Vibrational frequency results of the simulated structures are in good agreement with the solid-state infrared spectra. There is a 0.2 - 2 % difference in the imine stretching frequencies, 10 - 12 % difference for the V=O stretching frequencies and 0.5 - 9 % difference for the V-O stretching frequencies. The simulated frequencies were consistently higher than the experimental vibrational frequencies. Selected stretching frequencies for the simulated and experimental solid-state complexes are reported in *Table 6.3*.

**Table 6.3** C=N, V=O and V–O stretching frequencies ( $\text{cm}^{-1}$ ) for the DFT-simulated and solid-state oxovanadium complexes.

Neutral Complexes	C=N Experi mental	C=N DFT	V=O Experi mental	V=O DFT	V–O Experi mental	V–O DFT
[VO(PHA)(DPQ)]	1600	1636	958	1062	532	547
[VO(MEA)(DPQ)]	1599	1630	955	1062	533	549
[VO(TERTA)(DPQ)]	1603	1630	949	1061	535	551
[VO(CLA)(DPQ)]	1599	1635	945	1063	532	547
[VO(SOA)(DPQ)]	1600	1634	953	1064	533	547
[VO(NAA)(DPQ)]	1600	1624	954	1061	565	572
[VO(PHPHA)(DPQ)]	1597	1629	959	1062	534	549
[VO(MEA)(DPPZ)]	1601	1630	948	1054	533	549
Cationic Complexes	C=N Experi mental	C=N DFT	V=O Experi mental	V=O DFT	V–O Experi mental	V–O DFT
[VO(PHCA)(PHEN)] <sup>+</sup>	1582	1613	959	1069	555	584
[VO(MECA)(PHEN)] <sup>+</sup>	1604	1610	961	1069	557	553
[VO(TERTCA)(PHEN)] <sup>+</sup>	1600	1607	968	1069	557	553
[VO(PHPCA)(PHEN)] <sup>+</sup>	1601	1605	965	1069	556	598
[VO(MECA)(DPQ)] <sup>+</sup>	1581	1610	967	1071	556	553
[VO(TERTCA)(DPQ)] <sup>+</sup>	1581	1607	967	1071	556	553
[VO(MECA)(DPPZ)] <sup>+</sup>	1577	1610	966	1079	605	553

The comparisons of the experimental and simulated data above show a good level of agreement. This suggests that DFT methods are suitable to predict the structures of the complexes for which X-ray data are not available. The DFT-simulated structures are presented in *Figure 6.10* for those complexes where X-ray data are not available.

The DFT-simulated geometry-optimised structures for the complexes all show that the respective PHEN, DPQ or DPPZ ligand is free from steric hindrance by the tridentate ligand and protrudes from the molecule. This means it should be available to bind to DNA *in vitro* and *in vivo*.

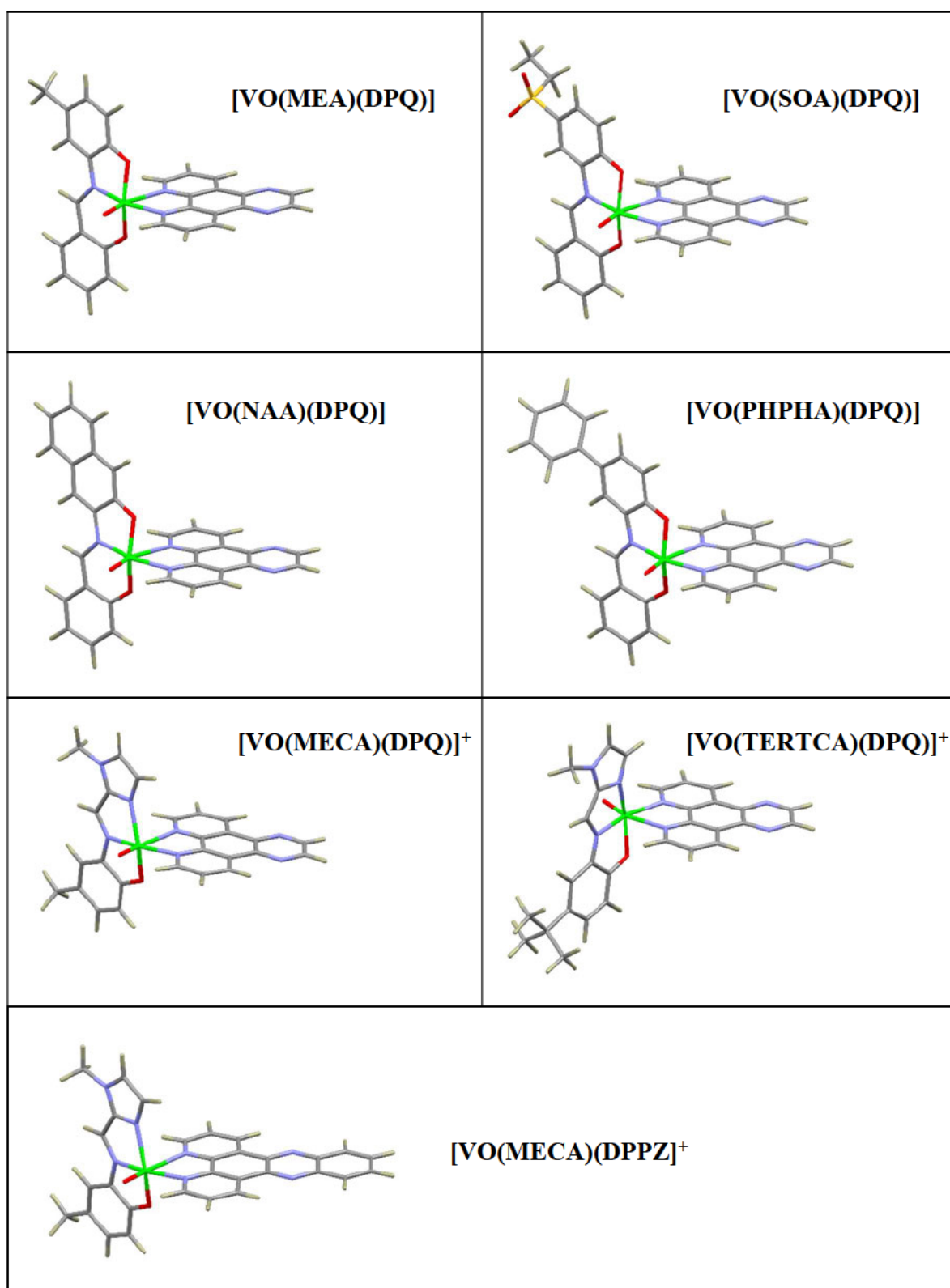


**Figure 6.10** DFT-simulated geometry-optimised structures (B3LYP/6-311G(dp) level of theory) of [VO(MEA)(DPQ)], [VO(SOA)(DPQ)], [VO(NAA)(DPQ)], [VO(PHPHA)(DPQ)], [VO(MECA)(DPQ)]<sup>+</sup>, [VO(TERTCA)(DPQ)]<sup>+</sup> and [VO(MECA)(DPPZ)]<sup>+</sup>.

The bond lengths for the DFT-simulated structures presented in *Figure 6.10*, indicate the V=O, V–O<sub>phenol</sub> and V–N<sub>DPQ/DPPZ</sub> *trans* bond lengths are shorter in the cationic complexes than in the analogous DPQ and DPPZ neutral complexes. The V–N<sub>imine</sub> bond is longer in the DFT-simulated cationic complexes than in the analogous neutral complexes (*Table 6.4*).

**Table 6.4** A comparison of selected dft-simulated V=O, V–O and V–N bond lengths (Å) for the analogous neutral and cationic oxovanadium(IV) complexes.

Complex	V=O	V–O ( <i>aminophenol</i> )	V–N <sub>imine</sub>	V– N <sub>DPQ/DPPZ</sub> <i>trans</i> V=O
[VO(MEA)(DPQ)]	1.582	1.955	2.096	2.455
[VO(MECA)(DPQ)] <sup>+</sup>	1.574	1.947	2.123	2.384
[VO(TERTA)(DPQ)]	1.583	1.956	2.096	2.454
[VO(TERTCA)(DPQ)] <sup>+</sup>	1.574	1.949	2.122	2.385
[VO(MEA)(DPPZ)]	1.583	1.955	2.096	2.449
[VO(MECA)(DPPZ)] <sup>+</sup>	1.575	1.949	2.123	2.380

The calculated NBO partial charges (measured in electrons) of selected atoms are shown in *Table 6.5* for the neutral complexes and in *Table 6.6* for the cationic complexes. The NBO partial charges of vanadium in the neutral and cationic complexes is less than its valence of +4. The charges of the coordinated O and N atoms indicate the vanadium ion has removed some electron density from the chelated ligands. Similar results have been reported in the literature for closely related [VO(ONO)(NN)] complexes with a salicylidene-glycinate Schiff base ligand.<sup>53</sup>

The effect of the electron-withdrawing sulfonyl group is evident by the higher partial charges of the oxo ligand and the aminophenol oxygen atom in [VO(SOA)(DPQ)] in comparison to the other neutral complexes (*Table 6.5*). Likewise, the coordinated imine nitrogen atom is affected by substituents on the Schiff base ligand. The complexes with electron-donating groups ([VO(MEA)(DPQ)] and [VO(TERTA)(DPQ)]) have a higher partial charge on the imine nitrogen atom than those with electron-withdrawing groups ([VO(CIA)(DPQ)] and [VO(SOA)(DPQ)]), (*Table 6.5*).

**Table 6.5** Partial NBO charges (e) of selected atoms in the neutral oxovanadium(IV) complexes.

Complex	V	O oxo	O amino phenol	N imine	O phenol	N DPQ trans Oxo	N DPQ trans imine N
[VO(PHA)(DPQ)]	1.460	-0.507	-0.728	-0.548	-0.721	-0.484	-0.496
[VO(MEA)(DPQ)]	1.461	-0.508	-0.729	-0.547	-0.721	-0.483	-0.495
[VO(TERTA)(DPQ)]	1.462	-0.508	-0.728	-0.546	-0.722	-0.483	-0.496
[VO(CLA)(DPQ)]	1.461	-0.503	-0.726	-0.553	-0.718	-0.486	-0.497
[VO(SOA)(DPQ)]	1.460	-0.497	-0.718	-0.556	-0.717	-0.488	-0.498
[VO(NAA)(DPQ)]	1.459	-0.506	-0.726	-0.556	-0.717	-0.485	-0.496
[VO(PHPHA)(DPQ)]	1.461	-0.505	-0.724	-0.550	-0.720	-0.485	-0.496
[VO(MEA)(DPPZ)]	1.461	-0.508	-0.729	-0.547	-0.721	-0.484	-0.496

**Table 6.6** Partial NBO charges (e) of selected atoms in the cationic oxovanadium(IV) complexes.

Complex	V	O oxo	O amino phenol	N imine	N imid- azole	N trans Oxo O	N trans imine N
[VO(PHCA)(PHEN)] <sup>+</sup>	1.456	-0.452	-0.692	-0.481	-0.562	-0.525	-0.518
[VO(MECA)(PHEN)] <sup>+</sup>	1.456	-0.453	-0.692	-0.481	-0.564	-0.524	-0.518
[VO(TERTCA)(PHEN)] <sup>+</sup>	1.456	-0.454	-0.692	-0.480	-0.565	-0.524	-0.518
[VO(PHPHCA)(PHEN)] <sup>+</sup>	1.455	-0.453	-0.691	-0.482	-0.563	-0.524	-0.518
[VO(MECA)(DPQ)] <sup>+</sup>	1.456	-0.454	-0.692	-0.482	-0.565	-0.527	-0.520
[VO(TERTCA)(DPQ)] <sup>+</sup>	1.456	-0.454	-0.692	-0.481	-0.565	-0.526	-0.521
[VO(MECA)(DPPZ)] <sup>+</sup>	1.457	-0.454	-0.692	-0.481	-0.564	-0.528	-0.521

The effect of changing the tridentate ligand from *O,N,O'*- to *O,N,N'*-donor is also evident in the electrostatic plots. Representative electrostatic potential (ESP) plots for [VO(MEA)(DPQ)], [VO(MECA)(DPQ)]<sup>+</sup> and [VO(SOA)(DPQ)] are shown in *Figure 6.11*. The ESP plots for the remaining complexes are reported in *Figures D6 and D7, Appendix D*. The ESP plots indicate there are more zones of positive potential (blue) in the cationic complexes as compared to the neutral complexes.

This highlights the cationic nature of these complexes and their ability to form electrostatic interactions with the negatively charged phosphate backbone of DNA.<sup>54</sup> The effect of the electron-withdrawing sulfonyl group is also noted. The ESP plots of the neutral complexes indicate that most of the electron density (red) is centred on the terminal oxo group (*Figure D6, Appendix D*). The exception being the sulfonyl complex, where most of the electron density is centred on the sulfonyl oxo groups (*Figure 6.11*). Amino-Schiff base ligands are known to not only be sterically-tuned, but electronically as well, by variation of the ligand pre-cursors.<sup>53</sup>

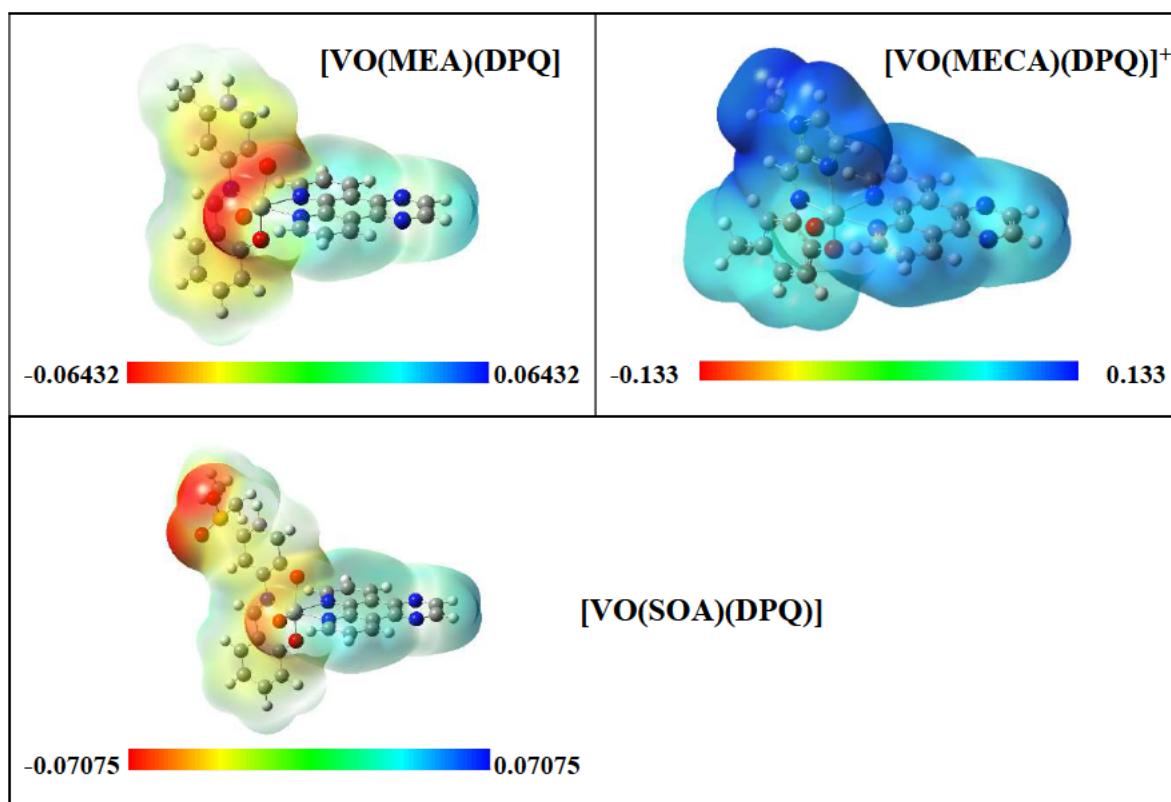


**Figure 6.11** ESP maps from the total SCF density for the neutral complexes [VO(MEA)(DPQ)] and [VO(SOA)(DPQ)] and the cationic complex [VO(MECA)(DPQ)]<sup>+</sup> highlighting the zones of positive (blue) and negative (red) electrostatic potential.

To better understand the electronic structure of the complexes, the UV/visible spectra were simulated for the geometry-optimised structures. The TD-DFT method was used, at the same level of theory as used for the geometry optimisations with an acetonitrile solvent Polarizable Continuum Model. Representative examples of superposition plots of the experimental and DFT-simulated UV/visible spectra are indicated in *Figure 6.12* for [VO(MEA)(DPQ)] and in *Figure 6.13* for [VO(MECA)(DPQ)]<sup>+</sup>.

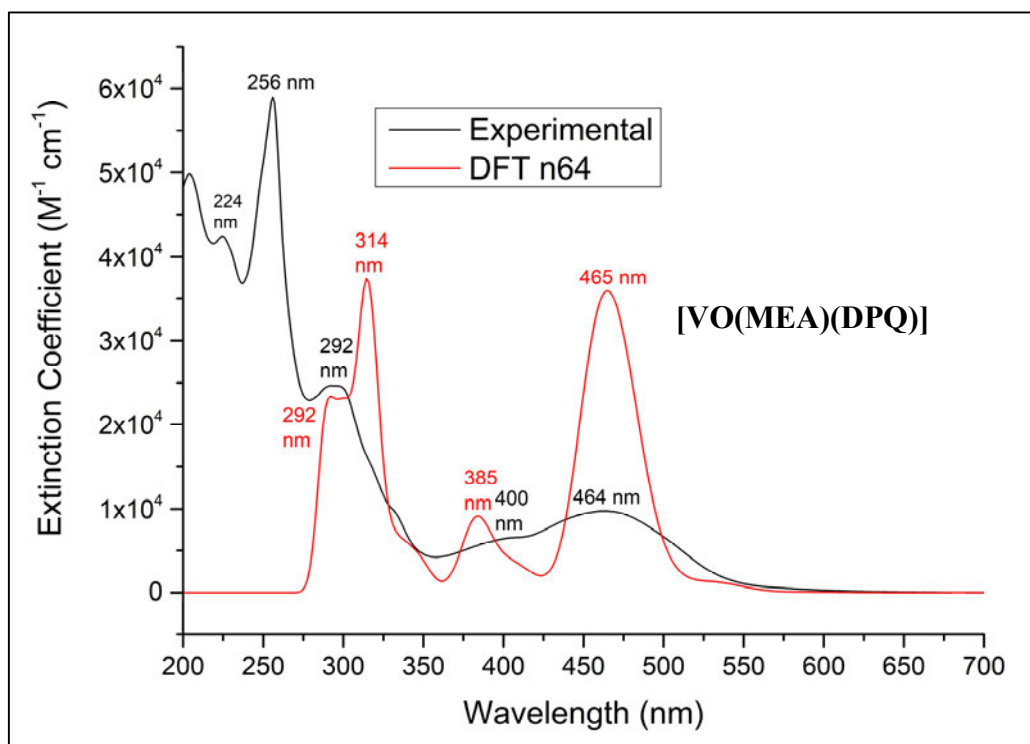


**Figure 6.12** Superposition plots of the experimental and the TD-DFT-simulated ( $CH_3CN$  solvent continuum) UV/visible spectra of  $[VO(MEA)(DPQ)]$ .

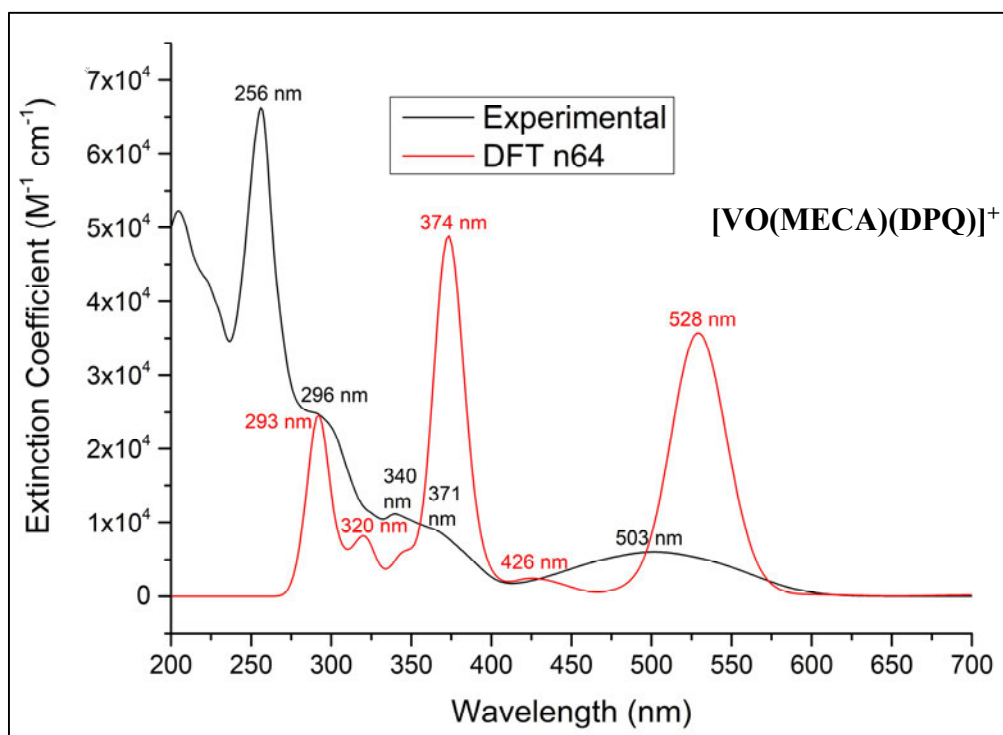


**Figure 6.13** Superposition plots of the experimental and the TD-DFT-simulated ( $CH_3CN$  solvent continuum) UV/visible spectra of  $[VO(MECA)(DPQ)]^+$ .

Superposition plots of the experimental and DFT-simulated UV/visible spectra for the remaining complexes are available in *Figures D8 – D10, Appendix D*. The superposition plots show good correlation between the experimental and simulated  $\lambda_{\max}$  values for the LMCT (ONO  $\rightarrow$  V<sup>IV</sup>) band around 460 nm in the neutral complexes (see *Figure 6.12* and *Figure D8* in *Appendix D*). For example, 465 nm versus 464 nm for the DFT-simulated and experimental LMCT bands, respectively for [VO(MEA)(DPQ)].

The DFT-simulations were also able to predict the higher energy of the LMCT (ONO  $\rightarrow$  V<sup>IV</sup>) band in the neutral analogous in comparison to the LMCT (ONN  $\rightarrow$  V<sup>IV</sup>) band in the cationic complexes. For example, 465 nm for [VO(MEA)(DPQ)] versus 528 nm for [VO(MECA)(DPQ)]<sup>+</sup> for the DFT-simulated LMCT band.

The  $\lambda_{\max}$  value for the LMCT band in the cationic complexes is, however, red-shifted to a greater extent in the simulated spectra compared to the experimental data (see *Figure 6.13* and *Figures D9 and D10* in *Appendix D*). For example, 528 nm versus 503 nm for the DFT-simulated and experimental LMCT bands, respectively for [VO(MECA)(DPQ)]<sup>+</sup>. The remaining high energy  $\pi \rightarrow \pi^*$  transitions are similarly red-shifted in the simulated spectra for both the neutral and cationic complexes.

The main electronic transitions with their associated oscillator strengths are summarised in *Table 6.7* for [VO(MEA)(DPQ)], *Table 6.8* for [VO(MECA)(DPQ)]<sup>+</sup>, *Table D13, Appendix D* for [VO(PHA)(DPQ)] and *Table D14, Appendix D* for [VO(SOA)(DPQ)]. GaussSum was used to assign the molecular orbital transitions and percentage contributions.<sup>55</sup> The spatial distribution of the molecular orbital isosurfaces were studied qualitatively. These data show that the absorption spectra are dominated by high energy  $\pi \rightarrow \pi^*$  transitions from both alpha and beta orbitals. The predicted energy transitions align with literature with respect to the vanadium *d*-orbitals. It is generally thought that transitions occur from  $d_{xy}$  to  $d_{xz}$ ,  $d_{yz}$ ;  $d_{xy}$  to  $d_x^2 - d_y^2$  and  $d_{xy}$  to  $d_z^2$  orbitals in increasing energies for vanadyl(IV) complexes.<sup>56</sup>

**Table 6.7** Summary of the major TD-DFT-simulated (CH<sub>3</sub>CN solvent continuum) electronic transitions, oscillator strengths and the corresponding molecular orbitals for [VO(MEA)(DPQ)].

$\lambda$ (nm)	Oscillator Strength, f	Molecular Orbitals	Contri- bution <sup>a</sup>	Assignment <sup>b</sup>
476.36	0.1051	HOMO (135A) $\rightarrow$ LUMO+2 (138A) HOMO (134B) $\rightarrow$ LUMO+2 (137B)	56% 22%	$\pi$ (Me, phenol <sub>a</sub> , imine, phenol <sub>b</sub> , O, Vd <sub>xy</sub> ) $\rightarrow$ $\pi^*$ (imine, phenol <sub>b</sub> , O, Vd <sub>xz</sub> , DPQ) $\pi$ (Me, phenol <sub>a</sub> , imine, phenol <sub>b</sub> , O) $\rightarrow$ $\pi^*$ (imine, phenol <sub>b</sub> , DPQ)
459.88	0.1247	HOMO (135A) $\rightarrow$ LUMO+3 (139A) HOMO (134B) $\rightarrow$ LUMO+2 (137B) HOMO (134B) $\rightarrow$ LUMO+3 (138B)	34% 11% 48%	$\pi$ (Me, phenol <sub>a</sub> , imine, phenol <sub>b</sub> , O, Vd <sub>xy</sub> ) $\rightarrow$ $\pi^*$ (phenol <sub>a</sub> , imine, phenol <sub>b</sub> , O, Vd <sub>xz</sub> , DPQ) $\pi$ (Me, phenol <sub>a</sub> , imine, phenol <sub>b</sub> , O) $\rightarrow$ $\pi^*$ (imine, phenol <sub>b</sub> , DPQ) $\pi$ (Me, phenol <sub>a</sub> , imine, phenol <sub>b</sub> , O) $\rightarrow$ $\pi^*$ (phenol <sub>a</sub> , imine, phenol <sub>b</sub> , O, Vd <sub>xz</sub> , DPQ)
384.17	0.0346	HOMO-2 (133A) $\rightarrow$ LUMO+2 (138A) HOMO-2 (133A) $\rightarrow$ LUMO+3 (139A) HOMO-1 (133B) $\rightarrow$ LUMO+2 (137B) HOMO-1 (133B) $\rightarrow$ LUMO+3 (138B)	27% 13% 23% 24%	$\pi$ (Me, phenol <sub>a</sub> , imine, phenol <sub>b</sub> , O, Vd <sub>xy</sub> ) $\rightarrow$ $\pi^*$ (imine, phenol <sub>b</sub> , O, Vd <sub>xz</sub> , DPQ) $\pi$ (Me, phenol <sub>a</sub> , imine, phenol <sub>b</sub> , O, Vd <sub>xy</sub> ) $\rightarrow$ $\pi^*$ (phenol <sub>a</sub> , imine, phenol <sub>b</sub> , O, Vd <sub>xz</sub> , DPQ) $\pi$ (Me, phenol <sub>a</sub> , imine, phenol <sub>b</sub> , O) $\rightarrow$ $\pi^*$ (imine, phenol <sub>b</sub> , DPQ) $\pi$ (Me, phenol <sub>a</sub> , imine, phenol <sub>b</sub> , O) $\rightarrow$ $\pi^*$ (phenol <sub>a</sub> , imine, phenol <sub>b</sub> , O, Vd <sub>xz</sub> , DPQ)
314.70	0.174	HOMO (135A) $\rightarrow$ LUMO+12 (148A) HOMO-2 (132B) $\rightarrow$ LUMO+2 (137B) HOMO-2 (132B) $\rightarrow$ LUMO+3 (138B)	10% 26% 10%	$\pi$ (Me, phenol <sub>a</sub> , imine, phenol <sub>b</sub> , O, Vd <sub>xy</sub> ) $\rightarrow$ $\pi^*$ (phenol <sub>a</sub> , phenol <sub>b</sub> , O, Vd <sub>z</sub> <sup>2</sup> ) $\pi$ (phenol <sub>a</sub> , imine, phenol <sub>b</sub> ) $\rightarrow$ $\pi^*$ (imine, phenol <sub>b</sub> , DPQ) $\pi$ (phenol <sub>a</sub> , imine, phenol <sub>b</sub> ) $\rightarrow$ $\pi^*$ (phenol <sub>a</sub> , imine, phenol <sub>b</sub> , O, Vd <sub>xz</sub> , DPQ)
288.21	0.0647	HOMO-5 (130A) $\rightarrow$ LUMO+1 (137A) HOMO-4 (130B) $\rightarrow$ LUMO+1 (136B)	17% 15%	$\pi$ (DPQ) $\rightarrow$ $\pi^*$ (DPQ) $\pi$ (DPQ) $\rightarrow$ $\pi^*$ (DPQ, Vd <sub>xy</sub> )

<sup>a</sup> Only orbitals with >10% contribution are listed.<sup>b</sup> Me = methyl substituent; phenol<sub>a</sub> = amino phenol benzene ring + OH; imine = C=N imine; phenol<sub>b</sub> = phenol benzene ring + OH; O = terminal O.

**Table 6.8** Summary of the major TD-DFT-simulated (CH<sub>3</sub>CN solvent continuum) electronic transitions, oscillator strengths and the corresponding molecular orbitals for [VO(MECA)(DPQ)]<sup>+</sup>.

$\lambda$ (nm)	Oscillator Strength, f	Molecular Orbitals	Contri- bution <sup>a</sup>	Assignment <sup>b</sup>
530.04	0.2207	HOMO (132A) → LUMO (133A) HOMO (131B) → LUMO (132B)	44% 46%	$\pi$ (Me, phenol, imine, imid, O, Vd <sub>xy</sub> ) → $\pi^*$ (phenol, imine, imid, O, Vd <sub>xz</sub> ) $\pi$ (Me, phenol, imine, imid, O) → $\pi^*$ (phenol, imine, imid, O, Vd <sub>xz</sub> )
375.62	0.1798	HOMO-2 (130A) → LUMO (133A) HOMO (132A) → LUMO+5 (138A) HOMO-1 (130B) → LUMO (132B)	35% 15% 38%	$\pi$ (Me, phenol, imine, imid) → $\pi^*$ (phenol, imine, imid, O, Vd <sub>xz</sub> ) $\pi$ (Me, phenol, imine, imid, O, Vd <sub>xy</sub> ) → $\pi^*$ (-O, O, Vd <sub>yz</sub> ) $\pi$ (phenol, imine, imid) → $\pi^*$ (phenol, imine, imid, O, Vd <sub>xz</sub> )
368.50	0.1109	HOMO (132A) → LUMO+5 (138A)	50%	$\pi$ (Me, phenol, imine, imid, O, Vd <sub>xy</sub> ) → $\pi^*$ (-O, O, Vd <sub>yz</sub> )
321.77	0.0369	HOMO (131B) → LUMO+6 (138B)	66%	$\pi$ (Me, phenol, imine, imid, O) → $\pi^*$ (-O, O, Vd <sub>yz</sub> )
297.07	0.0454	HOMO-5 (127A) → LUMO+1 (134A) HOMO-5 (127A) → LUMO+2 (135A) HOMO-3 (129A) → LUMO+2 (135A) HOMO-4 (127B) → LUMO+1 (133B)	23% 10% 11% 25%	$\pi$ (DPQ) → $\pi^*$ (DPQ) $\pi$ (DPQ) → $\pi^*$ (DPQ) $\pi$ (DPQ, Vd <sub>xy</sub> ) → $\pi^*$ (DPQ) $\pi$ (DPQ) → $\pi^*$ (dpq, Vd <sub>xy</sub> )
292.04	0.0822	HOMO-3 (129A) → LUMO+2 (135A) HOMO-2 (129B) → LUMO+2 (134B)	27% 25%	$\pi$ (DPQ, Vd <sub>xy</sub> ) → $\pi^*$ (DPQ) $\pi$ (DPQ) → $\pi^*$ (DPQ)

<sup>a</sup> Only orbitals with >10% contribution are listed.

<sup>b</sup> Me = phenolic methyl substituent; phenol = benzene ring + OH; imine = C=N imine; imid = imidazole; O = terminal O.

The HOMO and LUMO plots for the alpha spin states of [VO(PHA)(DPQ)], [VO(MEA)(DPQ)] and [VO(SOA)(DPQ)] are depicted in *Figure 6.14*. The alpha HOMO and LUMO plots for the remaining complexes are available in *Figures D11 – D13, Appendix D* and the beta HOMO and LUMO plots for all complexes are indicated in *Figures D14 – D17, Appendix D*. The HOMO and LUMO plots for both the neutral and cationic complexes indicate the orbitals are all of  $\pi$ -symmetry.

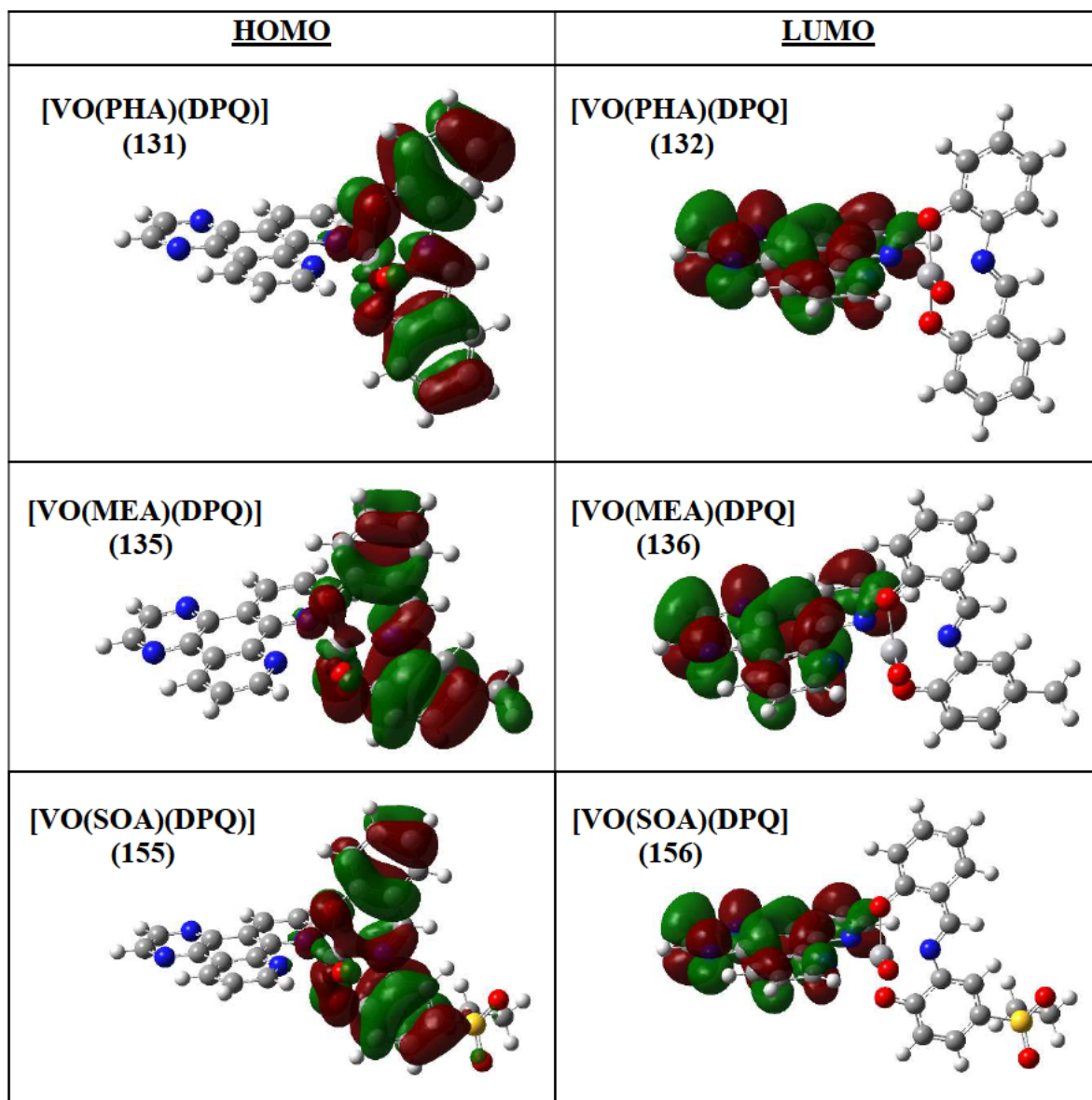


**Figure 6.14** DFT-simulated alpha HOMO and LUMO plots for the geometry-optimised (gas phase) of [VO(PHA)(DPQ)], [VO(MEA)(DPQ)] and [VO(SOA)(DPQ)].

The LUMOs reside predominantly on the DPQ/DPPZ co-ligands in the alpha and beta plots for the neutral complexes. The HOMOs in the alpha and beta plots reside predominantly on the tridentate ligand and vanadium ion for the neutral complexes.

In contrast to the neutral complexes, the molecular orbitals for both the alpha and beta HOMOs and LUMOs reside predominantly on the tridentate ligand for the cationic complexes. The HOMO-3, HOMO-2, HOMO-1, HOMO, LUMO, LUMO+1 and LUMO+2 molecular orbitals for the alpha spin state for  $[\text{VO}(\text{MECA})(\text{DPQ})]^+$  are shown in *Figure 6.15*.

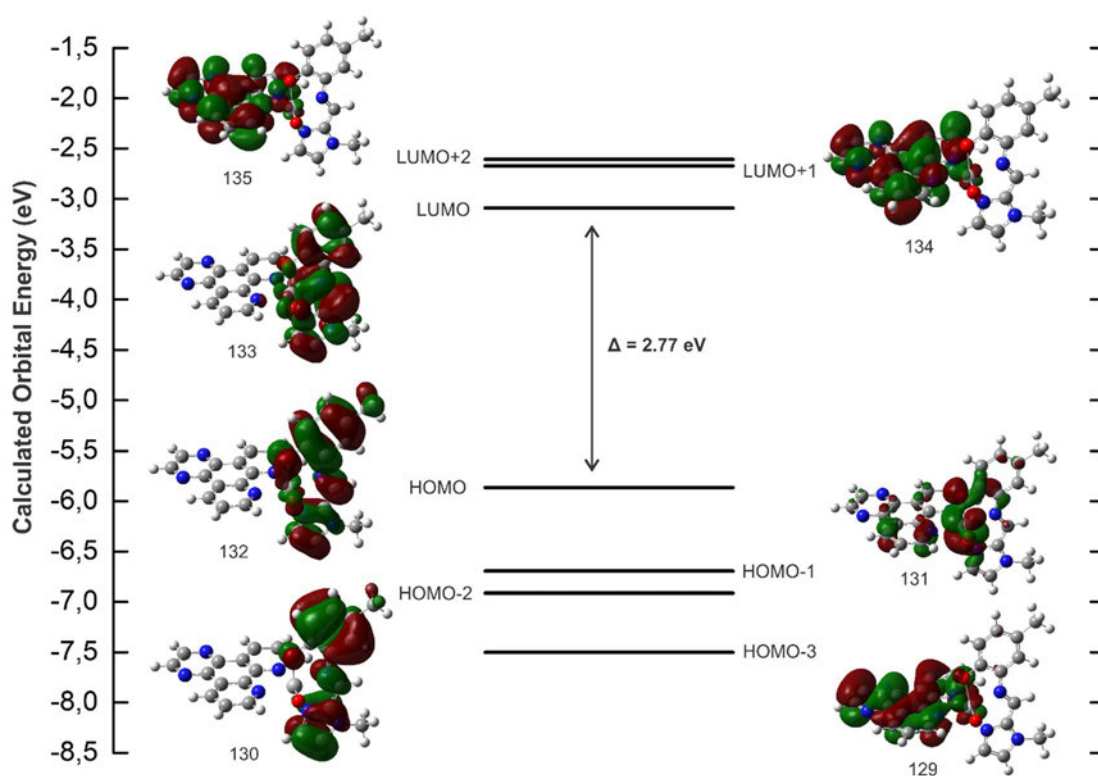


**Figure 6.15** DFT-simulated (B3LYP-/6-311G(dp)) alpha HOMO-3, HOMO-2, HOMO-1, HOMO, LUMO, LUMO+1 and LUMO+2 plots for  $[\text{VO}(\text{MECA})(\text{DPQ})]^+$ . The energy gap of the frontier molecular orbitals is 2.77 eV.

The energy gaps of the frontier molecular orbitals are summarised in *Table 6.9*.

**Table 6.9** Energy gap (in eV) between the frontier molecular orbitals for the oxovanadium(IV) compounds.

Neutral Compound	$\Delta E_{\alpha}$	$\Delta E_{\beta}$	Cationic Compound	$\Delta E_{\alpha}$	$\Delta E_{\beta}$
[VO(MEA)(DPPZ)]	2.42	2.43	[VO(PHPHCA)(PHEN)] <sup>+</sup>	2.70	2.74
[VO(MEA)(DPQ)]	2.88	2.87	[VO(MECA)(DPPZ)] <sup>+</sup>	2.76	2.79
[VO(TERTA)(DPQ)]	2.90	2.88	[VO(MECA)(PHEN)] <sup>+</sup>	2.77	2.81
[VO(PHPHA)(DPQ)]	2.91	2.90	[VO(MECA)(DPQ)] <sup>+</sup>	2.77	2.81
[VO(PHA)(DPQ)]	3.00	3.00	[VO(TERTCA)(DPQ)] <sup>+</sup>	2.79	2.83
[VO(NAA)(DPQ)]	3.01	3.00	[VO(TERTCA)(PHEN)] <sup>+</sup>	2.79	2.83
[VO(CLA)(DPQ)]	3.07	3.05	[VO(PHCA)(PHEN)] <sup>+</sup>	2.89	2.93
[VO(SOA)(DPQ)]	3.29	3.26			

Firstly, the neutral DPQ series of complexes will be analysed. Those neutral DPQ complexes with an electron-withdrawing substituent on the tridentate ligand (such as in [VO(CLA)(DPQ)] and [VO(SOA)(DPQ)]) have larger LUMO-HOMO gaps than those with an electron-donating group (such as in [VO(MEA)(DPQ)] and [VO(TERTA)(DPQ)]). The NBO charges indicate that the oxovanadium center in the neutral complexes with electron-withdrawing substituents on the tridentate ligand are only slightly more electrophilic than those with an electron-donating substituent (see *Table 6.5*).

Secondly, the neutral complexes have larger HOMO-LUMO energy gaps than the corresponding cationic complexes. For example,  $\Delta E_{\text{HOMO-LUMO}}(\alpha)$  is 2.88 eV for [VO(MEA)(DPQ)] but 2.77 eV for [VO(MECA)(DPQ)]<sup>+</sup>. The larger the difference between the frontier orbitals, the higher the kinetic stability of the molecular structure, indicating that the neutral complexes are more stable with respect to ligand substitution than the cationic complexes.<sup>53</sup>

The effect of the extended  $\pi$ -system of DPPZ is also evident in the neutral complexes. The HOMO-LUMO energy gap is lower in [VO(MEA)(DPPZ)] than in [VO(MEA)(DPQ)], indicating that [VO(MEA)(DPQ)] is more stable than [VO(MEA)(DPPZ)]. The reduction in the energy gap of the frontier molecular orbitals with increasing aromaticity of the bidentate co-ligand is, however, not seen in the cationic complexes.

This could be due to the spatial distribution of the frontier molecular orbitals being predominantly on the tridentate ligand in the cationic complexes. Conversely, the spatial distribution of the orbitals in the LUMO plots for the neutral complexes is predominantly on the DPQ/DPPZ co-ligand.

Similar correlations between the extent of aromaticity of the co-ligands and stability of the vanadium(IV) complexes have been reported in literature. Costa Pessoa and co-workers determined that PHEN complexes of the type [VO(ONO)(NN)] with tridentate salicylaldehyde semicarbazone ligands are more stable towards oxidation and solvolysis processes than the BIPY and even DPPZ analogues.<sup>4,57,58</sup> The stability of the oxovanadium(IV) complexes in this work will be further probed in *Chapter 7*.

## 6.5 Conclusions

The stability of the dimeric supramolecular structures of the *O,N,N'* ligands was confirmed through DFT simulations. The hydrogen-bonded dimers are significantly lower in energy than two independent monomer units by an average of 103 kJ mol<sup>-1</sup>. The TD-DFT simulations also suggest that the dimer is the dominant species in solution. The HOMO and LUMO plots of the dimers indicate they are of  $\pi$ -symmetry and that they span both molecules. The dimers can, therefore, be considered as supramolecular structures with  $\pi$ -electrons spread over both molecules.

The geometry-optimised lowest energy structures were found to be non-planar with a C5-N3-C6-C7 torsion angle of 144.74°, -22.33°, 23.75° and -28.53° for PHCA, MECA, TERTCA and PHPHCA, respectively. This out-of-plane rotation decreases the steric repulsion between the imine C-H and phenol moieties and leads to a lower energy than a co-planar arrangement. Due to two significantly different conformations of PHCA in the solid-state, the relative energies of the molecular geometries were probed using a scan simulation. The difference in energy between the conformations of PHCA with a planar arrangement of the phenyl and imidazole moieties versus the non-planar arrangement where the C5-N3-C6-C7 torsion angle is 144.74° was determined to be only 2.0 kJ mol<sup>-1</sup>. This low energy barrier likely explains why both conformations may exist in the solid-state.

Relative energies of the molecular geometries of PHPHCA were also probed using a scan simulation around the relative rotation of the phenol and phenyl rings. The DFT-simulated difference in energy between conformations with a  $141.7^\circ$  and  $-161.5^\circ$  C9-C10-C12-C17 torsion angle is relatively small at  $3.9 \text{ kJ mol}^{-1}$ .

A least-squares fit of the solid-state and DFT-simulated structures of the oxovanadium chelates shows good agreement with small root-mean-square deviations and low percentage differences between the bond lengths and bond angles. DFT methods were therefore used to predict the structures of the complexes for which X-ray data are not available. The geometry-optimised structures for the neutral and cationic complexes all indicate that the respective PHEN, DPQ or DPPZ ligands are free from steric hindrance by the tridentate ligand and so should be available to bind to DNA, which is their proposed cellular target.

The TD-DFT-simulated electronic transitions show that the absorption spectra are dominated by high energy  $\pi \rightarrow \pi^*$  transitions from both alpha and beta molecular orbitals. The molecular orbitals predominantly reside on the *O,N,O'*-tridentate ligand in the HOMO plots and on the DPQ/DPPZ ligand in the LUMO plots for the neutral complex's alpha and beta spin states. In contrast, the molecular orbitals are predominantly centred on the *O,N,N'*-tridentate ligand for both the HOMOs and the LUMOs in the cationic complexes' alpha and beta spin states.

The neutral complexes were determined to have larger HOMO-LUMO energy gaps than the corresponding cationic complexes. The neutral DPQ complexes with an electron-withdrawing substituent on the tridentate ligand have larger HOMO-LUMO energy gaps than those with electron-donating groups. This will likely influence their stability in a cellular environment.

## 6.6 References

1. Sasmal, P., Patra, A.K., Nethaji, M. and Chakravarty, A.R., *Inorg. Chem.*, **2007**, *46*, 11112.
2. Prasad, P., Sasmal, P.K., Majumdar, R., Dighe, R. and Chakravarty, A.R., *Inorg. Chim. Acta*, **2010**, *363*, 2743.
3. Guo, H., Lu, J., Ruan, Z., Zhang, Y., Liu, Y., Zang, L., Jiang, J. and Huang, J., *J. Coord Chem.*, **2012**, *65*, 191.
4. Benítez, J., Becco, L., Correia, I., Leal, S.M., Guiset, H., Costa Pessoa, J., Lorenzo J., Tanco, S., Escobar, P., Moreno, V., Garat, B. and Gambino, D., *J. Inorg. Biochem.*, **2011**, *105*, 303.
5. Zhai, S., Guo, Q., Dong, J., Xu, T. and Li, L., *Transit. Met. Chem.*, **2014**, *39*, 271.
6. Liao, X., Lu, J., Ying, P., Zhao, P., Bai, Y., Li, W. and Liu, M., *J. Biol. Inorg. Chem.*, **2013**, *18*, 975.
7. Bian, L., Li, L., Zhang, Q., Dong, J., Xu, T., Li, J. and Kong, J., *Transit. Met. Chem.*, **2012**, *37*, 783.
8. Jing, B.Q., Dong, J.F., Li, J.H., Xu T. and Li, L.Z., *J. Coord. Chem.*, **2013**, *66*, 520.
9. Haunschild, R., Barth, A. and Marx, W., *J. Cheminform.*, **2016**, *8*, 52.
10. Hohenberg, P. and Kohn, W., *Phys. Rev.*, **1964**, *136*, B864.
11. Kohn, W. and Sham, L. J., *Phys. Rev.*, **1965**, *140*, A1133.
12. Jensen, F., *Introduction to Computational Chemistry*, John Wiley & Sons Ltd, Chichester, **1999**, p. 150, 158, 159, 160, 177.
13. Hartree, D.R. and Hartree, W., *Proc. R. Soc. Lond. A.*, **1935**, *150*, 9.
14. Fock, V., *Z. Angew. Phys.*, **1930**, *61*, 126.
15. Baseden, K.A. and Tye, J.W., *J. Chem. Educ.*, **2014**, *91*, 2116.
16. Orio, M. and Pantazis, D.A., *Photosynth. Res.*, **2009**, *102*, 443.
17. Young, D., *Computational Chemistry: A Practical Guide for Applying Techniques to Real World Problems*, John Wiley & Sons Ltd, **2001**, 42, 43, 45, 78, 81, 231.
18. Yang, Y., Weaver, M.N. and Merz Jr., K.M., *J. Phys. Chem. A.*, **2009**, *113*, 9843.
19. Shit., M., Bera, S., Maity, S., Maji, S., Weyhermüller, T. and Ghosh, P., *Eur. J. Inorg. Chem.*, **2016**, 330.
20. Shit., M., Maity, S., Bera, S., Weyhermüller, T. And Ghosh, P., *New J. Chem.*, **2016**, *40*, 10305.

21. Bennie, R.B., Livingston, D.J., Joel, C., Jeyanthi, D., and Solomon, R.V., *Appl. Organomet. Chem.*, **2021**, *35*, e6106.
22. Adam, M.S.S. and Elsayw, H., *J. Photochem. Photobiol. B, Biol.*, **2018**, *184*, 34.
23. Biswas, N., Bera, S., Sepay, N., Mukhopadhyay, T.K., Acharya, K., Ghosh, S., Acharyya, S., Biswas, A.K., Drew, M.G.B. and Ghosh, T., *New. J. Chem.*, **2019**, *43*, 16714.
24. Becke, A.D., *J. Chem. Phys.*, **1993**, *98*, 5648.
25. Miehlich, B., Savin, A., Stoll, H. and Preuss, H., *Chem. Phys. Lett.*, **1989**, *157*, 200.
26. Lee, C., Yang, W. and Parr, R.G., *Phys. Rev. B: Condens. Matter*, **1988**, *37*, 785.
27. Krishnan, R., Binkley, J.S., Seeger, R. and Pople, J.A., *J. Chem. Phys.*, **1980**, *72*, 650.
28. *Gaussian 09, Revision E.01*,  
M. J. Frisch, G. W. Trucks, H. B. Schlegel, G. E. Scuseria, M. A. Robb, J. R. Cheeseman, G. Scalmani, V. Barone, B. Mennucci, G. A. Petersson, H. Nakatsuji, M. Caricato, X. Li, H. P. Hratchian, A. F. Izmaylov, J. Bloino, G. Zheng, J. L. Sonnenberg, M. Hada, M. Ehara, K. Toyota, R. Fukuda, J. Hasegawa, M. Ishida, T. Nakajima, Y. Honda, O. Kitao, H. Nakai, T. Vreven, J. A. Montgomery, Jr., J. E. Peralta, F. Ogliaro, M. Bearpark, J. J. Heyd, E. Brothers, K. N. Kudin, V. N. Staroverov, T. Keith, R. Kobayashi, J. Normand, K. Raghavachari, A. Rendell, J. C. Burant, S. S. Iyengar, J. Tomasi, M. Cossi, N. Rega, J. M. Millam, M. Klene, J. E. Knox, J. B. Cross, V. Bakken, C. Adamo, J. Jaramillo, R. Gomperts, R. E. Stratmann, O. Yazyev, A. J. Austin, R. Cammi, C. Pomelli, J. W. Ochterski, R. L. Martin, K. Morokuma, V. G. Zakrzewski, G. A. Voth, P. Salvador, J. J. Dannenberg, S. Dapprich, A. D. Daniels, O. Farkas, J. B. Foresman, J. V. Ortiz, J. Cioslowski, and D. J. Fox, Gaussian, Inc., Wallingford CT, **2013**.
29. Dennington, R.D., Keith, T., and Millam, J.M., *GaussView, Version 5*, Semichem Inc., Shawnee Mission, KS, **2009**.
30. Frisch, M.J., Pople, J.A., and Binkley, J.S., *J. Chem. Phys.*, **1984**, *80*, 3265.
31. Bauernschmitt, R. and Ahlrichs, R., *Chem. Phys. Lett.*, **1996**, *256*, 454.
32. Casida, M.E., Jamorski, C., Casida, K.C. and Salahub, D.R., *J. Chem. Phys.*, **1998**, *108*, 4439.
33. Stratmann, R. E., Scuseria, G. E. and Frisch, M. J., *J. Chem. Phys.*, **1998**, *109*, 8218.
34. Van Caillie, C. and Amos, R. D., *Chem. Phys. Lett.*, **1999**, *308*, 249.

35. Van Caillie, C. and Amos, R. D., *Chem. Phys. Lett.*, **2000**, 317, 159.
36. Furche, F. and Ahlrichs, R., *J. Chem. Phys.*, **2002**, 117, 7433.
37. Scalmani, G., Frisch, M. J., Mennucci, B., Tomasi, J., Cammi, R. and Barone, V., *J. Chem. Phys.*, **2006**, 124, 094107.
38. S. Miertuš, Scrocco, E. and Tomasi, J., *Chem. Phys.*, **1981**, 55, 117.
39. S. Miertuš and Tomasi, J., *Chem. Phys.*, **1982**, 65, 239.
40. Kabak, M., Elmali, A. and Elerman, Y., *J. Mol. Struct.*, **1999**, 477, 151.
41. Elmali, A., Kabak, M., Kavlakoglu, E., Elerman, Y. and Durlu, T.N., *J. Mol. Struct.*, **1999**, 510, 207.
42. Sun, Y., Wang, Y., Liu, Z., Huang, C. and Yu, C., *Spectrochim. Acta A*, **2012**, 96, 42.
43. Banerjee, A., Dash, S.P., Mohanty, M., Sanna, D., Sciortino, G., Ugone, V., Garriba, E., Reuter, H., Kaminsky, W. and Dinda, R., *J. Inorg. Biochem.*, **2019**, 199, 110786.
44. Barry, K.-L., Grimmer, C.D., Munro, O.Q. and Akerman, M.P., *RSC Adv.*, **2020**, 10, 7867.
45. Mercury CSD 2.0, C.F. Macrae, I.J. Bruno, J.A. Chisholm, P.R. Edgington, P. McCabe, E. Pidcock, L. Rodriguez-Monge, R. Taylor, J. van de Streek and P.A. Wood, *J. Appl. Cryst.*, **2008**, 41, 466.
46. Bürgi, H.B. and Dunitz, J.D., *Helv. Chim. Acta*, **1971**, 54, 1255.
47. Bürgi, H.B. and Dunitz, J.D., *Helv. Chim. Acta*, **1970**, 53, 1747.
48. Orr Jr, L.B., Parsons, E.J. and Pennington, W.T., *Acta Crystallogr., Sect. C: Cryst. Struct. Commun.*, **1992**, 48, 2042.
49. Akerman, M.P. and Chiazzari, V.A., *J. Mol. Struct.*, **2014**, 1058, 22.
50. Yang, Y., Weaver, M.N. and Merz Jr, K.M., *J. Phys. Chem. A*, **2009**, 113, 9843.
51. Allen, F.H., Kennard, O., Watson, D.G., Brammer, L., Orpen, A.G. and Taylor, R., *J. Chem. Soc. Perkin Trans. II*, **1987**, S1.
52. Gavranić, M., Kaitner, B. and Meštrović, E., *J. Chem. Crystallogr.*, **1996**, 26, 23.
53. Zhao, H.-Y., Xing, Y.-H., Cao, Y.-Z., Li, Z.-P., Wei, D.-M., Zeng, X.-Q. and Ge, M.-F., *J. Mol. Struct.*, **2009**, 938, 54.
54. Toney, J.H., Brock, C.P. and Marks, T.J., *J. Am. Chem. Soc.*, **1986**, 108, 7263.
55. O'Boyle, N.M., Tenderholt, A.L. and Langner, K.M., *J. Comp. Chem.*, **2008**, 29, 839.
56. Cao, Y.-Z., Zhao, H.-Y., Bai, F.-Y., Xing, Y.-H., Wei, D.-M., Niu, S.-Y. and Shi, Z., *Inorg. Chim. Acta*, **2011**, 368, 223.

57. Benítez, J., Guggeri, L., Tomaz, I., Arrambide, G., Navarro, M., Costa Pessoa, J., Garat, B. and Gambino, D., *J. Inorg. Biochem.*, **2009**, *103*, 609.
58. Fernández, M., Becco, L., Correia, I., Benítez, J., Piro, O.E., Echeverria, G.A., Medeiros, A., Comini, M., Lavaggi, M.L., González, M., Cerecetto, H., Moreno, V., Costa Pessoa, J., Garat, B. and Gambino, D., *J. Biol. Inorg. Chem.*, **2013**, *127*, 150.

## **Chapter Seven: Stability of Oxovanadium(IV)** **Complexes**

### **7.1 Introduction**

The vanadyl form of vanadium(IV) with the  $\text{VO}^{2+}$  core was selected for this study due to its stability in cells in comparison to other oxidation states of vanadium (*Section 1.6.1*).<sup>1</sup> Organic ligands have been shown to improve stability and absorption rates of vanadium species in comparison to inorganic vanadyl salts (*Section 1.6*).<sup>2,3</sup> That said, when vanadium(IV) drugs are administered (usually through intravenous injection) they tend to be thermodynamically unstable in the mammalian environment. Within the bloodstream most vanadium compounds undergo speciation and redox interconversion between the +4 and +5 oxidation state.<sup>1,2,4,6</sup> Oxovanadium(IV) complexes are susceptible to hydrolysis and loss of the original ligand(s).<sup>5</sup> Vanadate ( $\text{H}_2\text{V}^{\text{V}}\text{O}_4^-$ ) and vanadyl bound to transferrin ( $\text{V}^{\text{IV}}\text{O-Tf}$ ) are the main adducts formed in the blood serum (*Section 1.5*).<sup>1,7</sup> Less stable vanadium complexes are still able to have high cytotoxic activity as free coordination sites allow the complexes to be more reactive in polar environments within cells.<sup>8</sup> Despite vanadium coordination compounds degrading in physiological conditions, the complexes do show differing absorption, lifetimes and resorption into cells as compared to inorganic vanadium salts. Coordination of ligands to  $\text{VO}^{2+}$  has been shown to lower toxicity, and improve biological activities, such as insulin-mimetic properties and anticancer activities.<sup>2,4</sup> Organic ligands can, therefore, still be used to tune the properties of vanadium drugs.<sup>2</sup>

Tridentate Schiff base ligands and *N,N*-bidentate ligands, such as 1,10-phenanthroline, with strong sigma-donor capabilities have been used to stabilise oxovanadium(IV) complexes.<sup>9-13</sup> Improving the stability of a vanadium complex has many benefits. A vanadium compound that does not hydrolyse easily may prevent off-target binding events, which could alleviate side effects. In addition, chelated ligands of the vanadium complex can target specific tissues, and so, deliver the active metal centre to a specific cellular target. Oxovanadium complexes with tridentate *O,N,O*- or *O,N,N'*-donor Schiff base ligands and rigid aromatic rings such as PHEN, DPQ and DPPZ co-ligands, have been shown to have strong DNA binding affinities.<sup>9-12,14-24</sup>

Once at the active site, the chelated ligands can be hydrolysed, either partially or completely, to release the active form of vanadium.<sup>5,12</sup> There are several reports on the stabilities of oxovanadium complexes containing a *O,N,O'*- or *O,N,N'*-tridentate Schiff base ligand and a bidentate *N,N*-donor co-ligand, in various solvents and biological conditions. These are discussed below in Section 7.2.

## 7.2 Stabilities of Oxovanadium(IV) Complexes

Phenanthroline-derived co-ligands have been shown to stabilise oxovanadium(IV) complexes with *O,N,O'*-donor Schiff base ligands.<sup>25-29</sup> The degree of hydrolytic stability of oxovanadium(IV) complexes containing a *N,N*-bidentate co-ligand and an *O,N,O'*- or *O,N,N'*-tridentate Schiff base ligand can vary significantly depending on the nature of the ligands coordinated, solvent media, and pH.<sup>11,13,19,26,28,30-33</sup> Sasmal and co-workers briefly reported that the [VO(ONO)(NN)] complexes in Figure 7.1 are stable in solution based on the observation of a prominent molecular ion peak in the mass spectra in methanol.<sup>9,17</sup>

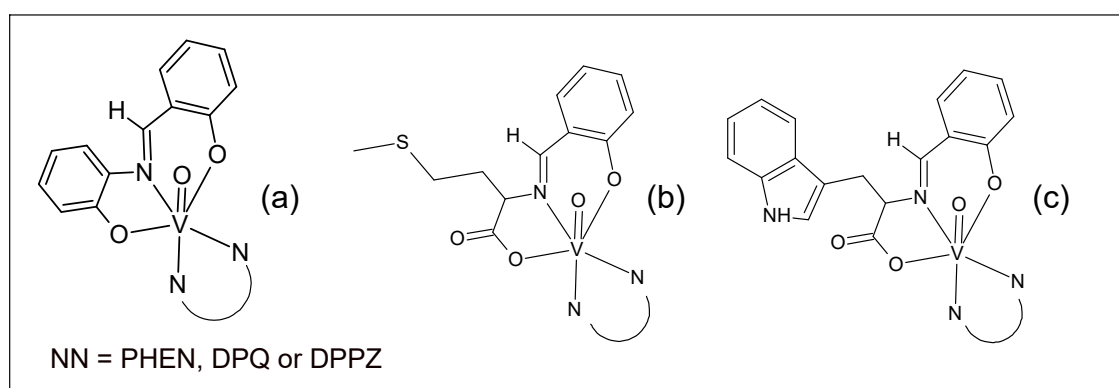


**Figure 7.1** [VO(ONO)(NN)] complexes reported, by Sasmal and co-workers to be stable in solution.<sup>9,17</sup>

Cationic oxovanadium(IV) complexes, shown in Figure 7.2 have also been reported to be stable in methanol.<sup>10,14</sup>

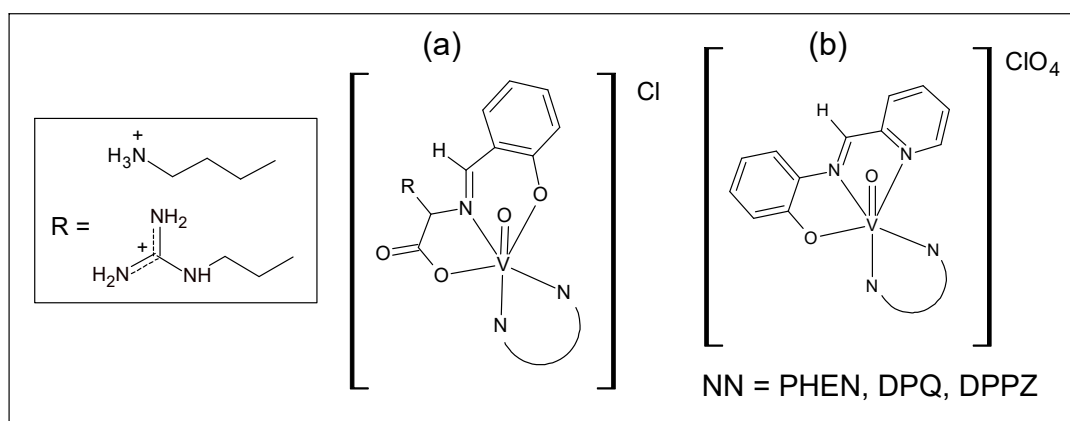


**Figure 7.2** Cationic oxovanadium(IV) complexes of the type  $[\text{VO}(\text{ONO})(\text{NN})](\text{Cl})$  (a) and  $[\text{VO}(\text{ONN})(\text{NN})](\text{ClO}_4)$  (b) for which stabilities were reported by Sasmal and co-workers.<sup>10,14</sup>

Certain solvents can cause solvolysis and/or oxidation of an oxovanadium(IV) complex. Solvolysis of oxovanadium(IV) complexes of the type  $[\text{VO}(\text{ONO})(\text{NN})]$  have been found to be more extensive in DMSO as compared to DMF.<sup>19,26,30</sup> Oxidation of oxovanadium(IV) complexes has been shown to be slower in 6-8% DMSO- $\text{H}_2\text{O}$  solutions than in neat DMSO.<sup>26,34</sup> DMSO is known to coordinate vanadium efficiently. For example, DMSO has been reported to substitute *O,N,O*-donor semicarbazone ligands and bidentate *N,N*-donor co-ligands from complexes of the type  $[\text{VO}(\text{ONO})(\text{NN})]$  to form  $[\text{V}^{\text{IV}}\text{O}(\text{DMSO})_4]_{\text{eq}}$ .<sup>30</sup>

The types of adducts formed from solvolysis processes include the oxidised species  $[\text{V}^{\text{V}}\text{O}_2(\text{ONO})(\text{solvent})]^-$ , with the solvent (DMSO or DMF) having displaced the *N,N*-bidentate ligand, and minor decomposition products of vanadate oligomers. Vanadium(IV) solvolysis products of the type  $[\text{V}^{\text{IV}}\text{O}(\text{ONO})(\text{DMF or DMSO})]$  may also be formed.<sup>19,26,30,34-36</sup> Substitution of solvent molecules from oxovanadium(IV) complexes may also occur. BIPY and PHEN ligands have been reported to substitute aqua ligands from an oxovanadium(IV)-iminodiacetate complex of the type  $[\text{VO}(\text{ONO})(\text{H}_2\text{O})_2]$ .<sup>25,29</sup>

Stability studies of oxovanadium(IV) complexes with pH considerations have been reported.<sup>11,12,25,28,35,37</sup> These studies have shown that the concentration of vanadium and the pH determine which vanadium species will be present.<sup>3</sup> The BIPY and PHEN complexes in *Figure 7.3 (a)* were determined to be stable in phosphate-buffered saline solution (pH 7.4) over 5 hours at room temperature.<sup>12</sup>

Pranczk *et al.* determined, through potentiometric titration studies, that the  $[\text{VO}(\text{ONO})(\text{PHEN})]$  complex in *Figure 7.3 (a)* is dominant in solution in the pH range 6.5 to 9.5, reaching the highest concentrations at pH 8 in aqueous solution.<sup>25</sup> At pH 2–6 complexes of  $[\text{VO}(\text{PHEN})_2]^{2+}$  and  $[\text{VO}(\text{HONO})(\text{ONO})]^-$  predominate. At higher pH, above 9.5, hydroxido complexes are favoured.<sup>26</sup> The complexes depicted in *Figure 7.3 (b)* were determined to be stable in 0.7% DMSO-water solution at pH = 7.<sup>37</sup> The complexes in *Figure 7.3 (c)* and *Figure 7.6 (d)* were the major species in solution at neutral pH in 50% $\text{H}_2\text{O}/50\%\text{DMSO}$  (v/v).<sup>35</sup>

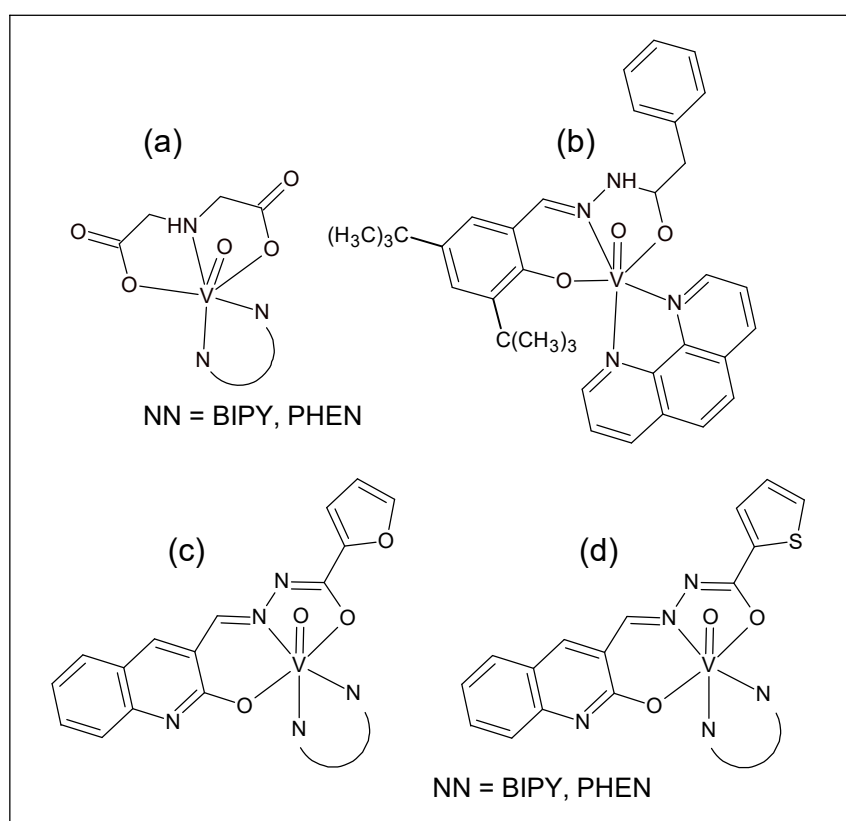


**Figure 7.3**  $[\text{VO}(\text{ONO})(\text{NN})]$  complexes for which stabilities have been studied with pH considerations.<sup>12,25,35,37</sup>

The oxovanadium(IV) complexes with hydrazone ligands depicted in *Figure 7.4* were also determined to be stable in 0.7% DMSO-water solution at pH = 7.<sup>11,28</sup> However, at lower pH of 2, these complexes are no longer stable.<sup>11,28</sup>

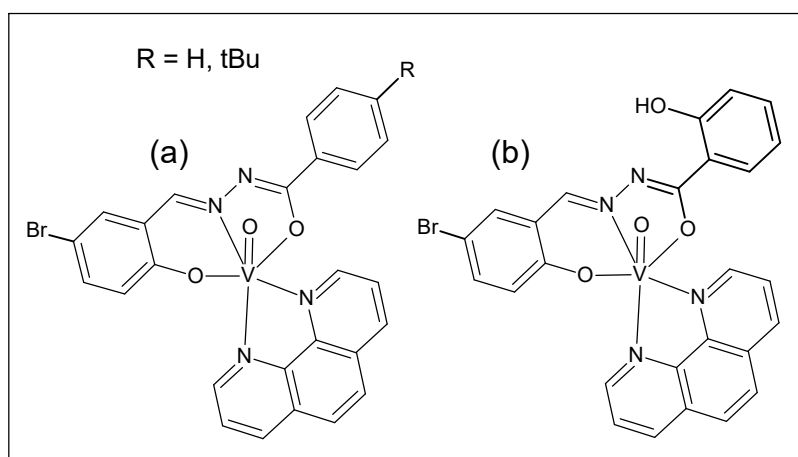


**Figure 7.4** Hydrazone oxovanadium(IV) complexes for which stabilities with pH considerations were reported by Szklarzewicz and co-workers.<sup>11,28</sup>

The identity of the bidentate *N,N*-donor co-ligand also impacts on the stability of oxovanadium(IV) complexes. Oxovanadium(IV) complexes of the type [VO(ONO)(NN)] in *Figure 7.3 (c) and (d)* and *Figure 7.5* with a PHEN co-ligand have been found to be more stable towards oxidation and solvolysis processes than the BIPY and even DPPZ analogues.<sup>19,30,34-36,38</sup> The lower stability of the BIPY complex was attributed to BIPY being more flexible than PHEN and thus more easily displaced by other ligands.<sup>37</sup>

The higher stability of the PHEN complexes in *Figure 7.5 (a)* led to higher antitrypanosomal activity, despite PHEN having lower intercalative DNA binding abilities than DPPZ.<sup>19,34</sup> DNA was the suspected biological target for activity.<sup>34</sup> The data suggest that the compound with the *N,N*-bidentate ligand is the species responsible for antitrypanosomal activity.<sup>34</sup> The formation of the oxidation/solvolysis products, however, makes it difficult to assign the antitrypanosomal activity of these complexes to a particular species. It additionally, makes determining which species are interacting with DNA, very challenging.<sup>30</sup>



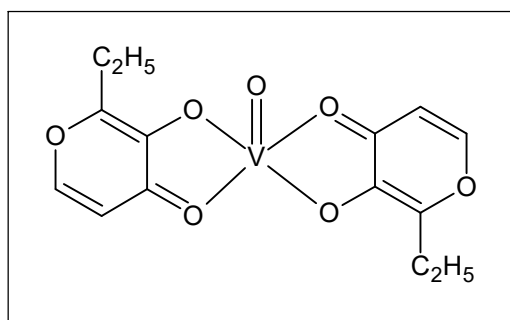


**Figure 7.6** Structure of BEOV, an oxovanadium(IV) complex that entered phase IIa human clinical trials for diabetes.<sup>1</sup> This compound acts as a pro-drug.

*In vitro* studies are conducted in aerated solutions with incubating times of several days. Knowledge about a potential vanadyl drug's stability to hydrolyse and/or oxidise over time in biological media must therefore be established.<sup>34</sup> It is important to determine the bio-active species. The ligand types and substituents on the tridentate ligand and type of co-ligand are important for imparting or changing pharmacological activity if these ligands remain fully or even partially coordinated to the vanadium centre.<sup>11</sup>

The tridentate Schiff base ligands in this study were chosen to impart stability to the  $\text{VO}^{2+}$  core by blocking coordination sites and by pushing electron density onto the electron deficient metal ion. The deprotonated oxygen atoms of the tridentate ligand bind strongly to the hard Lewis acid: vanadium.<sup>1,43</sup> The bidentate planar co-ligands of PHEN, DPQ and DPPZ were chosen based on the reported ability of these ligands, particularly PHEN, to stabilise vanadium(IV), as described above, and for the DNA targeting ability.<sup>44</sup> Therefore, it is important to determine the stability of these complexes, at least until uptake of the vanadium species into the cells.

The neutral and cationic compounds in this study are similar to those designed by Sasmal and co-workers in *Figures 7.1 (a)* and *Figure 7.2 (b)*, respectively. Although these complexes were reported to be stable in solution, various reports state that oxovanadium complexes can be susceptible to solvolysis/oxidation in solution.<sup>9,10</sup> For this study, the stability of selected complexes from this work were investigated using mass spectrometry, UV/visible and  $^{51}\text{V}$  NMR spectroscopy.

### 7.3 Mass Spectrometry Stability Studies of the Oxovanadium(IV) Complexes

Sasmal *et al.* reported the [VO(ONO)(NN)] and [VO(ONN)(NN)](ClO<sub>4</sub>) complexes in Figures 7.1 (a) and Figure 7.2 (b), respectively, are stable in solution due to the presence of a prominent molecular ion peak in the ESI-MS spectra in methanol.<sup>9,10</sup> This study did not take into account either the effect of the solvent or the stability of the complexes in solution as a function of time. In this work, prominent molecular ion peaks were also recorded in chloroform or dichloromethane for the neutral complexes and in acetonitrile for the cationic complexes.

Literature does, however, show that certain solvents, such as DMSO, can displace at least the bidentate ligand from an oxovanadium(IV) complex as discussed in Section 7.2.<sup>19,26,30</sup> Additional mass spectra studies were, therefore, conducted of selected complexes in 10%DMSO/90%water (v/v) over 24 hours on a Waters Micromass LCT Premier time-of-flight mass spectrometer using electrospray ionisation in positive mode with direct injection. The DMSO/water solvent system was selected for testing since it is commonly used in biological studies. DMSO is used to aid the solubility of the complexes in water. DMSO is suitable to use as it has applications as a solvent in many pharmaceuticals, such as being used to transfer substances across biological membranes.<sup>11,37</sup> Selected complexes chosen for the study include [VO(PHA)(DPQ)], [VO(MEA)(DPQ)], [VO(TERTA)(DPQ)], [VO(PHCA)(PHEN)](PF<sub>6</sub>), [VO(MECA)(PHEN)](PF<sub>6</sub>), [VO(MECA)(DPQ)](PF<sub>6</sub>), [VO(MECA)(DPPZ)](Cl), [VO(TERTCA)(PHEN)](PF<sub>6</sub>) and [VO(TERTCA)(DPQ)](PF<sub>6</sub>).

[VO(PHA)(DPQ)] was previously reported in the literature as stable with a prominent molecular ion peak of 511.08 *m/z* in methanol.<sup>9</sup> In this research, prominent molecular ion peaks at 510.0792 *m/z* and 511.0858 *m/z* corresponding to [M]<sup>+</sup> and [M+H]<sup>+</sup>, respectively, were also noted in chloroform (Figure 7.7).

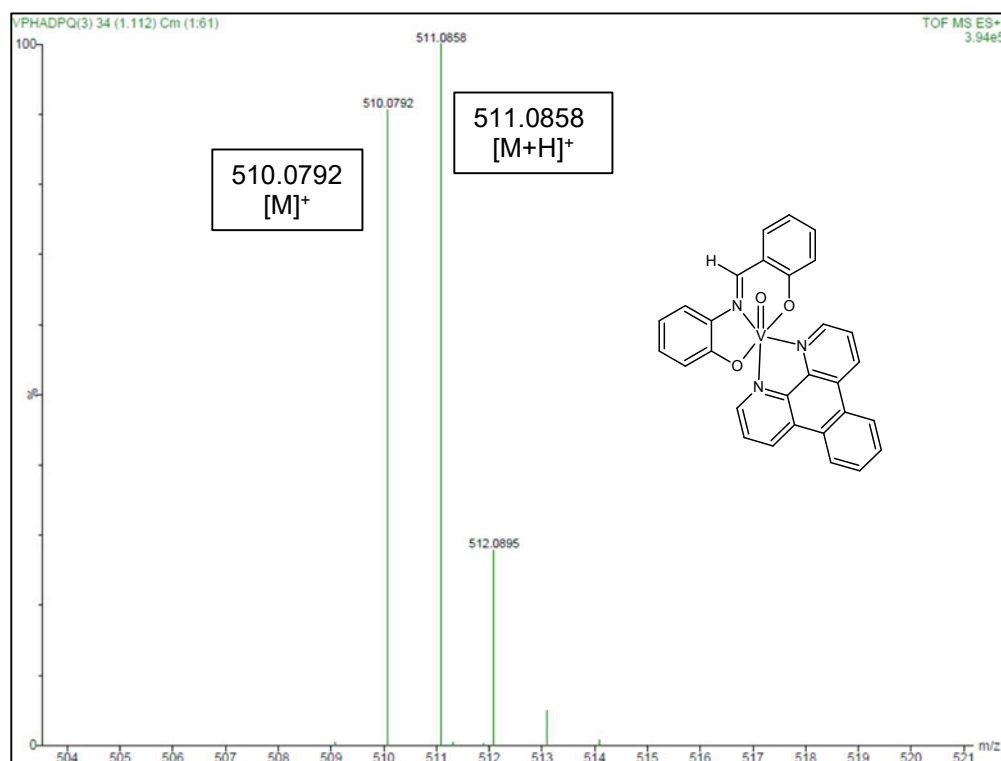


**Figure 7.7** ESI mass spectrum of  $[\text{VO}(\text{PHA})(\text{DPQ})]$  in chloroform indicating the prominent molecular ion peaks of  $510.0792\text{ m/z}$  and  $511.0858\text{ m/z}$  corresponding to  $[\text{M}]^+$  and  $[\text{M}+\text{H}]^+$  respectively.

However, a change of solvent to 10%DMSO/90%water (v/v) caused a dramatic change in the mass spectral data (*Figure E1* in *Appendix E*). Note: the same sample was used for preparing all solutions in each set of experiments. Multiple new species form, including compounds with molecular ion peaks at  $233.1031\text{ m/z}$  and  $255.0870\text{ m/z}$ , which could correspond to the free DPQ ligand ( $[\text{DPQ}+\text{H}]^+$  and  $[\text{DPQ}+\text{Na}]^+$ , respectively). The prominent molecular ion peaks of  $510.0792\text{ m/z}$  and  $511.0858\text{ m/z}$  are also diminished in the 10% DMSO/90% water (v/v) solvent mixture. The displacement of the bidentate ligand is consistent with previous literature reports.<sup>19,26,30</sup>

The addition of methyl and *tert*-butyl electron-donating substituents on the aminophenol ring of the tridentate ligand imparted some stability to the oxovanadium structures. The mass spectra at 2 minutes, 30 minutes, and 24 hours after the dissolution of  $[\text{VO}(\text{MEA})(\text{DPQ})]$  in 10%DMSO/90%water (v/v) and discussion thereof is in *Figure E2*, *Appendix E*.

For [VO(TERTA)(DPQ)] there is still a prominent molecular ion peak of 566.1644  $m/z$  immediately after dissolution in the 10%DMSO/90%water media, as in chloroform, corresponding to  $[M]^+$  for the intact complex (Figure 7.8).

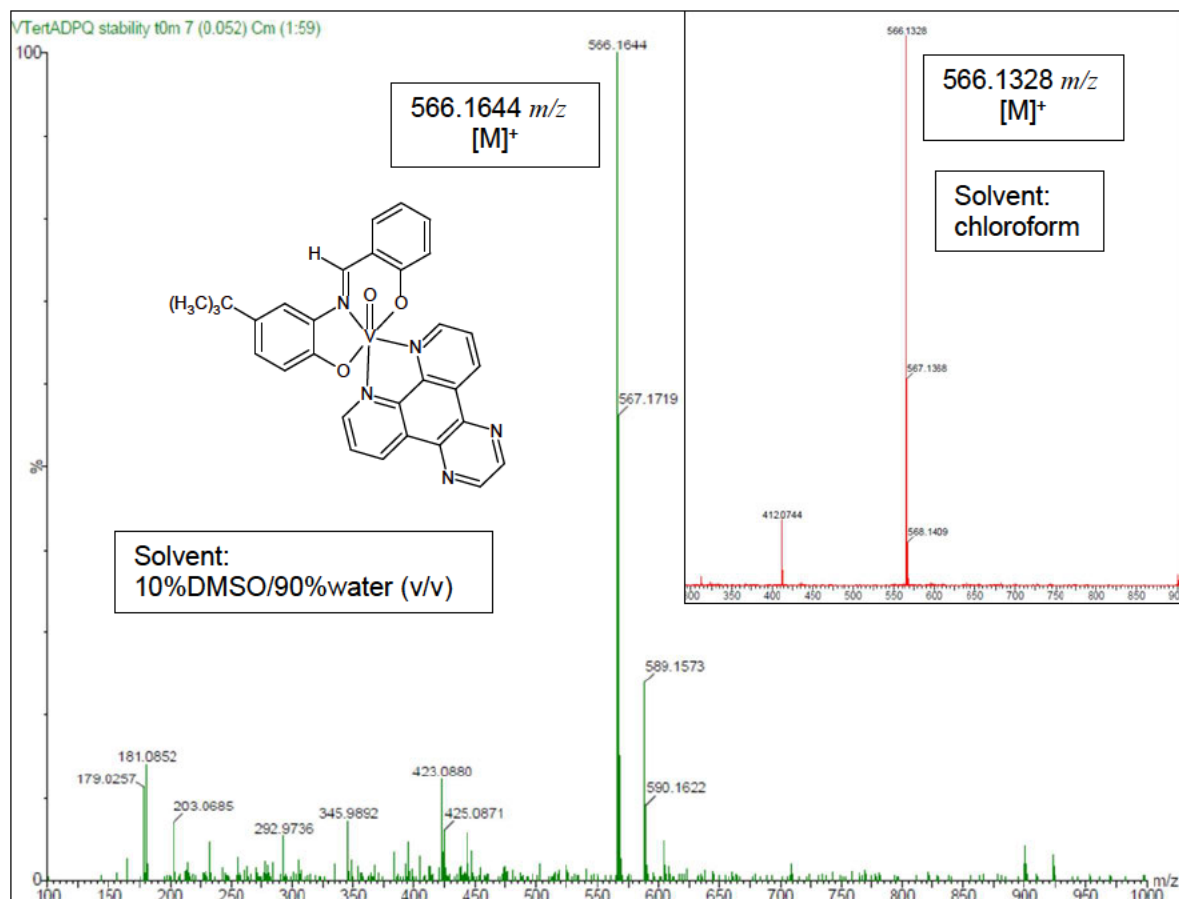


**Figure 7.8** ESI mass spectra of [VO(TERTA)(DPQ)] in 10%DMSO/90%water (v/v) and in chloroform (inset) indicating the prominent singular molecular ion peak  $[M]^+$  at 566.1644  $m/z$ .

Thirty minutes after the addition of the 10%DMSO/90%water solvent system, the  $[M]^+$  peak at 566.1667  $m/z$  is still present. Many other peaks, however, started to form, such as at 255.0773  $m/z$ , which is likely  $[DPQ+Na]^+$  (Figure 7.9). At 160 minutes after the addition, the 566  $m/z$   $[M]^+$  peak is still present (Figure E3, Appendix E). By 17.5 hours post-preparation the 566  $m/z$  is absent. At 24 hours after dissolution, the molecular ion peak is now at 412.1020  $m/z$ , which is most likely  $[VO(TERTA)(DMSO)]^+$  (Figure 7.9). The displacement of the bidentate co-ligand seems likely based on previous literature.<sup>19,26,30</sup>

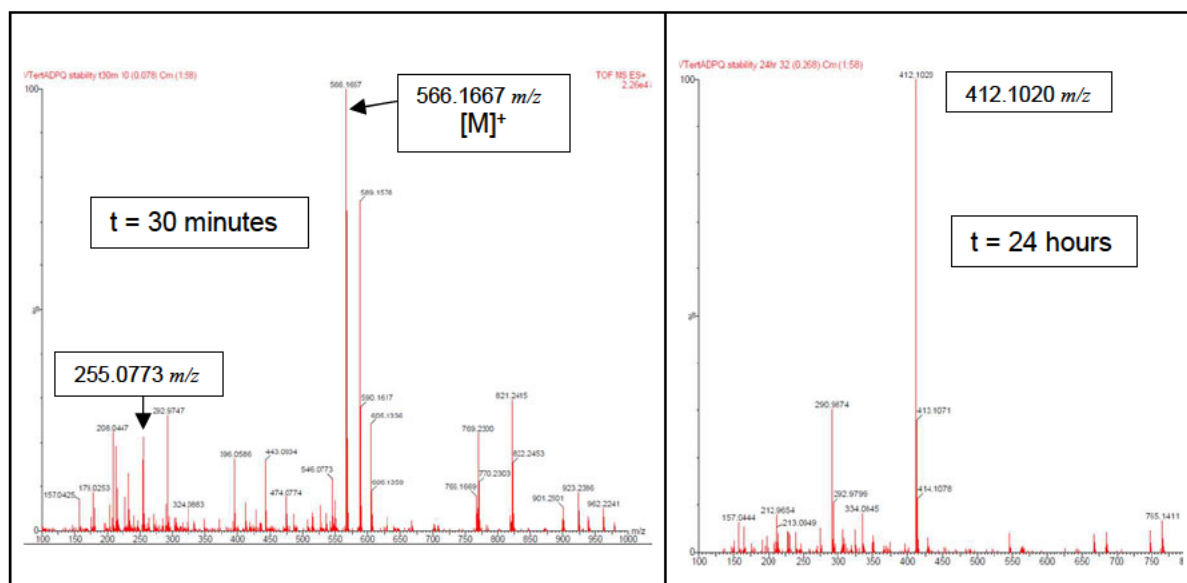


**Figure 7.9** ESI mass spectra at 30 minutes and 24 hours after dissolution of [VO(TERTA)(DPQ)] in a 10%DMSO/90%water (v/v) solvent system indicating the disappearance of the [VO(TERTA)(DPQ)] 566.1667  $m/z$  peak overtime and the appearance of the solvolysis species [VO(TERTA)(DMSO)]<sup>+</sup> at 412.1020  $m/z$ .

Similar solvent effects are noted for the cationic derivatives. ESI mass spectra recorded in acetonitrile show good purity with a single peak, corresponding to [M]<sup>+</sup>, for all the intact cationic complexes in the study (refer to *Appendix A*). Once again, changing the solvent system from acetonitrile to 10%DMSO/90%water (v/v) dramatically changed the structure of the cationic complexes. This shows that the changes observed in the DMSO/water solvent system are a consequence of hydrolysis or solvolysis, and not a low purity sample. As a representative example, there is one prominent molecular ion peak at 555.1563  $m/z$  corresponding to [VO(TERTCA)(DPQ)]<sup>+</sup> in acetonitrile (*Figure 7.10*). In 10%DMSO/90%water (v/v) additional species are also indicated, such as [DPQ+H]<sup>+</sup> at 233.0846  $m/z$ , along with the [VO(TERTCA)(DPQ)]<sup>+</sup> peak at 555.1624  $m/z$  initially present after dissolution (*Figure 7.10*).

The peak corresponding to [VO(TERTCA)(DPQ)]<sup>+</sup> then disappears more rapidly than [VO(TERTA)(DPQ)]. The [VO(TERTCA)(DPQ)]<sup>+</sup> peak is absent at three hours post-dissolution in 10%DMSO/90%water (v/v) (*Figure E4, Appendix E*). The prominent peak at 24 hours then becomes 233.1063  $m/z$ , which corresponds to the molecular ion of the DPQ co-ligand ([DPQ+H]<sup>+</sup>) in the positive ionisation mode (*Figure E4, Appendix E*).

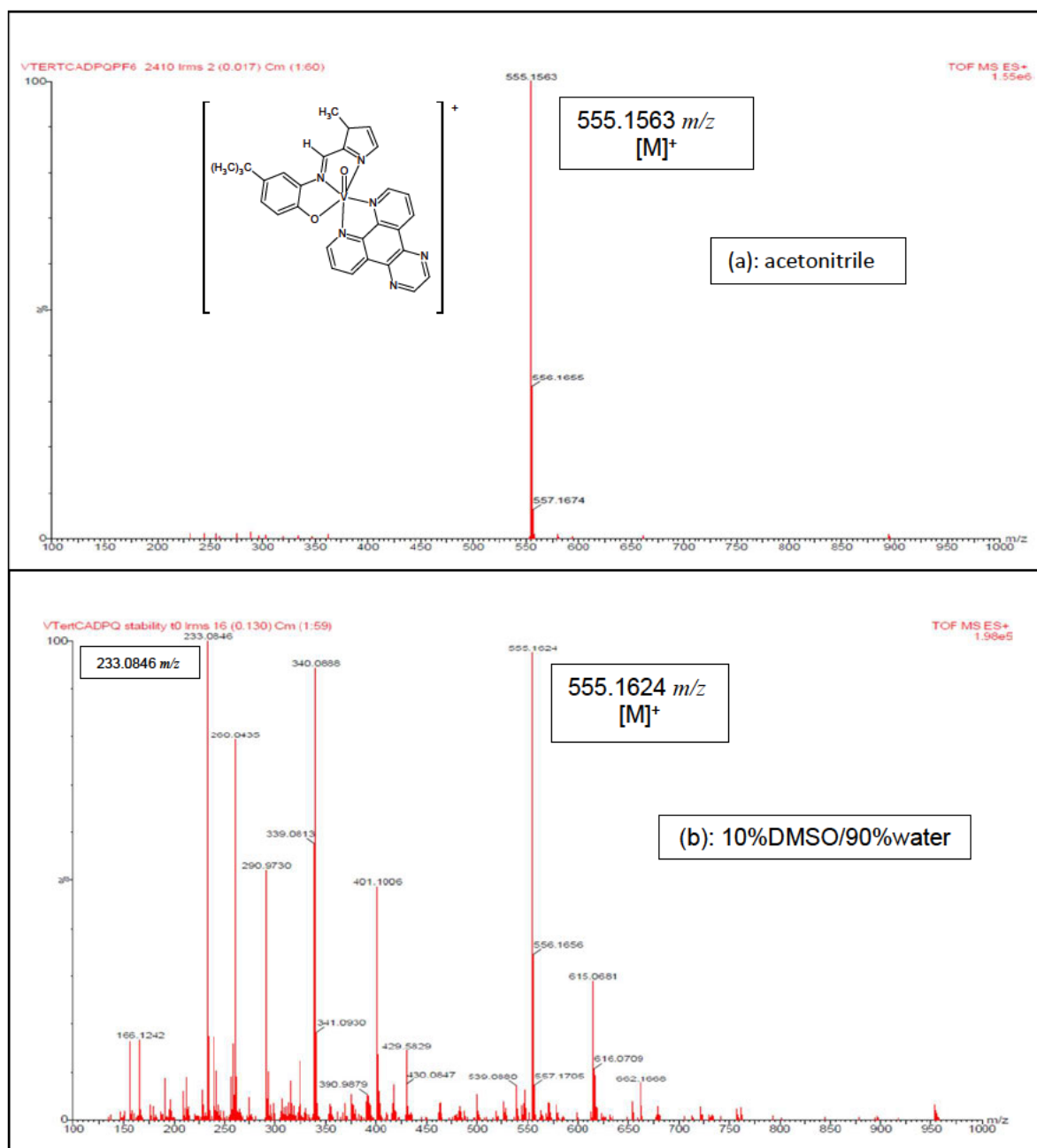


**Figure 7.10** ESI mass spectra of  $[\text{VO}(\text{TERTCA})(\text{DPQ})](\text{PF}_6)$  in  
(a): acetonitrile indicating the singular  $[\text{M}]^+$  peak at  $555.1563 \text{ m/z}$ .  
(b): 10%DMSO/90%water (v/v) - the  $[\text{VO}(\text{TERTCA})(\text{DPQ})]^+$  peak at  $555.1624 \text{ m/z}$  is indicated, along with many solvolysis/decomposition species including the  $[\text{DPQ}+\text{H}]^+$  peak at  $233.0846 \text{ m/z}$ . This illustrates the effect of solvent on the complex structure.

The same pattern, showing the presence of additional molecular ion peaks, along with the prominent molecular ion peak for the intact complex, is seen for [VO(TERTCA)(PHEN)](PF<sub>6</sub>), [VO(PHCA)(PHEN)](PF<sub>6</sub>), [VO(MECA)(PHEN)](PF<sub>6</sub>), and [VO(MECA)(DPQ)](PF<sub>6</sub>) immediately after dissolution in 10%DMSO/90%water (v/v), (Figures E5–E8, Appendix E). For example, a peak of 401.1147 *m/z* corresponding to [VO(TERTCA)(DMSO)]<sup>+</sup> appeared along with the prominent molecular ion peak of 503.1708 *m/z* corresponding to [VO(TERTCA)(PHEN)]<sup>+</sup> after dissolution of [VO(TERTCA)(PHEN)](PF<sub>6</sub>) in 10%DMSO/90%water (v/v) (Figure E5, Appendix E). The molecular ion peak then also diminishes over time for the above-mentioned cationic complexes in 10%DMSO/90%water (v/v) (Figures E5–E8, Appendix E).

The oxovanadium-DPPZ chloride complex salt was used to determine the effect of DMSO on metal complex stability as compared to water alone. The chloride salt has higher solubility in aqueous media compared to the hexafluorophosphate complexes and so the stability of [VO(MECA)(DPPZ)](Cl) could be determined in water alone. As expected, in the 10%DMSO/90%water (v/v) solvent mixture the molecular ion peak of 563.1688 *m/z* corresponding to [VO(MECA)(DPPZ)]<sup>+</sup> is present as the prominent molecular ion peak, along with other minor peaks, such as 283.1206 *m/z* for [DPPZ+H]<sup>+</sup>. At 30 minutes, the [VO(MECA)(DPPZ)]<sup>+</sup> peak is already diminished (Figure E9, Appendix E).

In contrast, the [VO(MECA)(DPPZ)](Cl) complex was stable in water with the molecular ion peak of 563.0673 *m/z* still prominent after 24 hours (Figure 7.11). Full ESI mass spectra at 2 minutes, 3, 6 and 24 hours after dissolution of [VO(MECA)(DPPZ)](Cl) in water are available in Figure E10, Appendix E. Costa Pessoa and co-workers also noted slower oxidation/solvolysis processes of oxovanadium complexes, in solutions that contained less DMSO.<sup>26,34</sup>

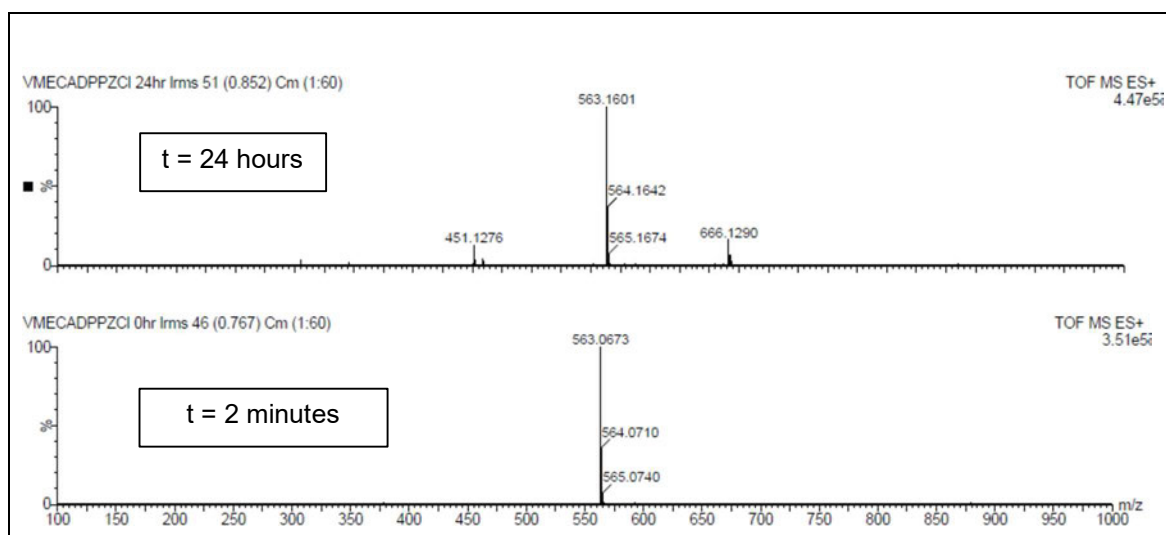


**Figure 7.11** ESI mass spectra at 2 minutes and 24 hours after dissolution of [VO(MECA)(DPPZ)](Cl) in water, indicating the stability of the prominent molecular ion peak of 563.1601  $m/z$  corresponding to [VO(MECA)(DPPZ)]<sup>+</sup>.

The above data show that although the samples of the various metal complexes are of high purity, solvolysis reactions do occur in various media. Based on this, it is likely that the complexes would act as pro-drugs, as is the case with other oxovanadium complexes.

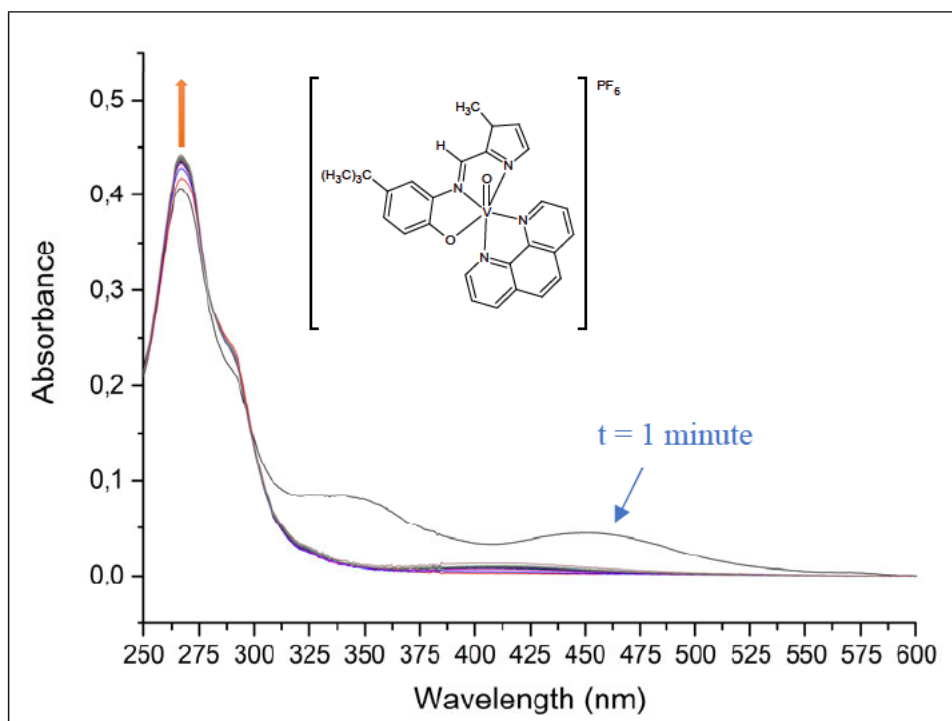
#### 7.4 UV/visible Spectroscopy Stability Studies of the Oxovanadium(IV) Complexes

The DNA binding absorption spectroscopy studies of the oxovanadium(IV) complexes were planned to be conducted using 10% v/v DMSO, 0.1 M Tris Buffer aqueous solution as the solvent media to aid dissolution while approximating biological media. The stability of the complexes in this solvent system, therefore, needs to be investigated to ensure the change in absorbance in the DNA binding studies can be attributed to the complex interactions with DNA alone and not to solvolysis processes.

The stability of selected complexes, namely [VO(TERTCA)(PHEN)](PF<sub>6</sub>), [VO(TERTCA)(DPQ)](PF<sub>6</sub>) and [VO(TERTA)(DPQ)], were studied by UV/visible spectroscopy over 18 hours.

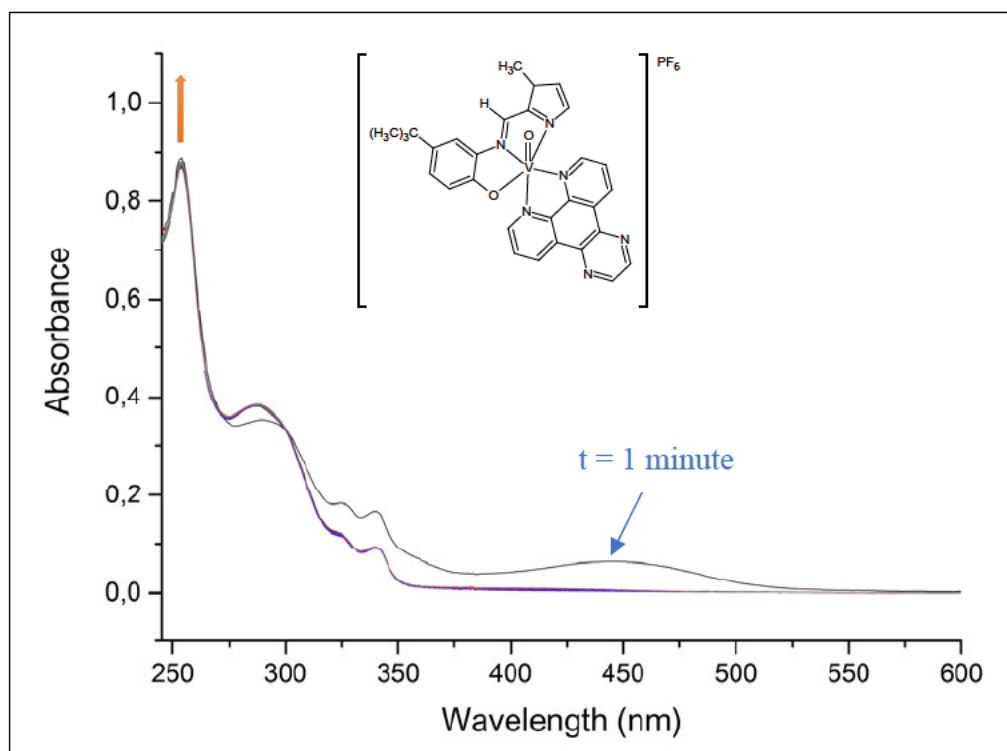
The solid complexes were first dissolved in DMSO and diluted with 0.1 M tris buffer ( $\text{NH}_2\text{C}(\text{CH}_2\text{OH})_3$ ), acidified with HCl to  $\text{pH} = 7.1$  to form a tris buffer aqueous solution containing 10% (v/v) DMSO. UV/visible absorption spectra were recorded at 1 minute, 15 minutes, 1 hour and every hour thereafter, for 18 hours after dissolution. Electronic spectra were recorded from 700 – 245 nm using a Perkin Elmer UV/visible Lambda 25 double-beam spectrometer (1.0 cm path length cuvette) equipped with a Perkin Elmer PTP-1 Peltier Temperature Programmer set to 37.0 °C. The UV WinLab-Run-Scan-Lambda 25 programme was used to record the spectra.

Figure 7.12 shows the UV/visible absorption spectra of  $[\text{VO}(\text{TERTCA})(\text{PHEN})](\text{PF}_6)$  over 18 hours in 10% DMSO, 0.1 M Tris Buffer ( $\text{pH} = 7.1$ ) solution. The first noticeable difference is the disappearance of the ligand-to-metal charge transfer (LMCT) band at 499 nm within the first 15 minutes. This could represent solvolysis processes with water, DMSO, or both, displacing original ligand and coordinating the  $\text{VO}^{2+}$  ion. The solvated-vanadium adduct thereafter appears stable, with only small spectral changes over the next 18 hours (6.07 % change at 267 nm).



**Figure 7.12** UV/visible spectra of  $[\text{VO}(\text{TERTCA})(\text{PHEN})](\text{PF}_6)$  (15  $\mu\text{M}$ ) in 10% v/v DMSO, 0.1 M Tris Buffer solution ( $\text{pH} = 7.1$ ) at 37 °C at  $t = 1$  min, 15 min, 1 hr and thereafter every hour until 18 hr after dissolution.

The UV/visible absorption spectra for  $[\text{VO}(\text{TERTCA})(\text{DPQ})](\text{PF}_6)$  over 18 hours in 10% DMSO, 0.1 M Tris Buffer (pH = 7.1) solution is shown in *Figure 7.13*. As in the cationic PHEN complex, the disappearance of the ligand-to-metal charge transfer (LMCT) band at 444 nm of  $[\text{VO}(\text{TERTCA})(\text{DPQ})](\text{PF}_6)$  occurs within the first 15 minutes. After this initial change, there is minimal change in absorbance over the next 18 hours (1.8 % change at 254 nm).



**Figure 7.13** UV/visible spectra of  $[\text{VO}(\text{TERTCA})(\text{DPQ})](\text{PF}_6)$  (14  $\mu\text{M}$ ) in 10% v/v DMSO, 0.1 M Tris Buffer solution (pH = 7.1) at 37  $^{\circ}\text{C}$ , at  $t = 1, 15 \text{ min}, 1 \text{ hr}$  and thereafter every hour until 18 hr after dissolution.

Considering the solvated complex of the cationic PHEN and DPQ analogues forms quickly, and is thereafter stable in the solvent media, this series of complexes are suitable for absorption DNA-binding studies in 10% v/v DMSO, 0.1 M Tris Buffer solution (pH = 7). However, prior to DNA binding studies, the solvolysis process must be allowed to reach equilibrium.

The mass spectroscopy study of  $[\text{VO}(\text{TERTCA})(\text{DPQ})]$  indicates that this complex is more stable with respect to solvolysis than the cationic analogues.

The DFT-simulations similarly suggest that the neutral complexes are more stable with respect to ligand substitution than the analogous cationic complexes based on the larger energy difference between the frontier molecular orbitals (Section 6.4). The absorption studies also indicate [VO(TERTA)(DPQ)] is more stable. The UV/visible absorption spectra for [VO(TERTA)(DPQ)] over 18 hours in 10% DMSO, 0.1 M Tris Buffer (pH 7.1) solution is shown in Figure 7.14. The absorbance of the LMCT band is still undergoing hypochromic and hypsochromic spectral changes 18 hours after dissolution. An isosbestic point is present at 281 nm. This could indicate slow solvolysis with the substitution of the bidentate ligand with the solvent, as described in literature.<sup>19,26,30,34,37</sup> The inset in Figure 7.14 shows an exponential decay in absorbance over time at 396 nm. This slower solvolysis process for [VO(TERTA)(DPQ)] complicates attaining meaningful DNA intrinsic binding constants for this series of complexes (discussed further in Section 8.3).

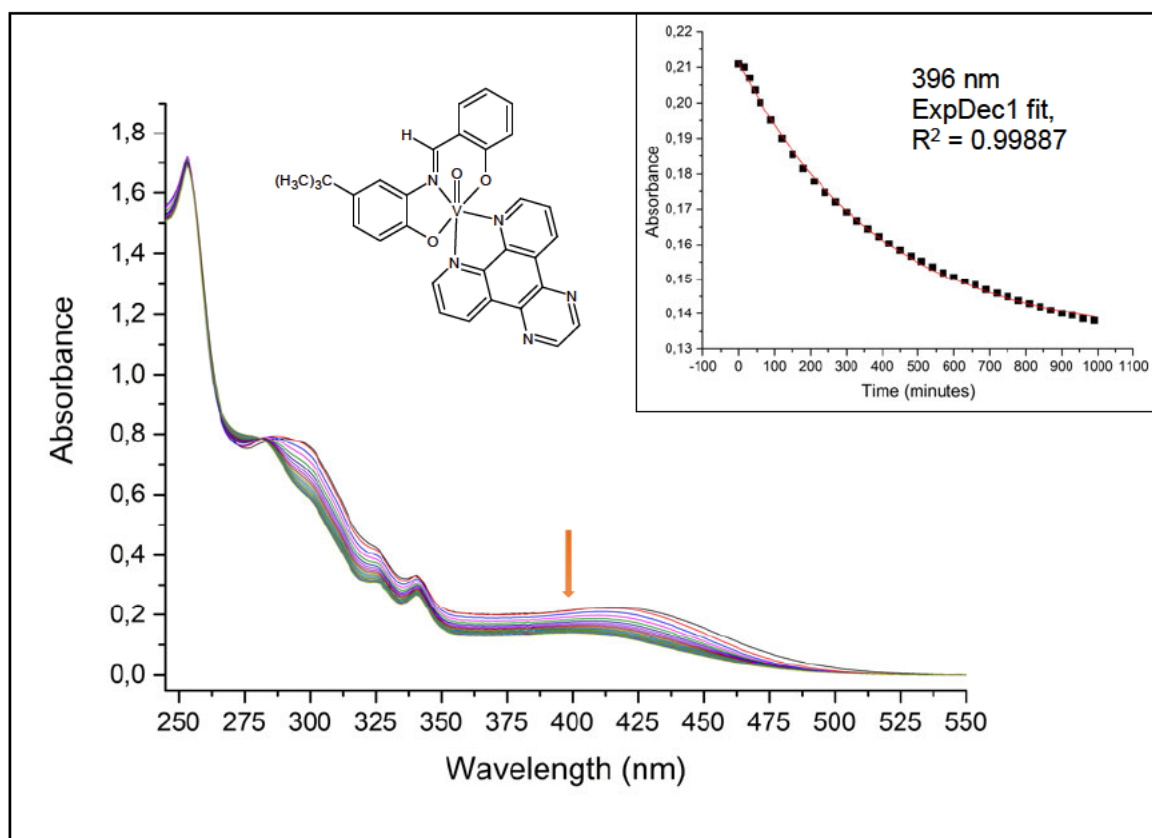


**Figure 7.14** UV/visible spectra of [VO(TERTA)(DPQ)] (30  $\mu$ M) in 10% v/v DMSO, 0.1 M Tris Buffer solution (pH = 7.1) at 37  $^{\circ}$ C at  $t = 1$  min, 15 min, 1 hr and thereafter every hour until 18 hr after dissolution.

*Inset:* Absorbance versus time plots at 396 nm.

## 7.5 NMR Spectroscopy Stability Studies of the Oxovanadium(IV) Complexes

The nature of the degradation/solvolysis products was further investigated using  $^{51}\text{V}$  NMR spectroscopy to detect possible oxidation products over time.  $^{51}\text{V}$  NMR spectra of 2 mM solutions of the complexes were recorded in  $\text{DMSO-}d_6$  on a Bruker Avance III 500 spectrometer equipped with an Oxford magnet (11.7 T) at a frequency of 131.4 MHz using a 5 mm BBOZ probe 19F/31P-109Ag-{1H} at 30 °C.  $^{51}\text{V}$  chemical shifts were referenced to neat  $\text{VOCl}_3$  as a primary external reference at 0 ppm. The oxidation process was monitored using sequential acquisitions over 21 hours for  $[\text{VO}(\text{PHA})(\text{DPQ})]$ ,  $[\text{VO}(\text{TERTA})(\text{DPQ})]$ ,  $[\text{VO}(\text{TERTCA})(\text{PHEN})](\text{PF}_6)$  and  $[\text{VO}(\text{TERTCA})(\text{DPQ})](\text{PF}_6)$ .

$[\text{VO}(\text{PHA})(\text{DPQ})]$  exhibited a broad singlet at  $-537$  ppm after dissolution which grew progressively more intense with time. An additional minor peak ( $-557$  ppm) appeared at *ca.* 3 hours (Figure 7.15).

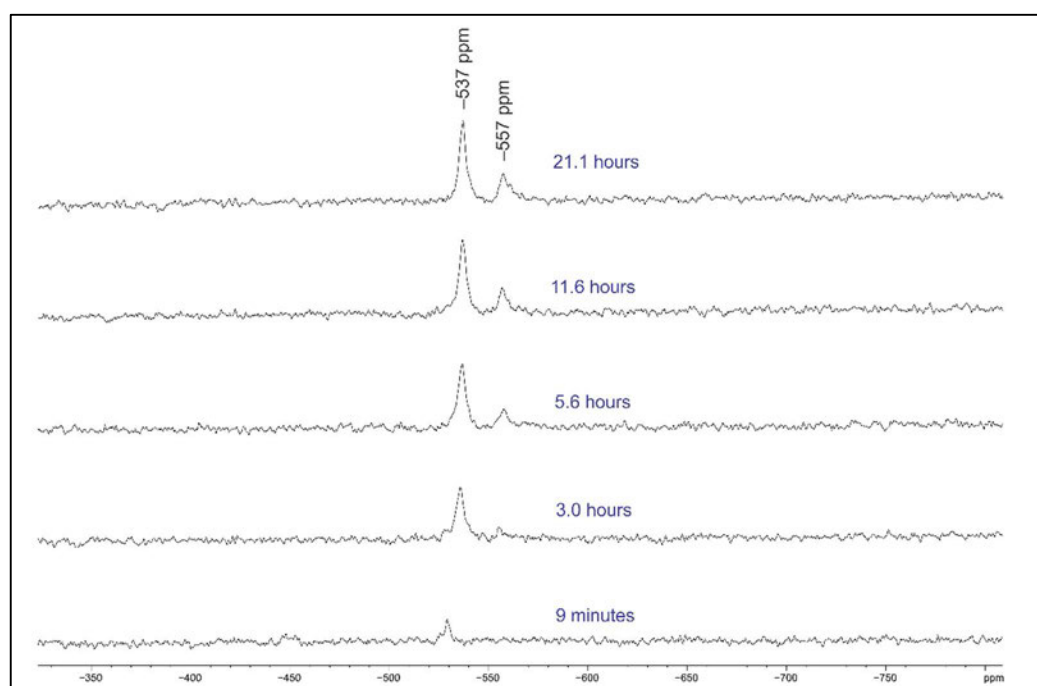


**Figure 7.15**  $^{51}\text{V}$  NMR spectra indicating the progressive oxidation of  $[\text{VO}(\text{PHA})(\text{DPQ})]$  (2 mM) in  $\text{DMSO-}d_6$ , over 21 hours. The minor peak appearing further upfield is attributed to the formation of vanadium oligomers.

Certain [VO(ONO)(PHEN)] complexes, represented by examples in *Figures 7.5 (a)* and the [VO(ONO)(DPPZ)] complexes in *Figure 7.5 (a)*, also showed minor oxidation products upfield from the major oxidation product, and are attributed to vanadate oligomers.<sup>19,26,34</sup>

The <sup>51</sup>V NMR spectra over 21 hours for [VO(TERTA)(DPQ)], [VO(TERTCA)(PHEN)](PF<sub>6</sub>) and [VO(TERTCA)(DPQ)](PF<sub>6</sub>) in DMSO-*d*<sub>6</sub> are shown in *Figures 7.16, 7.17* and *7.18*, respectively.

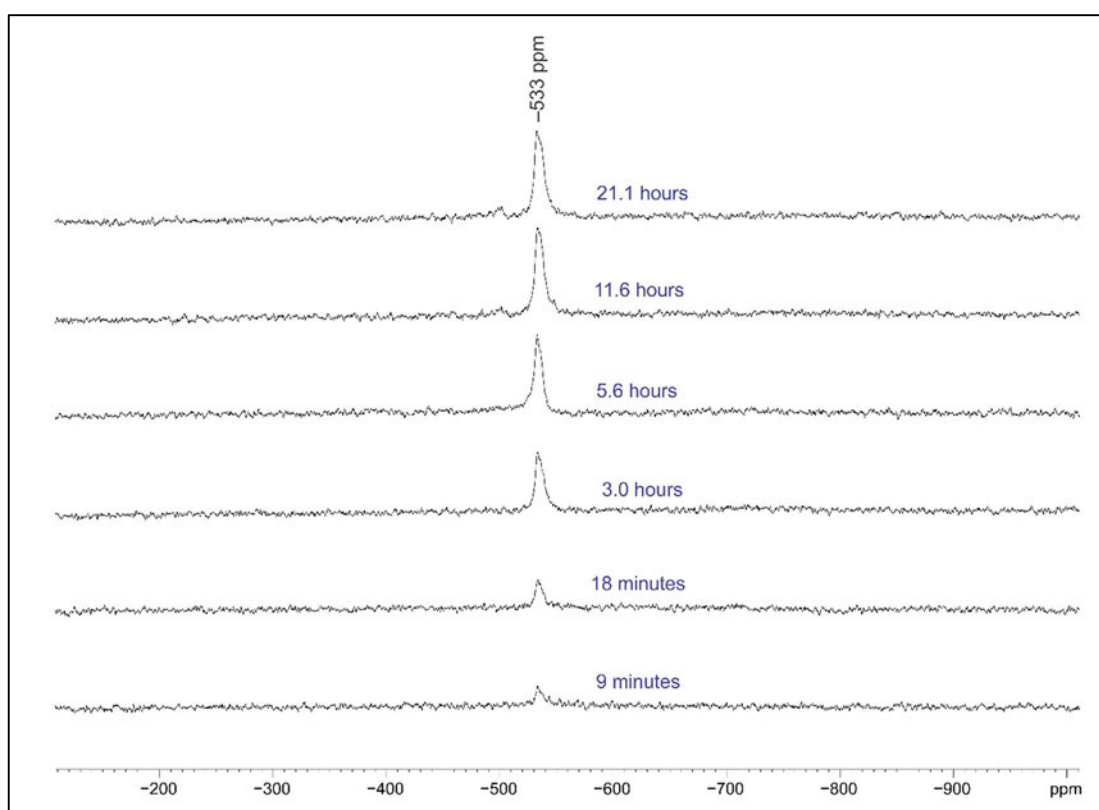


**Figure 7.16** <sup>51</sup>V NMR spectra indicating the progressive oxidation of [VO(TERTA)(DPQ)] (2 mM) in DMSO-*d*<sub>6</sub>, over 21 hours.

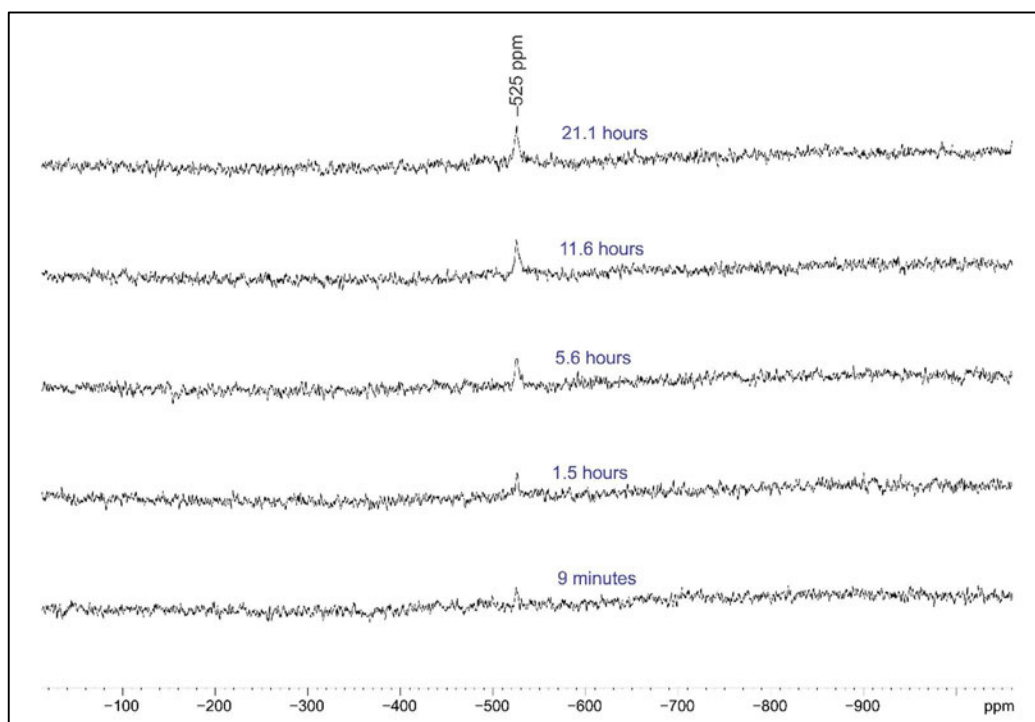


**Figure 7.17**  $^{51}\text{V}$  NMR spectra indicating the small amount of oxidised  $[\text{VO}(\text{TERTCA})(\text{PHEN})](\text{PF}_6)$  (2 mM) in  $\text{DMSO-}d_6$ , over 21 hours.

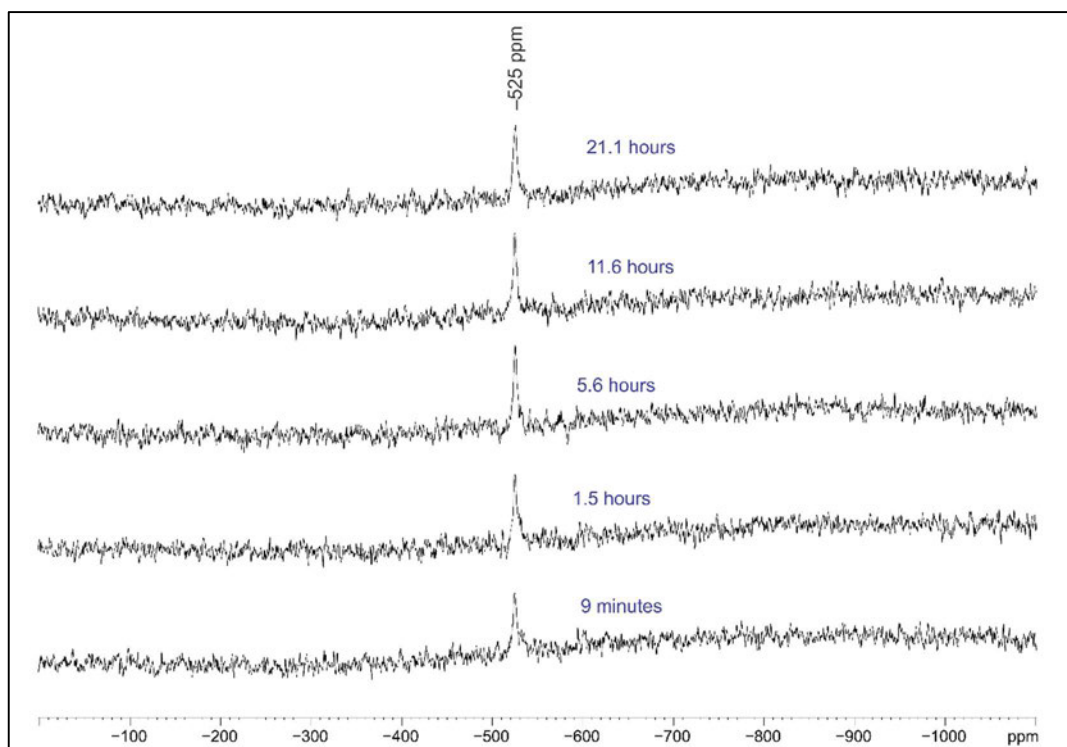


**Figure 7.18**  $^{51}\text{V}$  NMR spectra indicating the small amount of oxidised  $[\text{VO}(\text{TERTCA})(\text{DPQ})](\text{PF}_6)$  (2 mM) in  $\text{DMSO-}d_6$ , over 21 hours.

[VO(TERTA)(DPQ)] exhibited a broad singlet after dissolution at  $-533$  ppm, which grows progressively more intense with time. The cationic species [VO(TERTCA)(PHEN)](PF<sub>6</sub>) and [VO(TERTCA)(DPQ)](PF<sub>6</sub>) have the same chemical shift of oxidised product at  $-525$  ppm, although the <sup>51</sup>V peaks represent a minority of the total vanadium present.

The chemical shifts of the main oxidation product obtained for [VO(PHA)(DPQ)], [VO(TERTA)(DPQ)], [VO(TERTCA)(PHEN)](PF<sub>6</sub>) and [VO(TERTCA)(DPQ)](PF<sub>6</sub>) are similar to those reported in the literature of  $-529$  ppm to  $-547$  ppm for similar oxovanadium complexes.<sup>19,26,30,34</sup> The vanadium(V) complexes formed in this work probably correspond to [V<sup>V</sup>O<sub>2</sub>(ONO/ONN)(DMSO)] analogues, as reported in the literature.<sup>19,26,30,34</sup> The same cationic shift of the oxidised product of [VO(TERTCA)(PHEN)](PF<sub>6</sub>) and [VO(TERTCA)(DPQ)](PF<sub>6</sub>) indicate the possible substitution of the respective PHEN and DPQ ligand to form [V<sup>V</sup>O<sub>2</sub>(TERTCA)(DMSO)].

## 7.6 Conclusions on Stability of the Oxovanadium(IV) Complexes

The in-depth mass spectrometry, UV/visible and NMR spectroscopic studies indicate that the neutral and cationic complexes in this work are susceptible to solvolysis and oxidation processes in the presence of coordinating solvents, such as DMSO. Oxygen-donor ligands are favoured for coordination to vanadium(IV) over the *N,N*-bidentate ligands based on Lewis hard and soft acids and bases theory. The versatile nature of the coordination geometry and redox potential of vanadium(IV) itself, likely contribute to the observed solvolysis. The neutral oxovanadium(IV) complexes were more stable to solvolysis than the cationic analogues. The solvated adducts of the representative [VO(TERTCA)(PHEN/DPQ)](PF<sub>6</sub>) cationic complexes were considered suitable for absorption DNA-binding studies in 10% v/v DMSO, 0.1 M Tris Buffer solution (pH = 7).

## 7.7 References

1. Rehder, D., *Met. Ions Life Sci.*, **2013**, *13*, 139.
2. Rehder, D., 3.27 - Biological Activities of V and Cr. In: Reedijk, J. and Poeppelmeier, K., eds., *Comprehensive Inorganic Chemistry II* (Second Edition), Elsevier, **2013**, 821-824, 826-831, 833.
3. Azevedo, C.G., Correia, I., dos Santos, M.M.C., Santos, M.F.A., Santos-Silva, T., Douth, J., Fernandes, L. Santos, H.M., Capelo, J.L. and Costa Pessoa, J., *J. Inorg. Biochem.*, **2018**, *180*, 211.
4. Rehder, D., *Future Med. Chem.*, **2016**, *8*, 325.
5. Costa Pessoa, J., Etcheverry, S. and Gambino, D., *Coord. Chem. Rev.*, **2015**, *301-302*, 24.
6. Rehder, D., *Metallomics*, **2015**, *7*, 730.
7. Rehder, D., *Future Med. Chem.*, **2012**, *4*, 1823.
8. Nair, R.S., Kuriakose, M., Somasundaram, V., Shenoi, V., Kurup, M.R.P. and Srinivas, P., *Life Sci.*, **2014**, *116*, 90.
9. Prasad, P., Sasmal, P.K., Majumdar, R., Dighe, R. and Chakravarty, A.R., *Inorg. Chim. Acta*, **2010**, *363*, 2743.
10. Prasad, P., Sasmal, P.K., Khan, I., Kondaiah, P. and Chakravarty, A.R., *Inorg. Chim. Acta*, **2011**, *372*, 79.
11. Gryboś, R., Szklarzewicz, J., Jurowska, A. and Hodorowicz, M., *J. Mol. Struct.*, **2018**, *1171*, 880.
12. Ni, L., Zhao, H., Tao, L., Li, X., Zhou, Z., Sun, Y., Chen, C., Wei, D., Liu, Y., and Diao, G., *Dalton Trans.*, **2018**, *47*, 10035.
13. Tasiopoulus, A.J., Tolis, E.J., Tsangaris, J.M., Evangelou, A., Woollins, J.D., Slawin, A.M.Z., Costa Pessoa, J., Correia, I. and Kabanos, T.A., *J. Biol. Inorg. Chem.*, **2002**, *7*, 363.
14. Sasmal, P.K., Saha, S., Majumdar, R., Dighe, R.R. and Chakravarty, A.R., *Dalton Trans.*, **2010**, *39*, 7104.
15. Du, Y., Lu, J., Guo, H., Jiang, J., Chao, P., Chen, F. and Pan, J., *Transit. Met. Chem.*, **2010**, *35*, 859.
16. Zeng, P., He, L., Ye, Z., Yang, N., Song, Y. and Lu, J., *Transit. Met. Chem.*, **2015**, *40*, 779.

17. Sasmal, P., Patra, A.K., Nethaji, M. and Chakravarty, A.R., *Inorg. Chem.*, **2007**, *46*, 11112.
18. Bian, L., Li, L., Zhang, Q., Dong, J., Xu, T., Li, J. and Kong, J., *Transit. Met. Chem.*, **2012**, *37*, 783.
19. Benítez, J., Becco, L., Correia, I., Leal, S.M., Guiset, H., Costa Pessoa, J., Lorenzo J., Tanco, S., Escobar, P., Moreno, V., Garat, B. and Gambino, D., *J. Inorg. Biochem.*, **2011**, *105*, 303.
20. Guo, H., Lu, J., Ruan, Z., Zhang, Y., Liu, Y., Zang, L., Jiang, J. and Huang, J., *J. Coord. Chem.*, **2012**, *65*, 191.
21. Zhai, S., Guo, Q. and Dong, J., *Transit. Met. Chem.*, **2014**, *39*, 271.
22. Jing, B., Dong, J., Wei, Q., Xu, T. and Li, L., *Transit. Met. Chem.*, **2014**, *39*, 605.
23. Jing, B.Q., Dong, J.F., Li, J.H., Xu T. and Li, L.Z., *J. Coord. Chem.*, **2013**, *66*, 520.
24. Liao, X., Lu, J., Ying, P., Zhao, P., Bai, Y., Li, W. and Liu, M., *J. Biol. Inorg. Chem.*, **2013**, *18*, 975.
25. Pranczk, J., Jacewicz, D., Wyrzykowski, D., Wojtczak, A., Tesmar, A. and Chmurzyński, L., *Eur. J. Inorg. Chem.*, **2015**, 3343.
26. Benítez, J., de Queiroz, A.C., Correia, I., Alves, M.A., Alexandre-Moreira, M.S., Barreiro, E.J., Lima, L.M., Varela, J., González, M., Cerecetto, H., Moreno, V., Costa Pessoa, J. and Gambino, D. *Eur. J. Med.*, **2013**, *62*, 20.
27. Biswas, N., Bera, S., Sepay, N., Mukhopadhyay, T.K., Acharya, K., Ghosh, S., Acharyya, S., Biswas, A.K., Drew, M.G.B. and Ghosh, T., *New. J. Chem.*, **2019**, *43*, 16714.
28. Szklarzewicz, J., Jurowska, A., Hodorowicz, M., Gryboś, R., Kruczala, K., Gluch-Lutwin, M. and Kazek, G., *J. Coord. Chem.*, **2020**, *73*, 986.
29. Pranczk, J., Wyrzykowski, D., Jacewicz, D., Sikorski, A., Tesmar, A. and Chmurzyński, L., *Polyhedron*, **2015**, *100*, 74.
30. Benítez, J., Guggeri, L., Tomaz, I., Arrambide, G., Navarro, M., Costa Pessoa, J., Garat, B. and Gambino, D., *J. Inorg. Biochem.*, **2009**, *103*, 609.
31. Cavaco, I., Costa Pessoa, J., Costa, D., Duarte, M.T., Gillard, R.D. and Matias, P., *J. Chem. Soc. Dalton Trans.*, **1994**, 149.
32. Costa Pessoa, J., Calhorda, M.J., Cavaco, I., Correia, I., Duarte, M.T., Felix, V., Henriques, R.T., Piedade, M.F.M. and Tomaz, I., *J. Chem. Soc., Dalton Trans.*, **2002**, 4407.

33. Machado, I., Fernández, M., Becco, L., Garat, B., Brissos, R.F., Zabarska, N., Gamez, P., Marques, F., Correia, I., Costa Pessoa, J. and Gambino, D., *Inorg. Chim. Acta*, **2014**, *420*, 39.
34. Fernández, M., Becco, L., Correia, I., Benítez, J., Piro, O.E., Echeverria, G.A., Medeiros, A., Comini, M., Lavaggi, M.L., González, M., Cerecetto, H., Moreno, V., Costa Pessoa, J., Garat, B. and Gambino, D., *J. Biol. Inorg. Chem.*, **2013**, *127*, 150.
35. Banerjee, A., Dash, S.P., Mohanty, M., Sanna, D., Sciortino, G., Ugone, V., Garriba, E., Reuter, H., Kaminsky, W. and Dinda, R., *J. Inorg. Biochem.*, **2019**, *199*, 110786.
36. Scalese, G., Correia, I., Benítez, J., Rostán, S., Marques, F., Mendes, F., Matos, A.P., Costa Pessoa, J. and Gambino, D., *J. Inorg. Biochem.*, **2017**, *166*, 162.
37. Szklarzewicz, J., Jurowska, A., Hodorowicz, M., Gryboś, R. And Matoga, D., *J. Mol. Struc.*, **2019**, *1180*, 839.
38. Correia, I., Roy, S., Matos, C.P., Borovic, S., Butenko, N., Cavaco, I., Marques, F., Lorenzo, J., Rodríguez, A., Moreno, V. and Costa Pessoa, J., *J. Inorg. Biochem.*, **2015**, *147*, 134.
39. Corsello, S., Spangler, R., Nagari, R. and Golub, T., inventors; Vanadium Compositions and Methods for Treatment of Cancer, World Intellectual Property Organization WO 2020/102295 A1. patent application PCT/US2019/061108, **2020/05/22**.
40. Evangelou, A.M, *Cr. Rev. Oncol-Hem.*, **2002**, *42*, 249.
41. Thompson, K.H., Lichter, J., LeBel, C., Scaife, M.C., McNeill, J.H. and Orvig, C., *J. Inorg. Biochem.*, **2009**, *103*, 554.
42. Jakusch, T. and Kiss, T., *Coord. Chem. Rev.*, **2017**, *351*, 118.
43. Huheey, J.E., Keiter, E.A. and Keiter, R.L. *Inorganic Chemistry: Principles of Structure and Reactivity* (Fourth edition), HarperCollins College; **1993**, 345-347.
44. Sasmal, P., Patra, A.K. and Chakravarty, A.R., *J. Inorg. Biochem.*, **2008**, *102*, 1463.

## **Chapter Eight: Cytotoxicity and DNA Interaction**

### **Studies**

#### **8.1 Introduction**

As discussed in *Chapter One*, vanadium compounds, especially those with aromatic ligands, are cytotoxic towards certain forms of cancer. Oxovanadium complexes of the type [VO(ONO)(DPPZ)] have been reported to be photocytotoxic under visible light against cervical cancer cells.<sup>1</sup> Neutral oxovanadium complexes of the type [VO(ONO)(PHEN)] have been found to be cytotoxic against myeloma, gliomas, neuroblastoma, breast, ovarian, prostate, lung, liver and leukaemia cancer cell lines.<sup>2-7</sup> Cationic [VO(ONO)(DPPZ)](Cl), [VO(ONN)(DPPZ)](ClO<sub>4</sub>) and [VO(NNN)(DPPZ)](NO<sub>3</sub>)<sub>2</sub> complexes exhibit photocytotoxicity under visible light against cervical cancer HeLa cells.<sup>8-10</sup> Cytotoxicity studies of the oxovanadium complexes synthesised, in this work, are presented in *Section 8.2*. These data give an indication of the potential of these metallodrugs.

It is thought that DNA is a key biological target whereby the bidentate polypyridyl ligand interacts with DNA to control proliferation of the cells.<sup>4,7,11,12</sup> DNA binding studies of the synthesised oxovanadium complexes were, thus, included in the scope of this project.

Previous literature reports, on the DNA binding studies of oxovanadium complexes with an *O,N,O'*-tridentate ligand and a DPQ co-ligand, suggest that the neutral DPQ complexes in this work could be DNA groove binding agents with intrinsic DNA binding constants in the order of 10<sup>4</sup> M<sup>-1</sup>.<sup>1,13</sup> The cationic complexes are anticipated to be partial intercalators to DNA.<sup>10</sup> Their intrinsic DNA binding constants should be in the order of 10<sup>4</sup> M<sup>-1</sup> for the cationic complexes with a PHEN co-ligand and 10<sup>5</sup> M<sup>-1</sup> for the cationic complexes with a DPQ co-ligand of extended  $\pi$ -conjugation, based on previous studies of related compounds.<sup>10</sup>

The mode and strength of binding of the oxovanadium complexes was evaluated by UV/visible absorption titration (Section 8.3), emission fluorescence spectroscopy (Section 8.4) and DNA viscosity studies (Section 8.5). Computational molecular docking studies were also used to predict the binding mode and binding affinity of selected oxovanadium(IV) complexes to DNA (Section 8.6). The DNA cleavage ability of the complexes were assessed by gel electrophoresis (Section 8.7). The mechanism of DNA cleavage of selected oxovanadium complexes was, additionally, assessed through gel electrophoresis and EPR techniques (Section 8.8). Elemental analysis indicated sufficient purity of the compounds for biological testing.

## **8.2 Cell Cytotoxicity Studies**

### **8.2.1 Introduction and Experimental Cell Cytotoxicity Studies**

The cytotoxicity assay was conducted by Alexandré Delpont (Department of Biochemistry, UKZN, PMB) as per the following standard method.<sup>14,15</sup> Briefly, 96-well microtiter plates were seeded with HEK293 (Control, healthy renal cells), MDA-MB-231 (triple-negative breast cancer), HeLa (cervical cancer) and SH-SY5Y (neuroblastoma, brain cancer) cell lines at a concentration of  $2 \times 10^5$  cells/ml. The HEK293 healthy cell line was included to determine the toxicity of the oxovanadium compounds so that the selectivity index towards tumour cells can be calculated. The human-derived HeLa cell line is a commonly used model for cervical cancer as this cell line is robust and exhibits good growth characteristics.<sup>16</sup> Breast cancer has a high mortality rate in Africa (27 deaths per 100 000 women in Western Africa in 2020).<sup>17</sup> Breast cancer incidence rates are also increasing across the African continent (23 to 26 per 100 000 between 2000 and 2015).<sup>17</sup> In addition, triple negative breast cancer, which currently has limited treatment options, represents a high frequency of African woman with breast cancer (27%) across Africa and disproportionately affects African women across the globe.<sup>17,18</sup> MDA-MB-231 is an aggressive and invasive cell line commonly used as a model of triple negative late-stage breast cancer.<sup>18,19</sup> SH-SY5Y neuroblastoma cell line is widely used as a model for neurodegenerative disorders, neuronal outgrowth, and brain tumour progression owing to its neuronal characteristics and the expression of neuronal tumour markers.<sup>20</sup>

The cell culture media was DMEM supplemented with 10% foetal bovine serum (FBS) with 0.1 X penicillin-streptomycin and 50 ug/ml gentamicin. The cells were allowed to stabilise for 4 hours at 37 °C and 5% CO<sub>2</sub>. Thereafter, the neutral and cationic oxovanadium test compounds and cisplatin (a control) were added to the plate through two-fold serial dilutions to allow for eight final compound concentrations ranging from 50 to 0.391 μM in a total volume of 200 μL / well. All metal compounds were made up in DMSO and stored at -20 °C prior to use. The plate was then incubated for 96 hours at 37 °C and 5% CO<sub>2</sub>. 20 μL CellTiter 96® AQueous One Solution (Promega, Madison, WI, USA) was added to each well. The plates were then incubated for four hours. Absorbance, of the cell lysate, was read at 490 nm on a multiplate reader (Molecular Devices, San Jose, CA, USA). EC<sub>50</sub> values were calculated from the data as the concentration of each compound required to reduce cell viability by 50%. These values were calculated using GraphPad Prism 8.0 software (GraphPad Software, San Deigo, CA, USA).

### **8.2.2 Results and Discussion Cell Cytotoxicity Studies**

The average EC<sub>50</sub> values of at least three separate experiments with standard deviations of cisplatin (control) and oxovanadium(IV) compounds against healthy and cancer cell lines are reported in *Table 8.1*.

**Table 8.1** EC<sub>50</sub> of cisplatin (control) and oxovanadium(IV) compounds against healthy and cancer cell lines.

Compound	EC <sub>50</sub> ± Std Dev (µM)			
	HEK293	MDA-MB	HELA	SH-SY5Y
Cisplatin	14.2 ± 3.8	>50	22.68 ± 4.89	ND
[VO(PHA)(DPQ)]	≤ 1.56 (n = 4)	2.26 ± 1.40	≥ 50	5.47 ± 0.78
[VO(MEA)(DPQ)]	≤ 1.56 (n = 4)	4.42 ± 2.30	≥ 50	8.91 ± 2.09
[VO(TERTA)(DPQ)]	≤ 1.56 (n = 4)	3.49 ± 1.05	≥ 50	5.69 ± 0.2
[VO(CLA)(DPQ)]	≤ 1.56 (n = 4)	2.60 ± 1.21	≥ 50	11.73 ± 0.47
[VO(SOA)(DPQ)]	≤ 1.56 (n = 4)	5.48 ± 1.84	≥ 50	12.57 ± 0.08
[VO(NAA)(DPQ)]	≤ 1.56 (n = 4)	3.06 ± 2.41	≥ 50	7.87 ± 0.168
[VO(PHPHA)(DPQ)]	6.3 ± 0.05	46.82 ± 4.99	≥ 50	≥ 50
[VO(PHCA)(PHEN)](PF <sub>6</sub> )	4.3 ± 1.7	5.06 ± 1.49	2.86 ± 0.87	2.80 ± 0.02
[VO(MECA)(PHEN)](PF <sub>6</sub> )	3.6 ± 2.6	3.16 ± 3.81	4.84 ± 2.53	5.96 ± 0.16
[VO(TERTCA)(PHEN)](PF <sub>6</sub> )	≤ 1.56	3.19 ± 1.71	2.68 ± 0.12	3.35 ± 0.04
[VO(PHPHCA)(PHEN)](PF <sub>6</sub> )	1.8 ± 0.2	4.72 ± 2.95	4.09 ± 1.96	2.53 ± 0.64
[VO(MECA)(DPQ)](PF <sub>6</sub> )	35.1 ± 11.0	7.60 ± 6.95	4.73 ± 1.77	5.97 ± 0.13
[VO(TERTCA)(DPQ)](PF <sub>6</sub> )	≤ 1.56	23.76 ± 7.12	17.70 ± 2.15	7.19 ± 1.36
n = 3 unless otherwise indicated;				
ND = Not determined				
EC <sub>50</sub> : 50% cytotoxic concentration. Calculated as the concentration of compound that gives half-maximal response.				

The cell screening data in *Table 8.1* shows several interesting trends and remarkably different cytotoxicity profiles for each of the compounds against each cell line. In general, the oxovanadium compounds synthesised and screened for cytotoxicity in this work are active against the MDA-MB and SH-SY5Y tumour cell lines. It is interesting to note that the addition of a phenyl ring to the tridentate Schiff base ligand reduced the cytotoxicity of [VO(PHPHA)(DPQ)] by an order of magnitude against both MDA-MB and SHS5Y. This implies that substituents on the tridentate-*O,N,O'* ligand alter the physicochemical properties and subsequently the cytotoxicity of the active vanadium species.

The difference could be due to solubility limitations or aggregation of the neutral [VO(PHPHA)(DPQ)] compound causing a lower effective concentration of the compound in solution. Also, the added bulk of the ligand may prevent effective DNA binding or changing the mechanism of action. Although less noticeable, the compound [VO(SOA)(DPQ)], which has a bulky sulfonyl group, is also less cytotoxic. This again suggests an inverse relationship between steric bulk of the substituents and cytotoxicity. The [VO(PHA)(DPQ)] derivative, with no substituent on the phenyl ring, is the most active of the neutral series of complexes against both MDA-MB and SH-SY5Y.

The cytotoxicity of the compounds towards MDA-MB is a particularly exciting result as this represents a triple-negative breast cancer. If the data point of EC<sub>50</sub> of 46.82 μM for [VO(PHPHA)(DPQ)] is removed, the remaining neutral compounds have a mean (n = 6) EC<sub>50</sub> of 3.6 μM. The cationic compounds (excluding [VO(TERTCA)(DPQ)](PF<sub>6</sub>)) have a mean (n = 5) EC<sub>50</sub> of 4.7 μM against MDA-MB. This makes these compounds more effective against this cell line than commercially available compounds such as camptothecin, 5-fluorouracil and cisplatin.<sup>21</sup> This is an encouraging result. A comparison of the cytotoxicity of the oxovanadium compounds and commercially available drugs towards this particular cell line is shown in *Figure 8.1*.

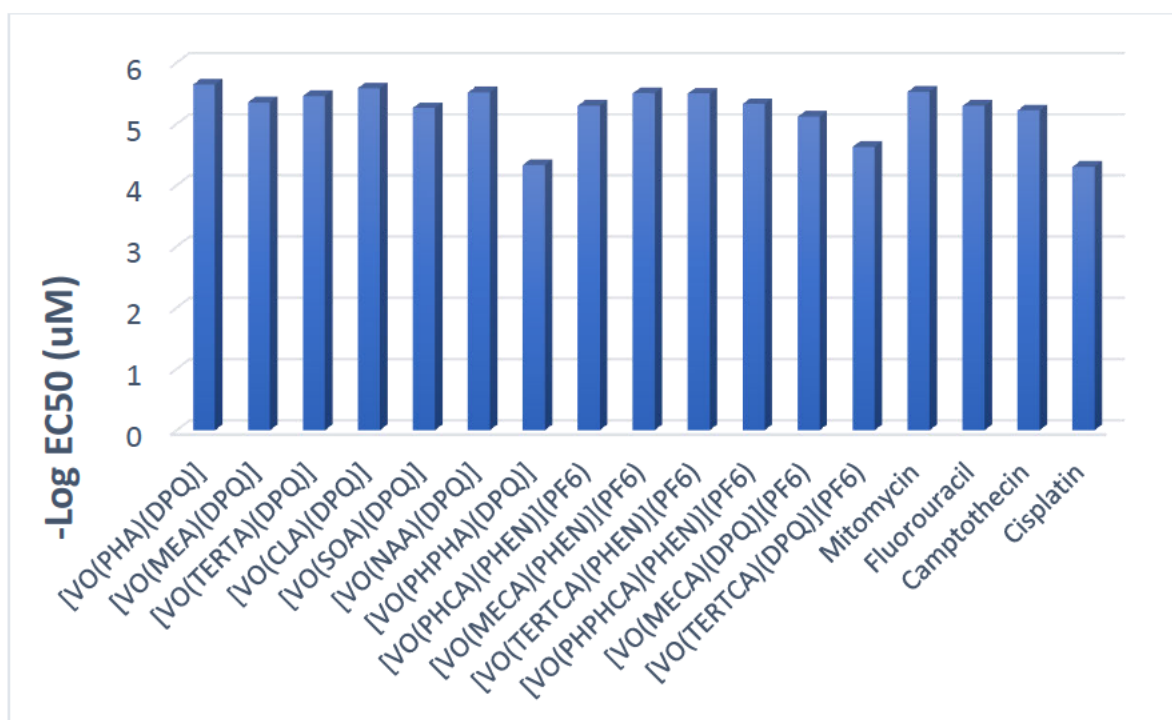


**Figure 8.1** Plot of  $-\text{Log}(\text{EC}_{50})$  data showing the cytotoxicity of the oxovanadium compounds synthesised in this work compared to commercially available drugs. The data is shown for cell line MDA-MB.<sup>21</sup>

The variation in cytotoxicity of each compound against each of the tested cell lines is also promising. This suggests that the compounds are genuine chemotherapeutics with a well-defined mechanism of action and not mere poisons. The cationic chelates are cytotoxic towards the HeLa cell line, which was entirely resistant to the neutral analogues. The  $\text{EC}_{50}$  values of the neutral analogues were all above the experimental range of concentrations, while the mean ( $n = 6$ )  $\text{EC}_{50}$  value of the cationic chelates is  $6.2 \mu\text{M}$ . This indicates the tridentate ligand and/or charge of the complex does influence the cytotoxic properties of the oxovanadium complexes. The cationic charge was a key design feature in this group of complexes to enable electrostatic attraction between the oxovanadium compounds and DNA (the intended cellular target), stabilising the DNA/drug conjugate. These data illustrate the importance of having an overall positive charge when developing metallodrugs.

All the cationic PHEN complexes had similar cytotoxicities towards the three cancerous cell lines. The mean ( $n = 4$ )  $\text{EC}_{50}$  for the four cationic chelates with PHEN co-ligands are  $4.0$ ,  $3.6$  and  $3.7 \mu\text{M}$  against the cell lines MDA-MB, HeLa and SH-SY5Y, respectively.

This could suggest that the same solvated vanadium species, formed by solvolysis of the cationic PHEN complex, is acting as a pro-drug and causing the cytotoxic effect. Interestingly, changing the co-ligand from PHEN to DPQ reduced the cytotoxicity of the *tert*-butyl cationic derivative against all three carcinoma cell lines. It is possible that the reduced aqueous solubility of the *tert*-butyl DPQ derivative may impact on its movement within a cell and hence reduces its cytotoxicity. The [VO(TERTCA)(DPQ)](PF<sub>6</sub>) derivative was also less cytotoxic than [VO(MECA)(DPQ)](PF<sub>6</sub>) against the MDA-MB and HeLa cell lines but of similar cytotoxicity against the SH-SY5Y cell line. These results indicate that a slight change in the tridentate ligand of a cationic oxovanadium complex can affect the cytotoxic properties of the compound. In this case the two compounds vary only by the functional group on the tridentate ligand.

Although the raw cytotoxicity data are encouraging, the high cytotoxicity towards HEK293, which represents healthy renal cells, is of concern. In almost all cases, the cytotoxicity towards this cell line is below the limit of detection of 1.56 μM.

In general, the cationic chelates are less toxic towards the healthy cell line than the neutral compounds. The selectivity index of each cationic chelate against each of the cell lines is summarised in *Table 8.2*. The selectivity index is a quick illustration of how the compounds affect the growth of healthy cells in comparison to neoplastic tissue. The renal cell line HEK293 is used as the reference point for calculating the selectivity index.

**Table 8.2** Selectivity index of the cationic oxovanadium compounds and cisplatin towards various tumour cell lines.

Cell line	MDA-MB	HeLa	SH-SY5Y
Cisplatin	<0.3*	0.6	Not determined
[VO(PHCA)(PHEN)](PF <sub>6</sub> )	0.8	1.5	1.5
[VO(MECA)(PHEN)](PF <sub>6</sub> )	1.1	0.7	0.6
[VO(TERTCA)(PHEN)](PF <sub>6</sub> )	<0.5*	<0.6*	<0.5*
[VO(PHPHCA)(PHEN)](PF <sub>6</sub> )	0.4	0.4	0.7
[VO(MECA)(DPQ)](PF <sub>6</sub> )	4.6	7.4	5.9
[VO(TERTCA)(DPQ)](PF <sub>6</sub> )	<0.1*	<0.1*	<0.2*

\*Selectivity index can only be reported as lower than indicated due to compounds having cytotoxicities outside of the experimental concentration range.

The data in *Table 8.2* show that in general, similar to the neutral compounds, the cationic metal complexes are more toxic towards healthy cells than tumour cells. The low selectivity of cisplatin is the cause of some of the side effects, suggesting that the current compounds would have the same issues. There is, however, a notable exception: [VO(MECA)(DPQ)](PF<sub>6</sub>). This compound is significantly more cytotoxic towards the tumour cells than the healthy cell line. This suggests that this is the lead compound developed in this series and warrants further investigation.

### 8.3 UV/visible Spectroscopic DNA Binding Studies

#### 8.3.1 Introduction and Experimental Absorption DNA Binding Studies

The binding of selected oxovanadium(IV) complexes to calf thymus DNA was studied by UV/visible absorption titrations in 100 mM Tris–HCl buffer (pH 7.1) containing 10% v/v DMSO (the DMSO was required to increase solubility of the metal chelates). The concentration of the oxovanadium(IV) complex was kept constant whilst increasing the concentration of the calf thymus DNA during the absorption titrations. The 100 mM Tris buffer (TRIZMA<sup>®</sup> base purchased from Sigma-Aldrich) was prepared with ultrapure water (resistivity = 18 MΩ) and acidified with HCl to pH = 7.1. DMSO (liquid chromatography grade) was purchased from Merck. *Ct*-DNA was purchased from Sigma-Aldrich. The absorption spectra were recorded from 700 – 220 nm using a Perkin Elmer UV/Vis Lambda 25 double-beam spectrometer (1.0 cm path length cuvette). The spectrometer was equipped with a Perkin Elmer PTP-1 Peltier Temperature Programmer set to 37.0 °C. The UV WinLab-Run-Scan-Lambda 25 programme was used to record the spectra.

*Ct*-DNA was stirred in 10% v/v DMSO 100 mM Tris-HCl buffer solution (pH 7.1) overnight and then filtered. The purity of the resultant DNA solution was checked by determining the absorbance ratio  $A_{260}/A_{280}$ . The  $A_{260}/A_{280}$  ratio of 1.9:1 indicated the DNA stock solution was free from protein impurities.<sup>1,22</sup> The concentration of the *ct*-DNA stock solution was determined from its absorption intensity at 260 nm using Beer's Law with the molar extension coefficient value of  $13\,200\text{ M}^{-1}\text{ cm}^{-1}$  per DNA base pair at 260 nm.<sup>23</sup>

The oxovanadium complex solutions were prepared by dissolving the solid complexes in DMSO and then diluting with the 100 mM Tris-HCl buffer (pH = 7.1) to form a 10% v/v DMSO 100 mM Tris-HCl buffer aqueous solution. The respective oxovanadium complex solutions were left overnight before any addition of DNA to allow for the solvolysis processes to finish. As with the cell cytotoxicity data, the DNA binding affinities are thus measured for the pro-drug. Samples were incubated for 10 minutes after the addition of each aliquot of the *ct*-DNA solution, at 37.0 °C, before the absorption spectrum was recorded. The intrinsic binding constants ( $K_b$ ) were obtained by monitoring the change in absorbance of the ligand  $\pi \rightarrow \pi^*$  band at 254 nm. The values were corrected for the absorbance of *ct*-DNA by adding equal aliquots of *ct*-DNA stock solution to both the sample cell and the reference cell.

$K_b$  (intrinsic DNA binding constant) is obtained by the ratio of the slope to intercept from a plot of  $\frac{[DNA]}{\epsilon_a - \epsilon_f}$  versus [DNA] using the Wolfe-Shimmer equation (Equation 8.1):<sup>24-26</sup>

$$\frac{[DNA]}{\epsilon_a - \epsilon_f} = \frac{[DNA]}{\epsilon_b - \epsilon_f} + \frac{1}{K_b(\epsilon_b - \epsilon_f)} \quad \text{Equation 8.1}$$

where [DNA] = Concentration of *ct*-DNA.

$\epsilon_a$  = Apparent extension coefficient ( $A_{\text{obs}} / [V \text{ complex}]$ ).

$\epsilon_f$  = Extension coefficient for the free oxovanadium complex.

$\epsilon_b$  = Extension coefficient for the oxovanadium complex in the fully bound form.

The plots were analysed using Origin Lab, version 9.1.

### 8.3.2 Results and Discussion Absorption DNA Binding Studies

The addition of *ct*-DNA to [VO(MECA)(DPQ)](PF<sub>6</sub>) (Figure 8.2) and [VO(TERTCA)(DPQ)](PF<sub>6</sub>) (Figure E11, Appendix E) resulted in hypochromism and a slight blue shift of 1 nm from 254 nm for both complexes. There was a slight red shift of 3 nm from 286 nm to 289 nm for [VO(TERTCA)(DPQ)](PF<sub>6</sub>) and of 1 nm from 287 nm to 288 nm for [VO(MECA)(DPQ)](PF<sub>6</sub>). Hypochromic shifts generally indicate stacking interactions between the DNA base pairs and aromatic chromophores of the complexes' ligands.<sup>27,28</sup>

The DFT-simulated geometry-optimised structures for  $[\text{VO}(\text{MECA})(\text{DPQ})]^+$  and  $[\text{VO}(\text{TERTCA})(\text{DPQ})]^+$  show that the DPQ ligand is free from steric hindrance by the tridentate ligand and so either ligand of the complex is available to bind to DNA (Section 6.4).

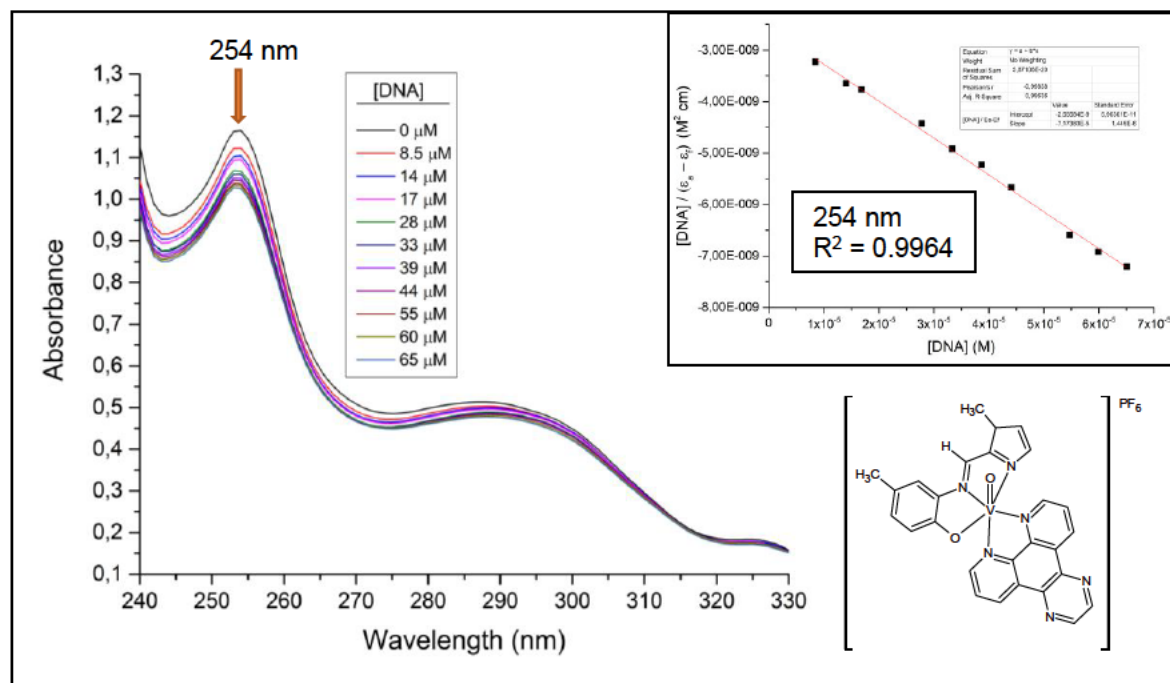


**Figure 8.2** UV/visible absorbance spectra of  $[\text{VO}(\text{MECA})(\text{DPQ})](\text{PF}_6)$  (15 μM) in the absence and presence of *ct*-DNA (0–65 μM) in 10% v/v DMSO/Tris buffer (pH 7.1) at 37 °C. *Inset*: Plots of  $[\text{DNA}] / (\epsilon_a - \epsilon_f)$  versus  $[\text{DNA}]$  for the titration of  $[\text{VO}(\text{MECA})(\text{DPQ})](\text{PF}_6)$  with *ct*-DNA at 254 nm. This plot was used to calculate the intrinsic DNA binding constant of  $2.8 \times 10^4 \text{ M}^{-1}$ .

The intrinsic binding constants were calculated to be  $2.8 \times 10^4$  and  $1.3 \times 10^4 \text{ M}^{-1}$  for  $[\text{VO}(\text{MECA})(\text{DPQ})](\text{PF}_6)$  and  $[\text{VO}(\text{TERTCA})(\text{DPQ})](\text{PF}_6)$ , respectively. Intrinsic binding constants of this order of magnitude are typically associated with DNA groove-binders.<sup>1,13</sup> The DFT-simulated ESP plots of  $[\text{VO}(\text{MECA})(\text{DPQ})]^+$  and  $[\text{VO}(\text{TERTCA})(\text{DPQ})]^+$  indicated positive potentials and so electrostatic interactions with the negatively charged phosphate backbone of DNA are also possible.

The lower intrinsic constant of  $[\text{VO}(\text{TERTCA})(\text{DPQ})](\text{PF}_6)$  is attributed to the steric bulk of the *tert*-butyl substituent on the tridentate ligand, in comparison to the methyl substituent of  $[\text{VO}(\text{MECA})(\text{DPQ})](\text{PF}_6)$ . The DFT-simulations determined the alpha and beta HOMOs and LUMOs molecular orbitals reside on the tridentate ligand for the cationic complexes (Section 6.4). Therefore, changing the substituent on the tridentate ligand would change the DNA binding properties of the complex.

Intrinsic DNA binding constants for the cationic complexes with PHEN co-ligands could not be determined as the UV/visible spectra showed minimal changes in absorption upon addition of DNA. This implies that the solvated adducts of the PHEN complexes have a low DNA binding affinity. Possible oxovanadium speciated drugs from  $[\text{VO}(\text{ONO})(\text{NN})]$  complexes have been reported to be  $[\text{VO}(\text{ONO})]$  and  $[\text{VO}(\text{NN})]$  species.<sup>29</sup> The DFT-simulated geometry-optimised structures for  $[\text{VO}(\text{MECA})(\text{DPQ})]^+$  and  $[\text{VO}(\text{TERTCA})(\text{DPQ})]^+$  (Section 6.4) and the solid-states structures for the PHEN complexes indicate the bidentate *N,N*-donor co-ligands are free from steric hindrance and so are available to bind to DNA. This implies that the DPQ complexes would have higher DNA binding constants than the PHEN complexes due to the extended conjugation of the DPQ ligand.

The UV/visible absorption stability studies of  $[\text{VO}(\text{TERTCA})(\text{DPQ})]$  (30  $\mu\text{M}$ ) in 10% v/v DMSO, 100 mM Tris Buffer solution (pH = 7.1), at 37 °C, indicated that hypochromic and hypsochromic changes in absorbance were still ongoing 18 hours post-preparation (Section 7.4, Figure 7.14). The changes in absorbance for the interaction of  $[\text{VO}(\text{TERTCA})(\text{DPQ})]$  with DNA also indicated hypochromic and hypsochromic changes in absorbance (Figure 8.3). The binding constants for the neutral DPQ complexes with DNA could, therefore, not be determined with any certainty. In future work, the DNA intrinsic constant could be more reliably measured by first allowing the slow solvolysis of the metal chelate to take place over several days and only then performing the DNA titration.

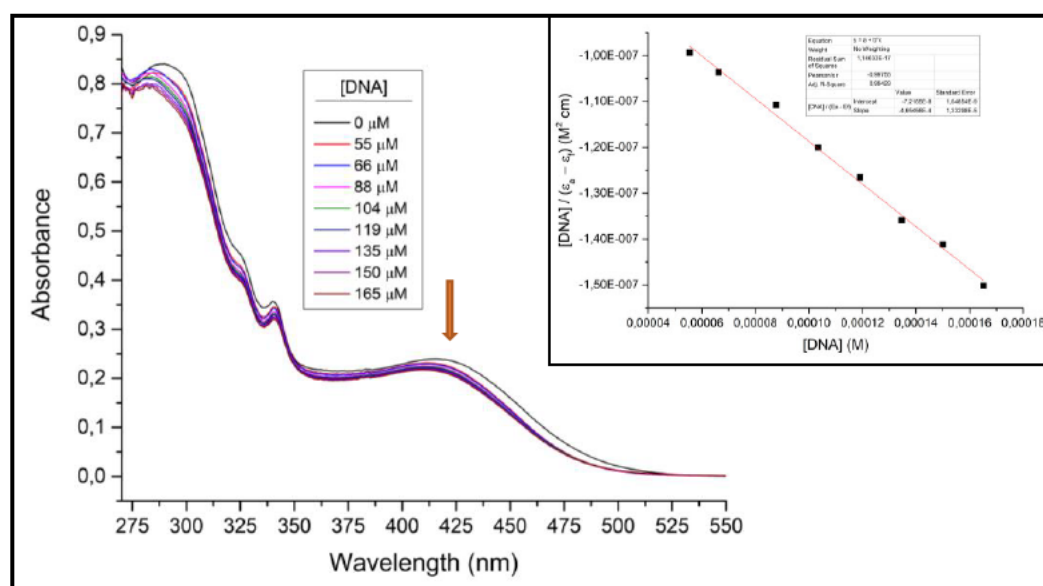


**Figure 8.3** UV/visible absorbance spectra of [VO(TERTA)(DPQ)] (30 μM) in the absence and presence of *ct*-DNA (0-165 μM) in 10% v/v DMSO, 100 mM Tris buffer (pH 7.1) at 37 °C. *Inset:* Plots of [DNA] / (ε<sub>a</sub> - ε<sub>f</sub>) versus [DNA] for the titration of [VO(TERTA)(DPQ)] with *ct*-DNA at 428 nm. Based on these spectral changes, a tentative DNA intrinsic constant of  $6.5 \times 10^3 \text{ M}^{-1}$  was calculated.

## 8.4 Competitive DNA Binding by Ethidium Bromide Displacement

### 8.4.1 Introduction Fluorescence Emission Studies

Competitive fluorescence DNA binding studies by ethidium bromide displacement of selected oxovanadium complexes were conducted to further investigate the binding mode of the complexes to DNA. Ethidium bromide is known to bind to DNA in an intercalative mode between the base pairs of DNA.<sup>22</sup> If a complex can competitively displace the bound ethidium bromide from the DNA helix, it could suggest that the complex binds to DNA in a similar mode to ethidium bromide, i.e. a DNA intercalator.<sup>22</sup> The fluorescence intensity of ethidium bromide in aqueous solution and of DNA itself is very weak. When ethidium bromide is bound to DNA, however, the fluorescence is intense due to a complex electron transfer process. If a metal complex displaces ethidium bromide from the DNA, this results in a decrease (quenching) of the fluorescence intensity.<sup>30-32</sup> If there is no significant change in the fluorescence intensity of the EB-DNA conjugate upon addition of the metal complex, this suggests that the complex binds to DNA in a non-intercalative mode, such as groove binding.<sup>22</sup>

### 8.4.2 Determination of the DNA Binding Constant of Ethidium Bromide

The binding constant of ethidium bromide to DNA is needed to calculate the apparent binding constants of the vanadium complexes to DNA. The equilibrium binding constant of ethidium bromide to *ct*-DNA was determined experimentally through direct UV/visible absorption titration.<sup>33</sup> The DNA solution was prepared and screened for purity as described in *Section 8.3.1*.

Ethidium bromide was purchased from Sigma Aldrich. The initial ethidium bromide solution was prepared in 0.100 M Tris-HCl Buffer (10% v/v DMSO, pH 7.0) at a concentration of  $9.58 \times 10^{-5}$  M. The absorption spectra of ethidium bromide were then recorded from 700 - 200 nm as increasing amounts of the *ct*-DNA stock solution were added. Samples were incubated for ten minutes after the addition of the DNA solution at 25.0 °C before each spectrum was recorded.

Bathochromism (red shifting) and hypochromism are expected upon addition of DNA to ethidium bromide. This is due to the concentration of free ethidium bromide decreasing and the consequent  $\pi$ -stacking between the aromatic chromophores of the base pairs of DNA and ethidium bromide.<sup>33-36</sup> *Figure 8.4* shows the large bathochromic shift of 33 nm from 488 nm to 521 nm. Hypochromism of 45% (at 488 nm) was also noted. The absorption spectra were corrected for dilution accordingly. The isosbestic point at 522 nm indicates the two forms of ethidium bromide in solution – bound and unbound.<sup>36</sup>

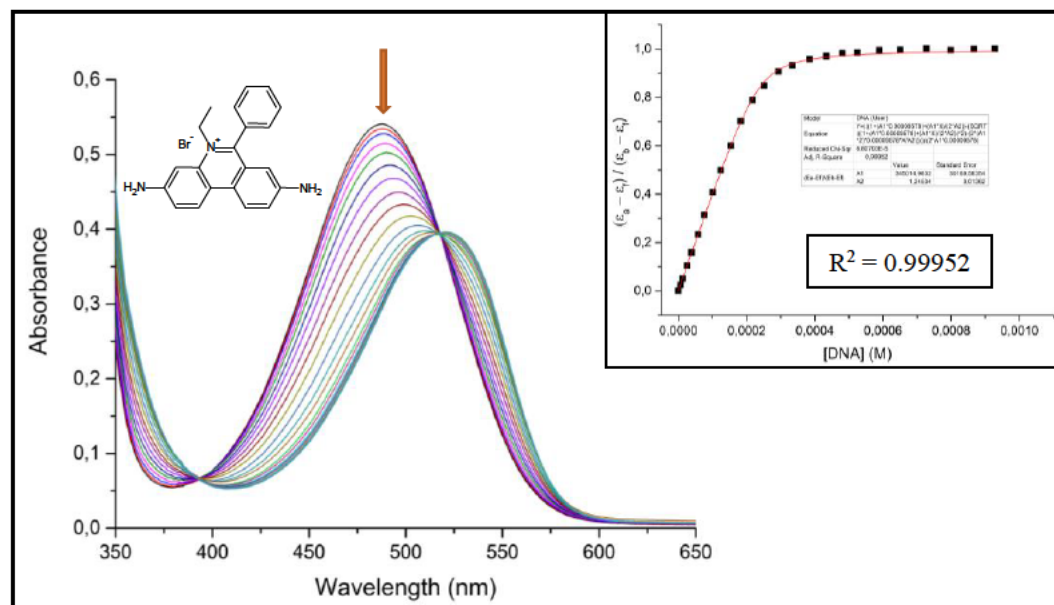


**Figure 8.4** UV/visible absorbance spectra of ethidium bromide (96  $\mu\text{M}$ ) as a function of *ct*-DNA concentration (0 – 929  $\mu\text{M}$ ) in 10% v/v DMSO and pH 7.0 Tris buffer at 25  $^{\circ}\text{C}$ . *Inset*: Plot of  $(\epsilon_a - \epsilon_f) / (\epsilon_b - \epsilon_f)$  versus [DNA] and the non-linear fit for the titration of ethidium bromide with *ct*-DNA at 492 nm.

The optical density data were then fitted to the expression by Bard and co-workers (Equation 8.2) (*inset Figure 8.7*):<sup>33,34,37</sup>

$$\frac{\epsilon_a - \epsilon_f}{\epsilon_b - \epsilon_f} = \frac{b - \left( b^2 - \frac{2K_b^2 C_t [\text{DNA}]}{s} \right)^{\frac{1}{2}}}{2K_b C_t} \quad \text{Equation 8.2(a)}$$

$$\text{Where } b = 1 + K_b C_t + K_b [\text{DNA}] / 2s \quad \text{Equation 8.2(b)}$$

[DNA] = Concentration of *ct*-DNA base pairs.

$\epsilon_a$  = Extinction coefficient of the absorption band at a given [DNA].

$\epsilon_f$  = Extinction coefficient of the free ethidium bromide (with no *ct*-DNA).

$\epsilon_b$  = Extinction coefficient of the fully intercalated ethidium bromide.

$K_b$  = Equilibrium binding constant.

$C_t$  = Concentration of ethidium bromide.

$s$  = Binding site size (number of nucleotides per ethidium bromide).

The binding constant of ethidium bromide to *ct*-DNA under these experimental conditions was determined to be  $3.5 \times 10^5 \text{ M}^{-1}$  (base pairs).

### 8.4.3 Experimental Fluorescence Emission Studies of the Oxovanadium(IV) Complexes

The competitive fluorescence emission studies of selected oxovanadium complexes were conducted by monitoring the emission spectra of ethidium bromide bound to DNA. The fluorescence was measured as increasing amounts of the respective oxovanadium complex were added to an initial solution of *ct*-DNA (15  $\mu\text{M}$  base pairs) and ethidium bromide (15  $\mu\text{M}$ ) in 4% v/v DMSO (starting ratio), 25 mM Tris-HCl buffer (pH 7.0). Stock solutions of the oxovanadium complexes were prepared in DMSO. The solutions were incubated for 10 minutes after each addition of the vanadium complex before emission spectra were recorded. The emission spectra were recorded on a Photon Technology Int. (PTI) fluorescence spectrometer equipped with PTI's XenoFlash™ 300 Hz pulsed light source, gated emission scans with a delay of 95  $\mu\text{s}$ , an integration window time of 100  $\mu\text{s}$  and 45 pulses per channel, controlled by PTI's Felix32© Version 1.1 software. Detection was done by PTI's Model 814 analog/photo-counting photomultiplier detector. Samples were recorded in a quartz emission cell at 25 °C. Excitation of the EB-DNA complex was kept at 500 nm and emission spectra were recorded from 530 to 800 nm. The apparent binding constants of the oxovanadium complexes to *ct*-DNA were calculated using the following equation:<sup>32</sup>

$$K_{app} = \frac{K_{(EB)}[EB]}{[Complex]_{50}} \quad \text{Equation 8.3}$$

Where  $K_{app}$  = Apparent binding constant.

$K_{(EB)}$  = Binding constant of ethidium bromide ( $3.45015 \times 10^5 \text{ M}^{-1}$ ).

$[EB]$  = Concentration of ethidium bromide ( $1.49 \times 10^{-5} \text{ M}$ ).

$[Complex]_{50}$  = Concentration of the oxovanadium complex that causes a 50% reduction of the initial fluorescence intensity.

The concentration of the oxovanadium complex that causes a 50% reduction of the initial fluorescence emission intensity was determined from the emission spectra processed with exponential decay using Origin 9.1.

#### 8.4.4 Results and Discussion Fluorescence Emission Studies of the Oxovanadium(IV) Complexes

Competitive emission data are shown for  $[\text{VO}(\text{TERTCA})(\text{DPQ})](\text{PF}_6)$  in Figure 8.5. Quenching of the fluorescence intensity of the EB-DNA adduct occurred, indicating that  $[\text{VO}(\text{TERTCA})(\text{DPQ})](\text{PF}_6)$  was able to displace ethidium bromide from DNA. This indicates that  $[\text{VO}(\text{TERTCA})(\text{DPQ})](\text{PF}_6)$  has the ability to at least partially intercalate to DNA, in line with the results from the absorption titration studies.

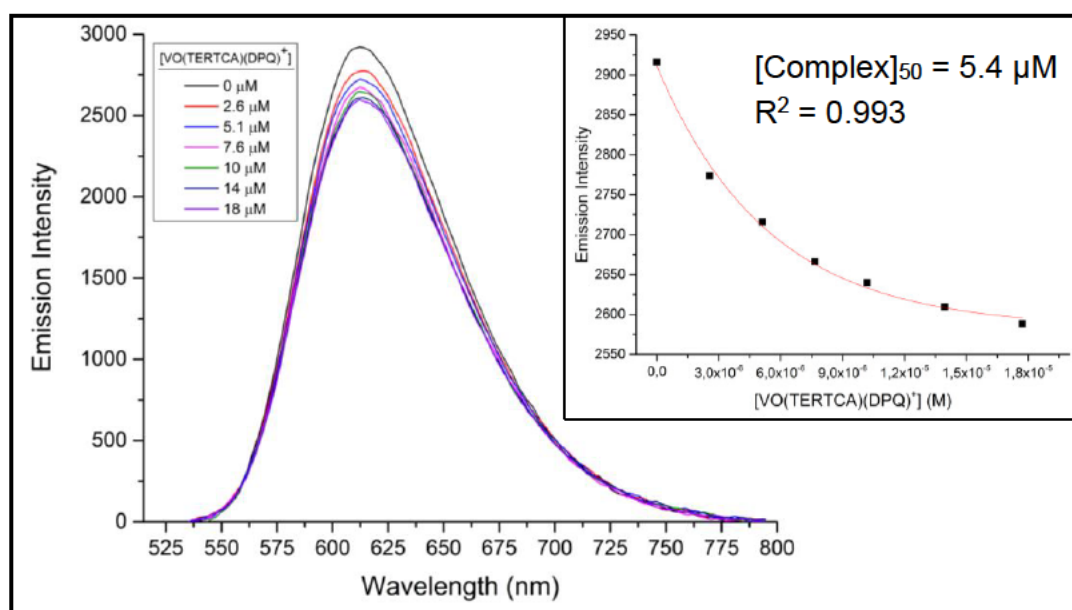


**Figure 8.5** Fluorescence emission spectra of ethidium bromide bound to *ct*-DNA in Tris-HCl buffer (25 mM, pH 7.0) and maximum 5.1% DMSO in the presence of increasing concentrations of  $[\text{VO}(\text{TERTCA})(\text{DPQ})](\text{PF}_6)$  (0 – 18  $\mu\text{M}$ ) at 25 °C. *Inset:* Plot of emission intensity of the EB-DNA adduct versus concentration of  $[\text{VO}(\text{TERTCA})(\text{DPQ})](\text{PF}_6)$  with an exponential decay fit at 614 nm.

The apparent binding constant of the neutral metal complex  $[\text{VO}(\text{PHA})(\text{DPQ})]$  was measured using the same protocol. The competitive emission data is shown in Figure E12, Appendix E.

The measurement of the apparent DNA binding constant of [VO(TERTA)(DPQ)] was complicated by the formation of a precipitate at concentrations above 45  $\mu\text{M}$  [VO(TERTA)(DPQ)]. This is likely a consequence of the reduced aqueous solubility caused by the *tert*-butyl groups. The apparent binding constant was, therefore, estimated from the initial exponential decay data from 0-38  $\mu\text{M}$  [VO(TERTA)(DPQ)] (Figure E13, Appendix E). The apparent binding constants for [VO(PHA)(DPQ)], [VO(TERTCA)(DPQ)](PF<sub>6</sub>) and [VO(TERTA)(DPQ)] (estimated) are indicated in Table 8.3.

**Table 8.3** Apparent DNA Binding Constants ( $K_{\text{app}}$ ) for selected neutral and cationic oxovanadium(IV) complexes.

Complex	$K_{\text{app}} / 10^5 \text{ M}$
[VO(TERTCA)(DPQ)](PF <sub>6</sub> )	9.50
[VO(PHA)(DPQ)]	3.87
[VO(TERTA)(DPQ)] (estimated value, due to precipitate formation)	1.51

The steric effect of the *tert*-butyl substituent on the tridentate ligand on the apparent binding constant is evident in the neutral complexes, as was noted for the intrinsic binding constants of the cationic DPQ complexes in Section 8.3. [VO(PHA)(DPQ)] has a higher apparent binding constant than [VO(TERTA)(DPQ)]. It is also interesting to note the higher apparent binding constant for the cationic [VO(TERTCA)(DPQ)](PF<sub>6</sub>) complex compared to its neutral analogue [VO(TERTA)(DPQ)]. This is likely a result of the electrostatic attraction between the negatively charged sugar-phosphate backbone of DNA and the positively charged complex. The DFT-simulated ESP plots and NBO charges indicate the higher positive potential in the cationic complexes as compared to the neutral complexes (Section 6.4). Also, the neutral complexes have larger DFT-simulated HOMO-LUMO energy gaps than the corresponding cationic complexes, indicating that the neutral complexes are more stable with respect to ligand substitution than the cationic complexes (Section 6.4). This would enable the cationic complexes to form speciated drugs more readily than the neutral species.

The speciated complexes could be more active by delivering the drug to the DNA of cancer cells more readily and enable DNA cleavage. Mass spectrometry and UV/visible spectroscopic studies also indicate the neutral oxovanadium(IV) complexes were more stable to solvolysis than the cationic analogues (*Chapter 7*). The higher DNA binding affinity of the cationic DPQ complexes may be the reason for the increased cytotoxicity against the HeLa cell line of the cationic chelates compared to the neutral compounds reported in *Section 8.2*.

The apparent binding constants for the cationic complexes with PHEN co-ligands, could not be determined, because the emission data showed minimal change upon addition of the metal complex. This implies that the cationic PHEN complexes do not bind to DNA through an intercalative binding mode. An intercalative binding mode is typically favoured when there is an extended aromatic ring system in the co-ligand. It is therefore somewhat expected that the PHEN and DPQ analogues may have different DNA binding modes.

## 8.5 *Viscosity DNA Binding Studies*

### 8.5.1 Introduction and Experimental DNA Viscosity

The above data show that the oxovanadium chelates likely have different binding modes, depending on the structure of the co-ligand. In an effort to better understand the DNA binding modes, DNA viscosity measurements were recorded. These measurements were done with an Anton Paar Lovis 2000 M rolling ball microviscometer. Each sample was tested three times to get an average viscosity. The measurements were conducted by keeping the DNA (sheared *ct*-DNA) concentration constant (237  $\mu\text{M}$ ) and varying the concentration of the oxovanadium complexes (0-300  $\mu\text{M}$ ) in 1X TAE buffer (Sigma-Aldrich, 10X, diluted with Type 1 ultrapure water, 40 mM Tris-acetate and 1 mM EDTA, pH 8.3) containing 10% v/v DMSO at 37°C. Data is presented as  $(\eta/\eta_0)^{1/4}$  versus  $[\text{complex}] / [\text{DNA}]$  where  $\eta$  and  $\eta_0$  are the dynamic viscosities of DNA in the presence and absence of the metal complex, respectively.<sup>22</sup>

### 8.5.2 Results and Discussion DNA Viscosity

The results of the effect of increasing concentrations of the neutral complexes with DPQ co-ligands on the relative DNA viscosities are presented in *Figures 8.6* and *8.7*.

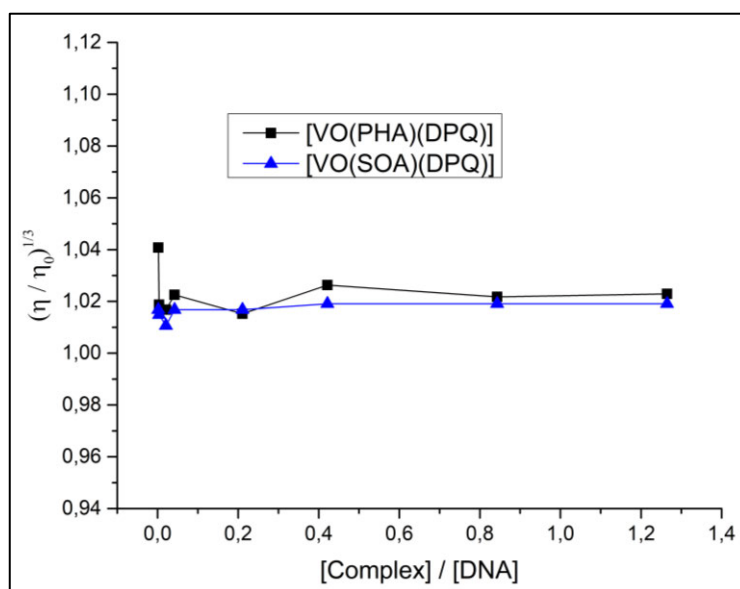


**Figure 8.6** Effect of increasing concentrations of [VO(PHA)(DPQ)] and [VO(SOA)(DPQ)] (0 – 300  $\mu\text{M}$ ) on the relative viscosities of *ct*-DNA (237  $\mu\text{M}$ ) in 1X TAE buffer (pH 8.3) containing 10% v/v DMSO at 37  $^\circ\text{C}$ .

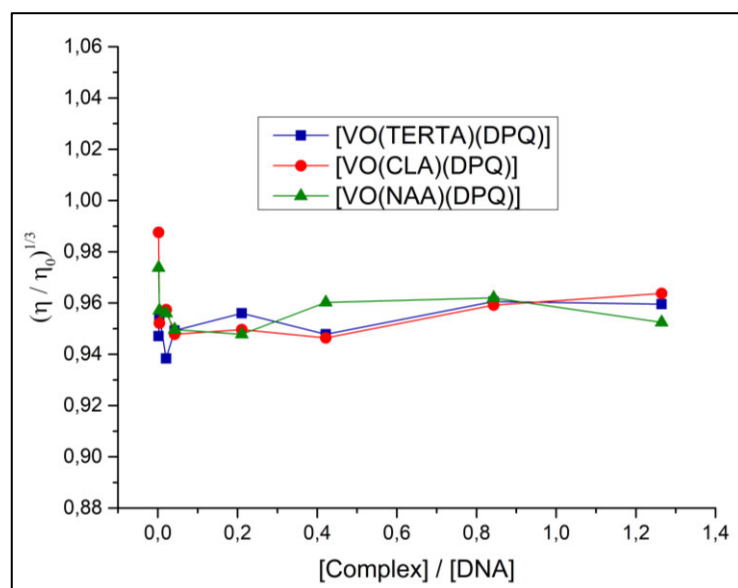


**Figure 8.7** Effect of increasing concentrations of [VO(TERTA)(DPQ)], [VO(CLA)(DPQ)] and [VO(NAA)(DPQ)] (0 – 300  $\mu\text{M}$ ) on the relative viscosities of *ct*-DNA (237  $\mu\text{M}$ ) in 1X TAE buffer (pH 8.3) containing 10% v/v DMSO at 37  $^{\circ}\text{C}$ .

For most of the neutral complexes, there was an initial small decrease in the relative viscosity of the DNA solution. This decrease was most pronounced for [VO(PHA)(DPQ)] (Figure 8.6) and [VO(CLA)(DPQ)] (Figure 8.7). A partial, non-classical intercalation mode of binding to DNA causes a decrease in the viscosity of DNA solution. This is due to a partial intercalator bending (or kinking) the DNA helix. In this way, the length of DNA is reduced, which decreases the viscosity.<sup>38</sup> This data therefore supports the earlier notion that [VO(PHA)(DPQ)] can at least partially intercalate DNA, based on the fluorescence emission studies.

For [VO(SOA)(DPQ)] and [VO(TERTA)(DPQ)] there was very little change in the relative viscosity of DNA overall (Figure 8.6 and 8.7, respectively). This is consistent with a groove-binding mode. A groove-binder is characterised by little to no change in the relative viscosity of DNA due to minor changes in the length of DNA. Metallointercalators on the other hand, cause a large increase in the viscosity of DNA solution. This is caused by the separation of DNA base pairs, increasing the contour length of DNA.<sup>25,26,33,38</sup> It is probable that the steric bulk associated with the *tert*-butyl and sulfonyl functional groups in these compounds inhibits DNA intercalation. This is an interesting result as it links to the cytotoxicity studies, which showed that increased steric bulk on the tridentate Schiff base ligand reduced the cytotoxicity.

For [VO(MEA)(DPQ)] (Figure 8.8 (a)), there was an initial small decrease followed by almost a complete recovery in the relative viscosity of the DNA solution. Thereafter, there was little change in the relative viscosity of the DNA-complex solution. This may indicate a dual-mode of binding of partial/non-classical intercalation and groove binding.<sup>38</sup> This could be a consequence of the intermediate steric volume of the methyl group which partially limits intercalation when compared to *tert*-butyl and sulfonyl. More than one type of DNA binding mode has also been reported for similar oxovanadium complexes of bidentate *N,N*-donor polypyridyl and tridentate-*O,N,O'* Schiff base ligands.<sup>39</sup>

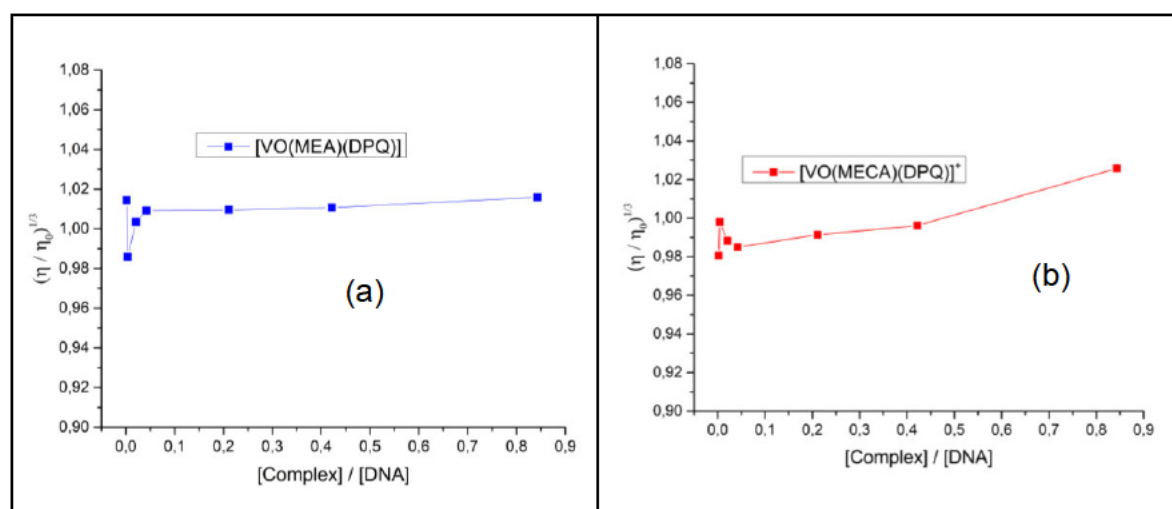


**Figure 8.8** Effect of increasing concentrations of [VO(MEA)(DPQ)] (a) and [VO(MECA)(DPQ)](PF<sub>6</sub>) (b) (0 – 200 μM) on the relative viscosities of *ct*-DNA (237 μM) in 1X TAE buffer (pH 8.3) containing 10% v/v DMSO at 37 °C.

The fluorescence spectroscopic studies showed that the cationic DPQ complex exhibited a stronger binding affinity for *ct*-DNA than the neutral DPQ analogue. The corresponding cationic DPQ complex [VO(MECA)(DPQ)](PF<sub>6</sub>) initially caused little change in the relative viscosity of the DNA solution, indicative of groove binding. As the concentration of the complex increased to approximately 100 μM, the relative viscosity of the DNA solution notably increased (Figure 8.8 (b)). This is indicative of intercalation.

The steric effect of the *tert*-butyl group in the cationic complex [VO(TERTCA)(DPQ)](PF<sub>6</sub>) inhibiting binding to DNA is also evident in the relative viscosity study. Increasing the concentration of [VO(TERTCA)(DPQ)](PF<sub>6</sub>) caused an initial decrease followed by minimal changes in the relative viscosity of the DNA solution (*Figure 8.9*). This is indicative of a partial intercalative mode of binding.<sup>38</sup> The stronger intercalative ability of [VO(MECA)(DPQ)](PF<sub>6</sub>) adduct in solution to DNA could further explain why this compound is significantly more cytotoxic towards the tumour cells than the healthy cell line in comparison to [VO(TERTCA)(DPQ)](PF<sub>6</sub>) (*Section 8.2*).

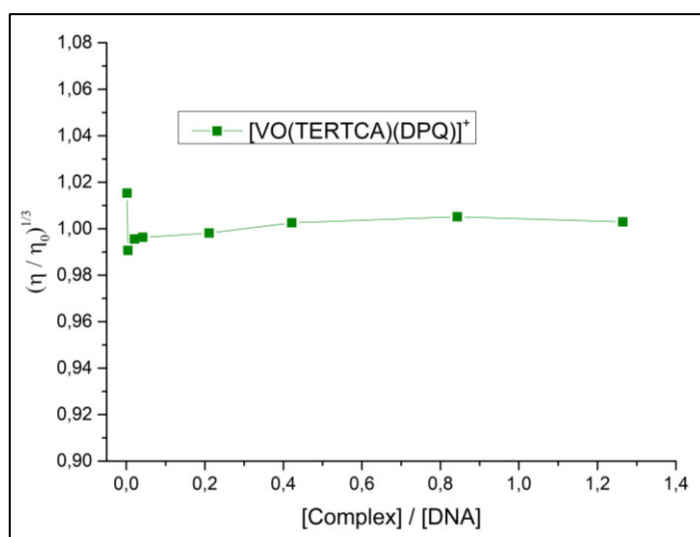


**Figure 8.9** Effect of increasing concentration of [VO(TERTCA)(DPQ)](PF<sub>6</sub>) (*b*) (0 – 300  $\mu$ M) on the relative viscosities of *ct*-DNA (237  $\mu$ M) in 1X TAE buffer (pH 8.3) containing 10% v/v DMSO at 37 °C.

The relative viscosity of the DNA solutions with increasing concentrations of the cationic PHEN complexes is shown in *Figure 8.10*. With the increasing concentrations of the cationic PHEN complexes, the relative viscosity of the DNA solutions remain almost unchanged. This confirmed that the cationic PHEN complexes do not intercalate into the DNA helix.<sup>22</sup> The absorption and emission studies also suggested that the cationic PHEN complexes do not intercalate DNA (*Sections 8.3.2 and 8.4.4*, respectively).

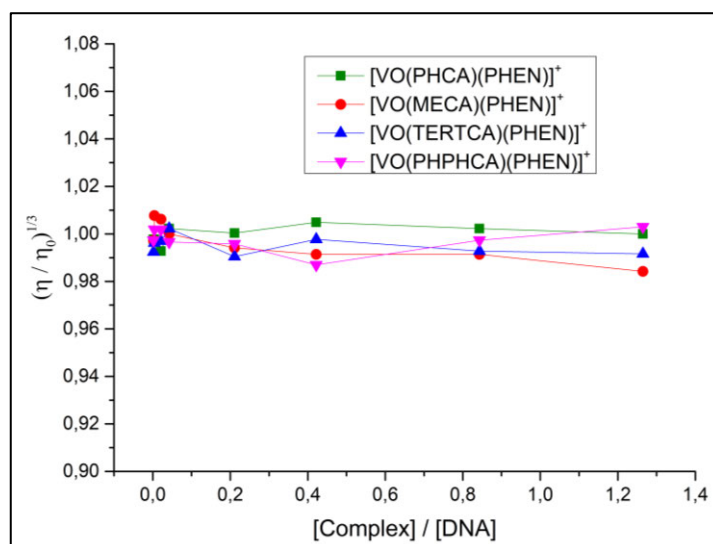


**Figure 8.10** Effect of increasing concentrations of  $[\text{VO}(\text{PHCA})(\text{PHEN})](\text{PF}_6)$ ,  $[\text{VO}(\text{MECA})(\text{PHEN})](\text{PF}_6)$ ,  $[\text{VO}(\text{TERTCA})(\text{PHEN})](\text{PF}_6)$  and  $[\text{VO}(\text{PHPHCA})(\text{PHEN})](\text{PF}_6)$  (0 – 300  $\mu\text{M}$ ) on the relative viscosities of *ct*-DNA (237  $\mu\text{M}$ ) in 1X TAE buffer (pH 8.3) containing 10% v/v DMSO at 37 °C.

In conjunction with the absorbance and fluorescence emission studies, the data collected from the viscosity measurements complement the cell cytotoxicity data. In particular, the different DNA binding modes as a function of steric volume of the functional groups on the tridentate ligand directly influence the cytotoxicity. The substituents with a large volume such as *tert*-butyl and sulfonyl are weak DNA binders and have reduced cytotoxicity. The length of conjugation of the *N,N*-donor heterocyclic ligand was also seen to decrease intercalative binding abilities of the complexes to DNA.

## 8.6 Molecular Docking Studies

Molecular docking studies were conducted to further understand the interactions of the neutral and cationic oxovanadium complexes with DNA. The molecular docking simulations of the interaction of selected oxovanadium complexes and DNA were conducted using PatchDock Beta 1.3 Version online server.<sup>40,41</sup> FireDock was used to refine the data sets.<sup>42</sup> Amongst ten solutions, only the lowest energy biomolecule-optimised conformer hybrid was considered. The crystal structure of B-DNA (PDB ID: 1F8N) was used as the receptor molecule. (The receptor molecule was prepared by Dr Sanam Maikoo, UKZN, by omitting water molecules of crystallisation and adding all hydrogens followed by the merging of non-polar hydrogens and computations of the Gasteiger charges.)

A set of atomic coordinates for the oxovanadium complexes were obtained from geometry optimisations of the individual metal complexes using Gaussian 09W at the B3LYP/6-311g level of theory.<sup>43</sup> They were converted into PDB format using Python Molecular Viewer.<sup>44</sup> The complex type in PatchDock was defined as protein-small ligand and the clustering RMSD was 4.0. YASARA view, Version 19.7.20 was used for the visualisation of the docked pose.<sup>45,46</sup>

The lowest global energy states for each of the complex-DNA systems range from  $-48.28 \text{ kJ mol}^{-1}$  to  $-66.73 \text{ kJ mol}^{-1}$  (Table 8.4). The negative value of the energies indicates the binding potential of the oxovanadium(IV) complexes with DNA.<sup>22</sup> The best binding energy for the interaction of the complex with DNA was found to be  $-66.73 \text{ kJ mol}^{-1}$  for the neutral [VO(MEA)(DPPZ)] complex, which indicates a strong interaction between this vanadium(IV) complex and DNA.<sup>47</sup>

**Table 8.4** Lowest global energy states for the docking of selected neutral and cationic oxovanadium(IV) species into B-DNA.

Complex	Lowest Global Energy (kJ mol <sup>-1</sup> )	Van der Waals Radius of Complexes (Å)
[VO(PHA)(DPQ)]	-53.94	8.432
[VO(MEA)(DPQ)]	-51.01	9.008
[VO(TERTA)(DPQ)]	-57.31	9.463
[VO(MECA)(PHEN)] <sup>+</sup>	-51.50	8.497
[VO(TERTCA)(PHEN)] <sup>+</sup>	-48.28	8.866
[VO(MECA)(DPQ)] <sup>+</sup>	-49.80	9.012
[VO(TERTCA)(DPQ)] <sup>+</sup>	-60.49	9.454
[VO(MEA)(DPPZ)]	-66.73	10.167
[VO(MECA)(DPPZ)] <sup>+</sup>	-63.00	9.978

Interestingly, [VO(TERTA)DPQ] has a lower global binding energy in comparison to the less sterically hindered [VO(PHA)(DPQ)] and [VO(MEA)(DPQ)]. In addition [VO(TERTCA)(DPQ)]<sup>+</sup> has a lower global binding energy in comparison to the less sterically hindered [VO(MECA)(DPQ)]<sup>+</sup>. It has been previously shown that lipophilicity can impact the DNA binding affinity and biological response.<sup>7,11,48-51</sup> Inside the DNA helix the aromatic base pairs create a lipophilic environment. The more lipophilic compounds, such as those with *tert*-butyl groups may therefore form stable adducts *in vacuo* when other factors are removed.

The molecular docking poses of selected oxovanadium(IV) complexes interacting with DNA are shown in *Figures 8.11 – 8.19*. The docked structures were edited in YASARA. The lowest-energy conformations indicate the complexes are DNA minor groove binders. The docking results support the experimental data of lower intrinsic binding constants in the order of 10<sup>4</sup> M<sup>-1</sup> determined for [VO(TERTCA)(DPQ)]<sup>+</sup> and [VO(MECA)(DPQ)]<sup>+</sup>, indicative of groove binding or non-classical intercalation mode (*Section 8.3*).

The cationic complexes [VO(TERTCA)(PHEN)]<sup>+</sup> (*Figure 8.15*) and [VO(TERTCA)(DPQ)]<sup>+</sup> (*Figure 8.17*) preferentially bind in the minor groove of DNA through the *O,N,N'*-tridentate ligand, rather than the planar DPQ ligand. As discussed in *Section 1.10*, previous DNA binding studies of oxovanadium(IV) complexes with tridentate ligands and planar bidentate *N,N*-donor co-ligands have shown that DNA binding affinities can be dependent on the electronic effects of the substituents on the aromatic chromophore of the tridentate ligands and not only on the nature of the *N,N*-bidentate ligand.<sup>52,53</sup> In this work, steric hindrance of the tridentate ligand also led to lower DNA binding constants (*Sections 8.3 and 8.4*) indicating that the tridentate ligand can be involved in DNA binding. The molecular docking studies are therefore in agreement with a number of aspects of the experimental data. This lends credibility to the results of these molecular simulations.

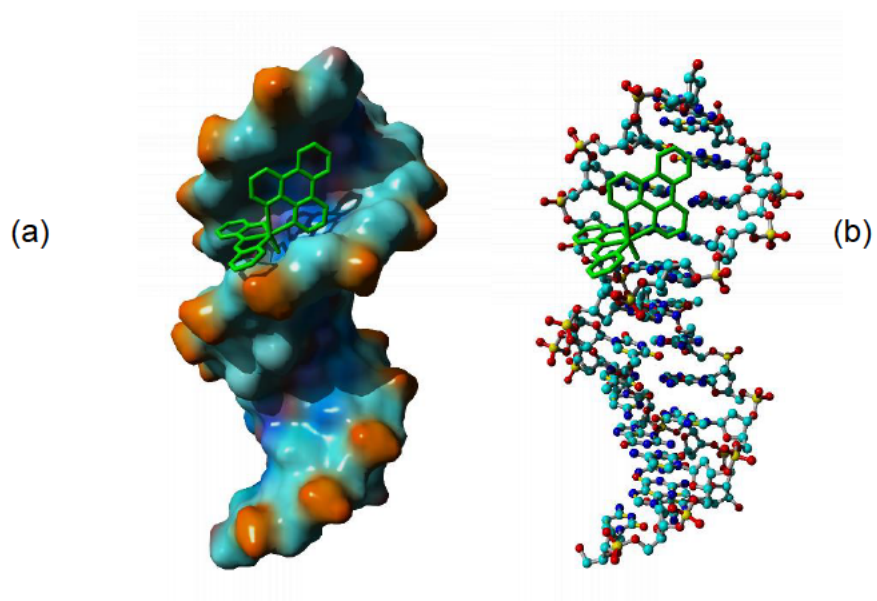


**Figure 8.11** [VO(PHA)(DPQ)] (shown as a green, capped-sticks model) docked into the minor groove of B-DNA:

(a) molecular surface view of DNA

(b) DNA in Ball and stick view

Global energy =  $-53.94 \text{ kJ mol}^{-1}$ .

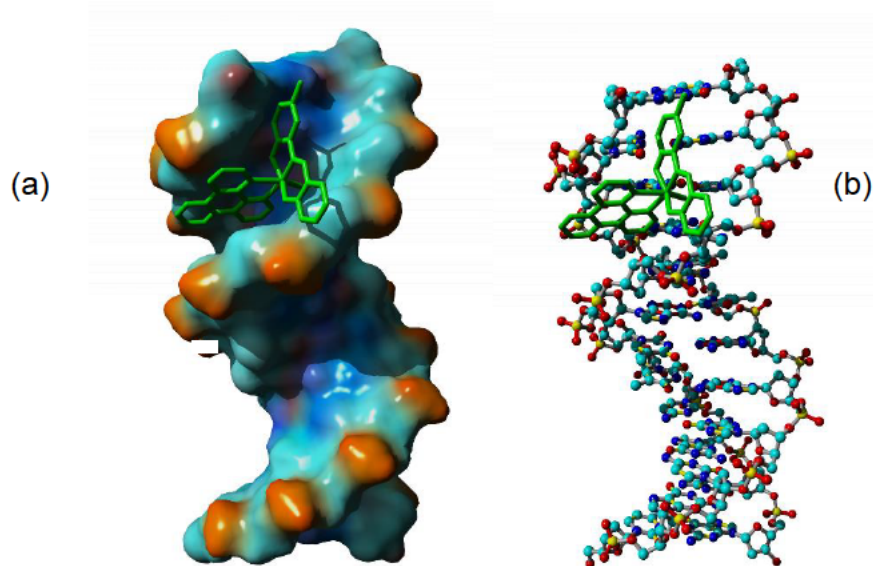


**Figure 8.12** [VO(MEA)(DPQ)] (shown as a green, capped-sticks model) docked into the minor groove of B-DNA:

(a) molecular surface view of DNA

(b) DNA in ball and stick view

Global energy =  $-51.01 \text{ kJ mol}^{-1}$ .

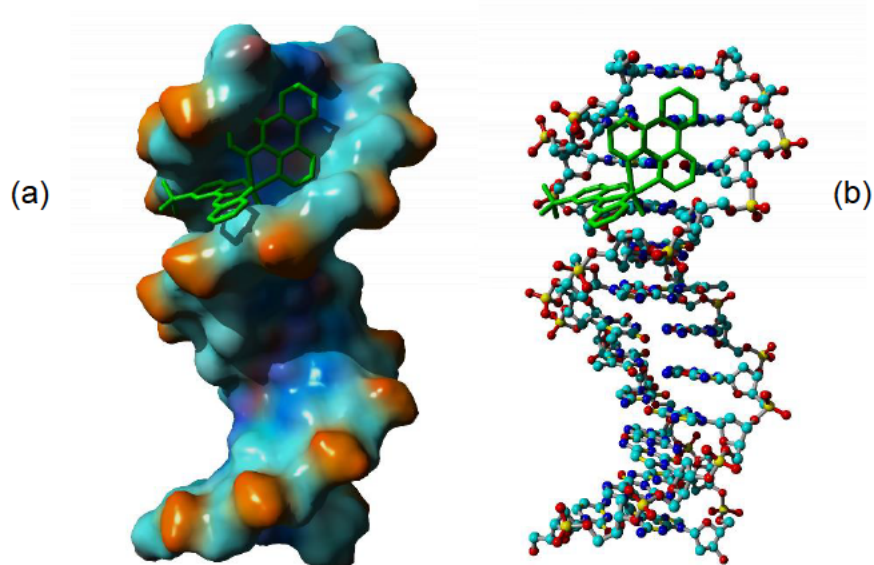


**Figure 8.13** [VO(TERTA)(DPQ)] (shown as a green, capped-sticks model) docked into the minor groove of B-DNA:

(a) molecular surface view of DNA

(b) DNA in ball and stick view

Global energy =  $-57.31 \text{ kJ mol}^{-1}$ .

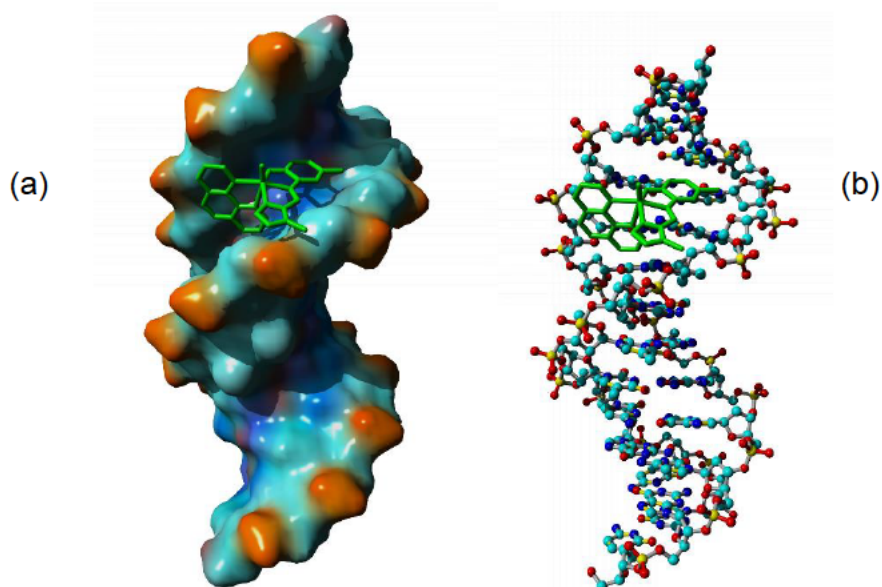


**Figure 8.14** [VO(MECA)(PHEN)]<sup>+</sup> (shown as a green, capped-sticks model) docked into the minor groove of B-DNA:

(a) molecular surface view of DNA

(b) DNA in ball and stick view

Global energy =  $-51.50 \text{ kJ mol}^{-1}$ .

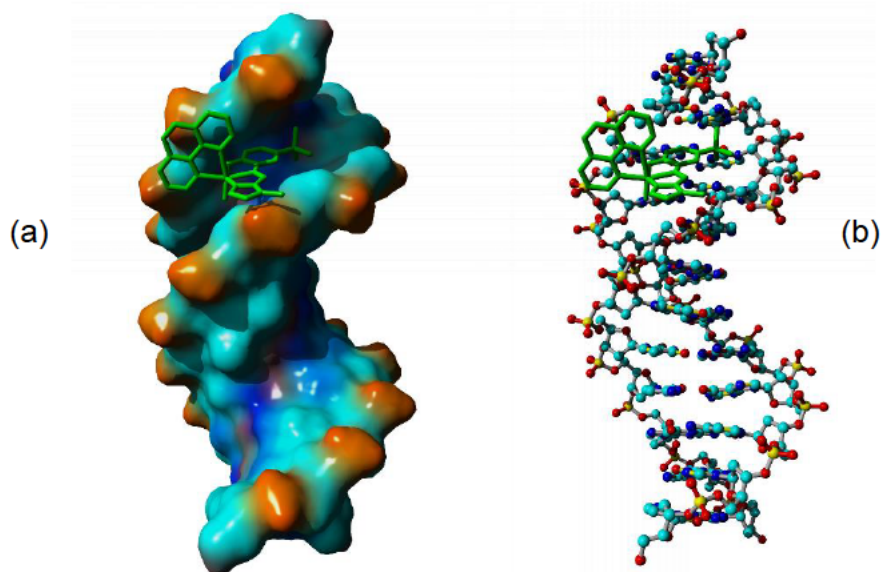


**Figure 8.15** [VO(TERTCA)(PHEN)]<sup>+</sup> (shown as a green, capped-sticks model) docked into the minor groove of B-DNA:

(a) molecular surface view of DNA

(b) DNA in ball and stick view

Global energy =  $-48.28 \text{ kJ mol}^{-1}$ .

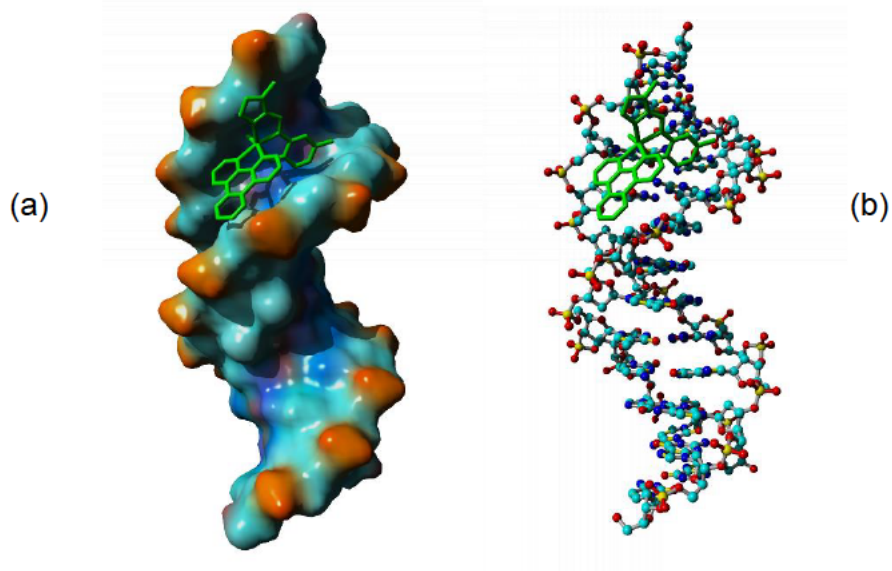


**Figure 8.16** [VO(MECA)(DPQ)]<sup>+</sup> (shown as a green, capped-sticks model) docked into the minor groove of B-DNA:

(a) molecular surface view of DNA

(b) DNA in ball and stick view

Global energy =  $-49.80 \text{ kJ mol}^{-1}$ .

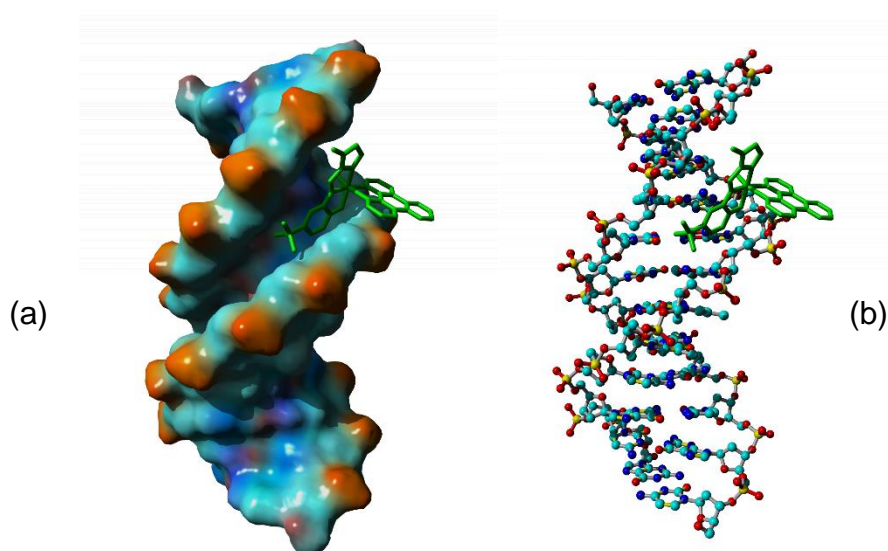


**Figure 8.17**  $[\text{VO}(\text{TERTCA})(\text{DPQ})]^+$  (shown as a green, capped-sticks model) docked into the minor groove of B-DNA:

(a) molecular surface view of DNA

(b) DNA in ball and stick view

Global energy =  $-60.49 \text{ kJ mol}^{-1}$ .

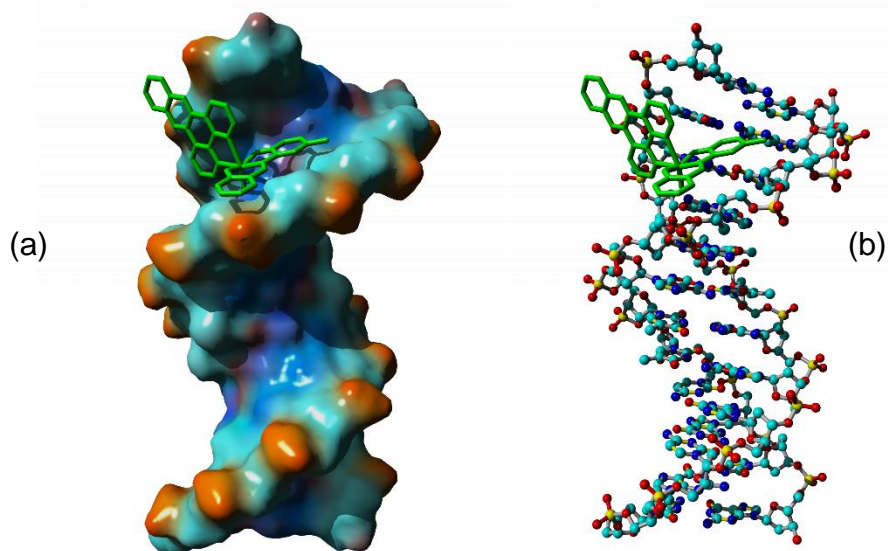


**Figure 8.18**  $[\text{VO}(\text{MEA})(\text{DPPZ})]$  (shown as a green, capped-sticks model) docked into the minor groove of B-DNA:

(a) molecular surface view of DNA

(b) DNA in ball and stick view

Global energy =  $-66.73 \text{ kJ mol}^{-1}$ .

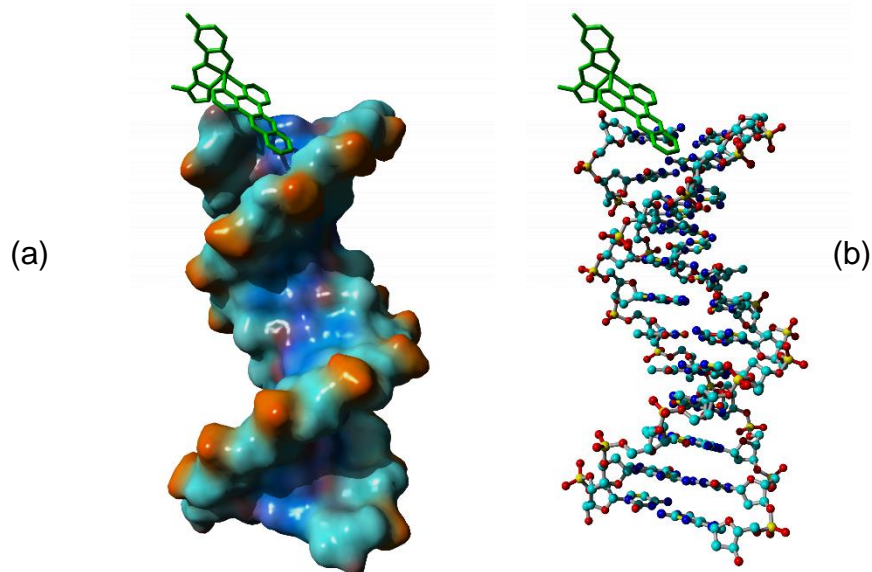


**Figure 8.19**  $[\text{VO}(\text{MECA})(\text{DPPZ})]^+$  (shown as a green, capped-sticks model) docked into the minor groove of B-DNA:

(a) molecular surface view of DNA

(b) DNA in ball and stick view

Global energy =  $-63.00 \text{ kJ mol}^{-1}$ .

YASARA view was used to compute short contact interactions between each metal compound and the respective biomolecular targets. Almost all of the complexes exhibited close contact interactions (under  $4\text{\AA}$ ) with the deoxyribose moieties of DNA.  $[\text{VO}(\text{MECA})(\text{PHEN})]^+$ ,  $[\text{VO}(\text{TERTCA})(\text{PHEN})]^+$ ,  $[\text{VO}(\text{MECA})(\text{DPQ})]^+$  and  $[\text{VO}(\text{MEA})(\text{DPPZ})]$  showed close contact interactions between guanine DNA bases and the aminophenol moiety of the respective metal complex. This highlights the involvement of the tridentate ligand in the DNA binding of the complexes.  $[\text{VO}(\text{MEA})(\text{DPQ})]$  exhibited close contact between DPQ and guanine.

Two of the complexes displayed hydrogen bonding to the DNA.  $[\text{VO}(\text{TERTA})(\text{DPQ})]$  has a hydrogen bond between the oxygen atom of the aminophenol moiety of the Schiff base ligand and a hydrogen atom from a guanine residue (*Figure 8.20 (a)*). The hydrogen bonding, which is a stabilising force, could explain the lower global binding energy of this complex in comparison to  $[\text{VO}(\text{PHA})(\text{DPQ})]$  and  $[\text{VO}(\text{MEA})(\text{DPQ})]$ , despite the bulkier *tert*-butyl substituent.  $[\text{VO}(\text{MECA})(\text{DPPZ})]^+$  also formed hydrogen bonds between the nitrogen atom of the DPPZ ligand and a hydrogen atom from a guanine residue (*Figure 8.20 (b)*).

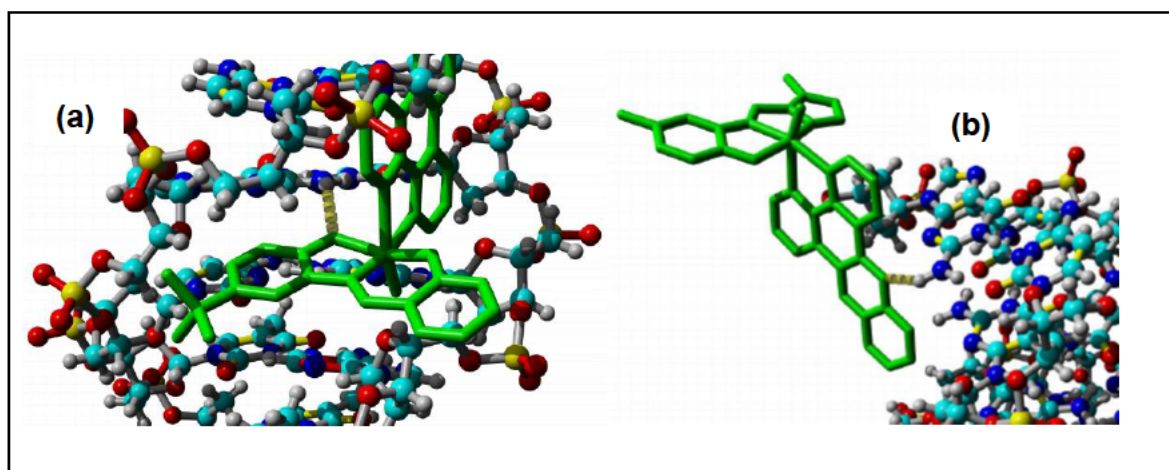


**Figure 8.20** Hydrogen bonding of the oxygen atom from the  $O,N,O'$ -donor ligand in  $[\text{VO}(\text{TERTA})(\text{DPQ})]$  (a) and the nitrogen atom from the DPPZ ligand of  $[\text{VO}(\text{MECA})(\text{DPPZ})]^+$  (b) to a  $\text{H}_{\text{amine}}$  atom from a guanine residue of B-DNA. Hydrogen bonds are shown as pale-yellow dashed lines.

## 8.7 Gel Electrophoresis DNA Cleavage Studies

### 8.7.1 Introduction and Experimental DNA Cleavage Studies

The production of ROS from vanadium(IV) complexes are an integral part of the mechanism of action of vanadium metallodrugs as they are able to induce either single or double-stranded DNA cleavage, inducing apoptosis.<sup>1,10,54-57</sup> The production of these ROS and the damage they do to DNA was studied by gel electrophoresis.

Gel electrophoresis studies can indicate DNA damage by a drug with the unwinding of supercoiled plasmid DNA to form nicked circular and/or linear conformations of DNA.<sup>22,32,58</sup> When electrophoresis is applied, the fastest migration will be for the closed circular supercoiled (SC) conformation (Form I). If cleavage occurs on one strand of DNA, then the nicked open-coil conformation (Form II) is formed, which moves more slowly than the SC conformation.<sup>32,59</sup> The linear form of DNA (Form III) migrates at a rate between that of Forms I and II.<sup>32</sup>

The cleavage of plasmid DNA by selected oxovanadium complexes was studied by agarose gel electrophoresis in 1X Tris-acetate-EDTA (TAE) buffer (40 mM Tris, 20 mM acetic acid, 1 mM EDTA, pH 8.0) containing 10% v/v DMSO. The pcDNA\_APP (made according to a previously reported method<sup>60</sup>), the TAE Buffer, agarose, DNA loading dye and DNA ladder were supplied by Dr Hewer, Biochemistry Department, University of KwaZulu-Natal, Pietermaritzburg.

Stock solutions of the metal complexes were prepared in DMSO. The complexes, DNA and TAE buffer were brought to a final sample volume of 10  $\mu$ L by adding Milli-Q® UltraPure water. The mixtures were then incubated at 37 °C for 30 minutes. The reactions were quenched after incubation by the addition of 2  $\mu$ L of gel loading dye (6X DNA loading dye (Thermo Fisher Scientific)). The solutions were finally loaded on 1% (w/v) agarose gel in 1X TAE buffer (pH 8.0) with the GeneRuler 1 kb DNA ladder (Thermo Fisher Scientific) included as a molecular weight marker.

Electrophoresis was then carried out at 80 V for 90 minutes at 500 mA in the 1X TAE buffer. The gel was then stained with a 0.5  $\mu$ g/mL ethidium bromide solution (10 mg/ml stock, MilliporeSigma) in Milli-Q® UltraPure water for 30 minutes. The gel was destained in Milli-Q® UltraPure water for 20 minutes. The gel was visualised by UV light and photographed for analysis using G:BOX Chemi XR5 (Syngene, India) in the GeneSys software (2012).

The first gel electrophoresis study involved incubating pcDNA\_APP plasmid DNA (0.15  $\mu$ g) with different concentrations of selected oxovanadium complexes, namely 0.5, 1.0, 5.0, 10, 50, 100, 200, 300 and 500  $\mu$ M, in 1X TAE buffer (pH 8.0) containing 10% v/v DMSO. Metal complexes selected for the gel electrophoresis study were [VO(SOA)(DPQ)], [VO(TERTA)(DPQ)], [VO(TERTCA)(PHEN)](PF<sub>6</sub>), [VO(TERTCA)(DPQ)](PF<sub>6</sub>) and [VO(MECA)(DPQ)](PF<sub>6</sub>). Control experiments were also run with DNA only and with DNA in 10% v/v DMSO in the 1X TAE buffer (pH 8.0).

## 8.7.2 Results and Discussion DNA Cleavage Studies

The gel electrophoresis patterns for the interactions of [VO(SOA)(DPQ)], [VO(TERTA)(DPQ)], [VO(TERTCA)(PHEN)](PF<sub>6</sub>), [VO(TERTCA)(DPQ)](PF<sub>6</sub>) and [VO(MECA)(DPQ)](PF<sub>6</sub>) and DNA are shown in *Figure 8.21*.

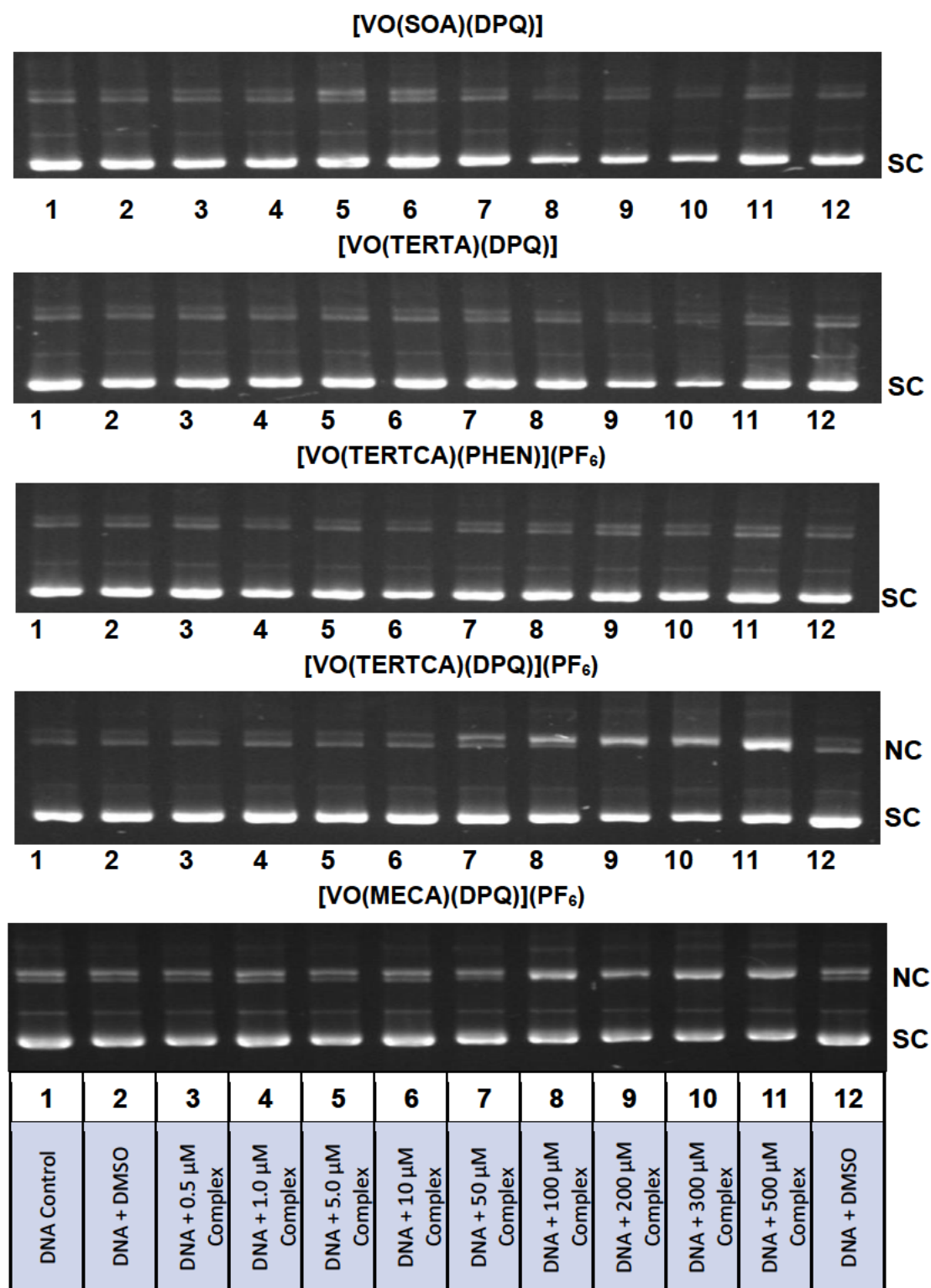


**Figure 8.21** Agarose gel electrophoresis experiments showing cleavage of pcDNA\_APP (0.15  $\mu$ g) by [VO(MECA)(DPQ)](PF<sub>6</sub>) and [VO(TERTCA)(DPQ)](PF<sub>6</sub>) above concentrations of 50  $\mu$ M in comparison to [VO(SOA)(DPQ)], [VO(TERTA)(DPQ)] and [VO(TERTCA)(PHEN)](PF<sub>6</sub>), which show no cleavage. Incubation was in 1X TAE buffer (pH 8.0) containing 10% DMSO, at 37 °C, for 30 minutes.

Upon electrophoresis, no obvious DNA cleavage was observed for the control experiments of DNA and of DNA in the presence of DMSO. The neutral complexes [VO(SOA)(DPQ)] and [VO(TERTA)(DPQ)] and the cationic complex [VO(TERTCA)(PHEN)](PF<sub>6</sub>) did not show DNA cleavage activity in the experimental concentration range 0-500 μM. The cationic DPQ complexes [VO(TERTCA)(DPQ)](PF<sub>6</sub>) and [VO(MECA)(DPQ)](PF<sub>6</sub>), however, showed DNA cleavage activity above concentrations of 50 μM. Additionally, these cationic DPQ complexes (or the solvated pro-drugs) could cleave DNA in the absence of external reagents such as ascorbate or hydrogen peroxide.

The converging concentration-dependent effect of [VO(TERTCA)(DPQ)](PF<sub>6</sub>) on pcDNA\_APP plasmid DNA is shown in *Figure 8.22*, illustrating how the relative amount of supercoiled DNA decreases as the relative amount of nicked circular increases as a function of increasing concentration of [VO(TERTCA)(DPQ)](PF<sub>6</sub>).

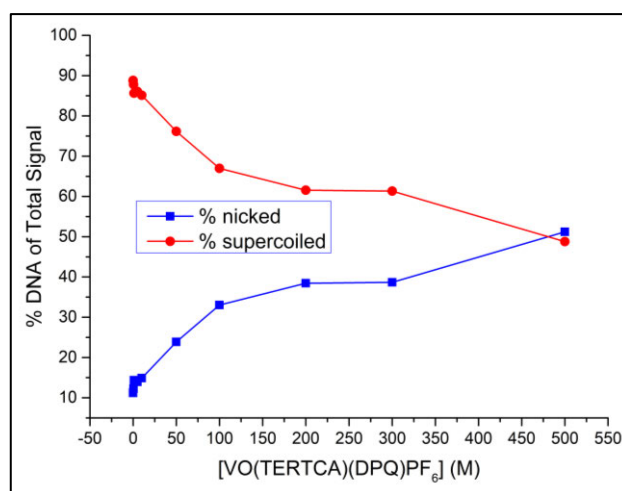


**Figure 8.22** The converging concentration-dependent effect of [VO(TERTCA)(DPQ)](PF<sub>6</sub>) on pcDNA\_APP plasmid DNA (0.15 μg) in 1X TAE buffer (pH 8.0) containing 10% v/v DMSO incubated at 37 °C for 30 min. The intensities were measured using the ImageJ software.<sup>61</sup>

Gel electrophoresis was also used to check that it is the specific combination of ligands and the vanadyl core that are needed for DNA cleavage. The cleavage activity of the cationic DPQ complexes was compared against the starting materials  $\text{VOSO}_4$ , the *O,N,N'*-tridentate ligands MECA and TERTCA as well as the bidentate *N,N*-donor ligand DPQ. This was done by incubating pcDNA\_APP plasmid DNA (0.15  $\mu\text{g}$ ) with 300  $\mu\text{M}$  of each of the above at 37  $^\circ\text{C}$  for 30 min in 1X TAE buffer (pH 8.0) containing 10% v/v DMSO. The resultant gel electrophoresis patterns are shown in *Figure 8.23*. The cleavage study indicates that the complex (or solvated pro-drug) is necessary for DNA cleavage rather than the independent ligands or metal salt.

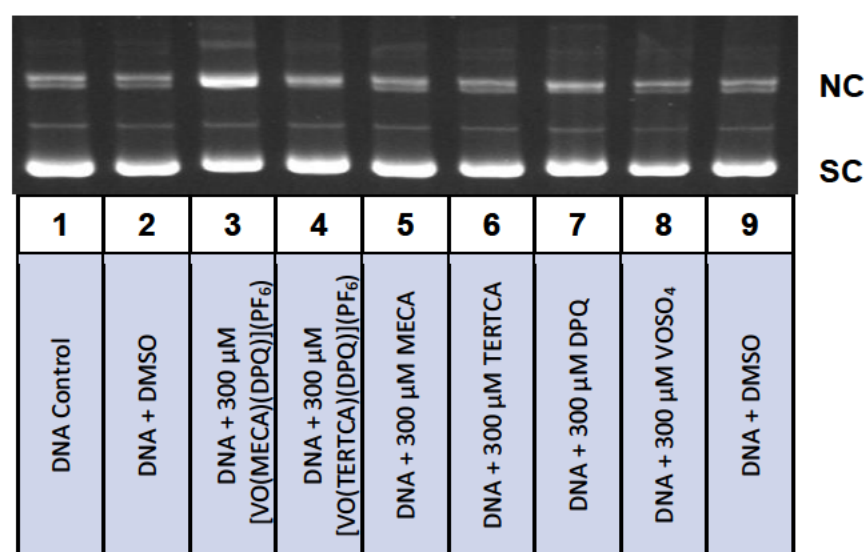


**Figure 8.23** Agarose gel electrophoresis pattern showing cleavage of pcDNA\_APP (0.15  $\mu\text{g}$ ) by [VO(MECA)(DPQ)](PF<sub>6</sub>) and [VO(TERTCA)(DPQ)](PF<sub>6</sub>) (300  $\mu\text{M}$ ) in comparison to VOSO<sub>4</sub> and the MECA, TERTCA and DPQ ligands (300  $\mu\text{M}$ ). Incubation was in 1X TAE buffer (pH 8.0) containing 10% v/v dmsO at 37  $^\circ\text{C}$  for 30 minutes.

Time dependence of the plasmid DNA cleavage by [VO(MECA)(DPQ)](PF<sub>6</sub>) and [VO(TERTCA)(DPQ)](PF<sub>6</sub>) was also studied by agarose gel electrophoresis. This experiment involved incubation of pcDNA\_APP plasmid DNA (0.15  $\mu\text{g}$ ) with 300  $\mu\text{M}$  of each complex in 1X TAE buffer (pH 8.0) containing 10% v/v DMSO at 37  $^\circ\text{C}$  for 15, 30, 45, 60, 75, 90, 105 and 120 minutes. The resulting time-dependent gel electrophoresis patterns are shown in *Figure 8.24* for [VO(MECA)(DPQ)](PF<sub>6</sub>) and [VO(TERTCA)(DPQ)](PF<sub>6</sub>).

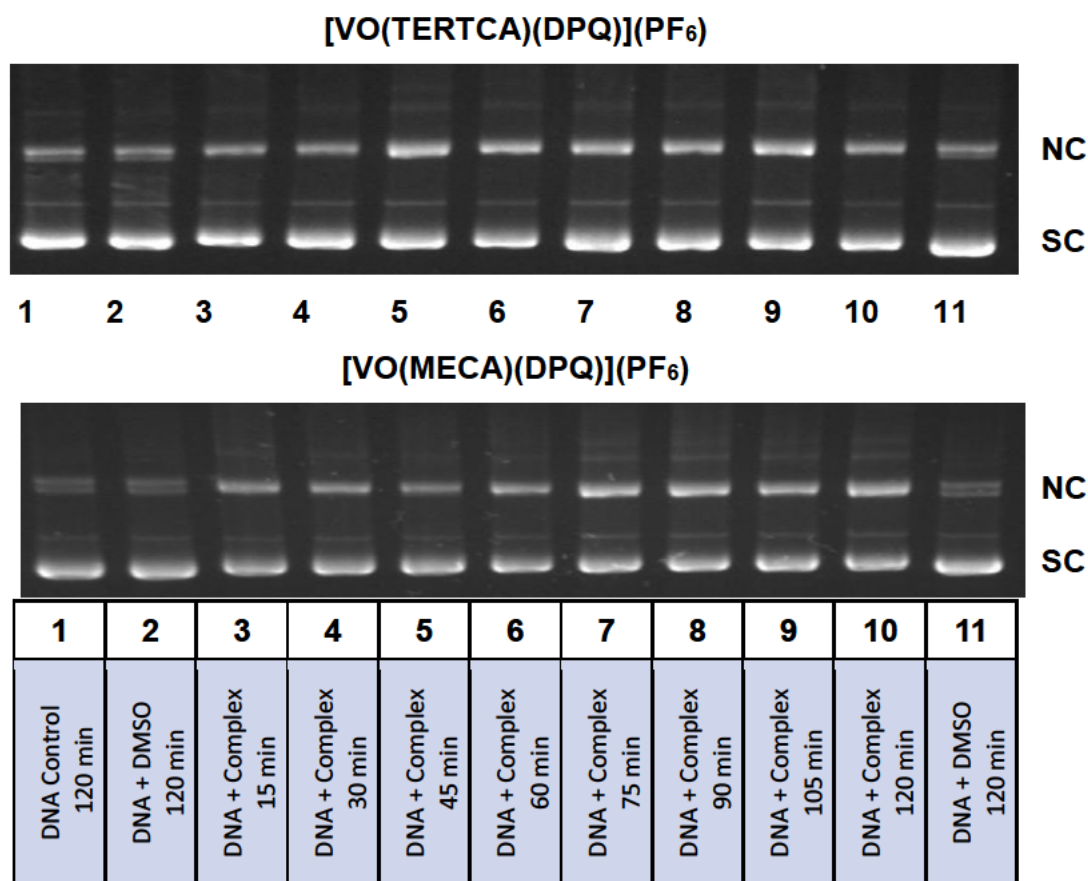


**Figure 8.24** Agarose gel electrophoresis pattern showing cleavage of pcDNA\_APP (0.15  $\mu$ g) by [VO(MECA)(DPQ)](PF<sub>6</sub>) (300  $\mu$ M) and [VO(TERTCA)(DPQ)](PF<sub>6</sub>) (300  $\mu$ M). Incubation was in 1X TAE buffer (pH 8.0) containing 10% v/v dms0 at 37 °C for 15, 30, 45, 60, 75, 90, 105 and 120 minutes.

The cationic complexes with DPQ co-ligands showed increased DNA cleavage activity as the incubation time was increased. The converging time-dependent effect of [VO(TERTCA)(DPQ)](PF<sub>6</sub>) and [VO(MECA)(DPQ)](PF<sub>6</sub>) (300  $\mu$ M) on the cleavage of pcDNA\_APP plasmid DNA (0.15  $\mu$ g) is shown in *Figure 8.25*. These results indicate that the complex with the methyl substituent was able to cleave DNA faster and more effectively than for [VO(TERTCA)(DPQ)](PF<sub>6</sub>). This again confirms the steric bulk of the tridentate Schiff base ligand of the metal complexes decreases DNA interaction (and decreases cytotoxicity). It also indicates that the active pro-drug species(s) involves the Schiff base ligand-vanadium moiety. These results further confirm that the [VO(MECA)(DPQ)](PF<sub>6</sub>) compound is the lead compound in the series.

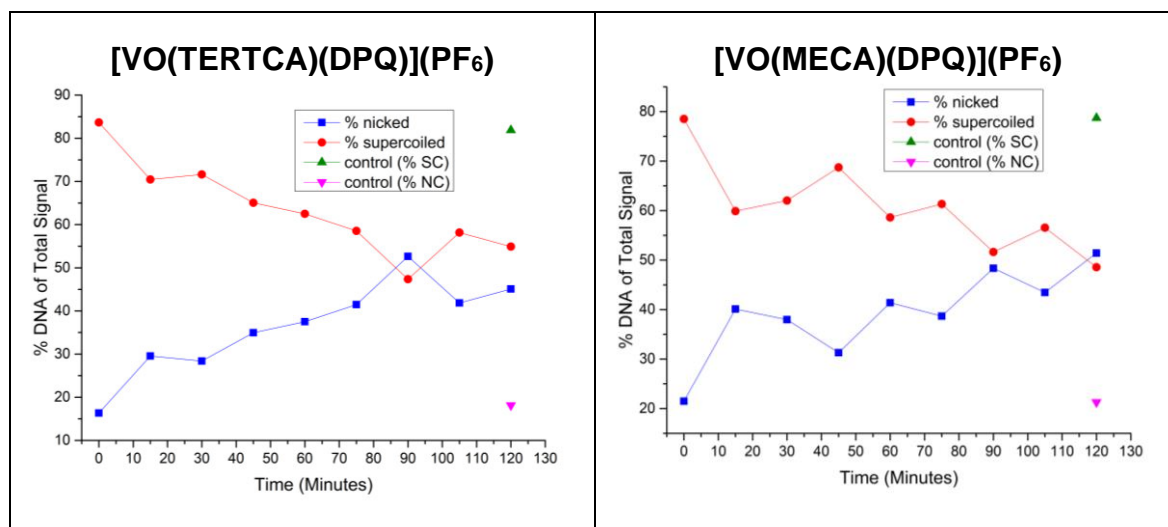


**Figure 8.25** The converging time-dependent effect of [VO(TERTCA)(DPQ)](PF<sub>6</sub>) and [VO(MECA)(DPQ)](PF<sub>6</sub>) (300 μM) on pcDNA\_APP plasmid DNA (0.15 μg) in 1X TAE buffer (pH 8.0) containing 10% v/v DMSO incubated at 37 °C for 15, 30, 45, 60, 75, 90, 105 and 120 minutes. The intensities were measured using the ImageJ software by Alexandré Delport (Biochemistry, UKZN).<sup>61</sup>

## 8.8 Mechanistic Studies of DNA Cleavage

### 8.8.1 Introduction and Experimental Gel Electrophoresis Mechanistic Studies of DNA Cleavage

The DNA cleavage studies, *Section 8.7*, revealed that the cationic complexes with DPQ co-ligands were able to cleave DNA in the presence of DMSO. This suggests a type-II singlet oxygen ROS mechanistic pathway (discussed in *Section 1.7.1*).<sup>1,13</sup> The cleavage mechanism of a representative complex, [VO(MECA)(DPQ)](PF<sub>6</sub>), was, therefore, studied by performing the DNA cleavage reactions in the presence of either a singlet oxygen quencher (DABCO) or a hydroxyl radical scavenger (DMSO).<sup>1</sup> In this way, it will be possible to determine the identity of the ROS responsible for DNA cleavage.

The mechanism of DNA cleavage was studied by the following method. A solution of plasmid DNA (0.15  $\mu\text{g}$ ) and 150  $\mu\text{M}$  [VO(MECA)(DPQ)](PF<sub>6</sub>) in 1X TAE buffer (pH 8.0) containing 10% v/v DMF was prepared.

The DNA, Milli-Q® UltraPure water and additives (DABCO or DMSO) were mixed before the addition of [VO(MECA)(DPQ)](PF<sub>6</sub>) (in DMF) and TAE buffer to make a final sample volume of 10  $\mu\text{L}$ . The final concentrations of the respective additives were 0.5 mM DABCO and 10% v/v DMSO. Control experiments with only DNA and with DNA in 10% v/v DMF in the 1X TAE buffer were also run. The mixtures were incubated at 37 °C for 60 minutes. The reactions were quenched after incubation by the addition of 2  $\mu\text{L}$  of gel loading dye (6X DNA loading dye (Thermo Fisher Scientific)).

The solutions were then finally loaded on 1% (w/v) agarose gel in 1X TAE buffer (pH 8.0) with the GeneRuler 1 kb DNA ladder (Thermo Fisher Scientific) included as a molecular weight marker. Electrophoresis was then carried out at 80 V for 90 minutes at 500 mA in the 1X TAE buffer. The gel was then stained with a 0.5  $\mu\text{g}/\text{mL}$  ethidium bromide solution (10 mg/ml stock, MilliporeSigma) in Milli-Q® UltraPure water for 30 minutes. It was then destained in Milli-Q® UltraPure water for 20 minutes. The gel was visualised by UV light and photographed for analysis using G:BOX Chemi XR5 (Syngene, India) in the GeneSys software (2012).

### **8.8.2 Results and Discussion Gel Electrophoresis Mechanistic Studies of DNA Cleavage**

The resultant gel electrophoresis patterns are shown in *Figure 8.26*. The control lanes (lanes 1 and 2) indicated no enhanced formation of the nicked form of DNA. The addition of DMSO (lane 5) leads to an enhancement of the DNA cleavage activity of [VO(MECA)(DPQ)](PF<sub>6</sub>) (lane 3) in comparison to the addition of DABCO (lane 4). These results suggest the cleavage of plasmid DNA by [VO(MECA)(DPQ)](PF<sub>6</sub>) involves singlet oxygen (<sup>1</sup>O<sub>2</sub>) via a type-II process.<sup>1</sup>

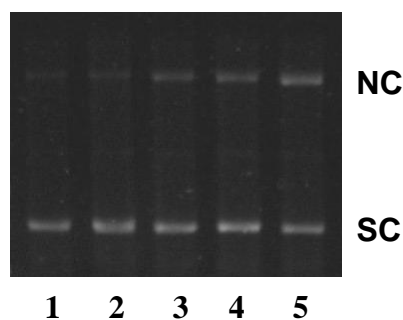


**Figure 8.26** Agarose gel electrophoresis pattern showing cleavage of pcDNA\_APP (0.15  $\mu\text{g}$ ) by  $[\text{VO}(\text{MECA})(\text{DPQ})](\text{PF}_6)$  (150  $\mu\text{M}$ ) in the presence of various additives. Incubation was in 1X TAE buffer (pH 8.0) containing 10% v/v DMF at 37  $^\circ\text{C}$  for 60 minutes. Lane 1: DNA control; Lane 2: DNA + 10% v/v DMF; Lane 3: DNA +  $[\text{VO}(\text{MECA})(\text{DPQ})](\text{PF}_6)$ ; Lane 4: DNA +  $[\text{VO}(\text{MECA})(\text{DPQ})](\text{PF}_6)$  + DABCO (0.5 mM); Lane 5: DNA +  $[\text{VO}(\text{MECA})(\text{DPQ})](\text{PF}_6)$  + DMSO (10% v/v).

The results in *Figures 8.21* and *8.26* indicate that the presence of DMSO did not inhibit the cleavage of plasmid DNA by the cationic complexes with DPQ co-ligands. In addition, these complexes did not require external oxidising or reducing agents to cleave the plasmid DNA. Conversely, the neutral complexes with DPQ co-ligands did not cleave DNA in the presence of DMSO (*Figure 8.21*). Further mechanistic studies were, therefore, conducted on the neutral analogue of  $[\text{VO}(\text{MECA})(\text{DPQ})](\text{PF}_6)$ , namely  $[\text{VO}(\text{MEA})(\text{DPQ})]$ , to ascertain whether the presence of DMSO was inhibiting the cleavage of DNA by the neutral complexes and/or whether an oxidising agent such as  $\text{H}_2\text{O}_2$  is required to induce DNA cleavage by the neutral complex.

The cleavage mechanism of  $[\text{VO}(\text{MEA})(\text{DPQ})]$  was studied using 150  $\mu\text{M}$   $[\text{VO}(\text{MEA})(\text{DPQ})]$  with 0.15  $\mu\text{g}$  pcDNA\_APP in the absence and the presence of 30 mM  $\text{H}_2\text{O}_2$ , 0.5 mM DABCO and 10% and 20% v/v DMSO following the same procedure as described for  $[\text{VO}(\text{MECA})(\text{DPQ})](\text{PF}_6)$ . Control experiments were also run with DNA only (Lane 1); DNA + 10% v/v DMF (lane 2); DNA + 10% v/v DMF + 10% v/v DMSO (lane 3); DNA + 10% v/v DMF + 20% v/v DMSO (lane 4) and DNA + 10% v/v DMF and 30 mM  $\text{H}_2\text{O}_2$  (lane 5) in the 1X TAE buffer (pH 8.0). The gel electrophoresis patterns are shown in *Figure 8.27*.

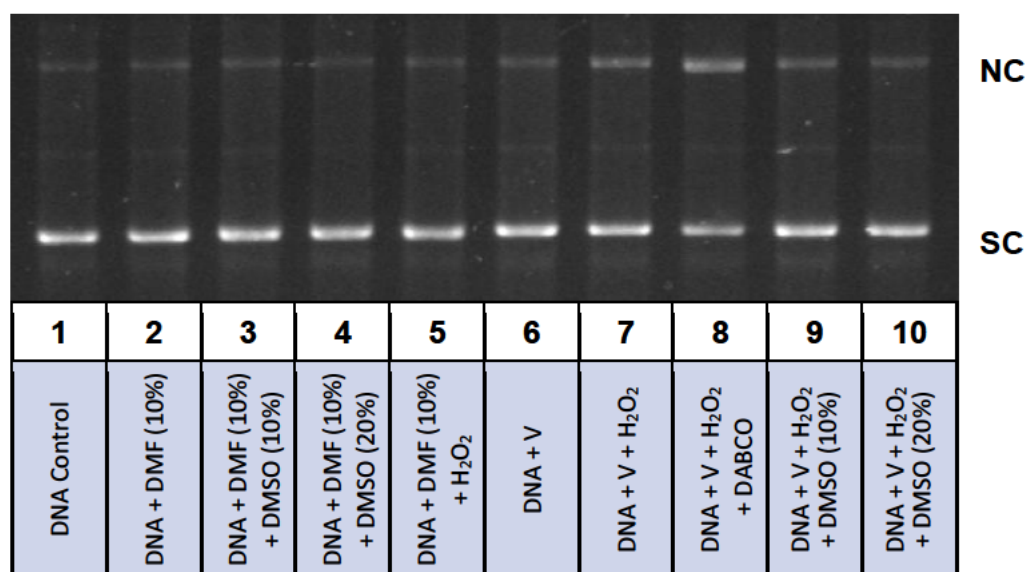


**Figure 8.27** Agarose gel electrophoresis pattern of pcDNA\_APP (0.15  $\mu$ g) with [VO(MEA)(DPQ)] (V) (150  $\mu$ M) in the absence (lane 6) and presence of various additives (H<sub>2</sub>O<sub>2</sub> (30 mM); DABCO (0.5 mM); 10% and 20% v/v DMSO). Incubation was in 1X TAE buffer (pH 8.0) containing 10% DMF at 37 °C for 60 minutes. V = [VO(MEA)(DPQ)].

[VO(MEA)(DPQ)] was not able to cleave DNA in the presence of DMSO or in the absence of an external oxidising agent (lane 6). [VO(MEA)(DPQ)] was able to cleave the DNA in the presence of 30 mM H<sub>2</sub>O<sub>2</sub> as indicated by the formation of the nicked form of plasmid DNA (lane 7). The presence of [VO(MEA)(DPQ)] is required to induce the cleavage as DNA with H<sub>2</sub>O<sub>2</sub> alone does not induce cleavage (lane 5). These results indicate that [VO(MEA)(DPQ)] can induce oxidative cleavage of plasmid DNA in the presence of H<sub>2</sub>O<sub>2</sub>.

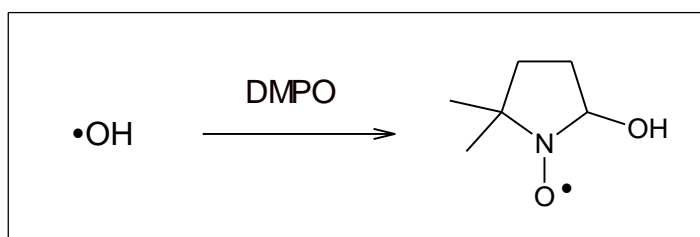
The mechanism of DNA cleavage by [VO(MEA)(DPQ)] was further probed by the additives DABCO and DMSO. The 20% v/v DMSO concentration suggested by previous mechanistic studies on oxovanadium complexes proved to be too high as the control lane (lane 4) was affected by 20% v/v DMSO.<sup>1,13</sup> The control lane of DNA + 10% v/v DMF + 10% v/v DMSO (lane 3) presented no different than the control lanes of DNA alone and of DNA + 10% v/v DMF (lanes 1 and 2, respectively) in the 1X TAE buffer. Based on this, 10% v/v DMSO was used for comparison.

In the presence of 10% v/v DMSO, the cleavage of the plasmid DNA by [VO(MEA)(DPQ)]/H<sub>2</sub>O<sub>2</sub> was inhibited (lane 9). In the presence of DABCO the cleavage of the plasmid DNA was enhanced (lane 8). Considering that DMSO is known to quench hydroxyl radicals while DABCO preserves them, these results suggest that the hydroxyl radical is most likely the reactive species inducing cleavage.<sup>1,2</sup> The hydroxyl radicals are most likely produced through the Fenton-type reaction from the oxidation of VO<sup>2+</sup> as discussed in *Section 1.7.1*:<sup>2</sup>



### 8.8.3 Introduction and Experimental Spin-Trapping Mechanistic Studies

To further verify if hydroxyl radicals are produced from the oxidation of [VO(MEA)DPQ] in a Fenton type reaction, an EPR spin-trapping experiment was conducted. Hydroxyl radicals are short-lived and highly reactive and so cannot be detected directly by EPR. Hydroxyl radicals can, however, be detected indirectly by reaction of the radicals with a spin-trap, such as 5,5-dimethyl-1-pyrroline N-oxide (DMPO) to form a more stable DMPO-OH adduct (*Scheme 8.1*). The longer-lived DMPO-OH adduct can be detected by EPR as a 1:2:2:1 quartet pattern.<sup>62-66</sup>



**Scheme 8.1** Spin-trapping of hydroxyl radicals to produce the DMPO-OH adduct.<sup>62</sup>

For the spin-trap experiment, DMPO (50 mM, Sigma-Aldrich) was added to [VO(MEA)(DPQ)] (0.5 mM) in acetonitrile (2470  $\mu\text{L}$ ) followed by the addition of H<sub>2</sub>O<sub>2</sub> (100 mM). After mixing, the solution was transferred to a quartz flat cell and the EPR spectrum recorded within 3 minutes of mixing. The EPR spectrum of [VO(MEA)(DPQ)] in acetonitrile in the absence of H<sub>2</sub>O<sub>2</sub> and DMPO was also recorded. The X-band EPR spectra were collected on a Bruker EMX Premium X spectrometer at room temperature with the following instrument settings: microwave bridge frequency, 9.8 GHz; modulation frequency, 100 kHz and centre field, 3500 G. Modulation amplitude was 3 G.

### 8.8.4 Results and Discussion Spin-Trapping Mechanistic Studies

The [VO(MEA)(DPQ)] complex in the absence of H<sub>2</sub>O<sub>2</sub> and DMPO exhibited an 8-line hyperfine pattern (Figure 8.28 (a)), indicative of the monomeric V<sup>IV</sup>O-bound species (Section 4.5). When [VO(MEA)(DPQ)] is mixed with H<sub>2</sub>O<sub>2</sub> in the presence of DMPO, the spectrum consists of the eight-line V<sup>IV</sup>O<sup>2+</sup> spectrum in addition to a spectrum consisting of four sharp lines (Figure 8.28 (b)). This four-line spectrum indicates the formation of the DMPO-OH spin adduct, further suggesting hydroxyl radicals are formed from the reaction of [VO(MEA)(DPQ)] and H<sub>2</sub>O<sub>2</sub>. Similar, superimposed spectra of the eight-line VO<sup>2+</sup> and four-line DMPO-OH spectra have also been reported for the reaction of vanadyl sulfate with H<sub>2</sub>O<sub>2</sub> in the presence of DMPO as confirmation of the ·OH radical formation.<sup>64</sup>

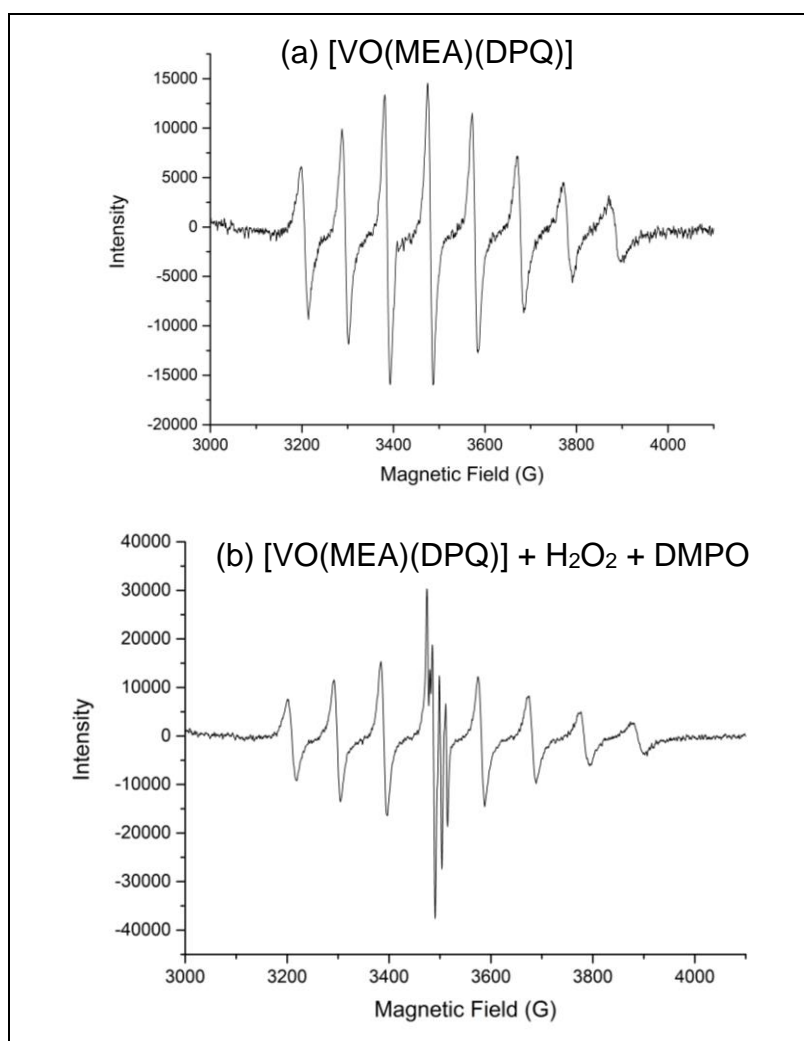


**Figure 8.28** EPR spectra of [VO(MEA)(DPQ)] at room temperature in acetonitrile (a) and of [VO(MEA)(DPQ)] (0.5 mM) following its reaction with H<sub>2</sub>O<sub>2</sub> (100 mM) in the presence of DMPO (50 mM) in acetonitrile (b).

## 8.9 Conclusions

The cytotoxicity screening of the oxovanadium complexes in this work revealed that the neutral complexes with DPQ co-ligands, except for the sterically hindered [VO(PHPHA)(DPQ)], were found to be cytotoxic against the MDA-MB and SH-SY5Y tumour cell lines with mean EC<sub>50</sub> values of 3.6 and 8.7  $\mu\text{M}$ , respectively. The same neutral complexes were found to be non-toxic towards the HeLa cell line.

The cationic complexes are, however, cytotoxic against all three tumour cell lines, with mean EC<sub>50</sub> values of 7.9, 6.2 and 4.6  $\mu\text{M}$  towards MDA-MB, HeLa and SH-SY5Y cell lines, respectively. This indicates that the charge of the complex influences the cytotoxicity. The effect of the substituent on the tridentate ligand is evident in the cationic complexes with DPQ co-ligands. The [VO(TERTCA)(DPQ)](PF<sub>6</sub>) complex is less cytotoxic than [VO(MECA)(DPQ)](PF<sub>6</sub>) against the three cancerous cell lines tested. It appears the steric bulk of the functional group influences cytotoxicity with larger functional groups, such as *tert*-butyl and sulfonyl, leading to lower cytotoxicity. The [VO(MECA)(DPQ)](PF<sub>6</sub>) complex is interesting as this complex was found to be significantly more toxic to neoplastic tissue than the healthy cell line HEK293. The selectivity index for MDA-MB, the triple-negative breast cancer, is 4.6. The selectivity indices for the HeLa and SH-SY5Y cell lines are even better: 7.4 and 5.9, respectively.

The DNA binding studies show that the compounds do have an affinity for DNA, and that DNA is a possible biological target. The effect of substituents on the tridentate ligand in the cationic complexes with DPQ co-ligands is evident in the *ct*-DNA binding absorption titration studies. [VO(TERTCA)(DPQ)](PF<sub>6</sub>), with the bulky *tert*-butyl substituent on the tridentate ligand, had a lower intrinsic *ct*-DNA binding constant than [VO(MECA)(DPQ)](PF<sub>6</sub>). The intrinsic binding constants were found to be  $2.8 \times 10^4 \text{ M}^{-1}$  and  $1.3 \times 10^4 \text{ M}^{-1}$  for [VO(MECA)(DPQ)](PF<sub>6</sub>) and [VO(TERTCA)(DPQ)](PF<sub>6</sub>), respectively, indicating moderate DNA binding affinity consistent with oxovanadium complexes. The DNA association constants for the cationic complexes with PHEN co-ligands could not be determined through absorption titrations or through competitive fluorescence studies with ethidium bromide. This is likely due to this class of compounds having low affinity for DNA.

Apparent binding constants for selected neutral DPQ complexes and [VO(TERTCA)(DPQ)](PF<sub>6</sub>) were determined through competitive fluorescence spectroscopic DNA studies with ethidium bromide, indicating at least partial DNA intercalative ability. The steric effect of the *tert*-butyl substituent is also evident in the neutral complexes, with [VO(TERTA)(DPQ)] having a lower apparent binding constant than [VO(PHA)(DPQ)]. The cationic charge seems to be a significant design feature leading to a higher apparent binding constant for [VO(TERTCA)(DPQ)](PF<sub>6</sub>) than for the neutral analogue [VO(TERTA)(DPQ)].

The viscosity studies indicate a partial intercalation mode of binding to DNA for [VO(PHA)(DPQ)], [VO(CLA)(DPQ)], [VO(NAA)(DPQ)] and [VO(TERTCA)(DPQ)](PF<sub>6</sub>). The cationic complexes with PHEN co-ligands, [VO(SOA)(DPQ)], [VO(TERTA)(DPQ)] and [VO(MEA)(DPQ)] are likely to be groove binders. [VO(MECA)(DPQ)](PF<sub>6</sub>) is most likely a DNA intercalator at higher concentrations. Molecular docking studies further highlighted the affinity of the metal chelates towards DNA, including interactions between DNA and the tridentate ligand. The lowest energy molecular docking poses range from *ca.* -48 to -67 kJ mol<sup>-1</sup>.

Gel electrophoresis studies were used to better understand the variations in cytotoxicity and revealed that the complexes [VO(MEA)(DPQ)], [VO(SOA)(DPQ)] and [VO(TERTA)(DPQ)] and [VO(TERTCA)(PHEN)](PF<sub>6</sub>) do not cleave DNA in the absence of external oxidising or reducing agents. The cationic complexes with DPQ co-ligands induced DNA cleavage activity in the absence of external reagents such as hydrogen peroxide. The cleavage studies importantly showed that the combination of metal ion and ligand is needed to induce DNA cleavage. Gel electrophoresis mechanistic studies indicated that the cleavage of plasmid DNA by [VO(MECA)(DPQ)](PF<sub>6</sub>) most likely occurs through a singlet oxygen pathway. [VO(MEA)(DPQ)] was shown to oxidatively cleave supercoiled plasmid DNA in the presence of H<sub>2</sub>O<sub>2</sub> through the generation of hydroxyl radicals. EPR spin-trapping studies with DMPO further suggested hydroxyl radicals are formed from the reaction of [VO(MEA)(DPQ)] and H<sub>2</sub>O<sub>2</sub>.

Collectively, these studies show that the charge of the complex, the nature of the tridentate ligand, the substituent on the tridentate ligand and the identity of the *N,N*-donor heterocyclic ligand affect the cytotoxic properties, DNA binding, DNA cleavage abilities and DNA cleavage mechanistic pathway of the metal chelates.

## 8.10 References

1. Prasad, P., Sasmal, P.K., Majumdar, R., Dighe, R. and Chakravarty, A.R., *Inorg. Chim. Acta*, **2010**, 363, 2743.
2. Guo, H., Lu, J., Ruan, Z., Zhang, Y., Liu, Y., Zang, L., Jiang, J. and Huang, J., *J. Coord Chem.*, **2012**, 65, 191.
3. Liao, X., Lu, J., Ying, P., Zhao, P., Bai, Y., Li, W. and Liu, M., *J. Biol. Inorg. Chem.*, **2013**, 18, 975.
4. Machado, I., Fernández, M., Becco, L., Garat, B., Brissos, R.F., Zabarska, N., Gamez, P., Marques, F., Correia, I., Costa Pessoa, J. and Gambino, D., *Inorg. Chim. Acta*, **2014**, 420, 39.
5. Cao, Y., Yi, C., Liu, H., Li, H., Li, Q., Yuan, Z. and Wei, G., *Transit. Met. Chem.*, **2016**, 41, 531.
6. Ni, L., Zhao, H., Tao, L., Li, X., Zhou, Z., Sun, Y., Chen, C., Wei, D., Liu, Y. and Diao, G., *Dalton Trans.*, **2018**, 47, 10035.
7. Benítez, J., Becco, L., Correia, I., Leal, S.M., Guiset, H., Costa Pessoa, J., Lorenzo J., Tanco, S., Escobar, P., Moreno, V., Garat, B. and Gambino, D., *J. Inorg. Biochem.*, **2011**, 105, 303.
8. Sasmal, P.K., Saha, S., Majumdar, R., Dighe, R.R. and Chakravarty, A.R., *Dalton Trans.*, **2010**, 39, 7104.
9. Banik., B., Sasmal, P.K., Roy, S., Majumdar, R., Dighe, R.R., Chakravarty, A.R., *Eur. J. Inorg. Chem.*, **2011**, 1425.
10. Prasad, P., Sasmal, P.K., Khan, I., Kondaiah, P. and Chakravarty, A.R., *Inorg. Chim. Acta*, **2011**, 372, 79.
11. Benítez, J., Guggeri, L., Tomaz, I., Arrambide, G., Navarro, M., Costa Pessoa, J., Garat, B. and Gambino, D., *J. Inorg. Biochem.*, **2009**, 103, 609.
12. Rehder, D., *Future Med. Chem.*, **2016**, 8, 325.
13. Sasmal, P., Patra, A.K., Nethaji, M. and Chakravarty, A.R., *Inorg. Chem.*, **2007**, 46, 11112.
14. Harrison, A.T., Kriel, F.H., Papathanasopoulos, M.A., Mosebi, S., Abrahams, S., and Hewer, R. *Chem. Biol. Drug Res.*, **2015**, 85, 290.
15. Mphahlele, M., Papathanasopoulos, M., Cinellu, M.A., Coyanis, M., Mosebi, S., Trait, T., Modise, R., Coates, J. and Hewer, R. *Bioorg. Med. Chem.*, **2012**, 20, 401.

16. Moradhaseli, S., Zare Mirakabadi, A., Sarzaeem, A., Kamalzadeh, M. and Haji Hosseini, R., *Iran J Pharm Res.*, **2013**, *12*, 155.
17. Hercules, S.M., Alnajjar, M., Chen, C., Mladjenovic, S.M., Shipeolu, B.A., Perkovic, O., Pond, G.R., Mbuagbaw, L., Blenman, K.R.M. and Daniel, J.M., *BMJ Open*, **2022**, *12*, e055735.
18. Mohammed, F., Rashid-Doubell, F., Taha, S., Cassidy, S. and Fredericks, S., *Int. J. Oncol.*, **2020**, *57*, 445.
19. Welsh, J., Chapter 40 - Animal Models for Studying Prevention and Treatment of Breast Cancer. In: P. Michael Conn, eds., *Animal Models for the Study of Human Disease*, Academic Press, **2013**, 997-1018.
20. Kovalevich, J. and Langford, D., *Methods Mol Biol.*, **2013**, *1078*, 9.
21. [https://ntp.niehs.nih.gov/databases\\_tools/data\\_search.htm](https://ntp.niehs.nih.gov/databases_tools/data_search.htm), 16 July 2022.
22. Rehman, S.U., Yaseen, Z., Husain, M.A., Sarwar, T., Ishqi, H.M. and Tabish, M., *PLoS One*, **2014**, *9*, e93913.
23. Felsenfeld, G.; Hirschman, S. Z. *J. Mol. Biol.* **1965**, *13*, 407.
24. Wolfe, A., Shimer, G.H. Jr. and Meehan, T., *Biochemistry*, **1987**, *26*, 6392.
25. Ying, P., Zeng, P., Lu, J., Yang, N. and Chen, H., *Open J. Inorg. Chem.*" **2014**, *4*, 51.
26. Shahabadi, N., Hakimi, M., Morovati, T. and Fatahi, N., *Nucleosides, Nucleotides and Nucleic Acids*, **2017**, *36*, 497.
27. Lima, S., Banerjee, A., Mohanty, M., Sahu, G., Kausar, C., Patra, S.K., Garriba, E., Kaminsky, W. and Dinda, R., *New. J. Chem.*, **2019**, *43*, 17711.
28. Banerjee, A., Dash, S.P., Mohanty, M., Sanna, D., Sciortino, G., Ugone, V., Garriba, E., Reuter, H., Kaminsky, W. and Dinda, R., *J. Inorg. Biochem.*, **2019**, *199*, 110786.
29. Scalese, G., Correia, I., Benítez, J., Rostán, S., Marques, F., Mendes, F., Matos, A.P., Costa Pessoa, J. and Gambino, D., *J. Inorg. Biochem.*, **2017**, *166*, 162.
30. Anjomshoa, M. and Torkzadeh-Mahani, M., *J. Fluoresc.*, **2016**, *26*, 1505.
31. Baguley, B.C. and Falkenhaus, E.-M., *Nucleic Acids Res.*, **1978**, *5*, 161.
32. Ragheb, M.A., Eldesouki, M.A. and Mohamed, M.S., *Spectrochim. Acta A*, **2015**, *138*, 585.
33. Banerjee, S., Hussain, A., Prasad, P., Khan, I., Banik, B., Kondaiah, P. and Chakravarty, A.R., *Eur. J. Inorg. Chem.*, **2012**, 3899.
34. Chen, L.-M., Liu, J., Chen, J.-C., Tan, C.-P., Shi, S., Zheng, K.-C., and Ji, L.-N., *J. Inorg. Biochem.*, **2008**, *102*, 330.

35. Waring, M.J., *J. Mol. Biol.*, **1965**, *13*, 269.
36. Vardevanyan, P.O., Antonyan, A.P., Parsadanyan, M.A., Davtyan, H.G. and Karapetyan, A.T., *Exp. Mol. Med.*, **2003**, *35*, 527.
37. Carter, T., Rodriguez, M. and Bard, A.J., *J. Am. Chem. Soc.*, **1989**, *111*, 8901.
38. Shahabadi, N. and Mohammadi, S., *Bioinorg. Chem. Appl.*, **2012**, *1*.
39. Correia, I., Roy, S., Matos, C.P., Borovic, S., Butenko, N., Cavaco, I., Marques, F., Lorenzo, J., Rodríguez, A., Moreno, V. and Costa Pessoa, J., *J. Inorg. Biochem.*, **2015**, *147*, 134.
40. Duhovny, D., Nussinov, R. and Wolfson, H.J., Efficient Unbound Docking of Rigid Molecules. In Gusfield *et al.*, editors, Proceedings of the 2'nd Workshop on Algorithms in Bioinformatics (WABI) Rome, Italy, Lecture Notes in Computer Science, **2002**, *2452*, 185-200, Springer Verlag.
41. Schneidman-Duhovny, D., Inbar, Y., Nussinov R. and Wolfson, H. J., *Nucleic Acids Res.*, **2005**, *33*, W363.
42. Andrusier, N., Nussinov, R. and Wolfson, H.J., *Proteins*, **2007**, *69*, 139.
43. Gaussian 09, Revision E.01, M. J. Frisch, G. W. Trucks, H. B. Schlegel, G. E. Scuseria, M. A. Robb, J. R. Cheeseman, G. Scalmani, V. Barone, B. Mennucci, G. A. Petersson, H. Nakatsuji, M. Caricato, X. Li, H. P. Hratchian, A. F. Izmaylov, J. Bloino, G. Zheng, J. L. Sonnenberg, M. Hada, M. Ehara, K. Toyota, R. Fukuda, J. Hasegawa, M. Ishida, T. Nakajima, Y. Honda, O. Kitao, H. Nakai, T. Vreven, J. A. Montgomery, Jr., J. E. Peralta, F. Ogliaro, M. Bearpark, J. J. Heyd, E. Brothers, K. N. Kudin, V. N. Staroverov, R. Kobayashi, J. Normand, K. Raghavachari, A. Rendell, J. C. Burant, S. S. Iyengar, J. Tomasi, M. Cossi, N. Rega, J. M. Millam, M. Klene, J. E. Knox, J. B. Cross, V. Bakken, C. Adamo, J. Jaramillo, R. Gomperts, R. E. Stratmann, O. Yazyev, A. J. Austin, R. Cammi, C. Pomelli, J. W. Ochterski, R. L. Martin, K. Morokuma, V. G. Zakrzewski, G. A. Voth, P. Salvador, J. J. Dannenberg, S. Dapprich, A. D. Daniels, O. Farkas, J. B. Foresman, J. V. Ortiz, J. Cioslowski, and D. J. Fox, Gaussian, Inc., Wallingford CT, **2009**.
44. ADT/PMV/ViewerFramework: Sanner, M.F., *J. Mol. Graphics Mod.*, **1999**, *17*, 57.
45. Krieger, E. and Vriend, G., *J. Comput. Chem.*, **2015**, *36*, 996.
46. Krieger, E. and Vriend, G., *Bioinformatics*, **2014**, *30*, 2981.
47. Abyar, F. and Tabrizi, L., *J. Biomol. Struct. Dyn.*, **2019**, 474.

48. Szklarzewicz, J., Jurowska, A., Hodorowicz, M., Gryboś, R., Kruczala, K., Gluch-Lutwin, M. and Kazek, G., *J. Coord. Chem.*, **2020**, 73, 986.
49. Fernández, M., Becco, L., Correia, I., Benítez, J., Piro, O.E., Echeverria, G.A., Medeiros, A., Comini, M., Lavaggi, M.L., González, M., Cerecetto, H., Moreno, V., Costa Pessoa, J., Garat, B. and Gambino, D., *J. Biol. Inorg. Chem.*, **2013**, 127, 150.
50. Benítez, J., de Queiroz, A.C., Correia, I., Alves, M.A., Alexandre-Moreira, M.S., Barreiro, E.J., Lima, L.M., Varela, J., González, M., Cerecetto, H., Moreno, V., Costa Pessoa, J. and Gambino, D. *Eur. J. Med.*, **2013**, 62, 20.
51. Bisel, P., Al-Momani, L. and Müller, M., *Org. Biomol. Chem.*, **2008**, 6, 2655.
52. Du, Y., Lu, J., Guo, H., Jiang, J., Chao, P., Chen, F. and Pan, J., *Transit. Met. Chem.*, **2010**, 35, 859.
53. Zeng, P., He, L., Ye, Z., Yang, N., Song, Y. and Lu, J., *Transit. Met. Chem.*, **2015**, 40, 779.
54. Sakurai, H., Tamura, H. and Okatani, K., *Biochem. And Biophys. Res. Commun.*, **1995**, 206, 133.
55. Kuwahara, J., Suzuki, T., Sugiura, Y., *Biochem. Biophys. Res. Commun.*, **1985**, 129, 368.
56. Chakravarty, A.R. and Roy, M., *Prog. Inorg. Chem.*, **2012**, 57, 119.
57. Aboafia, S.A., Elsayed, S.A., El-Sayed, A.K.A. and El-Hendawy, A.M., *J. Mol. Struct.*, **2018**, 1158, 39.
58. Pyle, A.M., Rehmann, J.P., Meshoyrer, R., Kumar, C.V., Turro, N.J. and Barton, J.K., *J. Am. Chem. Soc.*, **1989**, 111, 3051.
59. Islam, M.N., Kumbhar, A.A., Kumbhar, A.S., Zeller, M., Butcher, R.J., Dusane, M.B., and Joshi, B.N., *Inorg. Chem.*, **2010**, 49, 8237.
60. Delport, A and Hewer, R., *Protein J.*, **2019**, 38, 419.
61. Rasband, W.S., ImageJ, U. S. National Institutes of Health, Bethesda, Maryland, USA, <https://imagej.nih.gov/ij/docs/intro.html>, 1997-2016.
62. Finkelstein, E., Rosen, G.M. and Rauckman, E.J., *Arch. Biochem. Biophys.*, **1980**, 200, 1.
63. Verquin, G., Fontaine, G., Bria, M., Zhilinskaya, E., Abi-Aad, E., Aboukaïs, A., Baldeyrou, B., Bailly, C. and Bernier, J.-L., *J Biol. Inorg. Chem.*, **2004**, 9, 345.
64. Carmichael, A.J., *FEBS Lett.*, **1990**, 261, 165.
65. Carmichael, A.J., *Free Rad. Res. Commun.*, **1990**, 10, 37.

66. Buettner, G.R., *Free Rad. Biol. Med.*, **1987**, 3, 259.

## **Chapter Nine: Conclusions and Future Work**

### **9.1 Summary and Conclusions**

This thesis presented the synthesis of novel ternary oxovanadium(IV) complexes of the type [VO(ONO)(DPQ/DPPZ)], [VO(ONN)(PHEN/DPQ)](PF<sub>6</sub>) and [VO(ONN)(DPPZ)](Cl) for potential application as anticancer agents. DPQ and DPPZ were successfully synthesised and characterised by ESI-mass and <sup>1</sup>H and <sup>13</sup>C NMR spectroscopy. The *O,N,O'*-donor salicylidene-based ligands and tridentate *N*-methyl imidazole-derived *O,N,N'*-donor Schiff base ligands were successfully synthesised and fully characterised by elemental analysis, <sup>1</sup>H and <sup>13</sup>C NMR, IR, UV-Visible spectroscopy, and ESI-mass spectrometry. Crystal structures were obtained for MEA, TERTA, CLA, SOA and NAA: these compounds were found as the ketone tautomer in the solid-state. Novel X-ray structures were elucidated for the ligands PHCA, MECA, TERTCA, PHPHCA and the hemihydrate of PHCA. The *O,N,N'* ligands form hydrogen-bonded supramolecular dimeric structures. DFT simulations confirmed the stability of these dimeric structures *in vacuo*. The hydrogen-bonded dimers are significantly lower in energy than two independent monomer units by an average of 103 kJ mol<sup>-1</sup>. TD-DFT simulations suggest that the dimer is the dominant species in solution, this was confirmed by <sup>1</sup>H NMR titration. An in-depth X-ray, NMR and DFT study of the PHCA, MECA and TERTCA dimeric structures has been published.<sup>1</sup>

The oxovanadium(IV) complexes were successfully synthesised and characterised by elemental analysis, IR, UV-Visible spectroscopy and ESI-mass spectrometry. EPR spectra of the oxovanadium compounds confirmed the oxidation state of vanadium(IV) in the solid-state and in solution. Of the neutral complexes, single-crystal X-ray structures were elucidated for [VO(CLA)(DPQ)] and [VO(TERTA)(DPQ)]. Low-resolution X-ray structures were obtained for [VO(PHA)(DPQ)] and [VO(MEA)(DPPZ)]. The crystal structures indicated that the bidentate *N,N*-donor co-ligand and respective dianionic *O,N,O'*- tridentate ligand coordinate to the vanadyl (VO<sup>2+</sup>) moiety to form a monomeric VO<sub>3</sub>N<sub>3</sub> six-coordinate distorted octahedron.

Single crystal X-ray structures were also elucidated for the cationic complexes [VO(PHCA)(PHEN)](PF<sub>6</sub>), [VO(MECA)(PHEN)](PF<sub>6</sub>) and [VO(TERTCA)(PHEN)](PF<sub>6</sub>) indicating the six-coordinate monomeric [VO(ONN)(NN)]<sup>+</sup> species with a distorted octahedral geometry.

The *trans* effect was noted in all the metal chelates with the V-N bond *trans* to the V=O bond being significantly lengthened. The free ligands and metal complexes were studied by DFT methods using the B3LYP/6-311G(dp) level of theory. The comparison between the solid-state and DFT-simulated lowest energy conformations of the oxovanadium complexes showed good agreement. There were small root-mean-square deviations and small percentage differences between the bond lengths and bond angles. The DFT-optimised structures of the complexes for which X-ray structures could not be determined could, therefore, be regarded as accurate representations. The DFT-simulated and X-ray structures indicate that the aromatic rings of the respective PHEN, DPQ or DPPZ ligand are free from steric hindrance, and so, could be available to bind DNA through non-covalent binding modes.

DNA binding affinities of the oxovanadium complexes were measured through absorption titrations, competitive fluorescence, and viscosity studies. The cationic complexes with DPQ co-ligands bind *ct*-DNA with intrinsic binding constants of  $2.8 \times 10^4 \text{ M}^{-1}$  for [VO(MECA)(DPQ)](PF<sub>6</sub>) and  $1.3 \times 10^4 \text{ M}^{-1}$  for [VO(TERTCA)(DPQ)](PF<sub>6</sub>). This was determined through absorption spectroscopy. The difference in binding constants was attributed to the steric effect of the *tert*-butyl substituent on the tridentate ligand of the complex. Hypochromic shifts occurred in the absorption spectra upon increasing concentration of *ct*-DNA, implying stacking interactions between the DNA base pairs and aromatic chromophores of the complex ligands. Despite the bulky *tert*-butyl substituent, the [VO(TERTCA)(DPQ)](PF<sub>6</sub>) complex was also able to displace ethidium bromide from *ct*-DNA in competitive fluorescence emission binding studies. This indicates that [VO(TERTCA)(DPQ)](PF<sub>6</sub>) (or pro-drug) can at least partially intercalate *ct*-DNA. The neutral analogue of the *tert*-butyl complex, [VO(TERTA)(DPQ)], also displayed intercalative properties in the emission studies, however, with a lower apparent binding constant than [VO(TERTCA)(DPQ)](PF<sub>6</sub>). In addition, the [VO(TERTA)(DPQ)] complex was determined to have a lower apparent binding constant to *ct*-DNA than the less sterically hindered [VO(PHA)(DPQ)] complex.

This suggests that the steric bulk of the tridentate ligand similarly affected the DNA binding affinity of the neutral complexes. Intrinsic binding constants could not be determined for the neutral complexes with DPQ co-ligands as solvolysis/oxidation processes interfered with the absorption changes upon addition of *ct*-DNA. Intrinsic and apparent DNA binding constants could not be determined for the PHEN complexes as minimal changes occurred in the absorption and emission spectra, indicating a low DNA binding affinity.

The viscosity studies indicated a partial intercalation mode of binding to DNA is likely for [VO(PHA)(DPQ)], [VO(CLA)(DPQ)], [VO(NAA)(DPQ)] and [VO(TERTCA)(DPQ)](PF<sub>6</sub>). The cationic complexes with PHEN co-ligands, [VO(SOA)(DPQ)], [VO(TERTA)(DPQ)] and [VO(MEA)(DPQ)] are likely to be groove binders. [VO(MECA)(DPQ)](PF<sub>6</sub>) showed signs of intercalating DNA. Molecular docking studies indicated the complexes are DNA minor groove-binders, with the lowest energy molecular docking poses ranging from *ca.* -48 to -67 kJ mol<sup>-1</sup>.

The mechanism of action of vanadium-based chemotherapeutics typically involves the VO<sup>2+</sup> complexes binding to DNA *via* non-covalent interactions followed by oxidative DNA cleavage, which induces cell apoptosis. In the gel electrophoresis studies, the cationic complexes with DPQ co-ligands in this work were found to induce cleavage of plasmid DNA in the absence of external oxidising or reducing agents, most likely by a singlet oxygen pathway. The cleavage study also indicated that the complex is needed to induce DNA cleavage rather than the independent ligands or metal salt. The neutral DPQ complexes and cationic complexes with PHEN co-ligands did not induce DNA cleavage in the absence of external oxidising or reducing agents. The selected neutral complex [VO(MEA)(DPQ)] was, however, able to oxidatively cleave supercoiled plasmid DNA in the presence of H<sub>2</sub>O<sub>2</sub> *via* a hydroxyl radical pathway. EPR spin-trapping studies further suggested hydroxyl radicals are formed from the reaction of [VO(MEA)(DPQ)] and H<sub>2</sub>O<sub>2</sub>.

The cationic complexes were found to be cytotoxic against MDA-MB, SH-SY5Y and HeLa cancerous cell lines. The neutral DPQ oxovanadium complexes were found to be cytotoxic against the MDA-MB and SH-SY5Y cell lines and non-toxic towards the HeLa cell line. The cytotoxicity of the compounds towards the triple-negative breast cancer cell line MDA-MB is particularly interesting as this cancer does not generally respond to current treatments and has a high mortality rate as a result.

The mean cytotoxicity of the cationic metal chelates is 7.9  $\mu\text{M}$  against this cell line. Conversely, the cytotoxicity of cisplatin is lower than the experimental range used in this study. In general, the oxovanadium compounds synthesised in this work show promising cytotoxicity towards this cell line. Most of the complexes were, unfortunately, cytotoxic to the HEK293 healthy cell line. The  $[\text{VO}(\text{MECA})(\text{DPQ})](\text{PF}_6)$  complex is of significant interest since it has higher selectivity indices of 4.6, 7.4 and 5.9 against the tumour cell lines MDA-MB, HeLa and SH-SY5Y, respectively compared to the other metal chelates.

The cationic chelates are generally more cytotoxic than the neutral analogues. The mean ( $n = 4$ )  $\text{EC}_{50}$  for the four cationic chelates with PHEN co-ligands is 4.0, 3.6 and 3.7  $\mu\text{M}$  against the cell lines MDA-MB, HeLa and SHSY5Y, respectively. The cationic charge was a key design feature in this group of complexes to enable electrostatic attraction between the oxovanadium compounds and DNA (the intended cellular target), stabilising the DNA/drug conjugate. These data illustrate the importance of having an overall positive charge when developing metallodrugs.

In summary, the following factors impacted the cytotoxicity, DNA binding affinity and cleavage activity properties of the oxovanadium complexes:

- *The extent of aromaticity of the bidentate ligand:* the cationic complexes with DPQ co-ligands bind more strongly to DNA than the cationic complexes with PHEN co-ligands. The cationic complexes with DPQ co-ligands were able to cleave DNA in the absence of external oxidising agents whilst the cationic PHEN complex could not.
- *The charge of the complex/nature of tridentate ligand:* the cationic complex  $[\text{VO}(\text{TERTCA})(\text{DPQ})](\text{PF}_6)$  binds more strongly to DNA than the neutral analogue  $[\text{VO}(\text{TERTA})(\text{DPQ})]$  and it was able to cleave DNA in the absence of external oxidising agents whilst the neutral analogue could not. In addition, the cationic complexes were cytotoxic against the HeLa cancer cell line while the neutral analogues were not.
- *The type of substituent on tridentate ligand:* Less sterically hindered complexes bind more strongly to DNA than the analogous complexes with a bulky *tert*-butyl substituent on the tridentate ligand. In addition, the change from a methyl to a *tert*-butyl substituent in the cationic complexes increased toxicity against healthy cell line HEK293.

Mass spectrometry, UV/visible and NMR spectroscopy studies indicate that the neutral and cationic complexes, synthesised in this study, are susceptible to solvolysis processes. This is amplified in solvents which strongly coordinate vanadium.  $^{51}\text{V}$  NMR studies in  $\text{DMSO-}d_6$  suggest the solvated complex most likely corresponds to  $[\text{V}^{\text{V}}\text{O}_2(\text{ONO}/\text{ONN})(\text{DMSO})]$  analogues. UV-Visible studies indicate that the solvolysis product was formed within fifteen minutes after the dissolution of the cationic complex with the DPQ co-ligand, and was stable thereafter. It is likely that the vanadium compounds are cytotoxic as pro-drugs, as is common for vanadium compounds in clinical trials.

## 9.2 Future Work

The nature of the substituent on the tridentate ligand was found to influence the DNA binding, DNA cleavage ability and cytotoxic properties of the complexes. Future work on the lead complex,  $[\text{VO}(\text{MECA})(\text{DPQ})](\text{PF}_6)$ , can, therefore, be expanded to investigate more than the just the steric effect of the substituent on the tridentate ligand of the cationic complexes with DPQ co-ligands. Electronic effects such as electron-withdrawing substituents (eg. Cl), and substituents with hydrogen bonding capability (eg. OH) (*Figure 9.1*) could be investigated.<sup>2</sup> The future work could also include isolating the complexes as the chloride complex salt and include an ethylsulfonyl substituent on the tridentate ligand to improve the aqueous solubility of the complexes.

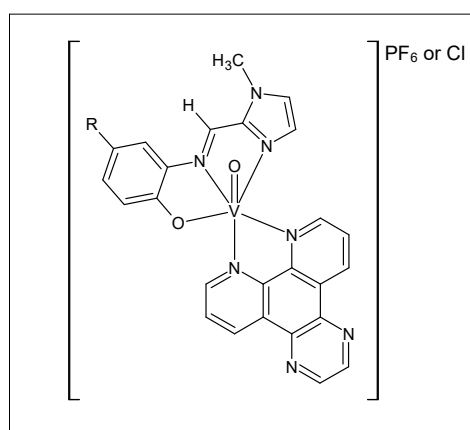


**Figure 9.1**  $[\text{VO}(\text{ONN})(\text{DPQ})](\text{PF}_6/\text{Cl})$  oxovanadium complexes with various substituents on the tridentate ligand where  $\text{R} = \text{H}, \text{Cl}, \text{OH}, \text{CH}_3, \text{CH}_3\text{CH}_2\text{SO}_2$ .

The role of the substituent on the properties of the complexes can be investigated in terms of stability, cytotoxicity, DNA binding and DNA cleavage properties.

The DNA binding studies can also be expanded upon to not only include absorption titrations, ethidium bromide fluorescence quenching and viscosity DNA binding studies but also include:

- Competitive emission studies with known minor groove binders, such as Hoescht 33258 and major groove binders, such as methyl green.<sup>3,4</sup> This will allow for a more definitive conclusion about the DNA binding mode to be drawn.
- Iodide fluorescence quenching studies to identify intercalators from electrostatic and groove binders.<sup>3</sup>
- Ionic strength fluorescence quenching studies with NaCl to investigate surface electrostatic interaction binders.<sup>3</sup>
- DNA melting curve studies to identify intercalators from groove binders.<sup>5</sup> Depending on the DNA binding mode, the DNA helix is either lengthened or shortened. This change affects the melting temperature of the DNA, measurable using DNA melting curves.

Speciated vanadium may be responsible for biological activity.<sup>6</sup> Oxovanadium complexes are known to undergo speciation and bind preferentially to transferrin protein.<sup>7,8</sup> The binding studies can also be expanded to include protein binding studies of transferrin and bovine or human serum albumin using fluorescence quenching or EPR spectroscopic methods.<sup>2,9-11</sup>

The mechanistic studies could also be expanded. The cationic complexes with DPQ co-ligands were found to cleave plasmid DNA, most likely by a singlet oxygen pathway as the presence of DMSO did not inhibit DNA cleavage activity in gel electrophoresis experiments. This could be further confirmed by expanding the range of reagents added to the reactions to include:

- Singlet oxygen quenchers such as sodium azide, L-histidine and 2,2,6,6-tetramethyl-4-piperidone (TEMP) in addition to DABCO.<sup>12-16</sup>
- Hydroxyl radical scavengers such as catalase, KI and mannitol in addition to DMSO.<sup>12-16</sup>
- Superoxide dismutase (SOD) to test for superoxide radical anions.<sup>12,13,15-17</sup>

The cleavage reactions can also be conducted in D<sub>2</sub>O, which allows for a longer lifetime of singlet oxygen,<sup>12,13,18</sup> and in an argon atmosphere to investigate the necessity of molecular oxygen for cleaving DNA.<sup>12,13</sup> The cleavage reactions can also be conducted in the dark to investigate the necessity of visible light.<sup>12</sup>

EPR spin trapping mechanistic studies could be expanded to include a singlet oxygen spin trap (TEMP) and singlet oxygen scavengers NaN<sub>3</sub> or DABCO. This would prove the existence of a singlet oxygen mechanism.<sup>19-21</sup> The hydroxyl radical DMPO spin trapping experiments can be further investigated. First, to resolve the 4 lines of the DMPO-OH adduct into the 1:2:2:1 pattern. The 4-line spectrum can be enhanced by optimising the vanadium complex, H<sub>2</sub>O<sub>2</sub> and DMPO concentrations or by varying instrument parameters. Carmichael suggests reducing the EPR instrument microwave power, scan range and modulation amplitude to resolve the DMPO-OH quartet.<sup>22</sup> In addition, the presence of hydroxyl radicals can be further verified as the quartet spectrum is not unique to the DMPO-OH adduct and DMPO-OH itself may be formed by pathways other than the reaction of  $\cdot\text{OH}$  and DMPO.<sup>22,23</sup> The presence of hydroxyl radicals may be further verified by adding compounds such as ethanol or DMSO. Ethanol and DMSO react with hydroxyl radicals to form carbon-based secondary radicals. These are then trapped by DMPO to form unique DMPO-hydroxyethyl and DMPO-CH<sub>3</sub> adducts for ethanol and DMSO, respectively.<sup>23-28</sup>

Many investigations are needed to identify which factors will impact the stability, cytotoxic and DNA binding properties of the oxovanadium complexes as well as their DNA cleavage abilities and mechanisms. This work has shown that mechanism of action is not as simple as a correlation between the conjugation of the polypyridyl co-ligand of the oxovanadium complexes and cytotoxicity.

The compound [VO(MECA)(DPQ)](PF<sub>6</sub>) was identified as the lead compound in the present study based on the enhanced selectivity index. Using this data as motivation, the National Cancer Institute (NCI) in the USA may screen the compound against their panel of 60 human tumour cell lines. This is a very useful test as the large amount of data collected allows for hierarchical cluster analysis using data from the NCI database. This statistical method may be used to group compounds according to their mechanism of action. This can then be used as a starting point for more detailed studies of the mechanism of action.<sup>29</sup>

## 9.3 Research Outputs

### 9.3.1 Conference Contributions

1. The Inorganic Chemistry Conference 2017 & Carman Physical Chemistry Symposium of the South African Chemical Institute (SACI), 25 – 29 June 2017, Arabella Hotel & Spa, Hermanus, Western Cape, South Africa. Barry, K.L., Akerman, M. and Munro, O., Poster entitled: “Synthesis and Structure of Novel Oxovanadium(IV) Complexes”.
2. Indaba 9 Conference, Modeling of Structures and Properties, 2 – 7 September 2018, Skukuza, Kruger National Park, South Africa. Barry, K.L., Akerman, M., Munro, O., Hewer, R. and Delpont, A., Poster entitled: “Synthesis and Structure of Novel Oxovanadium(IV) Complexes”.

### 9.3.2 Publications

1. Barry, K.L., Grimmer, C.D., Munro, O.Q. and Akerman, M.P., “Self-assembled supramolecular structures of O,N,N' tridentate imidazole-phenol Schiff base compounds”, *RSC Adv.*, **2020**, *10*, 7867.

## 9.4 References

1. Barry, K.L., Grimmer, C.D., Munro, O.Q. and Akerman, M.P., *RSC Adv.*, **2020**, *10*, 7867.
2. Banerjee, A., Dash, S.P., Mohanty, M., Sanna, D., Sciortino, G., Ugone, V., Garriba, E., Reuter, H., Kaminsky, W. and Dinda, R., *J. Inorg. Biochem.*, **2019**, *199*, 110786.
3. Rehman, S.U., Yaseen, Z., Husain, M.A., Sarwar, T., Ishqi, H.M. and Tabish, M., *PLoS One*, **2014**, *9*, e93913.
4. Lima, S., Banerjee, A., Mohanty, M., Sahu, G., Kausar, C., Patra, S.K., Garriba, E., Kaminsky, W. and Dinda, R., *New J. Chem.*, **2019**, *43*, 17711.
5. Banerjee, S., Hussain, A., Prasad, P., Khan, I., Banik, B., Kondaiah, P. and Chakravarty, A.R., *Eur. J. Inorg. Chem.*, **2012**, 3899.
6. Rehder, D., *Future Med. Chem.*, **2016**, *8*, 325.
7. Rehder, D., *Dalton Trans.*, **2013**, *42*, 11749.
8. Costa Pessoa, J., Etcheverry, S. and Gambino, D., *Coord. Chem. Rev.*, **2015**, *301-302*, 24.
9. Banerjee, A., Mohanty, M., Lima, S., Samanta, R., Garrriba, E., Sasamori, T. and Dinda, R., *New J. Chem.*, **2020**, *44*, 10946.
10. Liboiron, B.D., Thompson, K.H., Hanson, G.R., Lam, E., Aebischer, N. and Orvig, C., *J. Am. Chem. Soc.*, **2005**, *127*, 5104.
11. Du, H., Xiang, J., Zhang, Y., Tang, Y. and Xu, G., *J. Inorg. Biochem.*, **2008**, *102*, 146.
12. Sasmal, P., Patra, A.K., Nethaji, M. and Chakravarty, A.R., *Inorg. Chem.*, **2007**, *46*, 11112.
13. Prasad, P., Sasmal, P.K., Majumdar, R., Dighe, R. and Chakravarty, A.R., *Inorg. Chim. Acta*, **2010**, *363*, 2743.
14. Guo, H., Lu, J., Ruan, Z., Zhang, Y., Liu, Y., Zang, L., Jiang, J. and Huang, J., *J. Coord Chem.*, **2012**, *65*, 191.
15. Prasad, P., Sasmal, P.K., Khan, I., Kondaiah, P. and Chakravarty, A.R., *Inorg. Chim. Acta*, **2011**, *372*, 79.
16. Leichnetz, S., Heinrich, J. and Kulak, N., *Chem. Commun.*, **2018**, *54*, 13411.
17. Sreedhara, A., Freed, J.D. and Cowan, J.A., *J. Am. Chem. Soc.*, **2000**, *122*, 8814.
18. Khan, A.U., *J. Phys. Chem.*, **1976**, *80*, 2219.

19. Sun., Y., Zheng., Y., Lei, W.-H., Zhou, Q.-X., Hou, Y.-J., Zhang, B.-W. and Wang, X.-S., *Dalton Trans.*, **2012**, *41*, 651.
20. Hadjur, C., Jeunet, A. and Jardon, P., *J. Photochem. Photobiol., B.*, **1994**, *26*, 67.
21. Lion, Y., Delmelle, M. and Van De Vorst, A., *Nature*, **1976**, *263*, 442.
22. Carmichael, A.J., *FEBS Lett.*, **1990**, *261*, 165.
23. Finkelstein, E., Rosen, G.M. and Rauckman, E.J., *Arch. Biochem. Biophys.*, **1980**, *200*, 1.
24. Verquin, G., Fontaine, G., Bria, M., Zhilinskaya, E., Abi-Aad, E., Aboukaïs, A., Baldeyrou, B., Bailly, C. and Bernier, J.-L., *J Biol. Inorg. Chem.*, **2004**, *9*, 345.
25. Dixon, W.T. and Norman, R.O.C., *J. Chem. Soc.*, **1963**, 3119.
26. Dixon, W.T., Norman, R.O.C. and Buley, A.L., *J. Chem. Soc.*, **1964**, 3625.
27. Keller, R.J., Sharma, R.P., Grover, T.A. and Piette, L.H., *Arch. Biochem. Biophys.*, **1988**, *265*, 524.
28. Gilbert, B. C., Norman, R.O.C. and Sealy, R. C. *J. Chem. Soc., Perkin. Trans. 2*, **1975**, 303.
29. Akerman, K.J., Fagenson, A.M., Cyril V., Taylor, M., Muller, M.T., Akerman, M.P., and Munro, O.Q., *J. Am. Chem. Soc.*, **2014**, *136*, 5670.

## Appendix A: Characterisation Data

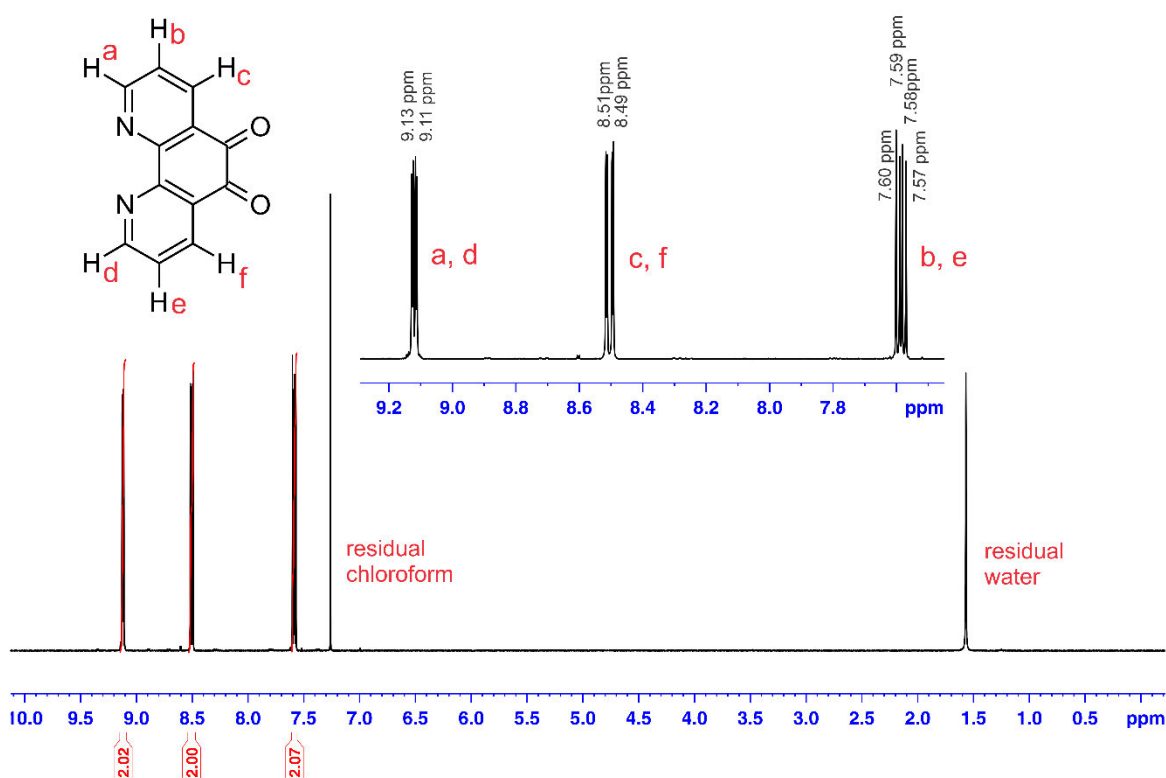


**Figure A1:** Fully assigned <sup>1</sup>H NMR spectrum of 1,10-phenanthroline-5,6-dione in CDCl<sub>3</sub>.

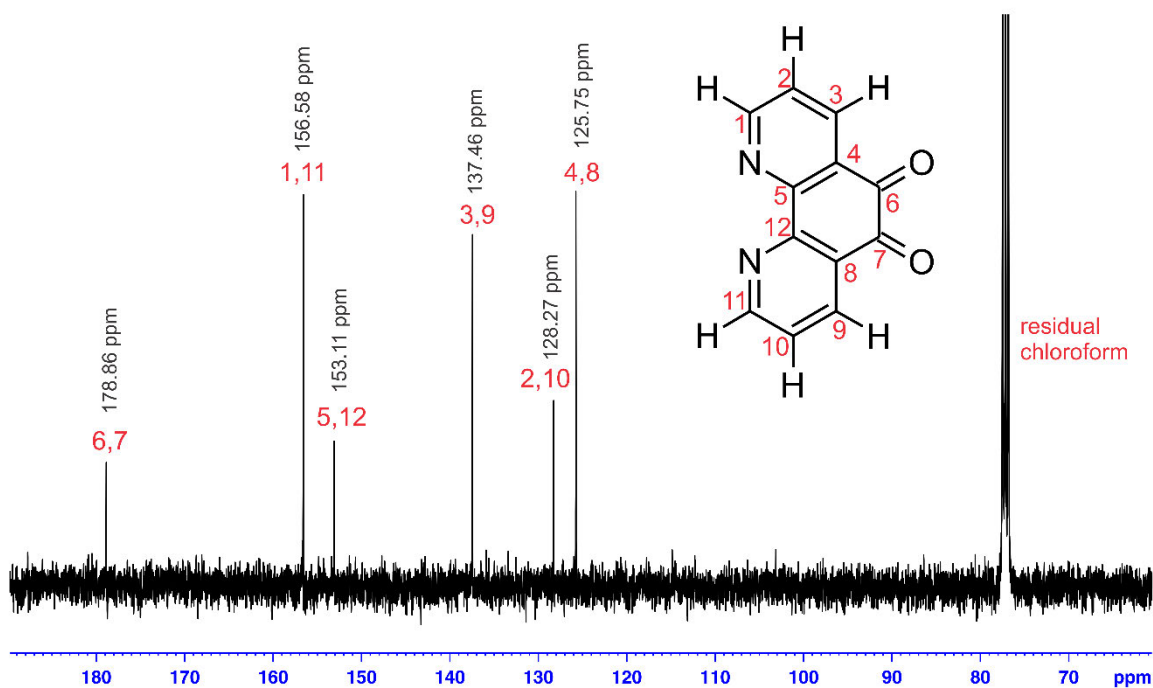


**Figure A2:** Fully assigned <sup>13</sup>C NMR spectrum of 1,10-phenanthroline-5,6-dione in CDCl<sub>3</sub>.

**Single Mass Analysis**

Tolerance = 5.0 PPM / DBE: min = -1.5, max = 100.0

Element prediction: Off

Number of isotope peaks used for i-FIT = 3

Monoisotopic Mass, Even Electron Ions

19 formula(e) evaluated with 1 results within limits (up to 20 closest results for each mass)

Elements Used:

C: 10-15 H: 5-10 N: 0-5 O: 0-5

Dione 2 (0.034) Cm (1:61)

TOF MS AP+

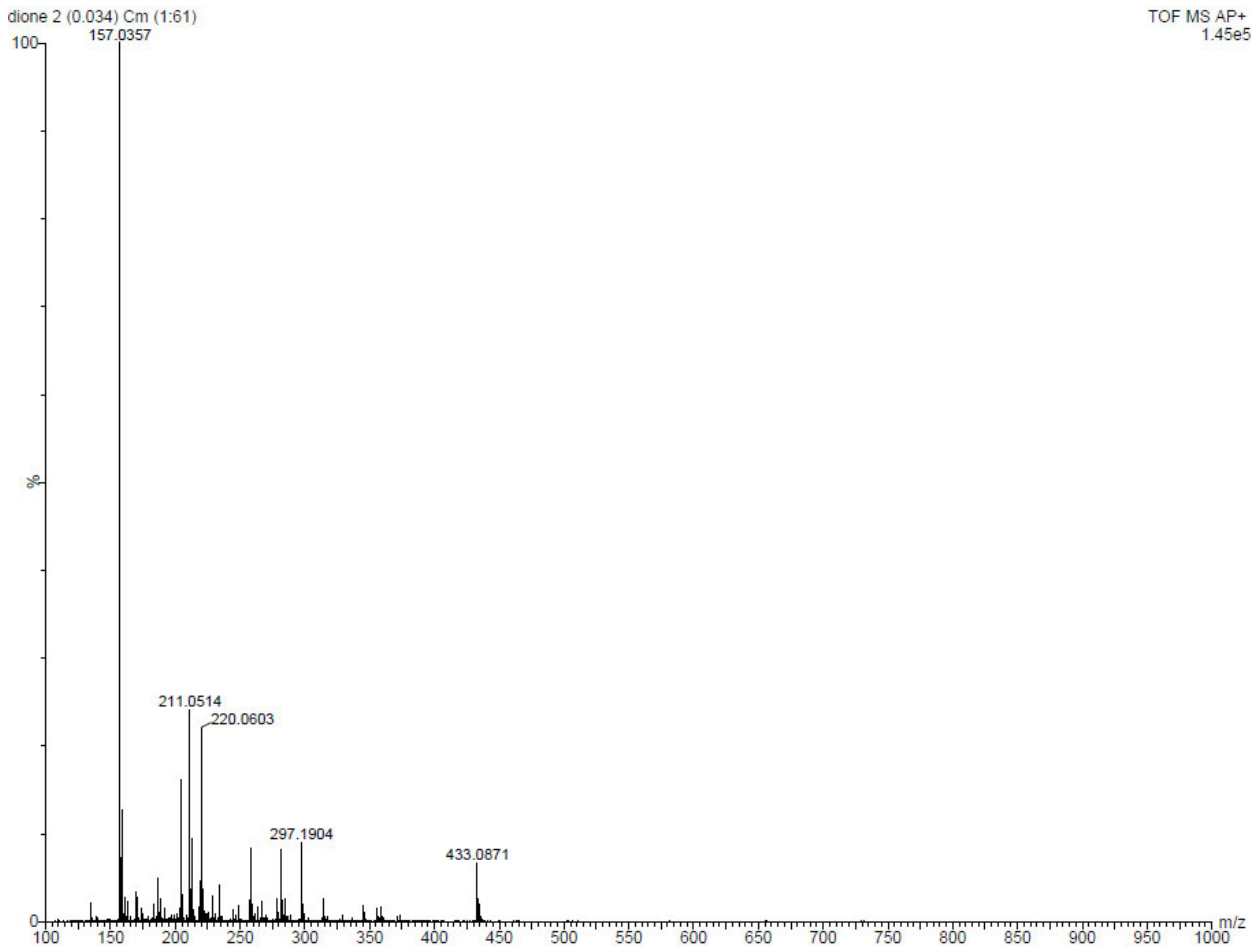
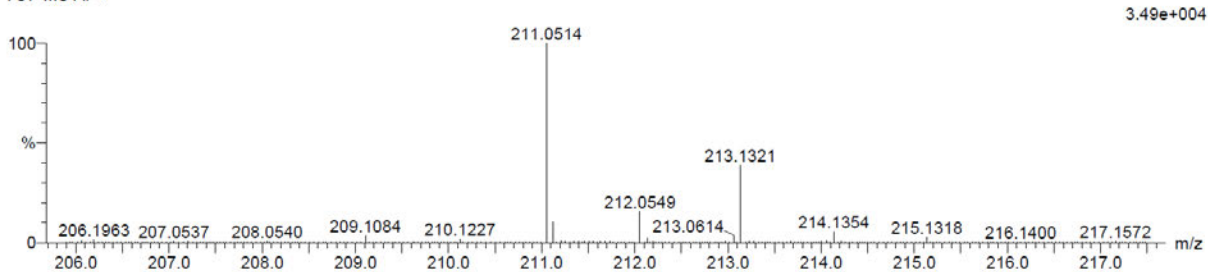


**Figure A3:** High resolution ESI mass spectrum of 1,10-phenanthroline-5,6-dione in methanol.

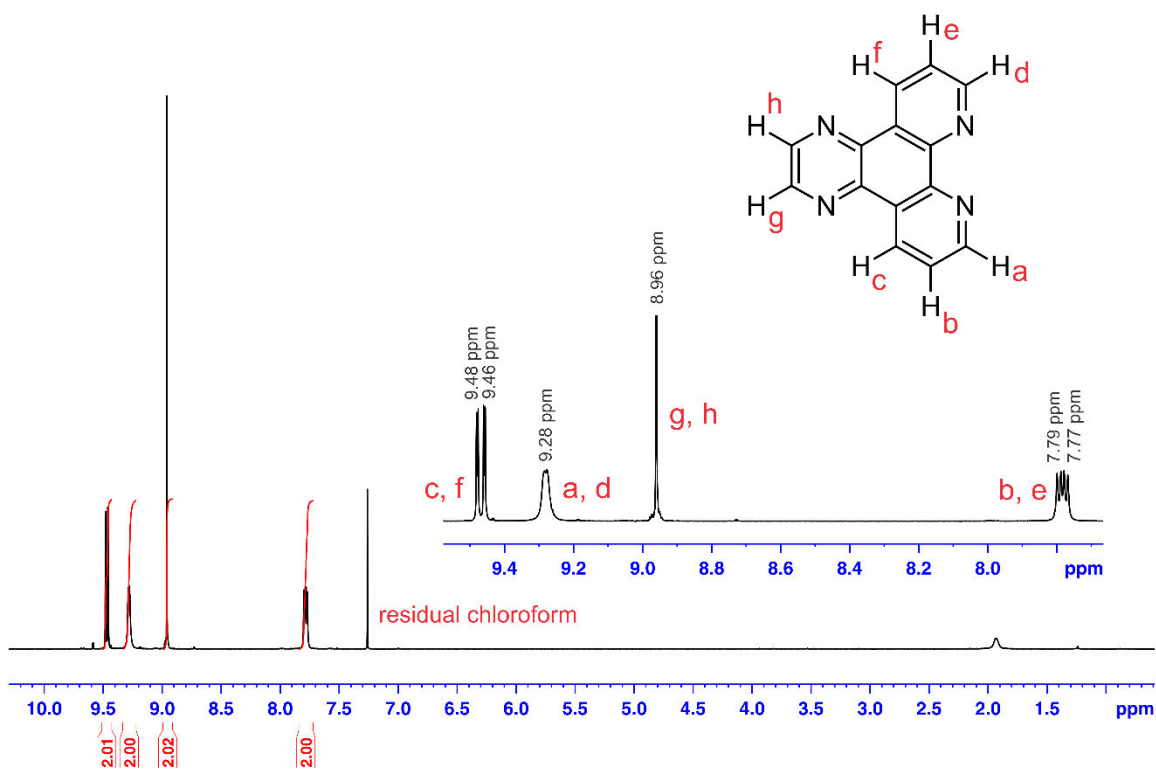


Figure A4: Fully assigned  $^1\text{H}$  NMR spectrum of DPQ in  $\text{CDCl}_3$ .

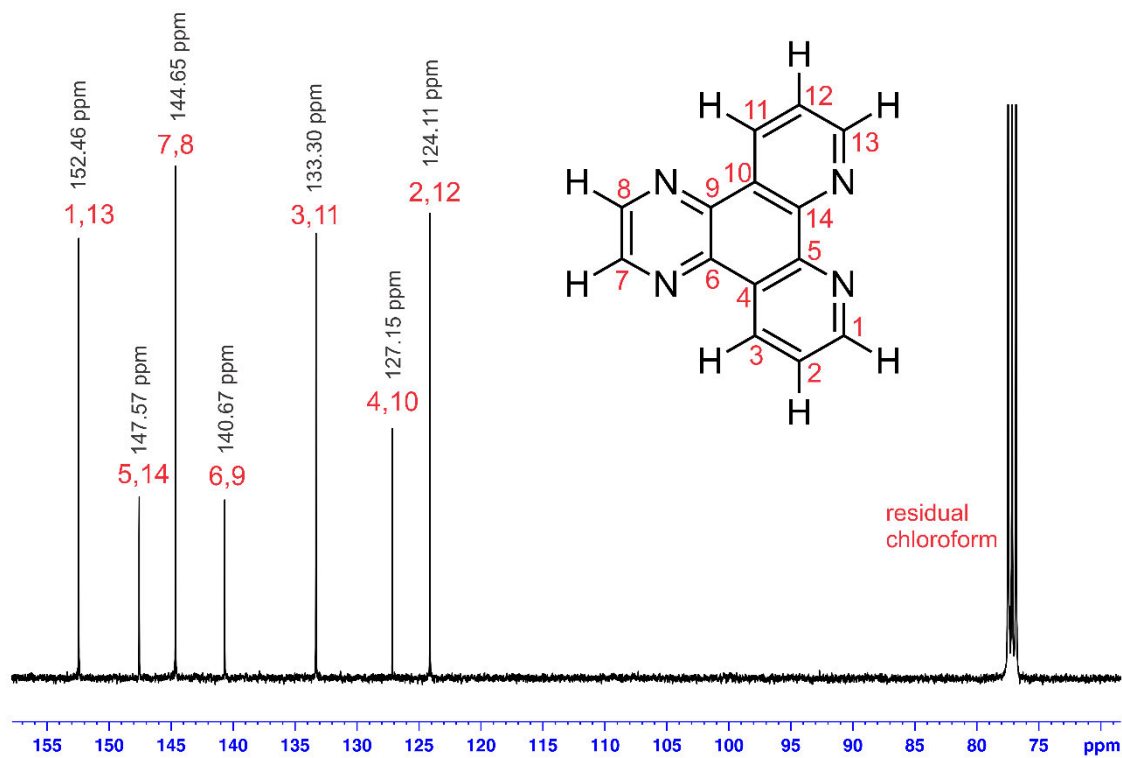


Figure A5: Fully assigned  $^{13}\text{C}$  NMR spectrum of DPQ in  $\text{CDCl}_3$ .

### Single Mass Analysis

Tolerance = 5.0 PPM / DBE: min = -1.5, max = 50.0

Element prediction: Off

Number of isotope peaks used for i-FIT = 3

Monoisotopic Mass, Even Electron Ions

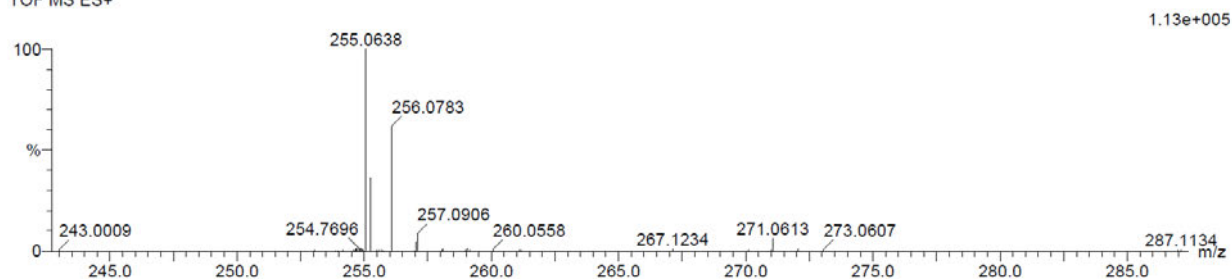
4 formula(e) evaluated with 1 results within limits (all results (up to 1000) for each mass)

Elements Used:

C: 10-15 H: 5-10 N: 0-5 Na: 1-1

DPQ-DMSO 32 (1.045) Cm (1.61)

TOF MS ES+



DPQ-DMSO Ims 13 (0.205) Cm (1:60)

TOF MS ES+  
9.64e4

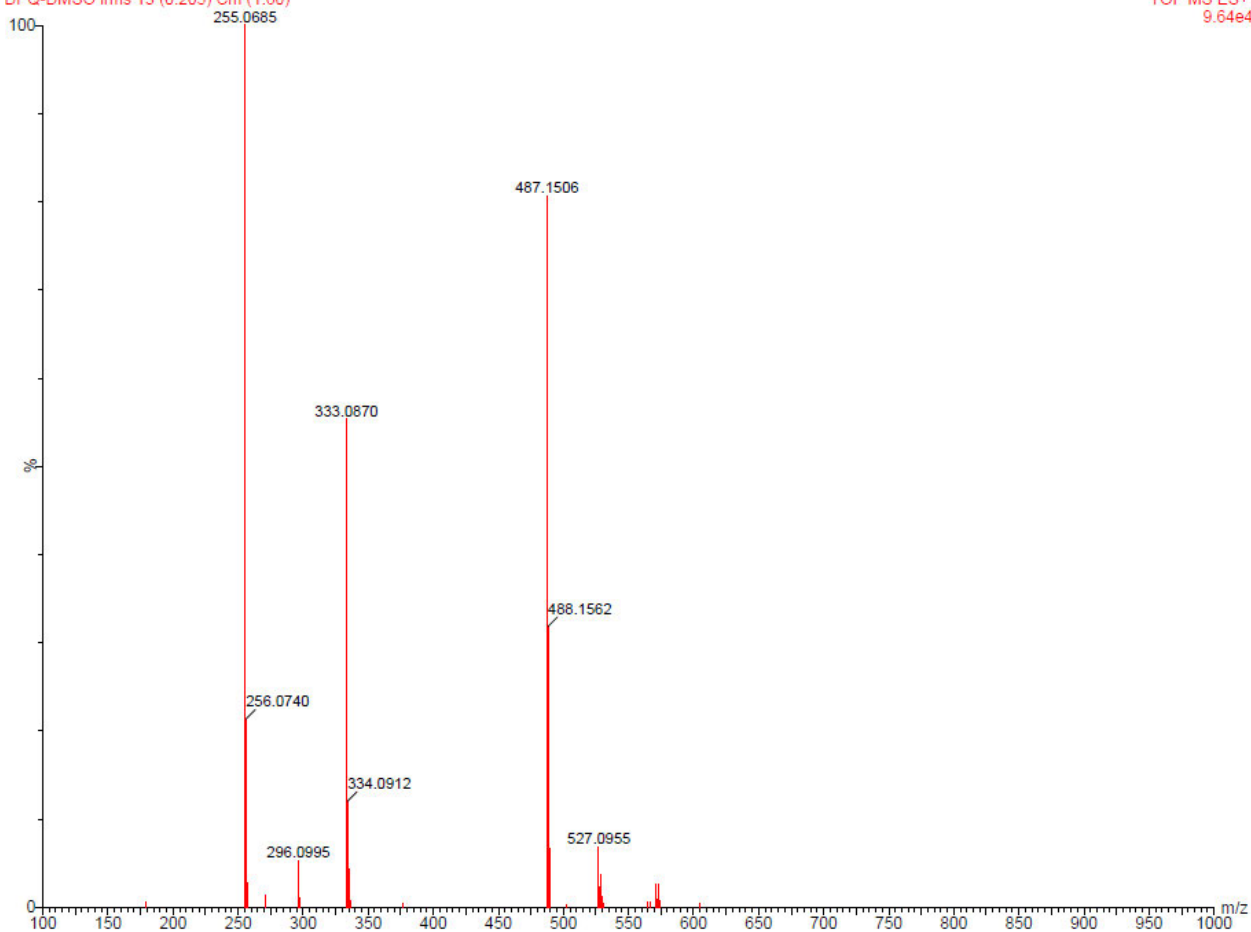


**Figure A6: High resolution ESI mass spectrum of DPQ in DMSO.**

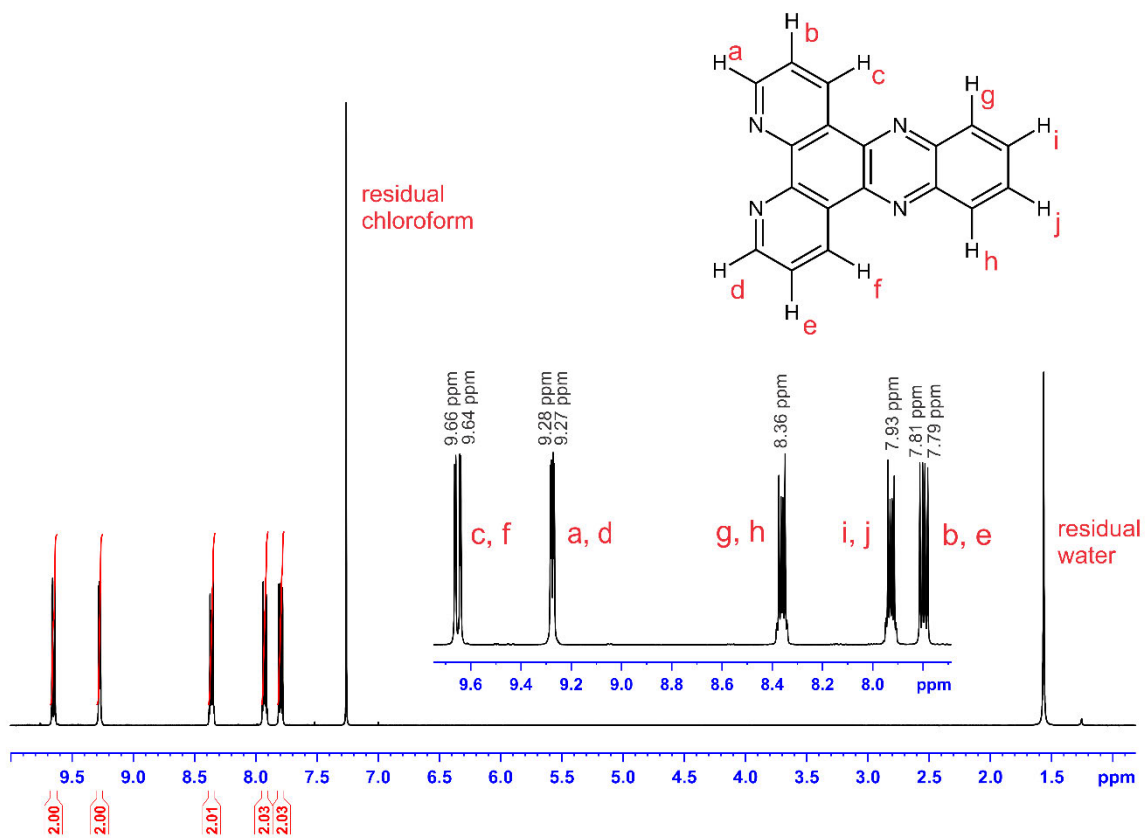


Figure A7: Fully assigned  $^1\text{H}$  NMR spectrum of DPPZ in  $\text{CDCl}_3$ .

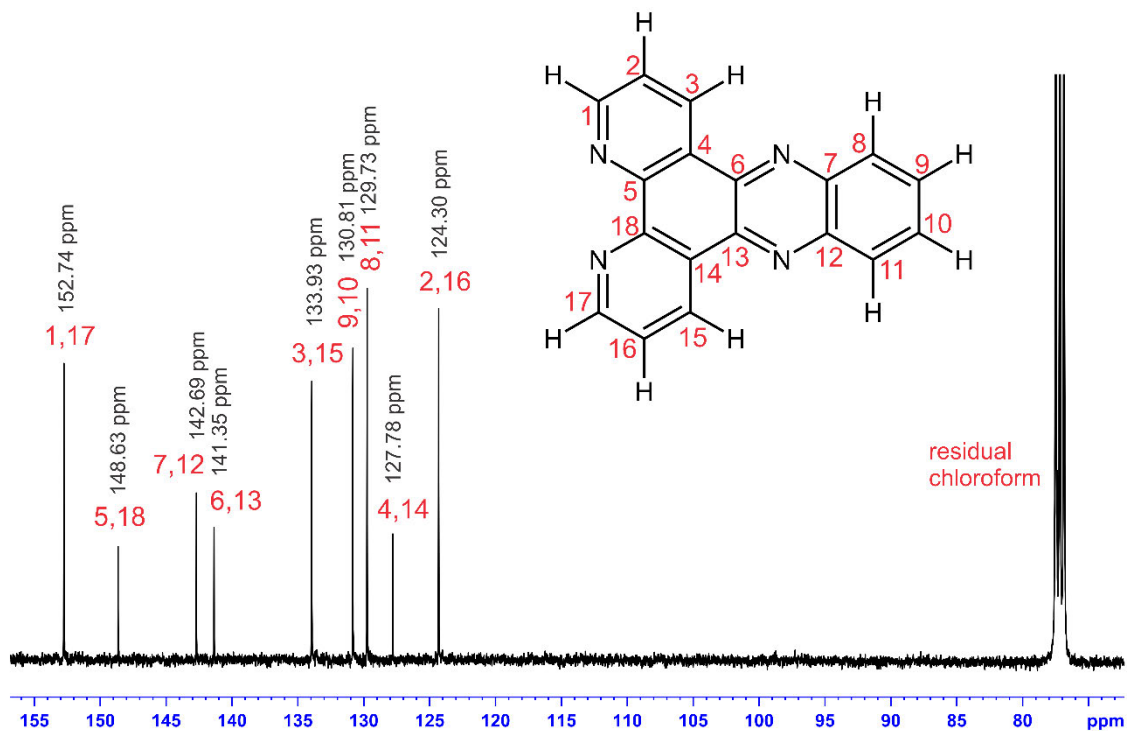


Figure A8: Fully assigned  $^{13}\text{C}$  NMR spectrum of DPPZ in  $\text{CDCl}_3$ .

### Single Mass Analysis

Tolerance = 4.0 PPM / DBE: min = -1.5, max = 100.0

Element prediction: Off

Number of isotope peaks used for i-FIT = 3

Monoisotopic Mass, Even Electron Ions

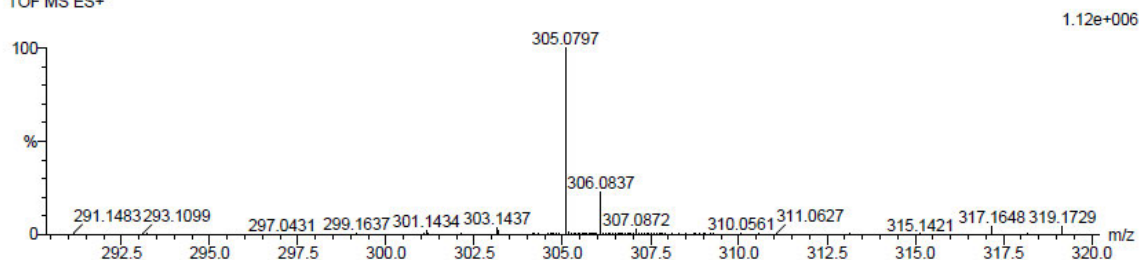
3 formula(e) evaluated with 1 results within limits (up to 20 closest results for each mass)

Elements Used:

C: 15-20 H: 10-15 N: 0-5 Na: 1-1

Dppz 23 (0.743) Cm (1.61)

TOF MS ES+



Dppz Ims 2 (0.017) Cm (1:59)

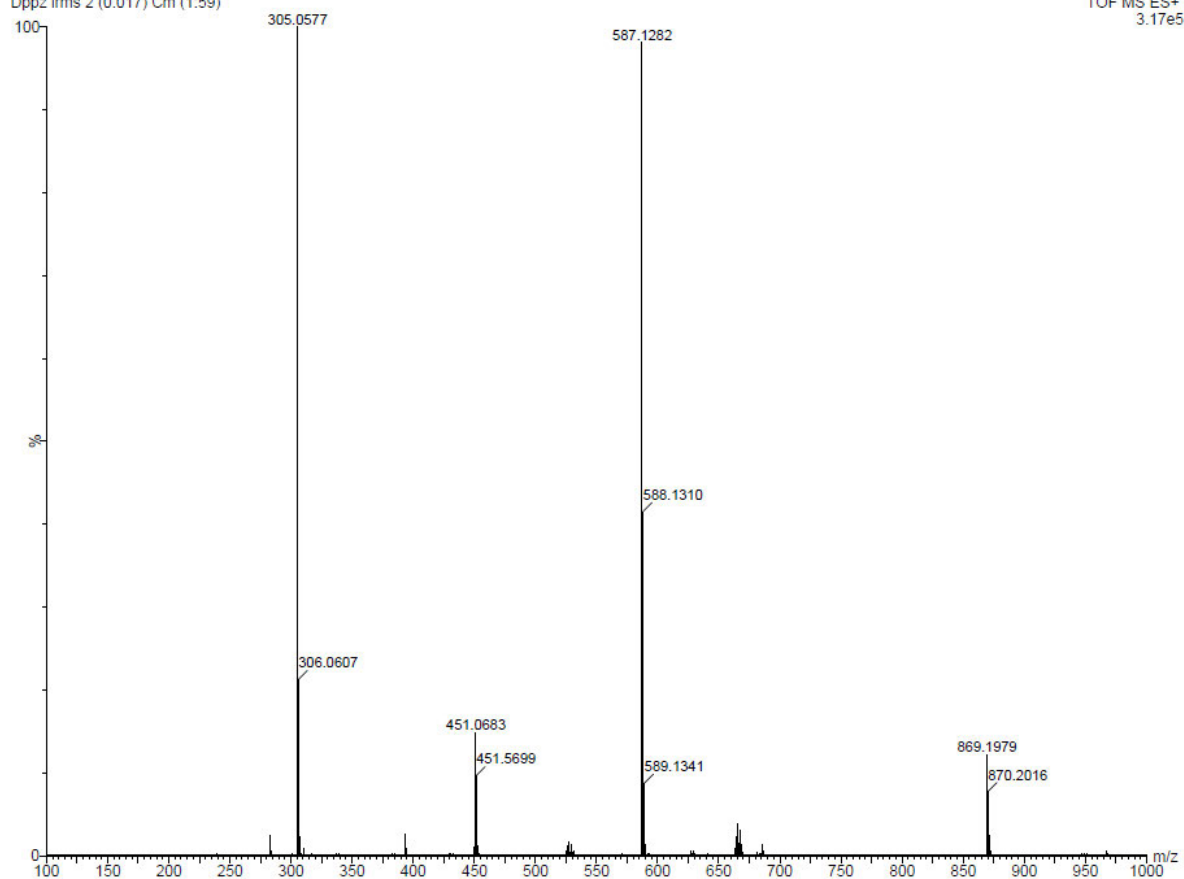


**Figure A9: High resolution ESI mass spectrum of DPPZ in methanol.**

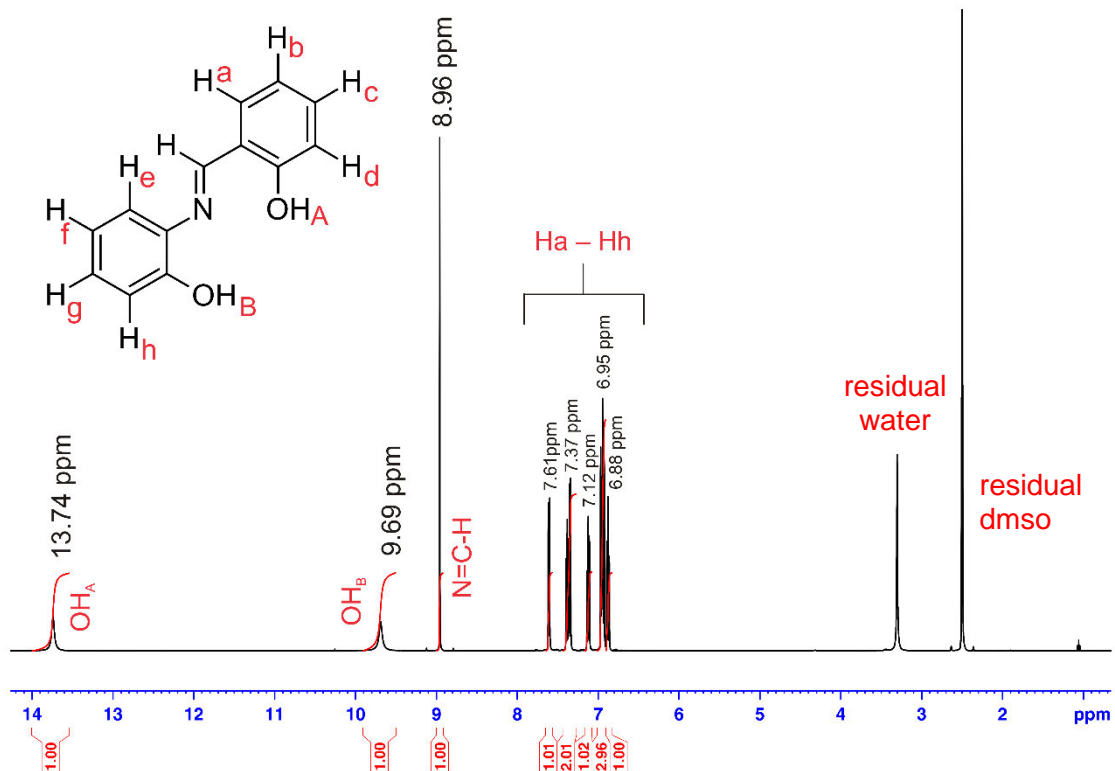


Figure A10: Assigned  $^1\text{H}$  NMR spectrum of PHA in  $\text{DMSO-}d_6$ .

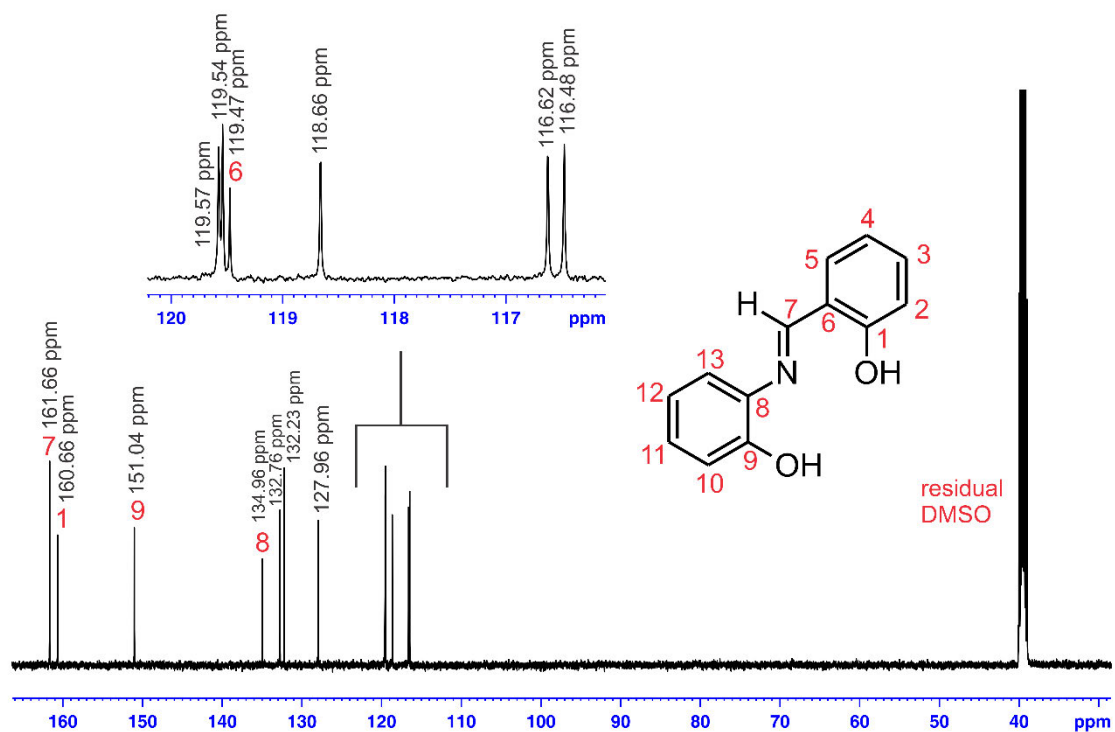
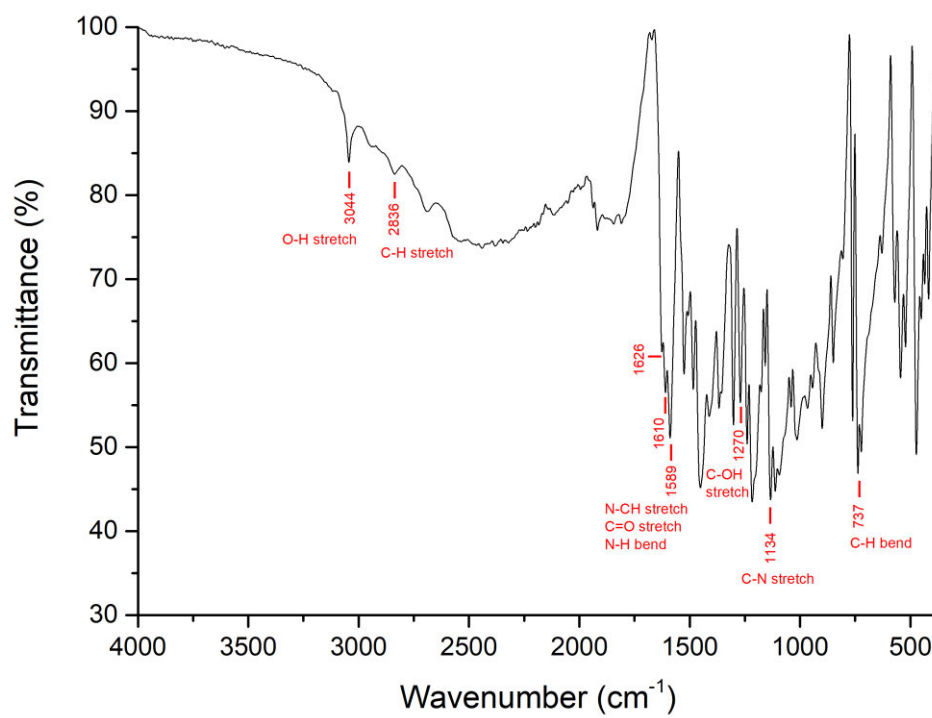
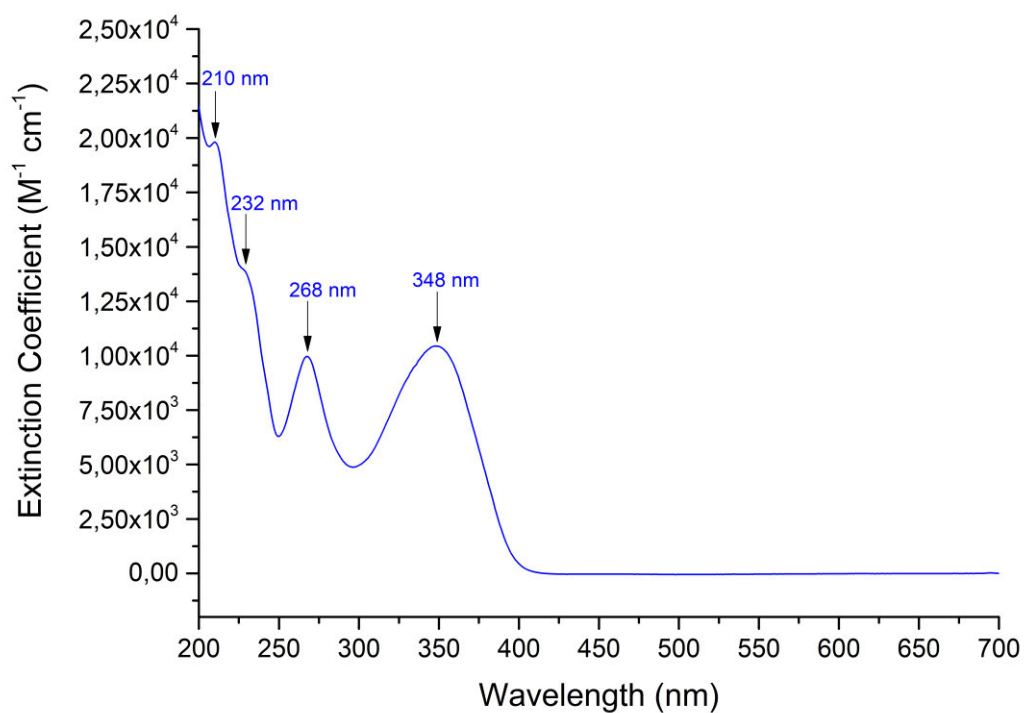


Figure A11: Assigned  $^{13}\text{C}$  NMR spectrum of PHA in  $\text{DMSO-}d_6$ .



**Figure A12: IR spectrum of PHA.**



**Figure A13: UV/visible spectrum of PHA. [PHA] =  $4.98 \times 10^{-5}$  M.**

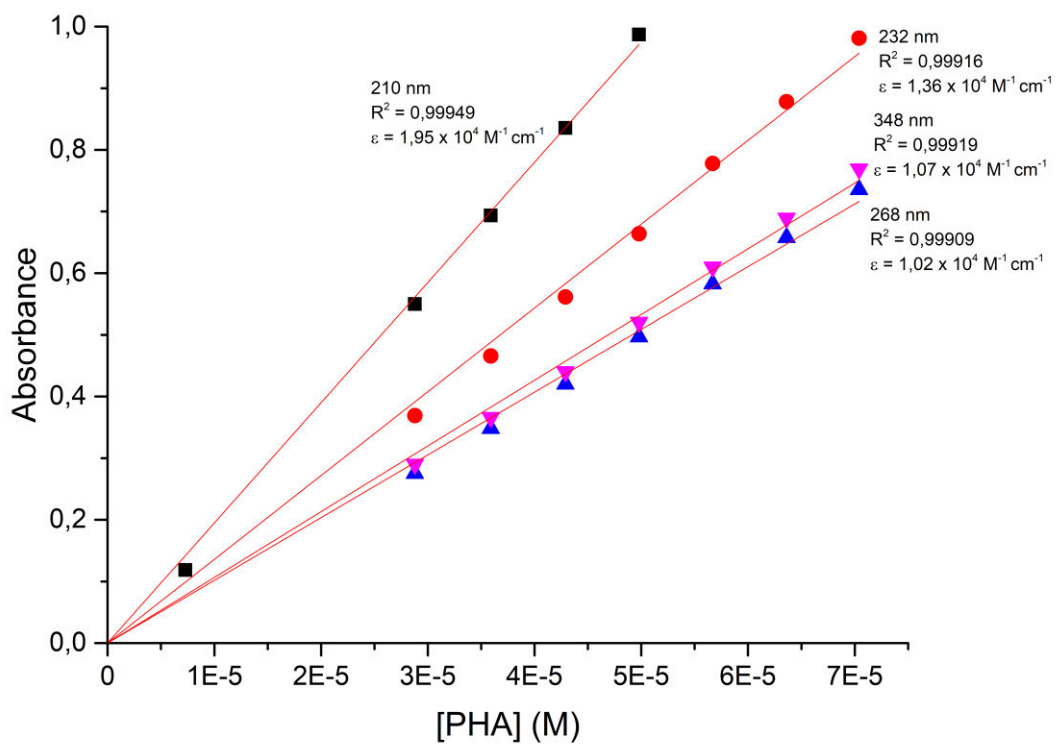


**Figure A14: Beer's Law Correlation of PHA.**

### Single Mass Analysis

Tolerance = 5.0 PPM / DBE: min = -1.5, max = 500.0

Element prediction: Off

Number of isotope peaks used for i-FIT = 2

Monoisotopic Mass, Even Electron Ions

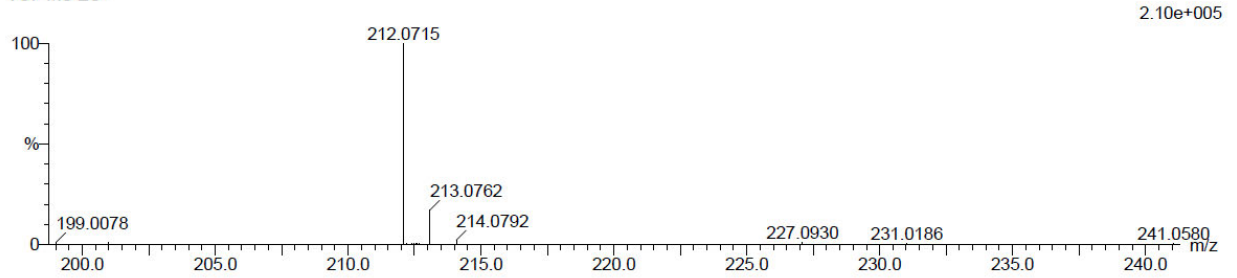
20 formula(e) evaluated with 1 results within limits (all results (up to 1000) for each mass)

Elements Used:

C: 10-15 H: 10-15 N: 0-5 O: 0-5

PHA(2) 24 (0.776) Cm (1:61)

TOF MS ES-



PHA(2) I rms 28 (0.461) Cm (1:60)

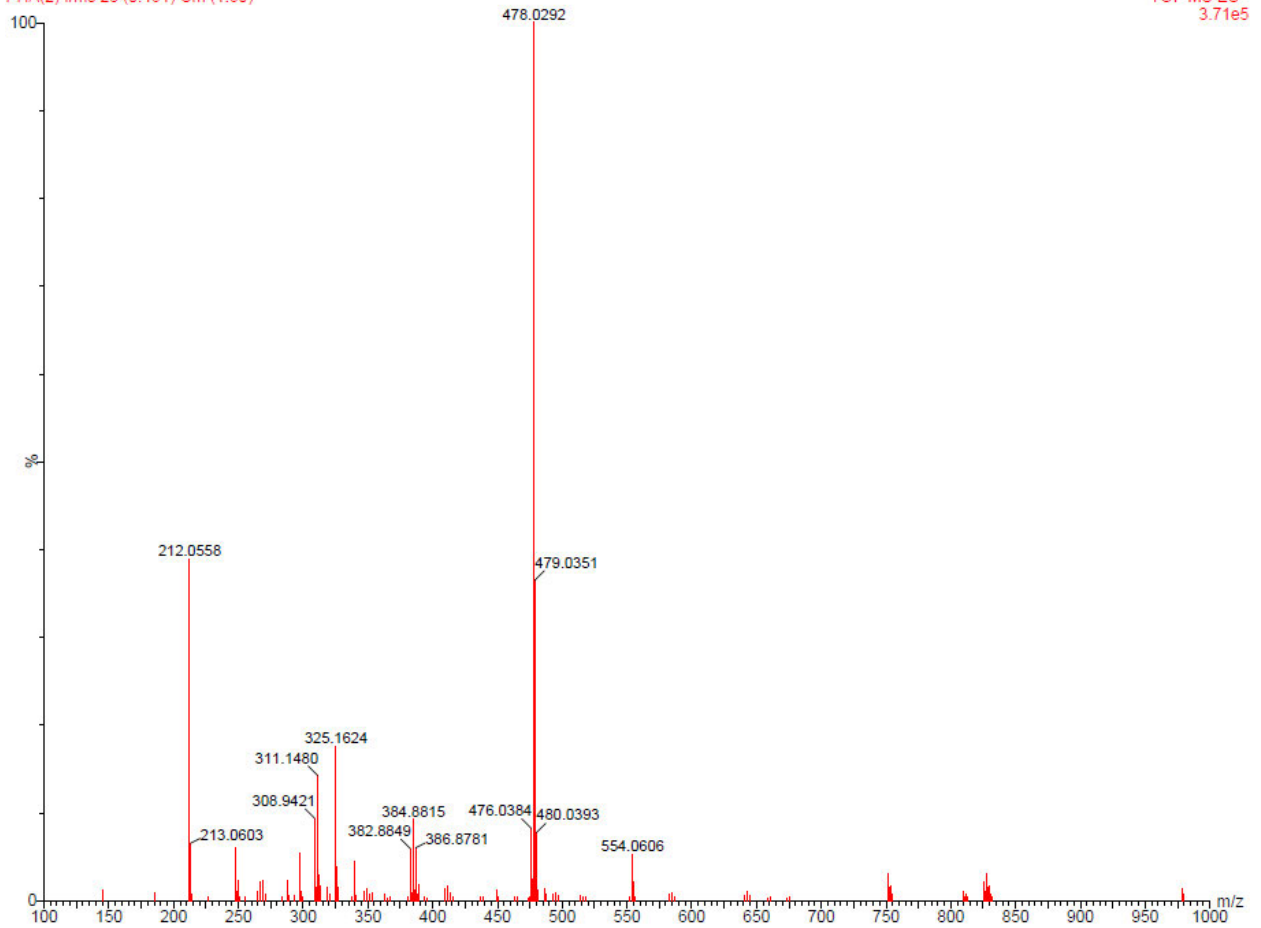


**Figure A15: High resolution ESI mass spectrum of PHA in chloroform.**

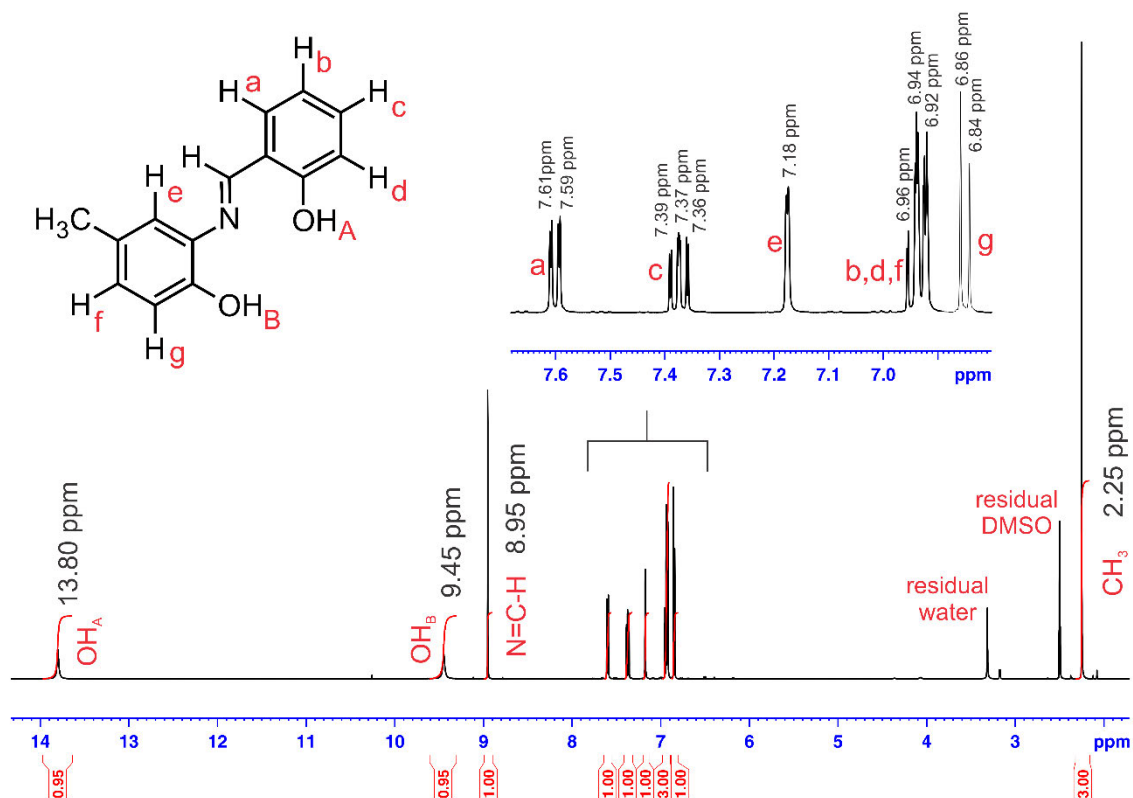


Figure A16: Fully assigned  $^1\text{H}$  NMR spectrum of MEA in  $\text{DMSO-}d_6$ .

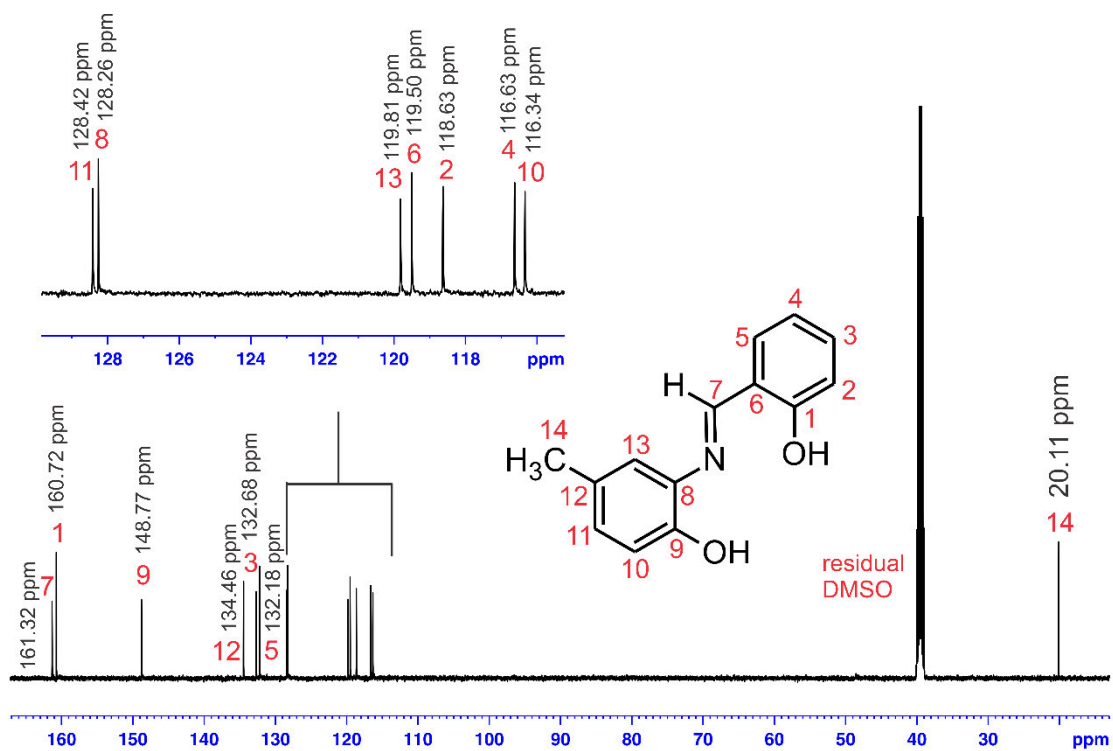
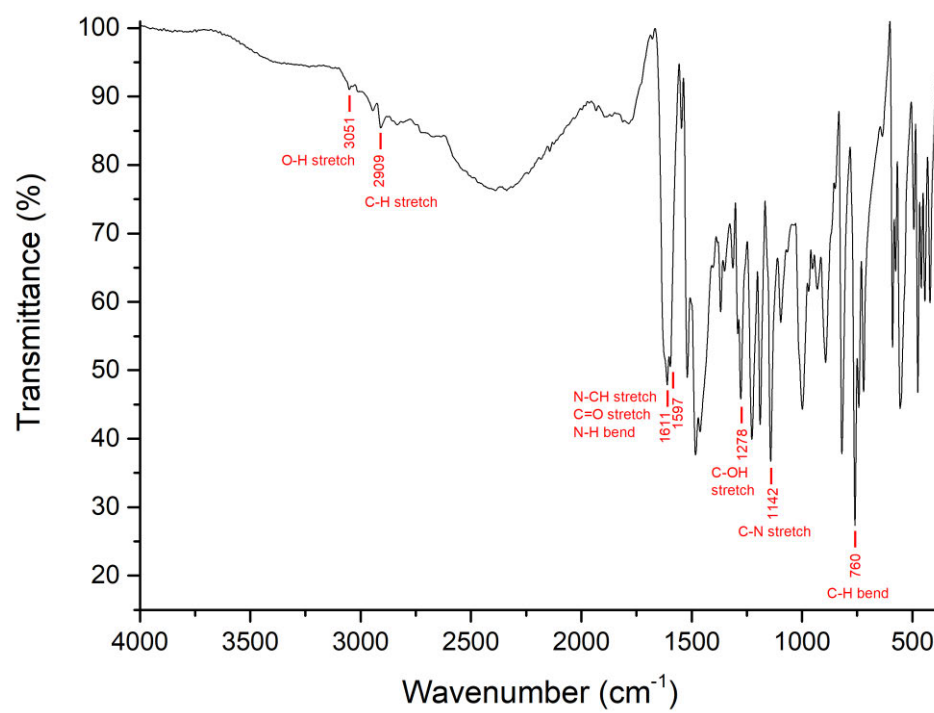
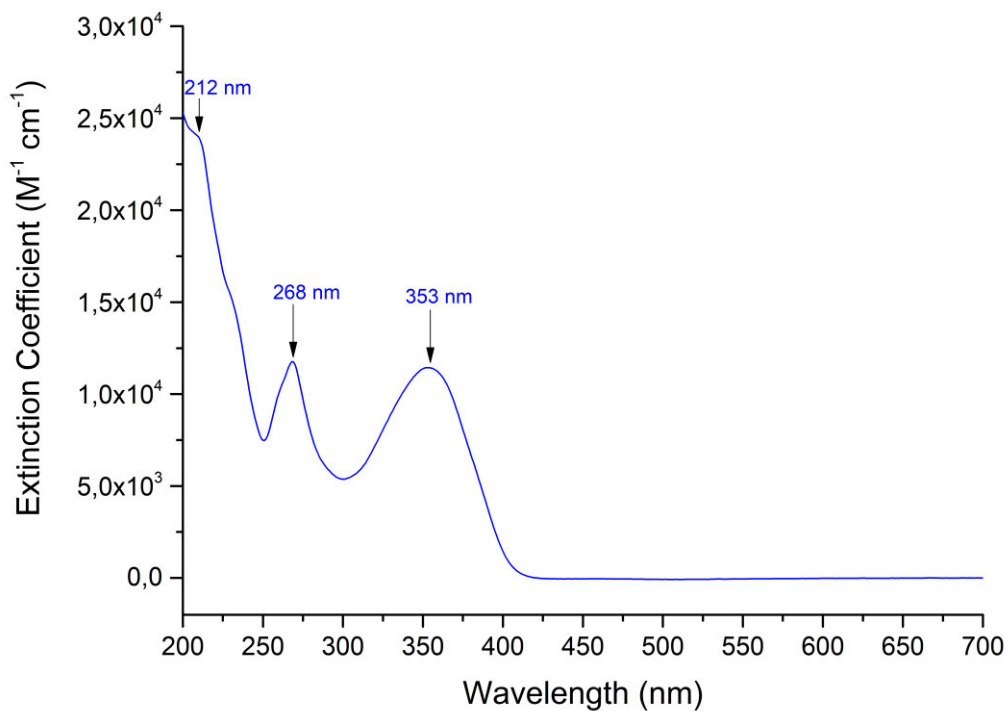


Figure A17: Fully assigned  $^{13}\text{C}$  NMR spectrum of MEA in  $\text{DMSO-}d_6$ .



**Figure A18:** IR spectrum of MEA.



**Figure A19: UV/visible spectrum of MEA.  $[\text{MEA}] = 3.71 \times 10^{-5} \text{ M}$ .**

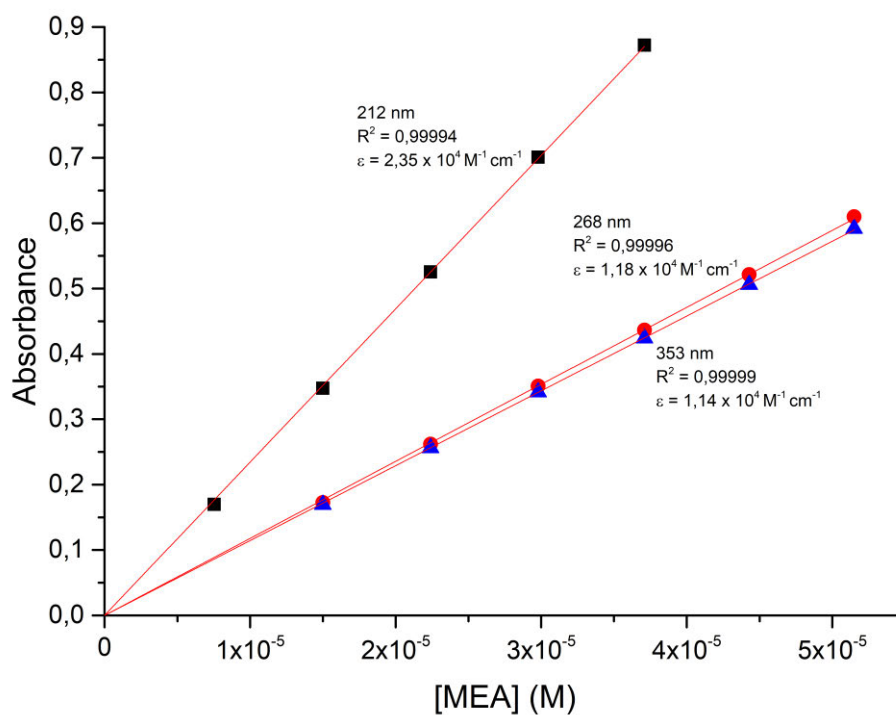


**Figure A20: Beer's Law Correlation of MEA.**

### Single Mass Analysis

Tolerance = 5.0 PPM / DBE: min = -1.5, max = 100.0

Element prediction: Off

Number of isotope peaks used for i-FIT = 3

Monoisotopic Mass, Even Electron Ions

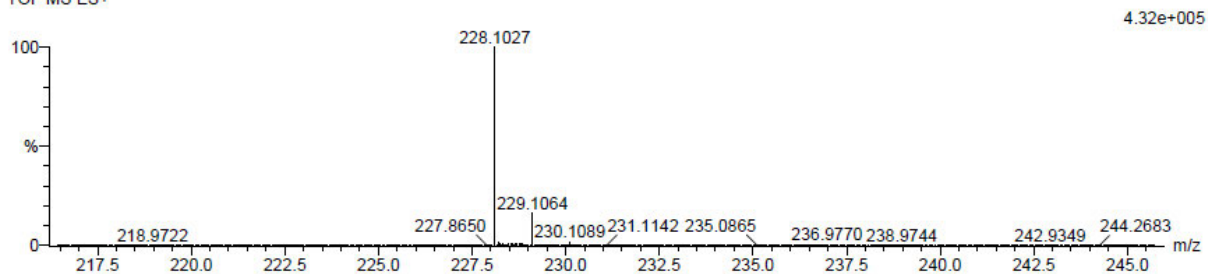
17 formula(e) evaluated with 1 results within limits (up to 20 closest results for each mass)

Elements Used:

C: 10-15 H: 10-15 N: 0-5 O: 0-5

1A - 4MESA 28 (0.911) Cm (1:61)

TOF MS ES+



1A - 4MESA lms 3 (0.034) Cm (1:60)

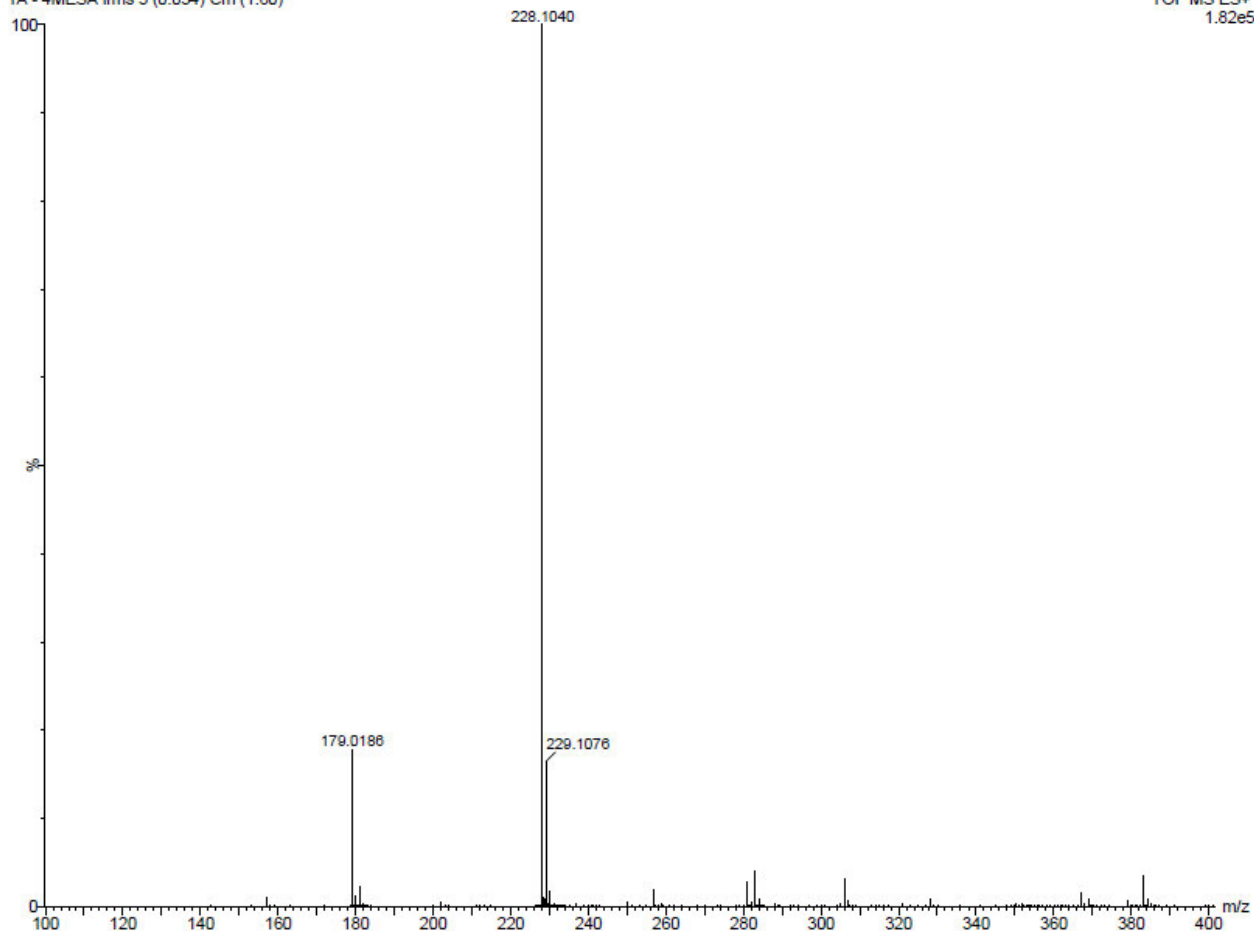


**Figure A21: High resolution ESI mass spectrum of MEA in methanol and DMSO.**

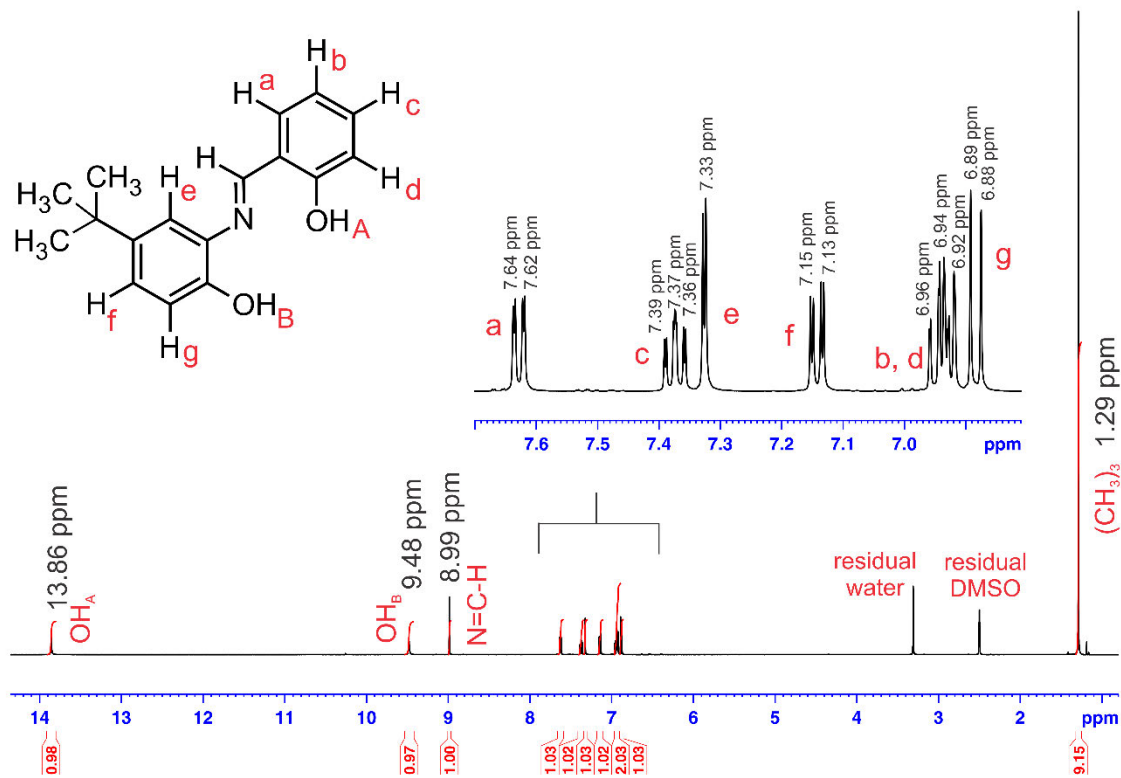


Figure A22: Fully assigned  $^1\text{H}$  NMR spectrum of TERTA in  $\text{DMSO-}d_6$ .

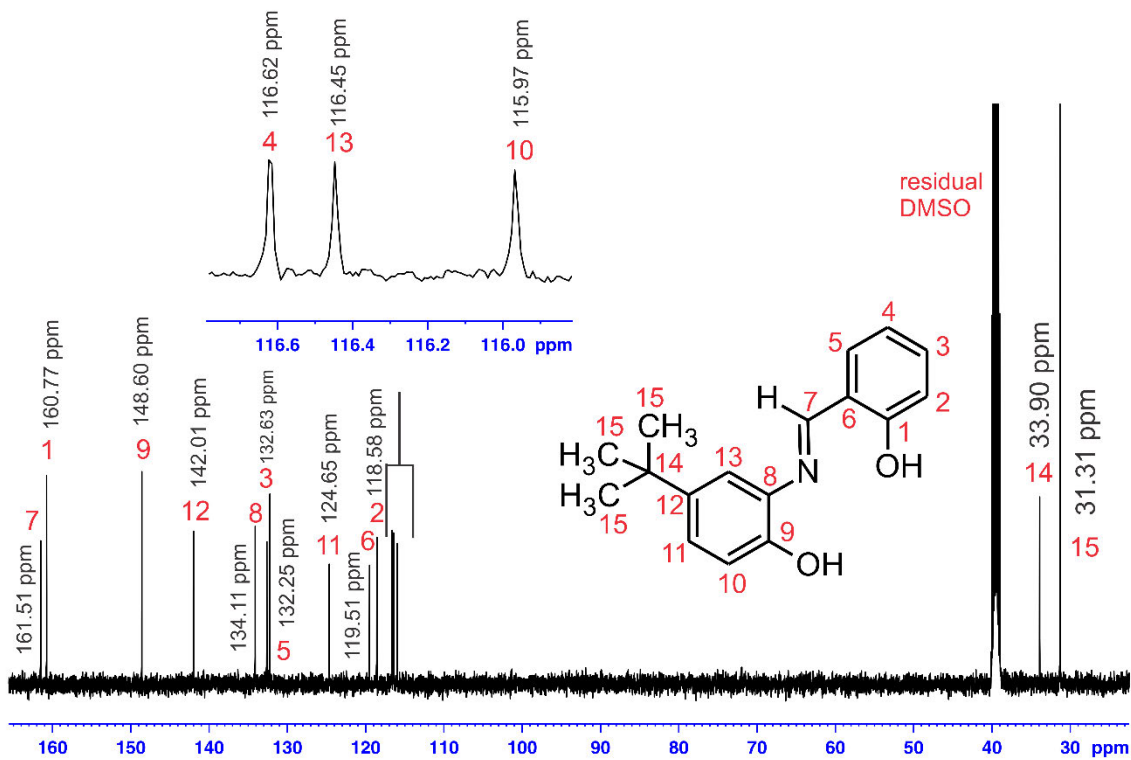
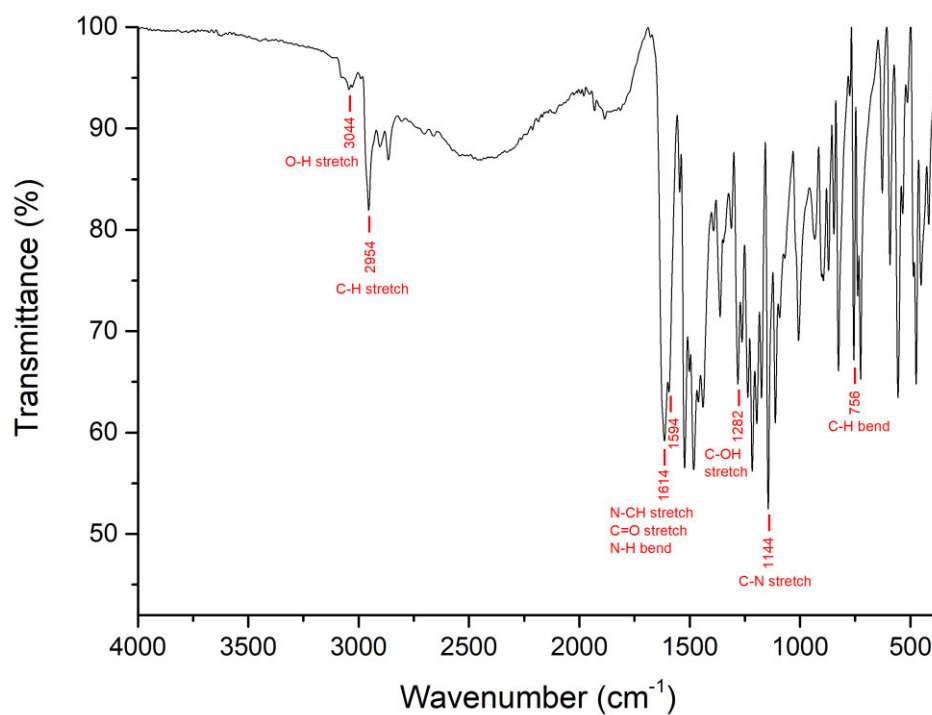
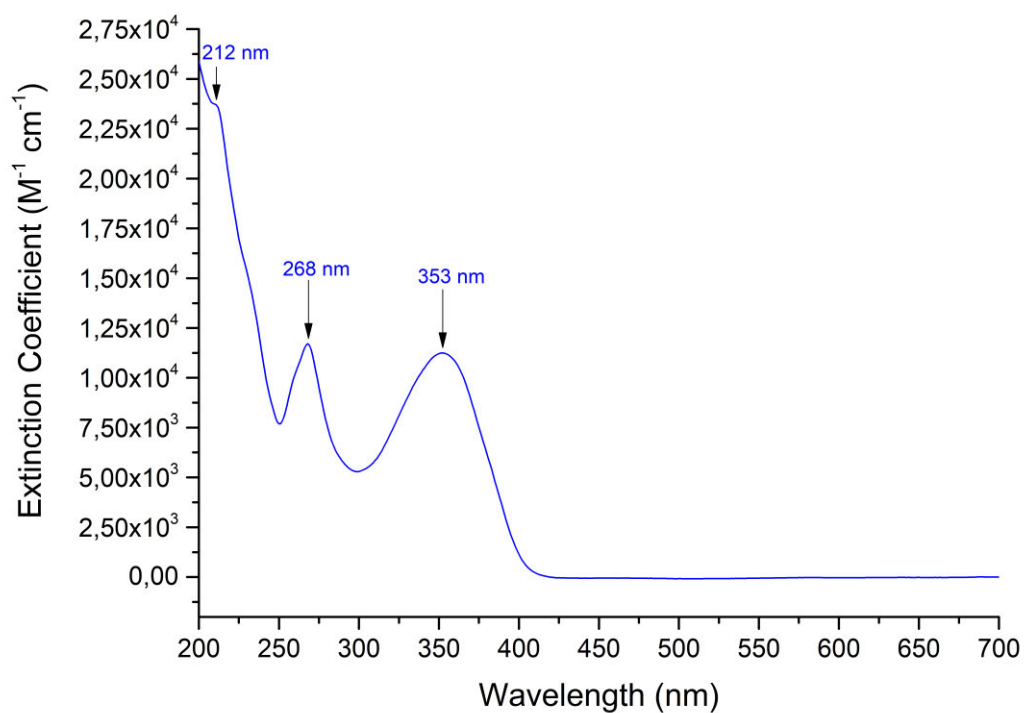


Figure A23: Fully assigned  $^{13}\text{C}$  NMR spectrum of TERTA in  $\text{DMSO-}d_6$ .



**Figure A24: IR spectrum of TERTA.**



**Figure A25: UV/visible spectrum of TERTA.  $[\text{TERTA}] = 4.06 \times 10^{-5} \text{ M}$ .**

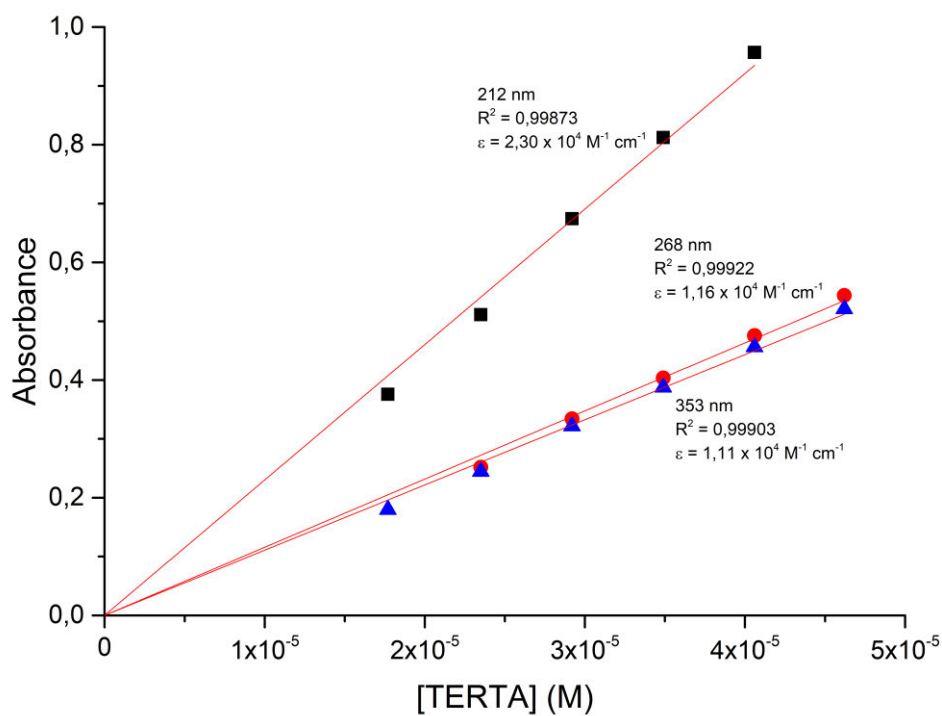


**Figure A26: Beer's Law Correlation of TERTA.**

### Single Mass Analysis

Tolerance = 5.0 PPM / DBE: min = -1.5, max = 100.0

Element prediction: Off

Number of isotope peaks used for i-FIT = 3

Monoisotopic Mass, Even Electron Ions

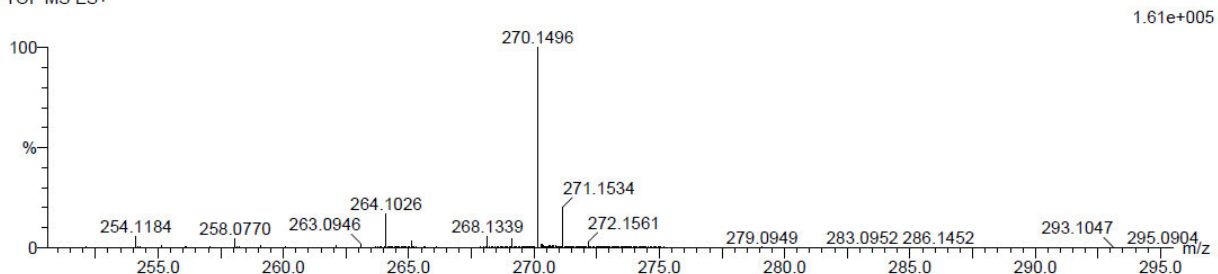
19 formula(e) evaluated with 1 results within limits (up to 20 closest results for each mass)

Elements Used:

C: 15-20 H: 15-20 N: 0-5 O: 0-5

4A - TERTSA 2 (0.009) Cm (1:57)

TOF MS ES+



4A - TERTSA Ims 2 (0.009) Cm (1:58)

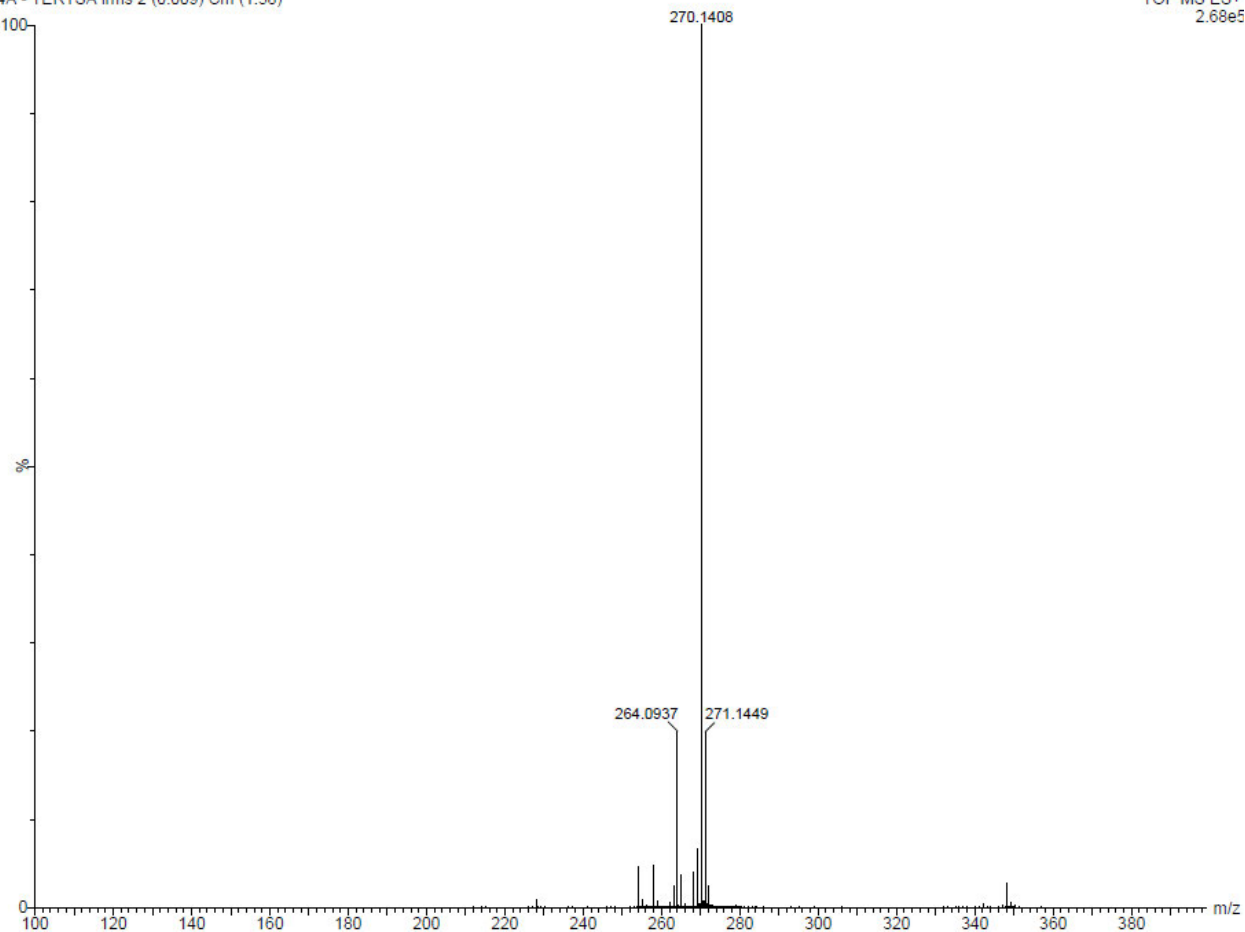


**Figure A27: High resolution ESI mass spectrum of TERTA in methanol.**

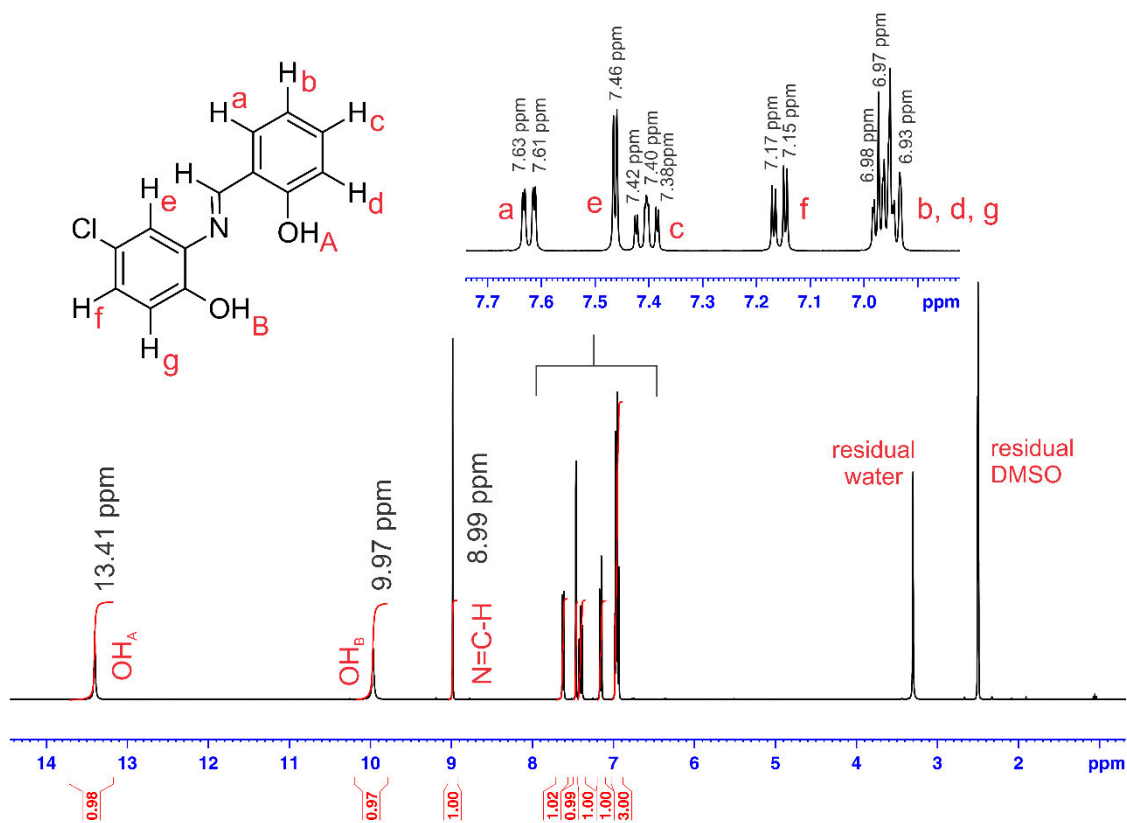


Figure A28: Fully assigned  $^1\text{H}$  NMR spectrum of CLA in  $\text{DMSO-}d_6$ .

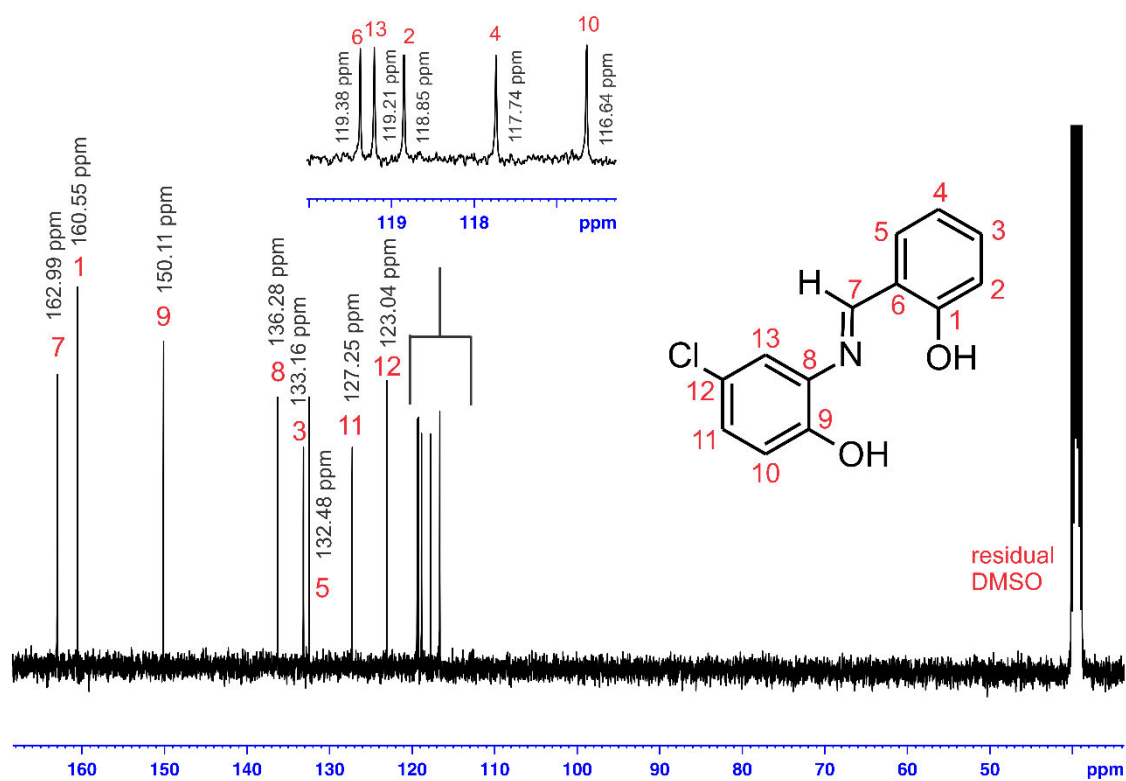
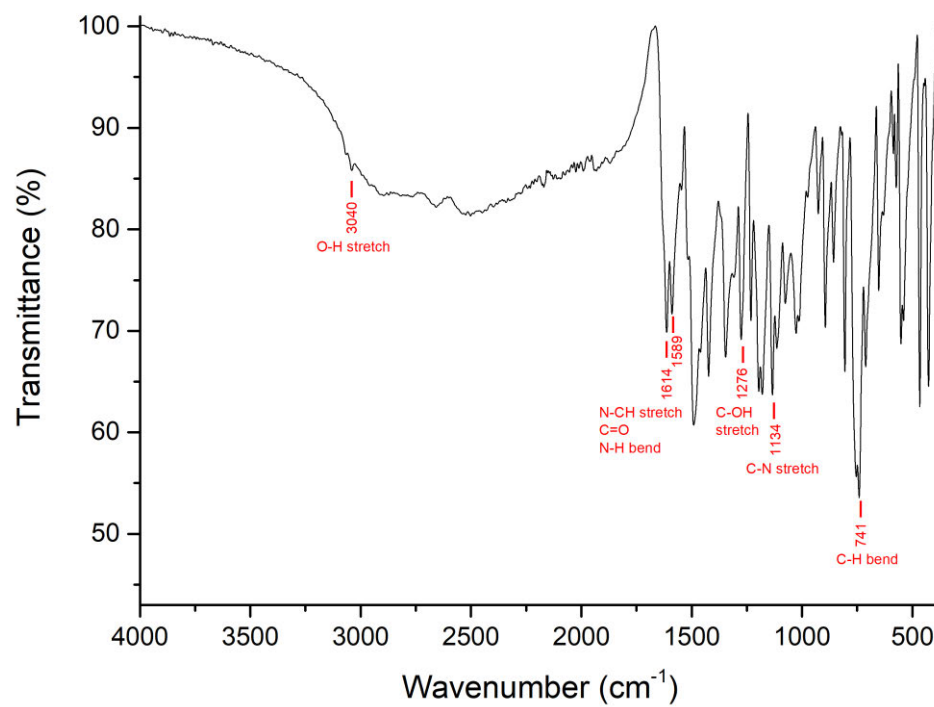
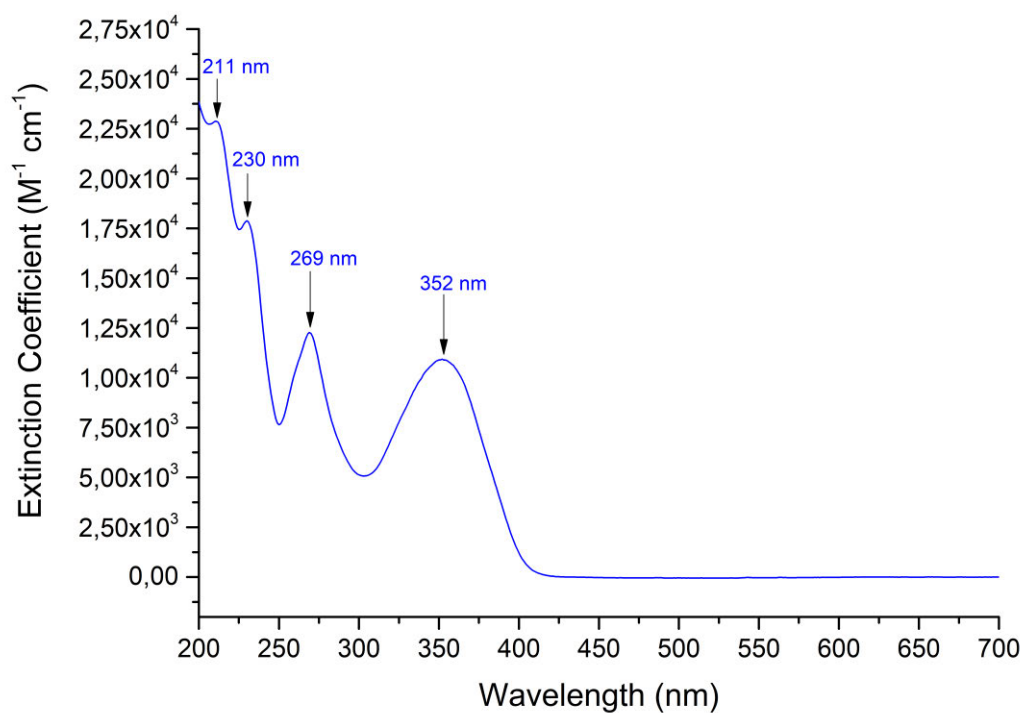


Figure A29: Fully assigned  $^{13}\text{C}$  NMR spectrum of CLA in  $\text{DMSO-}d_6$ .



**Figure A30: IR spectrum of CLA.**



**Figure A31: UV/visible spectrum of CLA. [CLA] =  $3.80 \times 10^{-5}$  M.**

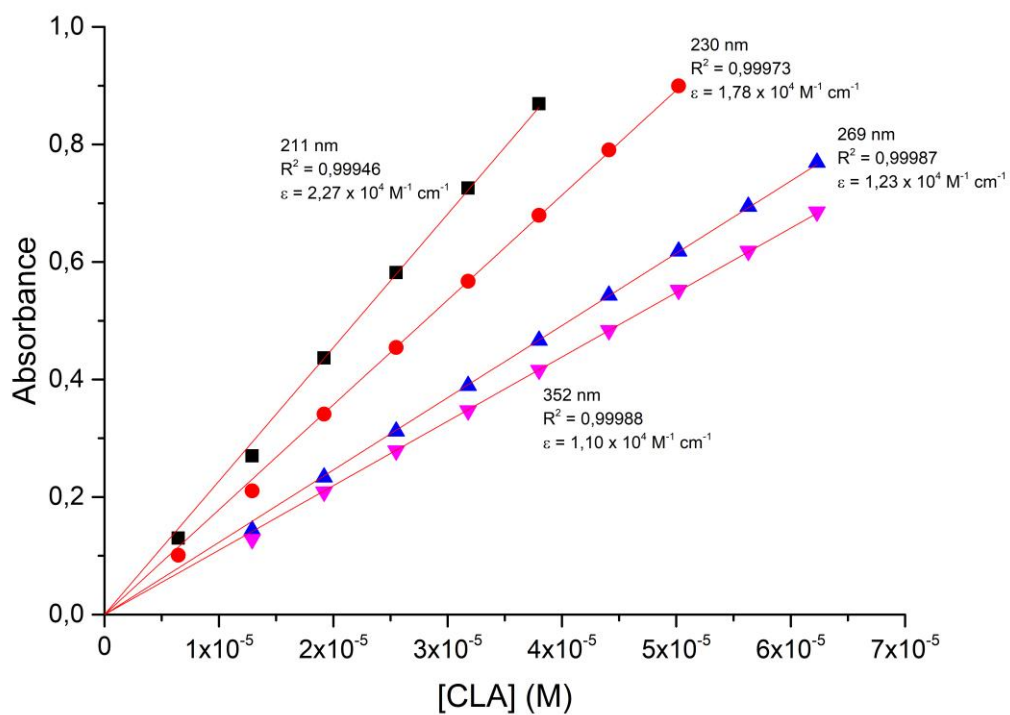


**Figure A32: Beer's Law Correlation of CLA.**

### Single Mass Analysis

Tolerance = 5.0 PPM / DBE: min = -1.5, max = 100.0

Element prediction: Off

Number of isotope peaks used for i-FIT = 2

Monoisotopic Mass, Even Electron Ions

37 formula(e) evaluated with 1 results within limits (up to 20 best isotopic matches for each mass)

Elements Used:

C: 10-15 H: 10-15 N: 0-5 O: 0-5 Cl: 0-1

CIA (chloroform) 24 (0.776) Cm (1:61)

TOF MS ES+

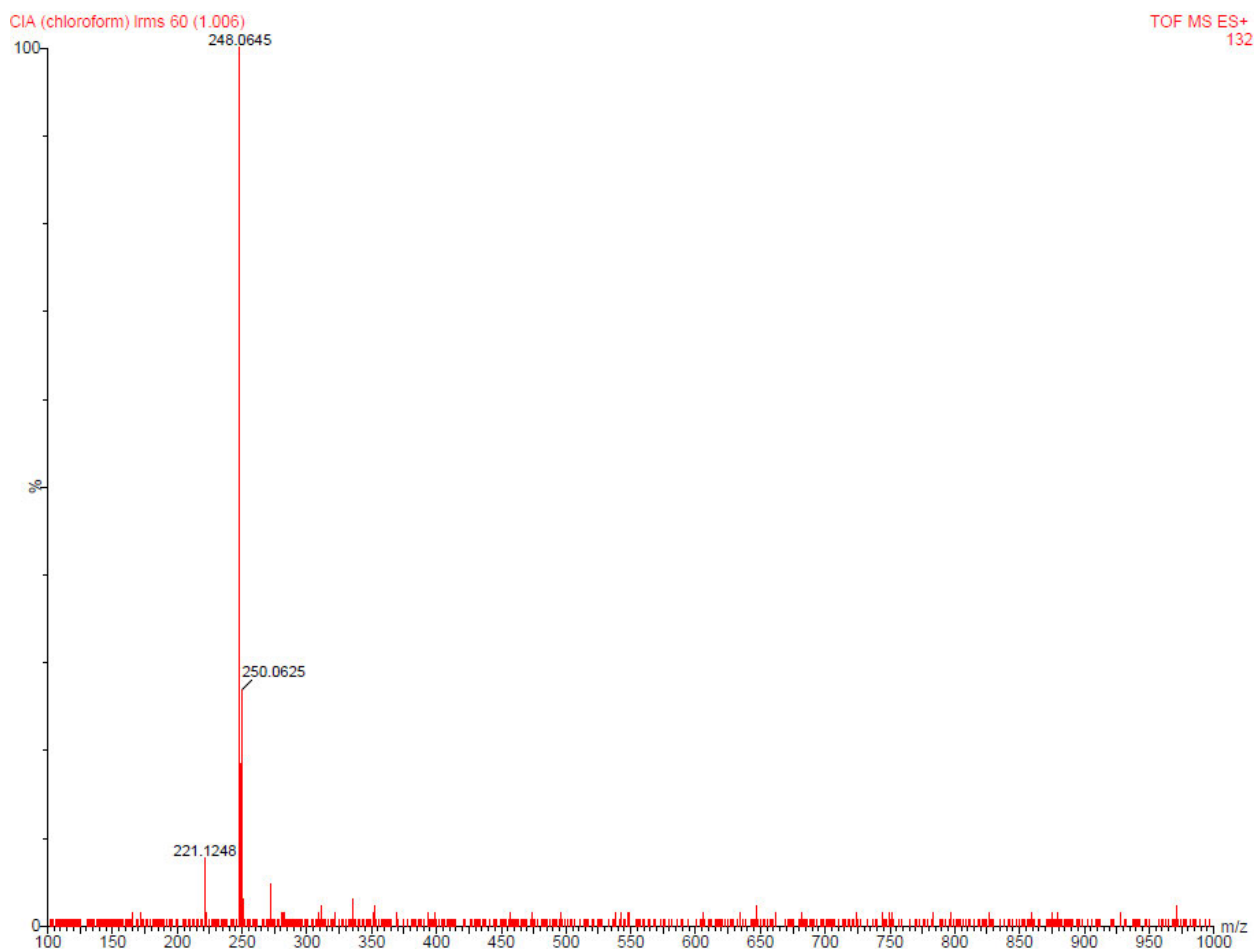
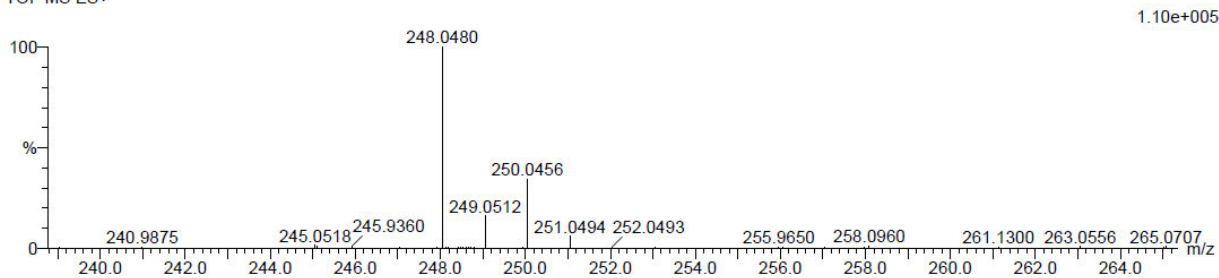


**Figure A33: High resolution ESI mass spectrum of CLA in chloroform.**

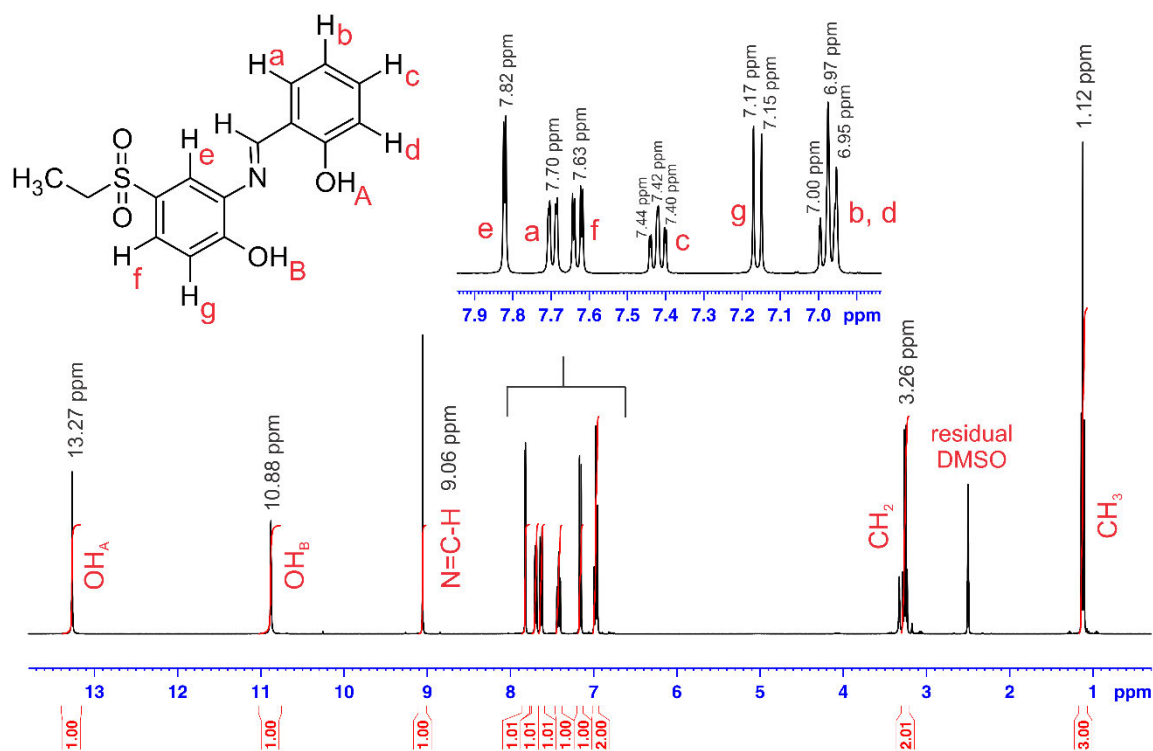


Figure A34: Fully assigned  $^1\text{H}$  NMR spectrum of SOA in  $\text{DMSO-}d_6$ .

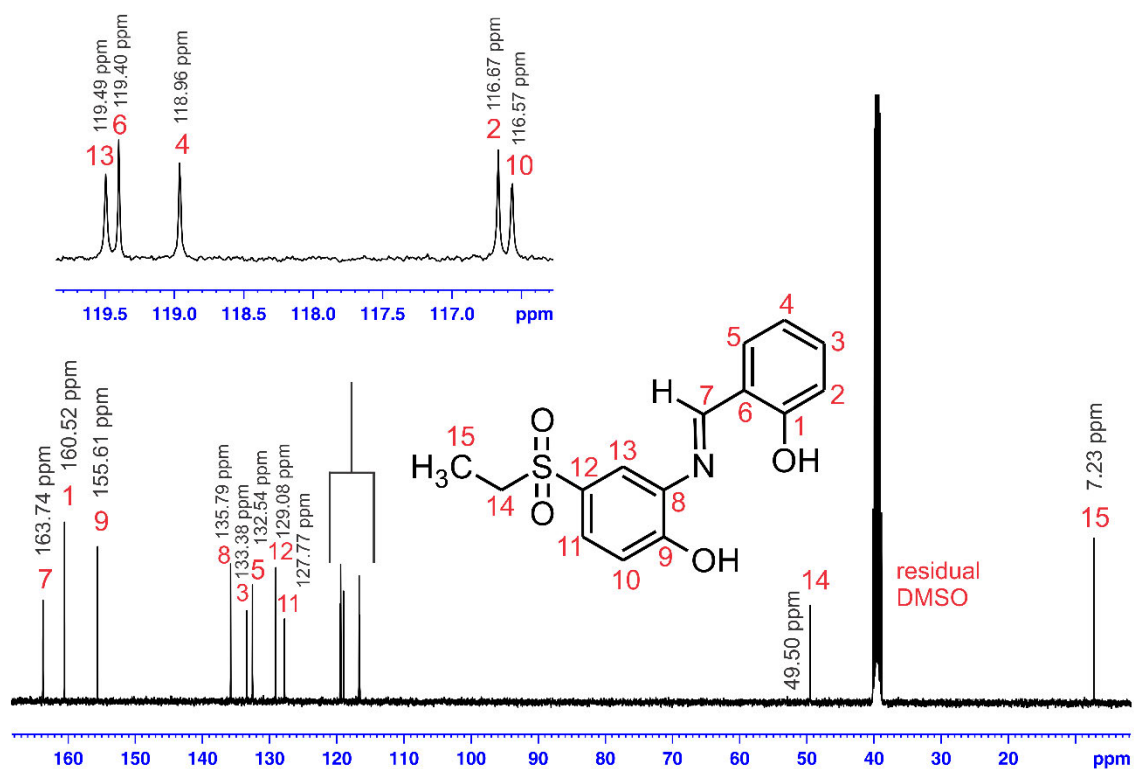
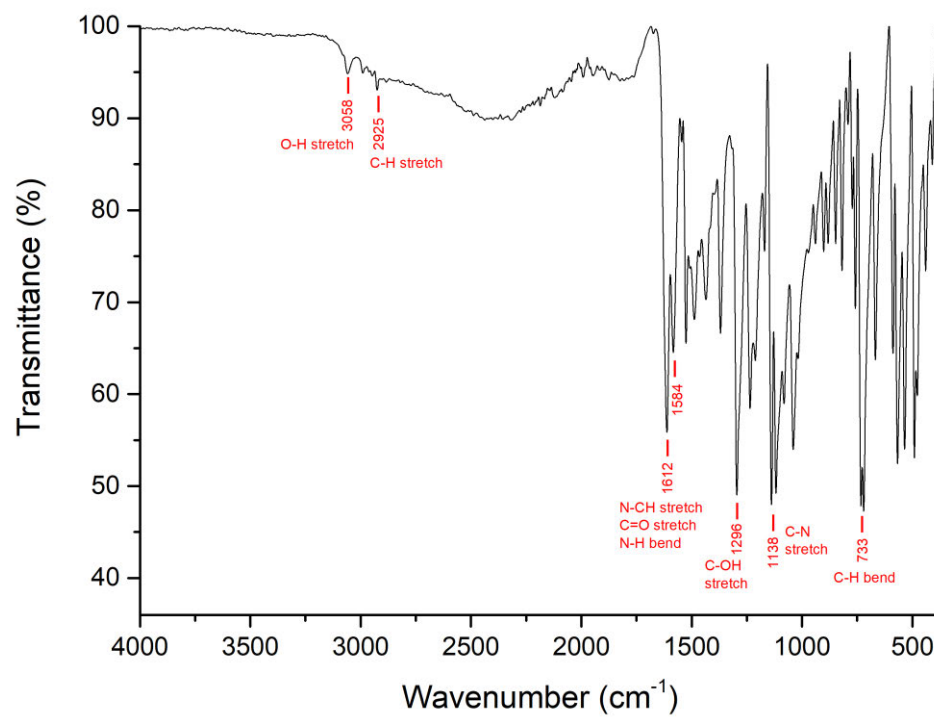
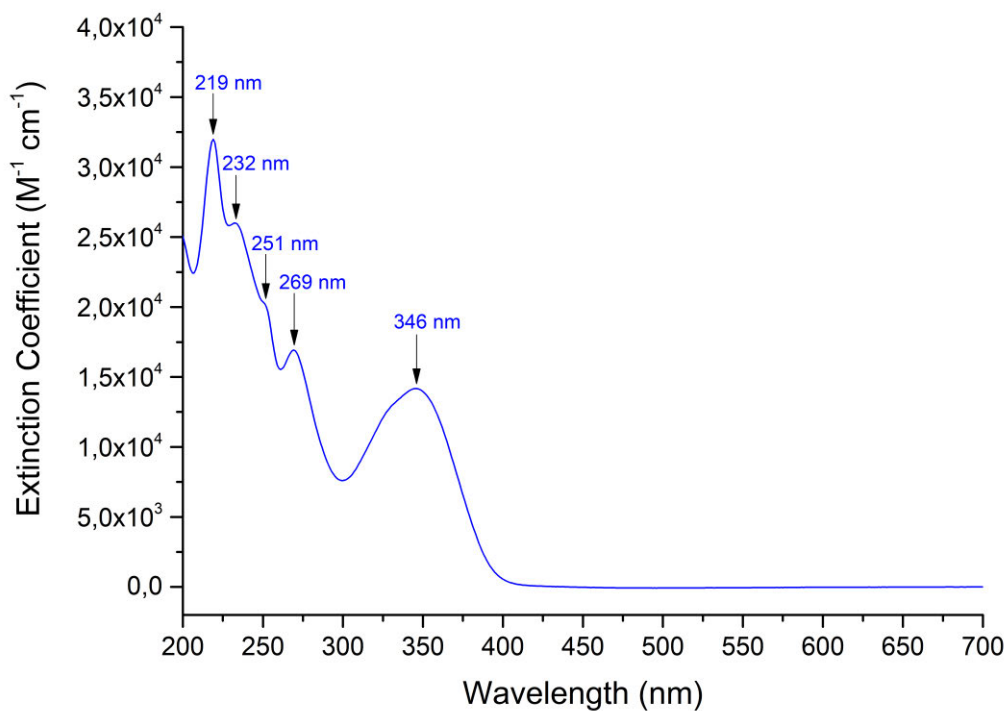


Figure A35: Fully assigned  $^{13}\text{C}$  NMR spectrum of SOA in  $\text{DMSO-}d_6$ .



**Figure A36: IR spectrum of SOA.**



**Figure A37: UV/visible spectrum of SOA.  $[\text{SOA}] = 3.02 \times 10^{-5} \text{ M}$ .**

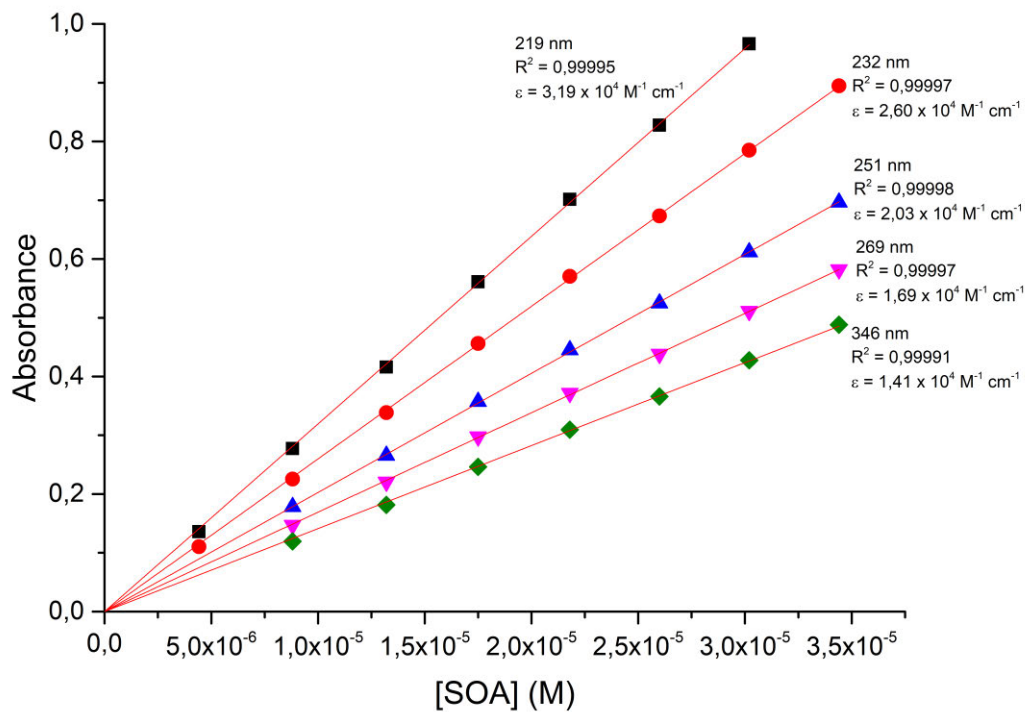


**Figure A38: Beer's Law Correlation of SOA.**

### Single Mass Analysis

Tolerance = 5.0 PPM / DBE: min = -1.5, max = 100.0

Element prediction: Off

Number of isotope peaks used for i-FIT = 2

Monoisotopic Mass, Even Electron Ions

29 formula(e) evaluated with 1 results within limits (up to 20 best isotopic matches for each mass)

Elements Used:

C: 15-20 H: 10-15 N: 0-5 O: 1-5 S: 0-1

SOA 22 (0.708) Cm (1:61)

TOF MS ES-

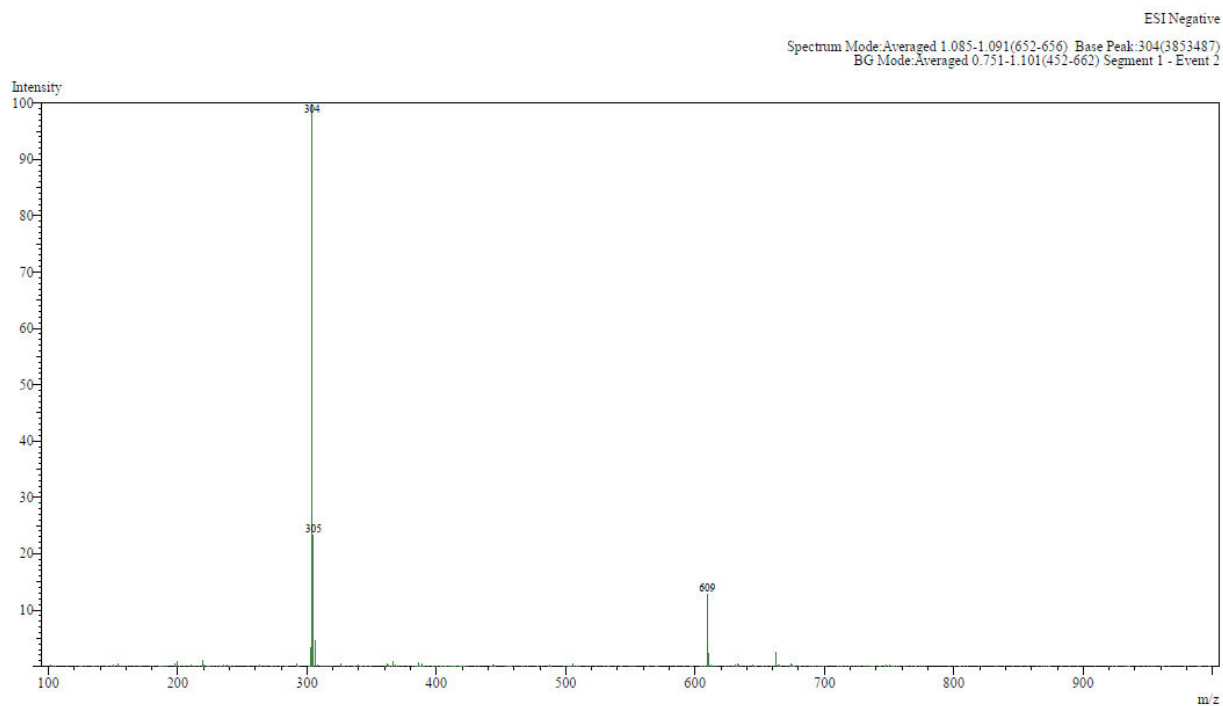
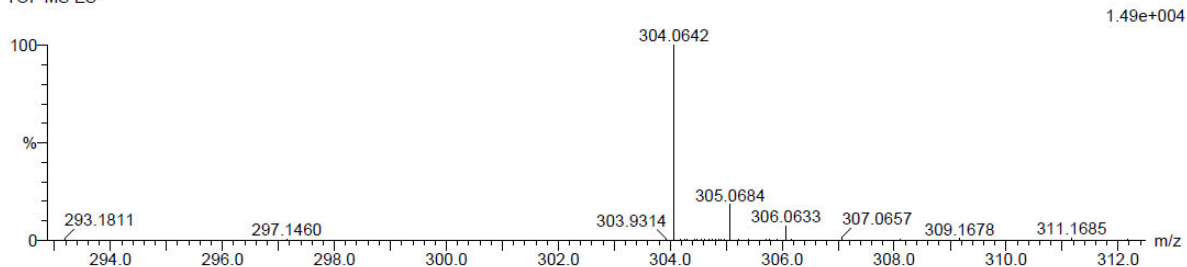


**Figure A39: High resolution ESI mass spectrum of SOA in acetonitrile.**

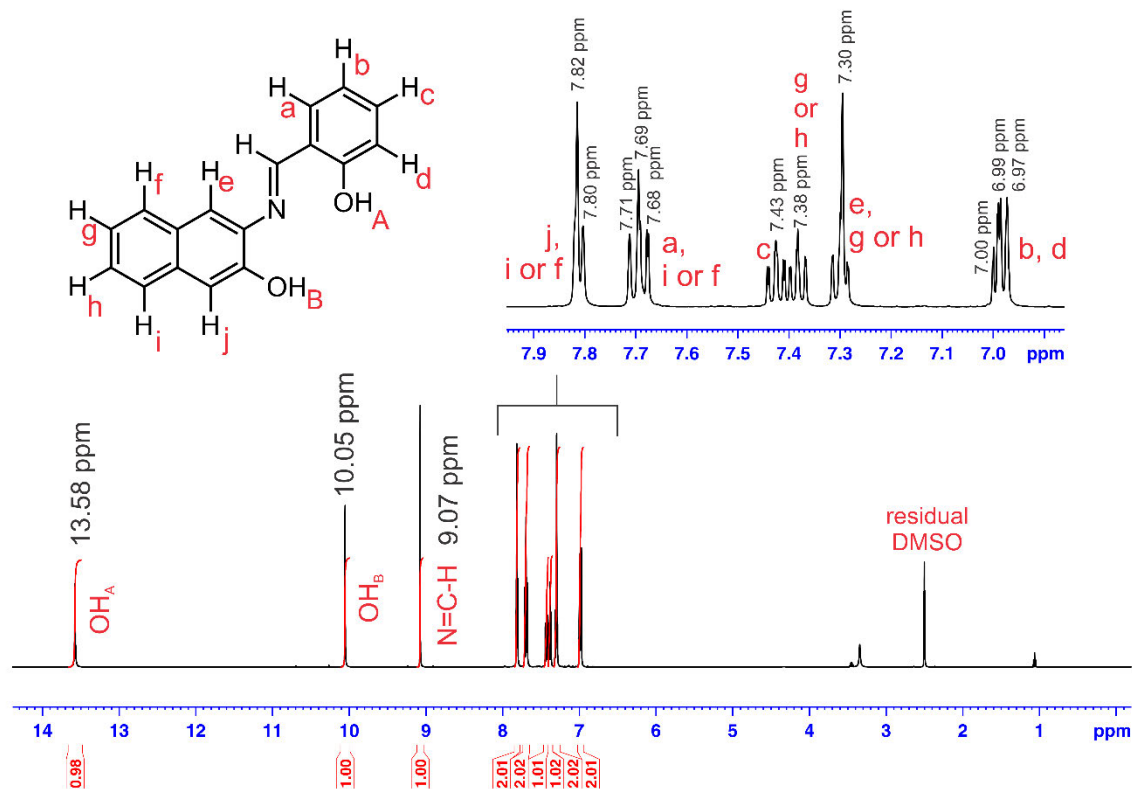


Figure A40: Assigned  $^1\text{H}$  NMR spectrum of NAA in  $\text{DMSO-}d_6$ .

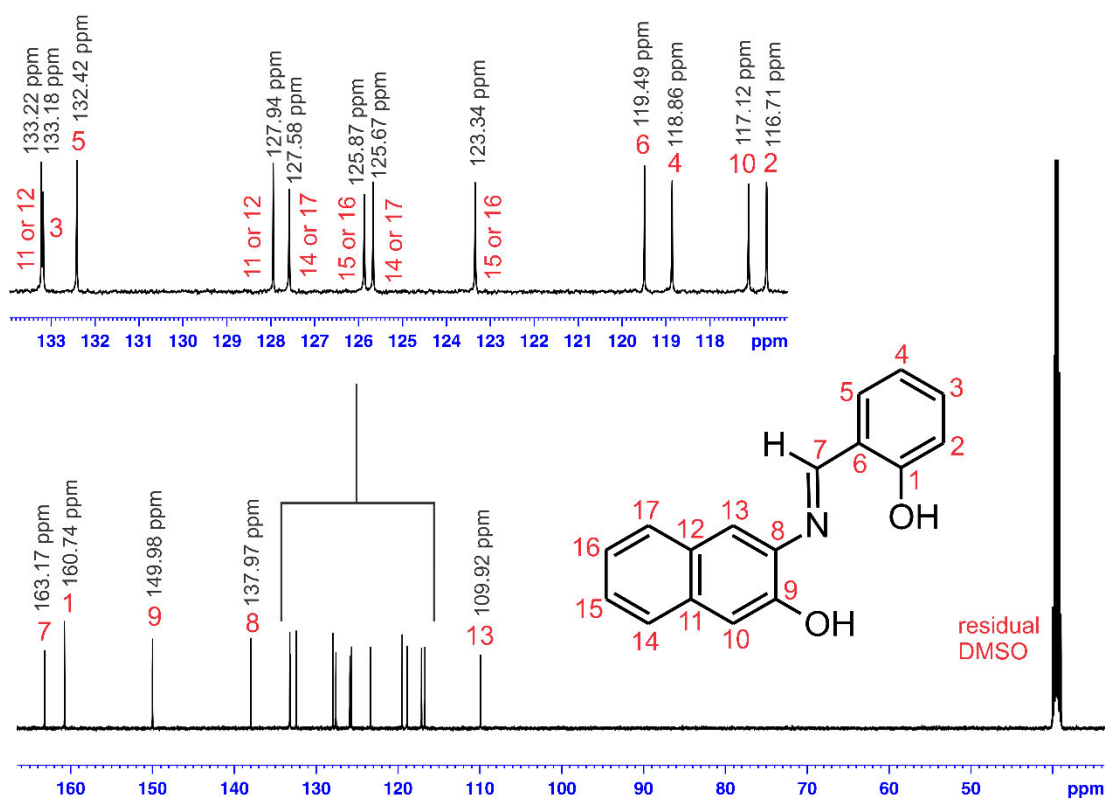
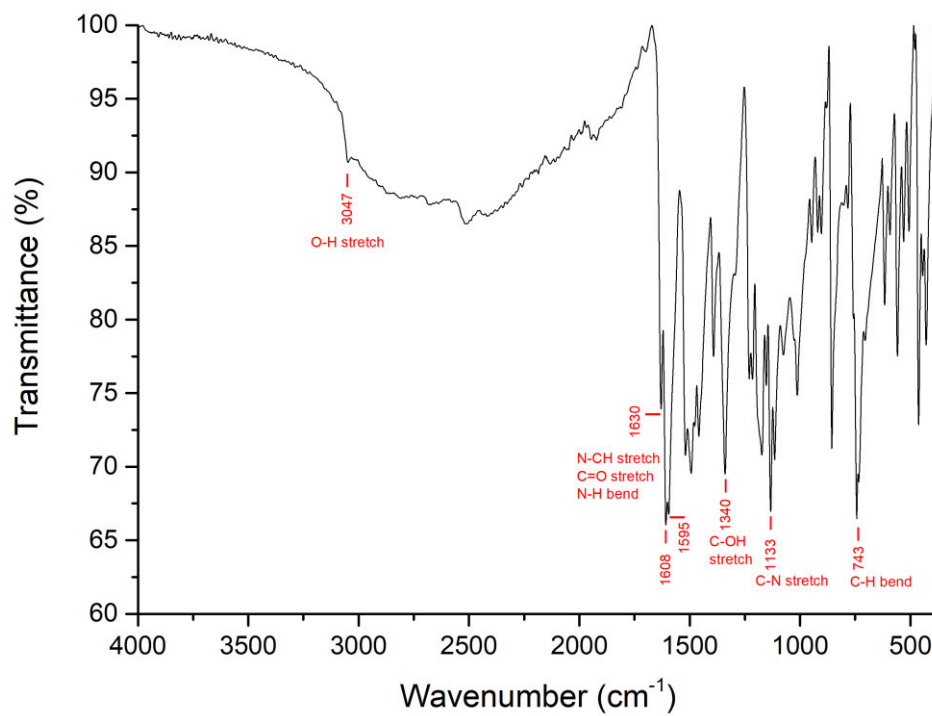
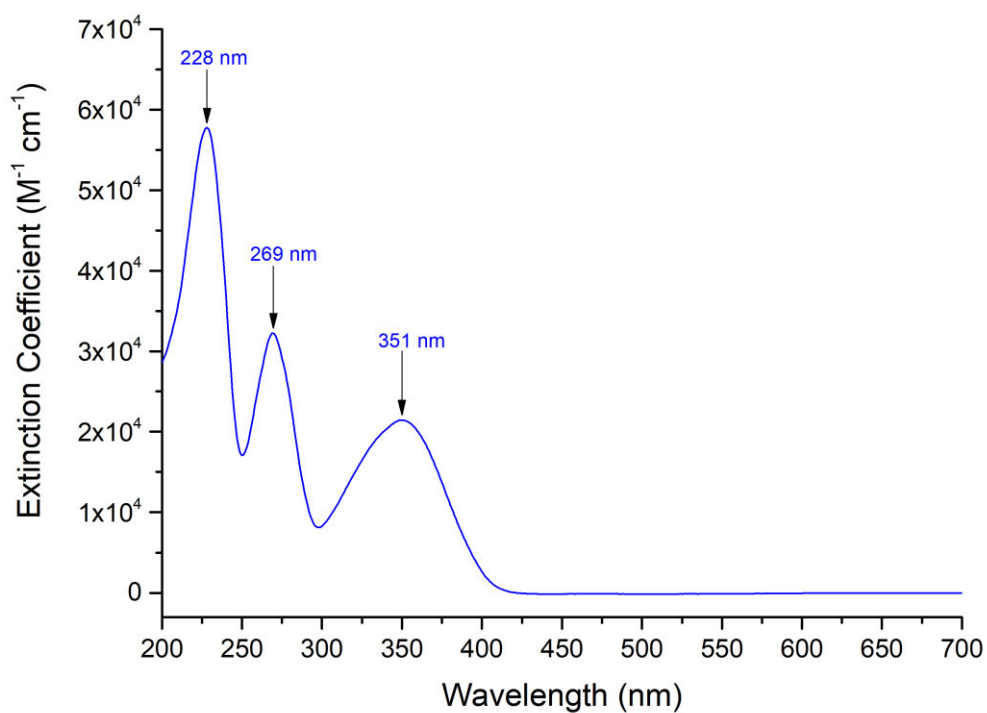


Figure A41: Assigned  $^{13}\text{C}$  NMR spectrum of NAA in  $\text{DMSO-}d_6$ .



**Figure A42: IR spectrum of NAA.**



**Figure A43:** UV/visible spectrum of NAA.  $[\text{NAA}] = 1.61 \times 10^{-5} \text{ M}$ .

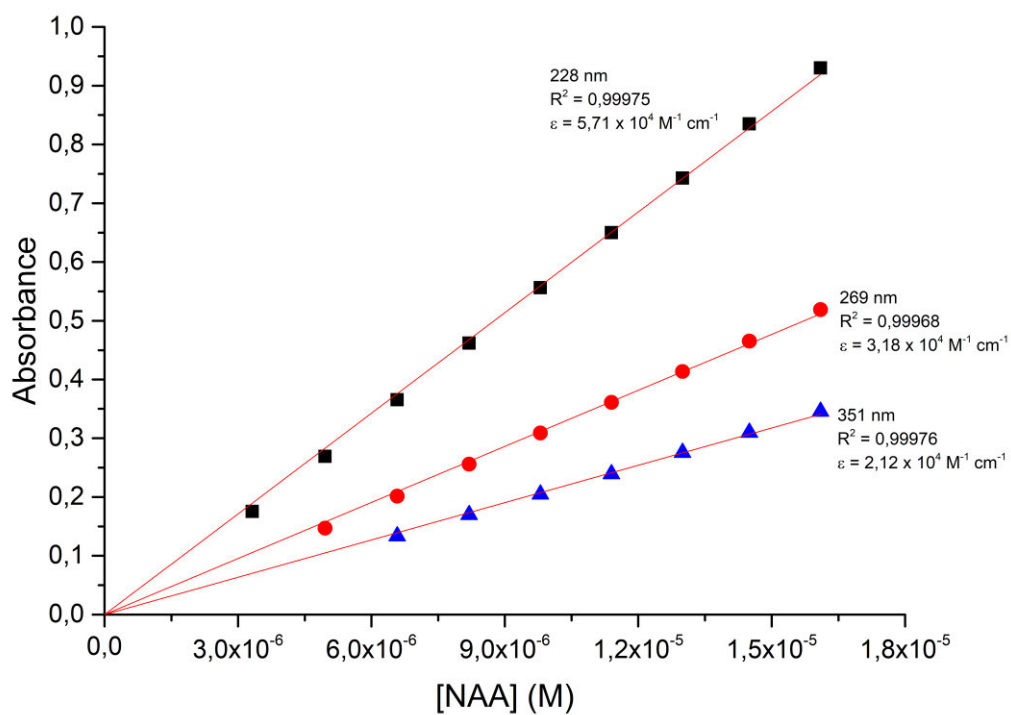


**Figure A44:** Beer's Law Correlation of NAA.

### Single Mass Analysis

Tolerance = 5.0 PPM / DBE: min = -1.5, max = 100.0

Element prediction: Off

Number of isotope peaks used for i-FIT = 3

Monoisotopic Mass, Even Electron Ions

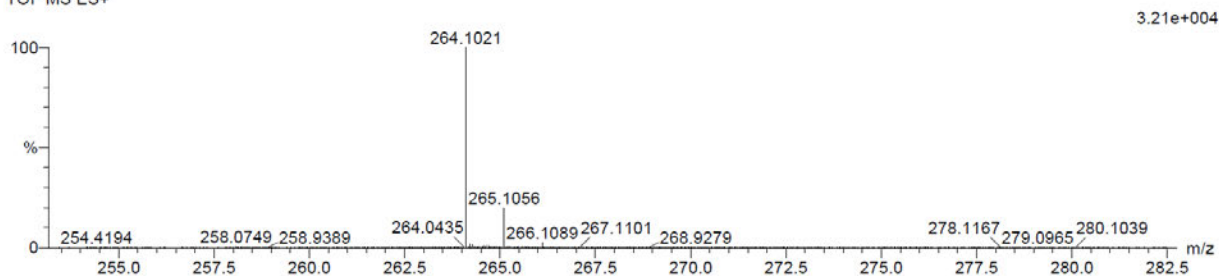
21 formula(e) evaluated with 1 results within limits (up to 20 closest results for each mass)

Elements Used:

C: 15-20 H: 10-15 N: 0-5 O: 0-5

2A - NAA 9 (0.069) Cm (1:58)

TOF MS ES+



2A - NAA Ims 32 (0.268) Cm (1:59)

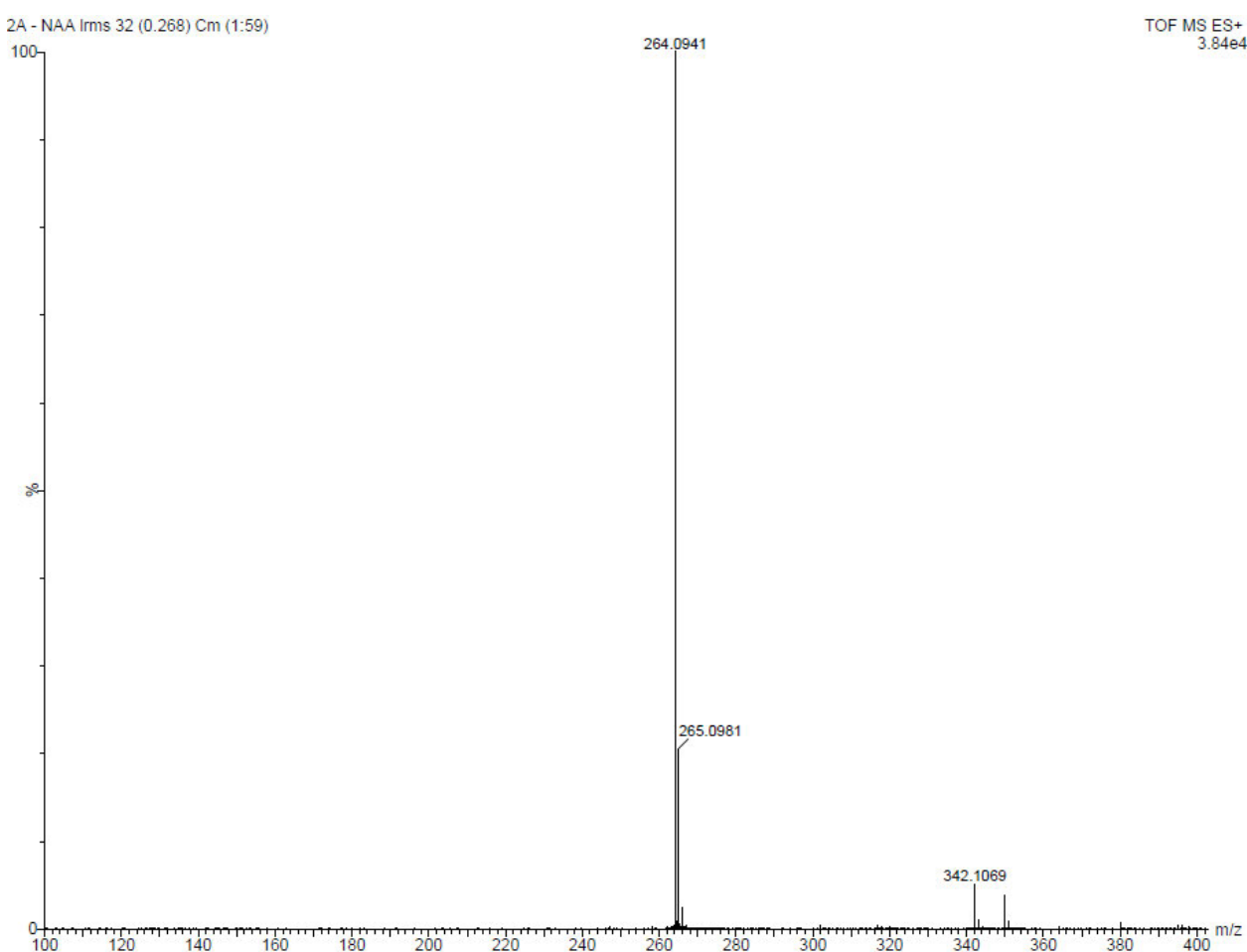


**Figure A45: High resolution ESI mass spectrum of NAA in methanol.**

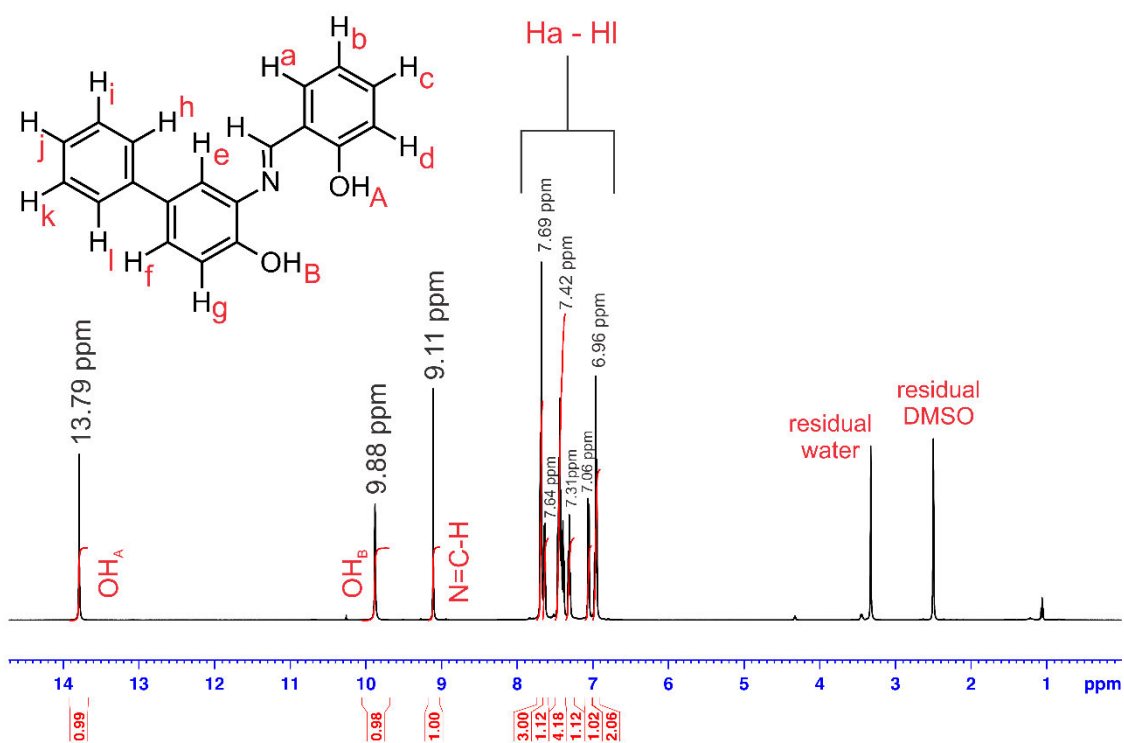


Figure A46: Assigned  $^1\text{H}$  NMR spectrum of PHPHA in  $\text{DMSO-}d_6$ .

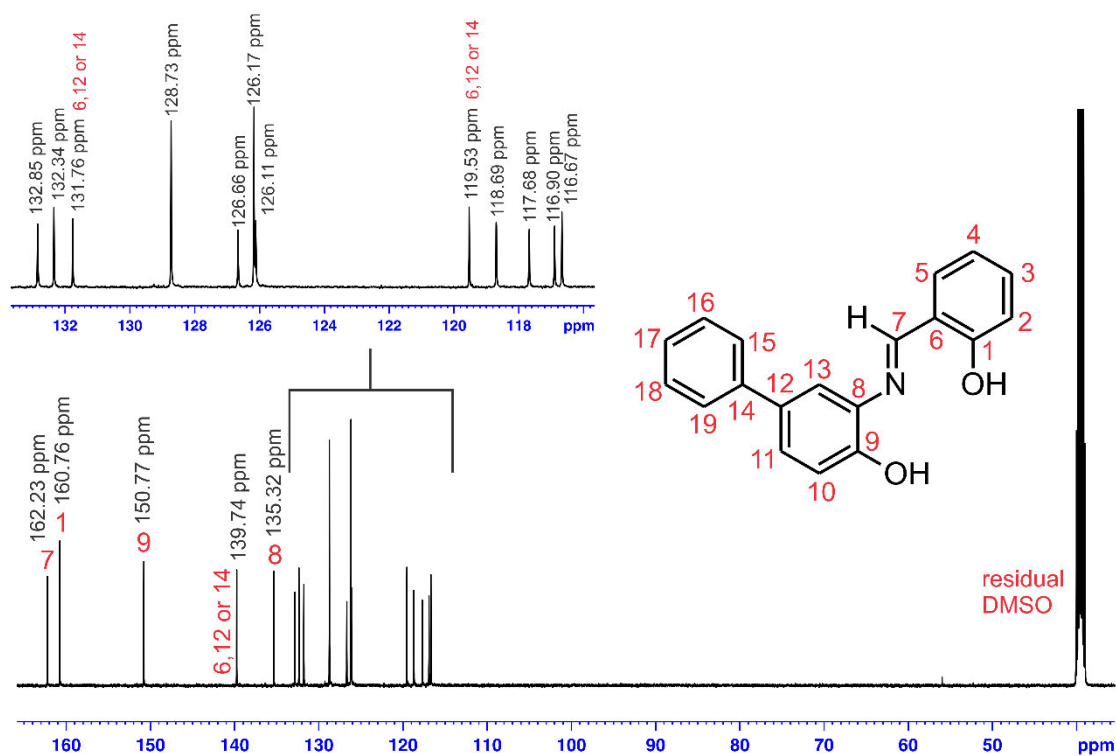
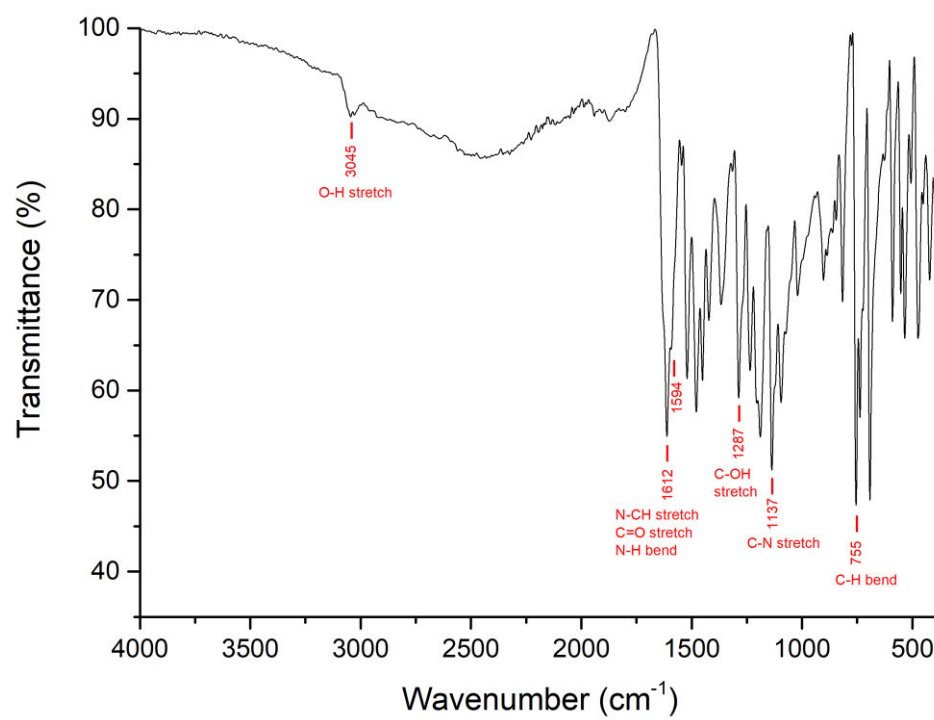
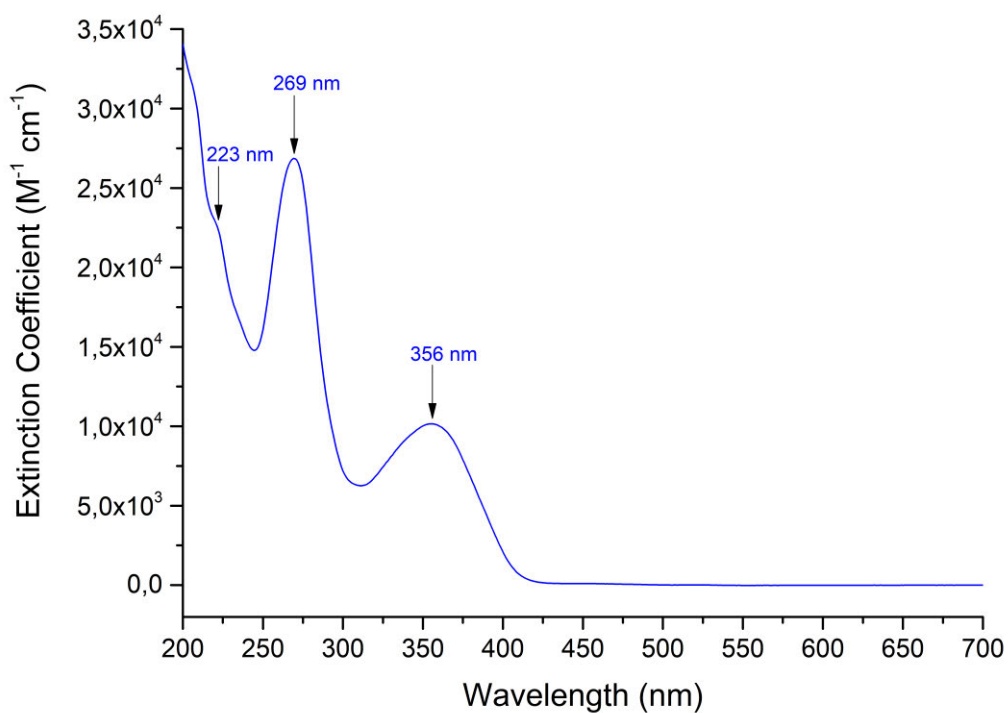


Figure A47: Assigned  $^{13}\text{C}$  NMR spectrum of PHPHA in  $\text{DMSO-}d_6$ .



**Figure A48: IR spectrum of PHPHA.**



**Figure A49: UV/visible spectrum of PHPHA.  $[\text{PHPHA}] = 3.40 \times 10^{-5} \text{ M}$ .**

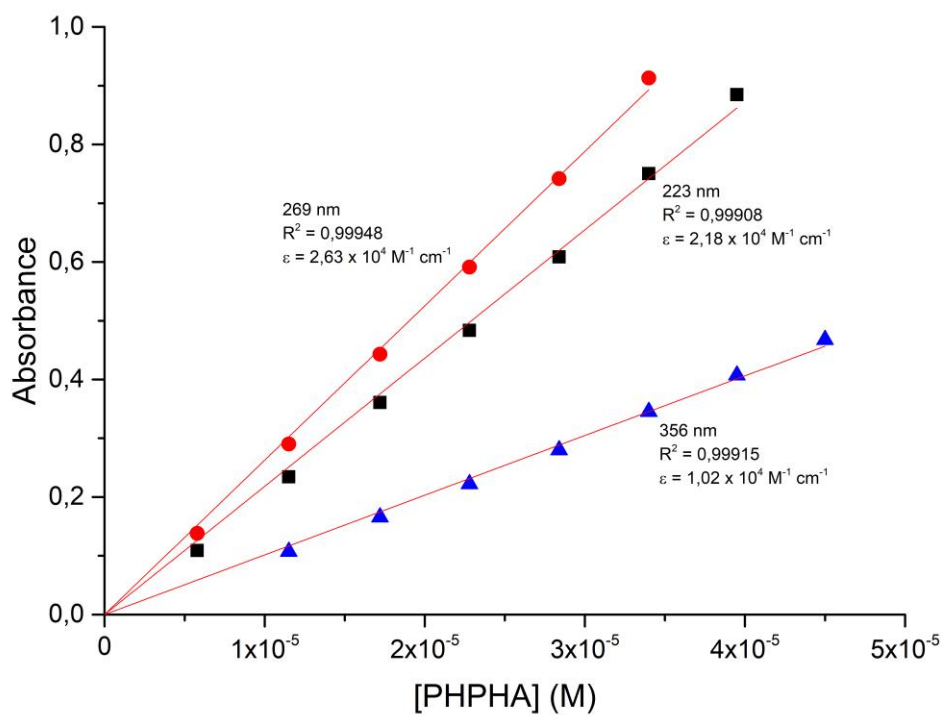


**Figure A50: Beer's Law Correlation of PHPHA.**

### Single Mass Analysis

Tolerance = 5.0 PPM / DBE: min = -1.5, max = 100.0

Element prediction: Off

Number of isotope peaks used for i-FIT = 2

Monoisotopic Mass, Even Electron Ions

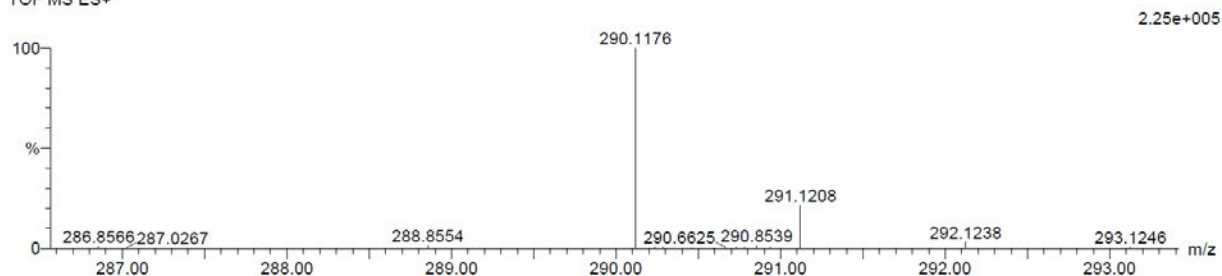
19 formula(e) evaluated with 1 results within limits (up to 20 best isotopic matches for each mass)

Elements Used:

C: 15-20 H: 15-20 N: 0-5 O: 0-5

PHPHA 61 (2.023) Cm (1:61)

TOF MS ES+



PHPHA Ims 14 (0.222) Cm (1:60)

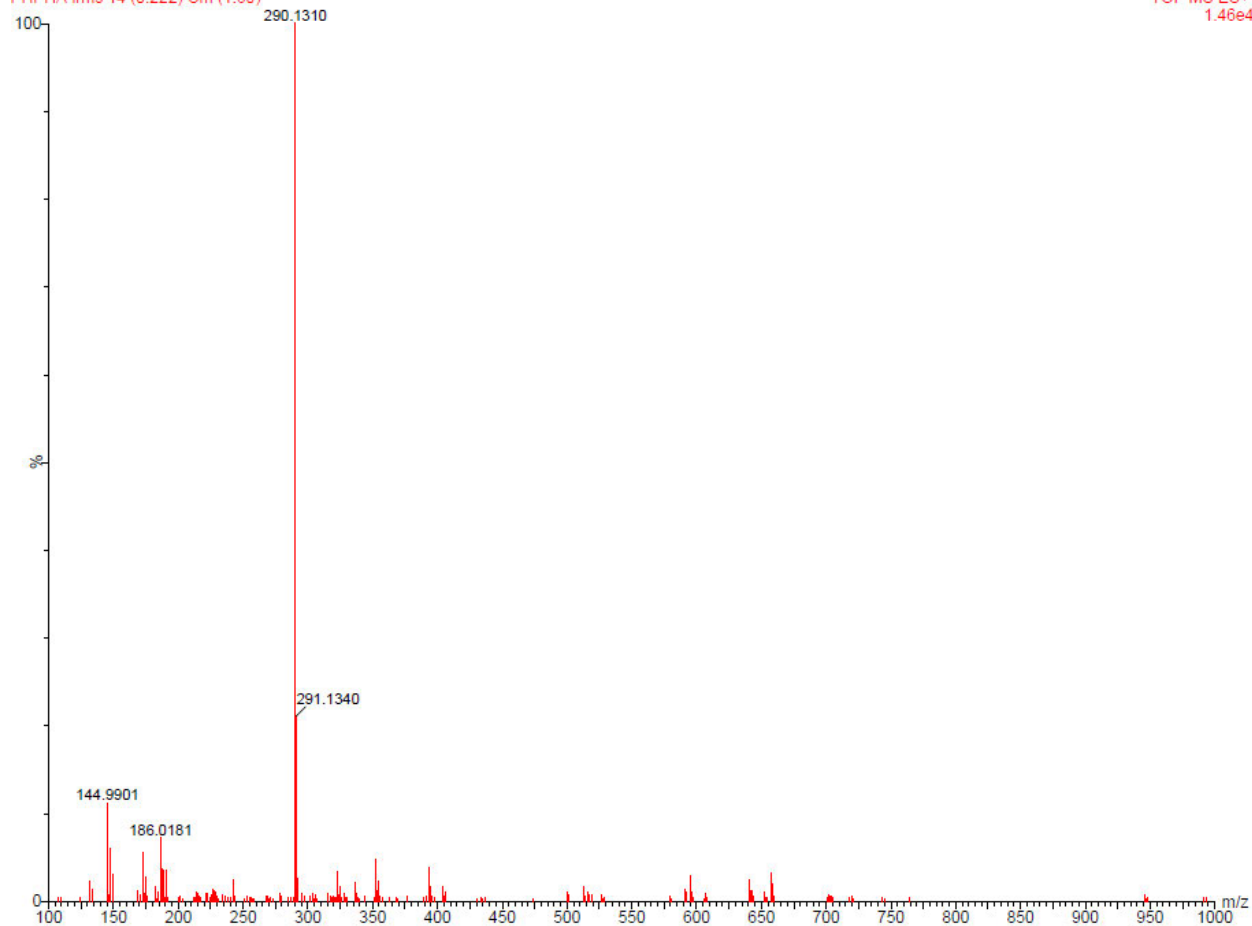


**Figure A51: High resolution ESI mass spectrum of PHPHA in chloroform.**

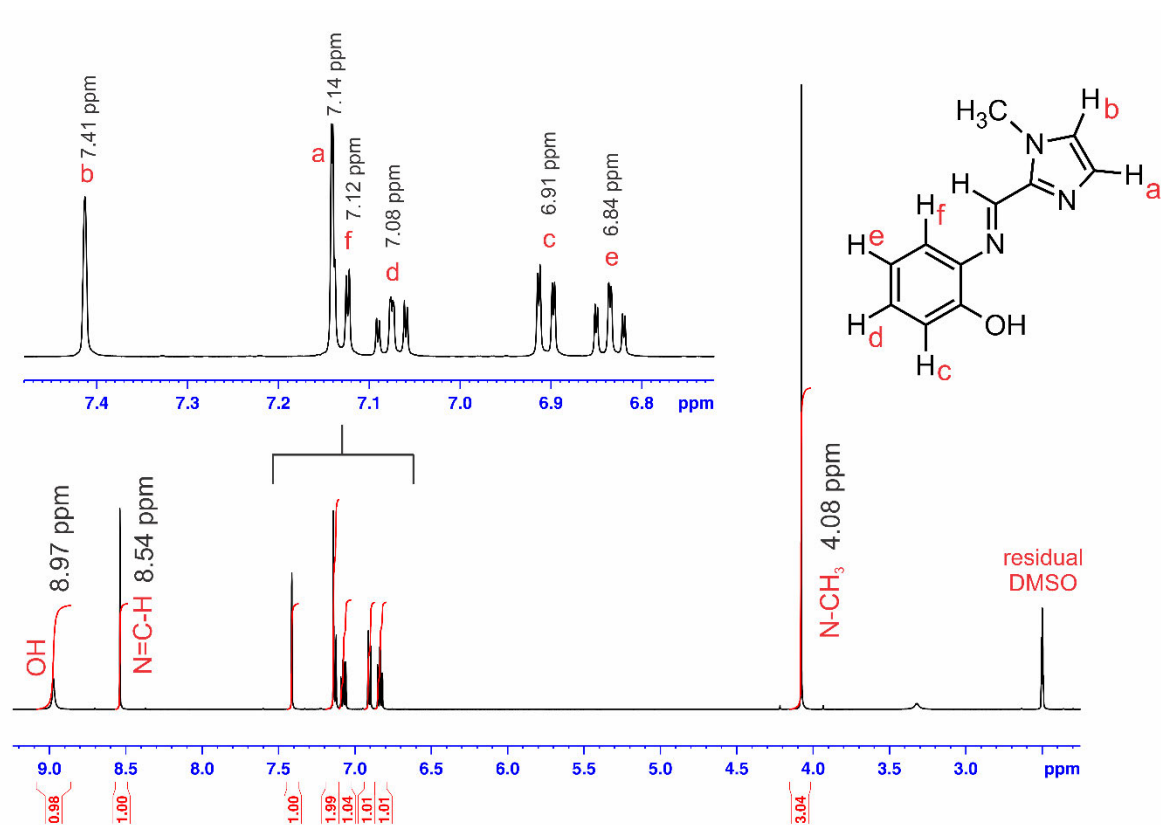


Figure A52: Fully assigned  $^1\text{H}$  NMR spectrum of PHCA in  $\text{DMSO-}d_6$ .

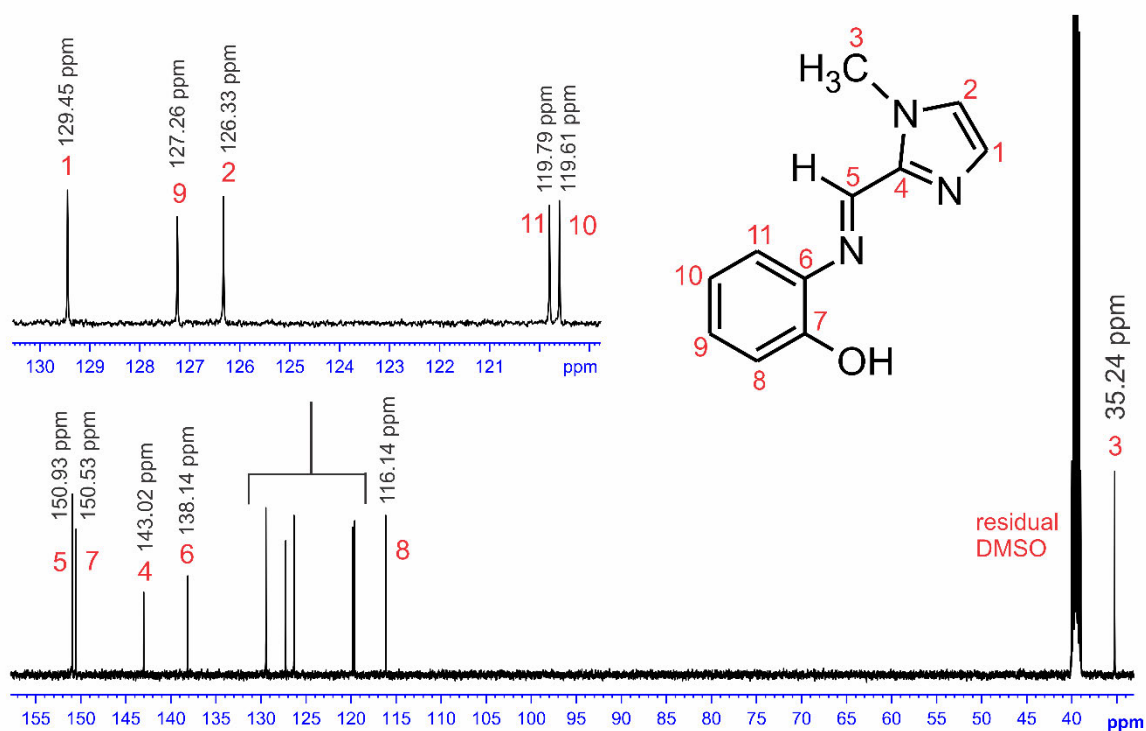
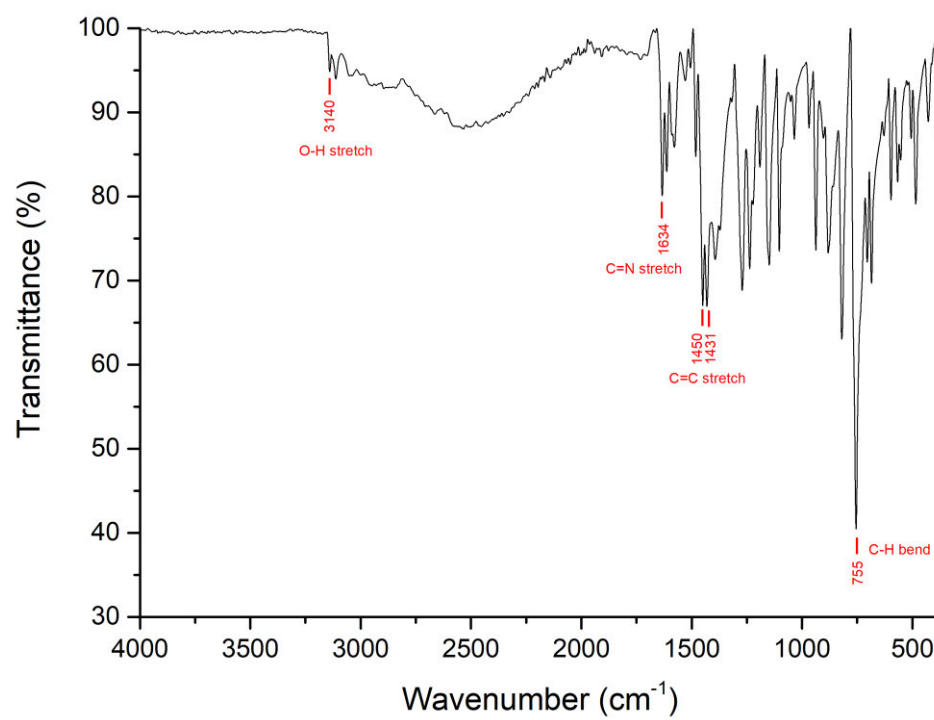
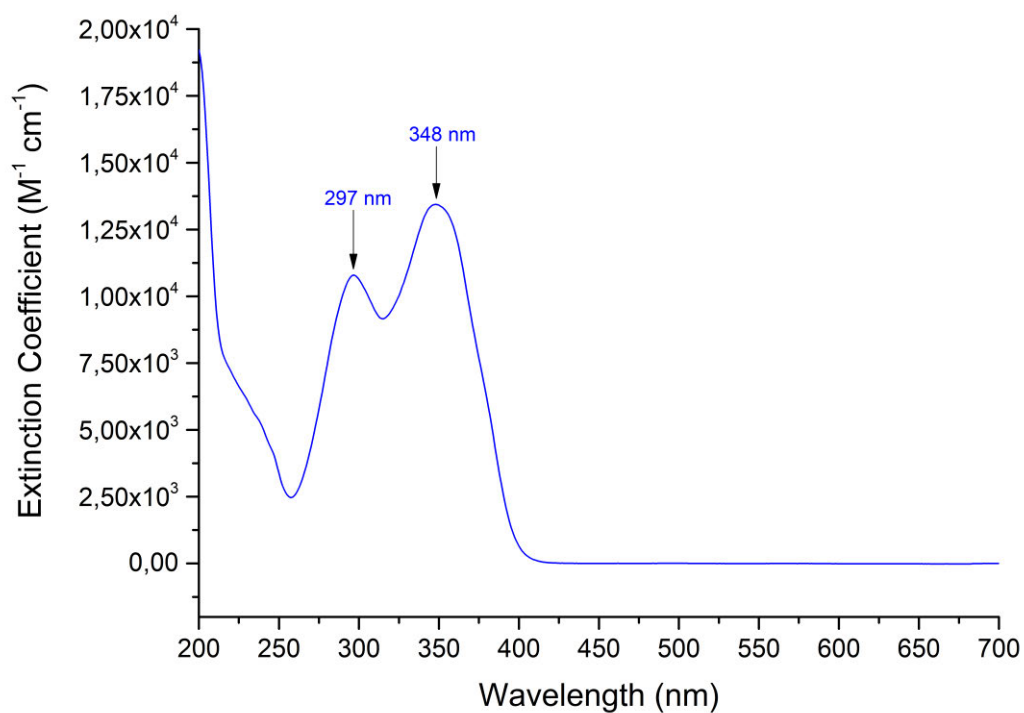


Figure A53: Fully assigned  $^{13}\text{C}$  NMR spectrum of PHCA in  $\text{DMSO-}d_6$ .



**Figure A54: IR spectrum of PHCA.**



**Figure A55: UV/visible spectrum of PHCA. [PHCA] =  $6.33 \times 10^{-5} \text{ M}$ .**

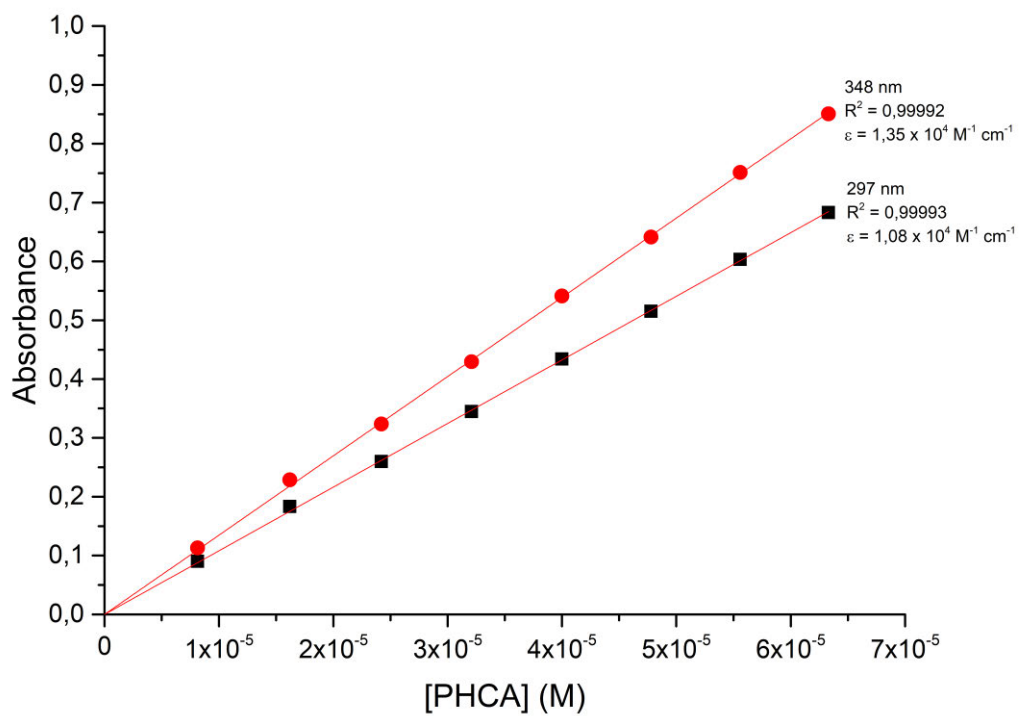


**Figure A56: Beer's Law Correlation of PHCA.**

### Single Mass Analysis

Tolerance = 5.0 PPM / DBE: min = -1.5, max = 100.0

Element prediction: Off

Number of isotope peaks used for i-FIT = 3

Monoisotopic Mass, Even Electron Ions

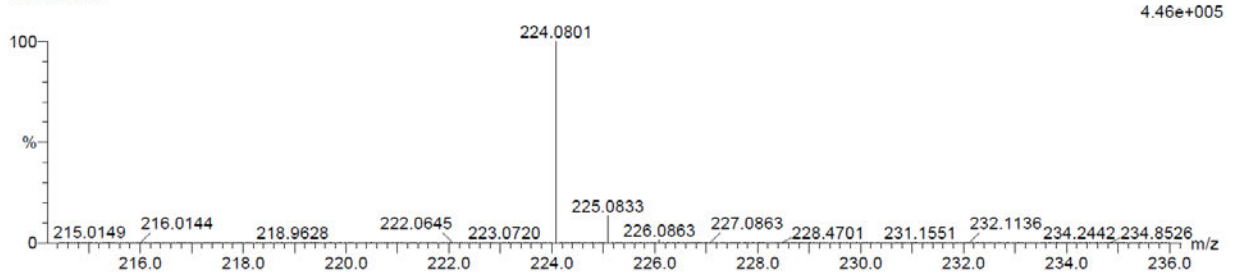
41 formula(e) evaluated with 1 results within limits (up to 20 closest results for each mass)

Elements Used:

C: 10-15 H: 10-15 N: 0-5 O: 0-5 Na: 0-1

PHCA (8) 9 (0.270) Cm (1.61)

TOF MS ES+



PHCA (8) I rms 1 (0.017) Cm (1:59)

TOF MS ES+  
2.18e5

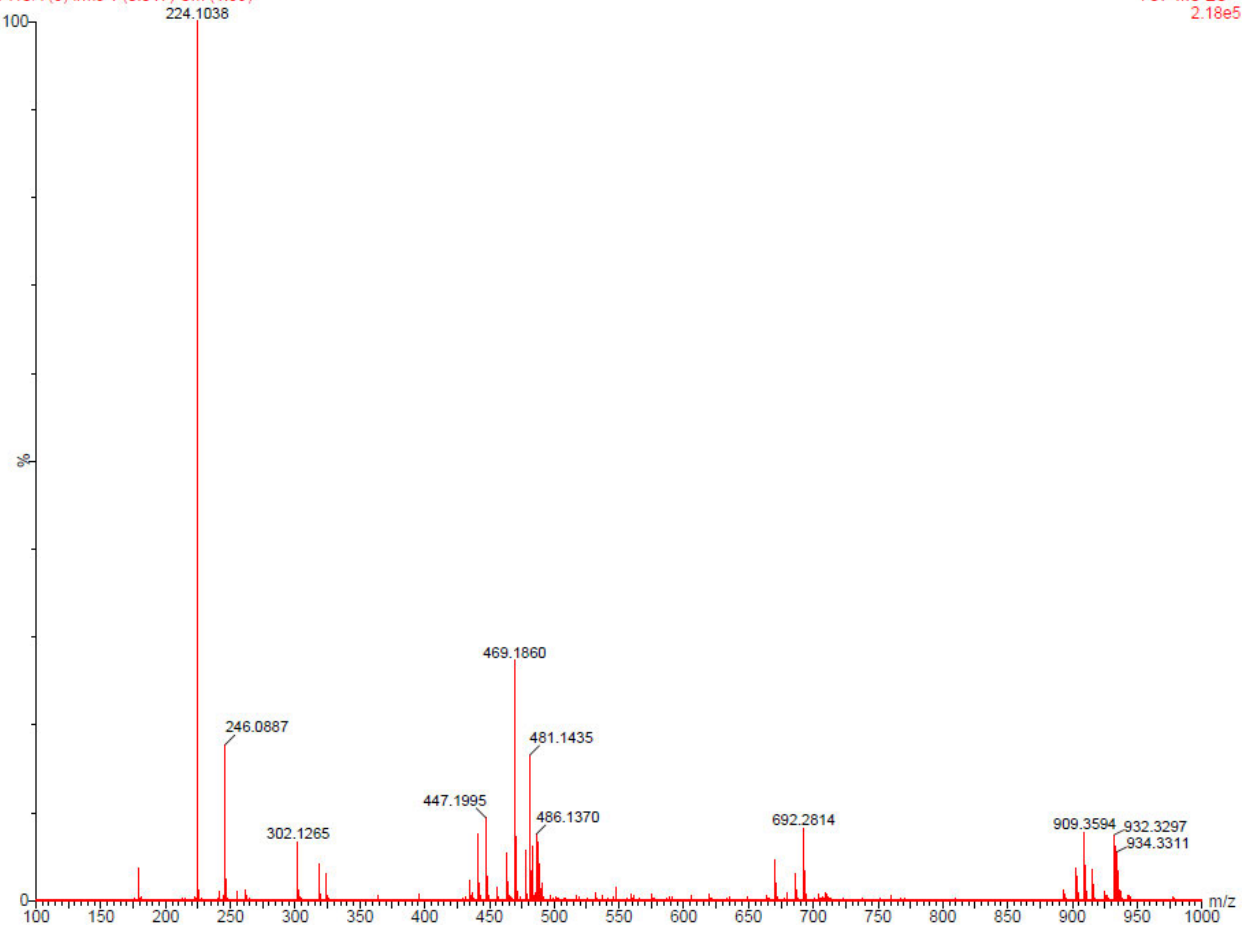


**Figure A57: High resolution ESI mass spectrum of PHCA in DMSO.**

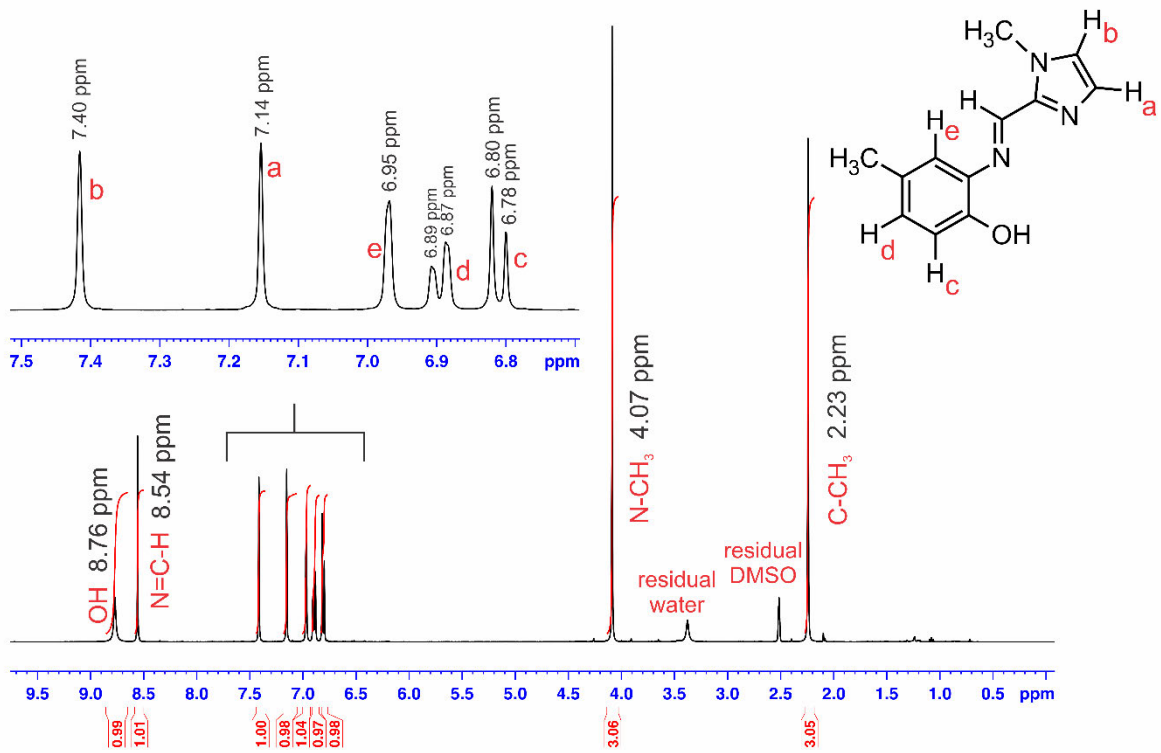


Figure A58: Fully assigned  $^1\text{H}$  NMR spectrum of MECA in  $\text{DMSO-}d_6$ .

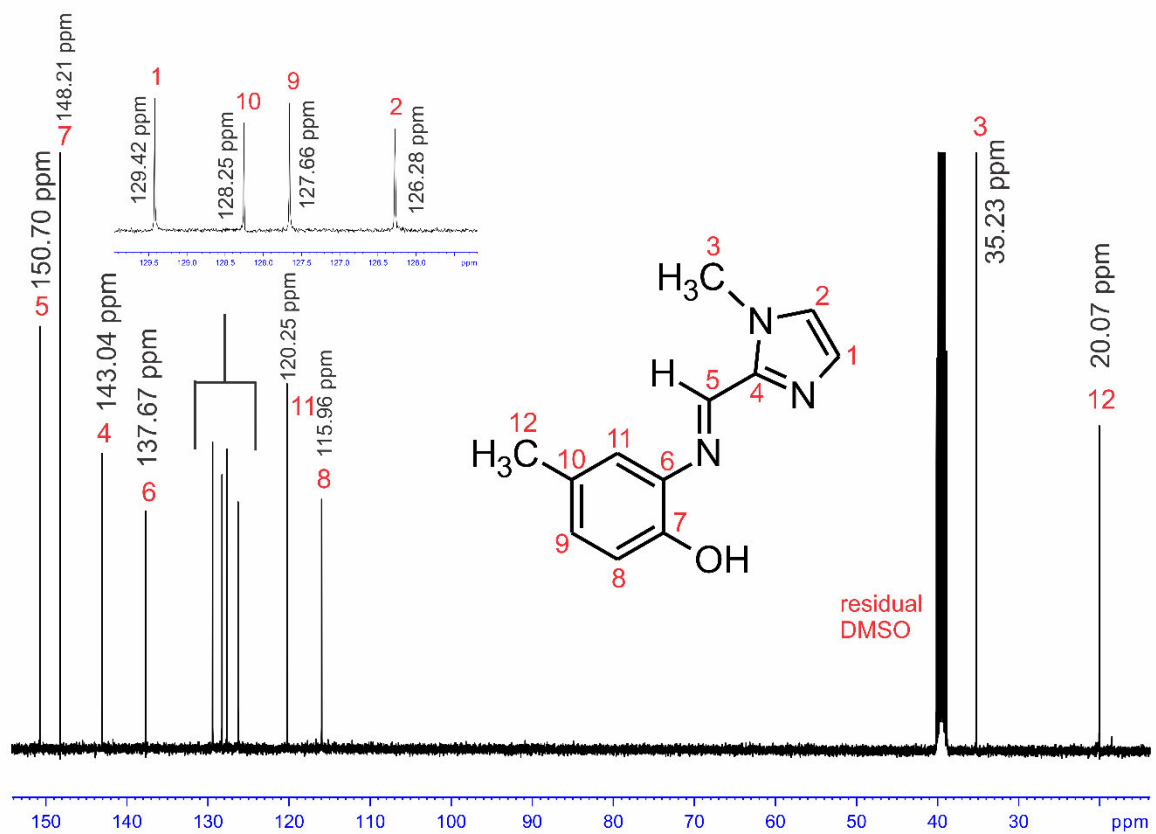
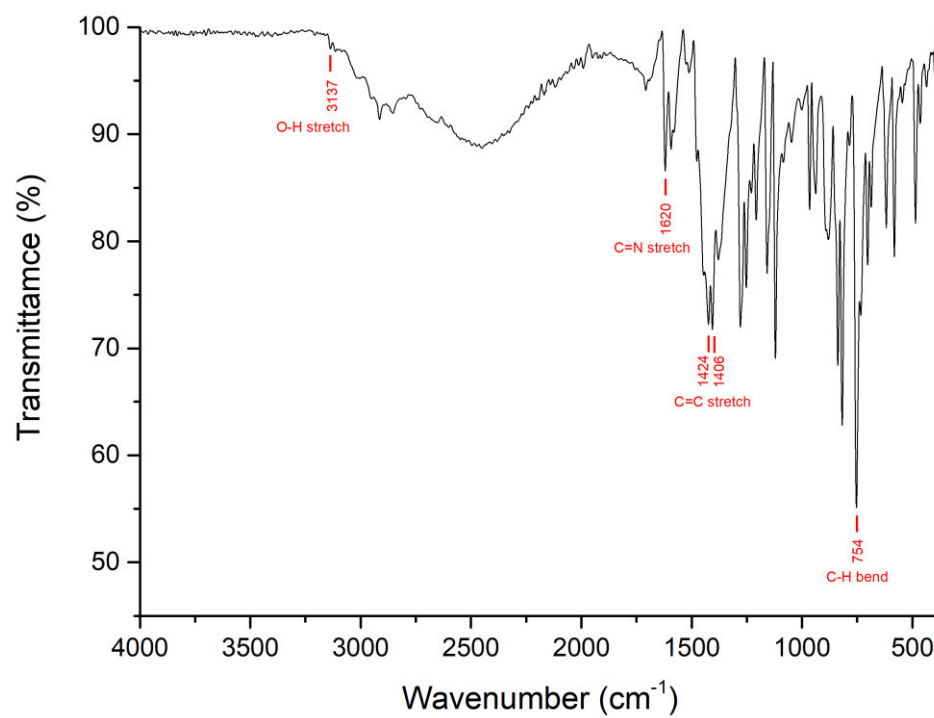
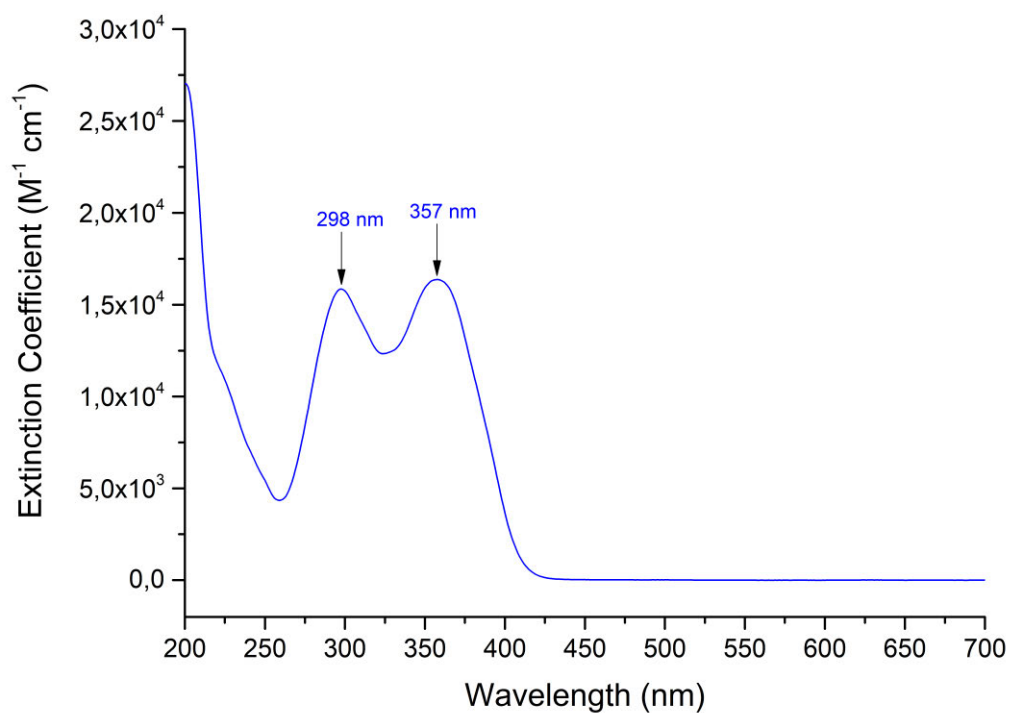


Figure A59: Fully assigned  $^{13}\text{C}$  NMR spectrum of MECA in  $\text{DMSO-}d_6$ .



**Figure A60: IR spectrum of MECA.**



**Figure A61: UV/visible spectrum of MECA. [MECA] =  $5.18 \times 10^{-5}$  M.**

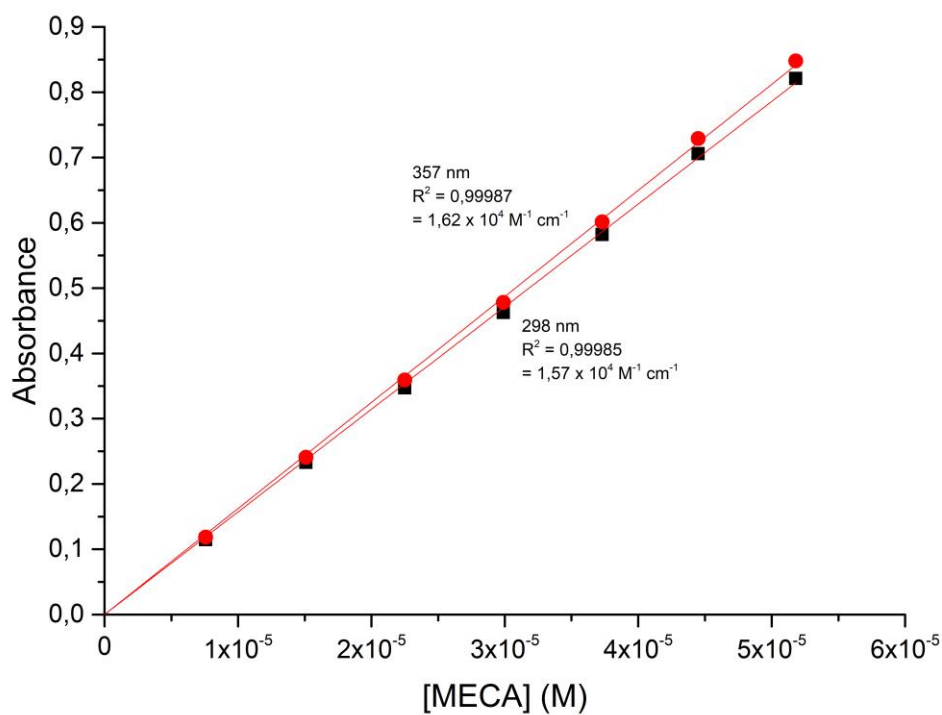


**Figure A62: Beer's Law Correlation of MECA.**

### Single Mass Analysis

Tolerance = 5.0 PPM / DBE: min = -1.5, max = 100.0

Element prediction: Off

Number of isotope peaks used for i-FIT = 3

Monoisotopic Mass, Even Electron Ions

38 formula(e) evaluated with 1 results within limits (up to 20 closest results for each mass)

Elements Used:

C: 10-15 H: 10-15 N: 0-5 O: 0-5 Na: 0-1

MECA (2) 50 (1.653) Cm (1:61)

TOF MS ES+

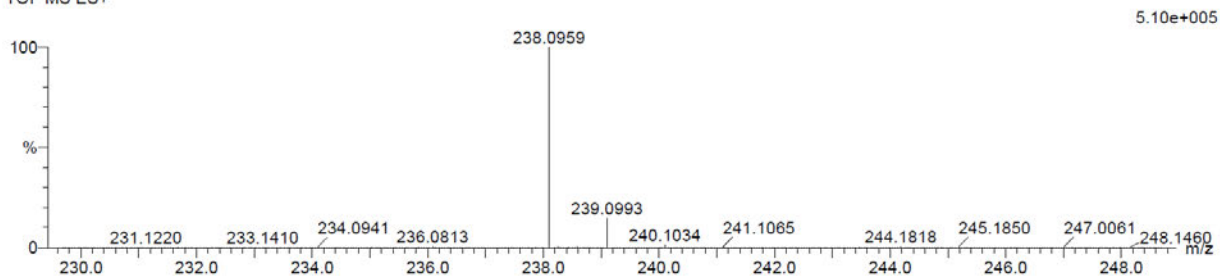


**Figure A63: High resolution ESI mass spectrum of MECA in methanol.**

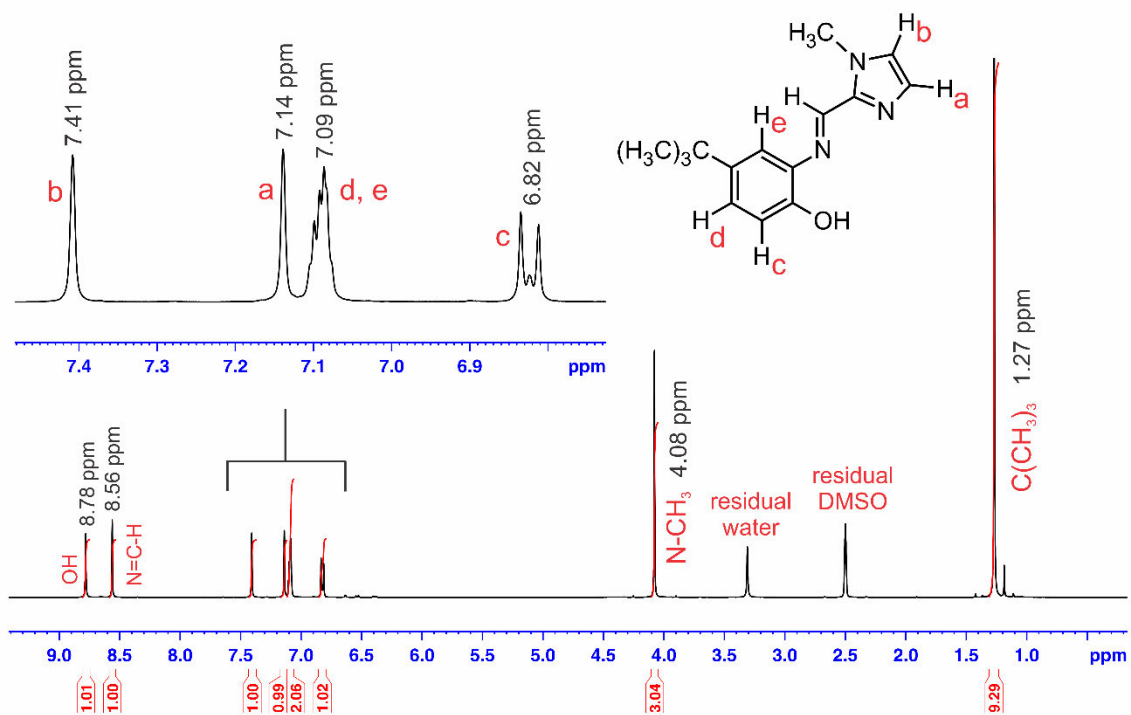


Figure A64: Fully assigned  $^1\text{H}$  NMR spectrum of TERTCA in  $\text{DMSO-}d_6$ .

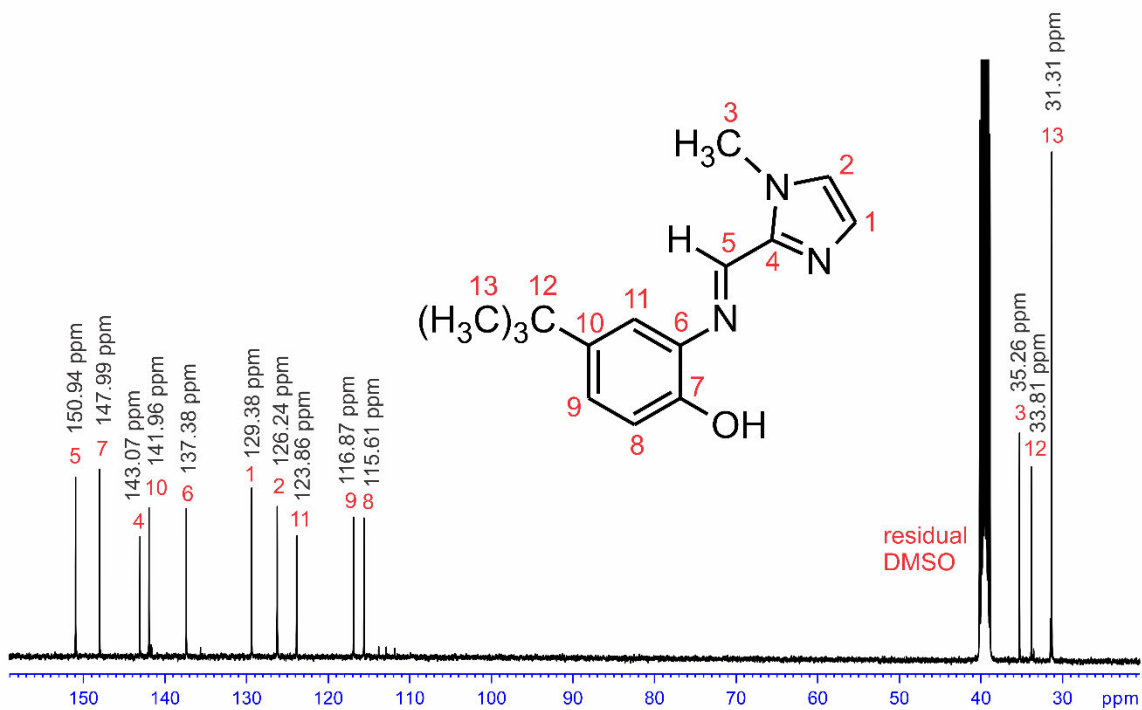
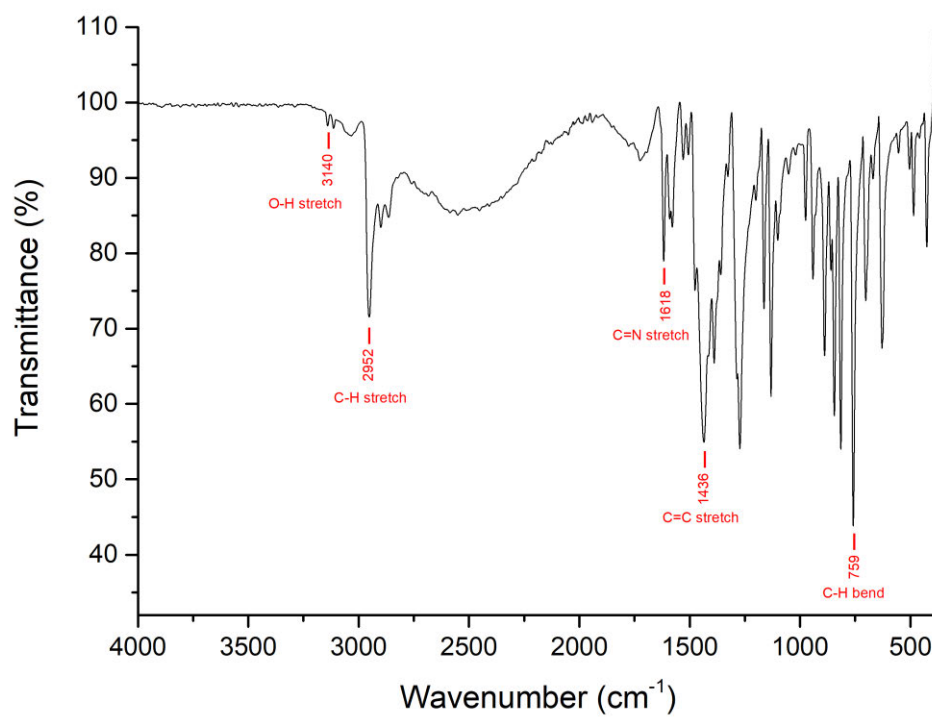
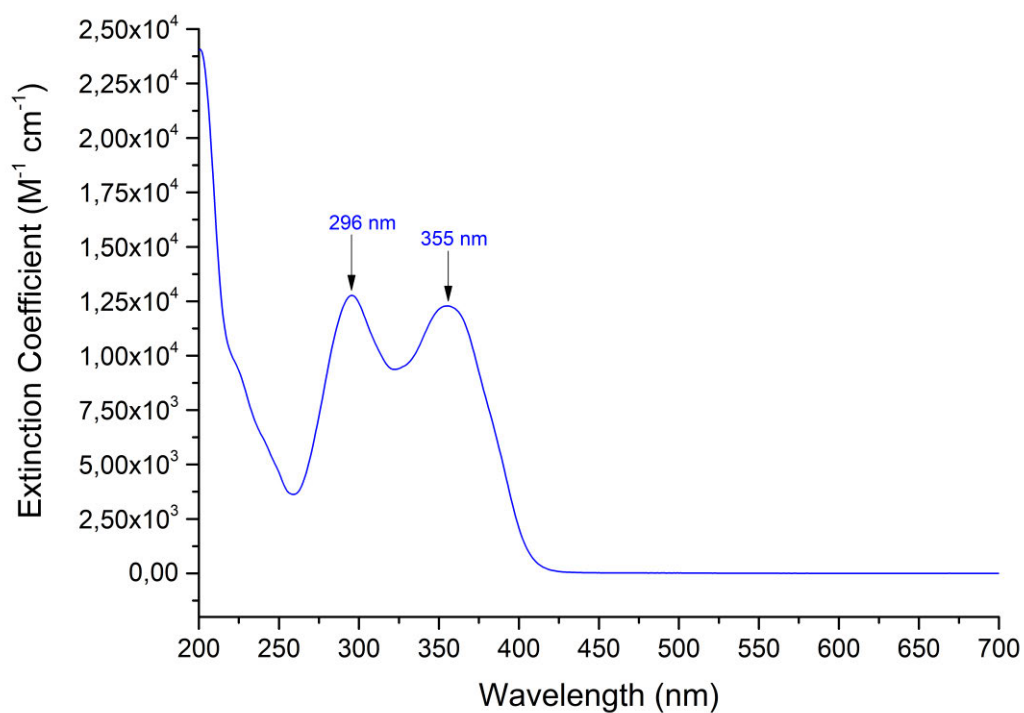


Figure A65: Fully assigned  $^{13}\text{C}$  NMR spectrum of TERTCA in  $\text{DMSO-}d_6$ .



**Figure A66: IR spectrum of TERTCA.**



**Figure A67: UV/visible spectrum of TERTCA.  $[\text{TERTCA}] = 4.93 \times 10^{-5} \text{ M}$ .**

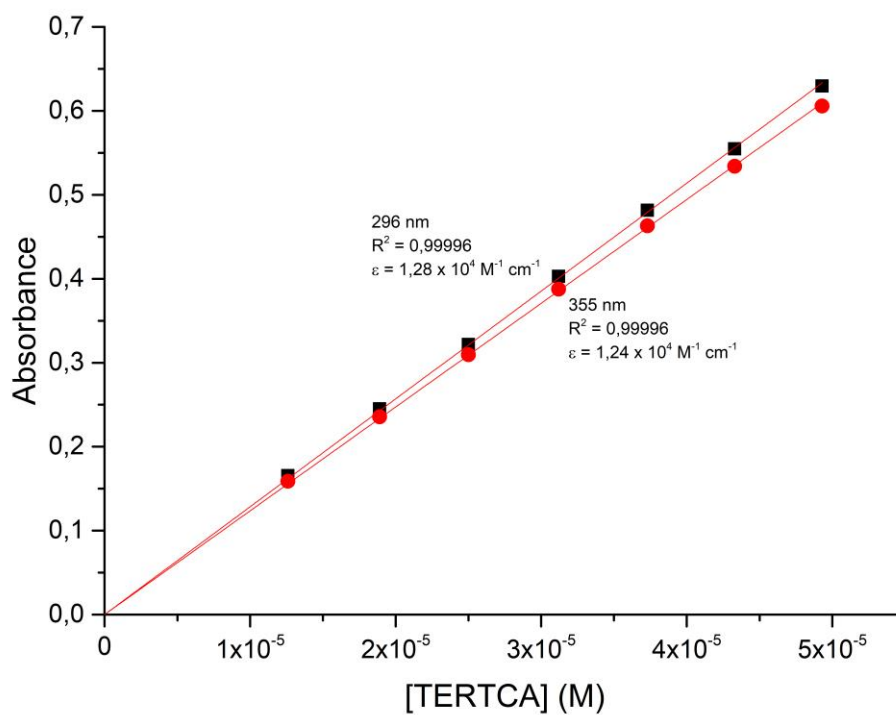


**Figure A68: Beer's Law Correlation of TERTCA.**

### Single Mass Analysis

Tolerance = 5.0 PPM / DBE: min = -1.5, max = 100.0

Element prediction: Off

Number of isotope peaks used for i-FIT = 3

Monoisotopic Mass, Even Electron Ions

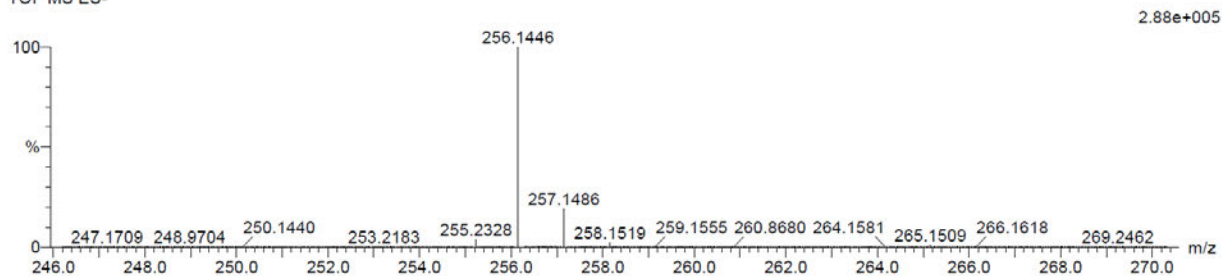
23 formula(e) evaluated with 1 results within limits (up to 20 closest results for each mass)

Elements Used:

C: 15-20 H: 15-20 N: 0-5 O: 0-5

TertCA 38 (1.248) Cm (1:61)

TOF MS ES-



TertCA Ims 55 (0.920) Cm (1:60)

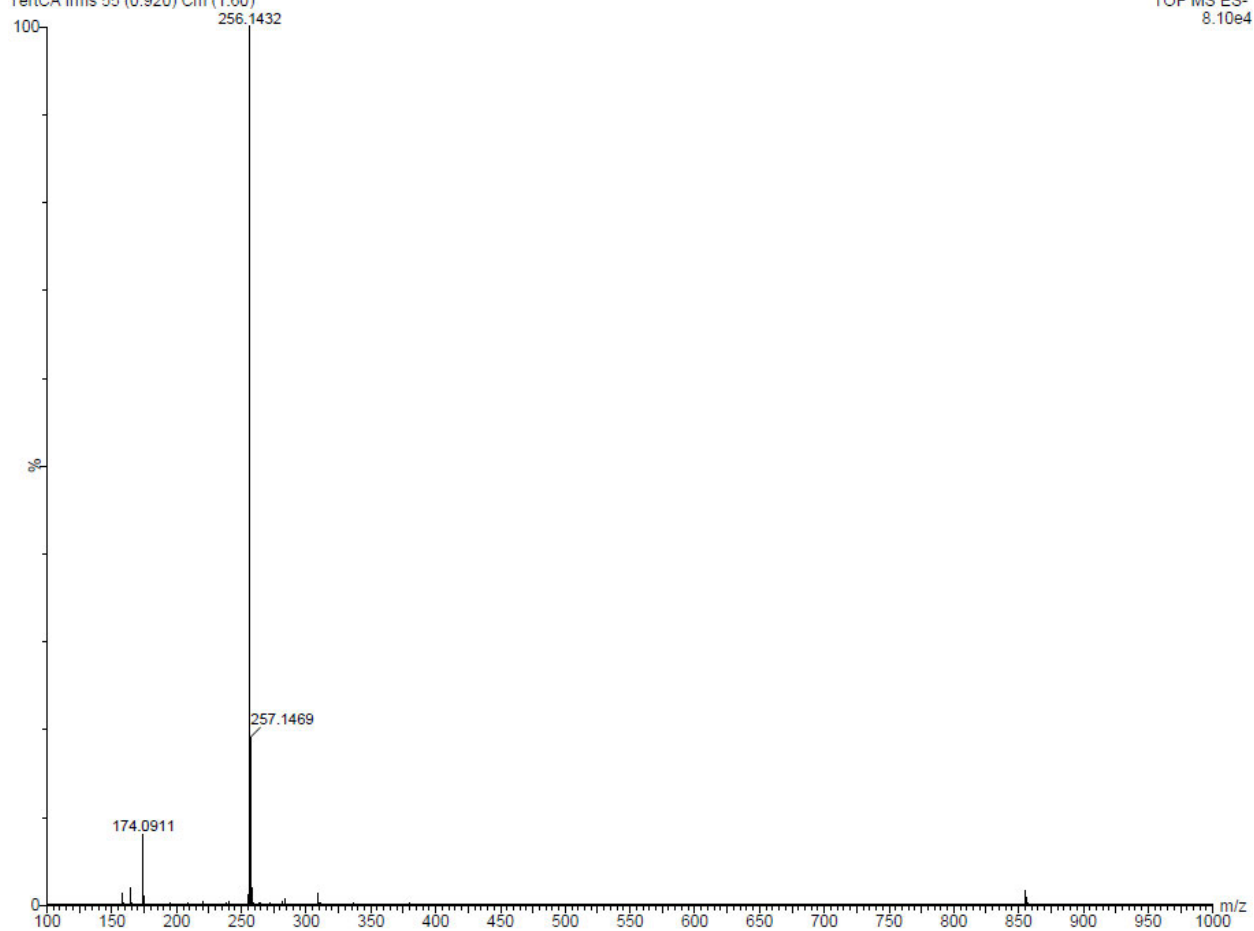


**Figure A69: High resolution ESI mass spectrum of TERTCA in methanol.**

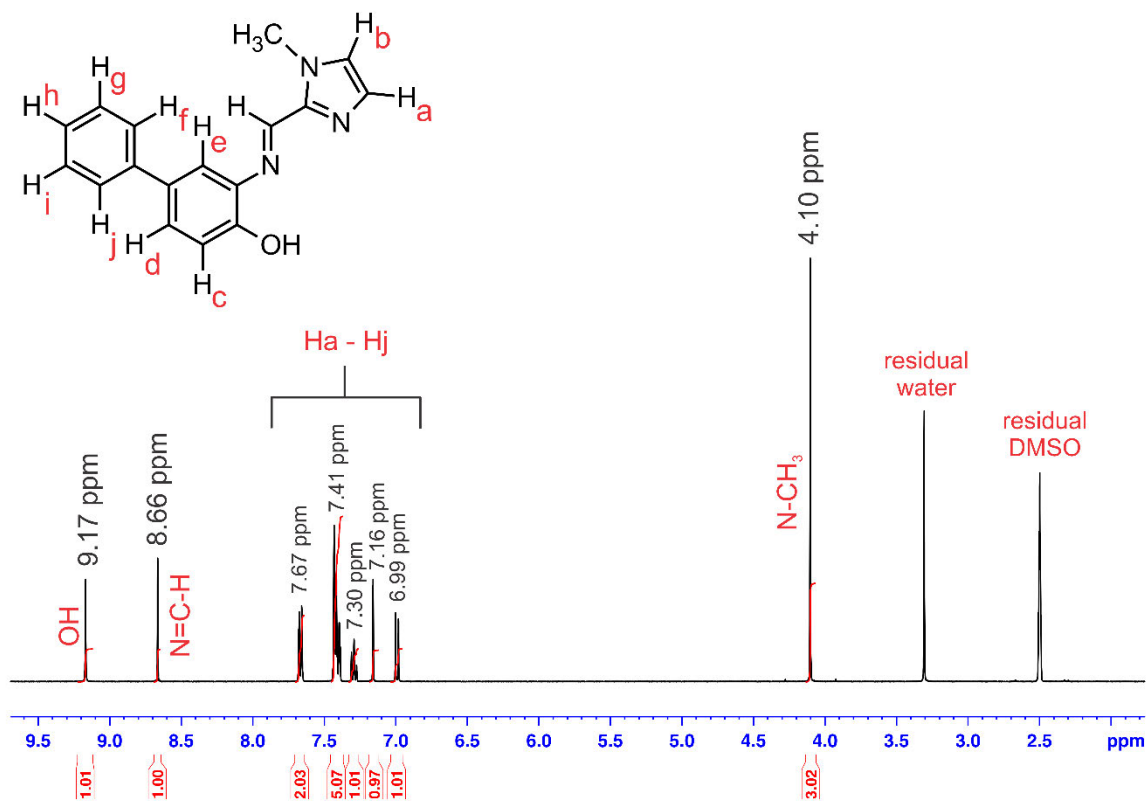


Figure A70: Assigned <sup>1</sup>H NMR spectrum of PHPHCA in DMSO-*d*<sub>6</sub>.

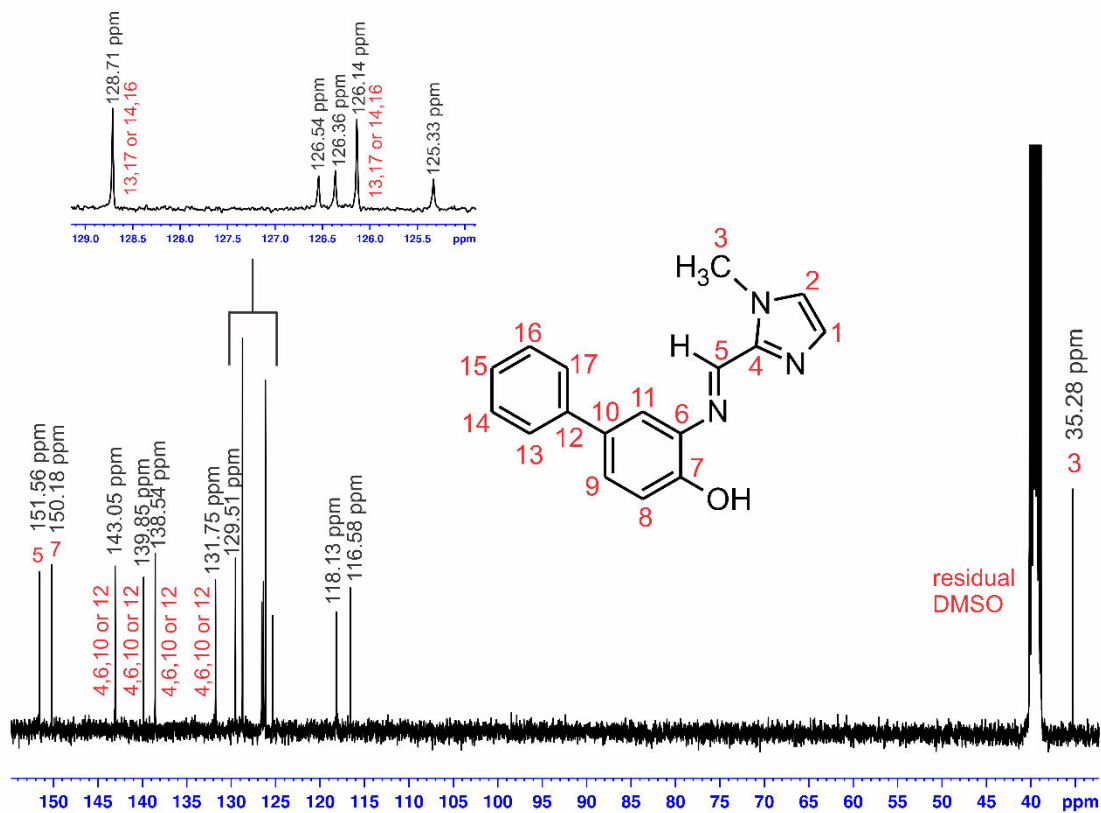
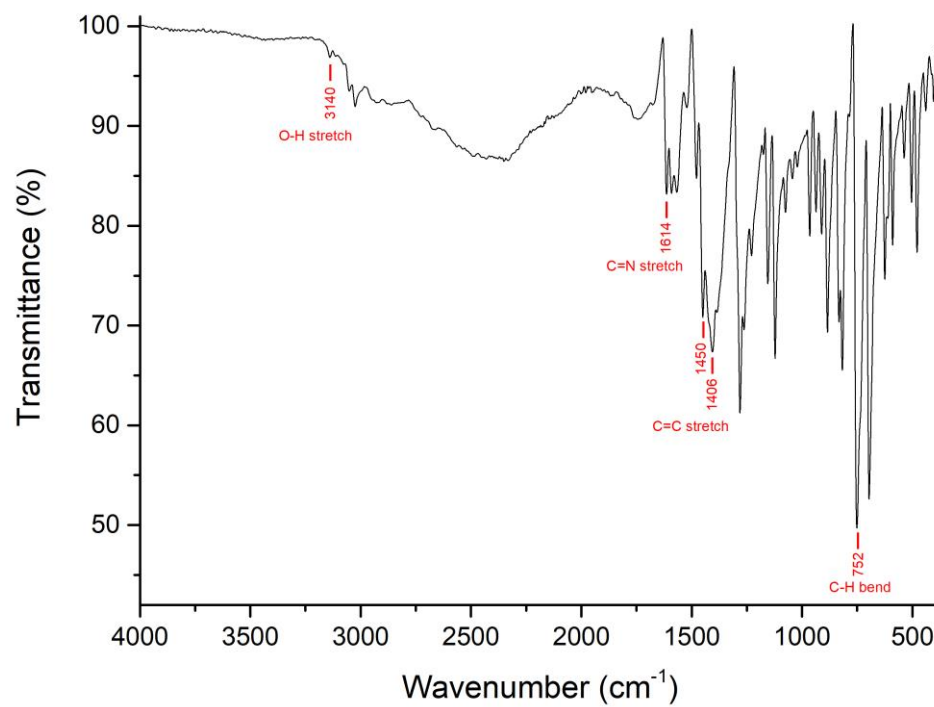
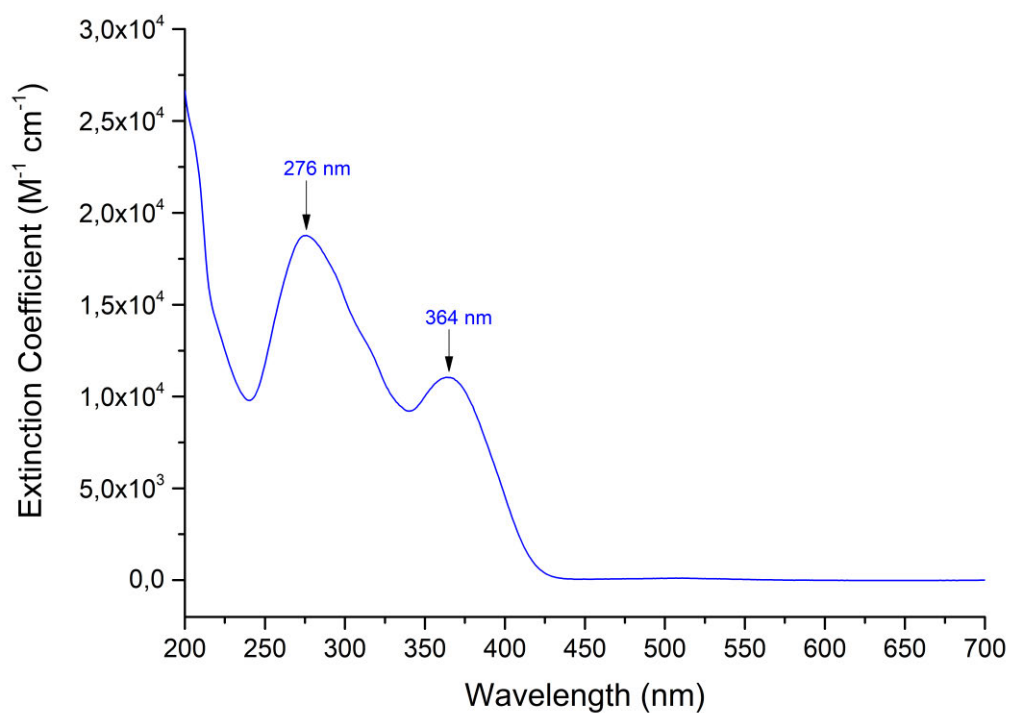


Figure A71: Assigned <sup>13</sup>C NMR spectrum of PHPHCA in DMSO-*d*<sub>6</sub>.



**Figure A72: IR spectrum of PHPHCA.**



**Figure A73: UV/visible spectrum of PHPHCA. [PHPHCA] =  $3.83 \times 10^{-5} \text{ M}$ .**

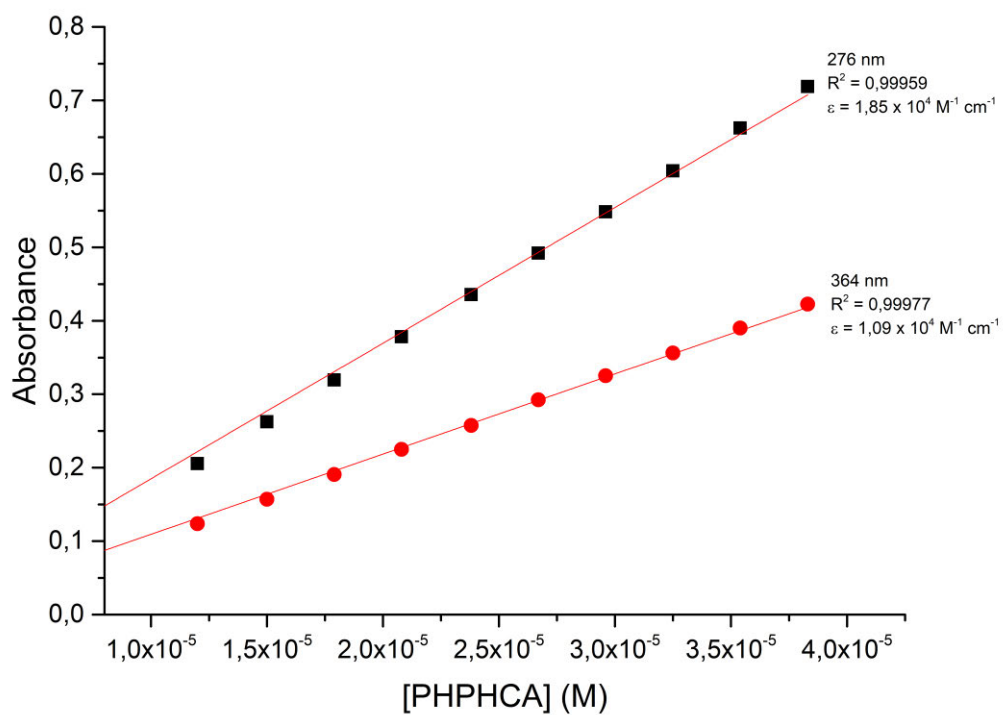


**Figure A74: Beer's Law Correlation of PHPHCA.**

### Single Mass Analysis

Tolerance = 5.0 PPM / DBE: min = -1.5, max = 500.0

Element prediction: Off

Number of isotope peaks used for i-FIT = 2

Monoisotopic Mass, Even Electron Ions

18 formula(e) evaluated with 1 results within limits (all results (up to 1000) for each mass)

Elements Used:

C: 15-20 H: 10-15 N: 0-5 O: 0-5

PHPHCA(3) 60 (2.022) Cm (1:60)

TOF MS ES-

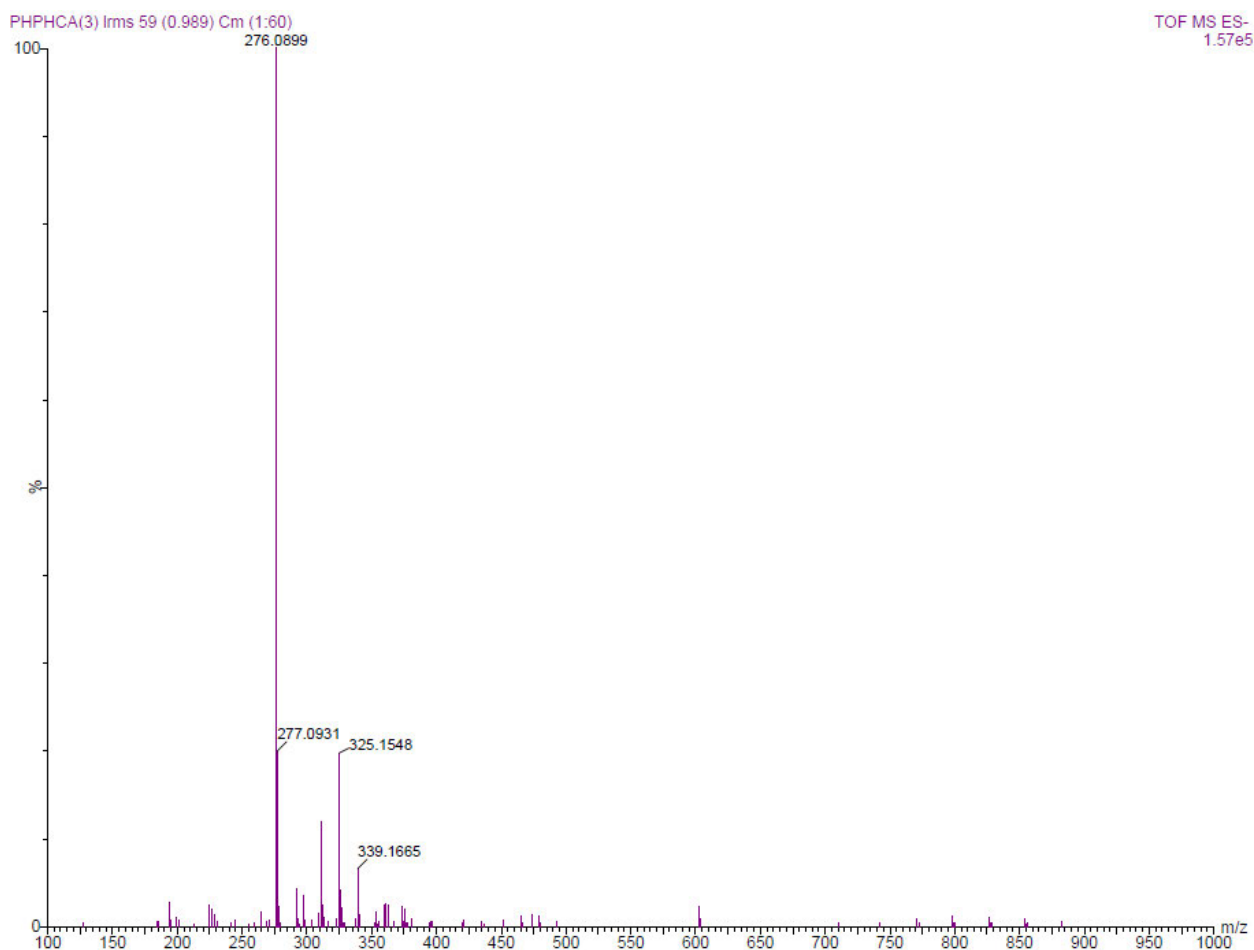
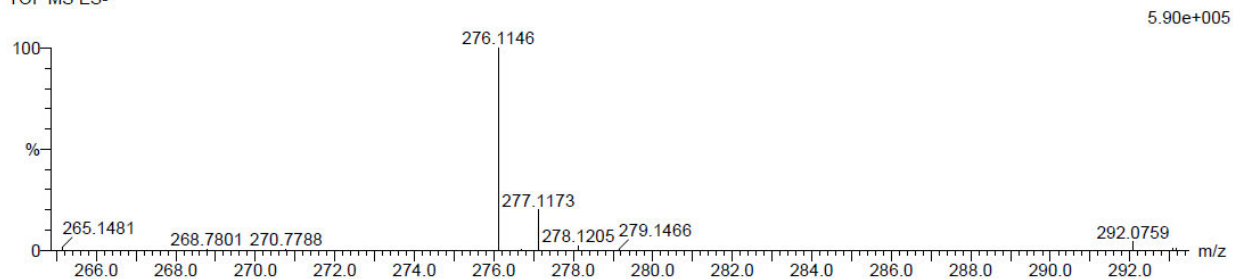


**Figure A75: High resolution ESI mass spectrum of PHPHCA in DMSO.**

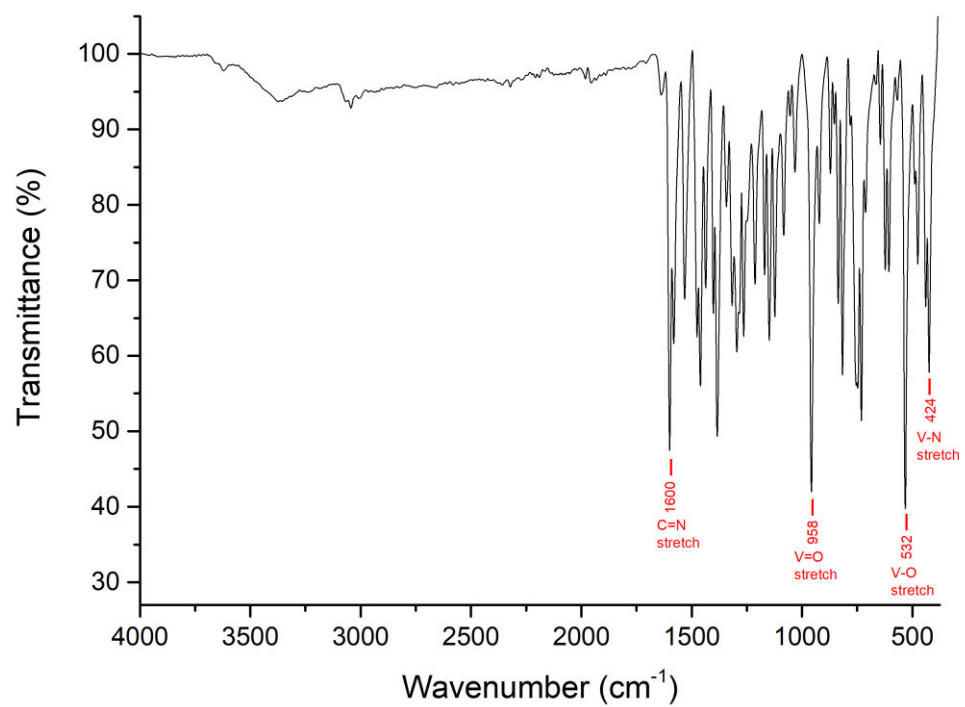


**Figure A76: IR spectrum of [VO(PHA)(DPQ)].**

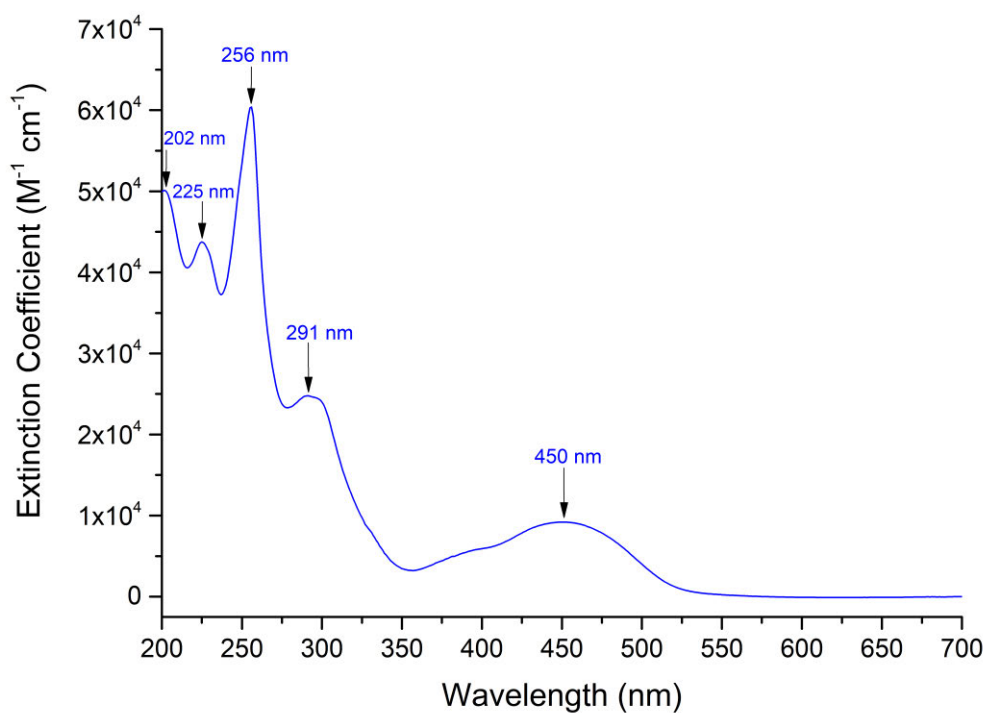


**Figure A77: UV/visible spectrum of [VO(PHA)(DPQ)].**  
**[VO(PHA)(DPQ)] = 1.65 x 10<sup>-5</sup> M.**

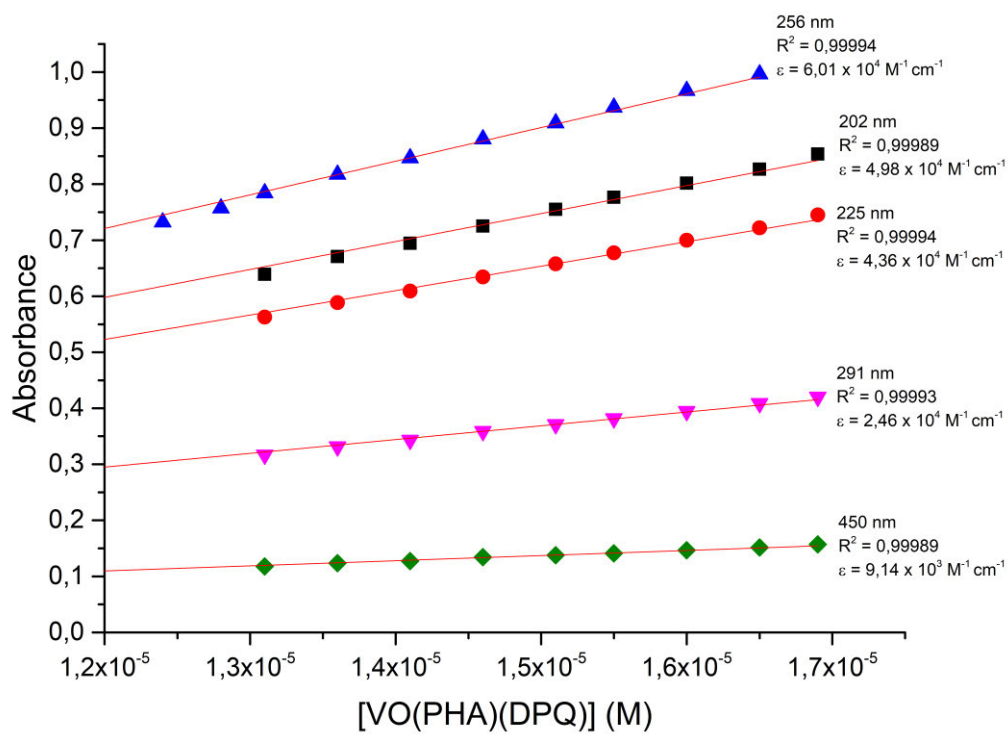


**Figure A78: Beer's Law Correlation of [VO(PHA)(DPQ)].**

### Single Mass Analysis

Tolerance = 5.0 PPM / DBE: min = -1.5, max = 100.0

Element prediction: Off

Number of isotope peaks used for i-FIT = 2

Monoisotopic Mass, Even Electron Ions

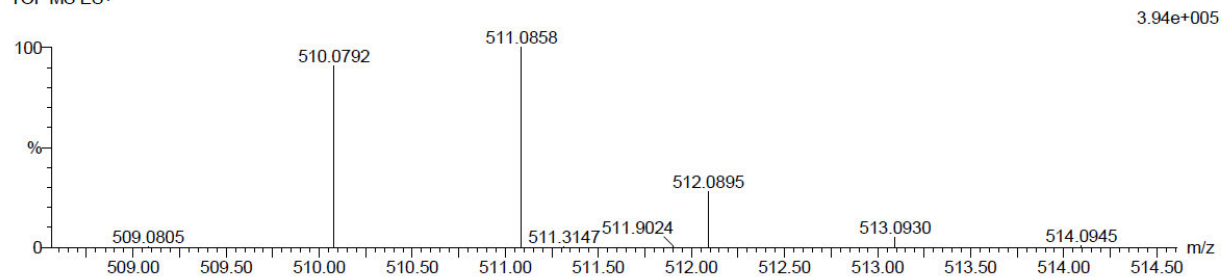
28 formula(e) evaluated with 1 results within limits (up to 20 best isotopic matches for each mass)

Elements Used:

C: 25-30 H: 15-20 N: 0-5 O: 0-5 V: 0-1

VPHADPQ(3) 34 (1.112) Cm (1:61)

TOF MS ES+



VPHADPQ(3) 34 (1.112) Cm (1:61)

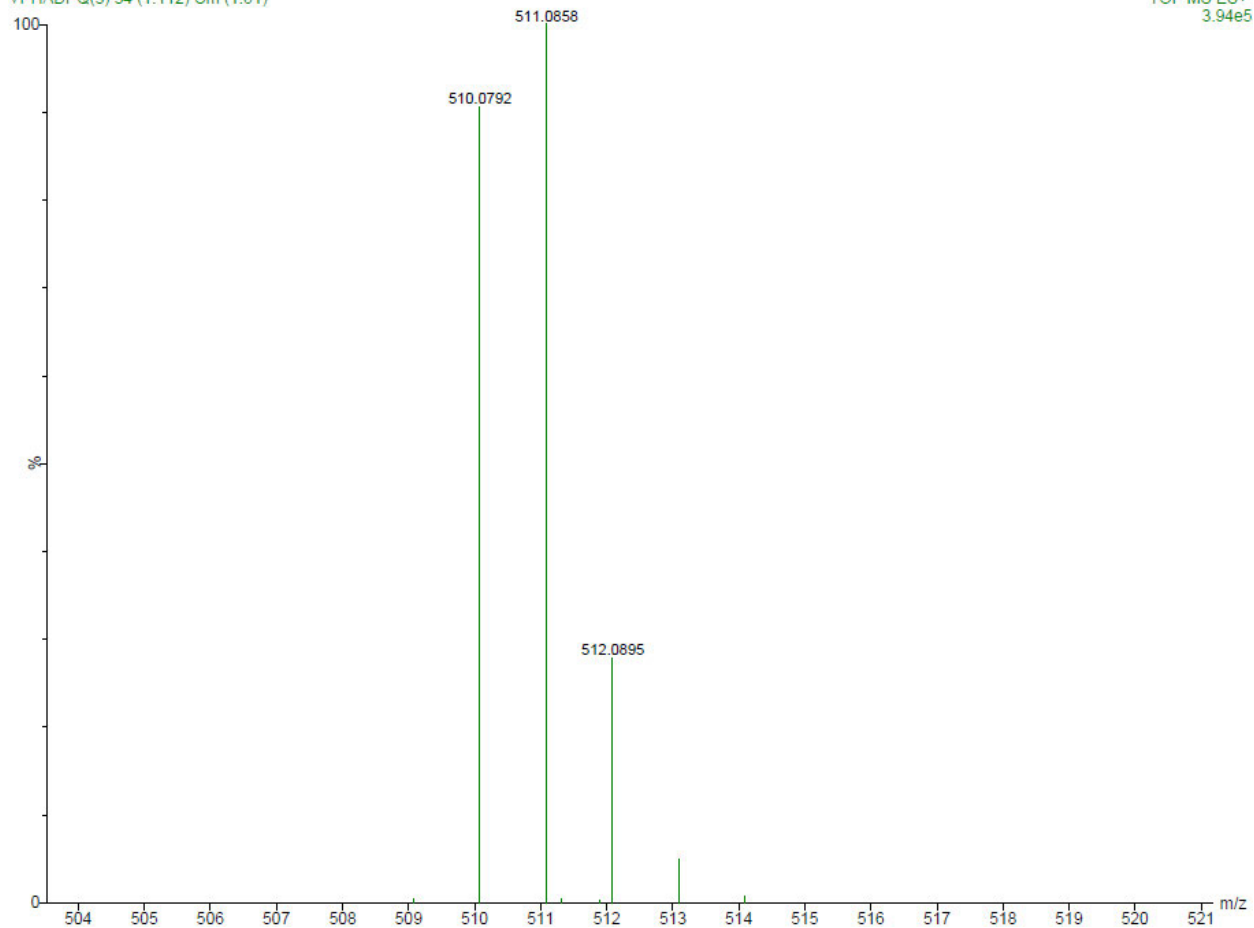


**Figure A79: High resolution ESI mass spectrum of [VO(PHA)(DPQ)] in chloroform.**

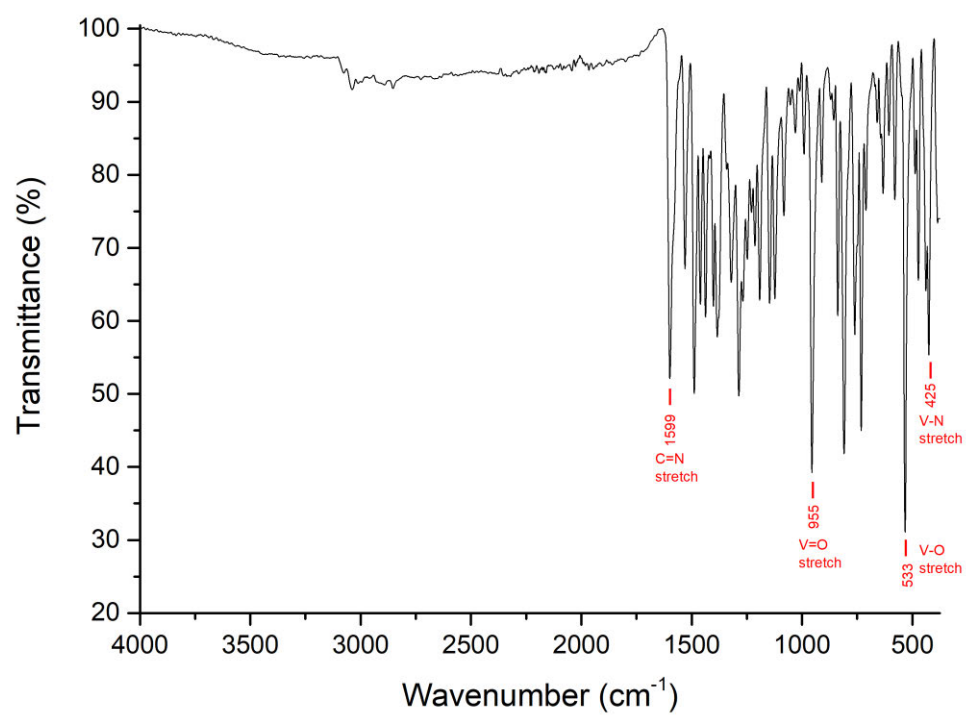


**Figure A80: IR spectrum of [VO(MEA)(DPQ)].**

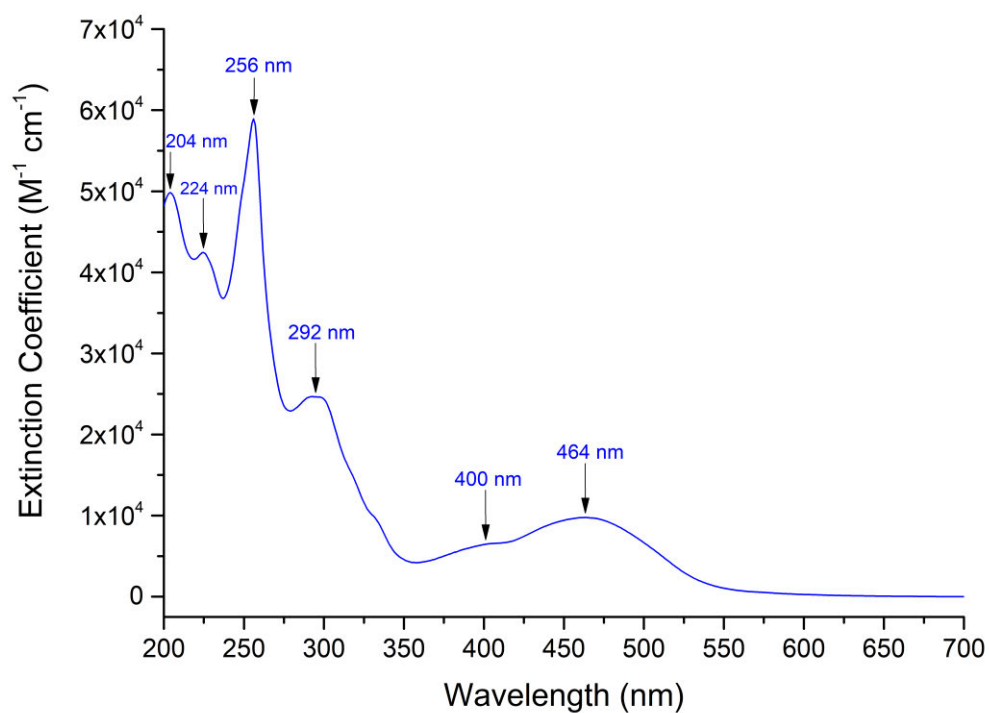


**Figure A81: UV/visible spectrum of [VO(MEA)(DPQ)].**  
**[VO(MEA)(DPQ)] =  $1.71 \times 10^{-5}$  M.**

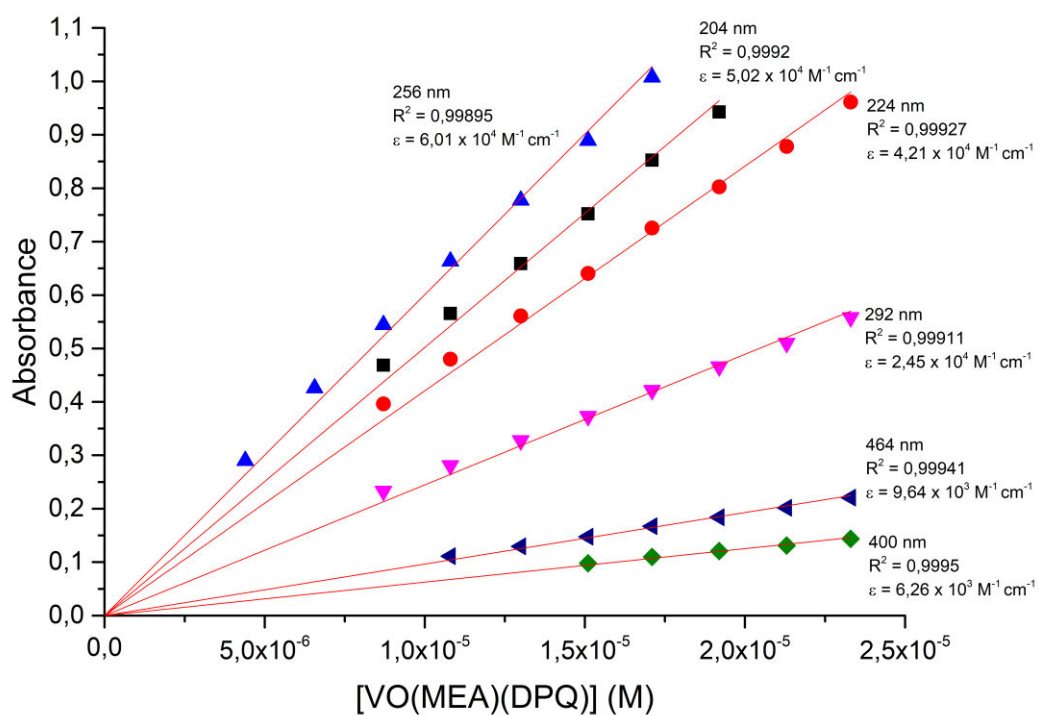


**Figure A82: Beer's Law Correlation of [VO(MEA)(DPQ)].**

### Single Mass Analysis

Tolerance = 5.0 PPM / DBE: min = -1.5, max = 100.0

Element prediction: Off

Number of isotope peaks used for i-FIT = 3

Monoisotopic Mass, Odd and Even Electron Ions

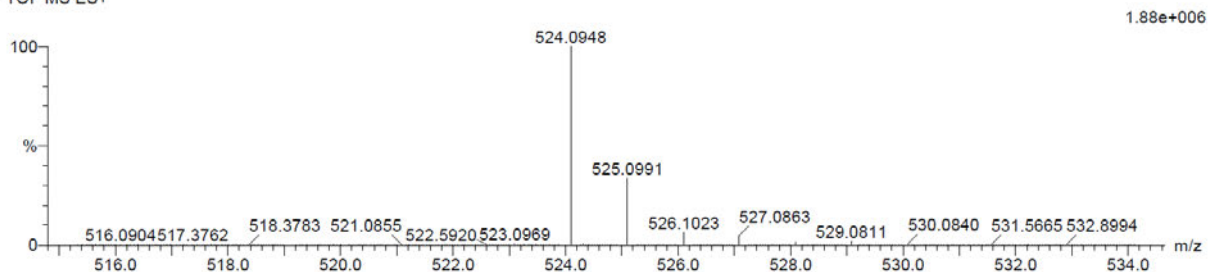
33 formula(e) evaluated with 1 results within limits (up to 20 closest results for each mass)

Elements Used:

C: 25-30 H: 15-20 N: 0-5 O: 0-5 V: 0-1

VMEADPQ(3) 59 (1.957) Cm (1:61)

TOF MS ES+



VMEADPQ(3) Ims 57 (0.955) Cm (1:60)

TOF MS ES+  
6.14e5

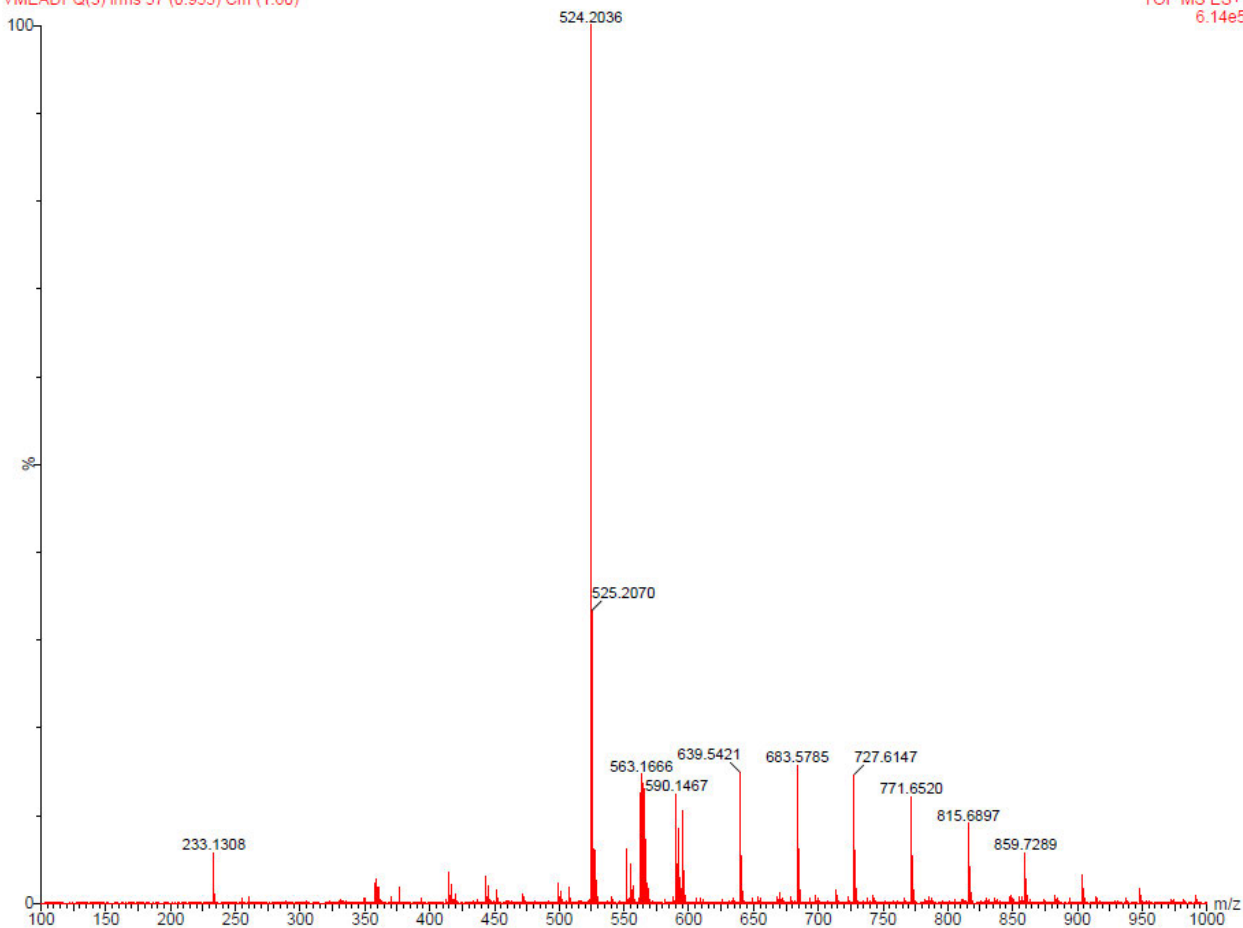


**Figure A83: High resolution ESI mass spectrum of [VO(MEA)(DPQ)] in chloroform.**

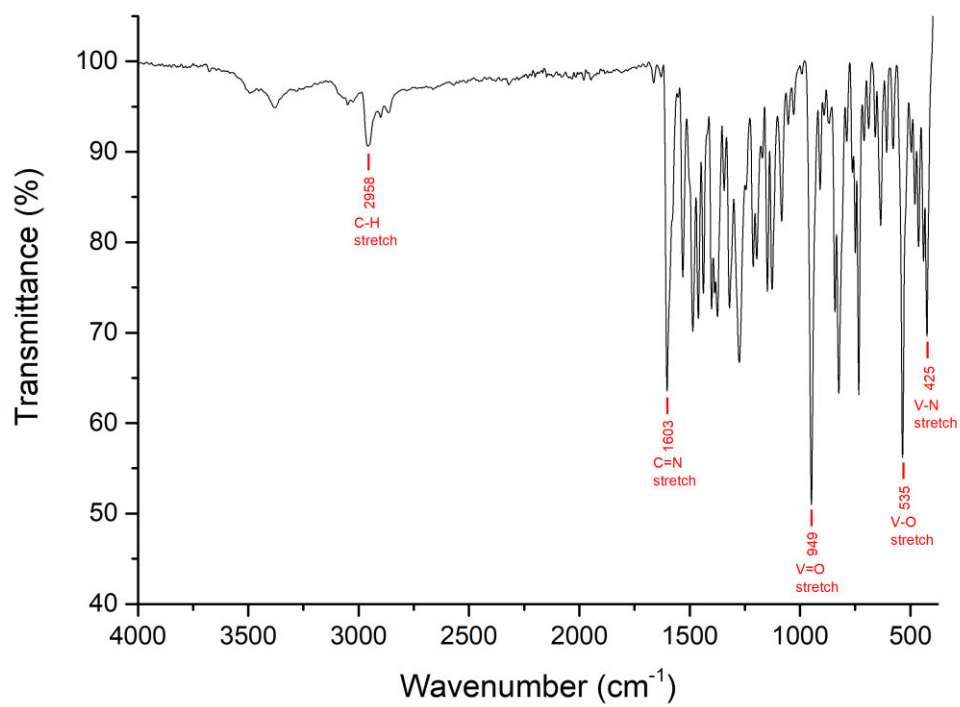


**Figure A84:** IR spectrum of [VO(TERTA)(DPQ)].

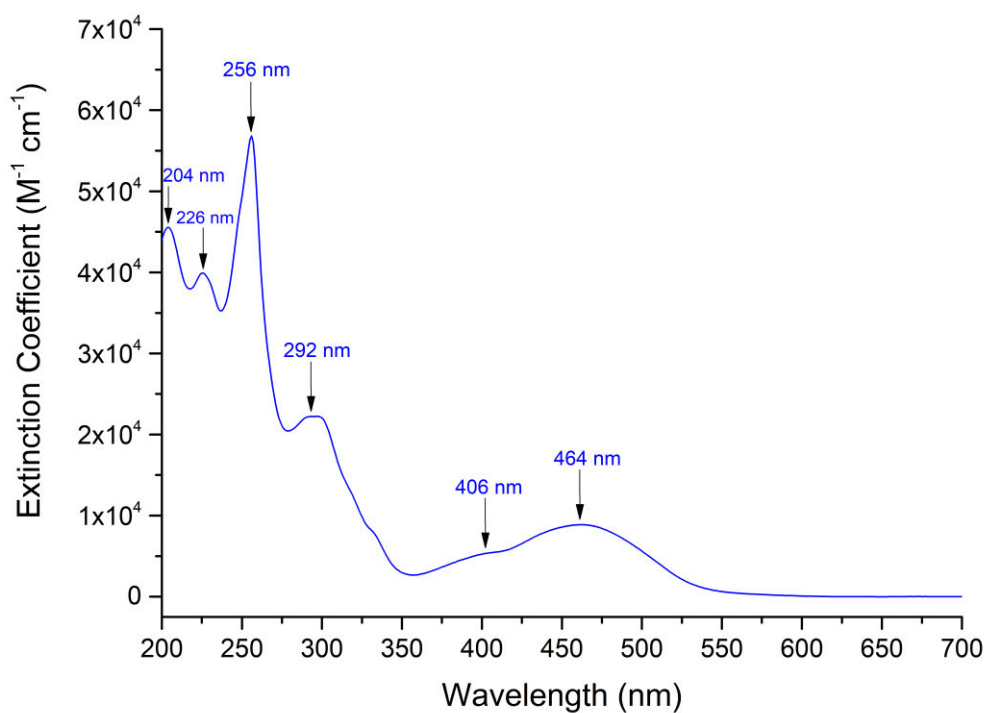


**Figure A85: UV/visible spectrum of [VO(TERTA)(DPQ)].**  
**[VO(TERTA)(DPQ)] =  $1.56 \times 10^{-5}$  M.**

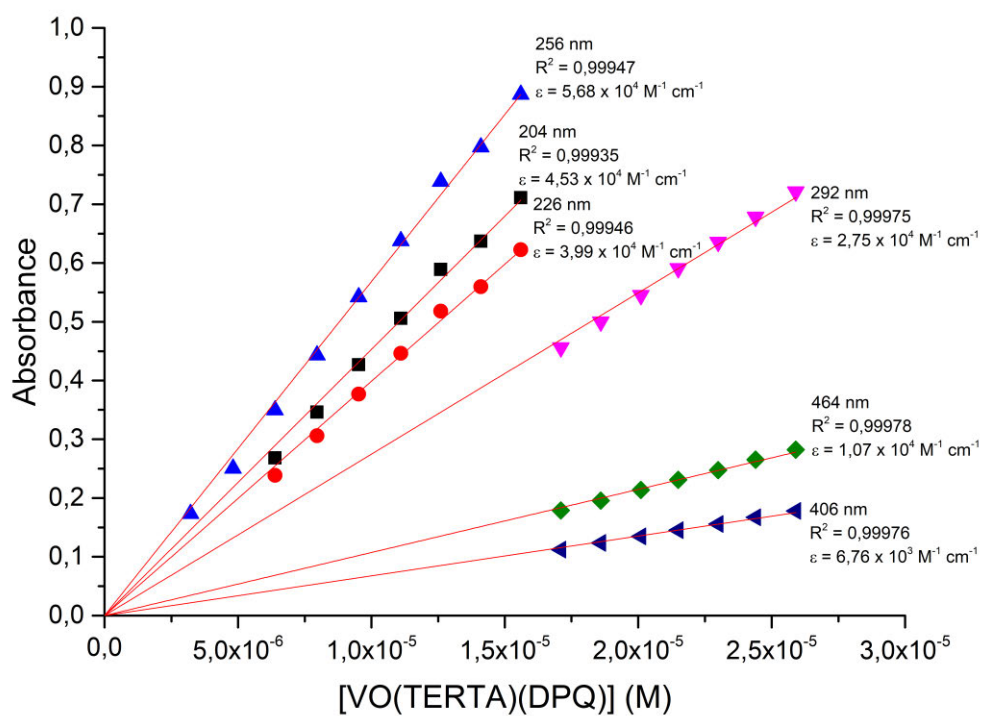


**Figure A86: Beer's Law Correlation of [VO(TERTA)(DPQ)].**

### Single Mass Analysis

Tolerance = 5.0 PPM / DBE: min = -1.5, max = 100.0

Element prediction: Off

Number of isotope peaks used for i-FIT = 3

Monoisotopic Mass, Odd Electron Ions

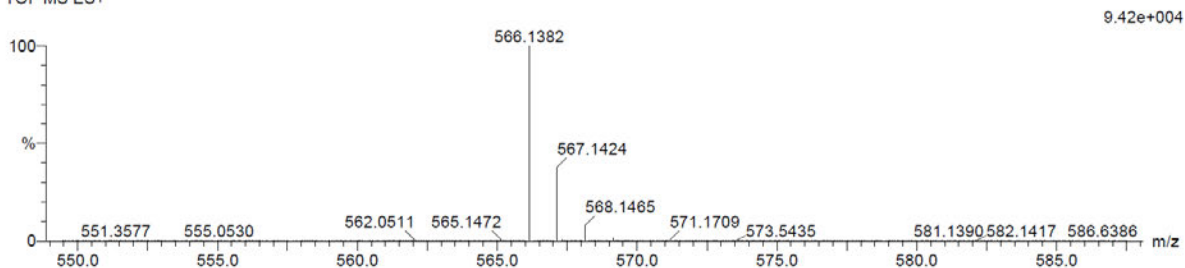
25 formula(e) evaluated with 1 results within limits (up to 20 closest results for each mass)

Elements Used:

C: 30-35 H: 20-25 N: 0-5 O: 0-5 V: 0-1

VTertADPQ 12 (0.188) Cm (1:60)

TOF MS ES+



VTertADPQ Ims 12 (0.188) Cm (1:59)

TOF MS ES+  
9.21e4

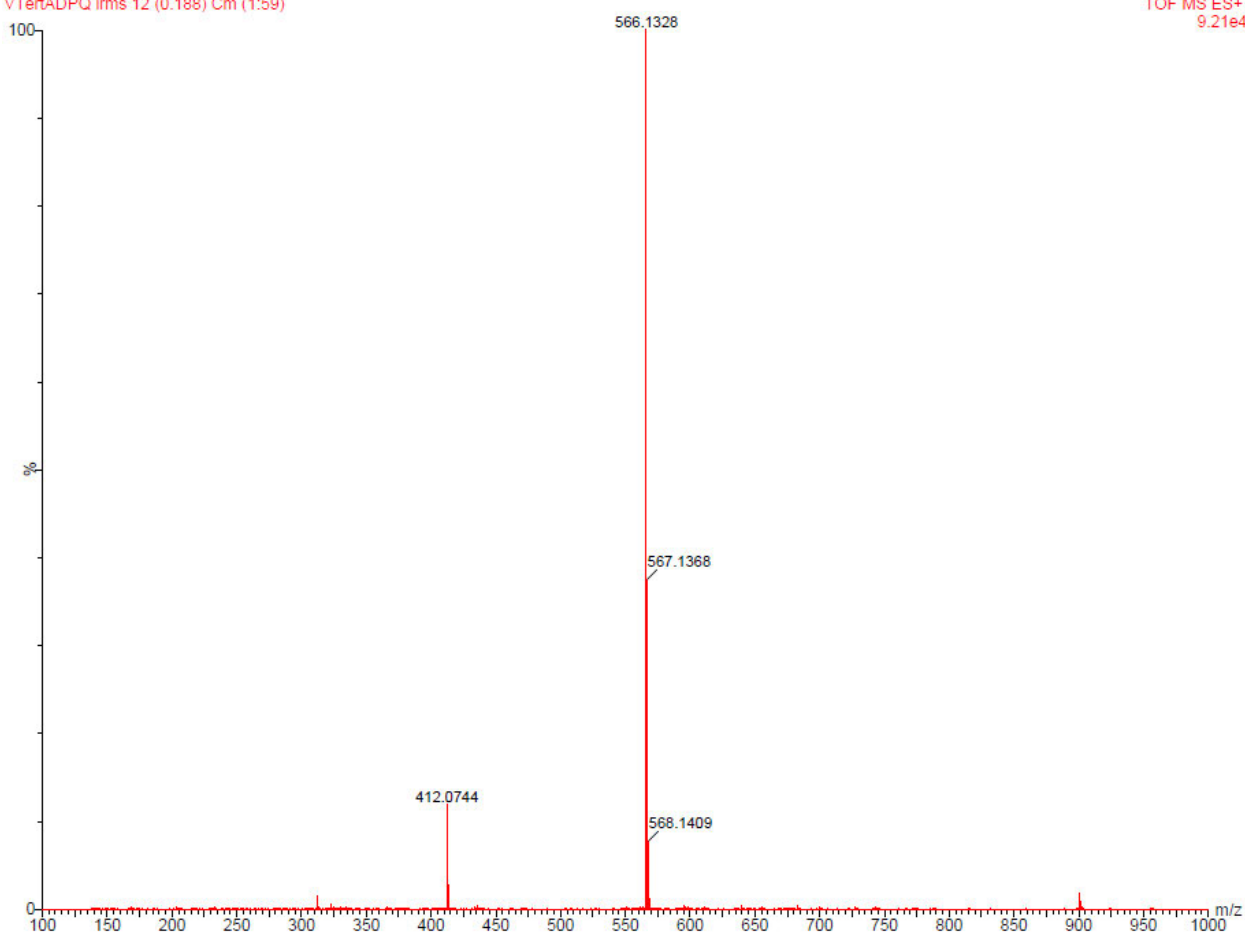


**Figure A87: High resolution ESI mass spectrum of [VO(TERTA)(DPQ)] in chloroform.**

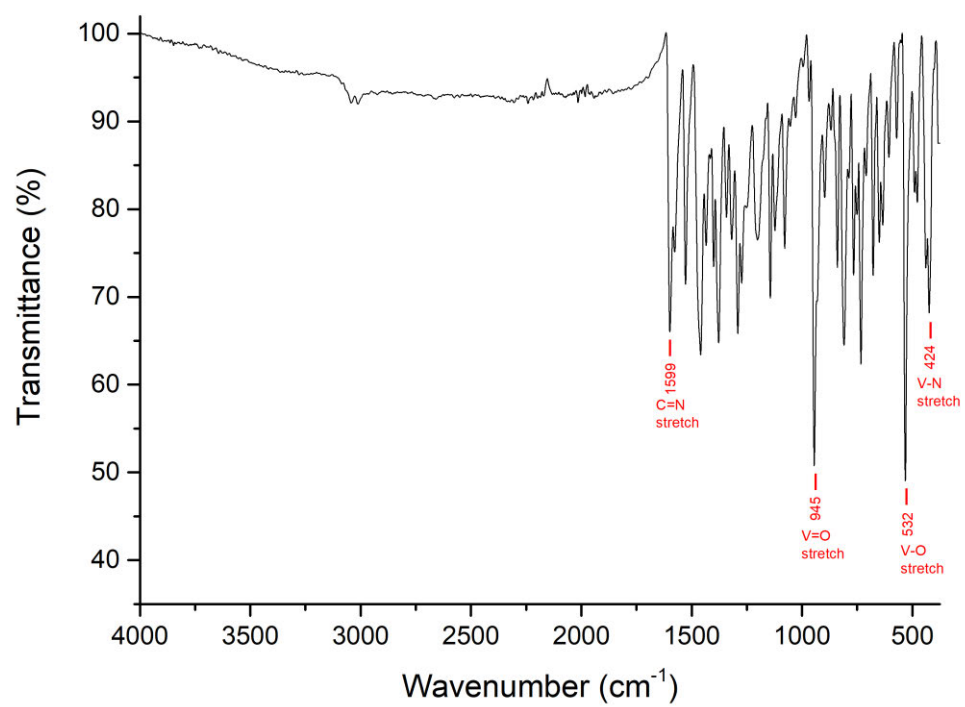


**Figure A88: IR spectrum of [VO(CLA)(DPQ)].**

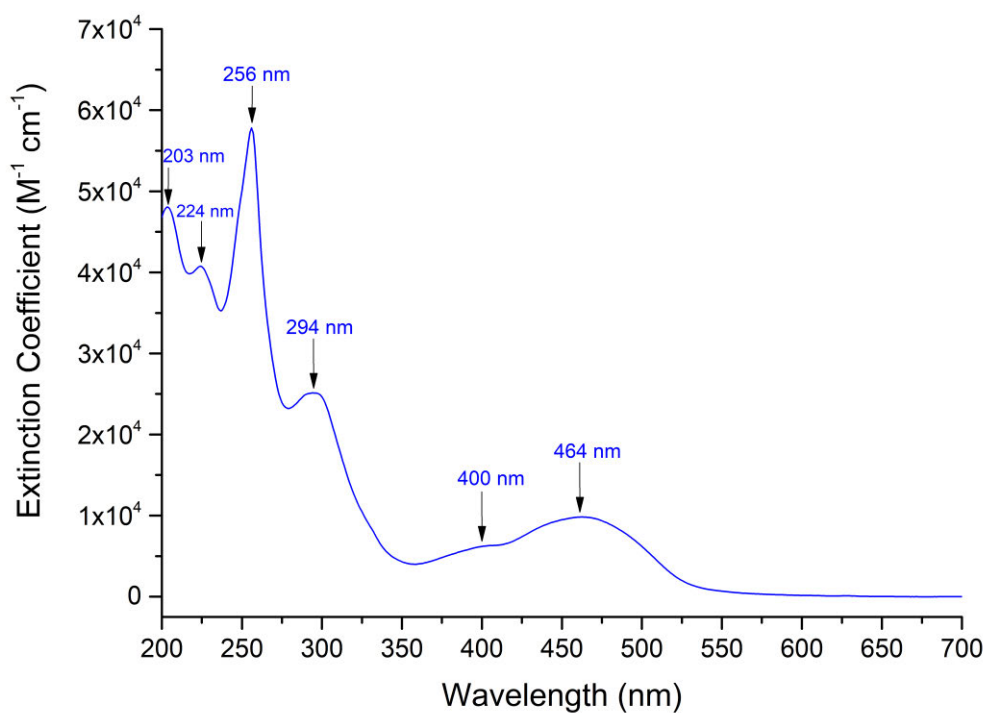


**Figure A89: UV/visible spectrum of [VO(CLA)(DPQ)].**  
**[VO(CLA)(DPQ)] =  $1.62 \times 10^{-5}$  M.**

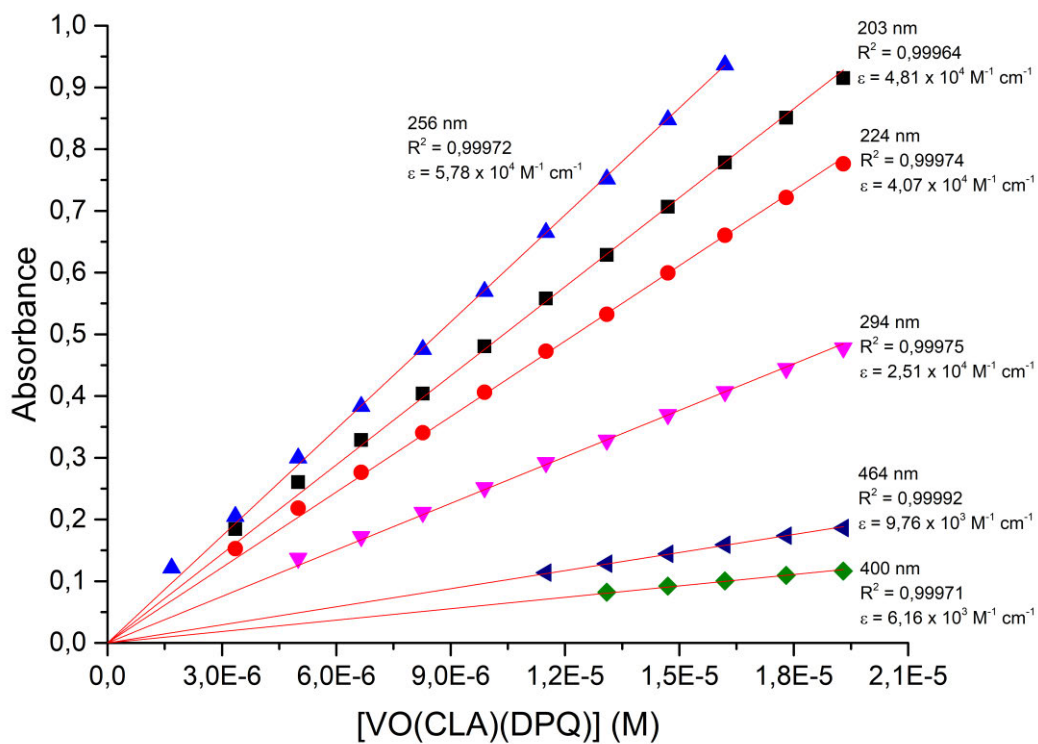


**Figure A90: Beer's Law Correlation of [VO(CLA)(DPQ)].**

### Single Mass Analysis

Tolerance = 5.0 PPM / DBE: min = -1.5, max = 100.0

Element prediction: Off

Number of isotope peaks used for i-FIT = 3

Monoisotopic Mass, Even Electron Ions

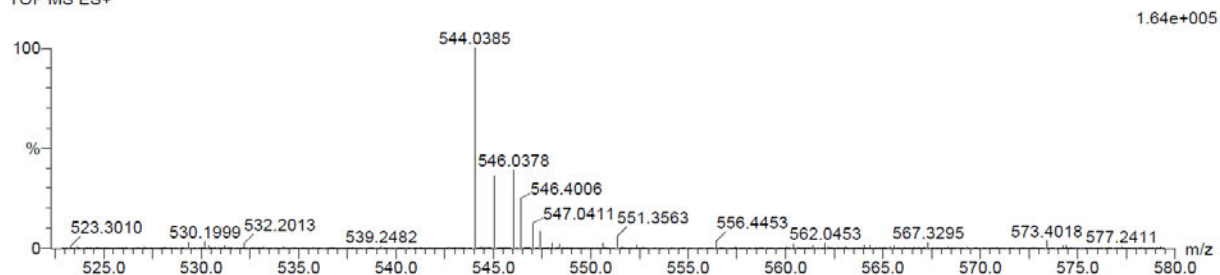
65 formula(e) evaluated with 1 results within limits (up to 20 closest results for each mass)

Elements Used:

C: 25-30 H: 15-20 N: 0-5 O: 0-5 Cl: 0-1 V: 0-1

VCIADPQ 5 (0.135) Cm (1:61)

TOF MS ES+



VCIADPQ I rms 60 (1.005) Cm (1:60)

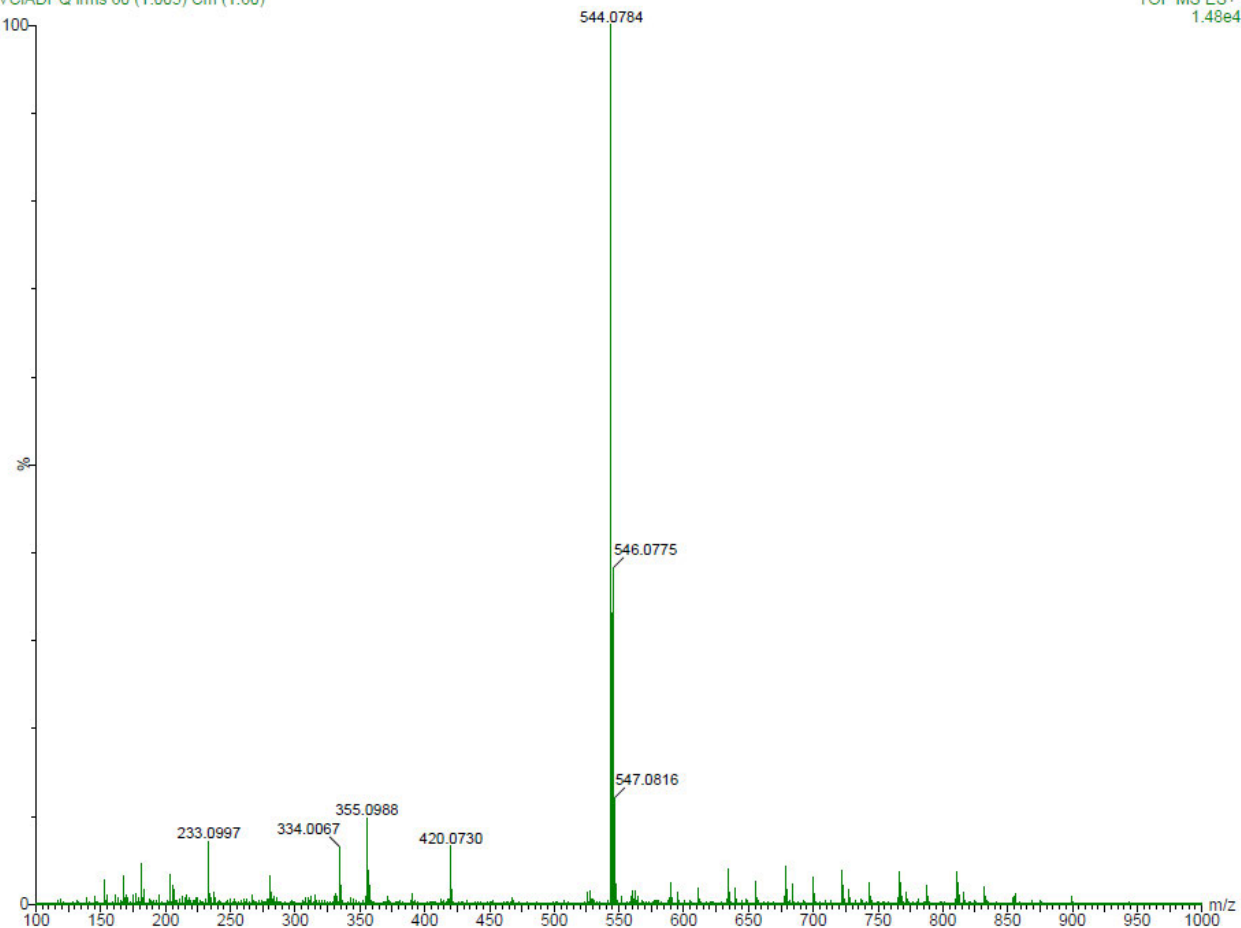


**Figure A91: High resolution ESI mass spectrum of [VO(CLA)(DPQ)] in chloroform.**

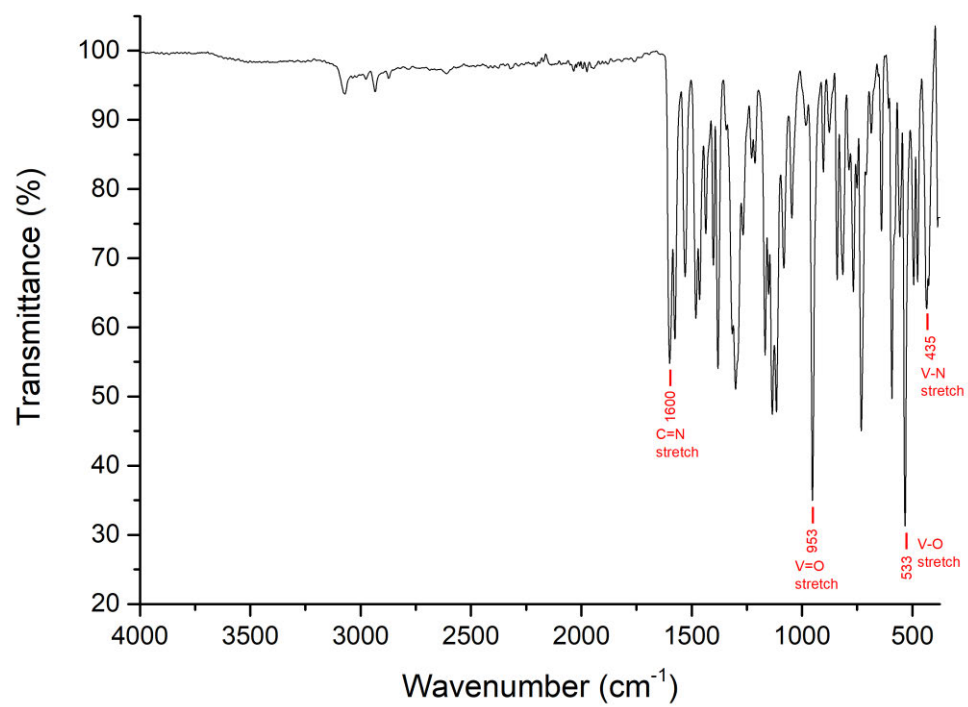


**Figure A92: IR spectrum of [VO(SOA)(DPQ)].**

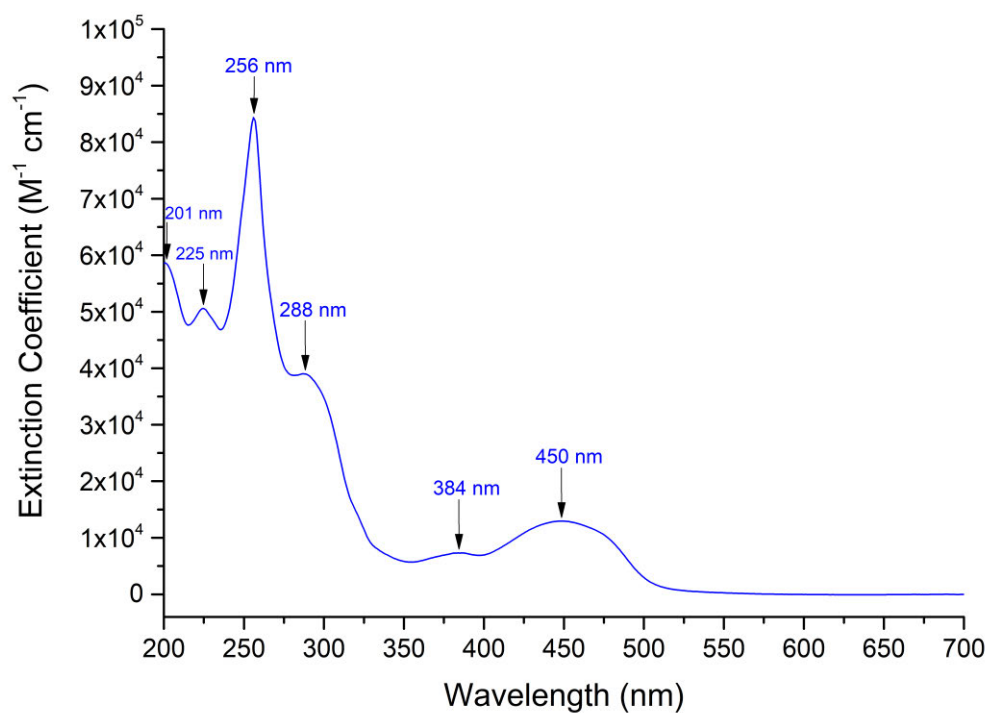


**Figure A93: UV/visible spectrum of [VO(SOA)(DPQ)].**  
**[VO(SOA)(DPQ)] =  $1.47 \times 10^{-5}$  M.**

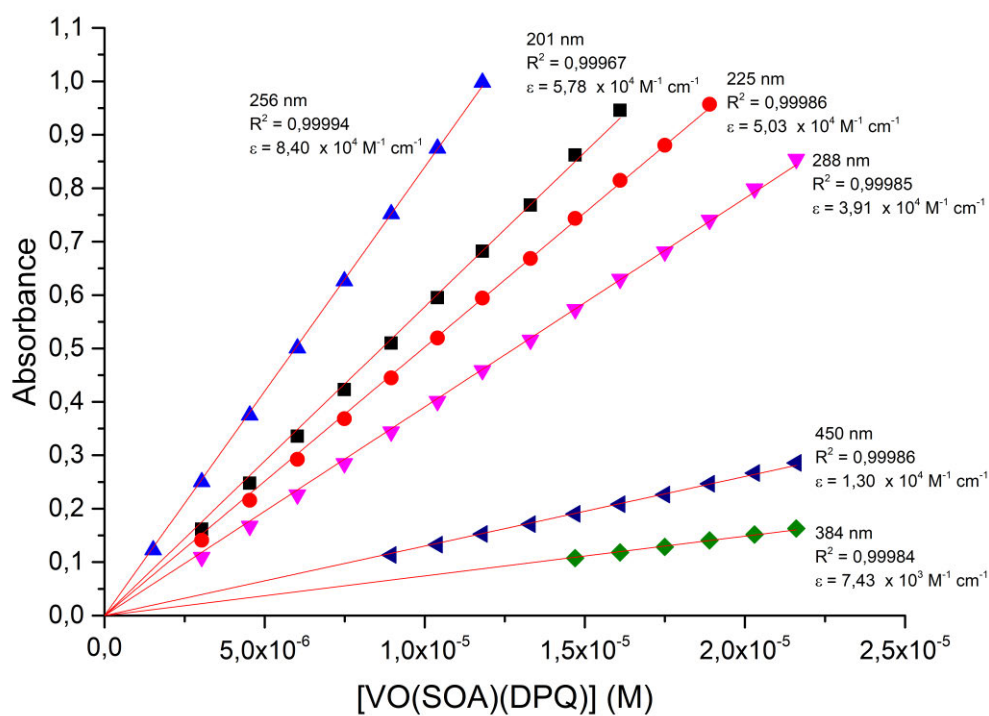


**Figure A94: Beer's Law Correlation of [VO(SOA)(DPQ)].**

### Single Mass Analysis

Tolerance = 5.0 PPM / DBE: min = -1.5, max = 100.0

Element prediction: Off

Number of isotope peaks used for i-FIT = 2

Monoisotopic Mass, Even Electron Ions

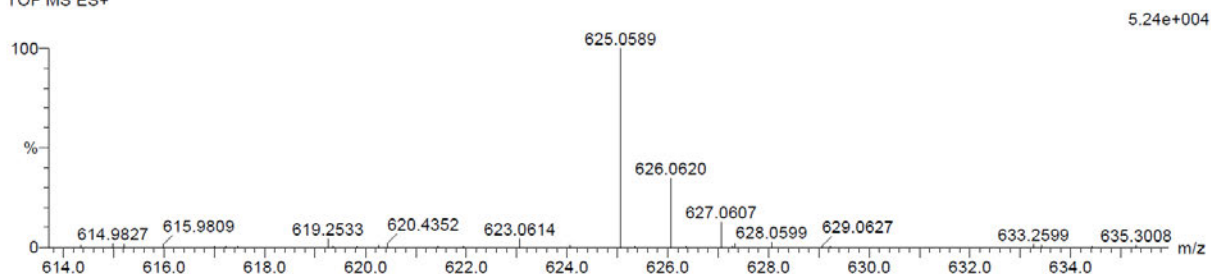
245 formula(e) evaluated with 1 results within limits (up to 20 best isotopic matches for each mass)

Elements Used:

C: 25-30 H: 20-25 N: 0-5 O: 0-5 Na: 0-1 S: 0-1 V: 0-1

VSOADPQ MeOH 55 (1.822) Cm (1:61)

TOF MS ES+



MS Spectrum  
VSOADPQ MeOH

ESI Positive

Spectrum Mode: Single 1.103(663) Base Peak: 633(1936208)  
BG Mode: Averaged 0.607-1.093(365-657) Segment 1 - Event 1

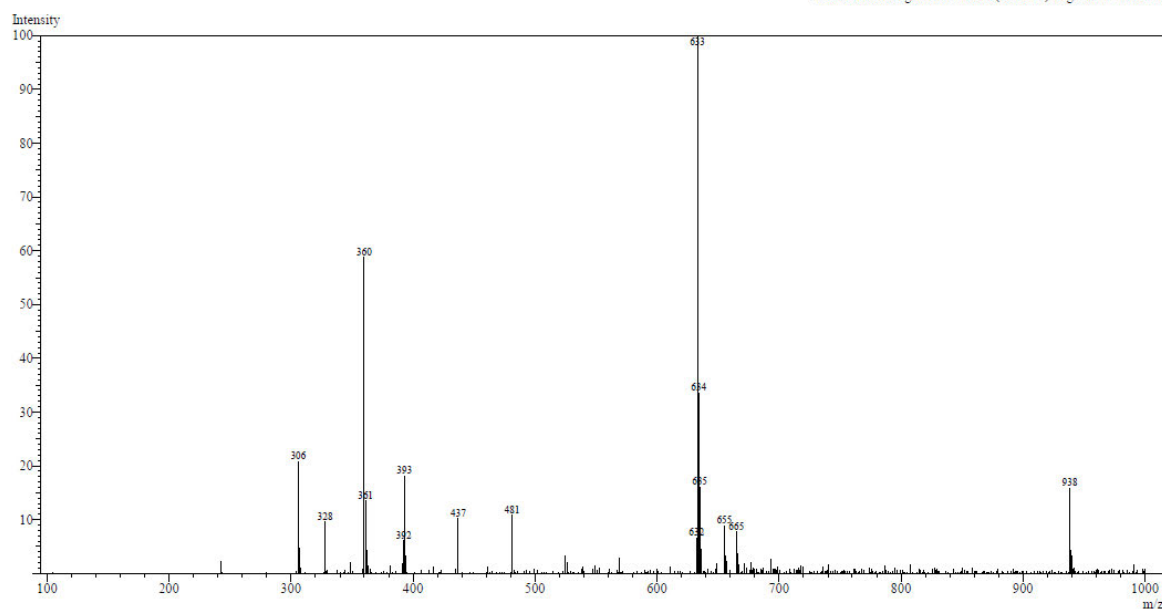


**Figure A95: High resolution ESI mass spectrum of [VO(SOA)(DPQ)] in methanol.**

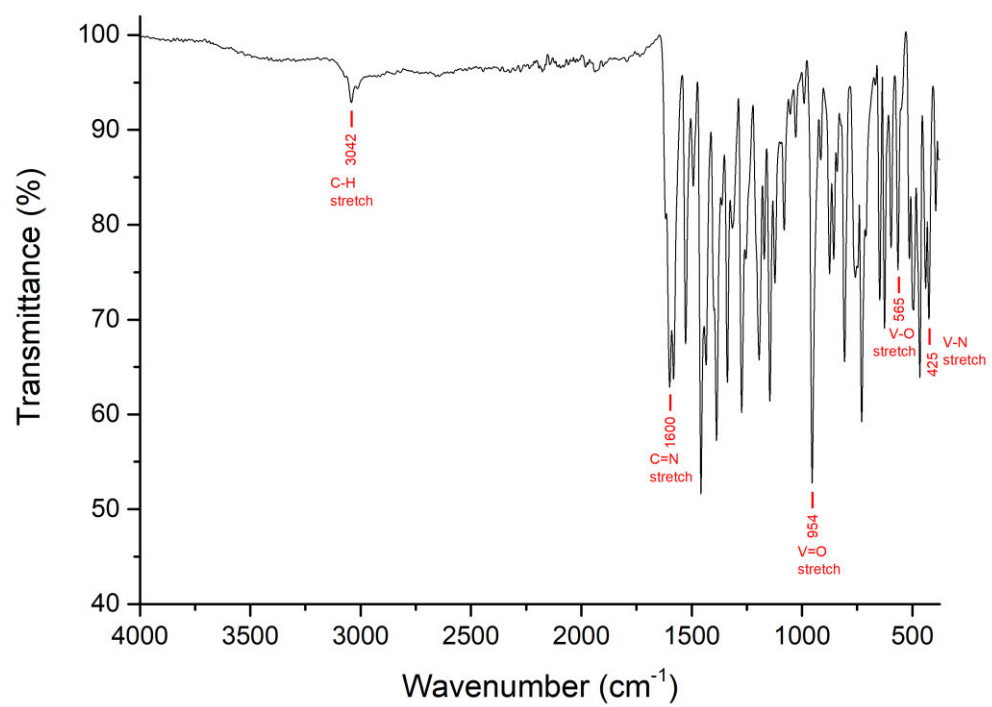


**Figure A96:** IR spectrum of [VO(NAA)(DPQ)].

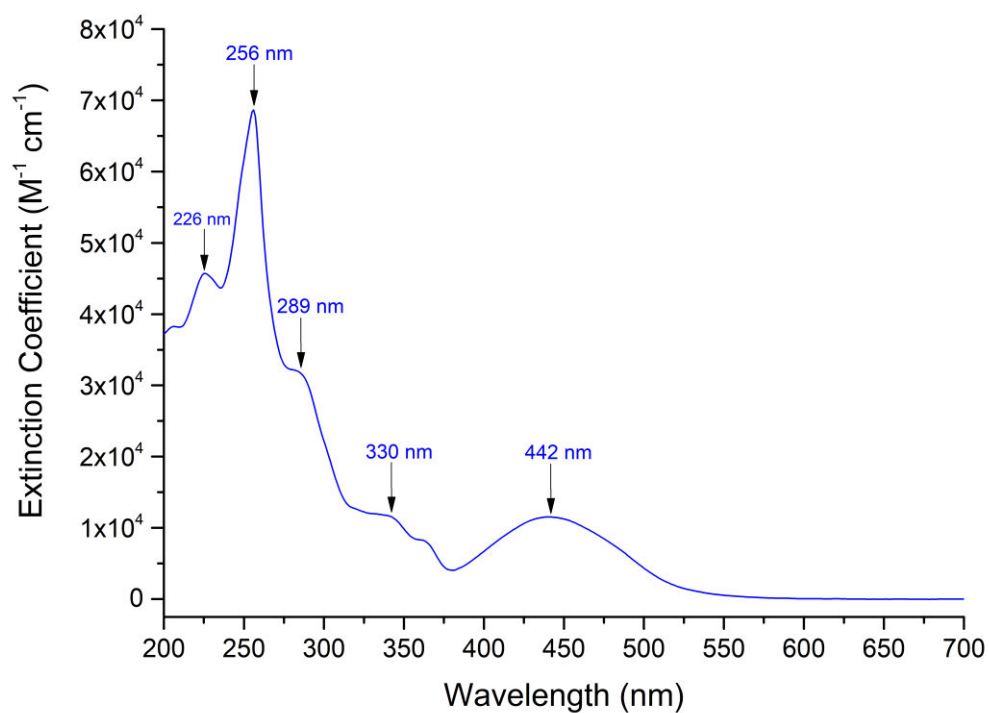


**Figure A97: UV/visible spectrum of [VO(NAA)(DPQ)].**  
**[VO(NAA)(DPQ)] =  $1.22 \times 10^{-5}$  M.**

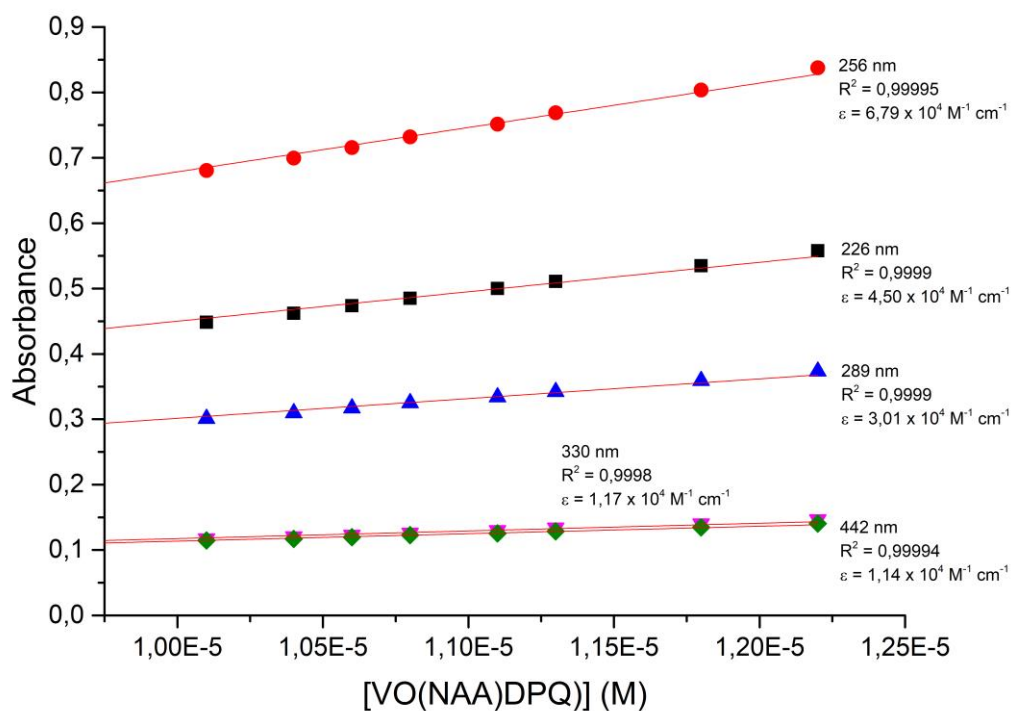


**Figure A98: Beer's Law Correlation of [VO(NAA)(DPQ)].**

### Single Mass Analysis

Tolerance = 5.0 PPM / DBE: min = -1.5, max = 100.0

Element prediction: Off

Number of isotope peaks used for i-FIT = 3

Monoisotopic Mass, Odd and Even Electron Ions

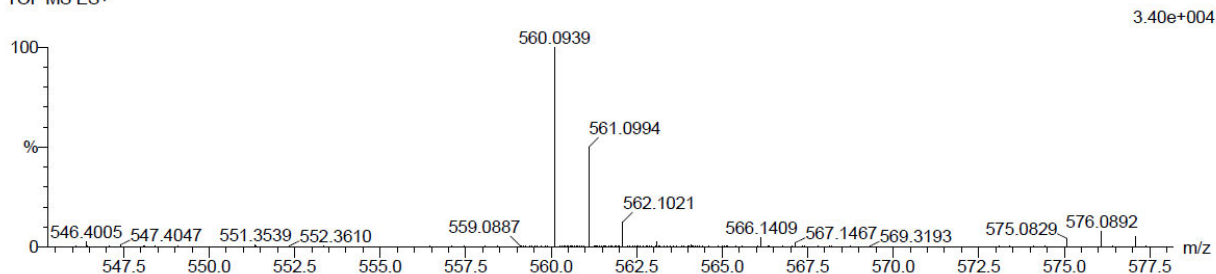
24 formula(e) evaluated with 1 results within limits (up to 20 closest results for each mass)

Elements Used:

C: 30-35 H: 15-20 N: 0-5 O: 0-5 V: 0-1

VNAADPQ 58 (1.922) Cm (1:61)

TOF MS ES+



VNAADPQ Ims 38 (0.630) Cm (2:60)

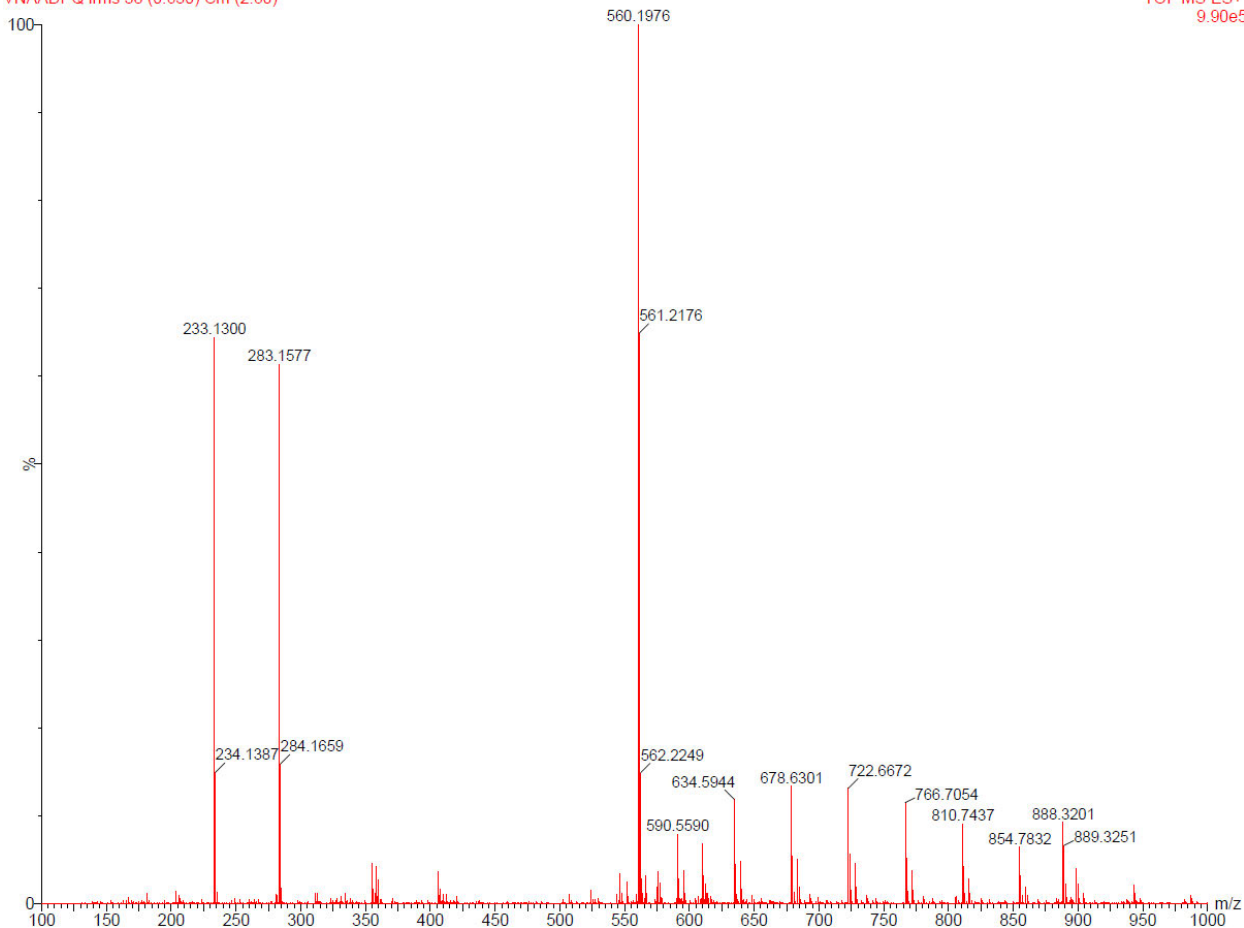


**Figure A99:** High resolution ESI mass spectrum of [VO(NAA)(DPQ)] in chloroform.

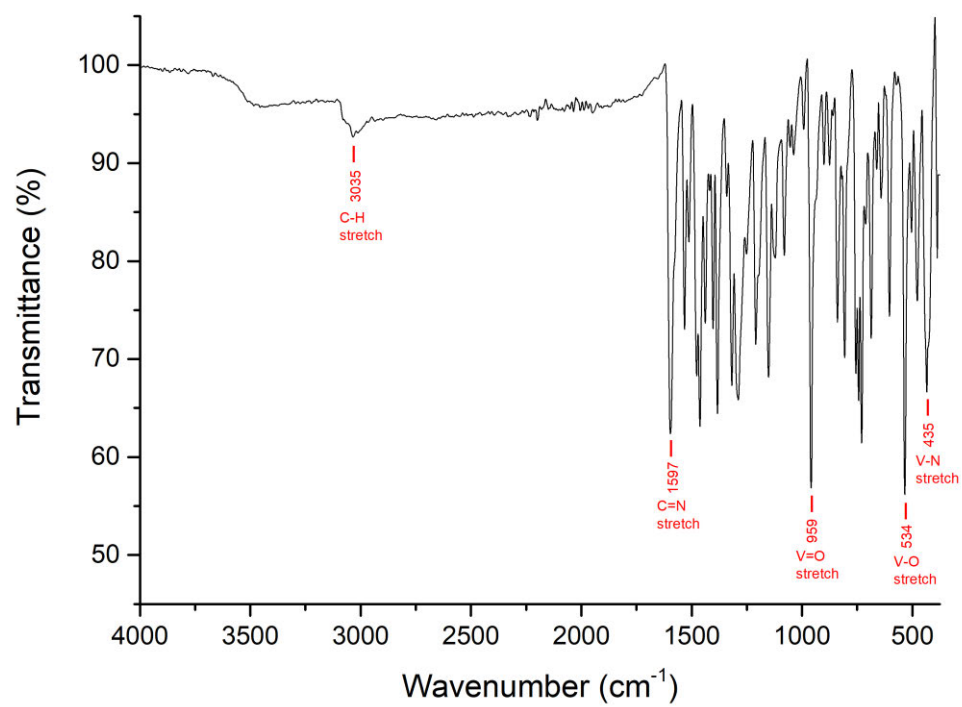


**Figure A100: IR spectrum of [VO(PHPA)(DPQ)].**

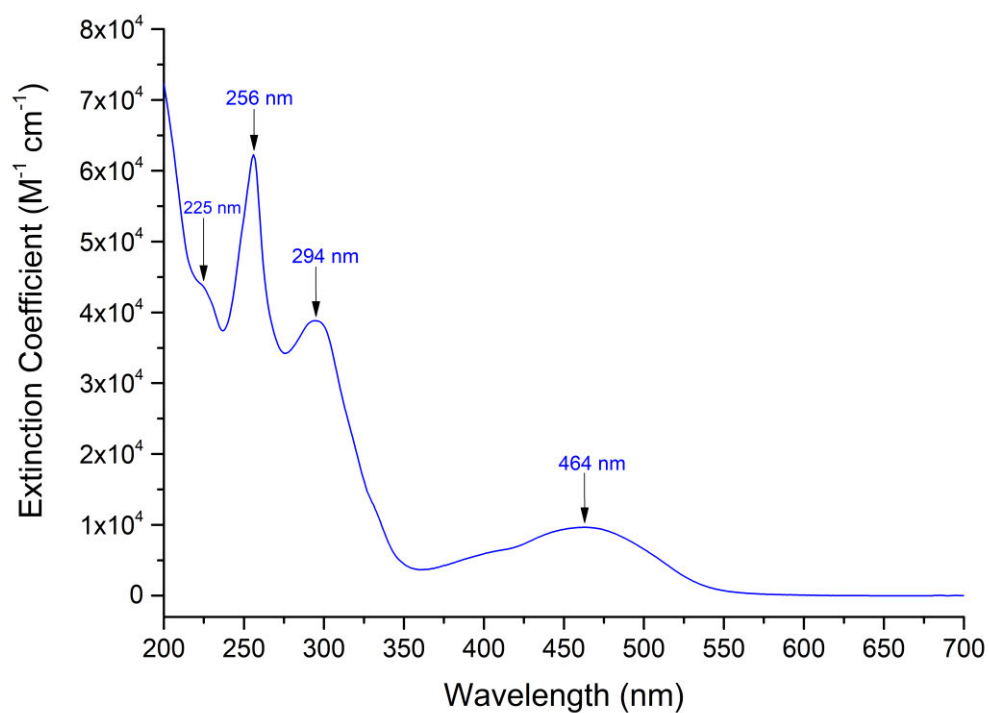


**Figure A101: UV/visible spectrum of [VO(PHPHA)(DPQ)].**  
**[VO(PHPHA)(DPQ)] =  $1.23 \times 10^{-5}$  M.**

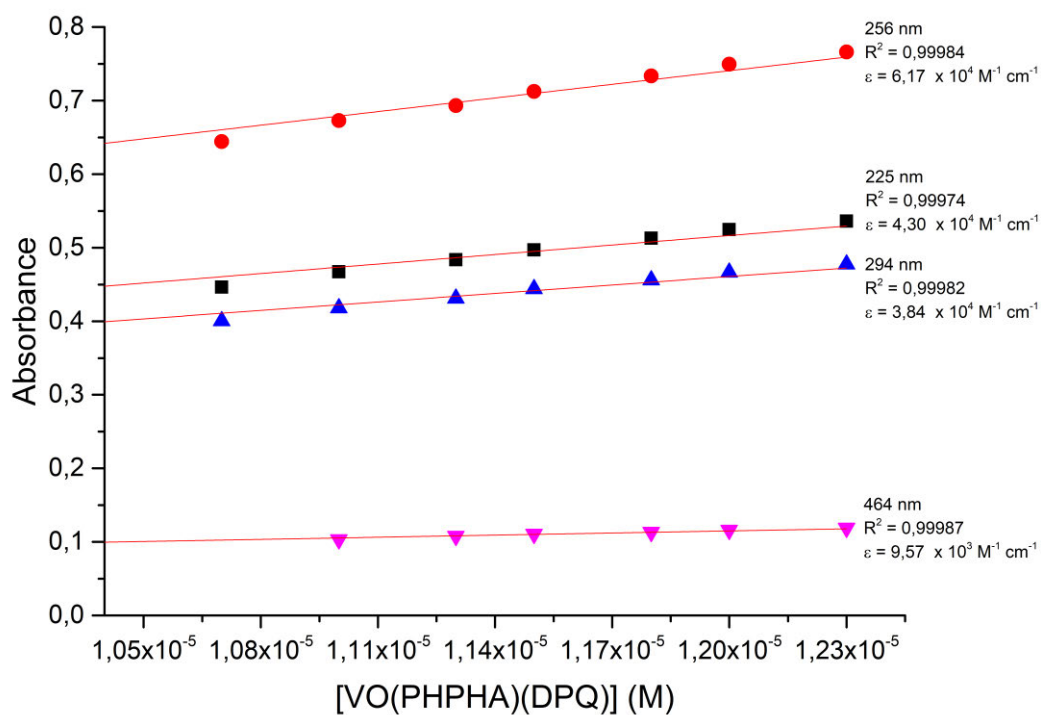


**Figure A102: Beer's Law Correlation of [VO(PHPHA)(DPQ)].**

### Single Mass Analysis

Tolerance = 5.0 PPM / DBE: min = -1.5, max = 100.0

Element prediction: Off

Number of isotope peaks used for i-FIT = 2

Monoisotopic Mass, Odd Electron Ions

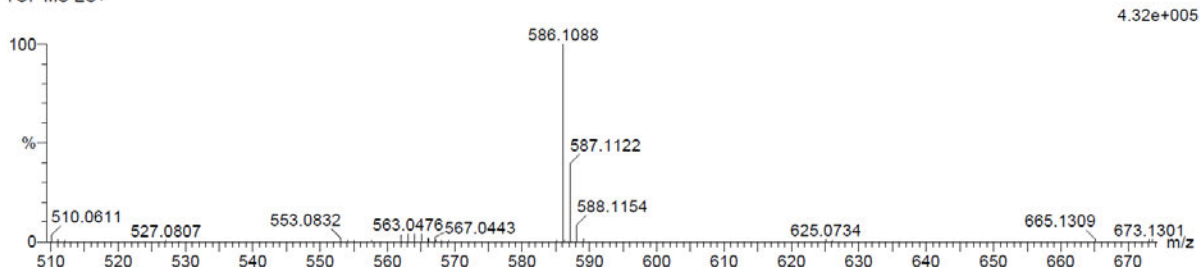
26 formula(e) evaluated with 1 results within limits (up to 20 best isotopic matches for each mass)

Elements Used:

C: 30-35 H: 20-25 N: 0-5 O: 0-5 V: 0-1

VPHPHADPQ 35 (1.147) Cm (1:61)

TOF MS ES+



VPHPHADPQ I rms 47 (0.784) Cm (1:60)

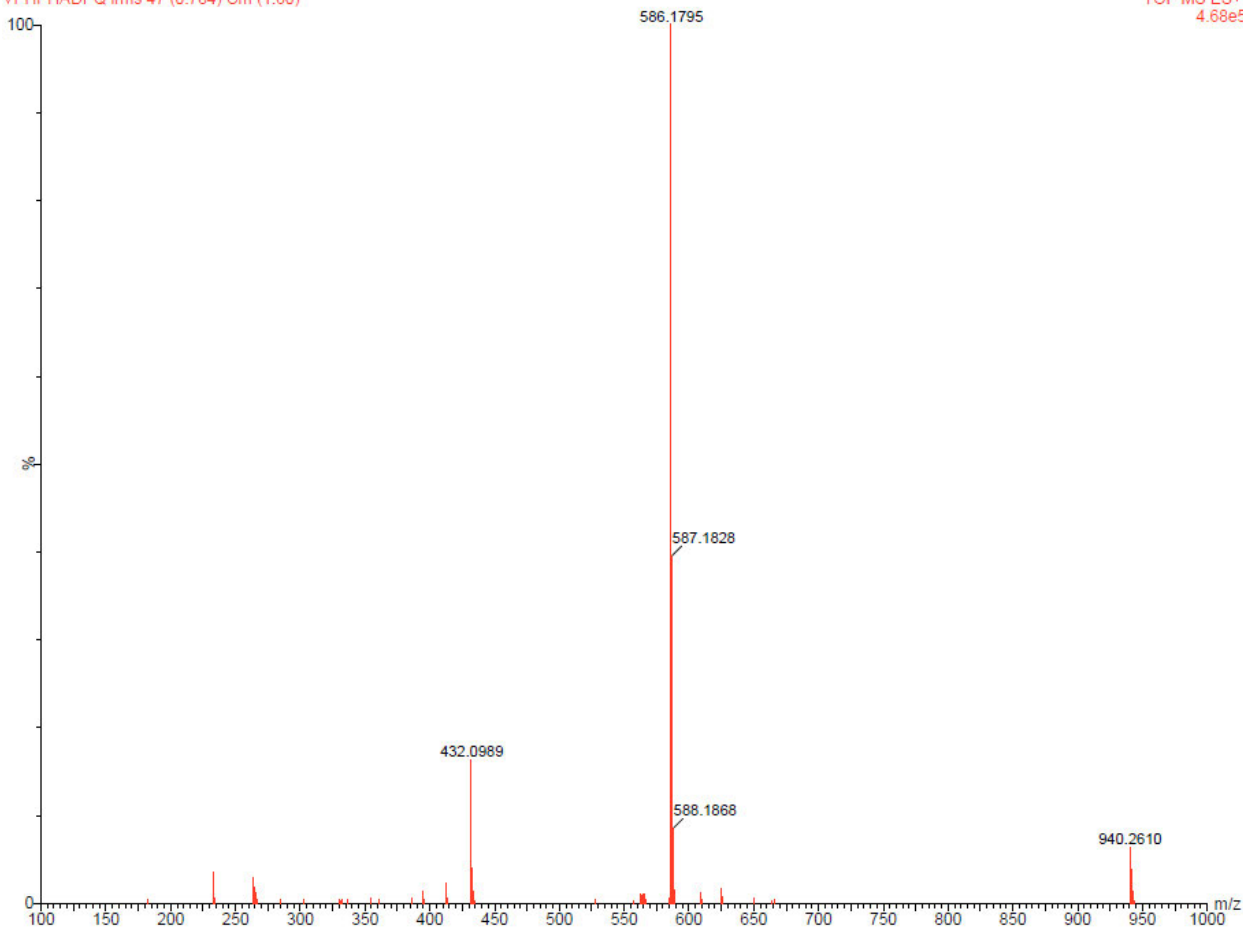


**Figure A103: High resolution ESI mass spectrum of [VO(PHPHA)(DPQ)] in acetonitrile.**

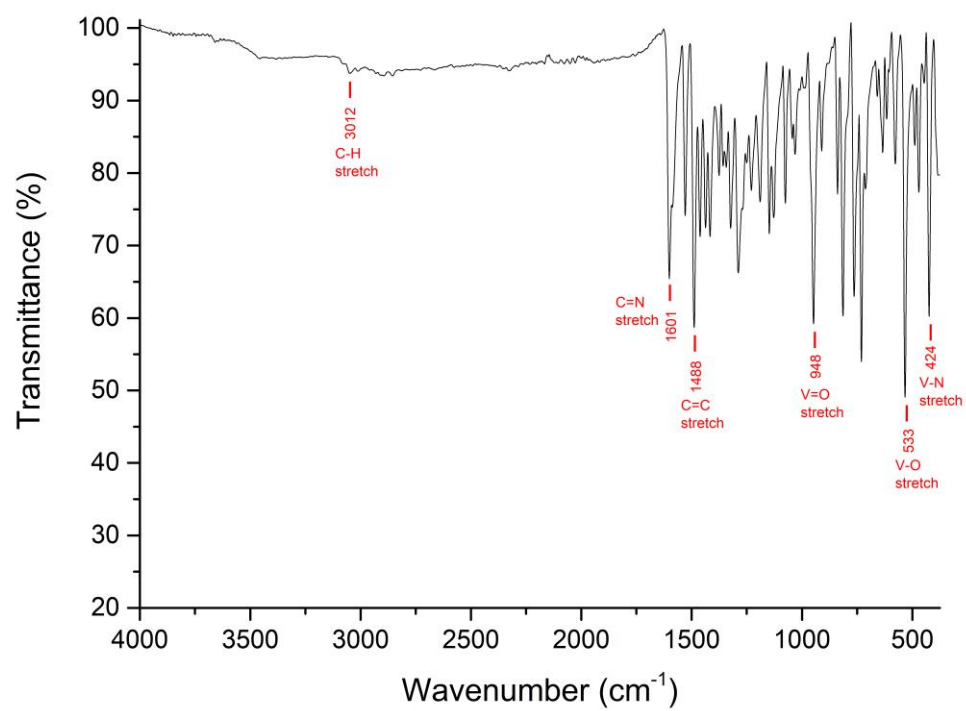


**Figure A104: IR spectrum of [VO(MEA)(DPPZ)].**

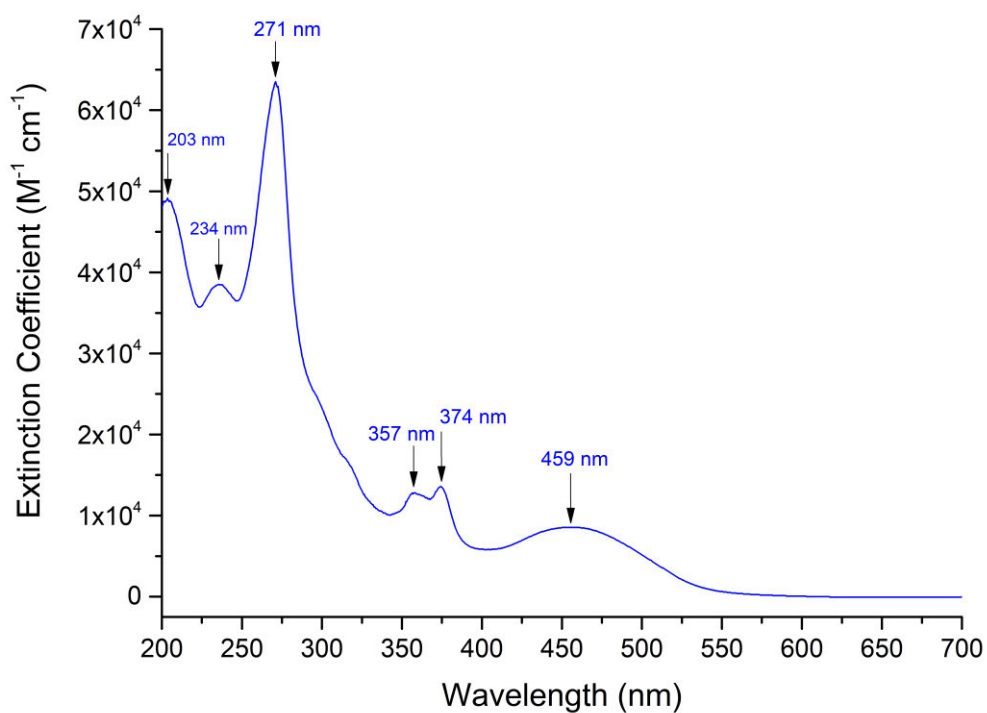


**Figure A105: UV/visible spectrum of [VO(MEA)(DPPZ)].**  
**[VO(MEA)(DPPZ)] =  $1.57 \times 10^{-5}$  M.**

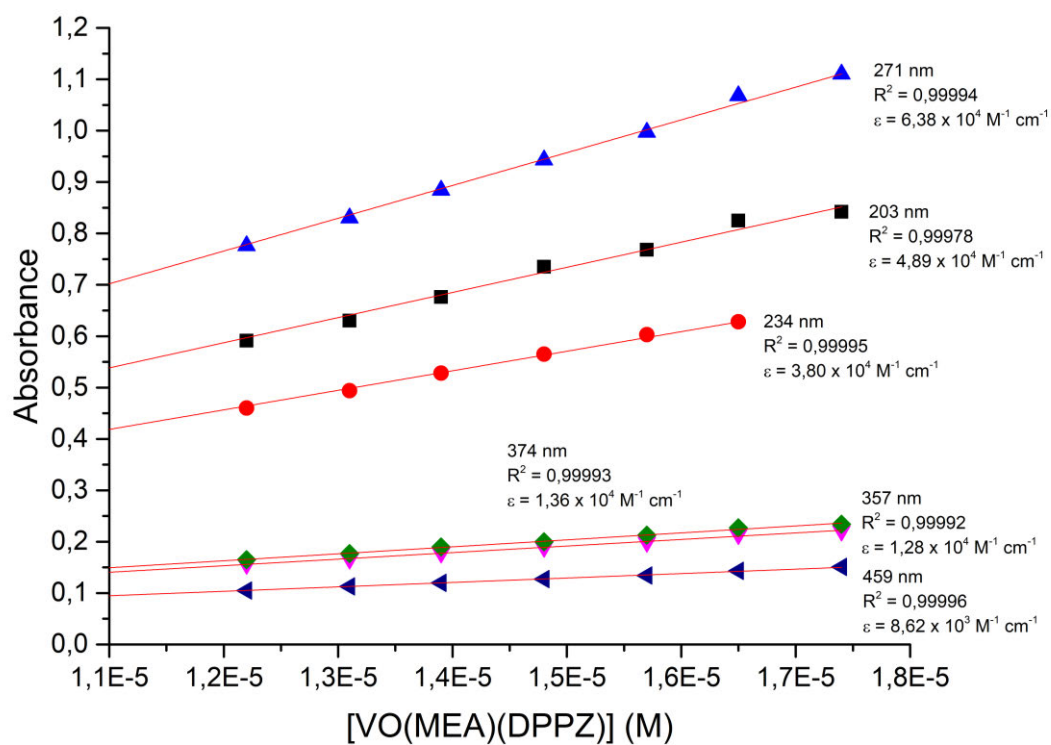


**Figure A106: Beer's Law Correlation of [VO(MEA)(DPPZ)]**

### Single Mass Analysis

Tolerance = 5.0 PPM / DBE: min = -1.5, max = 50.0

Element prediction: Off

Number of isotope peaks used for i-FIT = 3

Monoisotopic Mass, Odd Electron Ions

22 formula(e) evaluated with 1 results within limits (up to 50 best isotopic matches for each mass)

Elements Used:

C: 30-35 H: 20-25 N: 0-5 O: 0-5 V: 0-1

VMEADPPZ(6) rpt 33 (0.546) Cm (1:119)

TOF MS ES+

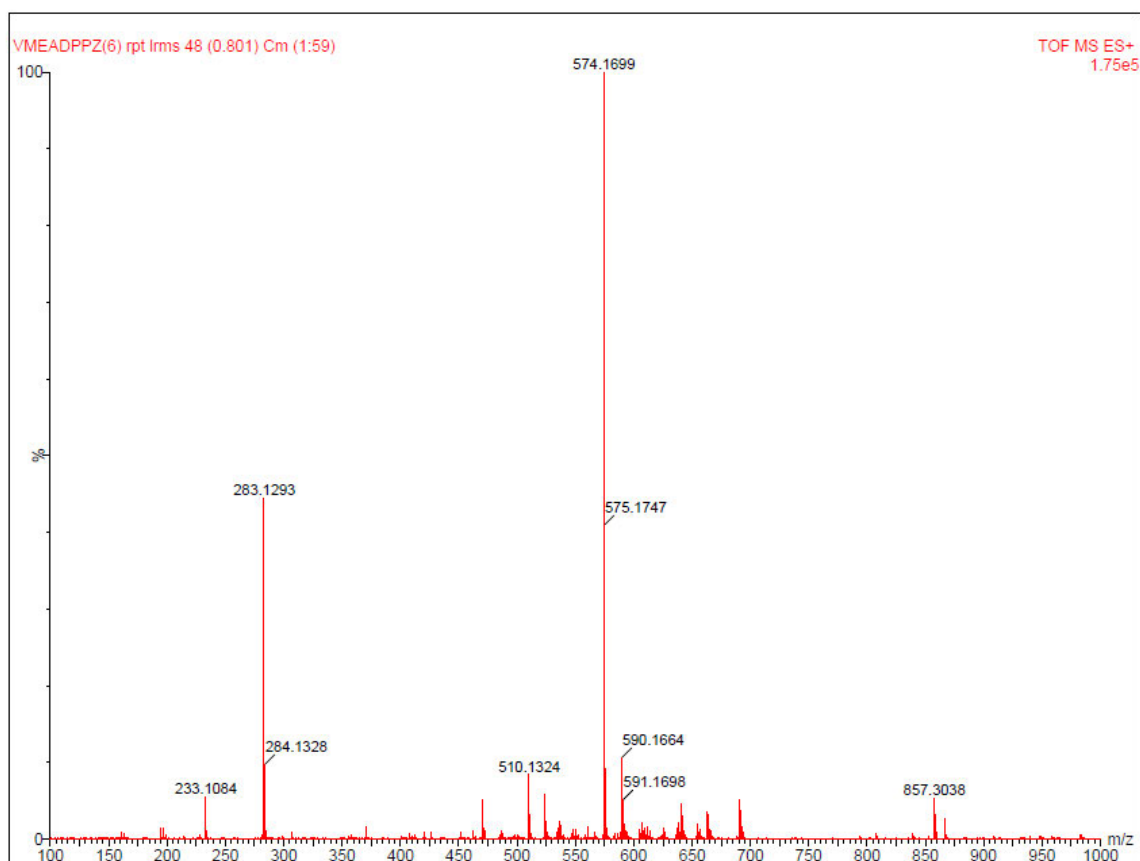
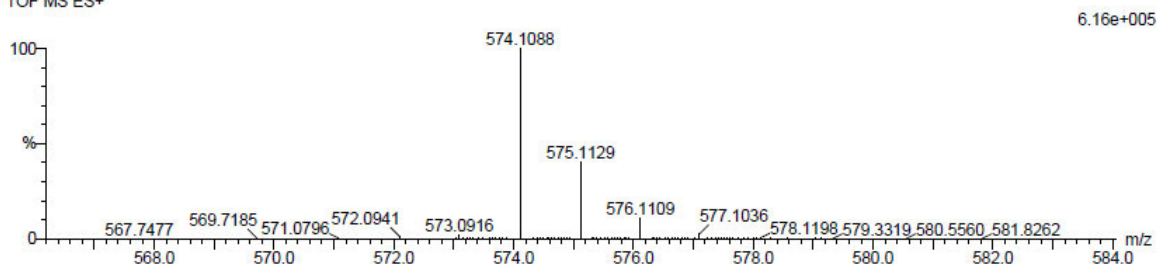


**Figure A107: High resolution ESI mass spectrum of [VO(MEA)(DPPZ)] in dichloromethane.**

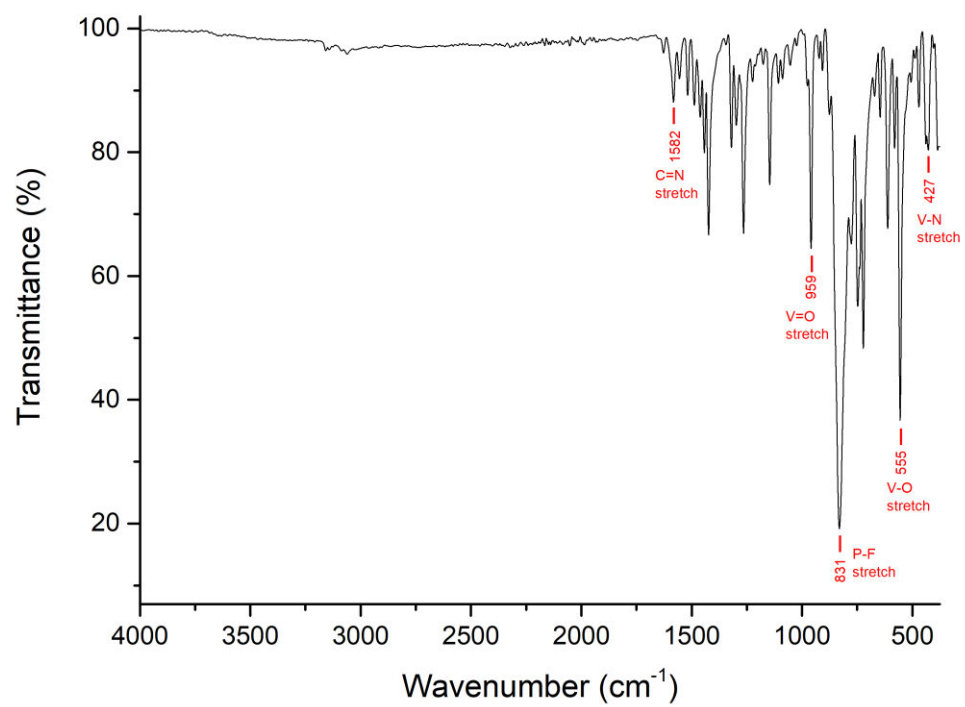


**Figure A108: IR spectrum of [VO(PHCA)(PHEN)](PF<sub>6</sub>).**

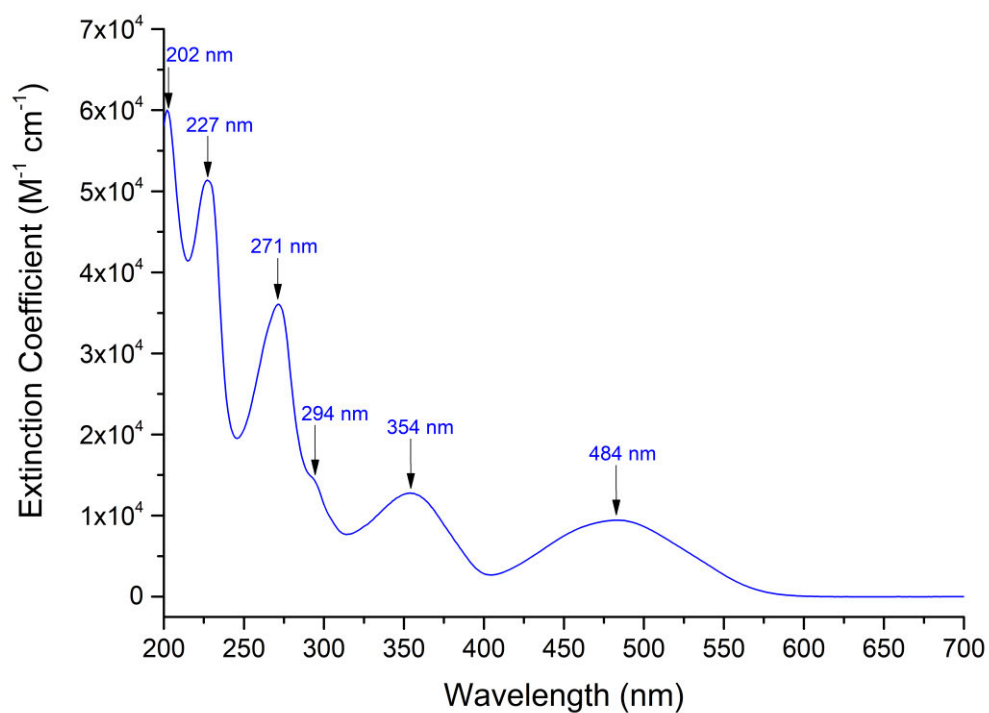


**Figure A109: UV/visible spectrum of [VO(PHCA)(PHEN)](PF<sub>6</sub>).**  
**[VO(PHCA)(PHEN)](PF<sub>6</sub>) = 1.64 x 10<sup>-5</sup> M.**

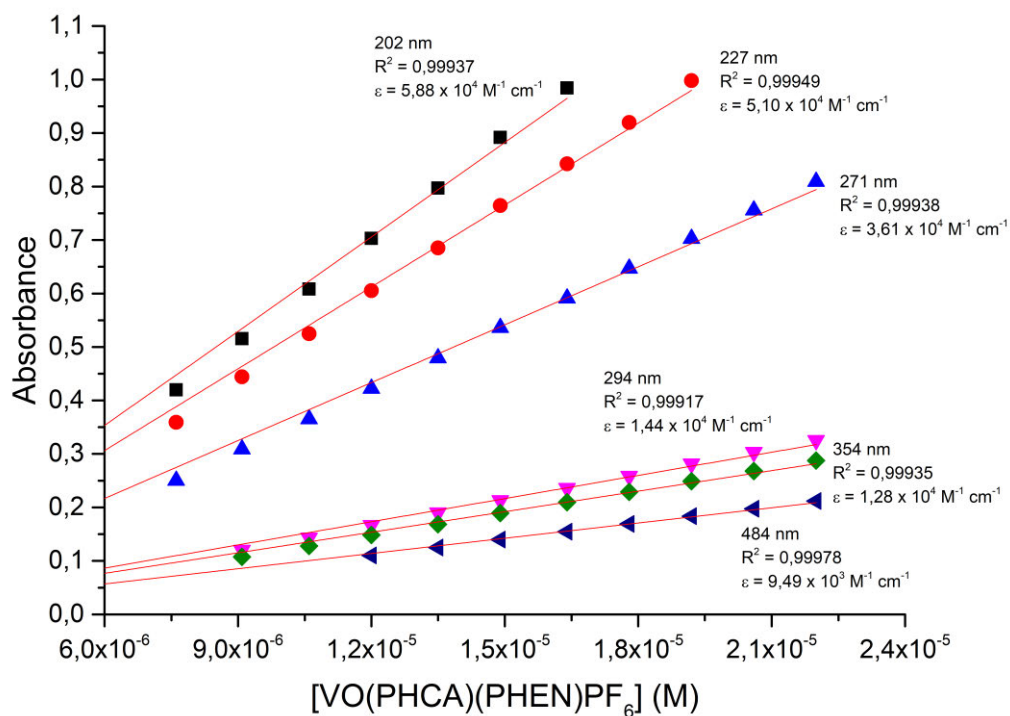


**Figure A110: Beer's Law Correlation of [VO(PHCA)(PHEN)](PF<sub>6</sub>).**

### Single Mass Analysis

Tolerance = 5.0 PPM / DBE: min = -1.5, max = 50.0

Element prediction: Off

Number of isotope peaks used for i-FIT = 2

Monoisotopic Mass, Even Electron Ions

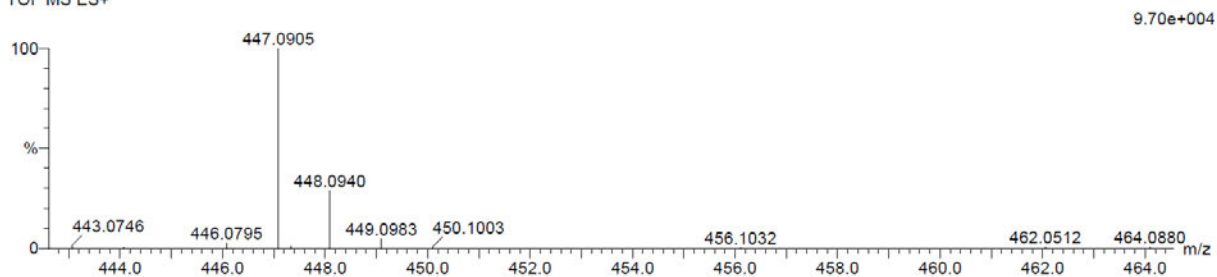
30 formula(e) evaluated with 1 results within limits (up to 20 closest results for each mass)

Elements Used:

C: 20-25 H: 15-20 N: 0-5 O: 0-5 V: 0-1

VPHCAPHENPF6(2) AN 20 (0.641) Cm (1:81)

TOF MS ES+



VPHCAPHENPF6(2) AN lms 60 (1.006) Cm (1:60)

TOF MS ES+  
3.85e5

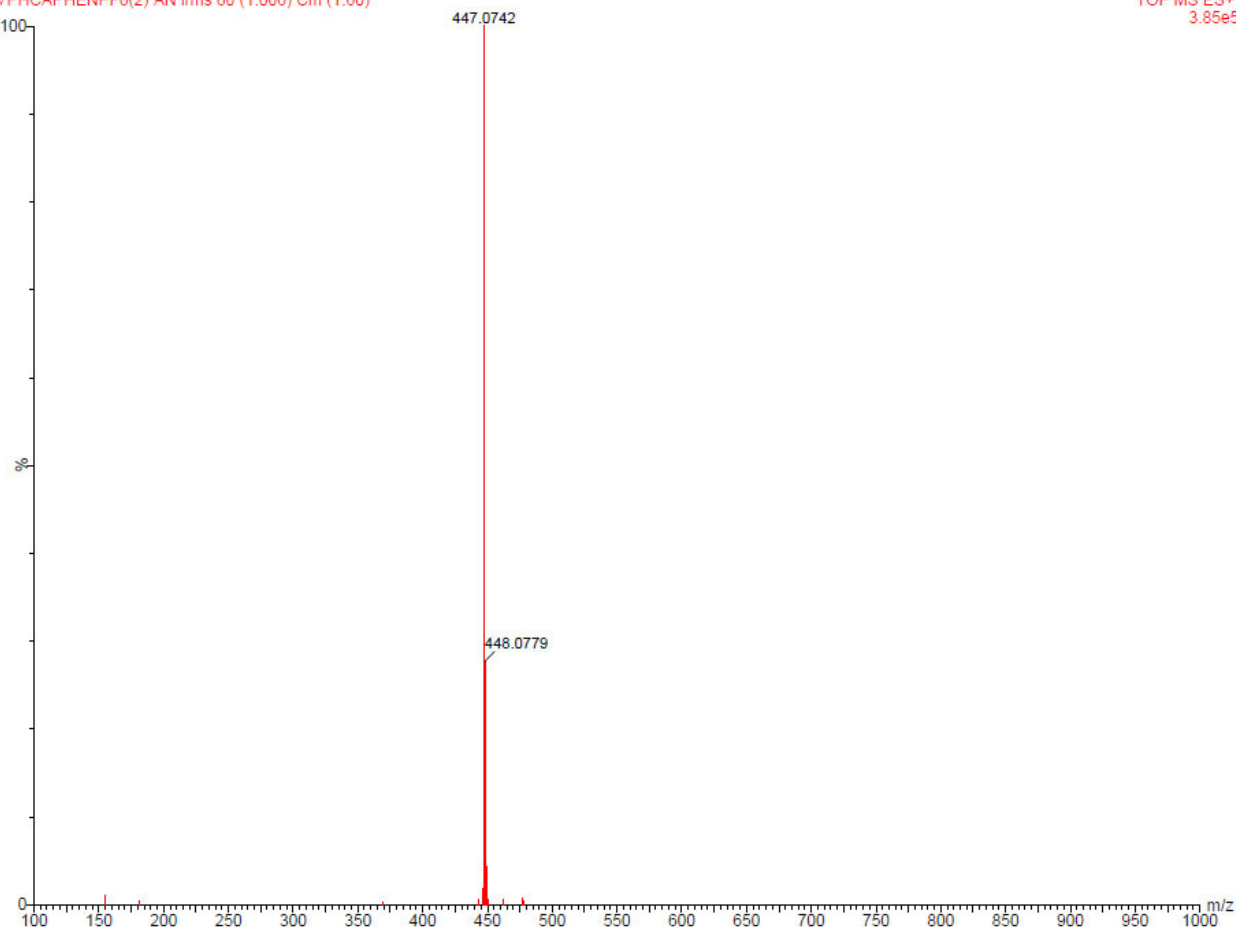


**Figure A111: High resolution ESI mass spectrum of [VO(PHCA)(PHEN)](PF<sub>6</sub>) in acetonitrile.**

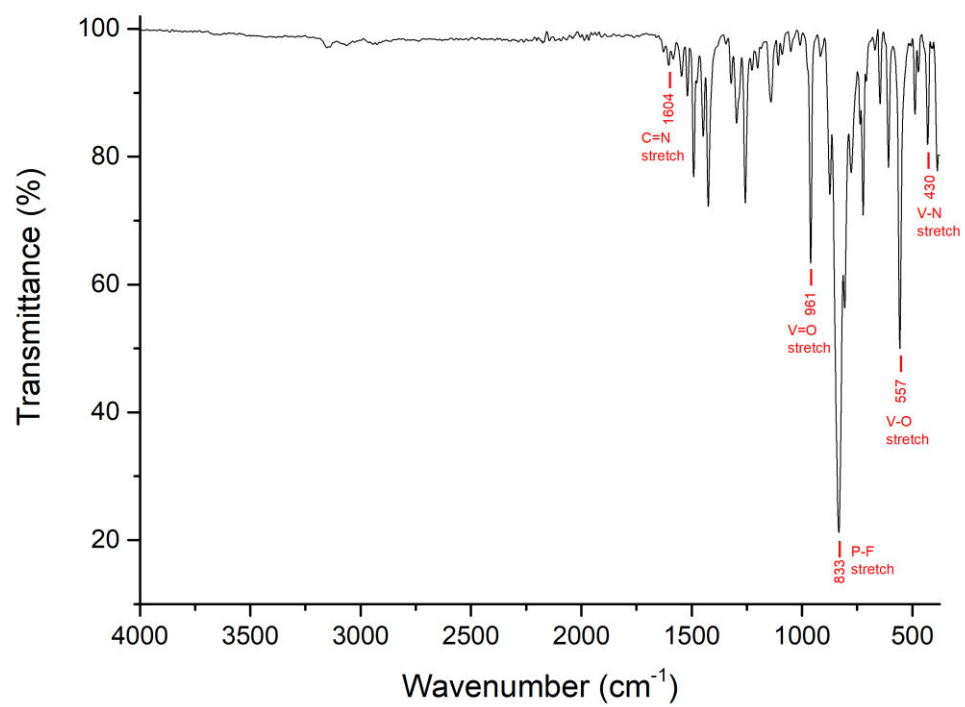


**Figure A112: IR spectrum of [VO(MECA)(PHEN)](PF<sub>6</sub>).**

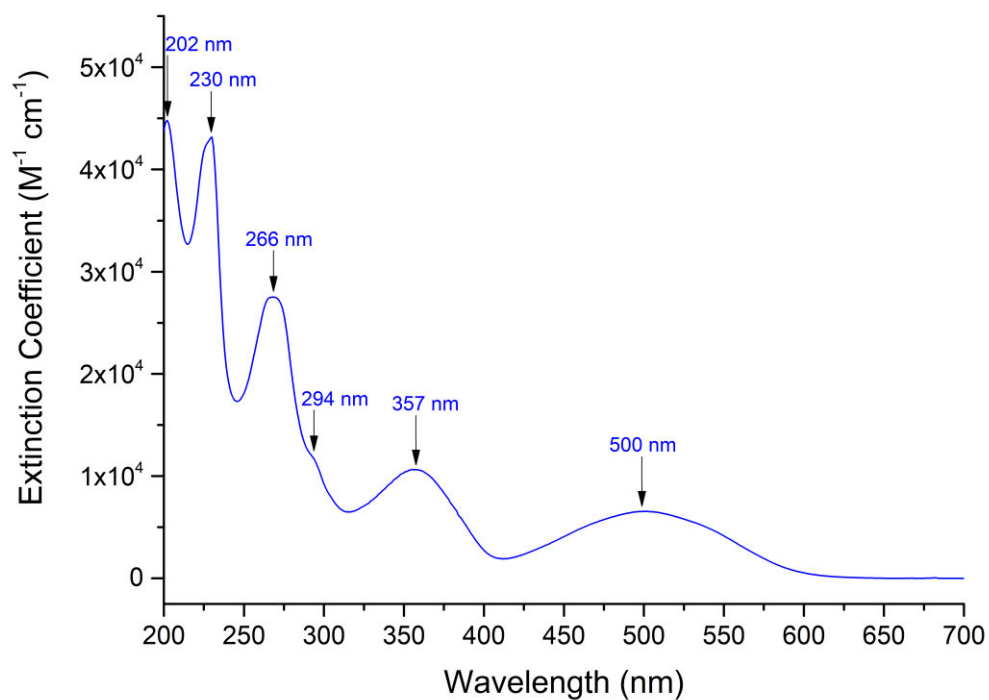


**Figure A113: UV/visible spectrum of [VO(MECA)(PHEN)](PF<sub>6</sub>).  
[VO(MECA)(PHEN)](PF<sub>6</sub>) = 2.10 x 10<sup>-5</sup> M.**

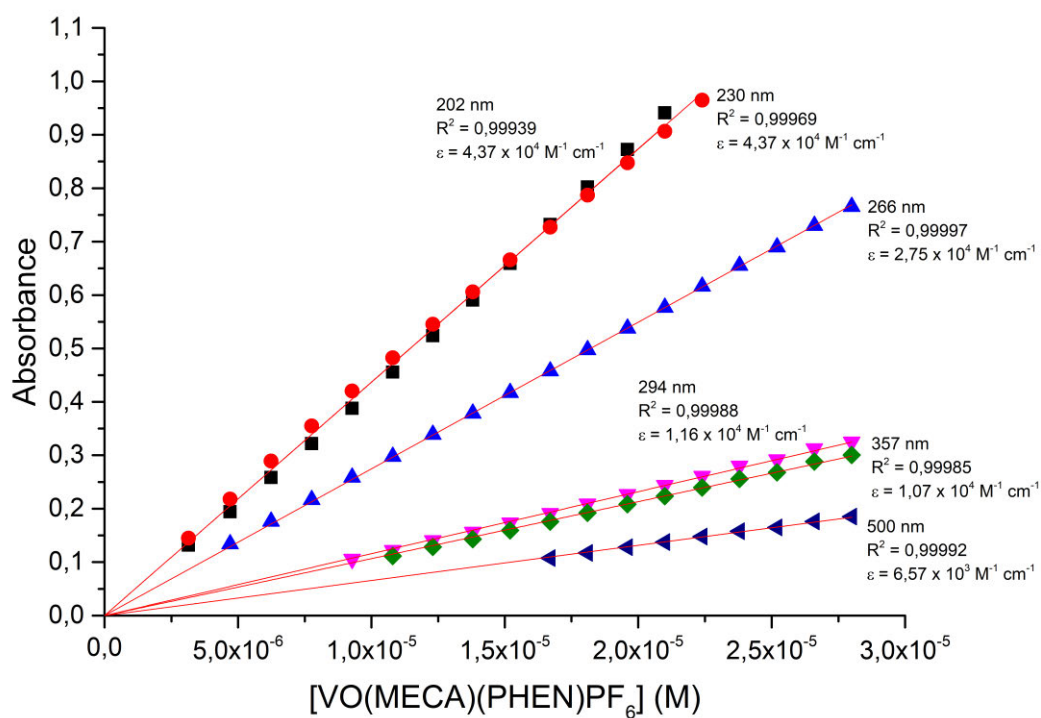


**Figure A114: Beer's Law Correlation of [VO(MECA)(PHEN)](PF<sub>6</sub>).**

### Single Mass Analysis

Tolerance = 5.0 PPM / DBE: min = -1.5, max = 100.0

Element prediction: Off

Number of isotope peaks used for i-FIT = 3

Monoisotopic Mass, Even Electron Ions

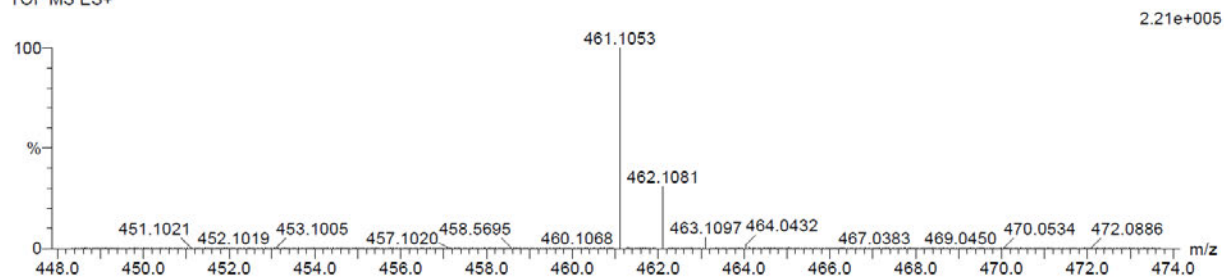
29 formula(e) evaluated with 1 results within limits (up to 20 closest results for each mass)

Elements Used:

C: 20-25 H: 20-25 N: 5-10 O: 0-5 V: 0-1

VMECA Phen PF6 recryst 38 (1.249) Cm (1:61)

TOF MS ES+



VMECA Phen PF6 recryst lms 17 (0.273) Cm (1:59)

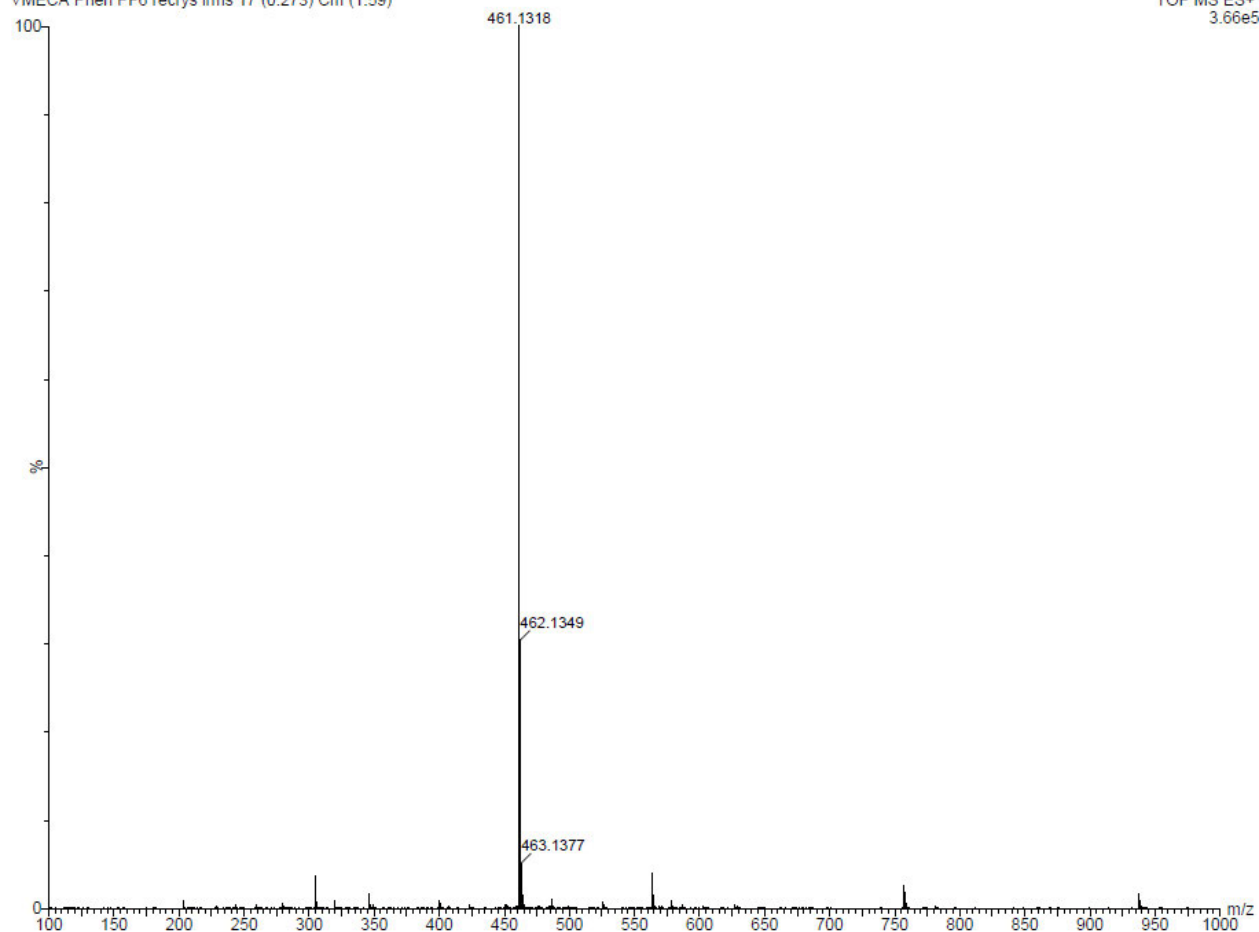


**Figure A115: High resolution ESI mass spectrum of [VO(MECA)(PHEN)](PF<sub>6</sub>) in acetonitrile.**

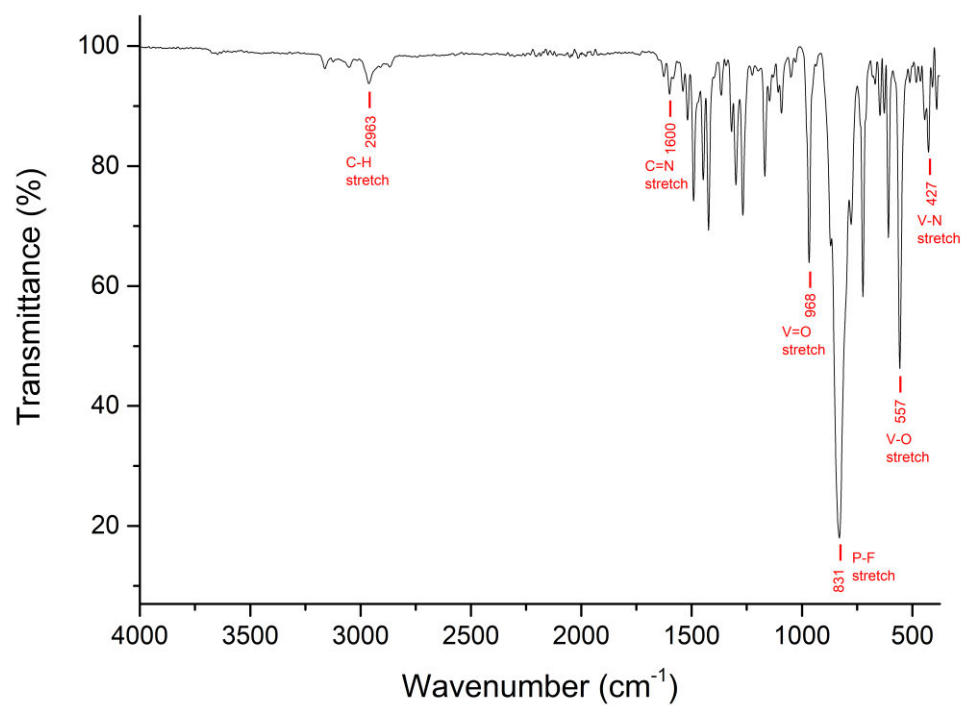


**Figure A116: IR spectrum of [VO(TERTCA)(PHEN)](PF<sub>6</sub>).**

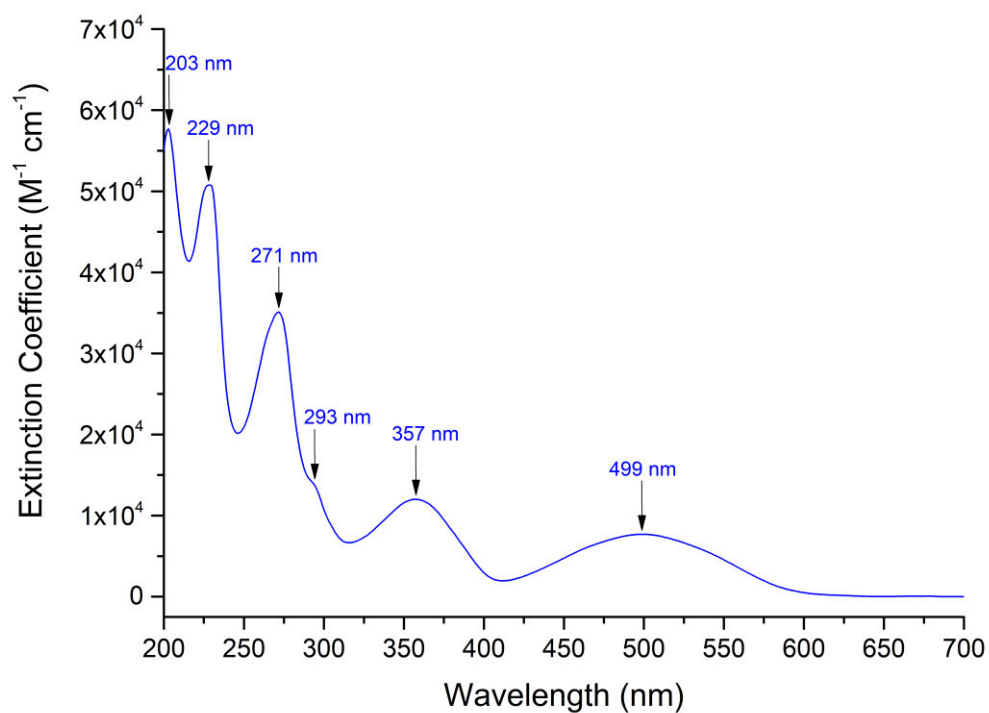


**Figure A117: UV/visible spectrum of [VO(TERTCA)(PHEN)](PF<sub>6</sub>).  
[VO(TERTCA)(PHEN)](PF<sub>6</sub>) = 1.63 x 10<sup>-5</sup> M.**

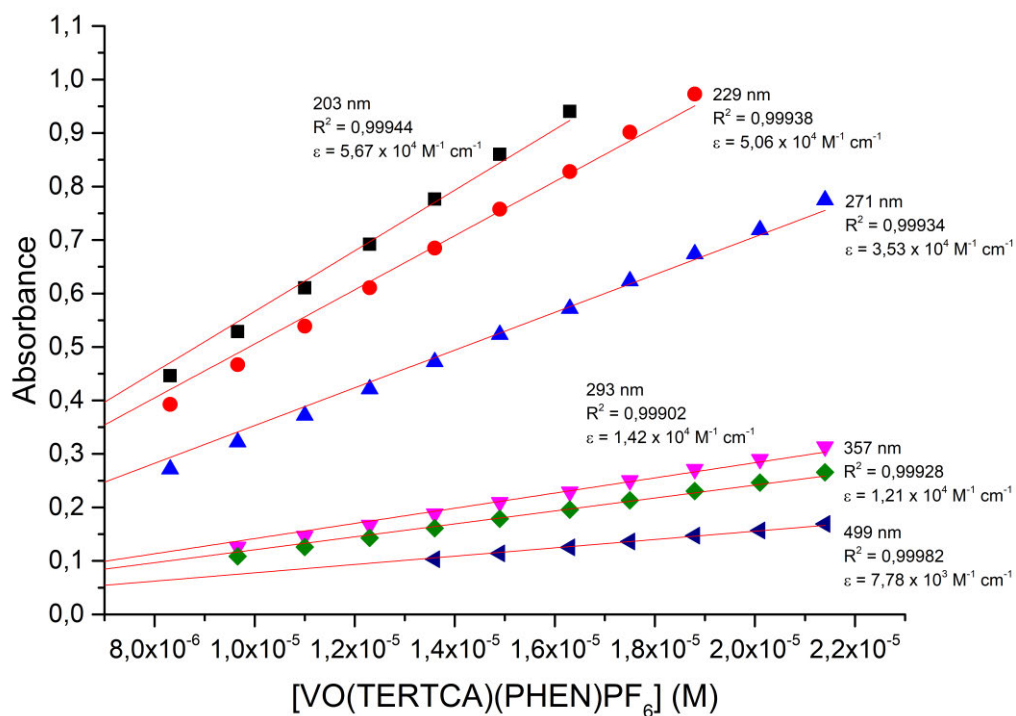


**Figure A118: Beer's Law Correlation of [VO(TERTCA)(PHEN)](PF<sub>6</sub>).**

### Single Mass Analysis

Tolerance = 5.0 PPM / DBE: min = -1.5, max = 50.0

Element prediction: Off

Number of isotope peaks used for i-FIT = 2

Monoisotopic Mass, Even Electron Ions

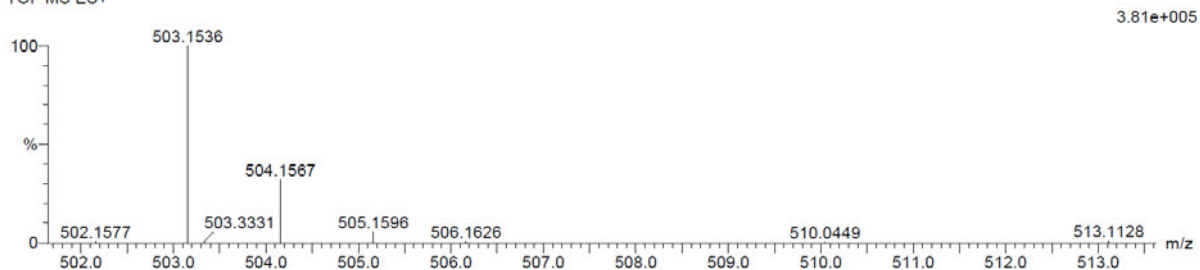
22 formula(e) evaluated with 1 results within limits (up to 20 closest results for each mass)

Elements Used:

C: 25-30 H: 25-30 N: 0-5 O: 0-5 V: 0-1

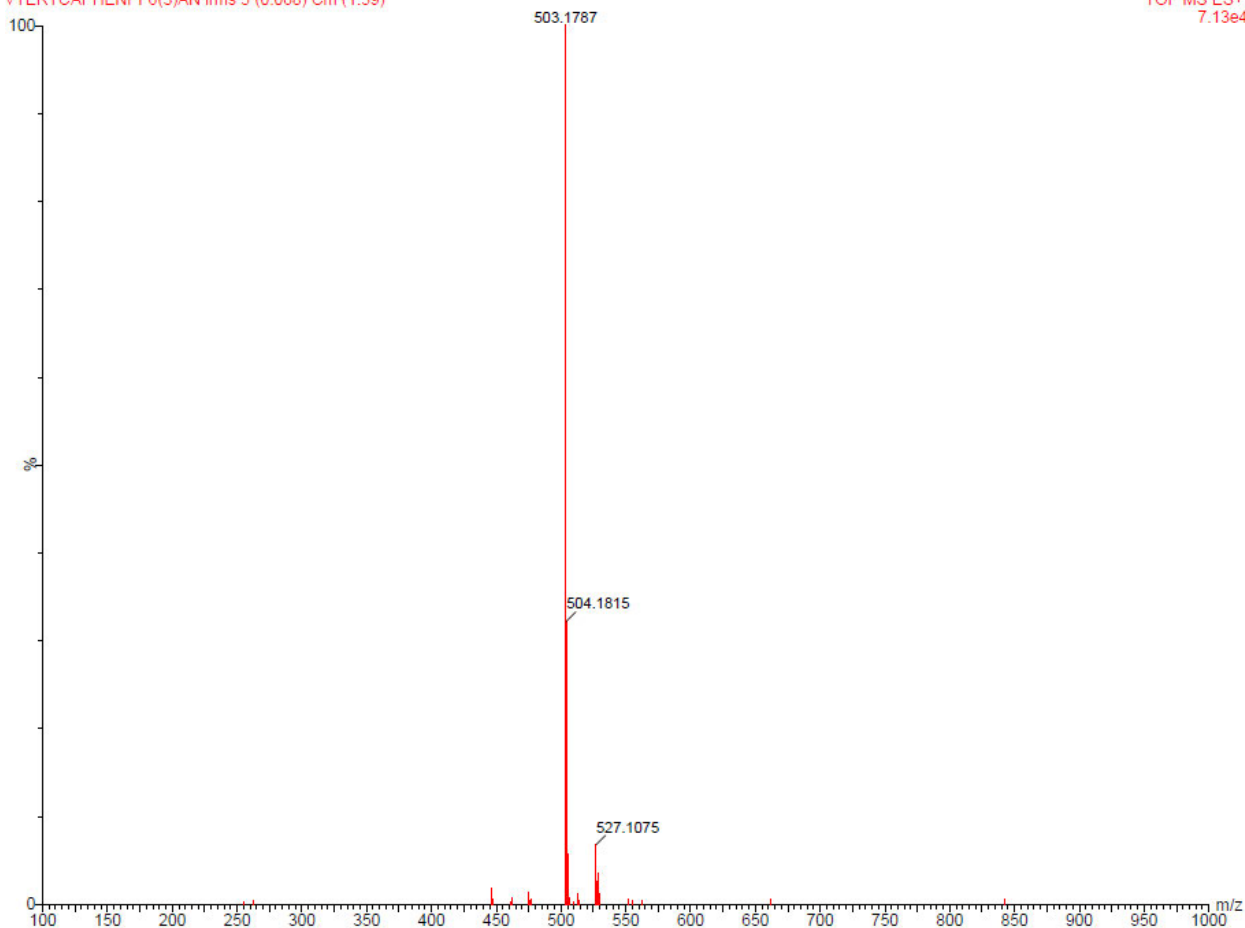
VTERTCAPHENPF6(3)AN 22 (0.709) Cm (1:61)

TOF MS ES+



3.81e+005

VTERTCAPHENPF6(3)AN Ims 5 (0.068) Cm (1:59)



TOF MS ES+  
7.13e4

**Figure A119: High resolution ESI mass spectrum of [VO(TERTCA)(PHEN)](PF<sub>6</sub>) in acetonitrile.**

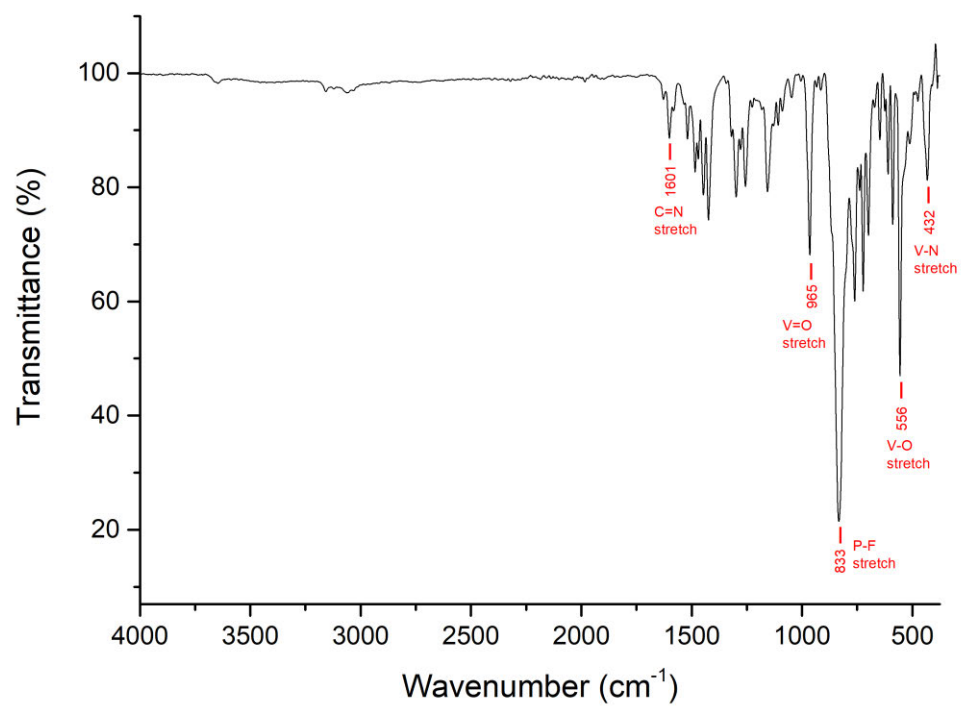


**Figure A120: IR spectrum of [VO(PHPHCA)(PHEN)](PF<sub>6</sub>).**

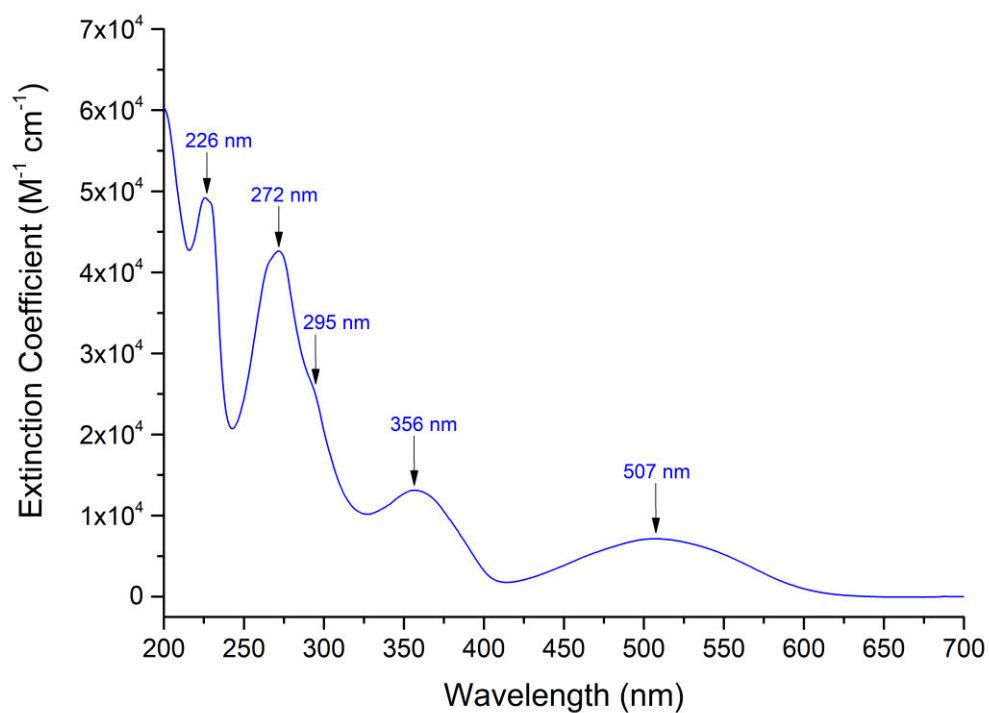


**Figure A121: UV/visible spectrum of [VO(PHPHCA)(PHEN)](PF<sub>6</sub>).  
[VO(PHPHCA)(PHEN)](PF<sub>6</sub>) = 1.98 x 10<sup>-5</sup> M.**

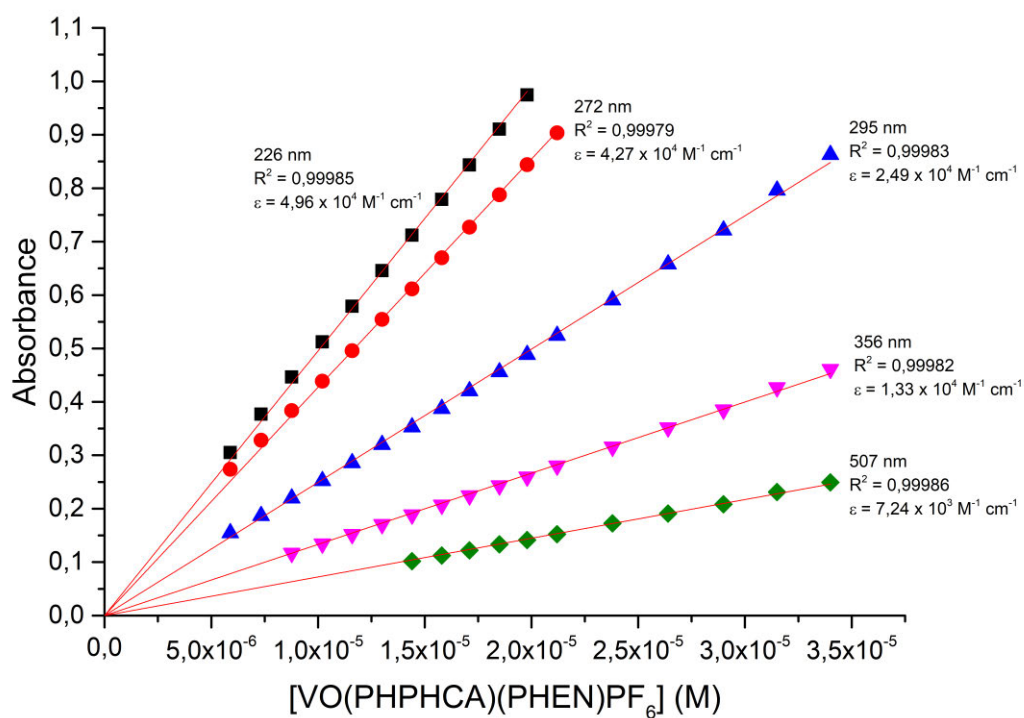


**Figure A122: Beer's Law Correlation of [VO(PHPHCA)(PHEN)](PF<sub>6</sub>).**

### Single Mass Analysis

Tolerance = 5.0 PPM / DBE: min = -1.5, max = 100.0

Element prediction: Off

Number of isotope peaks used for i-FIT = 2

Monoisotopic Mass, Even Electron Ions

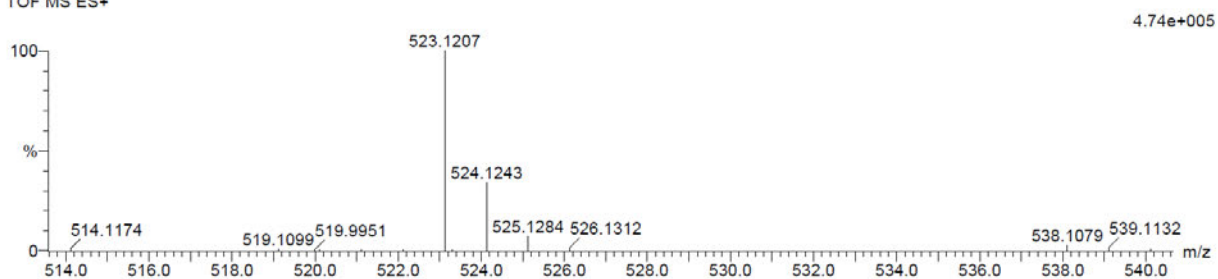
29 formula(e) evaluated with 1 results within limits (up to 20 best isotopic matches for each mass)

Elements Used:

C: 25-30 H: 20-25 N: 0-5 O: 0-5 V: 0-1

VPHPHCAPHENPF6(3) 8 (0.237) Cm (1:61)

TOF MS ES+



VPHPHCAPHENPF6(3) Ims 2 (0.017) Cm (1:59)

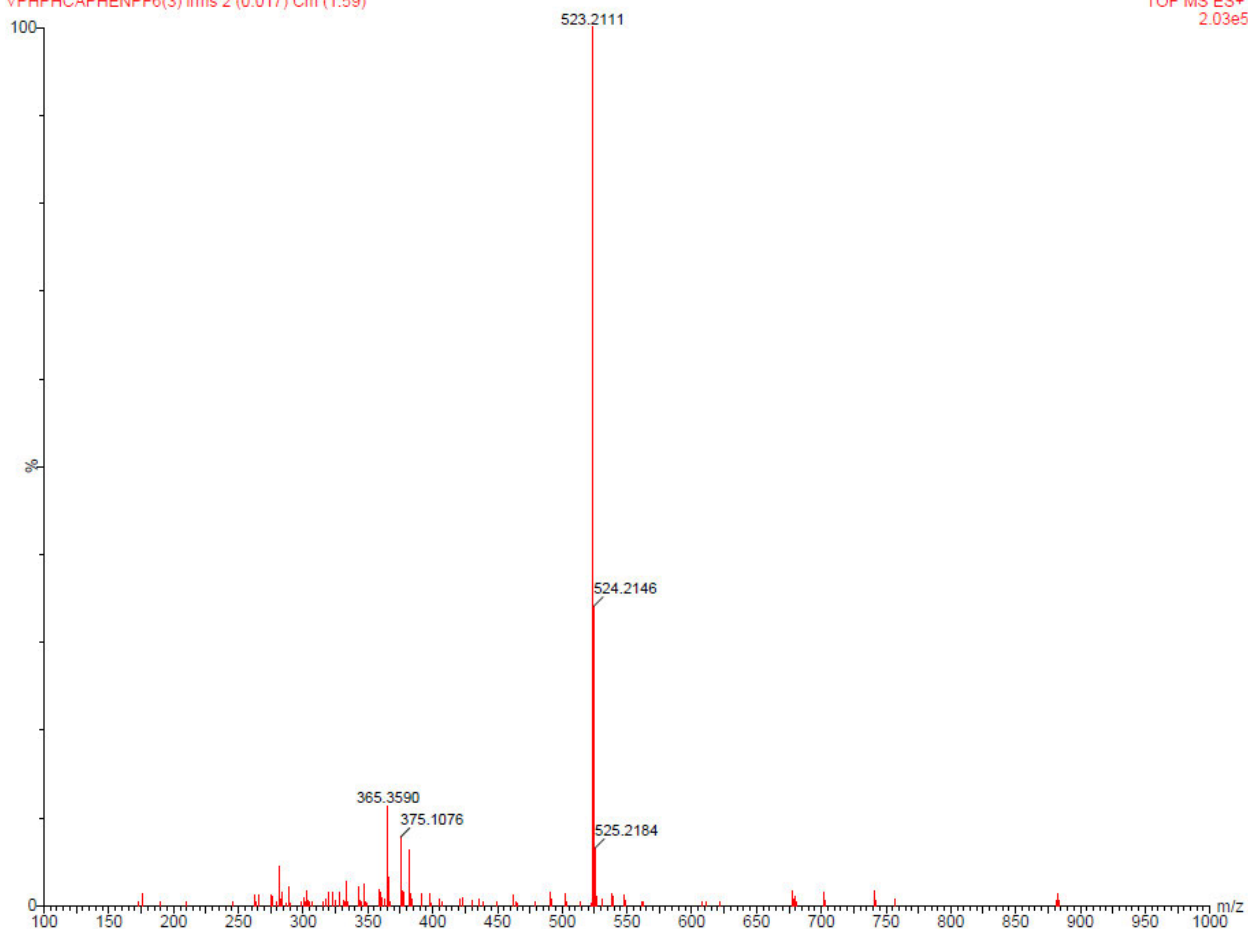


**Figure A123: High resolution ESI mass spectrum of [VO(PHPHCA)(PHEN)](PF<sub>6</sub>) in acetonitrile.**

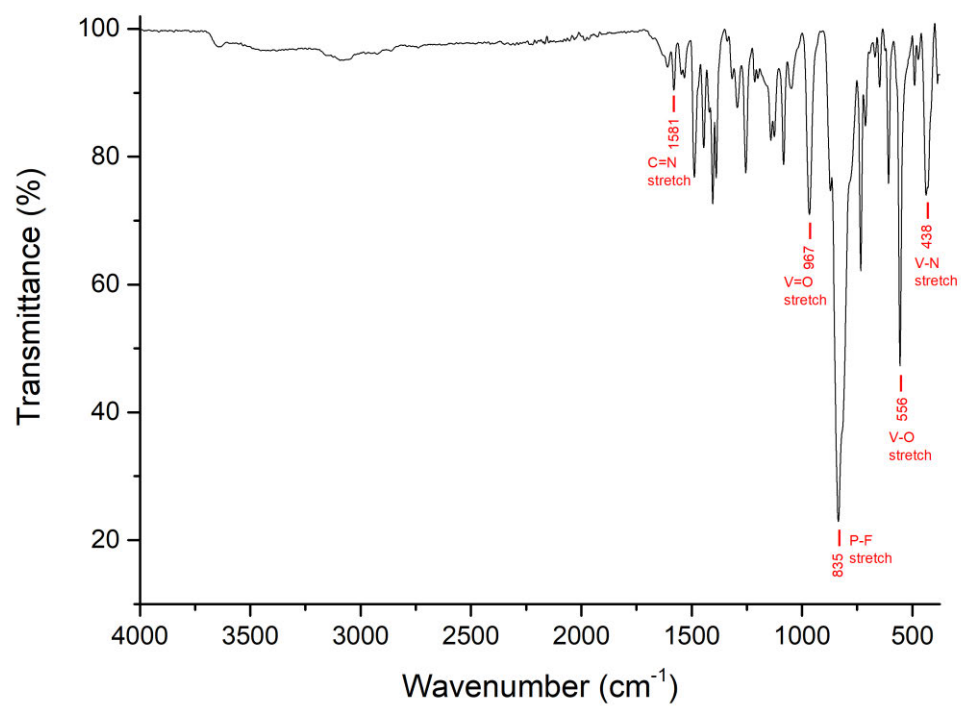


**Figure A124:** IR spectrum of [VO(MECA)(DPQ)](PF<sub>6</sub>).

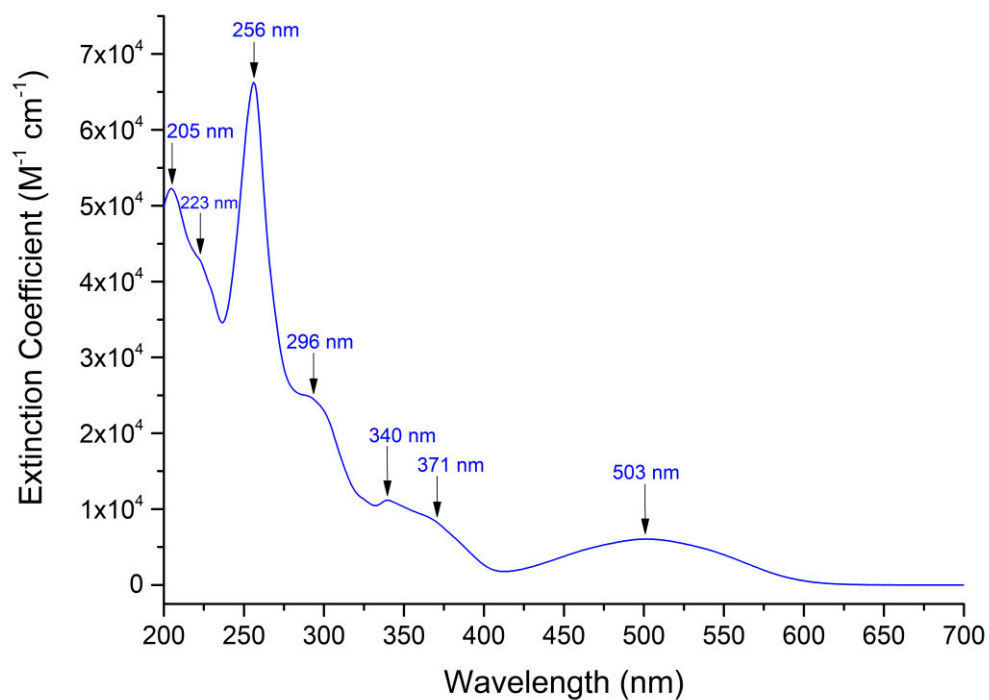


**Figure A125: UV/visible spectrum of [VO(MECA)(DPQ)](PF<sub>6</sub>).  
[VO(MECA)(DPQ)](PF<sub>6</sub>) = 1.74 x 10<sup>-5</sup> M.**

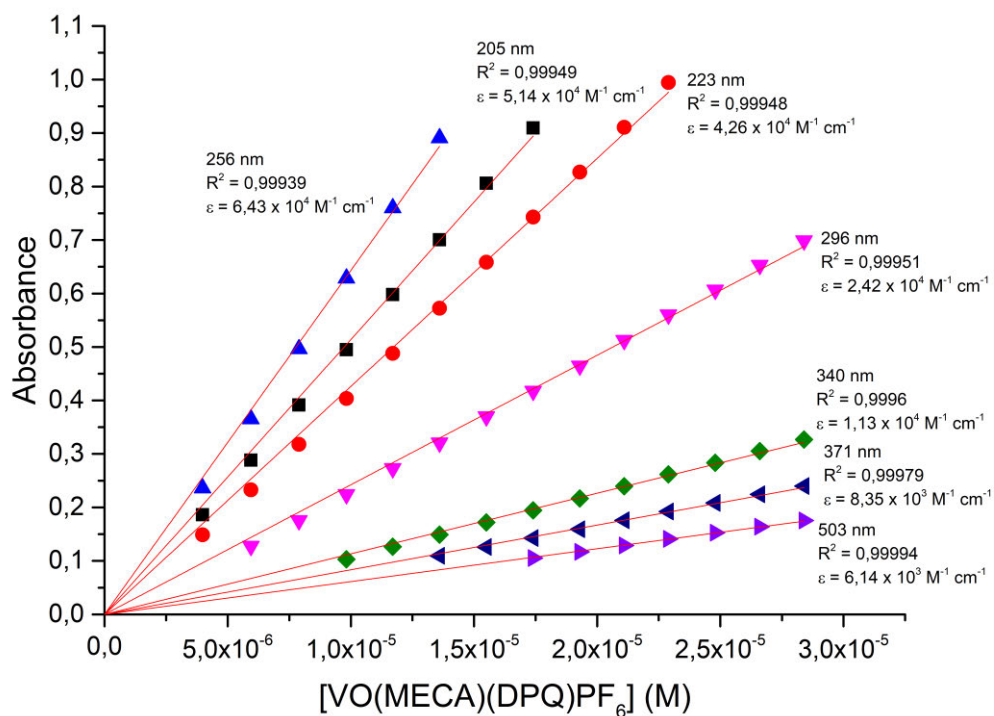


**Figure A126: Beer's Law Correlation of [VO(MECA)(DPQ)](PF<sub>6</sub>).**

### Single Mass Analysis

Tolerance = 5.0 PPM / DBE: min = -1.5, max = 50.0

Element prediction: Off

Number of isotope peaks used for i-FIT = 2

Monoisotopic Mass, Even Electron Ions

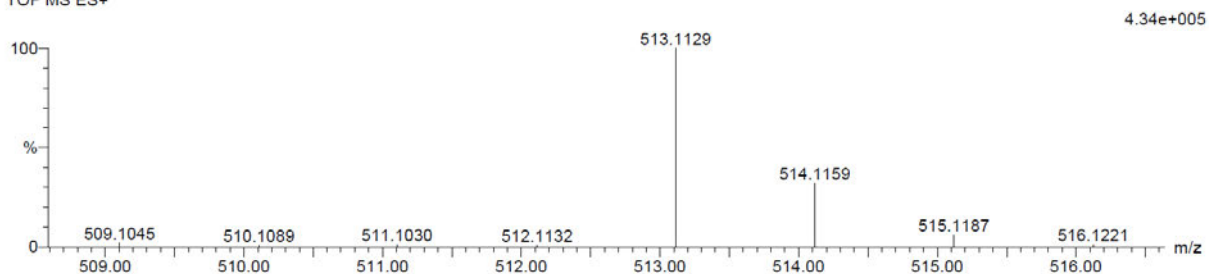
31 formula(e) evaluated with 1 results within limits (up to 20 closest results for each mass)

Elements Used:

C: 25-30 H: 15-20 N: 5-10 O: 0-5 V: 0-1

VMECADPQPF6(3)AN 32 (1.045) Cm (1:61)

TOF MS ES+



VMECADPQPF6(3)AN lms 7 (0.103) Cm (1:60)

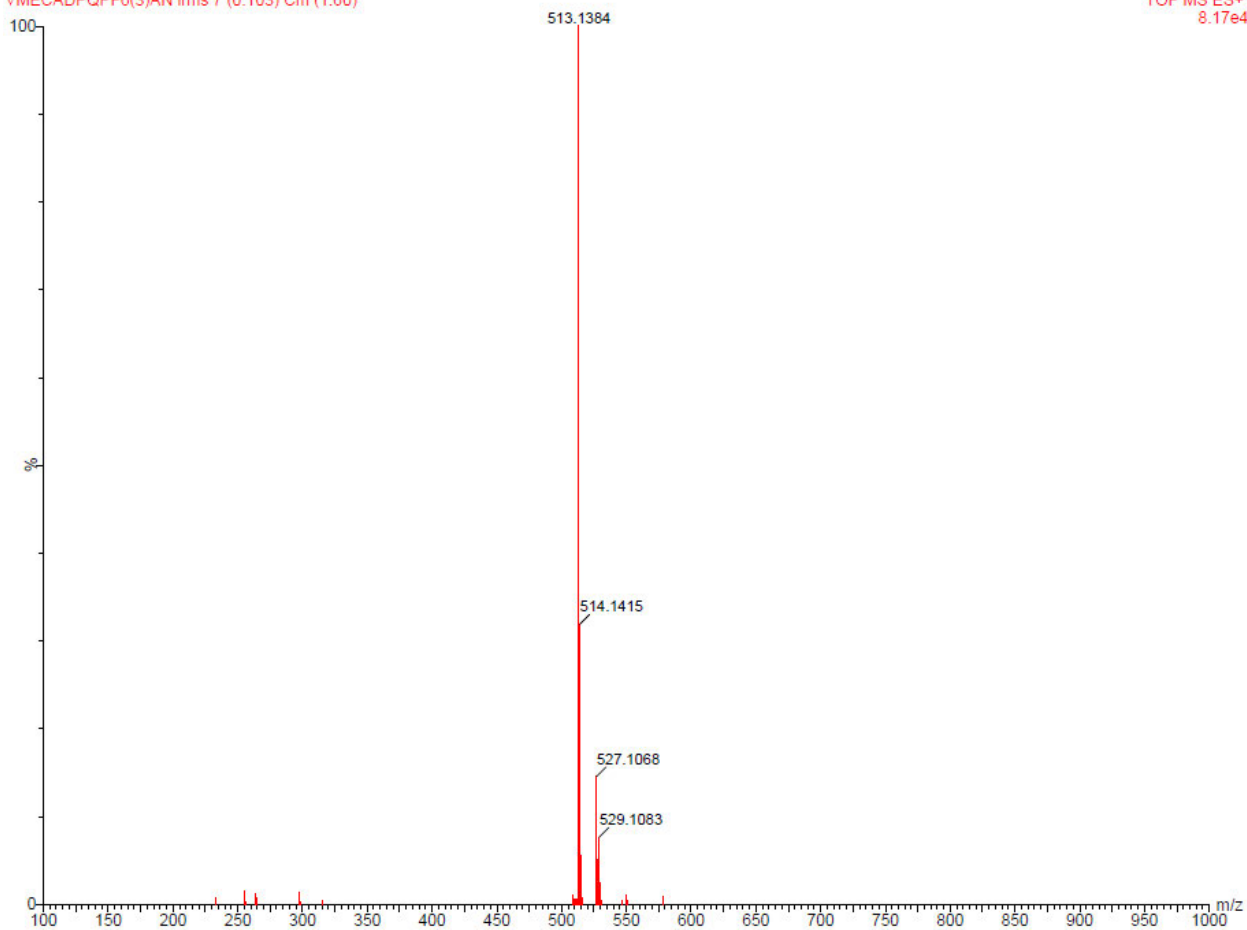


**Figure A127: High resolution ESI mass spectrum of [VO(MECA)(DPQ)](PF<sub>6</sub>) in acetonitrile.**

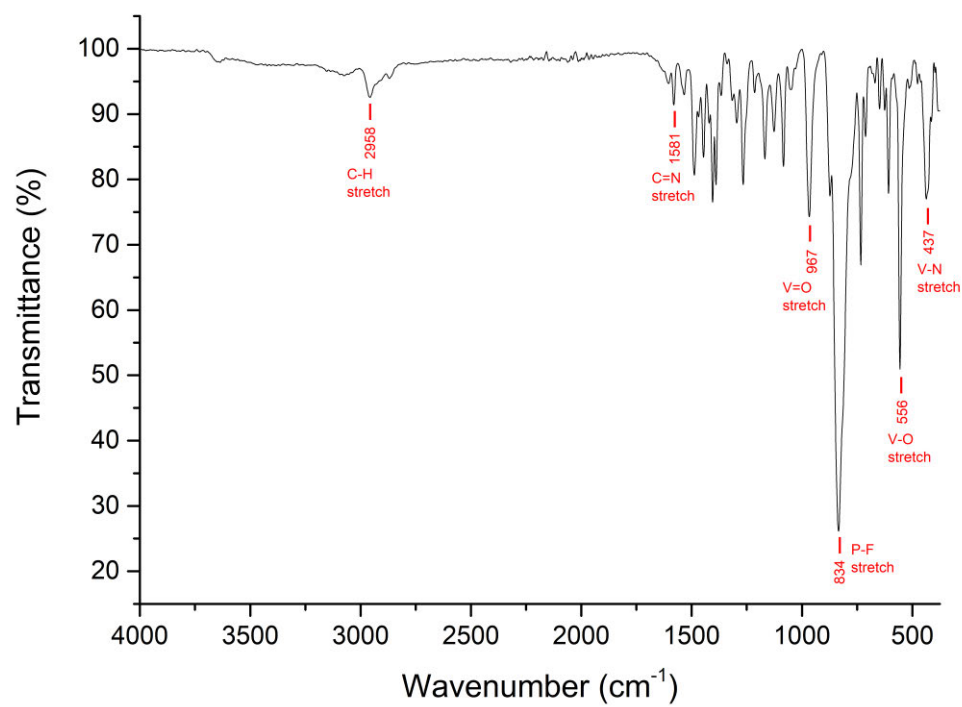


**Figure A128: IR spectrum of [VO(TERTCA)(DPQ)](PF<sub>6</sub>).**

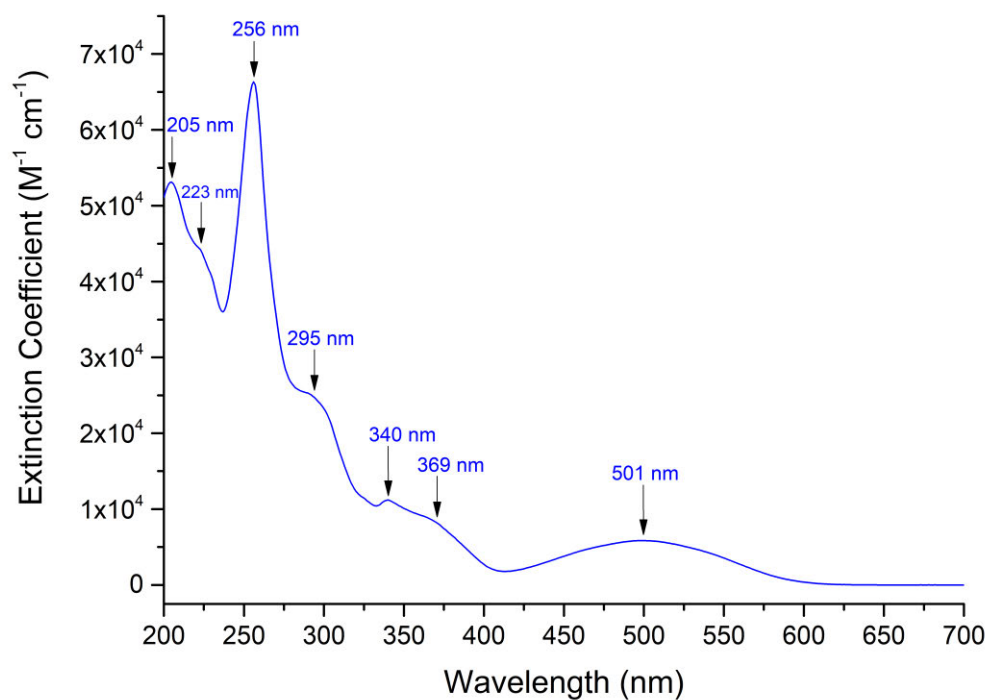


**Figure A129: UV/visible spectrum of [VO(TERTCA)(DPQ)](PF<sub>6</sub>).  
[VO(TERTCA)(DPQ)](PF<sub>6</sub>) = 1.74 x 10<sup>-5</sup> M.**

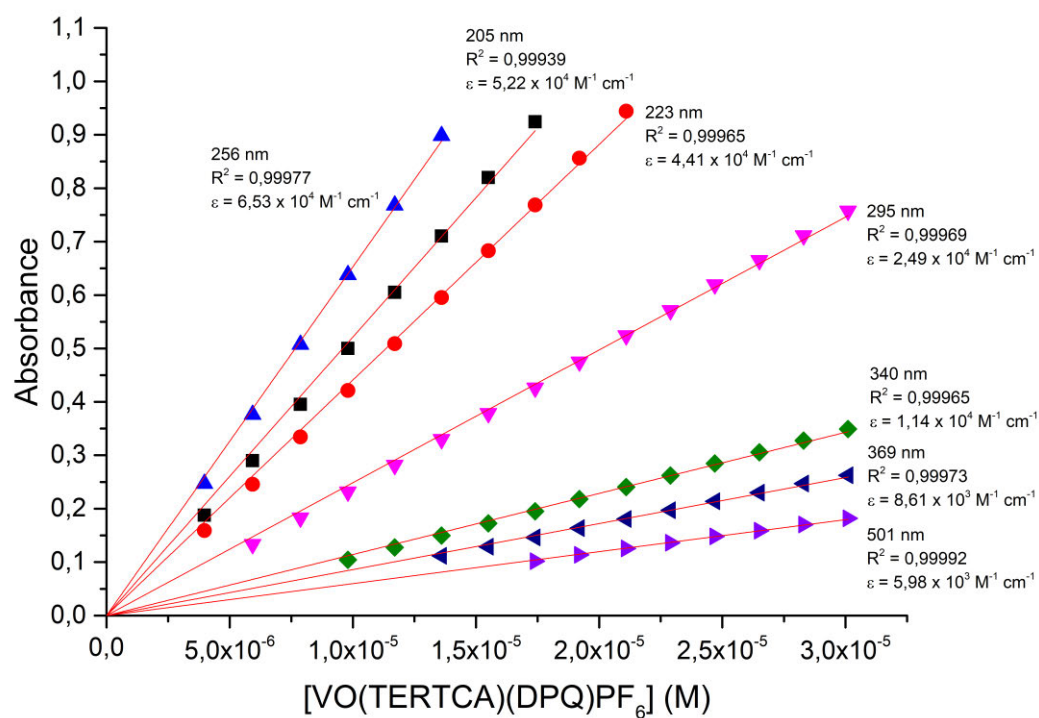


**Figure A130: Beer's Law Correlation of [VO(TERTCA)(DPQ)](PF<sub>6</sub>).**

### Single Mass Analysis

Tolerance = 5.0 PPM / DBE: min = -1.5, max = 100.0

Element prediction: Off

Number of isotope peaks used for i-FIT = 2

Monoisotopic Mass, Even Electron Ions

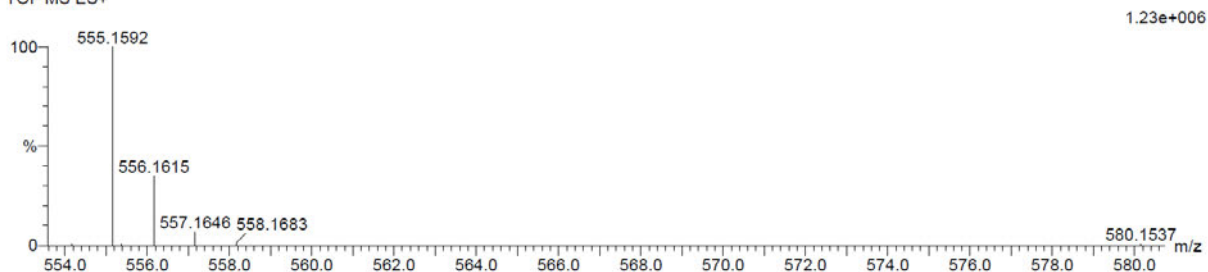
26 formula(e) evaluated with 1 results within limits (up to 20 best isotopic matches for each mass)

Elements Used:

C: 25-30 H: 25-30 N: 5-10 O: 0-5 V: 0-1

VTERTCADPQPF6 2410 47 (1.552) Cm (1:61)

TOF MS ES+



VTERTCADPQPF6 2410 lms 2 (0.017) Cm (1:60)

TOF MS ES+  
1.55e6

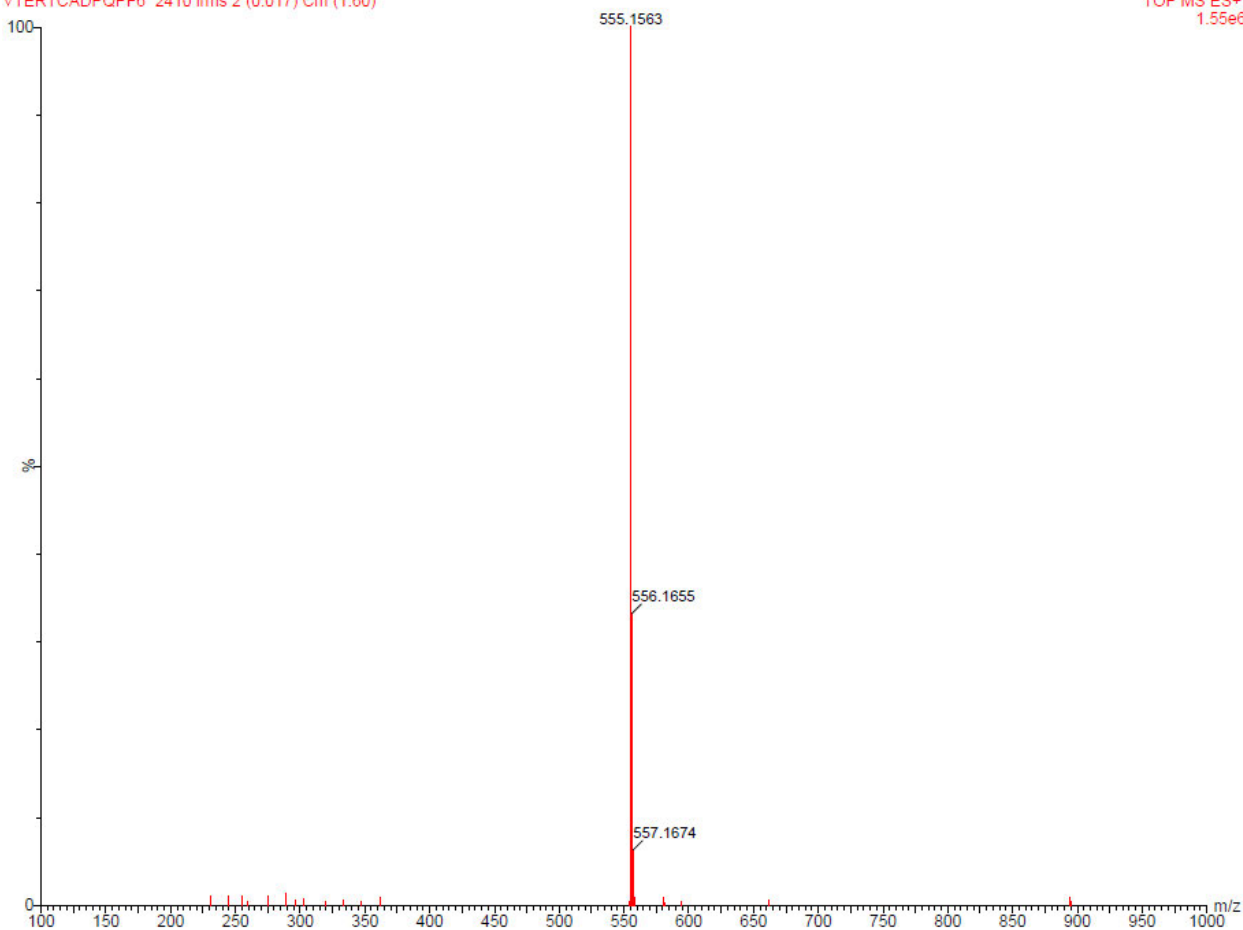


**Figure A131: High resolution ESI mass spectrum of [VO(TERTCA)(DPQ)](PF<sub>6</sub>) in acetonitrile.**

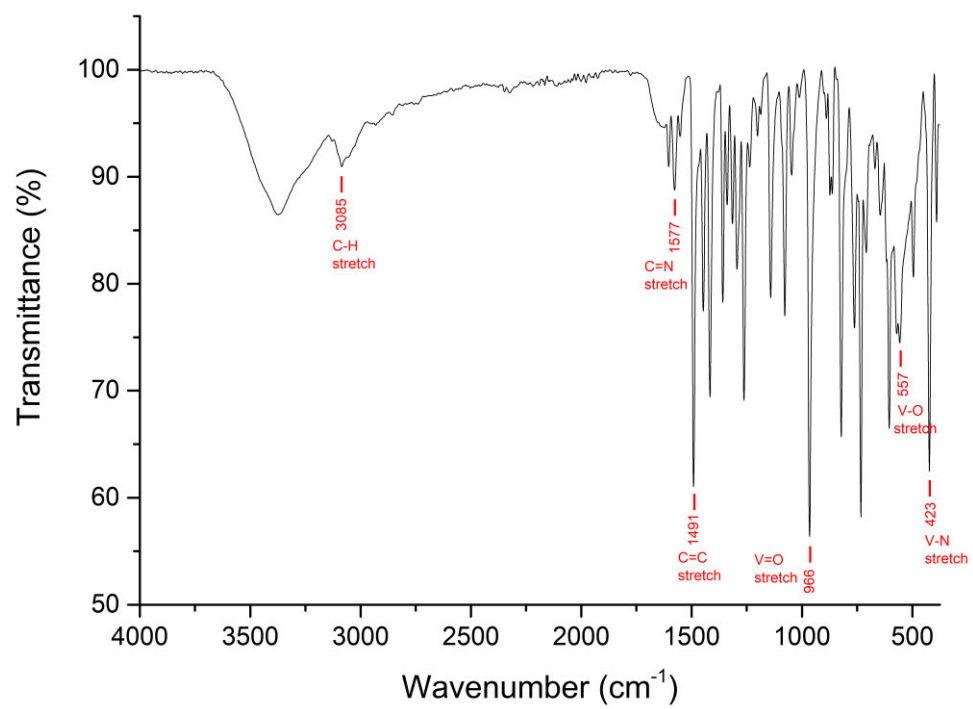


**Figure A132:** IR spectrum of [VO(MECA)(DPPZ)](Cl).

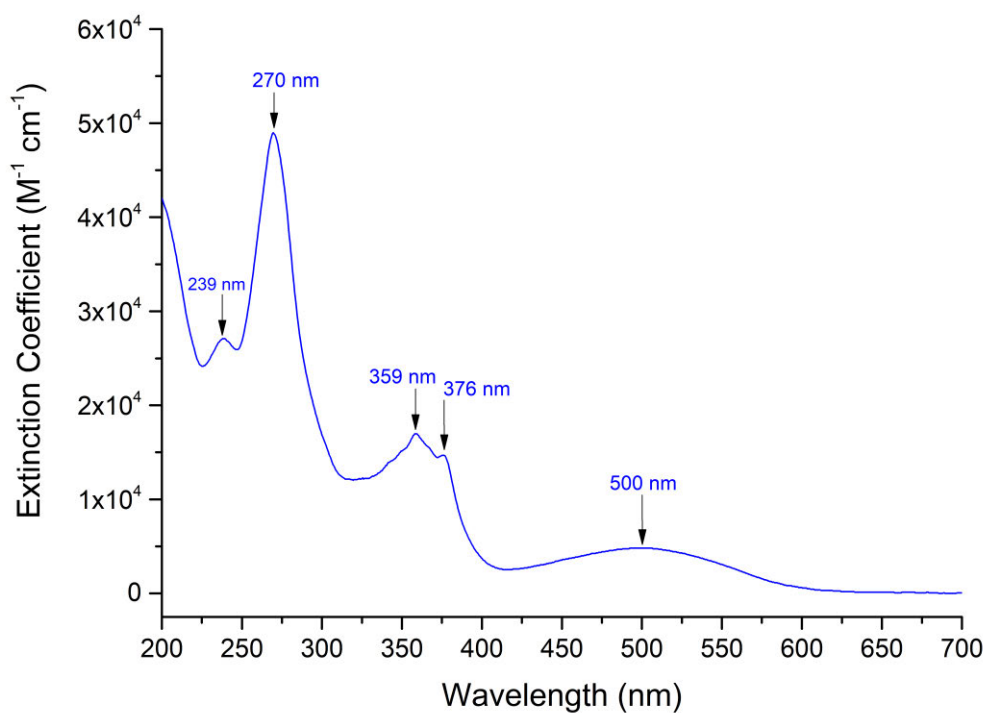


**Figure A133: UV/visible spectrum of [VO(MECA)(DPPZ)](Cl).  
[VO(MECA)(DPPZ)](Cl) = 1.58 x 10<sup>-5</sup> M.**

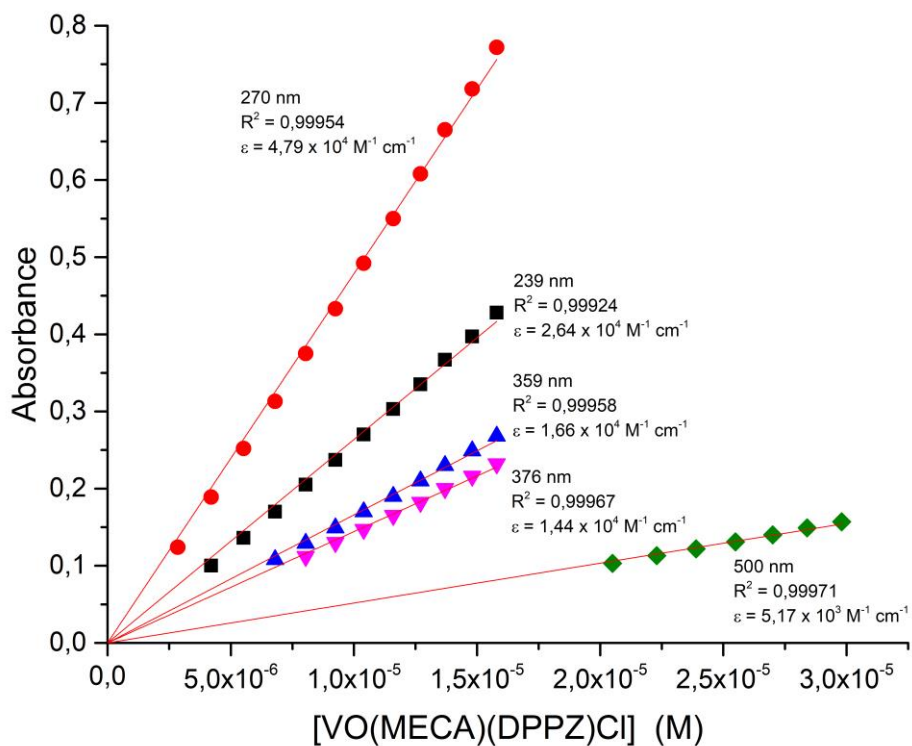


**Figure A134: Beer's Law Correlation of [VO(MECA)(DPPZ)](Cl).**

**Single Mass Analysis**

Tolerance = 5.0 PPM / DBE: min = -1.5, max = 100.0

Element prediction: Off

Number of isotope peaks used for i-FIT = 3

Monoisotopic Mass, Even Electron Ions

27 formula(e) evaluated with 1 results within limits (up to 20 closest results for each mass)

Elements Used:

C: 25-30 H: 20-25 N: 5-10 O: 0-5 V: 0-1

VMEA(dppz) 60 (2.024) Cm (1:60)

TOF MS ES+

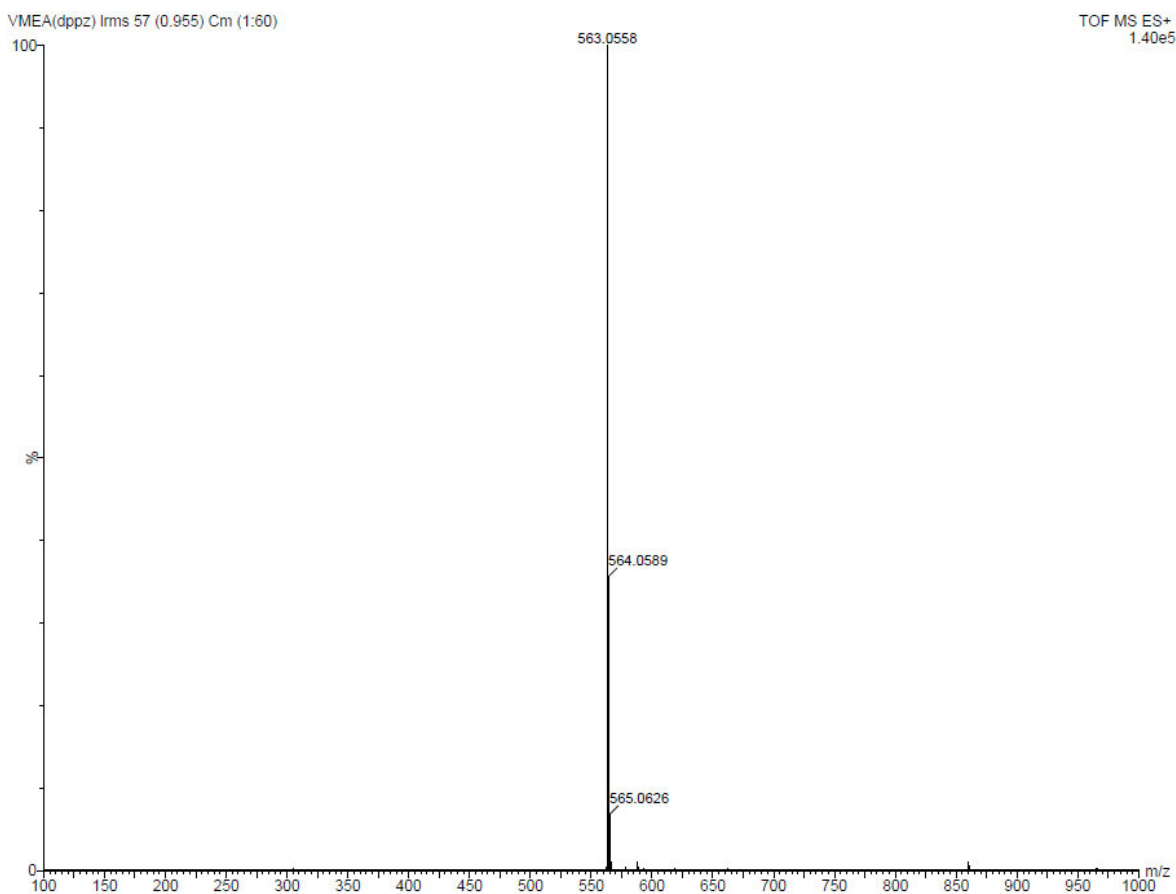
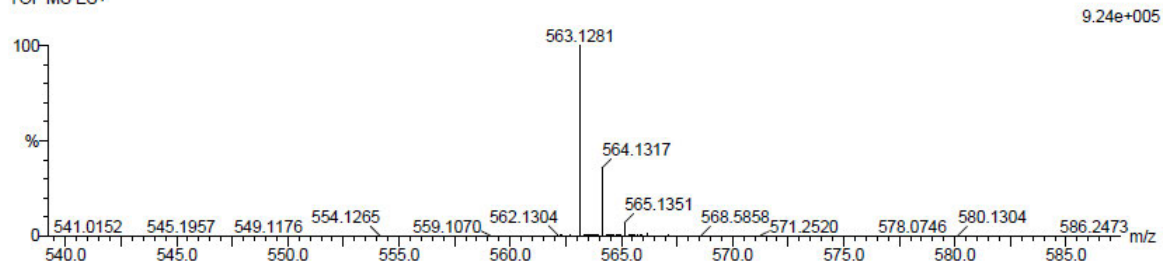


**Figure A135: High resolution ESI mass spectrum of [VO(MECA)(DPPZ)](Cl) in acetonitrile.**

## Appendix B: EPR Spectra

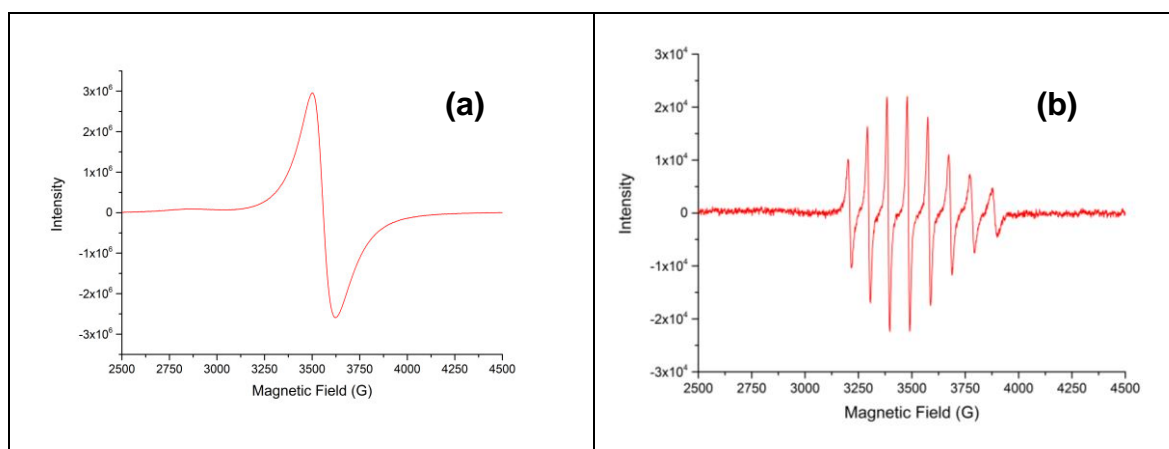


**Figure B1:** EPR Spectra of [VO(PHA)(DPQ)] in the solid-state at 9.859455 GHz (a) and in  $\text{CH}_2\text{Cl}_2$  at 9.792417 GHz (b) at 298 K.

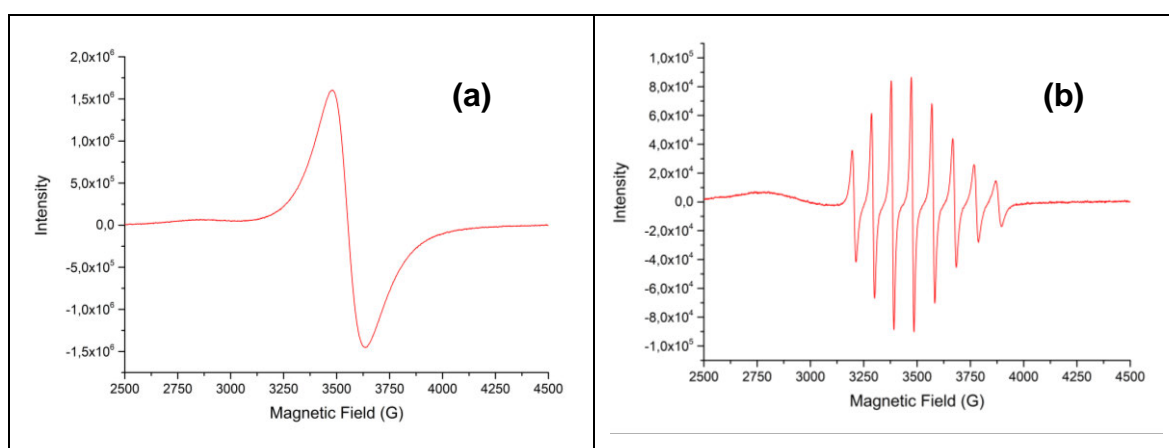


**Figure B2:** EPR Spectra of [VO(MEA)(DPQ)] in the solid-state at 9.847325 GHz (a) and in  $\text{CH}_2\text{Cl}_2$  at 9.777941 GHz (b) at 298 K.

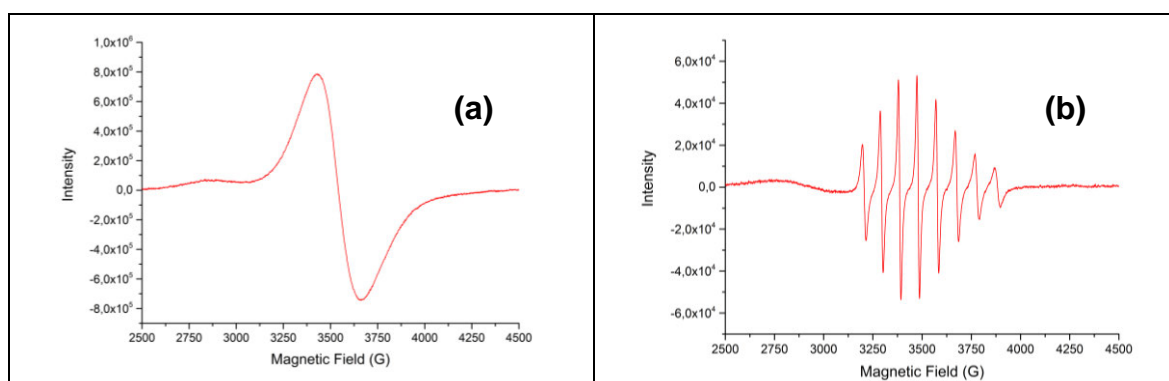


**Figure B3:** EPR Spectra of [VO(TERTA)(DPQ)] in the solid-state at 9.847624 GHz (a) and in  $\text{CH}_2\text{Cl}_2$  at 9.780834 GHz (b) at 298 K.

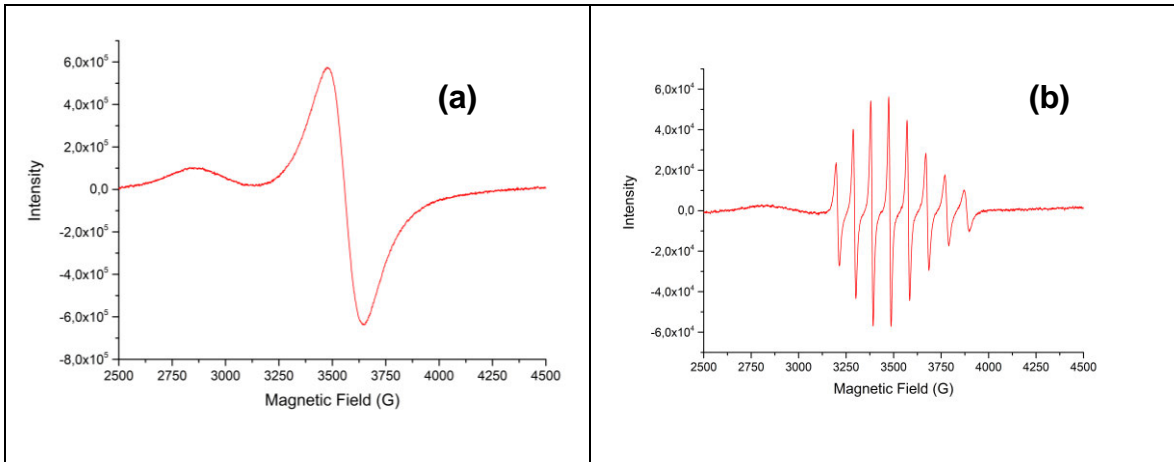


**Figure B4:** EPR Spectra of [VO(CLA)(DPQ)] in the solid-state at 9.864461 GHz (a) and in  $\text{CH}_2\text{Cl}_2$  at 9.781506 GHz (b) at 298 K.

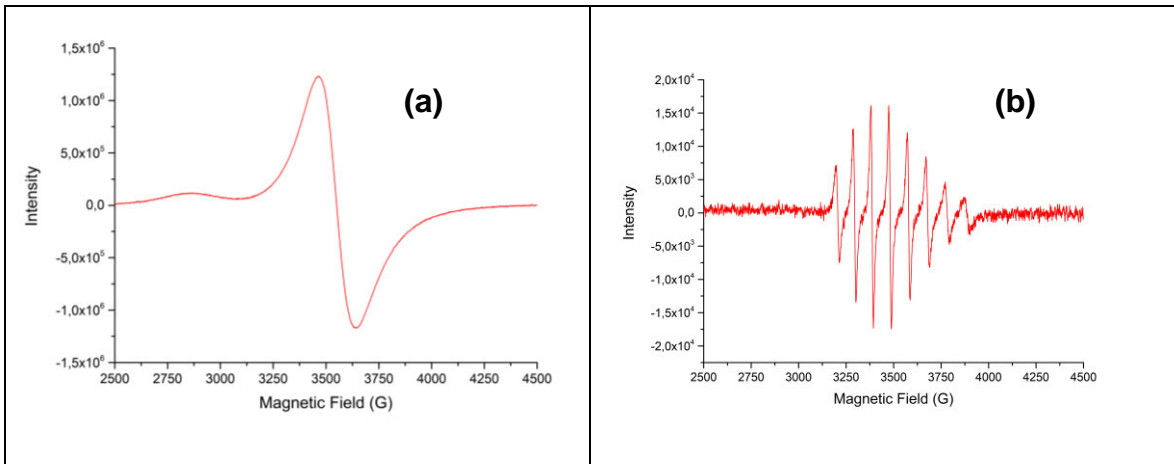


**Figure B5:** EPR Spectra of [VO(SOA)(DPQ)] in the solid-state at 9.866031 GHz (a) and in  $\text{CH}_2\text{Cl}_2$  at 9.785694 GHz (b) at 298 K.

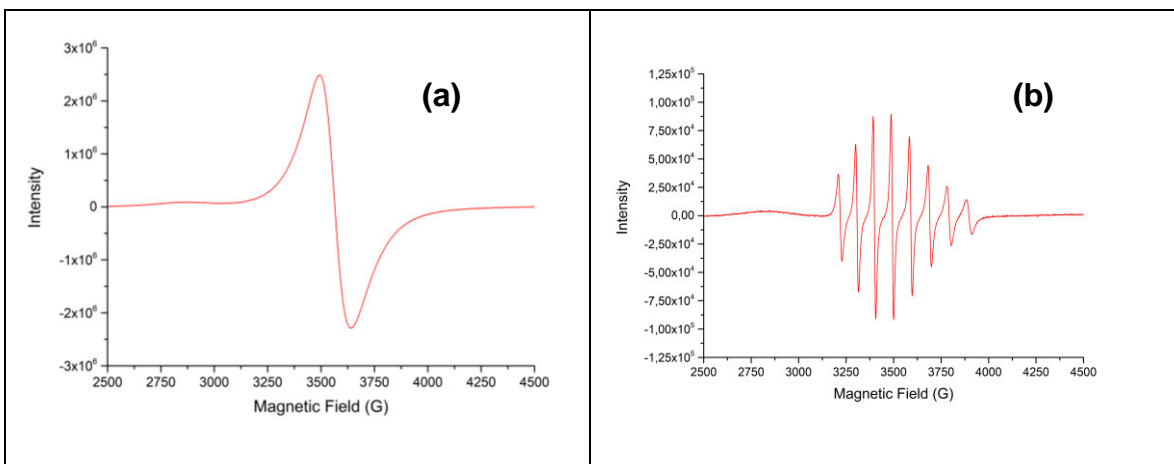


**Figure B6:** EPR Spectra of [VO(NAA)(DPQ)] in the solid-state at 9.859944 GHz (a) and in  $\text{CH}_2\text{Cl}_2$  at 9.817353 GHz (b) at 298 K.

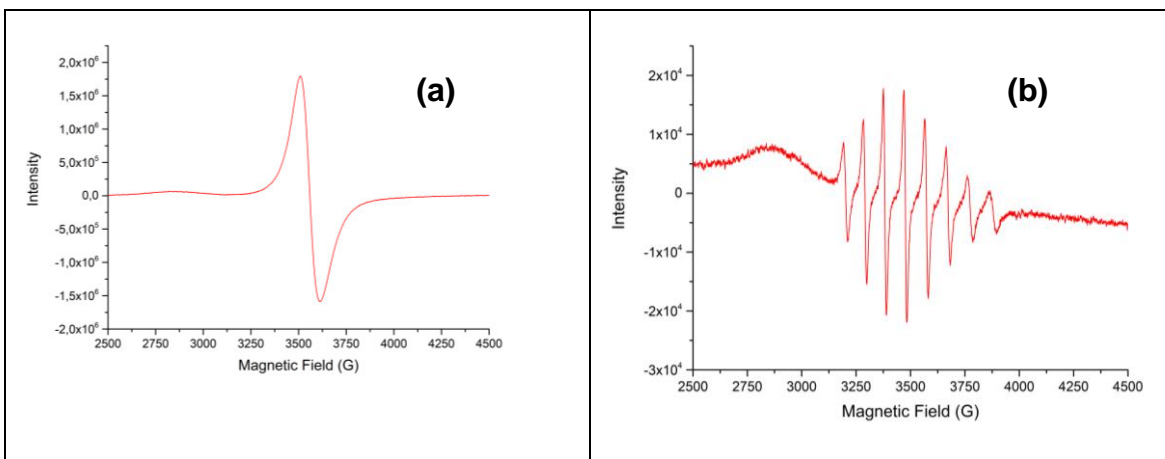


**Figure B7:** EPR Spectra of [VO(PHPHA)(DPQ)] in the solid-state at 9.846843 GHz (a) and in CH<sub>2</sub>Cl<sub>2</sub> at 9.772100 GHz (b) at 298 K.

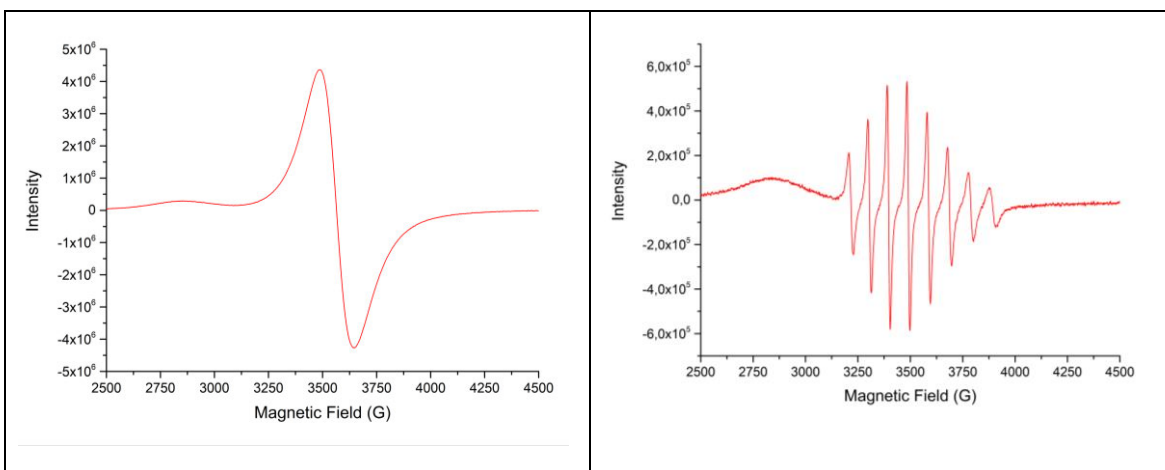


**Figure B8:** EPR Spectra of [VO(MEA)(DPPZ)] in the solid-state at 9.864484 GHz (a) and in CH<sub>2</sub>Cl<sub>2</sub> at 9.810435 GHz (b) at 298 K.

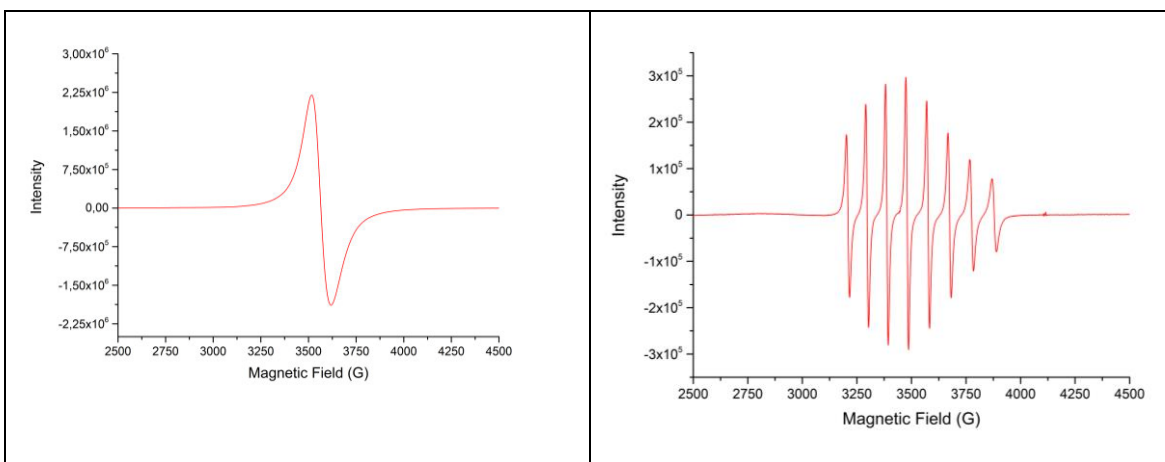


**Figure B9:** EPR Spectra of [VO(PHCA)(PHEN)](PF<sub>6</sub>) in the solid-state at 9.847960 GHz (a) and in acetonitrile at 9.782512 GHz (b) at 298 K.

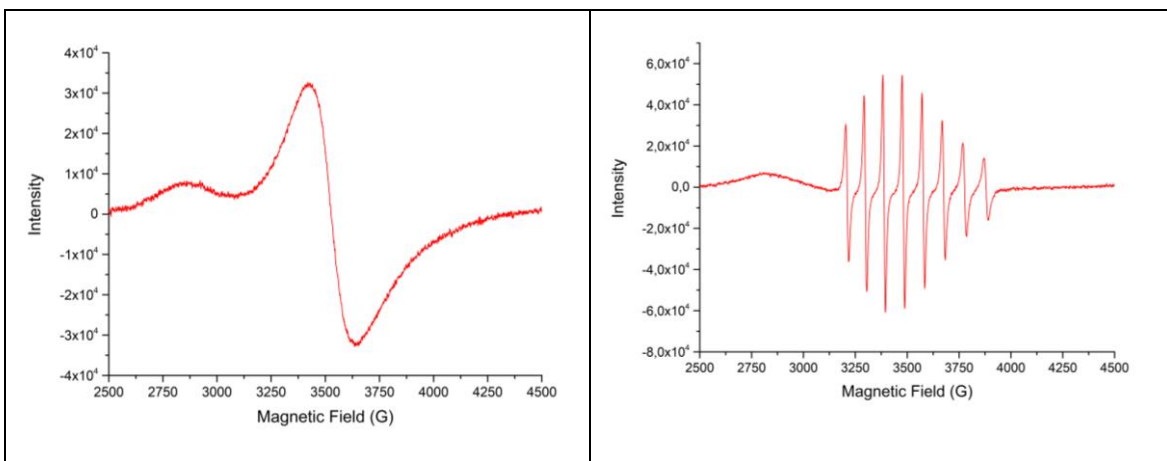


**Figure B10:** EPR Spectra of  $[\text{VO}(\text{MECA})(\text{PHEN})](\text{PF}_6)$  in the solid-state at 9.842512 GHz (a) and in acetonitrile at 9.787040 GHz (b) at 298 K.

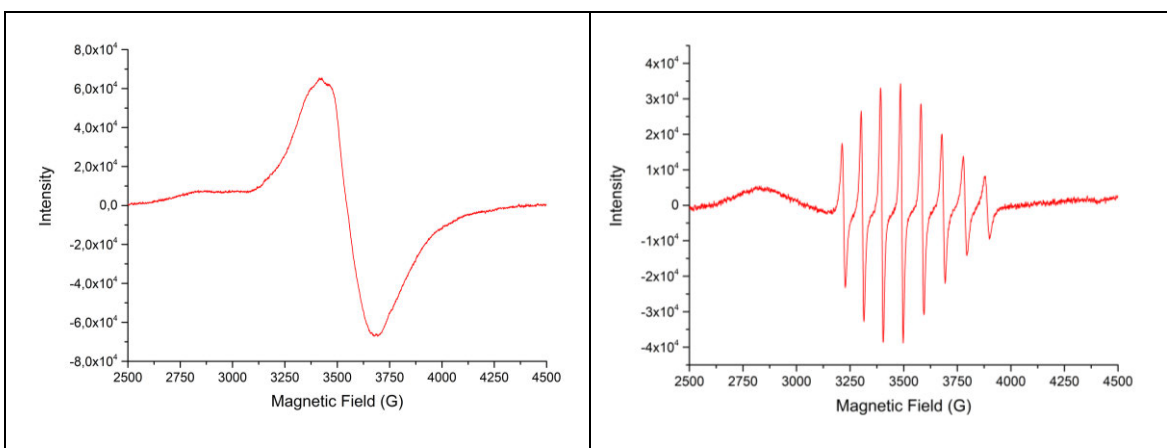


**Figure B11:** EPR Spectra of  $[\text{VO}(\text{TERTCA})(\text{PHEN})](\text{PF}_6)$  in the solid-state at 9.854115 GHz (a) and in acetonitrile at 9.812353 GHz (b) at 298 K.

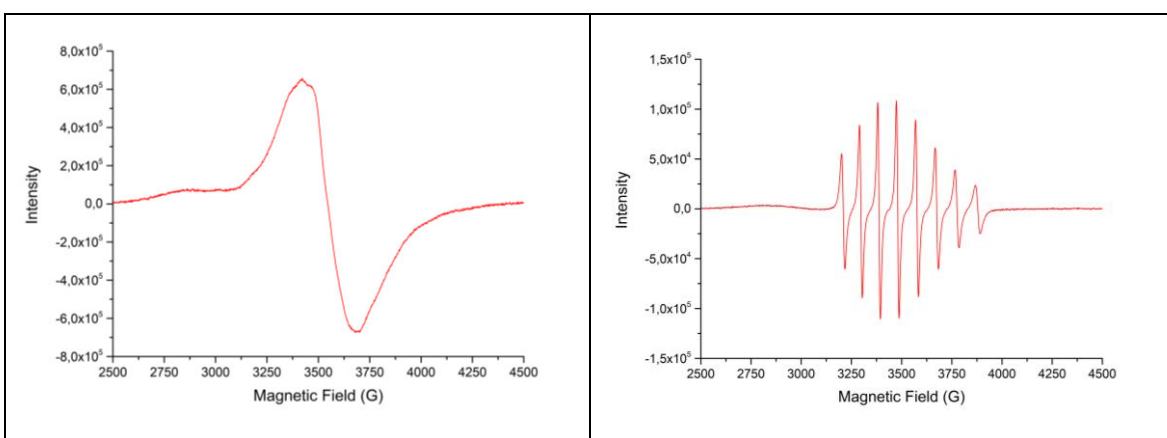


**Figure B12:** EPR Spectra of  $[\text{VO}(\text{PHPCA})(\text{PHEN})](\text{PF}_6)$  in the solid-state at 9.854104 GHz (a) and in acetonitrile at 9.783572 GHz (b) at 298 K.

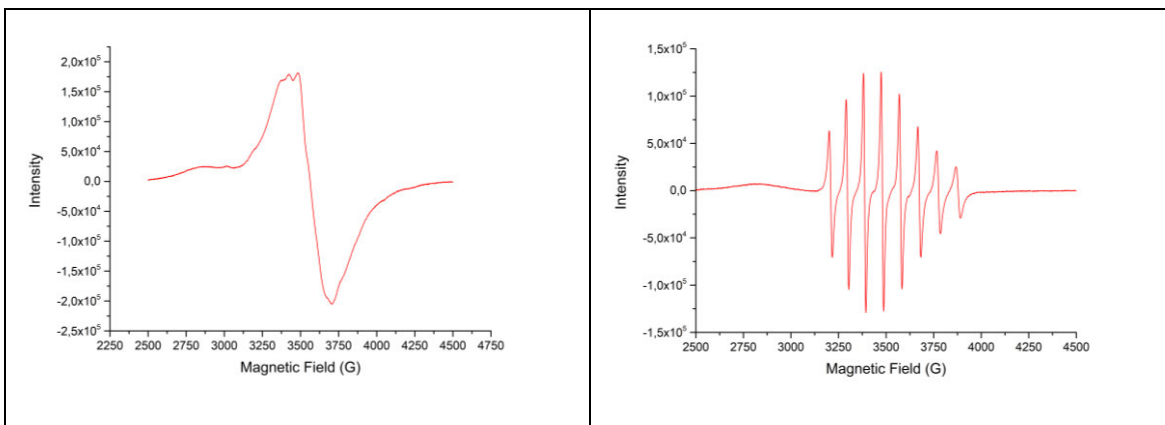


**Figure B13:** EPR Spectra of [VO(MECA)(DPQ)](PF<sub>6</sub>) in the solid-state at 9.869105 GHz (a) and in acetonitrile at 9.783366 GHz (b) at 298 K.

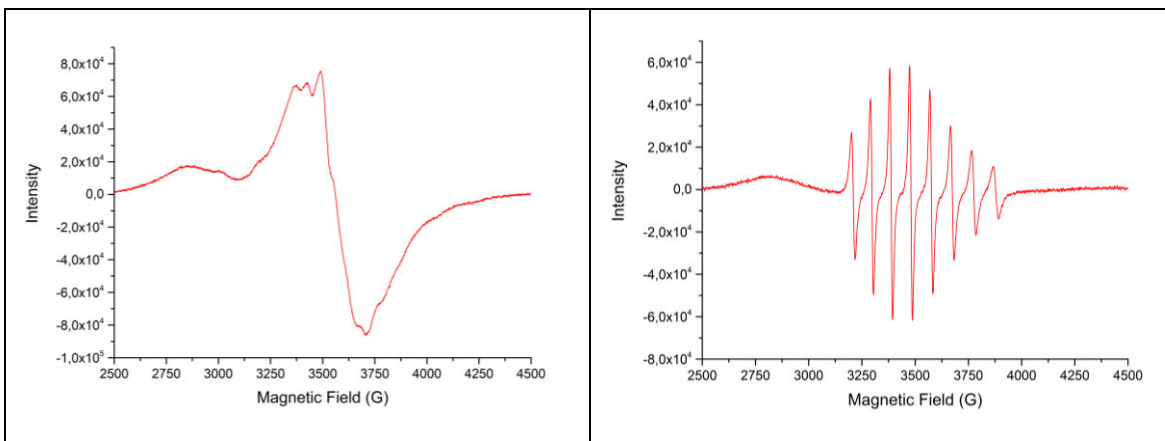


**Figure B14:** EPR Spectra of [VO(TERTCA)(DPQ)](PF<sub>6</sub>) in the solid-state at 9.869754 GHz (a) and in acetonitrile at 9.783182 GHz (b) at 298 K.

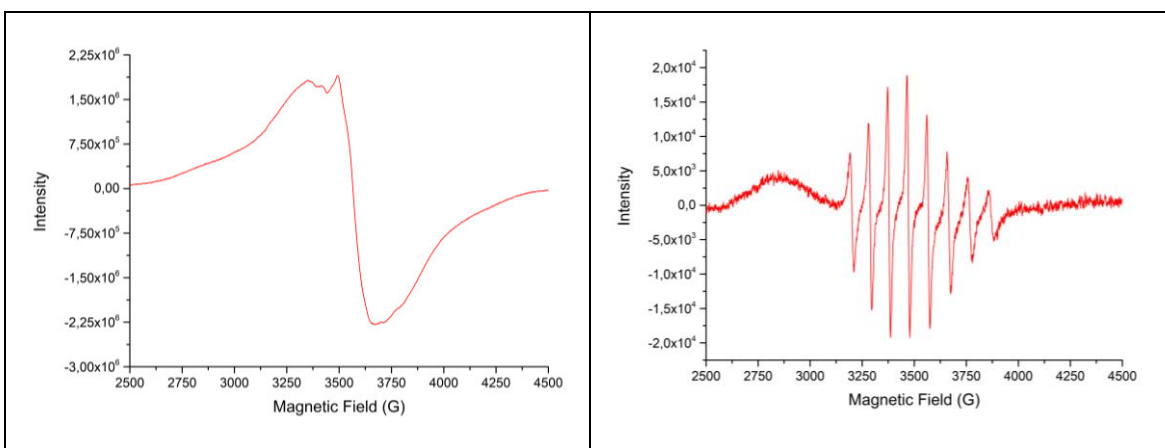


**Figure B15:** EPR Spectra of [VO(MECA)(DPPZ)](Cl) in the solid-state at 9.867162 GHz (a) and in acetonitrile at 9.762420 GHz (b) at 298 K.

## **Appendix C: Crystal Data and Structure Refinement**

**Table C1** Crystal data and structure refinement details for SOA and NAA.

<b>Crystal data</b>	<b>SOA</b>	<b>NAA</b>
Chemical formula	C <sub>15</sub> H <sub>15</sub> NO <sub>4</sub> S	C <sub>17</sub> H <sub>13</sub> NO <sub>2</sub>
Molar Mass (g mol <sup>-1</sup> )	305.35	263.28
Crystal system, space group	Monoclinic, P2 <sub>1</sub> /c	Orthorhombic, P <sub>ca</sub> 2 <sub>1</sub>
Temperature (K)	100	100
<i>a</i> , <i>b</i> , <i>c</i> (Å)	9.2665(4), 6.7112(2), 22.7298(8)	20.3416(13), 6.2785(4), 19.4841(14)
$\alpha$ , $\beta$ , $\gamma$ (°)	90, 98.092(2), 90	90, 90, 90
<i>V</i> (Å <sup>3</sup> )	1399.48(9)	2488.4(3)
<i>Z</i>	4	8
$\mu$ (mm <sup>-1</sup> )	0.25	0.09
Crystal size (mm)	0.23 x 0.13 x 0.09	0.22 x 0.17 x 0.12
<b>Data collection</b>		
Diffractometer	Bruker APEX-II CCD	Bruker APEX-II CCD
Absorption correction	Multi-scan, SADABS	Multi-scan, SADABS
Radiation type	Mo <i>K</i> $\alpha$	Mo <i>K</i> $\alpha$
<i>T</i> <sub>min</sub> , <i>T</i> <sub>max</sub>	0.697, 0.746	0.658, 0.746
No. of measured, independent and observed [ <i>I</i> > 2 $\sigma$ ( <i>I</i> )] reflections	13083, 3714, 3254	27783, 6177, 5673
<i>R</i> <sub>int</sub>	0.027	0.038
<b>Refinement</b>		
<i>R</i> [ <i>F</i> <sup>2</sup> > 2 $\sigma$ ( <i>F</i> <sup>2</sup> )], <i>wR</i> ( <i>F</i> <sup>2</sup> ), <i>S</i>	0.036, 0.099, 1.04	0.062, 0.166, 1.06
No. of reflections	3714	6177
No. of parameters	199	375
H-atom treatment	H atoms treated by a mixture of independent and constrained refinement	
$\Delta\rho_{\max}$ , $\Delta\rho_{\min}$ (e Å <sup>-3</sup> )	0.44, -0.38	1.00, -0.32

**Table C2** Crystal data and structure refinement details for PHCA.

<b>Crystal data</b>	<b>PHCA</b>	<b>PHCA·H<sub>2</sub>O</b>
Chemical formula	C <sub>11</sub> H <sub>11</sub> N <sub>3</sub> O	C <sub>11</sub> H <sub>11</sub> N <sub>3</sub> O, 0.5(H <sub>2</sub> O)
Molar Mass (g mol <sup>-1</sup> )	201.23	210.24
Crystal system, space group	Monoclinic, <i>P</i> 2 <sub>1</sub> / <i>c</i>	Monoclinic, <i>C</i> 2/ <i>c</i>
Temperature (K)	100	100
<i>a</i> , <i>b</i> , <i>c</i> (Å)	11.5123(13), 9.0527(8), 19.5365(18)	22.5522(16), 7.1022(5), 13.4620(9)
$\alpha$ , $\beta$ , $\gamma$ (°)	90, 96.232(4), 90	90, 110.400(3), 90
<i>V</i> (Å <sup>3</sup> )	2024.0(3)	2021.0(2)
<i>Z</i>	8	8
$\mu$ (mm <sup>-1</sup> )	0.09	0.10
Crystal size (mm)	0.38 x 0.19 x 0.12	0.31 x 0.16 x 0.11
<b>Data collection</b>		
Diffractometer	Bruker APEX-II CCD	Bruker APEX-II CCD
Absorption correction	Multi-scan, SADABS	Multi-scan, SADABS
Radiation type	Mo <i>K</i> $\alpha$	Mo <i>K</i> $\alpha$
<i>T</i> <sub>min</sub> , <i>T</i> <sub>max</sub>	0.688, 0.746	
No. of measured, independent and observed [ <i>I</i> > 2 $\sigma$ ( <i>I</i> )] reflections	19 119, 5328, 4559	9162, 2651, 2384
<i>R</i> <sub>int</sub>	0.026	0.021
<b>Refinement</b>		
<i>R</i> [ <i>F</i> <sup>2</sup> > 2 $\sigma$ ( <i>F</i> <sup>2</sup> )], <i>wR</i> ( <i>F</i> <sup>2</sup> ), <i>S</i>	0.041, 0.106, 1.03	0.042, 0.116, 1.06
No. of reflections	5328	2651
No. of parameters	279	150
H-atom treatment	H atoms treated by a mixture of independent and constrained refinement	
$\Delta\rho_{\max}$ , $\Delta\rho_{\min}$ (e Å <sup>-3</sup> )	0.34, -0.22	0.39, -0.20

**Table C3** Crystal data and structure refinement details for MECA, TERTCA and PHPHCA.

<b>Crystal data</b>	<b>MECA</b>	<b>TERTCA</b>	<b>PHPHCA</b>
Chemical formula	C <sub>12</sub> H <sub>13</sub> N <sub>3</sub> O	C <sub>15</sub> H <sub>19</sub> N <sub>3</sub> O	C <sub>17</sub> H <sub>15</sub> N <sub>3</sub> O
Molar Mass (g mol <sup>-1</sup> )	215.25	257.33	277.32
Crystal system, space group	Monoclinic, <i>P2<sub>1</sub>/n</i>	Monoclinic, <i>C2/c</i>	Monoclinic, <i>P2<sub>1</sub>/n</i>
Temperature (K)	100	100	100
<i>a</i> , <i>b</i> , <i>c</i> (Å)	12.849(5), 10.609(5), 16.349(5)	36.239(6), 7.1570(12), 11.2151(19)	13.1403(10), 7.2009(4), 28.993(2)
$\alpha$ , $\beta$ , $\gamma$ (°)	90, 96.668(5), 90	90, 104.478(3), 90	90, 98.731(4), 90
<i>V</i> (Å <sup>3</sup> )	2213.5(15)	2816.4(8)	2711.6(3)
<i>Z</i>	8	8	8
$\mu$ (mm <sup>-1</sup> )	0.09	0.08	0.09
Crystal size (mm)	0.30 x 0.12 x 0.09	0.41 x 0.23 x 0.09	0.31 x 0.18 x 0.08
<b>Data collection</b>			
Diffractometer	Bruker APEX-II CCD	Bruker APEX-II CCD	Bruker APEX-II CCD
Absorption correction	Multi-scan, <i>SADABS</i>	Multi-scan, <i>SADABS</i>	Multi-scan, <i>SADABS</i>
Radiation type	Mo <i>K</i> $\alpha$	Mo <i>K</i> $\alpha$	Mo <i>K</i> $\alpha$
<i>T</i> <sub>min</sub> , <i>T</i> <sub>max</sub>	0.684, 0.746	0.684, 0.746	0.673, 0.746
No. of measured, independent and observed [ <i>I</i> > 2 $\sigma$ ( <i>I</i> )] reflections	22 148, 5907, 4440	29 656, 3453, 2952	19126, 6679, 5157
<i>R</i> <sub>int</sub>	0.026	0.041	0.025
<b>Refinement</b>			
<i>R</i> [ <i>F</i> <sup>2</sup> > 2 $\sigma$ ( <i>F</i> <sup>2</sup> )], <i>wR</i> ( <i>F</i> <sup>2</sup> ), <i>S</i>	0.047, 0.144, 1.03	0.053, 0.140, 1.11	0.046, 0.127, 1.03
No. of reflections	5907	3453	6679
No. of parameters	301	180	389
H-atom treatment	H atoms treated by a mixture of independent and constrained refinement		
$\Delta\rho_{\max}$ , $\Delta\rho_{\min}$ (e Å <sup>-3</sup> )	0.42, -0.23	0.40, -0.25	0.35, -0.24

**Table C4** Crystal data and structure refinement details for [VO(CLA)(DPQ)] and [VO(TERTA)(DPQ)].

<b>Crystal data</b>	<b>[VO(CLA)(DPQ)]</b>	<b>[VO(TERTA)(DPQ)]</b>
Chemical formula	C <sub>27</sub> H <sub>16</sub> ClN <sub>5</sub> O <sub>3</sub> V·CH <sub>2</sub> Cl <sub>2</sub>	C <sub>31</sub> H <sub>25</sub> N <sub>5</sub> O <sub>3</sub> V
Molar Mass (g mol <sup>-1</sup> )	629.76	566.50
Crystal system, space group	Monoclinic, <i>P</i> 2 <sub>1</sub> / <i>c</i>	Triclinic, <i>P</i> -1
Temperature (K)	100	100
<i>a</i> , <i>b</i> , <i>c</i> (Å)	9.9796(14), 20.241(3), 13.5551(17)	11.873(5), 12.018 (5), 12.095 (5)
$\alpha$ , $\beta$ , $\gamma$ (°)	90, 109.441(6), 90	76.601 (5), 61.232 (5), 82.443 (5)
<i>V</i> (Å <sup>3</sup> )	2582.0 (6)	1471.2 (11)
<i>Z</i>	4	2
$\mu$ (mm <sup>-1</sup> )	0.74	0.38
Crystal size (mm)	0.18 x 0.10 x 0.02	0.41 x 0.14 x 0.06
<b>Data collection</b>		
Diffractometer	Bruker APEX-II CCD	Bruker APEX-II CCD
Absorption correction	Multi-scan, SADABS	Multi-scan, SADABS
Radiation type	Mo <i>K</i> $\alpha$	Mo <i>K</i> $\alpha$
<i>T</i> <sub>min</sub> , <i>T</i> <sub>max</sub>	0.665, 0.746	0.683, 0.746
No. of measured, independent and observed [ <i>I</i> > 2 $\sigma$ ( <i>I</i> )] reflections	18348, 5604, 4515	31198, 8532, 7342
<i>R</i> <sub>int</sub>	0.038	0.026
<b>Refinement</b>		
<i>R</i> [ <i>F</i> <sup>2</sup> > 2 $\sigma$ ( <i>F</i> <sup>2</sup> )], <i>wR</i> ( <i>F</i> <sup>2</sup> ), <i>S</i>	0.040, 0.108, 1.04	0.040, 0.112, 0.76
No. of reflections	5604	8532
No. of parameters	361	365
H-atom treatment	H atom parameters constrained	H atom parameters constrained
$\Delta\rho_{\max}$ , $\Delta\rho_{\min}$ (e Å <sup>-3</sup> )	1.07, -0.37	0.52, -0.67

**Table C5** Crystal data and structure refinement details for [VO(PHCA)(PHEN)](PF<sub>6</sub>) and [VO(MECA)(PHEN)](PF<sub>6</sub>).

<b>Crystal data</b>	<b>[VO(PHCA)(PHEN)](PF<sub>6</sub>)</b>	<b>[VO(MECA)(PHEN)](PF<sub>6</sub>)</b>
Chemical formula	C <sub>23</sub> H <sub>18</sub> N <sub>5</sub> O <sub>2</sub> V·F <sub>6</sub> P·CH <sub>2</sub> Cl <sub>2</sub>	C <sub>24</sub> H <sub>20</sub> N <sub>5</sub> O <sub>2</sub> V·F <sub>6</sub> P·CH <sub>2</sub> Cl <sub>2</sub>
Molar Mass (g mol <sup>-1</sup> )	677.26	691.28
Crystal system, space group	Triclinic, <i>P</i> $\bar{1}$	Triclinic, <i>P</i> $\bar{1}$
Temperature (K)	100	100
<i>a</i> , <i>b</i> , <i>c</i> (Å)	9.5935(10), 10.5630(11), 13.3748(14)	10.1490(6), 12.0502(8), 13.2243(9)
$\alpha$ , $\beta$ , $\gamma$ (°)	92.377(5), 96.459(5), 94.437(5)	116.979(2), 100.797(2), 94.141(2)
<i>V</i> (Å <sup>3</sup> )	1341.0(2)	1392.76(16)
<i>Z</i>	2	2
$\mu$ (mm <sup>-1</sup> )	0.71	0.68
Crystal size (mm)	0.19 x 0.10 x 0.06	0.19 x 0.12 x 0.03
<b>Data collection</b>		
Diffractometer	Bruker APEX-II CCD	Bruker APEX-II CCD
Absorption correction	Multi-scan, <i>SADABS</i>	Multi-scan, <i>SADABS</i>
Radiation type	Mo <i>K</i> $\alpha$	Mo <i>K</i> $\alpha$
<i>T</i> <sub>min</sub> , <i>T</i> <sub>max</sub>	0.701, 0.746	0.694, 0.745
No. of measured, independent and observed [ <i>I</i> > 2 $\sigma$ ( <i>I</i> )] reflections	26 649, 6941, 6302	15 969, 5447, 4844
<i>R</i> <sub>int</sub>	0.022	0.018
<b>Refinement</b>		
<i>R</i> [ <i>F</i> <sup>2</sup> > 2 $\sigma$ ( <i>F</i> <sup>2</sup> )], <i>wR</i> ( <i>F</i> <sup>2</sup> ), <i>S</i>	0.033, 0.085, 1.03	0.053, 0.123, 1.03
No. of reflections	6941	5447
No. of parameters	371	400
H-atom treatment	H-atom parameters constrained	H atoms treated by a mixture of independent and constrained refinement
$\Delta\rho_{\max}$ , $\Delta\rho_{\min}$ (e Å <sup>-3</sup> )	1.39, -0.39	1.97, -1.61

**Table C6** Crystal data and structure refinement details for [VO(TERTCA)(PHEN)](PF<sub>6</sub>).

<b>Crystal data</b>	<b>[VO(TERTCA)(PHEN)](PF<sub>6</sub>)</b>
Chemical formula	C <sub>27</sub> H <sub>26</sub> N <sub>5</sub> O <sub>2</sub> V·C <sub>6</sub> H <sub>5</sub> Cl·F <sub>6</sub> P
Molar Mass (g mol <sup>-1</sup> )	760.99
Crystal system, space group	Monoclinic, <i>P</i> 2 <sub>1</sub> / <i>n</i>
Temperature (K)	100
<i>a</i> , <i>b</i> , <i>c</i> (Å)	15.4347(7), 15.5428(7), 15.5623(7)
β (°)	117.516(2)
<i>V</i> (Å <sup>3</sup> )	3311.1(3)
<i>Z</i>	4
μ (mm <sup>-1</sup> )	0.50
Crystal size (mm)	0.06 x 0.06 x 0.04
<b>Data collection</b>	
Diffractometer	Bruker APEX-II CCD
Absorption correction	Multi-scan, <i>SADABS</i>
Radiation type	Mo <i>K</i> α
<i>T</i> <sub>min</sub> , <i>T</i> <sub>max</sub>	0.634, 0.745
No. of measured, independent and observed [ <i>I</i> > 2σ( <i>I</i> )] reflections	24 959, 6432, 4746
<i>R</i> <sub>int</sub>	0.050
<b>Refinement</b>	
<i>R</i> [ <i>F</i> <sup>2</sup> > 2σ( <i>F</i> <sup>2</sup> )], <i>wR</i> ( <i>F</i> <sup>2</sup> ), <i>S</i>	0.047, 0.123, 1.03
No. of reflections	6432
No. of parameters	446
H-atom treatment	H-atom parameters constrained
Δρ <sub>max</sub> , Δρ <sub>min</sub> (e Å <sup>-3</sup> )	0.64, -0.50

## **Appendix D: Density Functional Theory Results**

**Table D1** A comparison of selected solid-state and DFT-simulated bond lengths (Å) and bond angles (°) for PHCA. Atom numbers are indicated in the appended structure in *Table D3*.

Ligand	PHCA(a) solid-state	PHCA(b) solid-state	DFT- simulated	% Difference (a)	% Difference (b)
<b>Bond Lengths</b>					
C4–C5	1.460(2)	1.459(2)	1.447	0.89%	0.82%
C5–N3	1.278(2)	1.281(2)	1.285	–0.55%	–0.31%
N3–C6	1.426(1)	1.418(1)	1.401	1.8%	1.2%
C7–O1	1.369(1)	1.357(1)	1.368	0.07%	–0.81%
<b>Bond Angles</b>					
C4–C5–N3	123.2(1)	122.3(1)	122.65	0.45%	–0.29%
C5–N3–C6	118.2(1)	123.4(1)	123.44	–4.4%	–0.03%
N3–C6–C7	121.9(1)	127.3(1)	126.75	–4.0%	0.43%
N3–C6–C11	118.8(1)	114.4(1)	115.99	2.4%	–1.4%
<b>Torsion Angles</b>					
C4–C5–N3–C6	175.6(1)	–178.2(1)	179.32	2.1%	–0.63%
C5–N3–C6–C7	–59.1(2)	–7.6(2)	–25.26	57%	232%

**Table D2** A comparison of selected solid-state and DFT-simulated bond lengths (Å) and bond angles (°) for MECA. Atom numbers are indicated in the appended structure in *Table D3*.

Ligand	MECA(a) solid-state	MECA(b) solid-state	DFT- simulated	% Difference (a)	% Difference (b)
<b>Bond Lengths</b>					
C4–C5	1.448(2)	1.451(2)	1.447	0.07%	0.28%
C5–N3	1.281(2)	1.281(2)	1.285	–0.31%	–0.31%
N3–C6	1.410(2)	1.411(2)	1.401	0.64%	0.71%
C7–O1	1.352(1)	1.352(1)	1.369	–1.3%	–1.3%
<b>Bond Angles</b>					
C4–C5–N3	122.5(1)	122.3(1)	122.55	–0.04%	–0.20%
C5–N3–C6	122.4(1)	122.3(1)	123.65	–1.0%	–1.1%
N3–C6–C7	126.8(1)	126.6(1)	127.04	–0.19%	–0.35%
N3–C6–C11	115.1(1)	115.1(1)	115.63	–0.46%	–0.46%
<b>Torsion Angles</b>					
C4–C5–N3–C6	174.6(1)	–175.8(1)	179.37	2.7%	–2.0%
C5–N3–C6–C7	–15.4(2)	16.3(2)	–22.33	45%	–37%

**Table D3** A comparison of selected solid-state and DFT-simulated bond lengths (Å) and bond angles (°) for TERTCA. Atom numbers are indicated in the appended structure.

Ligand	TERTCA solid-state	DFT- simulated	% Difference
<b>Bond Lengths</b>			
C4–C5	1.456(2)	1.447	0.62%
C5–N3	1.284(2)	1.285	–0.08%
N3–C6	1.421(2)	1.402	1.3%
C7–O1	1.354(2)	1.369	–1.1%
<b>Bond Angles</b>			
C4–C5–N3	123.4(1)	122.68	0.58%
C5–N3–C6	120.8(1)	123.41	–2.2%
N3–C6–C7	126.8(1)	126.88	–0.06%
N3–C6–C11	114.6(1)	115.51	–0.79%
<b>Torsion Angles</b>			
C4–C5–N3–C6	176.4(1)	–179.29	–1.6%
C5–N3–C6–C7	19.1(2)	23.87	–25.0%

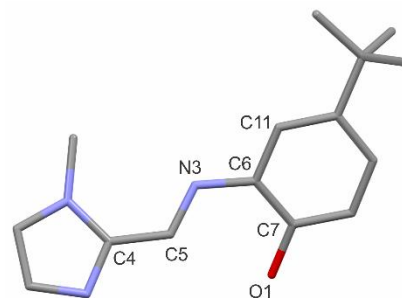


**Table D4** A comparison of selected solid-state and DFT-simulated bond lengths (Å) and bond angles (°) for PHPHCA. Atom numbers are indicated in the appended structure in Table D3.

Ligand	PHPHCA (a) solid-state	PHPHCA (b) solid-state	DFT- simulated	% Difference (a)	% Difference (b)
<b>Bond Lengths</b>					
C4–C5	1.457(2)	1.456(2)	1.447	0.69%	0.62%
C5–N3	1.284(2)	1.274(2)	1.284	0%	–0.78%
N3–C6	1.416(2)	1.416(2)	1.401	1.1%	1.1%
C7–O1	1.341(2)	1.350(2)	1.367	–1.9%	–1.3%
<b>Bond Angles</b>					
C4–C5–N3	122.2(1)	121.5(1)	122.73	–0.43%	–1.0%
C5–N3–C6	122.9(1)	122.4(1)	123.03	–0.11%	–0.51%
N3–C6–C7	126.8(1)	127.7(1)	126.38	0.33%	1.0%
N3–C6–C11	114.9(1)	114.0(1)	116.03	–0.98%	–1.8%
<b>Torsion Angles</b>					
C4–C5–N3–C6	174.1(1)	177.8(1)	179.05	2.8%	0.70%
C5–N3–C6–C7	0.6(2)	11.2(2)	–28.53	–4655%	–155%

**Table D5** Experimental and DFT-simulated monomer and dimer imine C=N stretching vibrational frequencies ( $\text{cm}^{-1}$ ) of the *O,N,N'* ligands.

<i>O,N,N'</i> Ligand	Experimental $\nu$ (C=N) ( $\text{cm}^{-1}$ )	DFT Monomer $\nu$ (C=N) ( $\text{cm}^{-1}$ )	DFT Dimer $\nu$ (C=N) ( $\text{cm}^{-1}$ )
<b>PHCA</b>	1634	1674	1668
<b>MECA</b>	1620	1675	1672
<b>TERTCA</b>	1618	1674	1669
<b>PHPHCA</b>	1614	1675	1670

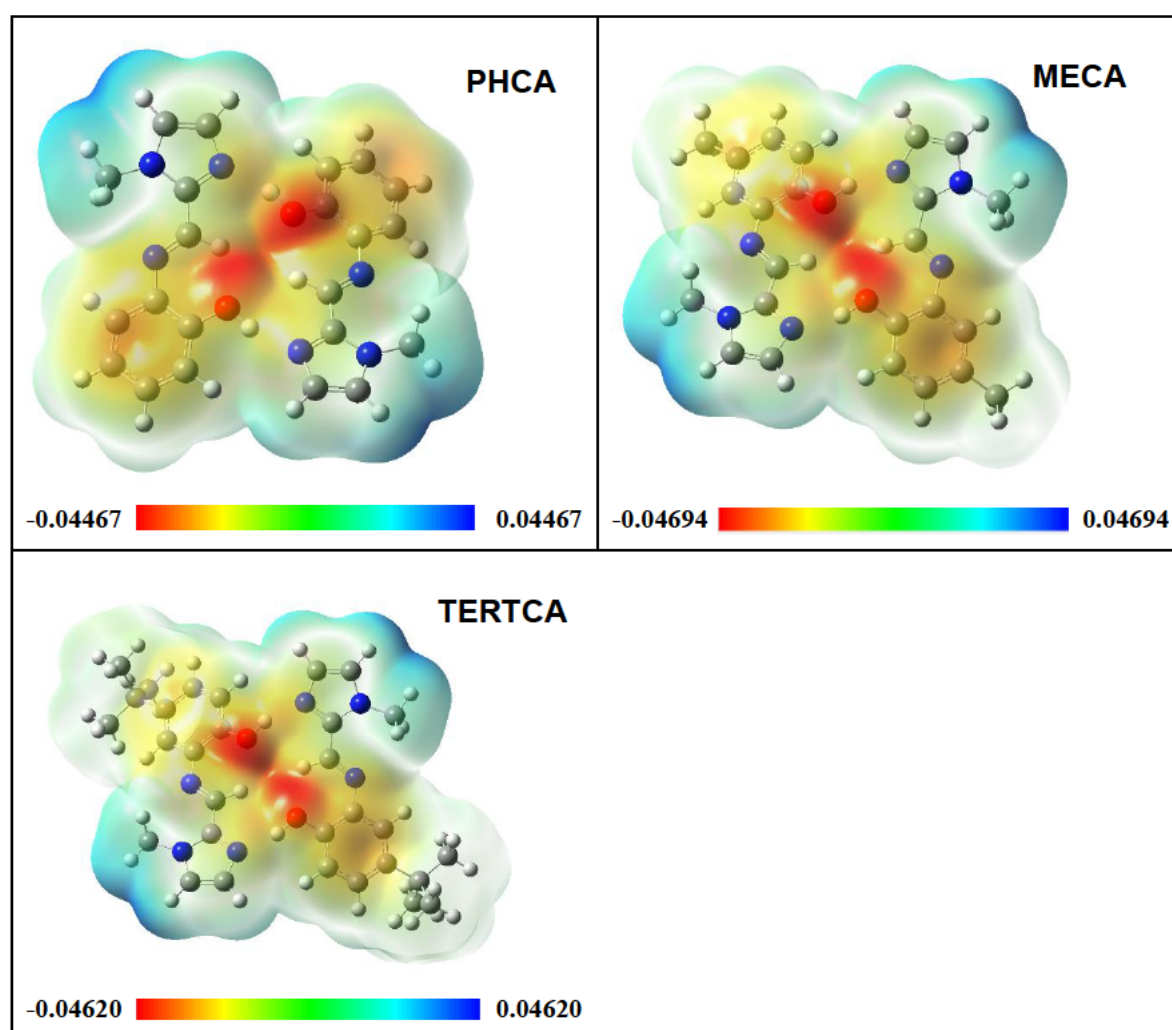


**Figure D1** Electrostatic potential (ESP) maps from the total SCF density for the PHCA, MECA and TERTCA dimers highlighting the zones of positive (blue) and negative (red) electrostatic potential.

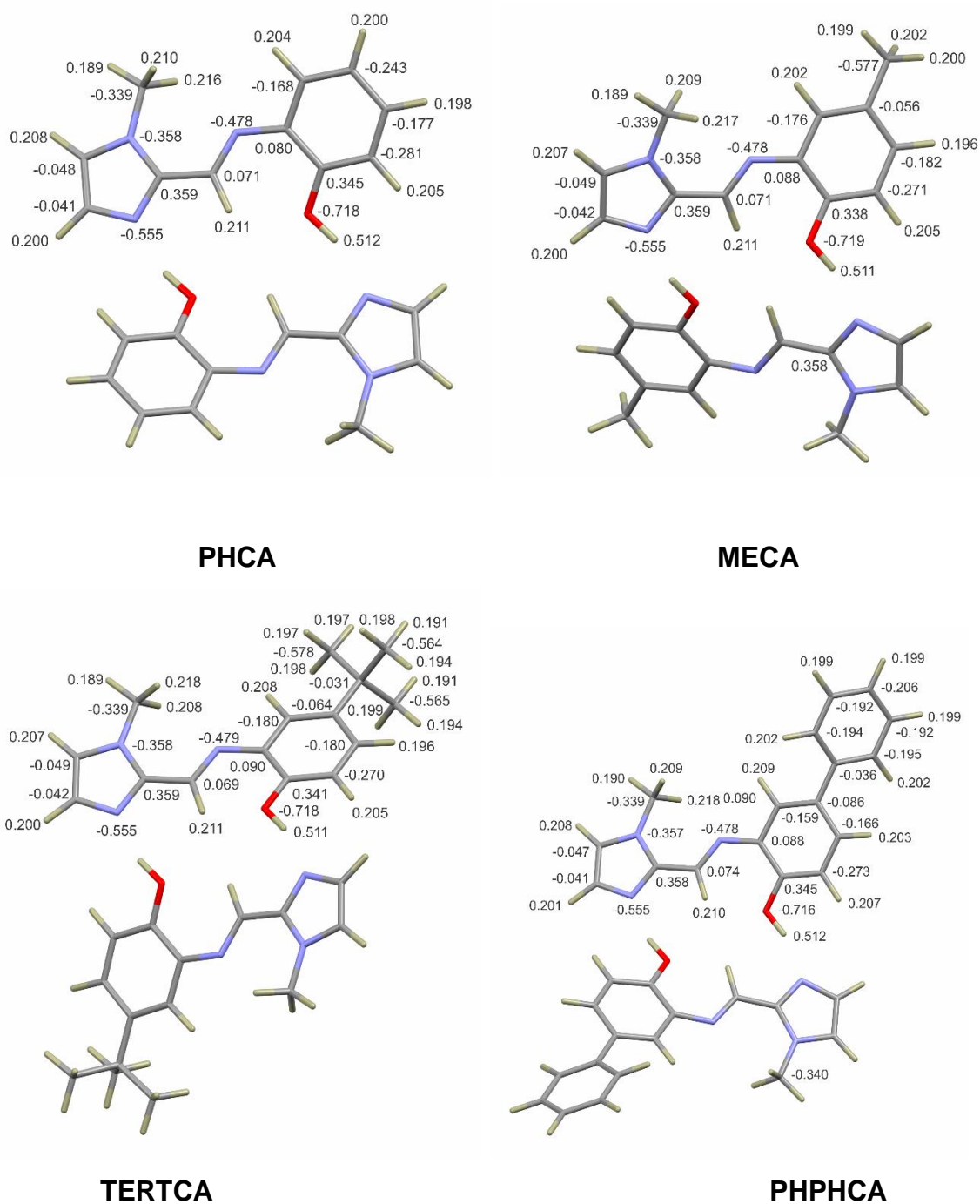


**Figure D2** DFT-calculated NBO partial charges (e) for the dimeric species of the *O,N,N'* ligands. NBO charges are not repeated for those atoms that have the same NBO charges in the dimeric structures. The OH hydrogen atom and oxygen have the most positive and negative charges respectively.

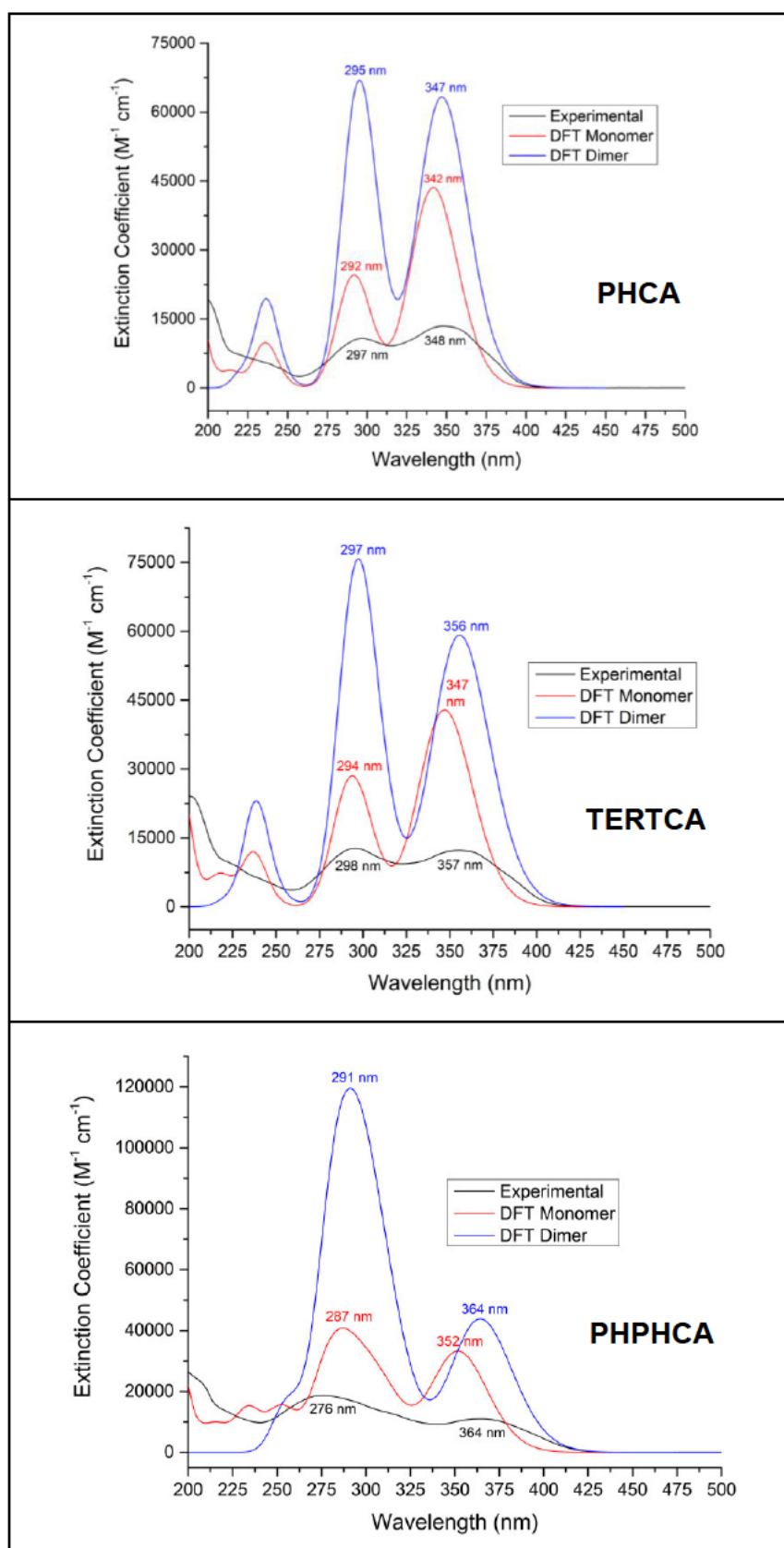


**Figure D3** Superposition plots of the experimental and the TD-DFT-simulated ( $\text{CH}_3\text{CN}$  solvent continuum) monomer and dimer UV/visible spectra of PHCA, TERTCA and PHPHCA.

**Table D6** Summary of the major TD-DFT-simulated (CH<sub>3</sub>CN solvent continuum) electronic transitions and oscillator strengths for the monomeric and dimeric structures of PHCA and the corresponding molecular orbitals.

$\lambda$ (nm) <sup>a</sup>	Oscillator Strength, f	Molecular Orbitals	Contri- bution <sup>b</sup>	Assignment <sup>c</sup>
<b>PHCA Monomer</b>				
341.68	0.6008	53 (HOMO) → 54 (LUMO)	88%	$\pi$ (Imd, Im, Phenol) → $\pi^*$ (Imd, Im, Phenol)
293.25	0.1219	50 (HOMO-3) → 54 (LUMO)	12%	$\pi$ (N-Me, Imd, Im, Phen) → $\pi^*$ (Imd, Im, Phenol)
		51 (HOMO-2) → 54 (LUMO)	75%	$\pi$ (N-Me, Imd, Im, Phen) → $\pi^*$ (Imd, Im, Phenol)
291.00	0.2186	52 (HOMO-1) → 54 (LUMO)	88%	$\pi$ (Imd, Im, Phenol) → $\pi^*$ (Imd, Im, Phenol)
236.32	0.1280	50 (HOMO-3) → 54 (LUMO)	38%	$\pi$ (N-Me, Imd, Im, Phen) → $\pi^*$ (Imd, Im, Phenol)
		51 (HOMO-2) → 54 (LUMO)	13%	$\pi$ (N-Me, Imd, Im, Phen) → $\pi^*$ (Imd, Im, Phenol)
		53 (HOMO) → 55 (LUMO+1)	34%	$\pi$ (Imd, Im, Phenol) → $\pi^*$ (Phenol)
<b>PHCA Dimer</b>				
345.60	0.7240	105 (HOMO-1) → 107 (LUMO)	81%	$\pi$ (Imd, Im, Phenol) → $\pi^*$ (Imd, Im, Phenol)
		106 (HOMO) → 108 (LUMO+1)	10%	$\pi$ (Imd, Im, Phenol) → $\pi^*$ (Imd, Im, Phenol)
295.01	0.8542	103 (HOMO-3) → 108 (LUMO+1)	41%	$\pi$ (Imd, Im, Phenol) → $\pi^*$ (Imd, Im, Phenol)
		104 (HOMO-2) → 107 (LUMO)	29%	$\pi$ (Imd, Im, Phenol) → $\pi^*$ (Imd, Im, Phenol)
236.91	0.2321	99 (HOMO-7) → 108 (LUMO+1)	10%	$\pi$ (Imd, Im, Phenol) → $\pi^*$ (Imd, Im, Phenol)
		100 (HOMO-6) → 107 (LUMO)	15%	$\pi$ (Imd, Im, Phenol) → $\pi^*$ (Imd, Im, Phenol)
		105 (HOMO-1) → 109 (LUMO+2)	12%	$\pi$ (Imd, Im, Phenol) → $\pi^*$ (Phenol)
		106 (HOMO) → 110 (LUMO+3)	41%	$\pi$ (Imd, Im, Phenol) → $\pi^*$ (Phenol)

<sup>a</sup> Three-Four of the 24 calculated excited states with the highest oscillator strengths are listed.

<sup>b</sup> Only orbitals with >10% contribution are listed.

<sup>c</sup> Imd = imidazole; Im = imine; Phenol = benzene ring + OH; Phen = benzene ring; N-Me = imidazole N-CH<sub>3</sub>.

**Table D7** Summary of the major TD-DFT-simulated (CH<sub>3</sub>CN solvent continuum) electronic transitions and oscillator strengths for the monomeric and dimeric structures of TERTCA and the corresponding molecular orbitals.

$\lambda$ (nm) <sup>a</sup>	Oscillator Strength, f	Molecular Orbitals	Contri- bution <sup>b</sup>	Assignment <sup>c</sup>
<b>TERTCA Monomer</b>				
347.00	0.5911	69 (HOMO) → 70 (LUMO)	91%	$\pi$ (Imd, Im, Phenol, Tert) → $\pi^*$ (Imd, Im, Phenol)
292.90	0.3268	66 (HOMO-3) → 70 (LUMO)	12%	$\pi$ (N-Me, Imd, Im, Phen) → $\pi^*$ (Imd, Im, Phenol)
		67 (HOMO-2) → 70 (LUMO)	45%	$\pi$ (N-Me, Imd, Im, Phen) → $\pi^*$ (Imd, Im, Phenol)
		68 (HOMO-1) → 70 (LUMO)	32%	$\pi$ (Imd, Im, Phenol, Tert) → $\pi^*$ (Imd, Im, Phenol)
237.07	0.1581	66 (HOMO-3) → 70 (LUMO)	35%	$\pi$ (N-Me, Imd, Im, Phen) → $\pi^*$ (Imd, Im, Phenol)
		67 (HOMO-2) → 70 (LUMO)	13%	$\pi$ (N-Me, Imd, Im, Phen) → $\pi^*$ (Imd, Im, Phenol)
		69 (HOMO) → 71 (LUMO+1)	35%	$\pi$ (Imd, Im, Phenol, Tert) → $\pi^*$ (Phenol, Tert)
<b>TERTCA Dimer</b>				
354.45	0.7013	137 (HOMO-1) → 139 (LUMO)	79%	$\pi$ (Imd, Im, Phenol, Tert) → $\pi^*$ (Imd, Im, Phenol)
		138 (HOMO) → 140 (LUMO+1)	14%	$\pi$ (Imd, Im, Phenol, Tert) → $\pi^*$ (Imd, Im, Phenol)
296.78	0.7722	134 (HOMO-4) → 139 (LUMO)	10%	$\pi$ (N-Me, Imd, Im, Phenol) → $\pi^*$ (Imd, Im, Phenol)
		135 (HOMO-3) → 140 (LUMO+1)	68%	$\pi$ (Imd, Im, Phenol, Tert) → $\pi^*$ (Imd, Im, Phenol)
238.64	0.2807	131 (HOMO-7) → 140 (LUMO+1)	11%	$\pi$ (Imd, Im, Phenol) → $\pi^*$ (Imd, Im, Phenol)
		132 (HOMO-6) → 139 (LUMO)	18%	$\pi$ (Imd, Im, Phenol) → $\pi^*$ (Imd, Im, Phenol)
		137 (HOMO-1) → 141 (LUMO+2)	14%	$\pi$ (Imd, Im, Phenol, Tert) → $\pi^*$ (Phenol)
		138 (HOMO) → 142 (LUMO+3)	34%	$\pi$ (Imd, Im, Phenol, Tert) → $\pi^*$ (Phenol)

<sup>a</sup> Three of the 24 calculated excited states with the highest oscillator strengths are listed.

<sup>b</sup> Only orbitals with >10% contribution are listed.

<sup>c</sup> Imd = imidazole; Im = imine; Phenol = benzene ring + OH; Phen = benzene ring; N-Me = imidazole N-CH<sub>3</sub>; Tert = phenolic *tert*-butyl substituent.

**Table D8** Summary of the major TD-DFT-simulated (CH<sub>3</sub>CN solvent continuum) electronic transitions and oscillator strengths for the monomeric and dimeric structures of PHPHCA and the corresponding molecular orbitals.

$\lambda$ (nm) <sup>a</sup>	Oscillator Strength, f	Molecular Orbitals	Contri- bution <sup>b</sup>	Assignment <sup>c</sup>
<b>PHPHCA Monomer</b>				
352.00	0.4562	73 (HOMO) → 74 (LUMO)	91%	$\pi$ (Imd, Im, Phenol, Phenyl) → $\pi^*$ (Imd, Im, Phenol)
292.04	0.3238	71 (HOMO-2) → 74 (LUMO)	64%	$\pi$ (N-Me, Imd, Im, Phen) → $\pi^*$ (Imd, Im, Phenol)
		72 (HOMO-1) → 74 (LUMO)	16%	$\pi$ (Imd, Im, Phenol, Phenyl) → $\pi^*$ (Imd, Im, Phenol)
278.22	0.3464	73 (HOMO) → 75 (LUMO+1)	88%	$\pi$ (Imd, Im, Phenol, Phenyl) → $\pi^*$ (Phenol, Phenyl)
<b>PHPHCA Dimer</b>				
361.82	0.3235	145 (HOMO-1) → 147 (LUMO)	95%	$\pi$ (Imd, Im, Phenol, Phenyl) → $\pi^*$ (Imd, Im, Phenol)
313.42	0.4014	141 (HOMO-5) → 148 (LUMO+1)	15%	$\pi$ (Imd, Im, Phenol) → $\pi^*$ (Imd, Im, Phenol)
		142 (HOMO-4) → 147 (LUMO)	17%	$\pi$ (N-Me, Imd, Im, Phenol) → $\pi^*$ (Imd, Im, Phenol)
		143 (HOMO-3) → 148 (LUMO+1)	18%	$\pi$ (Imd, Im, Phenol, Phenyl) → $\pi^*$ (Imd, Im, Phenol)
		144 (HOMO-2) → 147 (LUMO)	41%	$\pi$ (Imd, Im, Phenol, Phenyl) → $\pi^*$ (Imd, Im, Phenol)
296.91	0.9438	141 (HOMO-5) → 148 (LUMO+1)	23%	$\pi$ (Imd, Im, Phenol) → $\pi^*$ (Imd, Im, Phenol)
		142 (HOMO-4) → 147 (LUMO)	27%	$\pi$ (N-Me, Imd, Im, Phenol,) → $\pi^*$ (Imd, Im, Phenol)
		143 (HOMO-3) → 148 (LUMO+1)	12%	$\pi$ (Imd, Im, Phenol, Phenyl) → $\pi^*$ (Imd, Im, Phenol)
		144 (HOMO-2) → 147 (LUMO)	23%	$\pi$ (Imd, Im, Phenol, Phenyl) → $\pi^*$ (Imd, Im, Phenol)
282.24	0.8567	145 (HOMO-1) → 149 (LUMO+2)	22%	$\pi$ (Imd, Im, Phenol, Phenyl) → $\pi^*$ (Phenola, Phenyla)
		145 (HOMO-1) → 150 (LUMO+3)	15%	$\pi$ (Imd, Im, Phenol, Phenyl) → $\pi^*$ (Phenolb, Phenylb)
		146 (HOMO) → 149 (LUMO+2)	23%	$\pi$ (Imd, Im, Phenol, Phenyl) → $\pi^*$ (Phenola, Phenyla)
		146 (HOMO) → 150 (LUMO+3)	34%	$\pi$ (Imd, Im, Phenol, Phenyl) → $\pi^*$ (Phenolb, Phenylb)

<sup>a</sup> Three-Four of the 24 calculated excited states with the highest oscillator strengths are listed.

<sup>b</sup> Only orbitals with >10% contribution are listed.

<sup>c</sup> Imd = imidazole; Im = imine; Phenol = benzene ring + OH; Phen = benzene ring; N-Me = imidazole N-CH<sub>3</sub>; Phenyl = phenolic phenyl substituent.

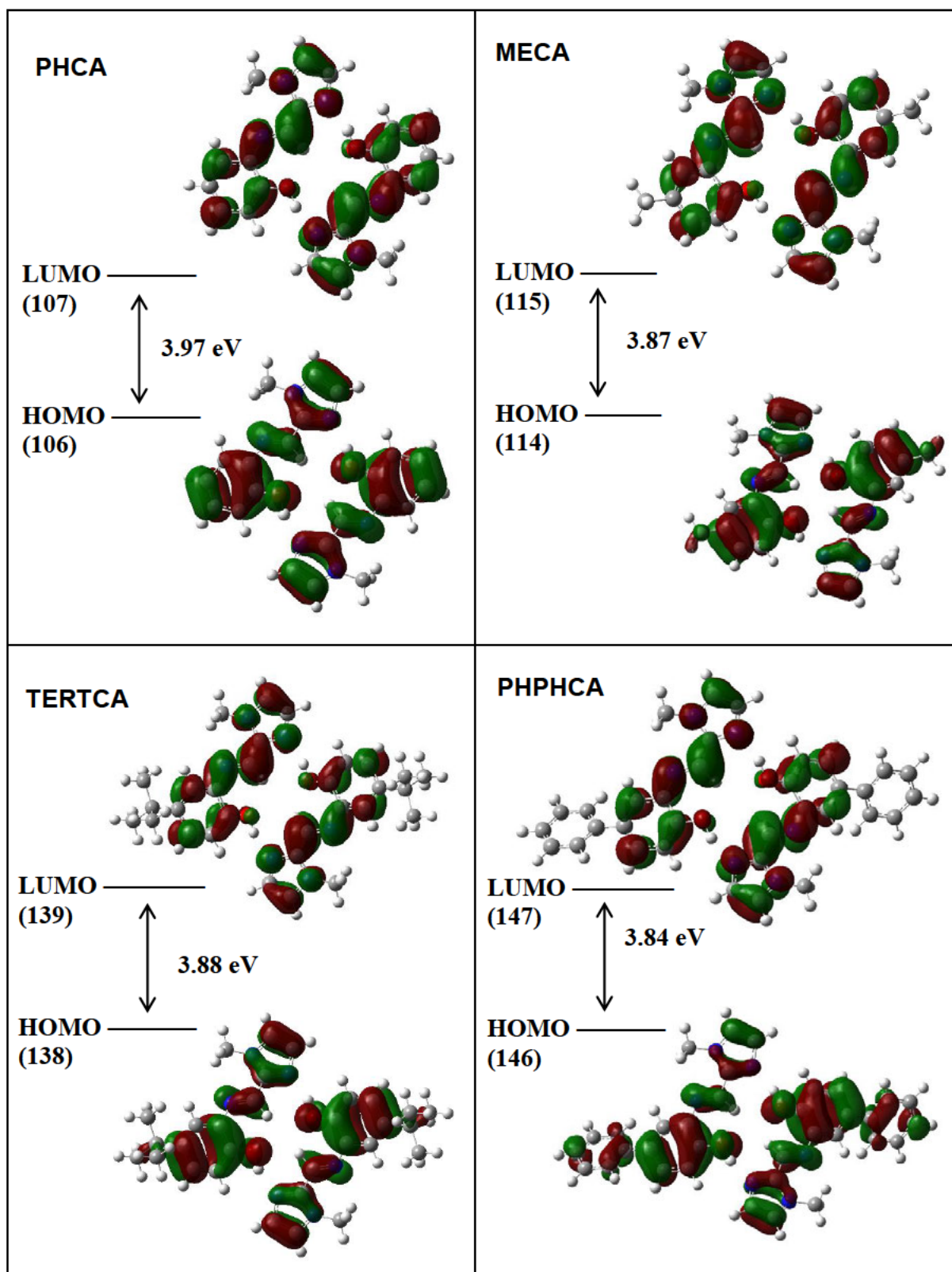


**Figure D4** HOMO and LUMO plots for the geometry-optimised (gas phase) dimers of PHCA, MECA, TERTCA and PHPHCA, illustrating how the orbitals span both molecules. The energy gap of the frontier molecular orbitals is also indicated for each ligand.

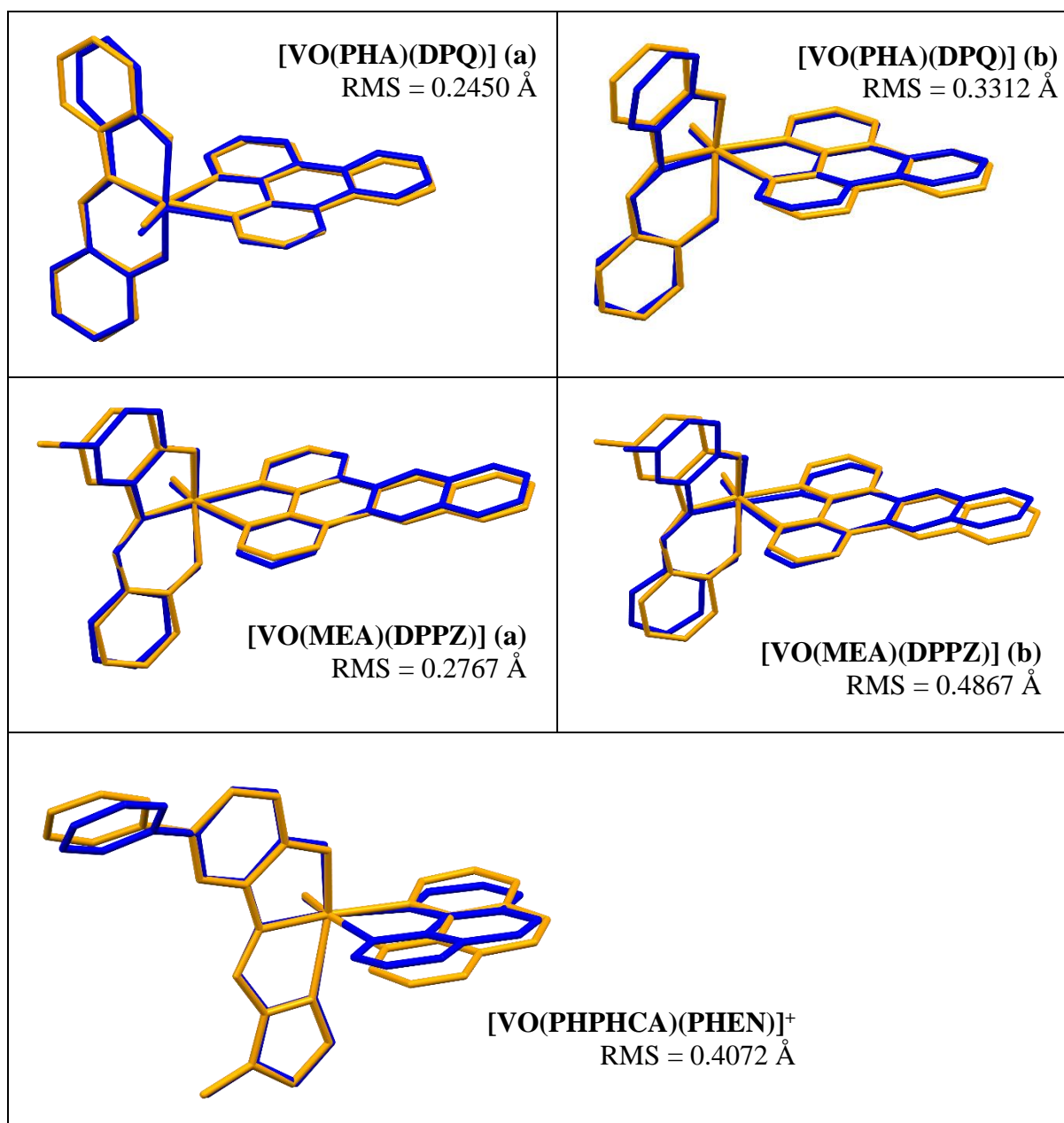


**Figure D5** Least-squares-fits of the optimised (yellow) and low-resolution solid-state (blue) structures of [VO(PHA)(DPQ)], [VO(MEA)(DPPZ)] and [VO(PHPHCA)(PHEN)]<sup>+</sup>. Root mean square deviations (RMSD) for all non-hydrogen atoms are indicated on the diagram.

**Table D9** A comparison of selected solid-state and DFT-simulated bond lengths (Å) and bond angles (°) for [VO(TERTA)(DPQ)]. Atom numbers are indicated in the appended structure.

Bond Lengths	Solid-state	Calculated	% Difference
V1–O1	1.977(1)	1.963	0.71
V1–O2	1.981(1)	1.956	1.3
V1–O3	1.606(2)	1.583	1.4
V1–N1	2.070(1)	2.096	-1.3
V1–N2	2.151(1)	2.202	-2.4
V1–N3	2.337(2)	2.454	-5.0
C6–C7	1.434(2)	1.432	0.14
C7–N1	1.295(2)	1.302	-0.54
N1–C8	1.421(2)	1.417	0.28
Bond Angles	Solid-state	Calculated	% Difference
O3–V1–N1	103.68(6)	103.99	-0.30
O3–V1–N2	94.55(6)	91.14	3.6
O3–V1–N3	167.30(6)	161.22	3.6
O3–V1–O1	100.35(6)	102.37	-2.0
O3–V1–O2	102.14(6)	104.92	-2.7
C6–C7–N1	125.8(2)	126.12	-0.3

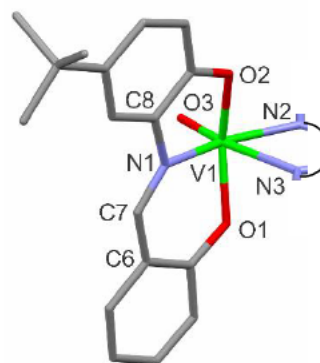


**Table D10** A comparison of selected solid-state and DFT-simulated bond lengths (Å) and bond angles (°) for [VO(PHCA)(PHEN)]<sup>+</sup>. Atom numbers are indicated in the appended structure.

Bond Lengths	Solid-state	Calculated	% Difference
V1–O1	1.951(1)	1.947	0.21
V1–O2	1.607(1)	1.574	2.1
V1–N1	2.151(1)	2.173	-1.0
V1–N3	2.085(1)	2.123	-1.8
V1–N4	2.126(1)	2.154	-1.3
V1–N5	2.301(1)	2.390	-3.9
C4–C5	1.441(2)	1.442	-0.07
C5–N3	1.290(2)	1.299	-0.70
N3–C6	1.401(2)	1.383	1.3
Bond Angles	Solid-state	Calculated	% Difference
O2–V1–N1	94.34(5)	94.94	-0.64
O2–V1–N4	94.82(5)	92.38	2.6
O2–V1–N5	165.15(5)	163.69	0.88
O2–V1–O1	103.66(5)	105.43	-1.7
O2–V1–N3	103.86(5)	104.93	-1.0
C4–C5–N3	112.9(1)	114.29	-1.2

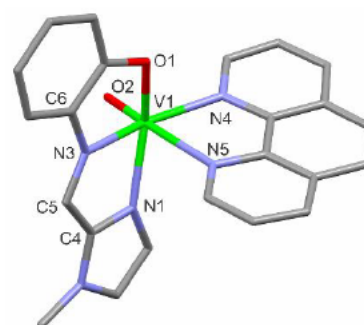


**Table D11** A comparison of selected solid-state and DFT-simulated bond lengths (Å) and bond angles (°) for [VO(MECA)(PHEN)]<sup>+</sup>. Atom numbers are indicated in the appended structure.

Bond Lengths	Solid-state	Calculated	% Difference
V1–O1	1.967(2)	1.948	0.97
V1–O2	1.604(3)	1.574	1.9
V1–N1	2.122(3)	2.170	-2.3
V1–N3	2.080(3)	2.123	-2.1
V1–N4	2.116(3)	2.154	-1.8
V1–N5	2.311(3)	2.391	-3.5
C4–C5	1.445(5)	1.441	0.28
C5–N3	1.295(4)	1.301	-0.46
N3–C6	1.404(4)	1.381	1.6
Bond Angles	Solid-state	Calculated	% Difference
O2–V1–N1	96.1(1)	95.17	1.0
O2–V1–N4	91.8(1)	92.35	-0.6
O2–V1–N5	165.5(1)	163.70	1.1
O2–V1–O1	101.9(1)	105.34	-3.4
O2–V1–N3	106.9(1)	104.96	1.8
C4–C5–N3	113.1(3)	114.21	-1.0

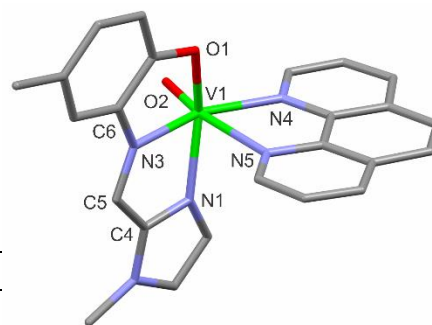


**Table D12** A comparison of selected solid-state and DFT-simulated bond lengths (Å) and bond angles (°) for [VO(TERTCA)(PHEN)]<sup>+</sup>. Atom numbers are indicated in the appended structure in *Table D11*.

Bond Lengths	Solid-state	Calculated	% Difference
V1–O1	1.952(2)	1.948	0.20
V1–O2	1.603(2)	1.574	1.8
V1–N1	2.139(2)	2.169	-1.4
V1–N3	2.087(2)	2.122	-1.7
V1–N4	2.108(2)	2.154	-2.2
V1–N5	2.312(3)	2.391	-3.4
C4–C5	1.434(4)	1.441	-0.49
C5–N3	1.293(3)	1.301	-0.62
N3–C6	1.397(3)	1.381	1.1
Bond Angles	Solid-state	Calculated	% Difference
O2–V1–N1	95.4(1)	95.06	0.4
O2–V1–N4	94.4(1)	92.44	2.1
O2–V1–N5	165.9(1)	163.70	1.3
O2–V1–O1	102.93(9)	105.36	-2.4
O2–V1–N3	105.4(1)	105.20	0.2
C4–C5–N3	112.8(3)	114.19	-1.2

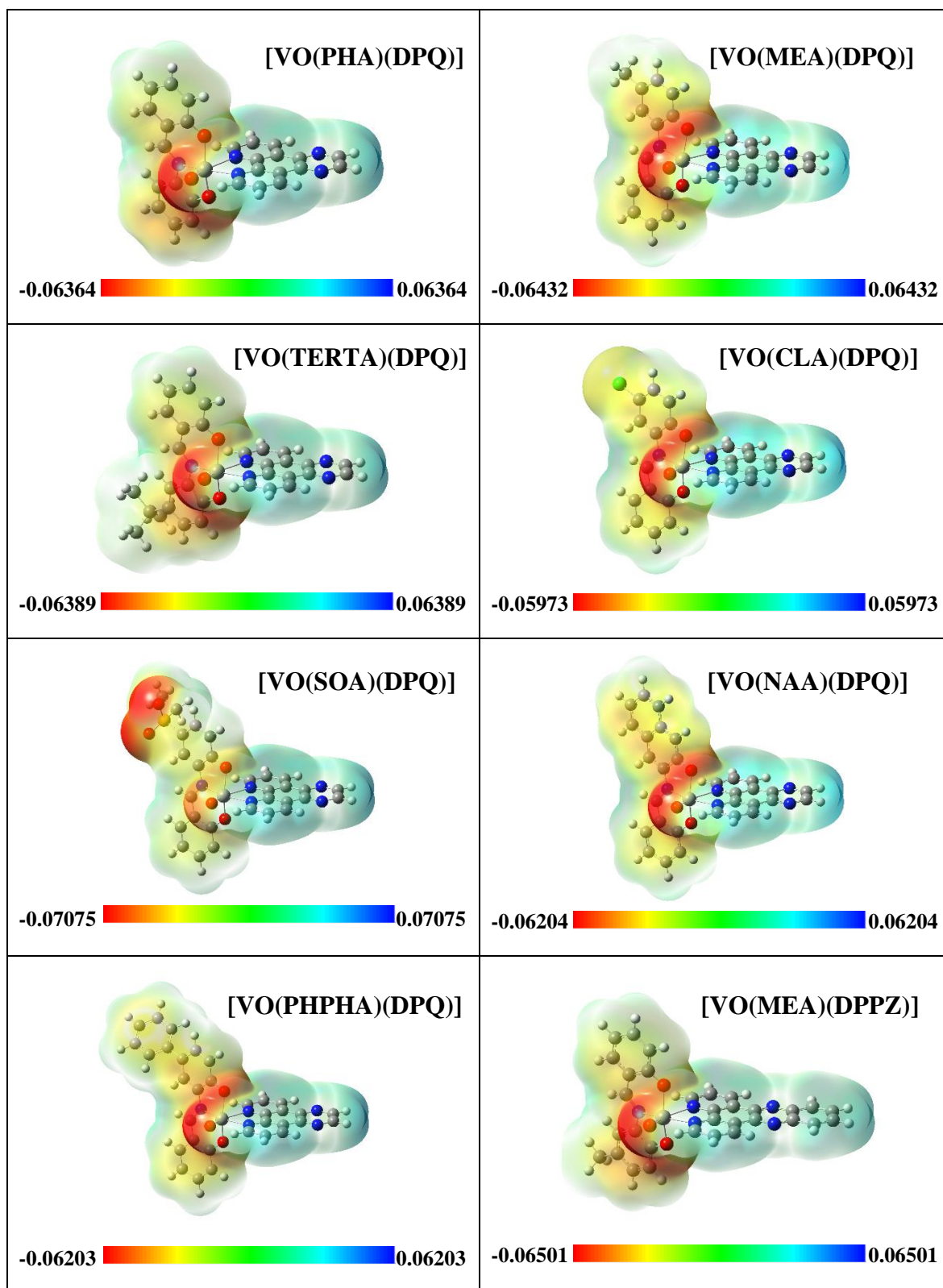


**Figure D6** Electrostatic potential (ESP) plots from the total SCF density for the neutral oxovanadium(IV) complexes highlighting the zones of positive (blue) and negative (red) electrostatic potential.

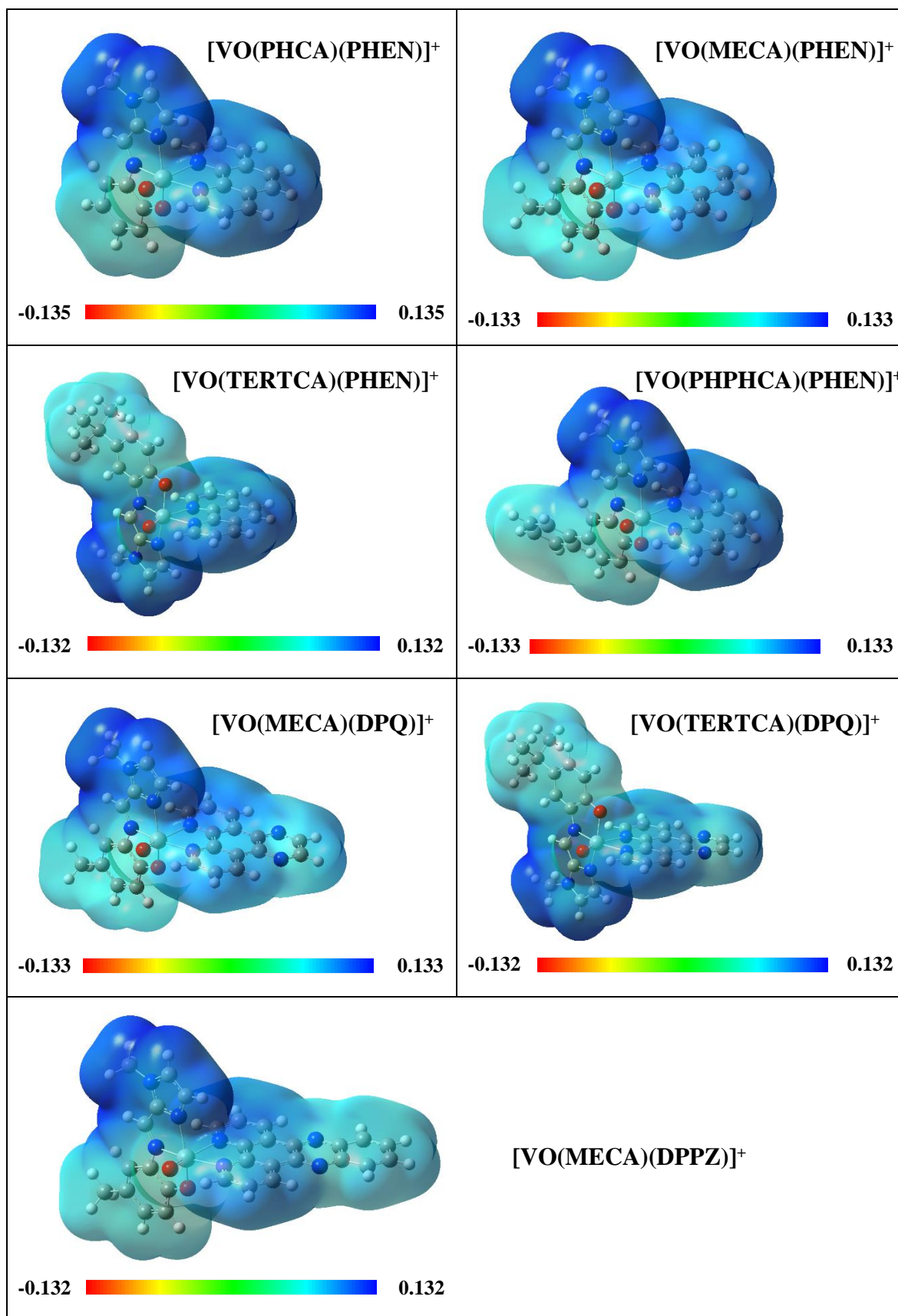


**Figure D7** Electrostatic potential (ESP) plots from the total SCF density for the cationic oxovanadium(IV) complexes highlighting the zones of positive (blue) and negative (red) electrostatic potential.

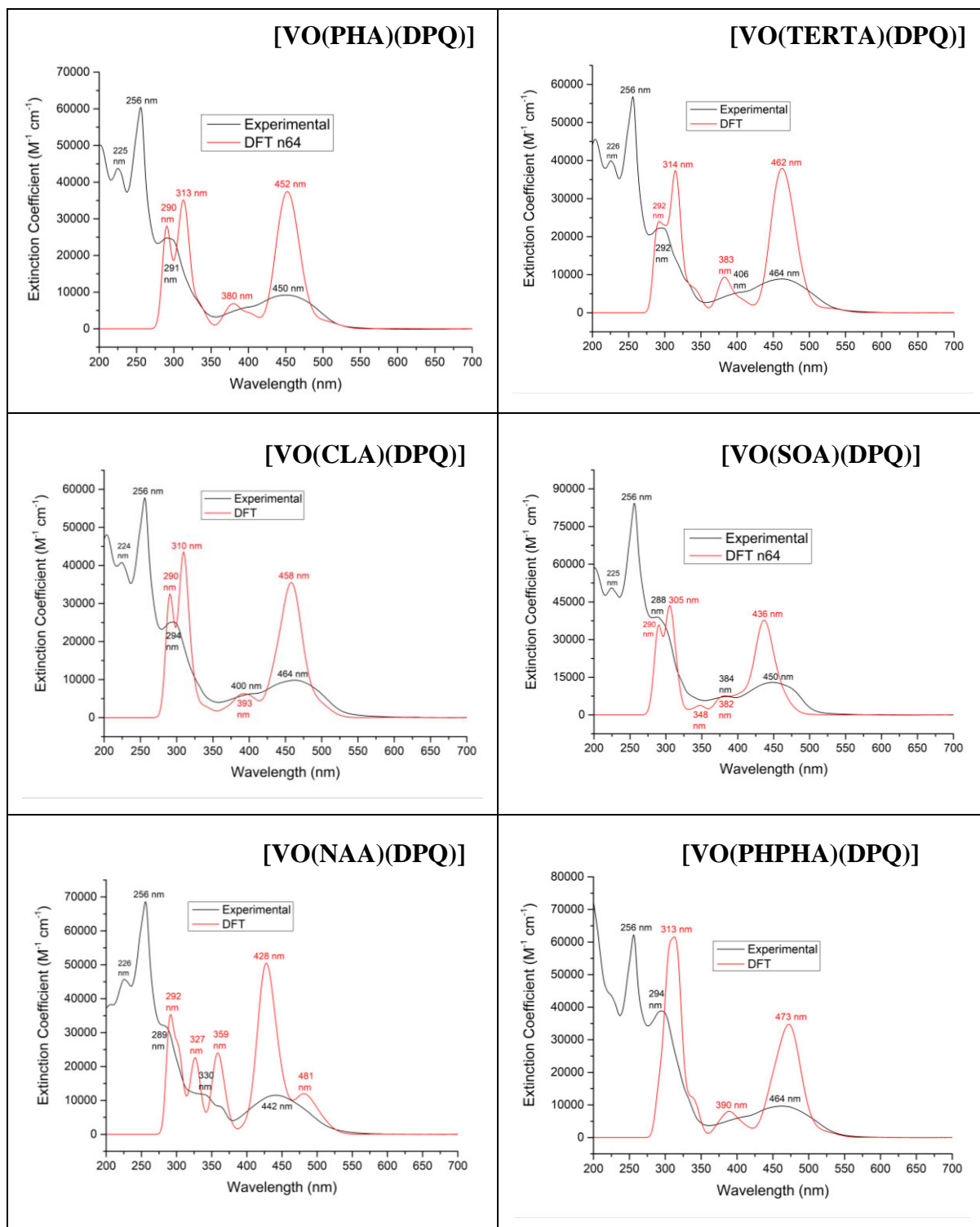


**Figure D8** Superposition plots of the experimental and the TD-DFT-simulated ( $CH_3CN$  solvent continuum) UV/visible spectra of the neutral  $[VO(ONO)(DPQ)]$  complexes.

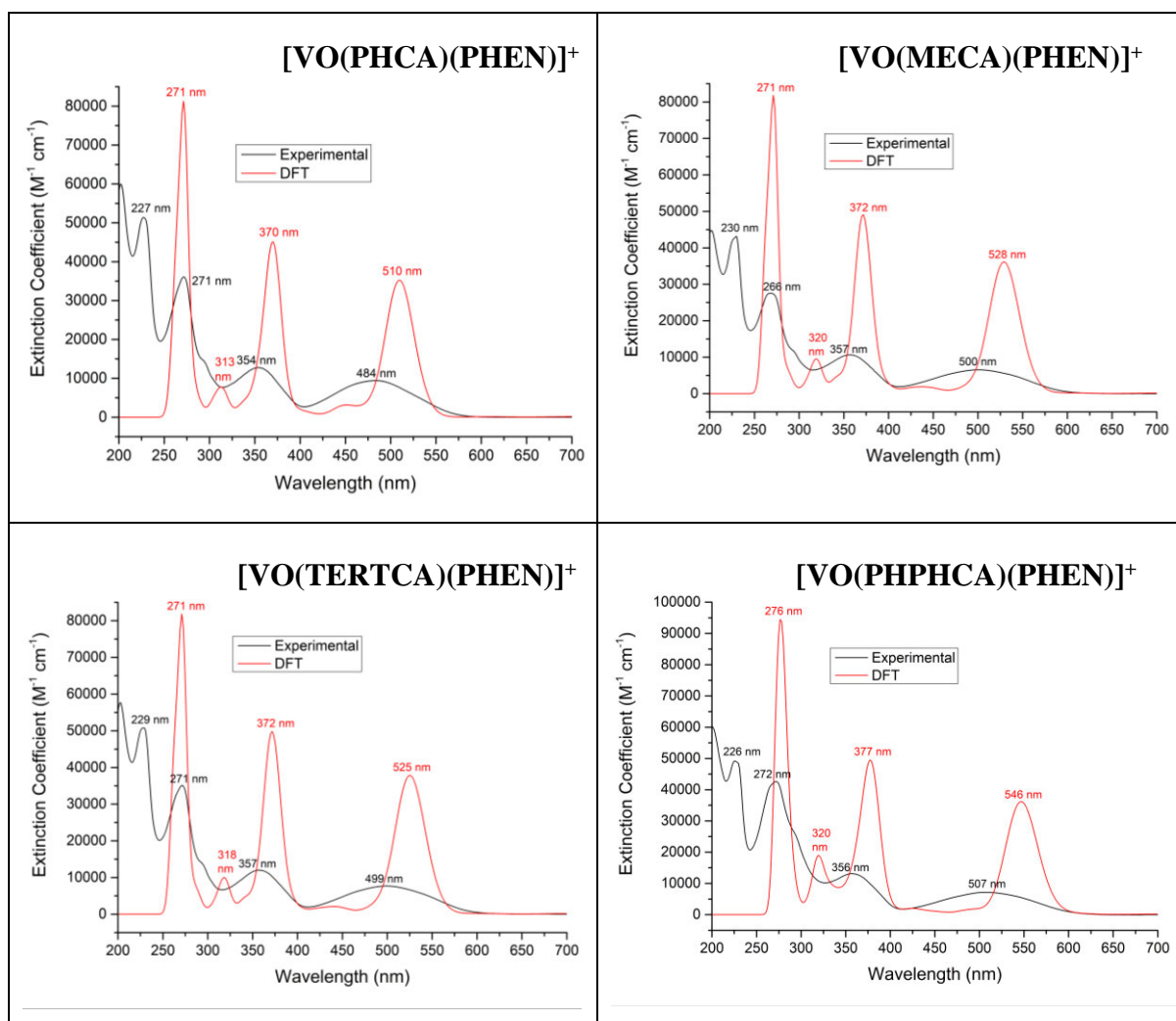


**Figure D9** Superposition plots of the experimental and the TD-DFT-simulated (CH<sub>3</sub>CN solvent continuum) UV/visible spectra of the cationic [VO(ONN)(PHEN)]<sup>+</sup> complexes.

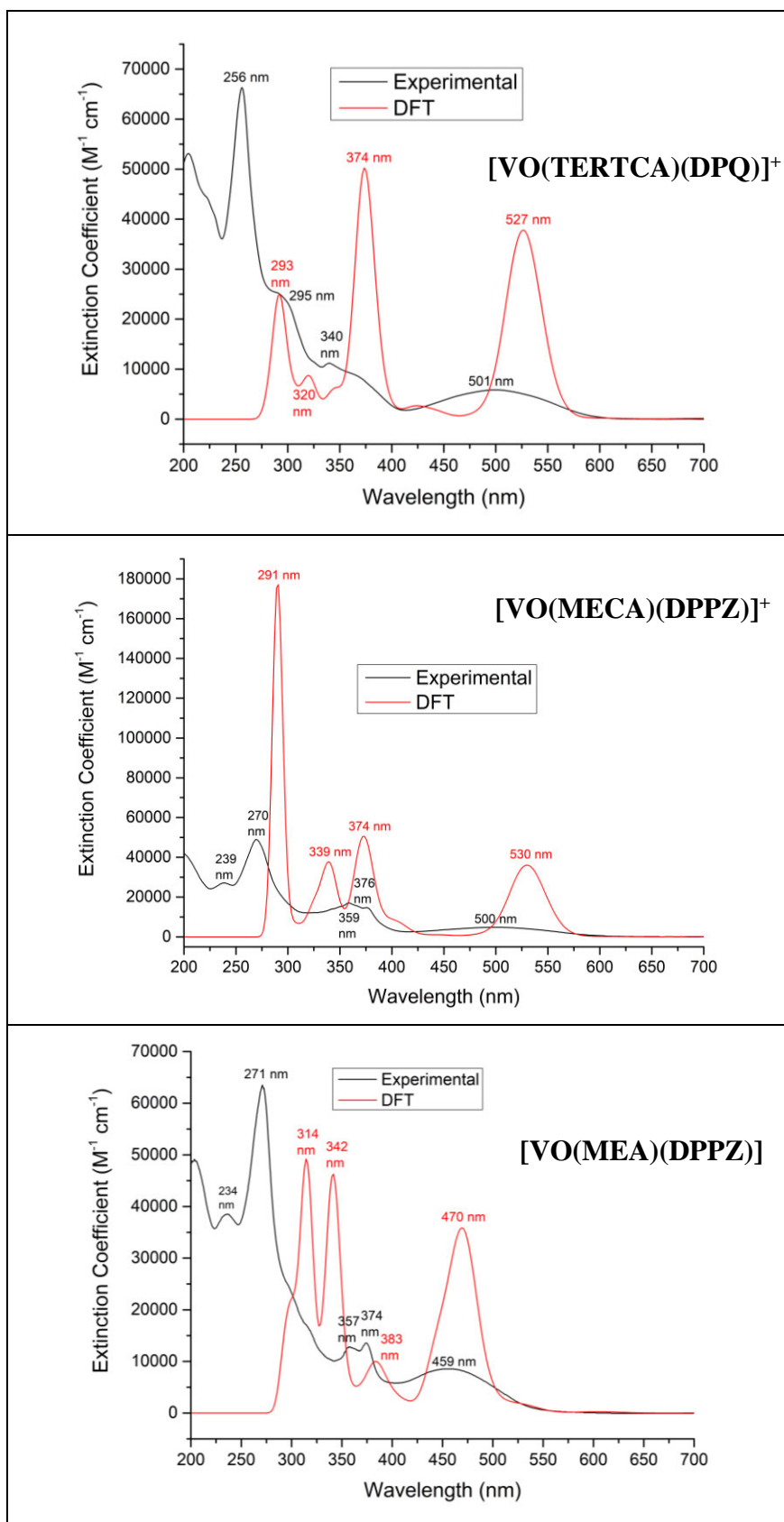


**Figure D10** Superposition plots of the experimental and the TD-DFT-simulated ( $\text{CH}_3\text{CN}$  solvent continuum) UV/visible spectra of  $[\text{VO}(\text{TERTCA})(\text{DPQ})]^+$ ,  $[\text{VO}(\text{MECA})(\text{DPPZ})]^+$  and  $[\text{VO}(\text{MEA})(\text{DPPZ})]$ .

**Table D13** Summary of the major TD-DFT-simulated (CH<sub>3</sub>CN solvent continuum) electronic transitions, oscillator strengths and the corresponding molecular orbitals for [VO(PHA)(DPQ)].

$\lambda$ (nm)	Oscillator Strength, f	Molecular Orbitals	Contr i- butio n	Assignment
459.45	0.1334	HOMO (131A) → LUMO+2 (134A) HOMO (130B) → LUMO+2 (133B) HOMO (130B) → LUMO+3 (134B)	49% 24% 11%	$\pi$ (phenol <sub>a</sub> , imine, phenol <sub>b</sub> , O, Vd <sub>xy</sub> ) → $\pi^*$ (phenol <sub>a</sub> , imine, phenol <sub>b</sub> , O, Vd <sub>xz</sub> , DPQ) $\pi$ (phenol <sub>a</sub> , imine, phenol <sub>b</sub> , O) → $\pi^*$ (imine, phenol <sub>b</sub> , O, Vd <sub>xz</sub> , DPQ) $\pi$ (phenol <sub>a</sub> , imine, phenol <sub>b</sub> , O) → $\pi^*$ (phenol <sub>a</sub> , imine, phenol <sub>b</sub> , O, Vd <sub>xz</sub> , DPQ)
442.20	0.0915	HOMO (131A) → LUMO+3 (135A) HOMO (130B) → LUMO+2 (133B) HOMO (130B) → LUMO+3 (134B)	21% 16% 53%	$\pi$ (phenol <sub>a</sub> , imine, phenol <sub>b</sub> , O, Vd <sub>xy</sub> ) → $\pi^*$ (phenol <sub>a</sub> , imine, phenol <sub>b</sub> , O, Vd <sub>xz</sub> , DPQ) $\pi$ (phenol <sub>a</sub> , imine, phenol <sub>b</sub> , O) → $\pi^*$ (imine, phenol <sub>b</sub> , O, Vd <sub>xz</sub> , DPQ) $\pi$ (phenol <sub>a</sub> , imine, phenol <sub>b</sub> , O) → $\pi^*$ (phenol <sub>a</sub> , imine, phenol <sub>b</sub> , O, Vd <sub>xz</sub> , DPQ)
380.68	0.0278	HOMO-2 (129A) → LUMO+2 (134A) HOMO-2 (129A) → LUMO+3 (135A) HOMO-1 (129B) → LUMO+2 (133B) HOMO-1 (129B) → LUMO+3 (134B)	27% 10% 26% 20%	$\pi$ (phenol <sub>a</sub> , imine, phenol <sub>b</sub> , O, Vd <sub>xy</sub> ) → $\pi^*$ (phenol <sub>a</sub> , imine, phenol <sub>b</sub> , O, Vd <sub>xz</sub> , DPQ) $\pi$ (phenol <sub>a</sub> , imine, phenol <sub>b</sub> , O, Vd <sub>xy</sub> ) → $\pi^*$ (phenol <sub>a</sub> , imine, phenol <sub>b</sub> , O, Vd <sub>xz</sub> , DPQ) $\pi$ (phenol <sub>a</sub> , imine, phenol <sub>b</sub> , O) → $\pi^*$ (imine, phenol <sub>b</sub> , O, Vd <sub>xz</sub> , DPQ) $\pi$ (phenol <sub>a</sub> , imine, phenol <sub>b</sub> , O) → $\pi^*$ (phenol <sub>a</sub> , imine, phenol <sub>b</sub> , O, Vd <sub>xz</sub> , DPQ)
311.53	0.1225	HOMO-2 (128B) → LUMO+2 (133B)	22%	$\pi$ (phenol <sub>a</sub> , imine, phenol <sub>b</sub> ) → $\pi^*$ (imine, phenol <sub>b</sub> , O, Vd <sub>xz</sub> , DPQ)
302.52	0.057	HOMO-4 (127A) → LUMO (132A) HOMO-4 (127A) → LUMO+1 (133A) HOMO-3 (127B) → LUMO (131B)	29% 10% 27%	$\pi$ (DPQ) → $\pi^*$ (DPQ) $\pi$ (DPQ) → $\pi^*$ (DPQ) $\pi$ (DPQ) → $\pi^*$ (DPQ, Vd <sub>xy</sub> )
289.00	0.0452	HOMO-5 (126A) → LUMO+1 (133A) HOMO-4 (126B) → LUMO+1 (132B)	11% 10%	$\pi$ (DPQ) → $\pi^*$ (DPQ) $\pi$ (DPQ) → $\pi^*$ (DPQ, Vd <sub>xy</sub> )

<sup>a</sup> Only orbitals with >10% contribution are listed.

<sup>b</sup> phenol<sub>a</sub> = amino phenol ring + OH; imine = C=N imine; phenol<sub>b</sub> = phenol ring + OH; O = terminal O.

**Table D14** Summary of the major TD-DFT-simulated (CH<sub>3</sub>CN solvent continuum) electronic transitions, oscillator strengths and the corresponding molecular orbitals for [VO(SOA)(DPQ)].

$\lambda$ (nm)	Oscillator Strength, f	Molecular Orbitals	Contri- bution	Assignment
436.93	0.1863	HOMO (155A) $\rightarrow$ LUMO+1 (157A)	24%	$\pi$ (phenol <sub>a</sub> , imine, phenol <sub>b</sub> , O, Vd <sub>xy</sub> ) $\rightarrow$ $\pi^*$ (phenol <sub>a</sub> , imine, phenol <sub>b</sub> , O, Vd <sub>xz</sub> )
		HOMO (154B) $\rightarrow$ LUMO+2 (157B)	43%	$\pi$ (phenol <sub>a</sub> , imine, phenol <sub>b</sub> , O) $\rightarrow$ $\pi^*$ (phenol <sub>a</sub> , imine, phenol <sub>b</sub> , O, Vd <sub>xz</sub> )
374.24	0.0276	HOMO-2 (153A) $\rightarrow$ LUMO (156A)	11%	$\pi$ (phenol <sub>a</sub> , phenol <sub>b</sub> , O, Vd <sub>xy</sub> ) $\rightarrow$ $\pi^*$ (DPQ)
		HOMO-2 (153A) $\rightarrow$ LUMO+1 (157A)	26%	$\pi$ (phenol <sub>a</sub> , phenol <sub>b</sub> , O, Vd <sub>xy</sub> ) $\rightarrow$ $\pi^*$ (phenol <sub>a</sub> , imine, phenol <sub>b</sub> , O, Vd <sub>xz</sub> )
		HOMO-1 (153B) $\rightarrow$ LUMO+2 (157B)	43%	$\pi$ (phenol <sub>a</sub> , phenol <sub>b</sub> , O) $\rightarrow$ $\pi^*$ (phenol <sub>a</sub> , imine, phenol <sub>b</sub> , O, Vd <sub>xz</sub> )
313.17	0.0593	HOMO-2 (152B) $\rightarrow$ LUMO (155B)	67%	$\pi$ (phenol <sub>a</sub> , imine, phenol <sub>b</sub> ) $\rightarrow$ $\pi^*$ (DPQ, Vd <sub>xy</sub> )
305.99	0.1133	HOMO-3 (152A) $\rightarrow$ LUMO+1 (157A)	30%	$\pi$ (phenol <sub>a</sub> , imine, phenol <sub>b</sub> ) $\rightarrow$ $\pi^*$ (phenol <sub>a</sub> , imine, phenol <sub>b</sub> , O, Vd <sub>xz</sub> )
		HOMO-2 (152B) $\rightarrow$ LUMO+2 (157B)	32%	$\pi$ (phenol <sub>a</sub> , imine, phenol <sub>b</sub> ) $\rightarrow$ $\pi^*$ (phenol <sub>a</sub> , imine, phenol <sub>b</sub> , O, Vd <sub>xz</sub> )
302.94	0.0596	HOMO-2 (152B) $\rightarrow$ LUMO+2 (157B)	11%	$\pi$ (phenol <sub>a</sub> , imine, phenol <sub>b</sub> ) $\rightarrow$ $\pi^*$ (phenol <sub>a</sub> , imine, phenol <sub>b</sub> , O, Vd <sub>xz</sub> )
290.94	0.0538	HOMO-4 (150B) $\rightarrow$ LUMO+1 (156B)	12%	$\pi$ (DPQ) $\rightarrow$ $\pi^*$ (DPQ)

<sup>a</sup> Only orbitals with >10% contribution are listed.

<sup>b</sup> phenol<sub>a</sub> = amino phenol benzene ring + OH; imine = C=N imine; phenol<sub>b</sub> = phenol benzene ring + OH; O = terminal O.

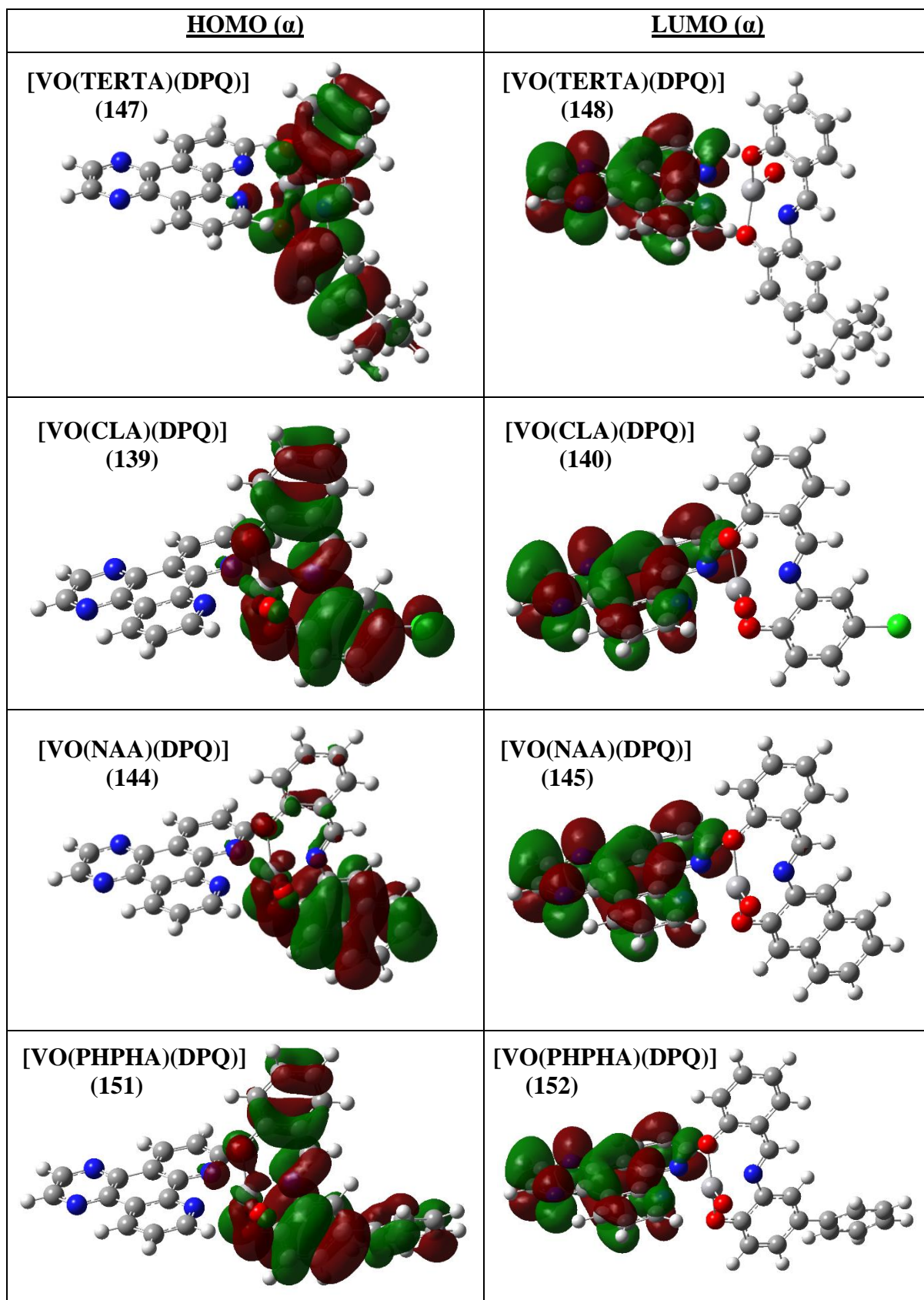


**Figure D11** DFT-simulated (B3LYP-/6-311G(dp)) alpha HOMO and LUMO plots of [VO(TERTA)(DPQ)], [VO(CLA)(DPQ)], [VO(NAA)(DPQ)] and [VO(PHPHA)(DPQ)].

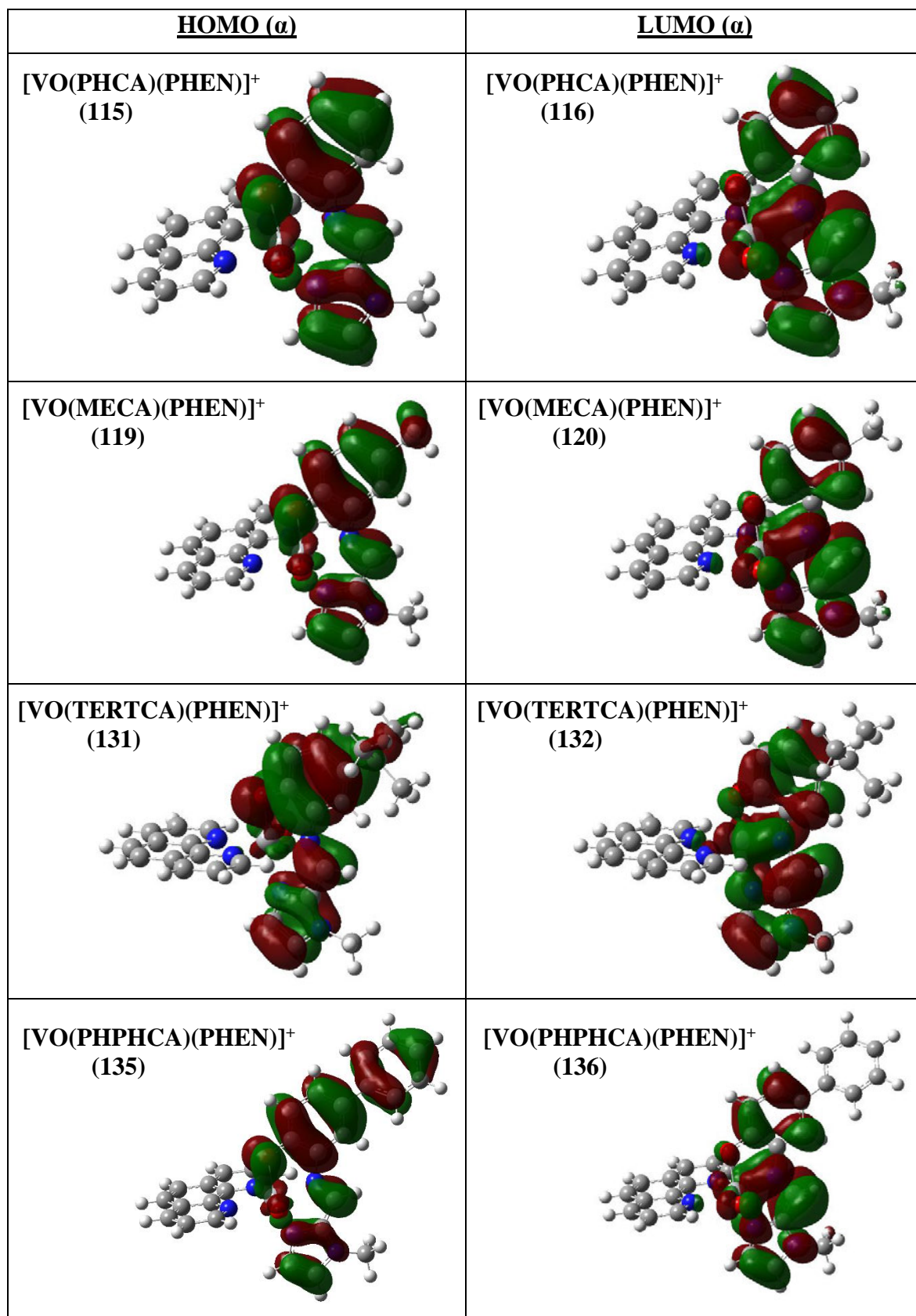


**Figure D12** DFT-simulated (B3LYP-/6-311G(dp)) alpha HOMO and LUMO plots of [VO(PHCA)(PHEN)]<sup>+</sup>, [VO(MECA)(PHEN)]<sup>+</sup>, [VO(TERTCA)(PHEN)]<sup>+</sup> and [VO(PHPHCA)(PHEN)]<sup>+</sup>.

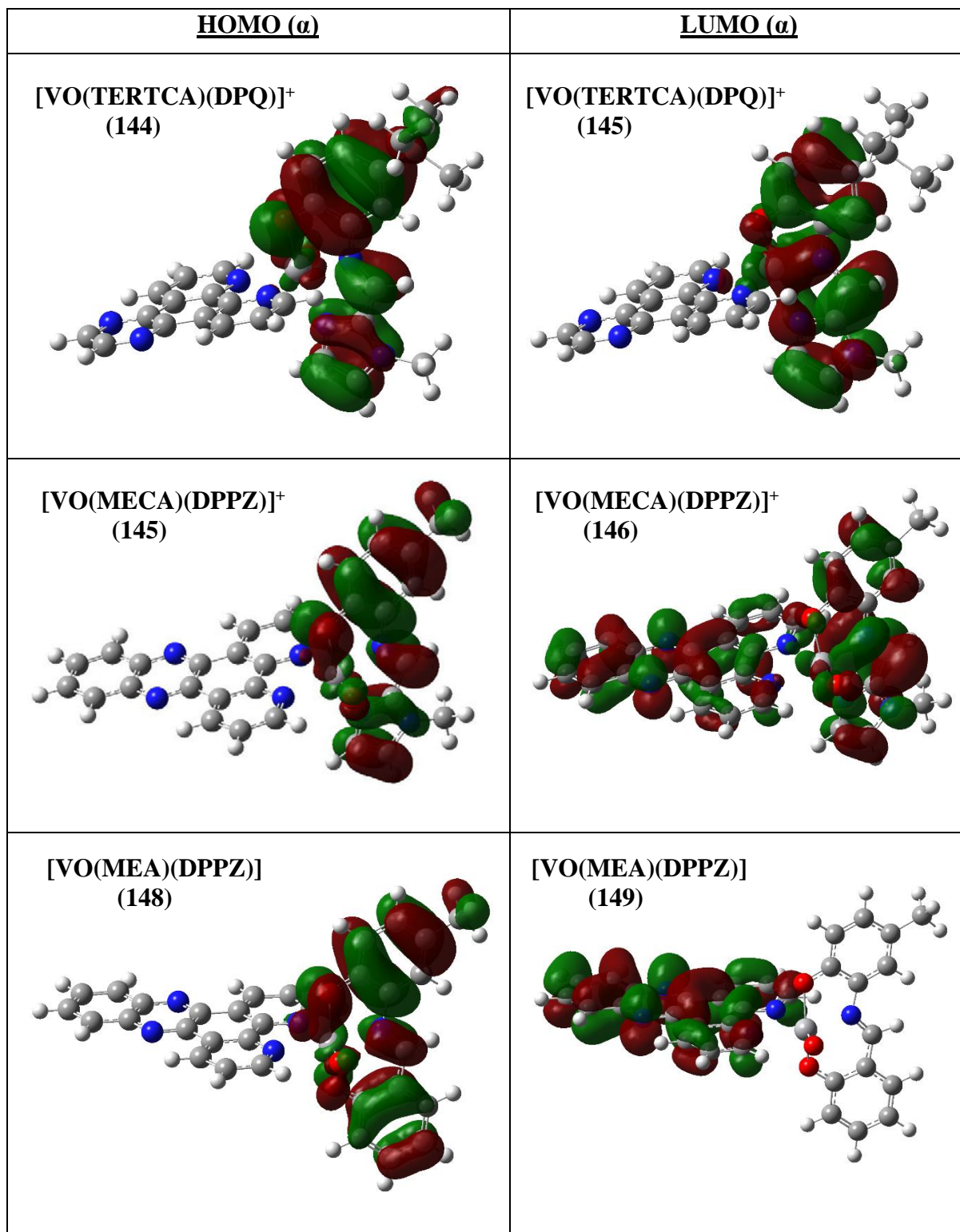


**Figure D13** DFT-simulated (B3LYP-/6-311G(dp)) alpha HOMO and LUMO plots of [VO(TERTCA)(DPQ)]<sup>+</sup>, [VO(MECA)(DPPZ)]<sup>+</sup> and [VO(MEA)(DPPZ)].

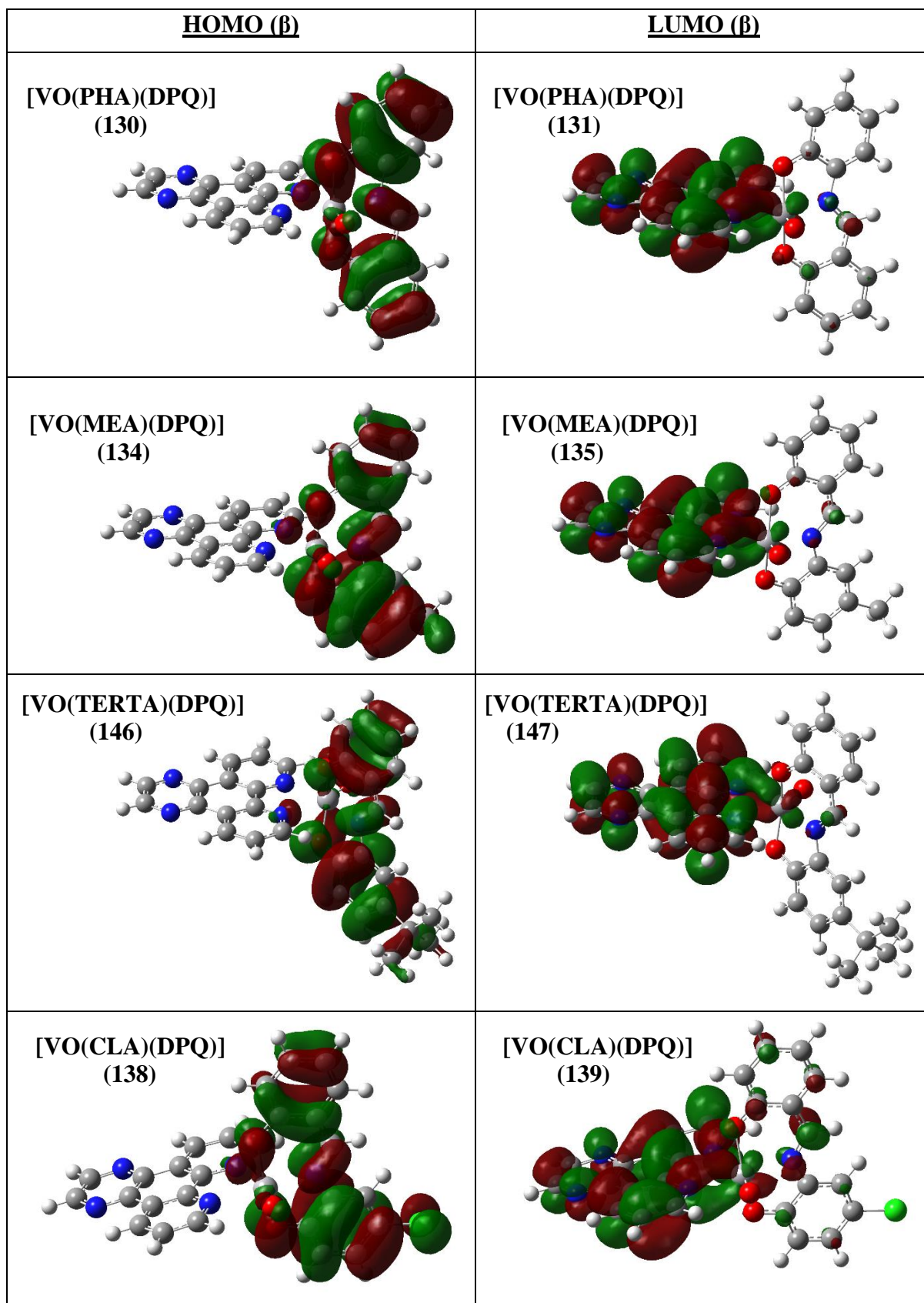


**Figure D14** DFT-simulated (B3LYP-/6-311G(dp)) beta HOMO and LUMO plots of [VO(PHA)(DPQ)], [VO(MEA)(DPQ)], [VO(TERTA)(DPQ)] and [VO(CLA)(DPQ)].

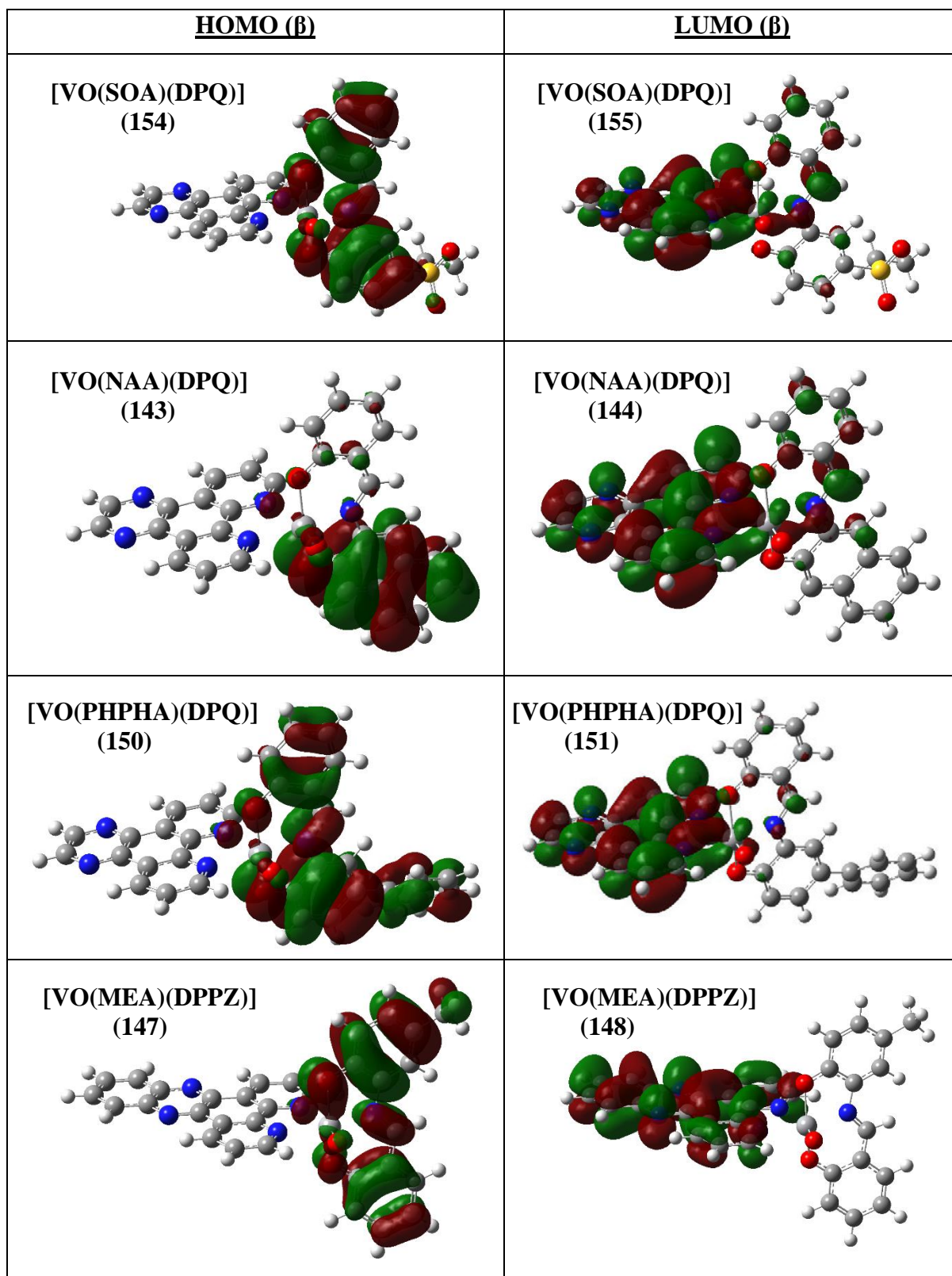


**Figure D15** DFT-simulated (B3LYP-/6-311G(dp)) beta HOMOs and LUMO plots of [VO(SOA)(DPQ)], [VO(NAA)(DPQ)], [VO(PHPHA)(DPQ)] and [VO(MEA)(DPPZ)].

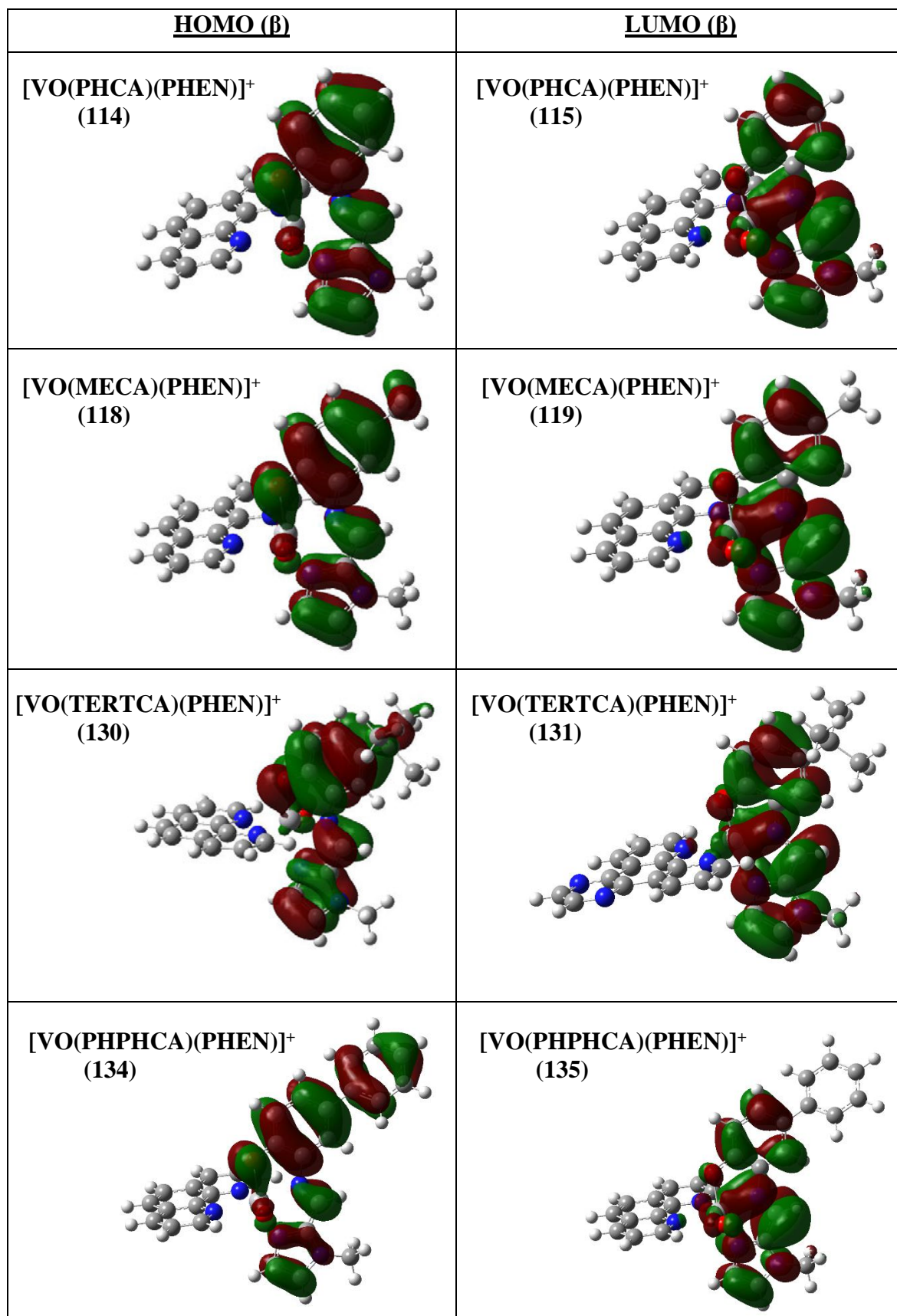


**Figure D16** DFT-simulated (B3LYP-/6-311G(dp)) beta HOMO and LUMO plots of [VO(PHCA)(PHEN)]<sup>+</sup>, [VO(MECA)(PHEN)]<sup>+</sup>, [VO(TERTCA)(PHEN)]<sup>+</sup> and [VO(PHPHCA)(PHEN)]<sup>+</sup>.

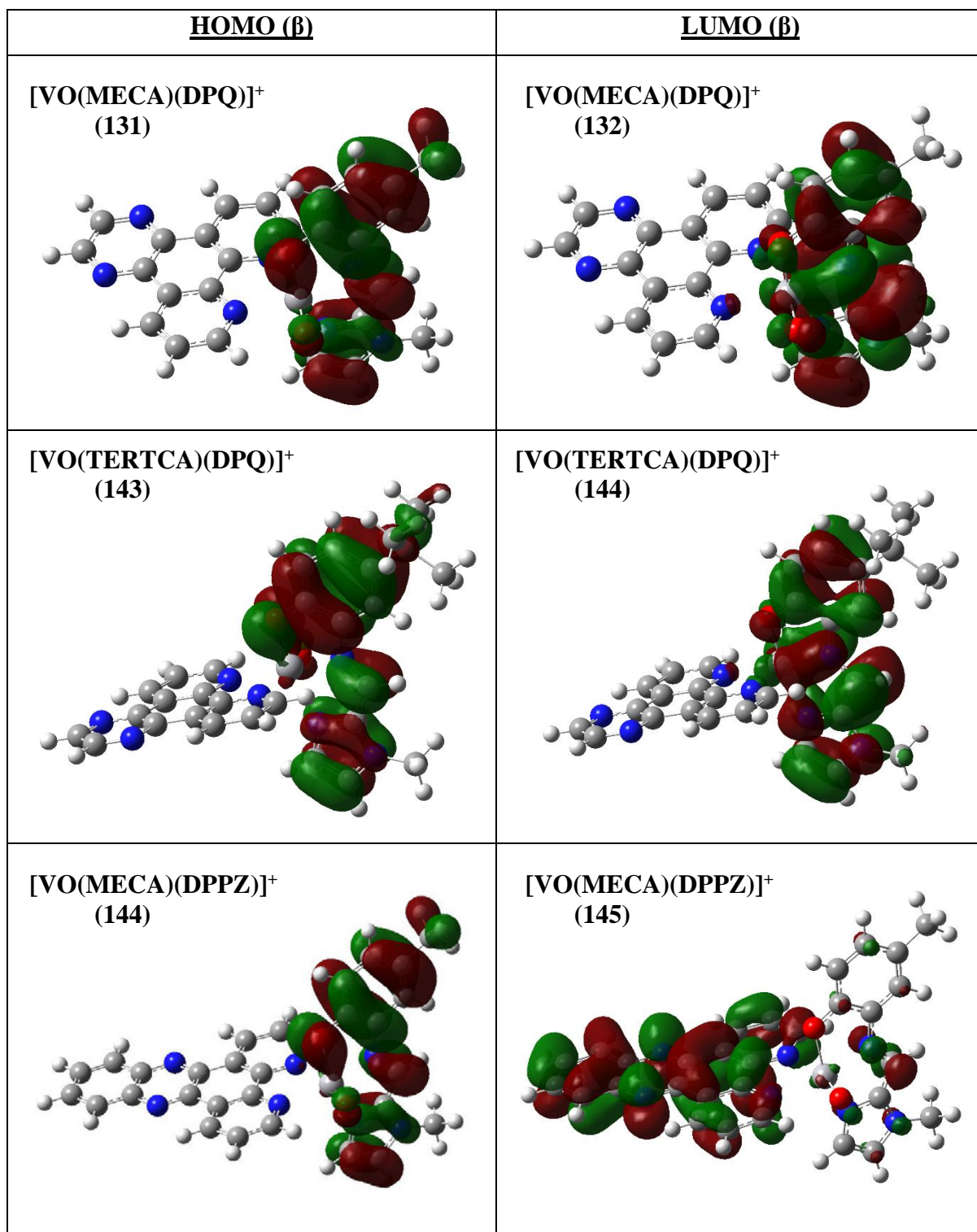


**Figure D17** DFT-simulated (B3LYP-/6-311G(d,p)) beta HOMO and LUMO plots of [VO(MECA)(DPQ)]<sup>+</sup>, [VO(TERTCA)(DPQ)]<sup>+</sup> and [VO(MECA)(DPPZ)]<sup>+</sup>.

## Appendix E: Stability and DNA Binding Studies

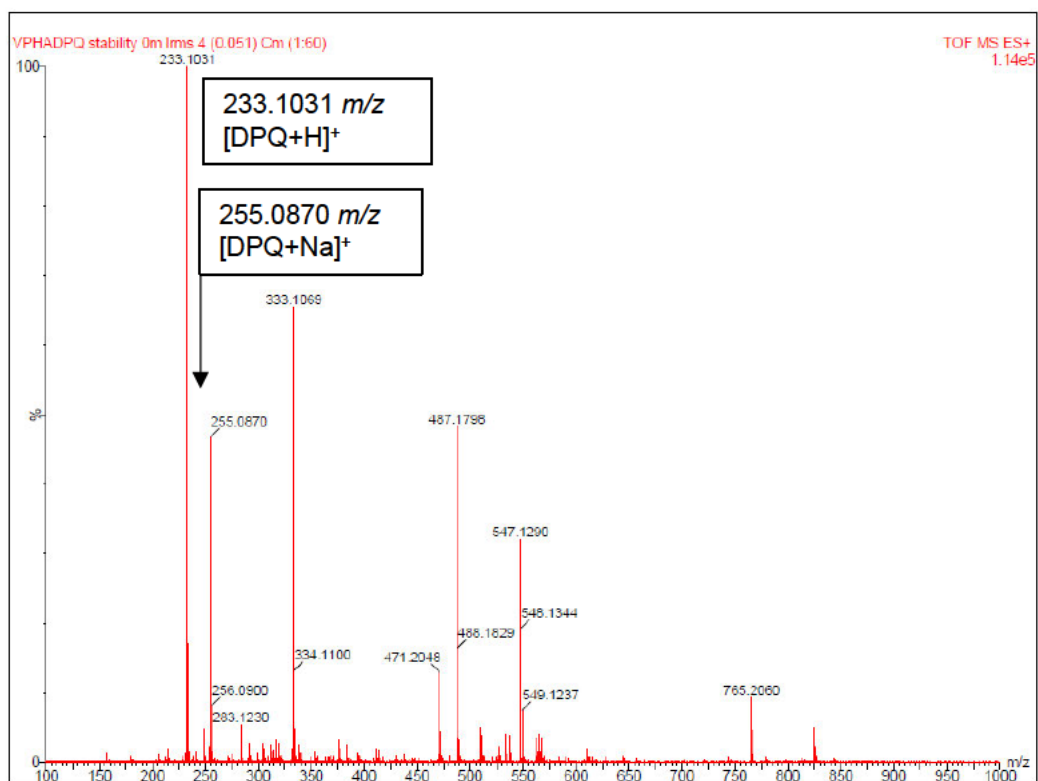


**Figure E1** ESI mass spectrum immediately after dissolution of [VO(PHA)(DPQ)] in 10%DMSO/90%water (v/v) indicating many solvolysis/decomposition species including the [DPQ+H]<sup>+</sup> and [DPQ+Na]<sup>+</sup> peaks at 233.1031 *m/z* and 255.0870 *m/z*, respectively.

Upon addition of [VO(MEA)(DPQ)] to 10%DMSO/90%water (v/v) the prominent molecular ion peak at 525.1450 *m/z* for [VO(MEA)(DPQ)+H]<sup>+</sup> is present but already with additional peaks, such as 233.1038 *m/z*, which corresponds to [DPQ+H]<sup>+</sup> (Figure E2). These additional peaks were absent for the sample prepared in chloroform (Figure A83, Appendix A). Thirty minutes after dissolution of [VO(MEA)(DPQ)] in the 10%DMSO/90%water (v/v) solvent system, the molecular ion peak at 525.1450 *m/z* has already diminished. The prominent molecular ion peak is now 443.1115 *m/z*, which corresponds to a complex where DPQ has exchanged with DMSO. For the [VO(TERTA)(DPQ)] complex the molecular ion peak for the intact complex was still present at 160 minutes. The mass spectra at 2 minutes, 30 minutes, and 24 hours after the dissolution of [VO(MEA)(DPQ)] in 10%DMSO/90%water (v/v) are shown in Figure E2.

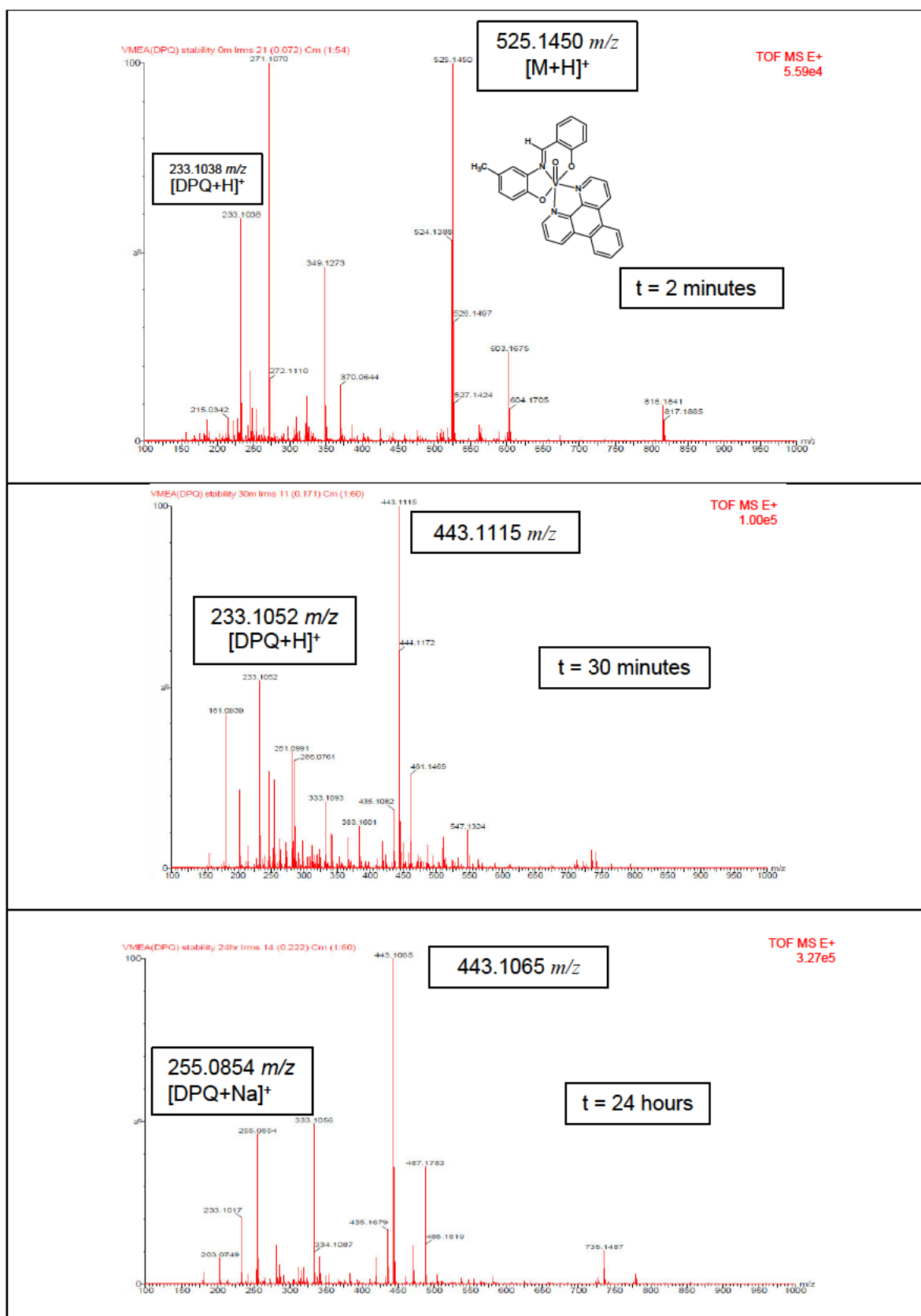


**Figure E2** ESI mass spectra at 2 minutes, 30 minutes and 24 hours after dissolution of [VO(MEA)(DPQ)] in 10%DMSO/90%water (v/v) indicating the disappearance of the 525.1450 m/z [M+H]<sup>+</sup> complex molecular ion peak and appearance of many other species, such as 233.1038 m/z [DPQ+H]<sup>+</sup>.

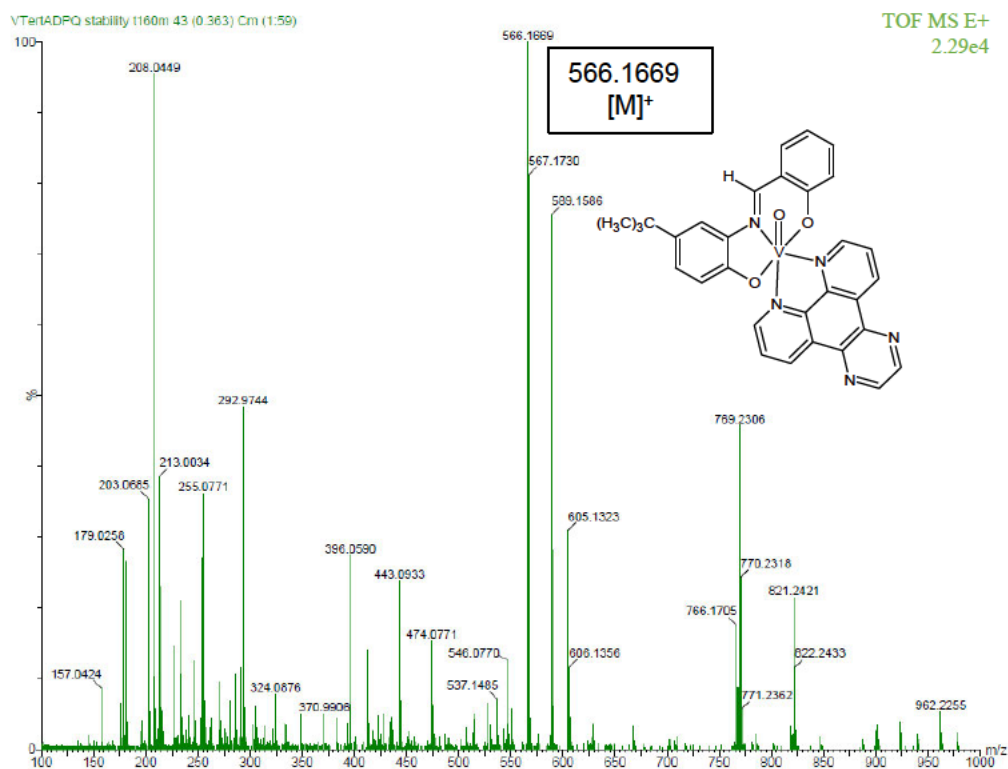


**Figure E3** ESI mass spectrum 160 minutes post-dissolution of [VO(TERTA)(DPQ)] in 10%DMSO/90%water (v/v) indicating the complex molecular ion peak of [M]<sup>+</sup> at 566.1669 *m/z* is still present (along with many other solvolysis/decomposition products).

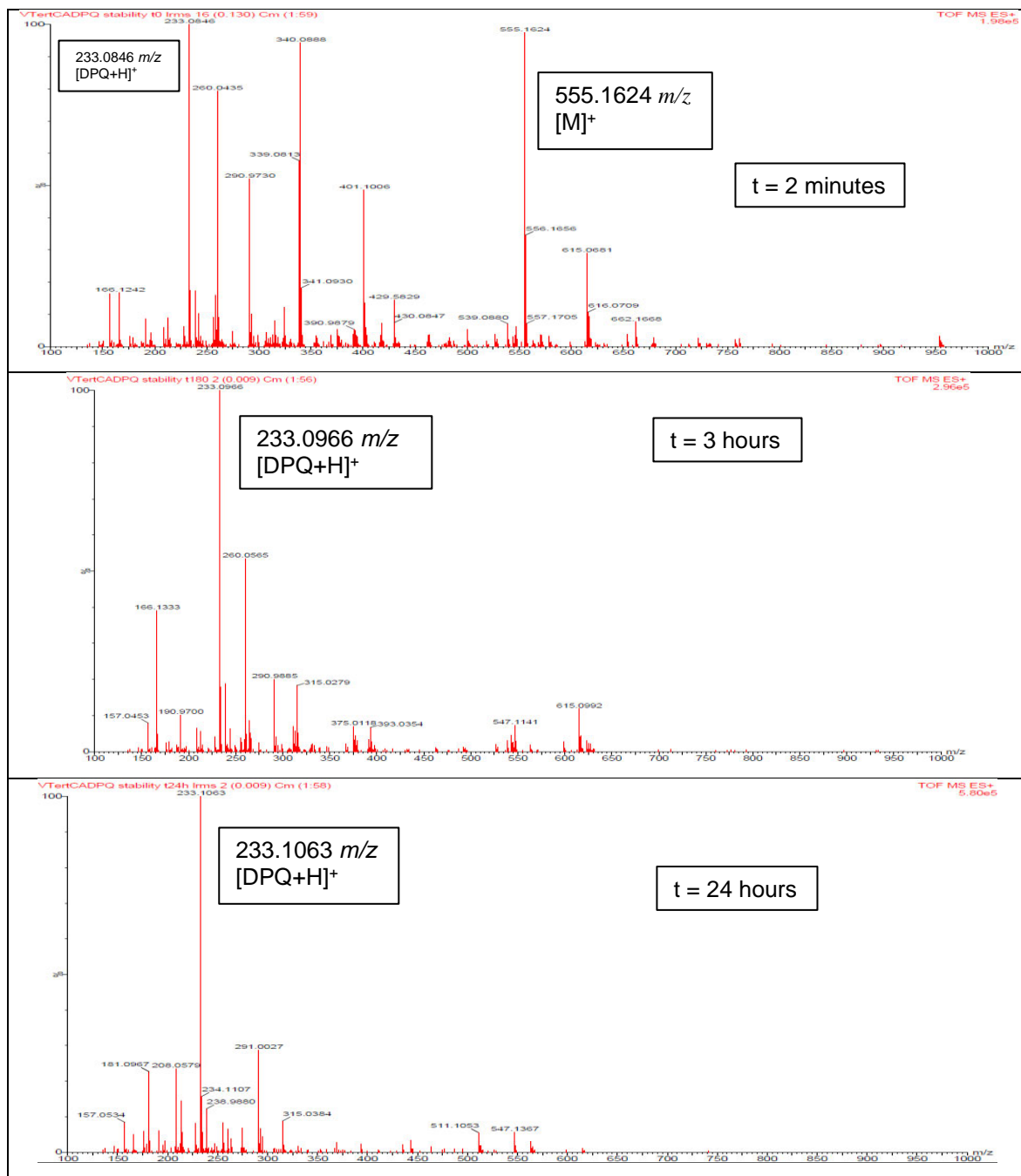


**Figure E4** ESI mass spectra at 2 minutes, 3 hours and 24 hours after dissolution of  $[\text{VO}(\text{TERTCA})(\text{DPQ})](\text{PF}_6)$  in 10%DMSO/90%water indicating the appearance of decomposition species, such as  $[\text{DPQ}+\text{H}]^+$  at 233.1063  $m/z$  and the disappearance of the  $[\text{VO}(\text{TERTCA})(\text{DPQ})]^+$  555.1624  $m/z$  peak over time.

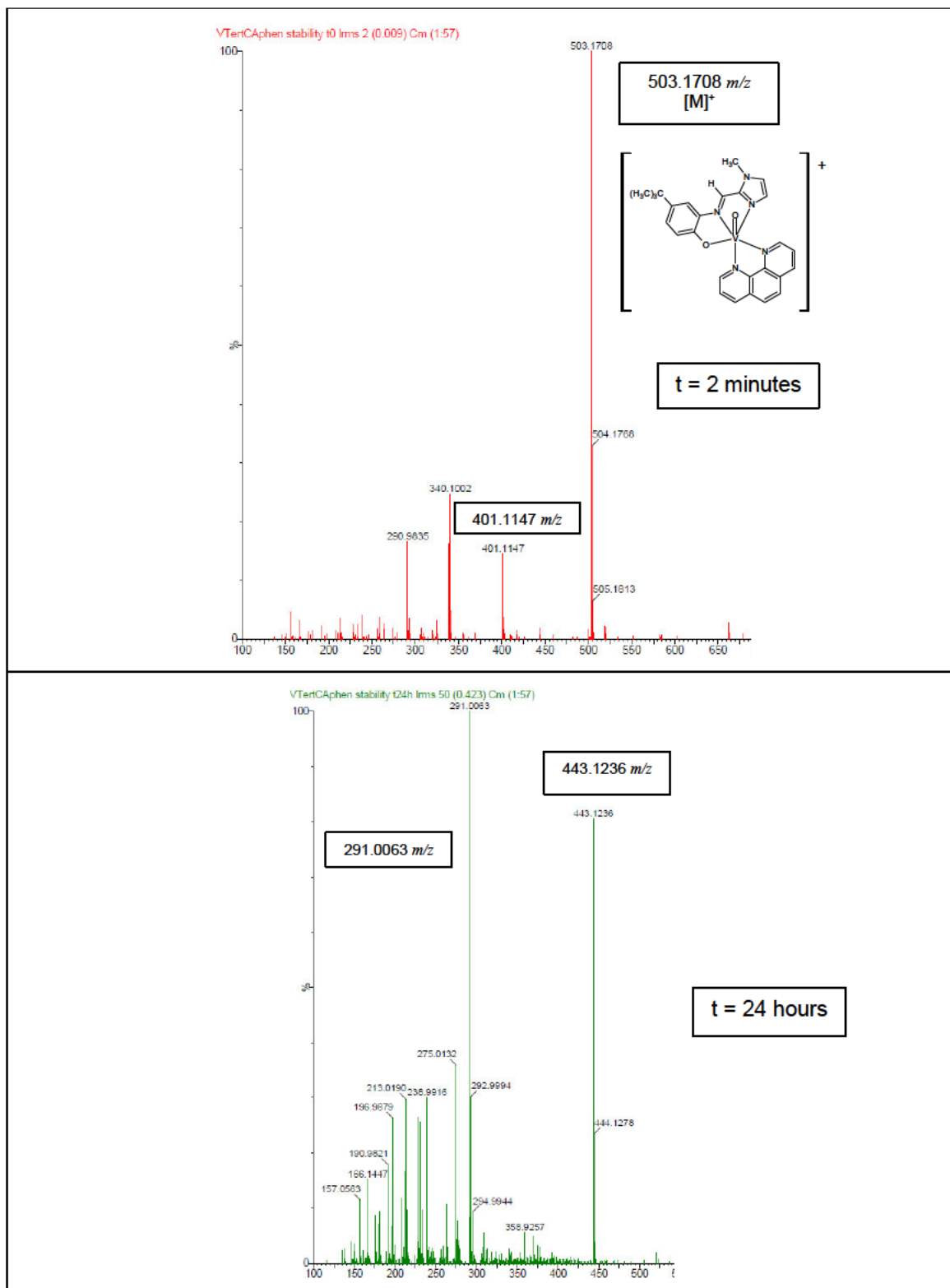


**Figure E5** ESI mass spectra at 2 minutes and 24 hours after dissolution of  $[\text{VO}(\text{TERTCA})(\text{PHEN})](\text{PF}_6)$  in 10%DMSO/90% water (v/v) indicating solvolysis/decomposition species, including 401.1147  $m/z$  for  $[\text{VO}(\text{TERTCA})(\text{DMSO})]^+$  and the disappearance of the molecular ion peak of 503.1708  $m/z$  for  $[\text{VO}(\text{TERTCA})(\text{PHEN})]^+$  over time.

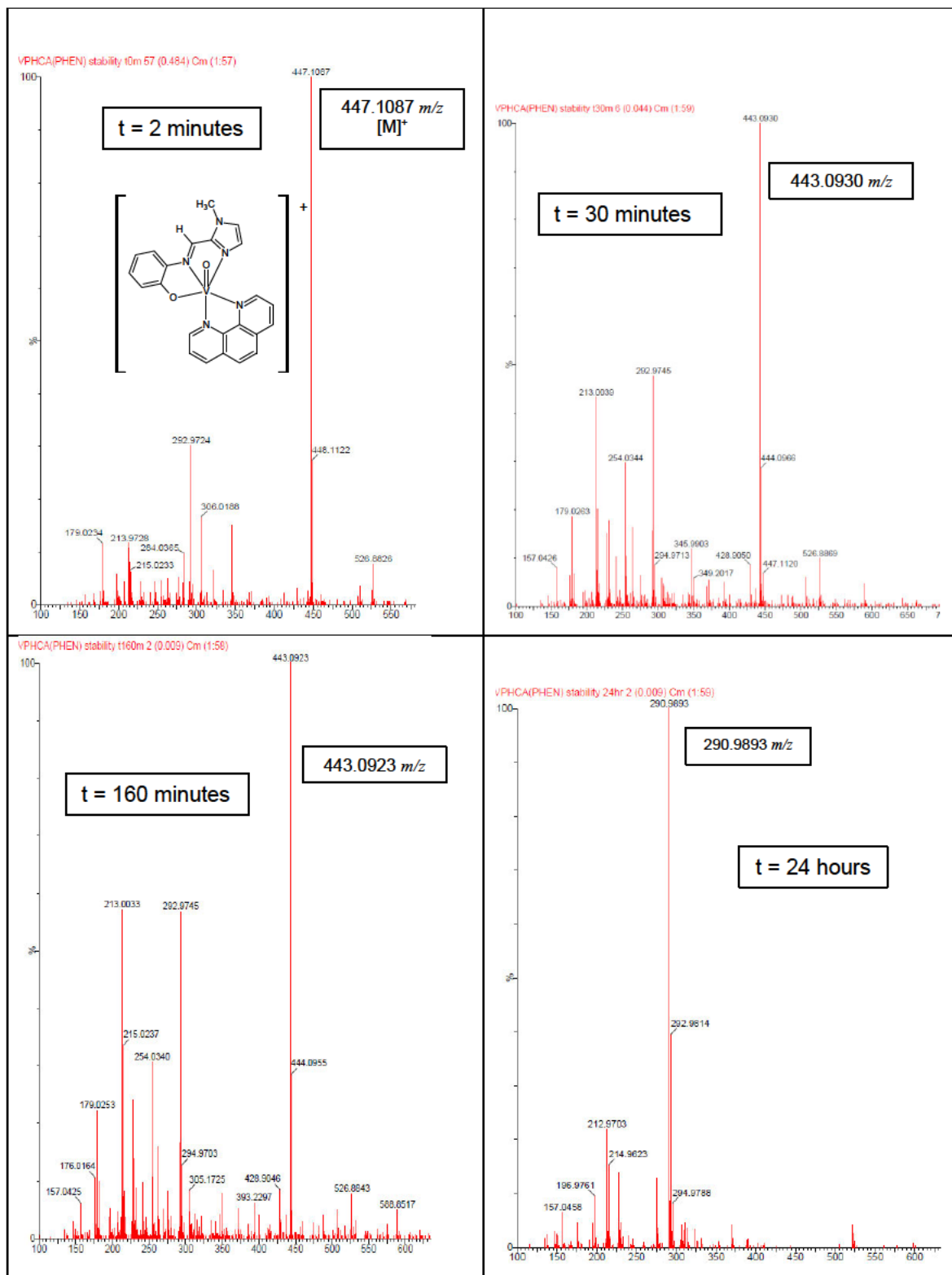


**Figure E6** ESI mass spectra at 2, 30, 160 minutes and 24 hours after dissolution of  $[\text{VO}(\text{PHCA})(\text{PHEN})](\text{PF}_6)$  in 10%DMSO/90%water (v/v) indicating solvolysis/decomposition species and the disappearance of the molecular ion peak of 447.1087  $m/z$  for  $[\text{VO}(\text{PHCA})(\text{PHEN})]^+$  over time.

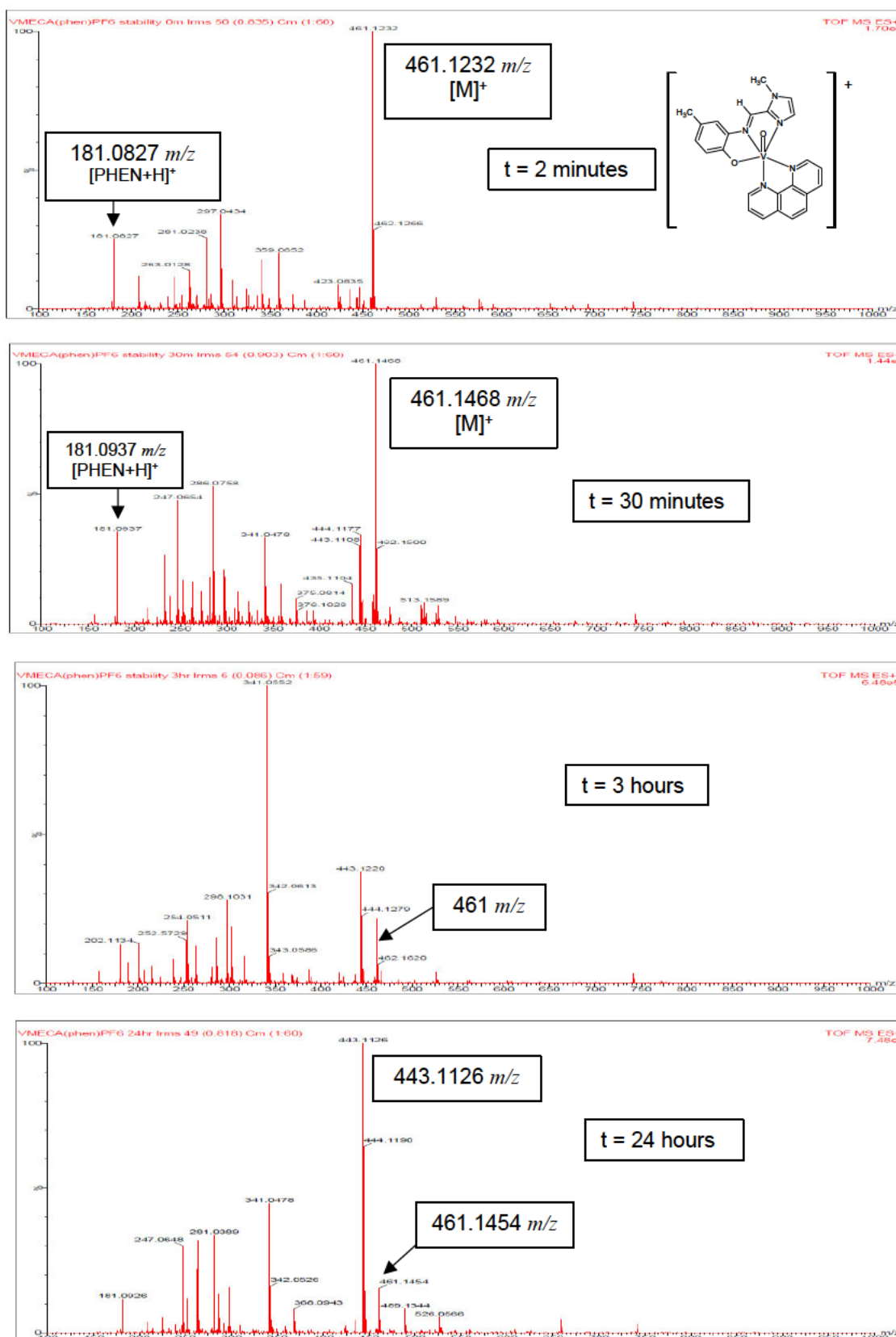


**Figure E7** ESI mass spectra at 2 minutes, 30 minutes, 3 hours and 24 hours after dissolution of [VO(MECA)(PHEN)](PF<sub>6</sub>) in 10%DMSO/90%water indicating solvolysis/decomposition species, including 181.0827 m/z for [PHEN+H]<sup>+</sup> and the diminishing 461.1232 m/z peak for [VO(MECA)(PHEN)]<sup>+</sup> over time.

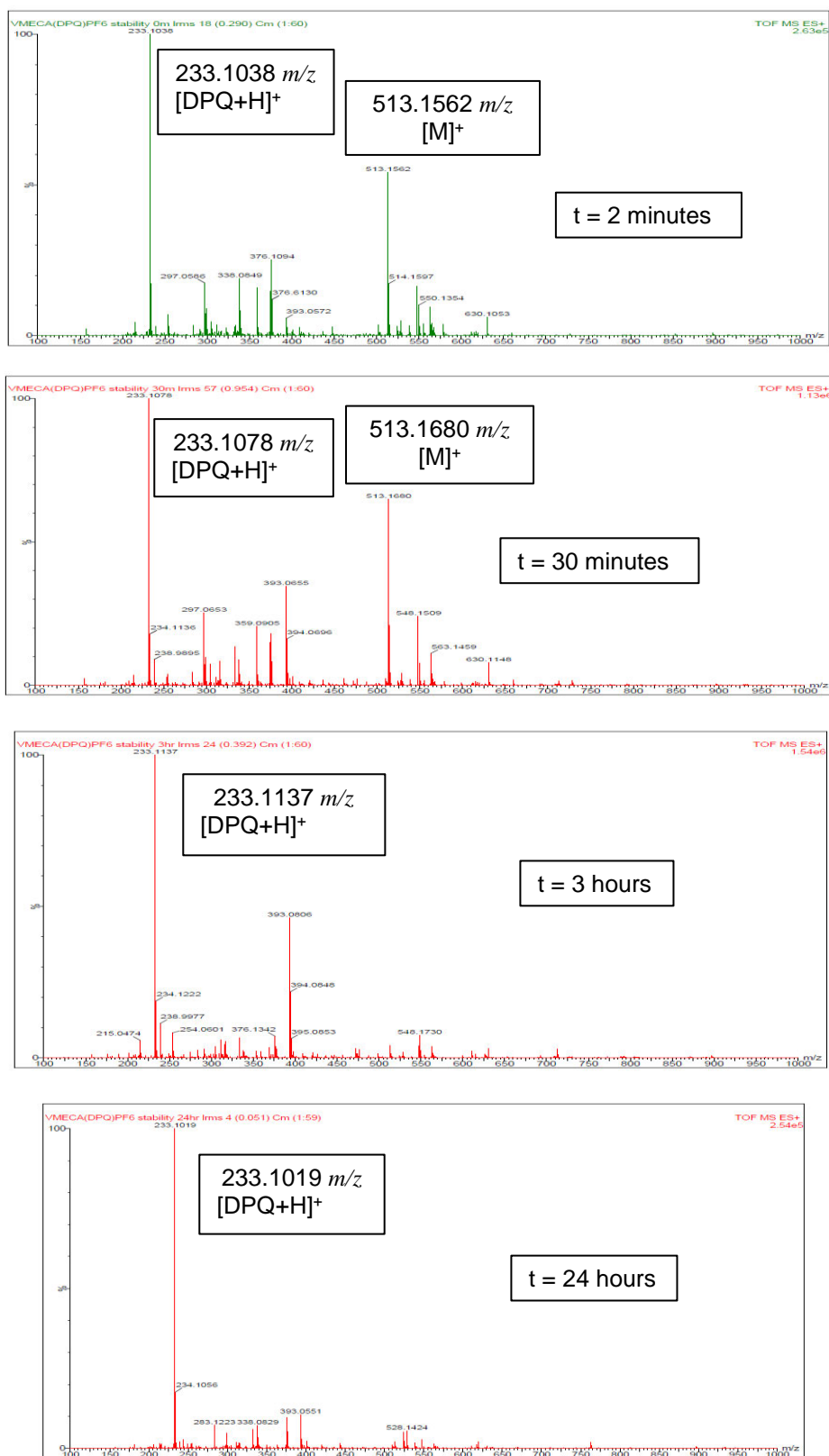


**Figure E8** ESI mass spectra at 2 minutes, 30 minutes, 3 hours and 24 hours after dissolution of [VO(MECA)(DPQ)](PF<sub>6</sub>) in 10%DMSO/90%water (v/v) indicating the diminishing 513.1562 m/z peak for [VO(MECA)(DPQ)]<sup>+</sup> over time and the appearance of additional solvolysis/decomposition species, including 233.1038 m/z for [DPQ+H]<sup>+</sup>.

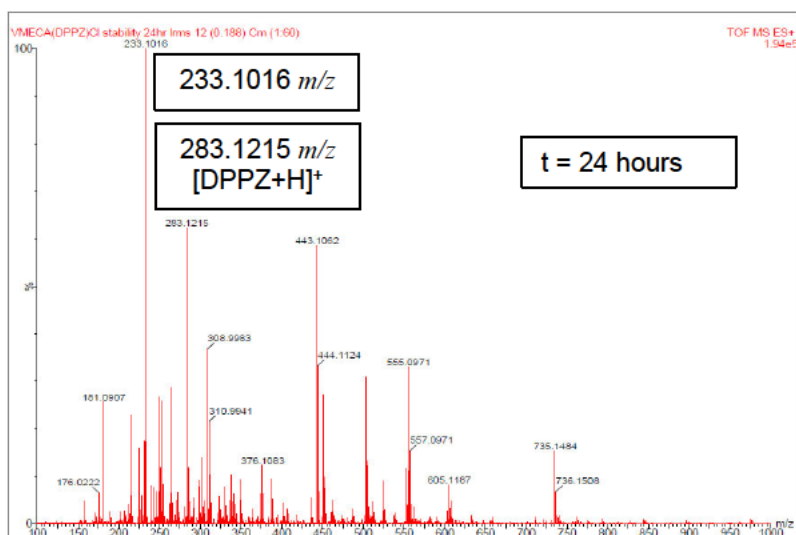
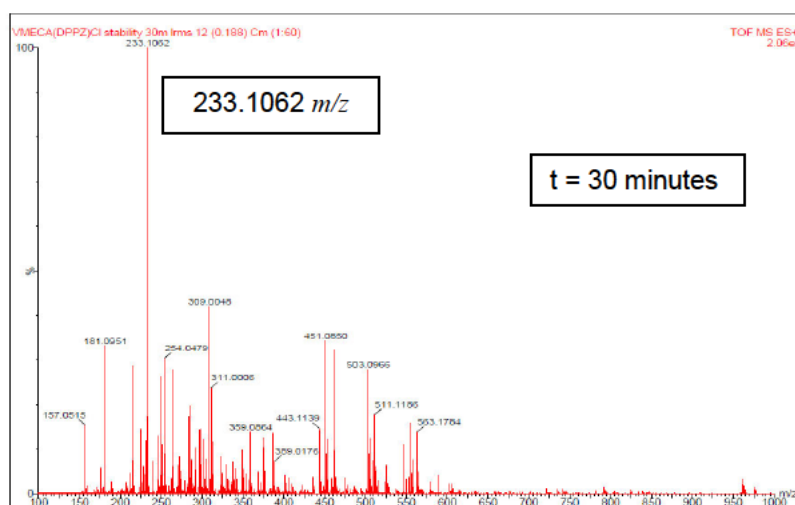
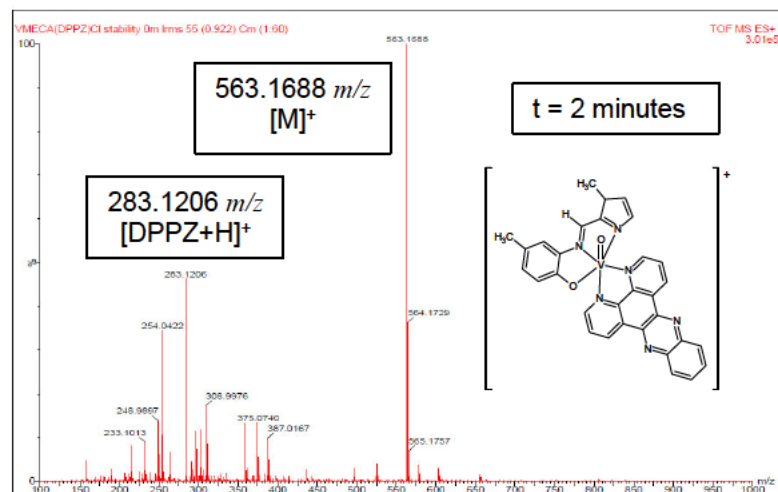


**Figure E9** ESI mass spectra at 2 minutes, 30 minutes and 24 hours after dissolution of [VO(MECA)(DPPZ)](Cl) in 10%DMSO/90%water indicating the diminishing molecular ion peak of 563.1688  $m/z$  for [VO(MECA)(DPPZ)]<sup>+</sup> and the appearance of solvolysis/decomposition species, including [DPPZ+H]<sup>+</sup> at 283.1206  $m/z$ .

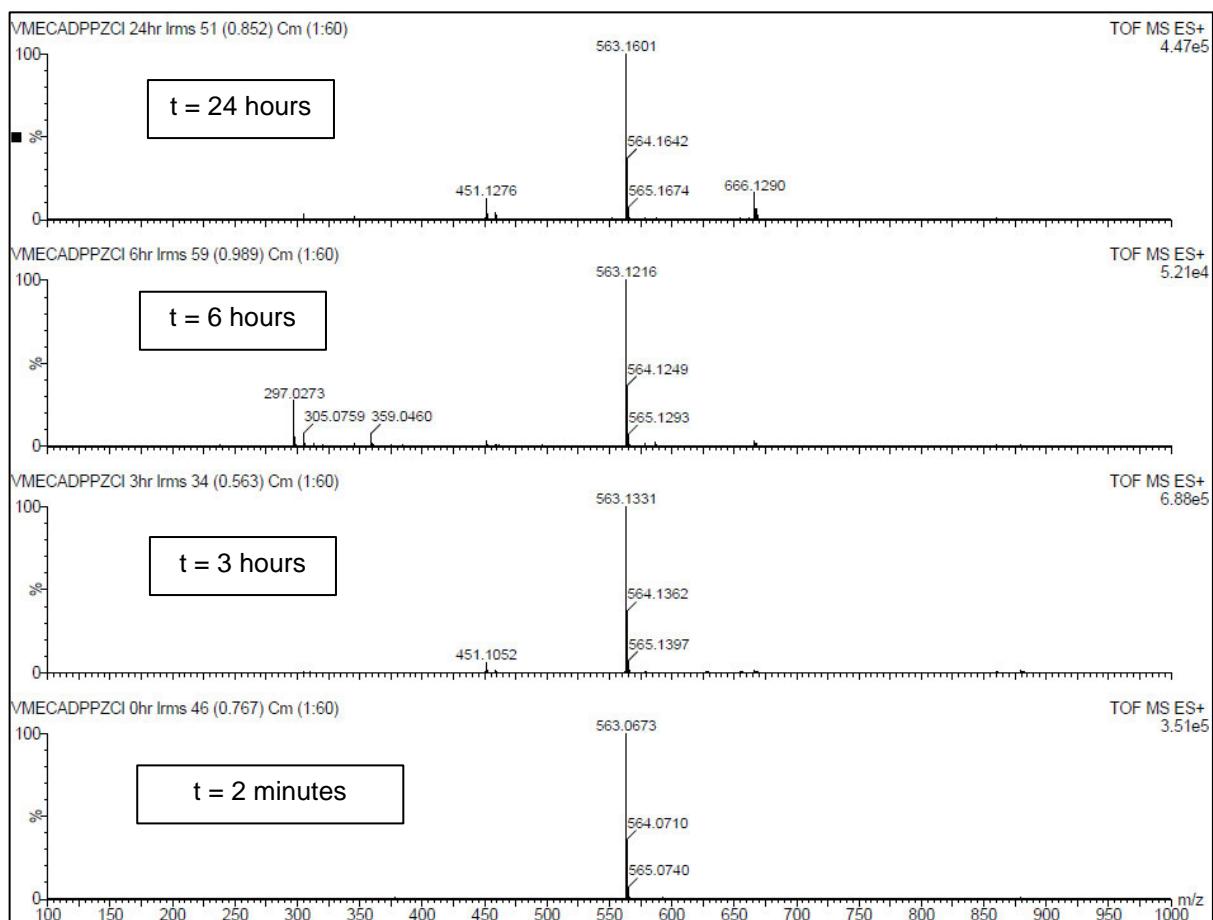


**Figure E10** ESI mass spectra at 2 minutes, 3, 6 and 24 hours after dissolution of [VO(MECA)(DPPZ)](Cl) in water indicating the stability of the prominent molecular ion peak of 563.1601  $m/z$  for [VO(MECA)(DPPZ)]<sup>+</sup>.

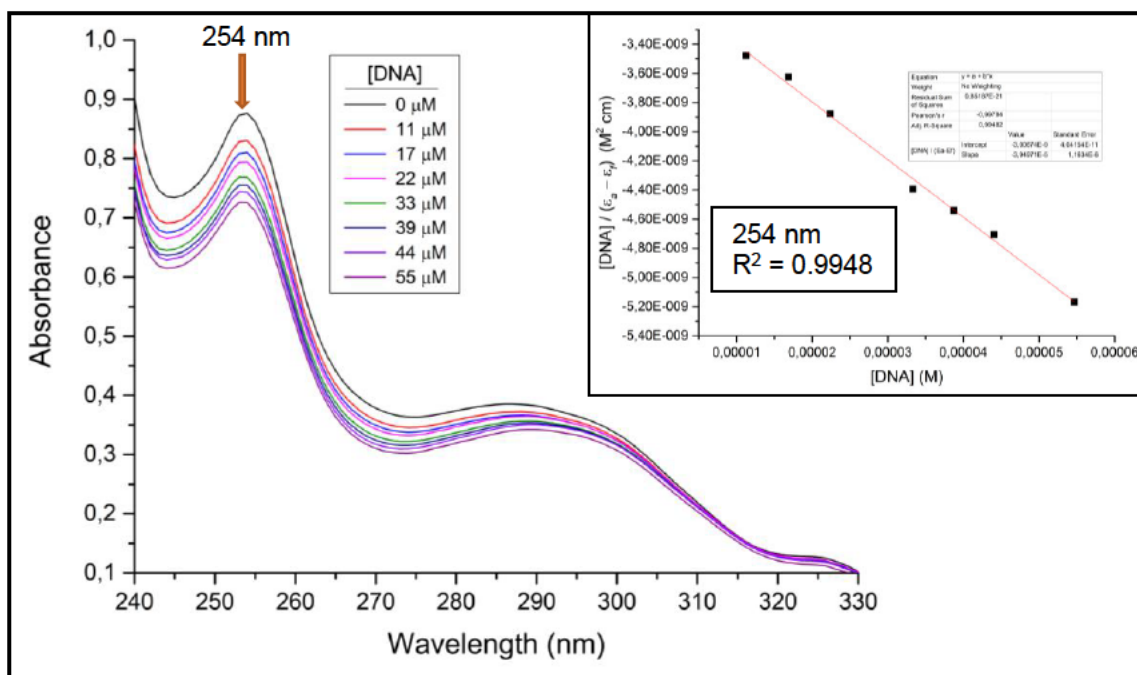


**Figure E11** UV/visible absorbance spectra of  $[\text{VO}(\text{TERTCA})(\text{DPQ})](\text{PF}_6)$  ( $14 \mu\text{M}$ ) in the absence and presence of *ct*-DNA ( $0\text{--}55 \mu\text{M}$ ) in 10% v/v DMSO/ Tris buffer (pH 7.1) at  $37^\circ\text{C}$ . *Inset*: Plots of  $[\text{DNA}] / (\epsilon_a - \epsilon_f)$  versus  $[\text{DNA}]$  for the titration of  $[\text{VO}(\text{TERTCA})(\text{DPQ})]^+$  with *ct*-DNA at 254 nm. This plot was used to calculate the intrinsic binding constant of  $1.3 \times 10^4 \text{ M}^{-1}$ .

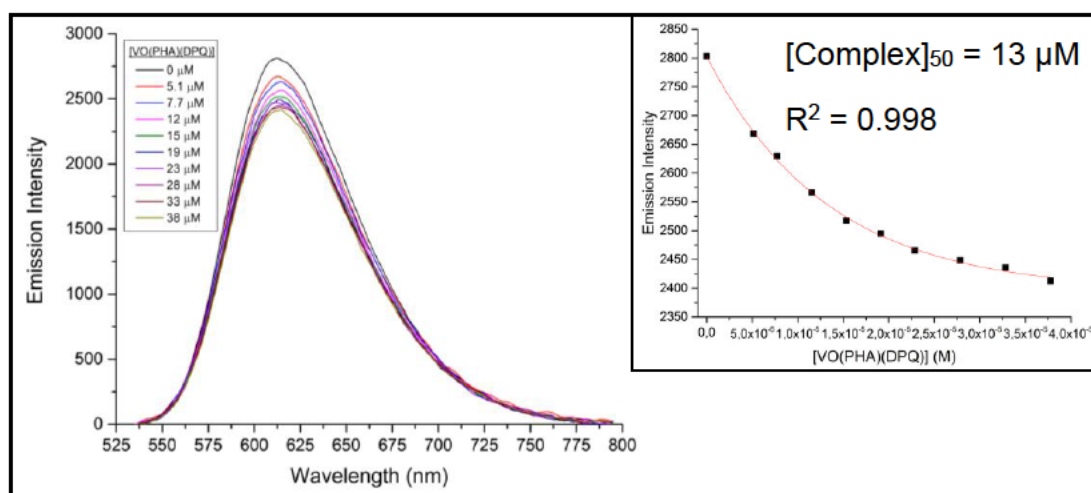


**Figure E12** Fluorescence emission spectra of ethidium bromide bound to *ct*-DNA in Tris-HCl buffer (25 mM, pH 7.0) and maximum 6.3% DMSO in the presence of increasing concentrations of  $[\text{VO}(\text{PHA})(\text{DPQ})]$  ( $0\text{--}38 \mu\text{M}$ ) at  $25^\circ\text{C}$ . *Inset*: Plot of emission intensity of EB-DNA adduct versus concentration of  $[\text{VO}(\text{PHA})(\text{DPQ})]$  with an exponential decay fit at 614 nm.

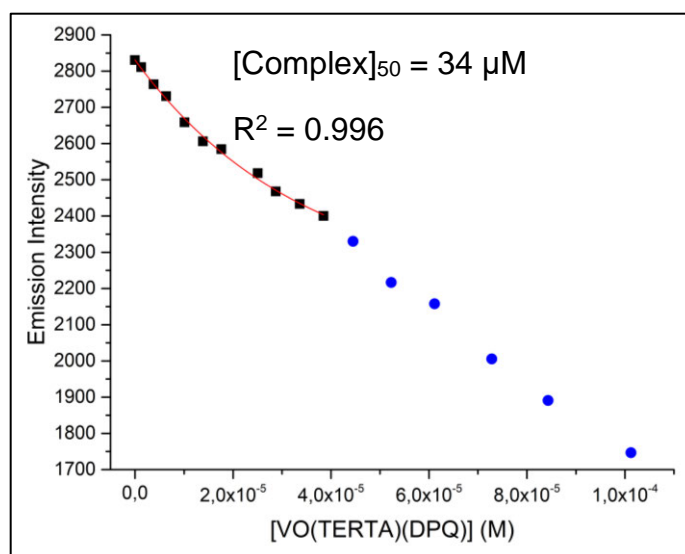


**Figure E13.** Plot of emission intensity at 614 nm of ethidium bromide bound to *ct*-DNA versus concentration of [VO(TERTA)(DPQ)] (0 – 101  $\mu$ M) in Tris-HCl buffer (25 mM, pH 7.0) and maximum 10% v/v DMSO, at 25  $^{\circ}$ C. Exponential decay fit at 614 nm over 0 – 38  $\mu$ M [VO(TERTA)(DPQ)].